Finite antenna arrays : an eigencurrent approach

Finite Antenna Arrays:

An Eigencurrent Approach

Dave Bekers

This PhD thesis is the result of a project carried out under sponsorship of Thales Nederland, the Netherlands, and the Stan Ackermans Institute of the Technische Universiteit Eindhoven, the Netherlands. The project was carried out at Thales Nederland.

Finite Antenna Arrays:

An Eigencurrent Approach

PROEFONTWERP

ter verkrijging van de graad van doctor aan de
Technische Universiteit Eindhoven, op gezag van de
Rector Magnificus, prof.dr. R.A. van Santen, voor een
commissie aangewezen door het College voor
Promoties in het openbaar te verdedigen
op maandag 13 december 2004 om 16.00 uur

door

Dave Johannes Bekers

geboren te Breda

De documentatie van het proefontwerp is goedgekeurd door de promotoren:

prof.dr. A.G. Tijhuis
en
prof.dr.ir. C.J. van Duijn

Copromotor:
dr.ir. S.J.L. van Eijndhoven

CIP-DATA LIBRARY TECHNISCHE UNIVERSITEIT EINDHOVEN

Bekers, Dave Johannes

Finite antenna arrays : an eigencurrent approach / by Dave Johannes Bekers.
Eindhoven : Technische Universiteit Eindhoven, 2004.
Proefontwerp. - ISBN 90-386-1012-2
NUR 919
Subject headings: antenna arrays / antennas / electromagnetic waves / mathematical models / mathematical moment problems / eigenvalue problems / numerical simulation / sensitivity analysis
2000 Mathematics Subject Classification: 35Q60, 78M05, 47N99, 31B10, 00A73, 35B34

Press: Universiteitsdrukkerij, Technische Universiteit Eindhoven

Cover design: Jeroen Willekens
Paul Verspaget & Carin Bruinink, Grafische Vormgeving – Communicatie

Preface

”Why do we need a(n) (industrial) mathematician?” It is a frequently asked question in industry. Probably the answers are even more numerous: to carry out a specific calculational step, to develop a(n) (numerical) algorithm, to find an optimal strategy, and to test a hypothesis are only some examples. A more profound answer is that an abstract look at a certain problem may give a deeper insight and may establish links with other fields, where a solution to the problem is available. One of the strongest unifying concepts in mathematics is the concept of eigenvalue. As L.N. Trefethen [115] wrote: “They [Eigenvalues] give an operator a personality”. Represented in the complex plane, eigenvalues are much easier to digest by the human brain than the abstract notion of an operator that describes a certain process or phenomenon. Moreover, eigenvalues may provide insight into physical phenomena like resonance, stability, and rate of increase or decay. More specifically, in mechanics, eigenvalues may determine under which conditions a bridge will collapse or an music instrument will give a proper sound. In electromagnetism, they may determine whether a certain signal is propagating. In ecology, they may predict whether layers of salt become unstable. In heat transfer, they may determine the cooling time of a molded compact disc or the heating time of a copying machine.

In this thesis an approach based on the concept of eigenvalue is proposed for the analysis of antenna arrays. Examples revealed that eigenvalues, and the related eigenfunctions or eigencurrents, are one-to-one related to the specific array functions like scanning and the technique of monopulse. Moreover, the excitation of specific, resonant, eigencurrents explains various effects observed in practice, like variations of element impedances attributed to array surface waves and modulations of element impedances. The visual power of eigenvalues is exploited as well in the sense that their distribution in the complex plane may reveal suitable (surface) loading to reduce resonant behavior.

The preceding paragraph illustrates the strong relation between the concept of eigenvalue and antenna-array design. Moreover, it illustrates how an abstract look at antenna arrays may provide practical information for design. In the past four years, these relations were not always as clear for me as they are now. The hardest part of the project was probably to keep believing that the approach based on eigencurrents was appropriate and to explain why such an approach

was needed. An additional difficulty was that electrical engineers and mathematicians talk different 'languages'. Moreover, both 'languages' consist of many 'sublanguages'. To write one thesis for several languages was not an easy task. To put it differently, trying to be mathematically strict and industrially applied at the same time is for a mathematician like climbing one of the ridges of a mountain: the danger is to disappear into the deep ravines on either of the sides. In this respect, joining the program Mathematics for Industry before carrying out a PhD project was very useful.

Many people have guided or helped me in this project. First of all, I would like to mention dr.ir. Stef van Eijndhoven, dr.ir. Fons van de Ven, and prof.dr. Anton Tijhuis. Stef, many, many thanks, not only for reading this thesis up to the 'milimeter', but also for all your suggestions and advice with respect to the interpretation of the many generated (numerical) results. Moreover, your mental support encouraged me a lot. Fons, thank you for all your support and advice over the past years and for always having a listening ear. Anton, I appreciate all your help and support very much and I would like to thank you especially for the extensive time you took to read my thesis and to give suggestions for improvement. Through your advice, a lot of 'language difficulties' of the nature mentioned above were resolved, although during our enthusiastic discussions, we sometimes ran ourselves into such a 'difficulty'. Many thanks go also to my present and previous supervisors at Thales Nederland: dr.ir. Peter-Paul Borsboom and ir. Evert Kolk. Peter-Paul, thank you for all your advice and support in the last three years, especially for all the effort you took to find application areas for my work, both inside and outside Thales. Evert, thank you for your guidance in the first year and for giving me the opportunity to continue my final project of Mathematics for Industry as a PhD project.

I would like to express my gratitude to prof.dr.ir. Hans van Duijn and prof.dr.ir. Guy Vandenbosch for their comments on the first versions of my thesis. I am also thankful to the members and several former members of the group JRS-TU antenna at Thales Nederland for their interest and many worthwhile discussions from which I learned a lot. In particular, I would like to thank Joris Buijnsters, Eddy van Ewijk, and Bertus ter Heijde, Bart Morsink, and Gertjan van Werkhoven for the discussions about the development of radar systems and the relation with my work. Moreover, I would like to thank Kiman Velt for the HFSS simulations that could not be described in this thesis anymore unfortunately. Warm thanks also go to Emiel Stolp, Frank Leferink, Hans Schurer, Hans Driessen, and Monique Kedde, for the stimulating discussions about work and my work in particular. Last but not least, I would like to thank Geert Vulink, Dolf Boompaal, and Rein Eggens for the pleasant atmosphere in our cubical throughout the years.

From the Laboratoire d'Electromagnétisme et d'Acoustique, I would like to thank prof. Juan Mosig for giving me the opportunity to work in his group from April till June 2000 and to present my work in June 2001. Moreover, I would like to thank Michael Mattes for the pleasant cooperation during my three-months stay and for the warm welcome at my visit in June 2001.

From the Technische Universiteit Eindhoven, I would like to thank the (former) students of Mathematics for Industry, the members of the Electromagnetics group of the department of electrical engineering, and the members of the applied analysis group, nowadays CASA, of the department of mathematics and computer science. In particular, I would like to thank Friso Hagman, Martijn van Beurden, Tom Gierstberg, Kamyar Malakpoor, Gertjan Pieters, and Jan Kroot for their mental support and encouraging discussions.

Finally, I would like to thank all my friends and relatives for their friendship and support. In particular, I would like to thank Jeroen Willekens for designing the cover. Moreover, I would like to thank my mother Yvonne, my father Frans, and my brother Colin for their patience, understanding, and support. Last, but definitely not least, I would like to thank my girlfriend Shirley for all her love, patience, understanding, support, and of course for drawing several pictures in this thesis and typing several parts of the text.

Dave Bekers, Eindhoven, 1 november 2004

Glossary of Notation

General remarks:

- If more equations correspond to the same equation number, they are indicated by superscript numbers at the equation number. For example, $(2.1)^2$ is the second equation in Equation (2.1).
- A superscript symbol connected to a word indicates a footnote, e.g., representation*.
- Except for the time-domain quantities in Section 2.1, vectors and vector functions are indicated by boldface characters, e.g., $\boldsymbol{E}$ and $\boldsymbol{w}$. Matrices and column vectors are denoted by Roman capitals, e.g., Z and W. Operators and vector spaces are in general denoted by calligraphic characters, e.g., $\mathcal{A}$ and $\mathcal{Z}$.
- If a super- or subscript of a mathematical symbol is typeset in the normal Roman font, the script indicates the abbreviation of a word or word group, e.g., N_{sub}. If a super- or subscript is typeset in the italic Roman font, the script indicates a mathematical symbol (a variable or a coordinate-axis label), e.g., $\boldsymbol{e}_x$ and $\boldsymbol{u}_{nq}$.
- A dot in an argument of a function or an operator indicates that the corresponding variable is free. For example, if g is a function of two variables, then $f = g(\,\cdot\,, \eta)$ is a function of one variable, where g is evaluated with respect to its second argument only. The function f evaluated at ξ equals $g(\xi, \eta)$.
- The dB scale is in general defined as $10\,{}^{10}\!\log|\,\cdot\,|$. The definition $20\,{}^{10}\!\log|\,\cdot\,|$ is adopted for (electric) far-field components only.
- The word group 'absolute value(s) of the ...' is often abbreviated to 'the absolute ...', e.g., 'absolute eigenvalue' instead of 'absolute value of the eigenvalue'.
- The word 'element' is used for both elements of sets and elements of an antenna.
- Normalized quantities or variables are denoted by hats, e.g., $\hat{\xi}$ an $\hat{A}_{pq}$.

Vector spaces

Throughout this thesis, we identify in the usual way the Euclidean space $\mathbb{E}^3$ of points and vectors, and the set $\mathbb{R}^3$ of 3-tuples with real components. In other words, points and vectors in $\mathbb{E}^3$ are identified with 3-tuples in $\mathbb{R}^3$. We interpret $\mathbb{R}^3$ as a vector space equipped with the usual scalar product $(\,.\,\bullet\,.\,)$, shortly $\bullet$, and the usual vector product $\times$. Moreover, we equip $\mathbb{R}^3$ with the standard basis $\boldsymbol{e}_x = (1,0,0)$, $\boldsymbol{e}_y = (0,1,0)$, and $\boldsymbol{e}_z = (0,0,1)$ with associated Cartesian coordinate system. A 3-tuple or vector in $\mathbb{R}^3$ is written as $\boldsymbol{x} = x\boldsymbol{e}_x + y\boldsymbol{e}_y + z\boldsymbol{e}_z$, or shortly (x,y,z), and $\boldsymbol{E} = E_x\boldsymbol{e}_x + E_y\boldsymbol{e}_y + E_z\boldsymbol{e}_z$, or shortly, (E_x, E_y, E_z).

Vector fields in $\mathbb{E}^3$ assign to each point in $\mathbb{E}^3$ a vector with length and direction. With the identification above, a vector field in $\mathbb{E}^3$ is a vector function from $\mathbb{R}^3$ to $\mathbb{R}^3$. In turn, these vector functions can be interpreted as vector fields in $\mathbb{R}^3$. Therefore, we use both the term vector function and the term vector field. Vector functions from $\mathbb{R}^3$ to $\mathbb{C}^3$ are complex-valued vector fields in $\mathbb{R}^3$. Here, $\mathbb{C}^3$ is the (complex) vector space of 3-tuples with complex components, which is equipped with the same scalar product, vector product, and standard basis as $\mathbb{R}^3$.

In Section 2.3, we introduce complex-valued vector functions of which the range is a subset of $\mathbb{C}^N$, i.e., the set of N-tuples with complex components. The components of such a vector function $\boldsymbol{w}$ are denoted by w_p, $p = 1, \ldots, N$. In Section 2.4, this notation is changed to $w(\,\cdot\,; p)$ to avoid confusion between the components of vector functions and the indices of vectors in a set, e.g., $\{\boldsymbol{w}_1, \ldots, \boldsymbol{w}_M\}$. Analogously, the notation for the components of a vector $\boldsymbol{\alpha}$ is $\alpha(n)$ instead of α_n and the notation for the components of a matrix G is $G(m,n)$ instead of G_{mn}.

The following notations are used in this thesis. Some symbols that appear locally are not listed; they are defined within the text. Moreover, symbols related to the algebraic concepts employed in this thesis are defined in Subsection 2.4.1. For details on notation of function spaces, we refer to Section 3.1.

Roman symbols

$\boldsymbol{A}$	magnetic vector potential
$\boldsymbol{A}_{pq}$	magnetic vector potential at the surface S_p induced by the current at the surface S_q.
$A(\Psi), A(\theta_{\mathrm{scan}})$	infinite-array moment matrix
a, a_q	radius of a ring
b, b_q	half the width of a strip or ring
$\mathrm{bas}(\mathcal{W})$	the set $\{\mathcal{W}\boldsymbol{e}_1, \ldots, \mathcal{W}\boldsymbol{e}_N\}$ for a mapping $\mathcal{W}$ from $\mathbb{C}^N$ to a vector space $\mathcal{X}$, defined in Subsection 2.4.1
$C^\infty(A)$	
c	speed of light, $c = 1/\sqrt{\varepsilon_0\mu_0}$
$\boldsymbol{c}_q$	centers of elements in an array

D	generalized derivative
d_{pq}	distances between strips in a line array
d	distances between elements in a uniform line array
div	divergence of a vector field
$\mathrm{dom}(\,\cdot\,)$	domain of an operator
$\boldsymbol{E}$	time-independent part of the time-harmonic strength of the electric field $\mathscr{E}$, shortly electric field
$\boldsymbol{E}_S$	(tangential) excitation field at S (tangential vector field at S)
$\boldsymbol{E}^{\mathrm{ext}}$	externally applied electric field ($\boldsymbol{E}_S = -(\boldsymbol{E}^{\mathrm{ext}})_{\tan}$)
$\boldsymbol{E}^{\mathrm{i}}$	incident electric field
E_n	set of eigencurrents of an array in which mutual coupling is ignored, corresponding to the eigencurrent $\boldsymbol{u}_n^{\mathrm{sub}}$ of the generating subarray, where $n = 1, \ldots, N_{\mathrm{eig}}^{\mathrm{sub}}$
E	union of the sets E_n
$\boldsymbol{e}_\xi$, $\boldsymbol{e}_\eta$	1. tangent vectors of S 2. idem, where S represents a line array of strips
$\boldsymbol{e}_\zeta$	normal on S corresponding to $\boldsymbol{e}_\xi$ and $\boldsymbol{e}_\eta$, $\boldsymbol{e}_\zeta = \boldsymbol{e}_\xi \times \boldsymbol{e}_\eta$
$\boldsymbol{e}_\xi^{\mathrm{ext}}$, $\boldsymbol{e}_\eta^{\mathrm{ext}}$, $\boldsymbol{e}_\zeta^{\mathrm{ext}}$	extension of the tangent vectors of S and their normal to a global or locally global coordinate system
$\boldsymbol{e}_n$	unit vector of the standard basis of $\mathbb{C}^N$
$F(A, B)$	a linear space of functions that map the elements of a set A into a set B
F_{pq}	kernel of $\mathcal{F}_{pq}$
$\tilde{F}_{pq}$	kernel of $\tilde{\mathcal{F}}_{pq}$
f	frequency
G	Gram matrix
g_{free}	a fundamental solution of the Helmholtz operator: $e^{-jkR}/4\pi R$
$\hat{g}_{\mathrm{free}}$	$g_{\mathrm{free}}(R) = k\hat{g}_{\mathrm{free}}(\hat{R})$
grad	gradient of a scalar function
$\boldsymbol{H}$	time-independent part of the time-harmonic strength of the magnetic field $\mathscr{H}$, shortly magnetic field
$\boldsymbol{H}^{\mathrm{ext}}$	externally applied magnetic field
$H_{2,n}(A, \mathbb{C}^N)$	subspace of $L_2(A, \mathbb{C}^N)$ consisting of all functions on a set A with nth derivative in L_2, denoted by $H_{2,n}(A)$ for $N = 1$
$H_{2,n,\mathrm{per}}(A, B)$	consists of all functions in $H_{2,n}(A, B)$ that are periodic on the real line with period 2π
$\boldsymbol{J}$	time-independent part of the time-harmonic current density $\mathscr{J}$, shortly current
$\boldsymbol{J}_{\mathcal{A}}$	averaged current $\boldsymbol{J}_{\mathcal{A}} = \mathcal{A}\boldsymbol{J}$

j	$\sqrt{-1}$
$K_{1i,pq}, K_{2,pq}$	kernels of $\mathcal{K}_{1i,pq}, \mathcal{K}_{2,pq}$
$\tilde{K}_{1i,pq}, \tilde{K}_{2,pq}$	approximated kernels
k	wave number defined by $k = \omega\sqrt{\varepsilon_0\mu_0}$
$L(A, \mathbb{C}^N)$	vector space of linear mappings from a set A to a set B
$L_2(A, \mathbb{C}^N)$	space of square integrable functions from a set A to the set $\mathbb{C}^N$, denoted by $L_2(A)$ for $N = 1$
ℓ	length of a strip.
N_{el}	number of (antenna) elements or surfaces S_q
$N_{\mathrm{exp}}, \boldsymbol{N}_{\mathrm{exp}}$	number of expansion functions
$N_{\mathrm{test}}, \boldsymbol{N}_{\mathrm{test}}$	number of test functions
$N_{\mathrm{cos}}, \boldsymbol{N}_{\mathrm{cos}}$	number of cosine expansion functions
$N_{\mathrm{sin}}, \boldsymbol{N}_{\mathrm{sin}}$	number of sine expansion functions
N_{sub}	number of subarrays
$N_{\mathrm{eig}}^{\mathrm{sub}}$	number of eigencurrents of the generating subarray
N_{int}	number of intervals for integration
$\boldsymbol{n}$	normal of S
$O(\,\cdot\,)$	order symbol
P^{rad}	radiated power
P^{ex}	complex power
R	function defined by $R(\,\cdot\,) = \|\,\cdot\,\|$, where $\|\,\cdot\,\|$ is the module
r	radial coordinate corresponding to the parameter description of rings
$\mathrm{ran}(\,\cdot\,)$	range of an operator
rot	rotation of a vector field
S	smooth oriented surface in $\mathbb{R}^3$ that represents the array elements
∂S	boundary curve of S
$S^{\pm}$	the two sides of S with normals $\boldsymbol{n}^{\pm}$ that point into the areas at the $S^{\pm}$-sides of S.
S_q	surfaces of which the union is S; these surfaces represent the array elements
$\mathrm{Tang}(S, (\xi, \eta))$	Tangent plane of S at the point $\boldsymbol{x}_S$
t	time
$\boldsymbol{u}_n, \boldsymbol{u}_{nq}$	eigenfunctions or eigencurrents with indices $_n$ and $_{nq}$
U_n, U_{nq}	Eigenvectors with indices $_n$ and $_{nq}$, represent the expansion coefficients of $\boldsymbol{u}_n, \boldsymbol{u}_{nq}$
$v^{\mathrm{ex}}, \boldsymbol{v}^{\mathrm{ex}}$	centerline component(s) of the width-averaged excitation field on the surface S,
$V^{\mathrm{ex}}, V^{\mathrm{ex}}(q)$	voltage of a feed gap (voltage or delta gap, or finite feed gap)

$w, \boldsymbol{w}$	1. centerline components of the width-averaged current on the surfaces S_q 2. element of an inner-product space in Subsections 2.4.1 and 2.4.2
W	(column) vector, consists in general of the expansion coefficients of w or $\boldsymbol{w}$
$\boldsymbol{x}$	3-tuple or vector in $\mathbb{R}^3$
$\boldsymbol{x}_S$	parameter representation of the surface S
$\boldsymbol{x}_S(\,\cdot\,,0)$	centerline of S in case $\Pi(S)$ is given by $\Pi(S) = \Pi_\xi(S) \times [-\eta_1, \eta]$
$\boldsymbol{y}_n, \boldsymbol{y}_{nq}$	functions in the bi-orthogonal set $\mathcal{Y}$ with indices $_n$ and $_{nq}$, defined in Subsection 5.2.1
Z	moment impedance matrix
Z_0	characteristic impedance of free space defined by $Z_0 = \sqrt{\mu_0/\epsilon_0}$
$Z_{\rm inp}$	input impedance

Calligraphic symbols

$\mathcal{A}$	averaging operator defined for tangential vector fields on S, where $\Pi(S) = \Pi_\xi(S) \times [-\eta_1, \eta]$
$\mathscr{B}$	density of the magnetic flux
$\mathscr{D}$	density of the electric flux
$\mathcal{D}$	differential operator defined by $\mathcal{D} = -jZ_0k(\mathcal{I} + (1/k^2)\,\mathrm{grad}\,\mathrm{div}\,)$
$\mathcal{D}_S$	$(\mathcal{D}\,\cdot)_{\tan} = \mathcal{D}_S(\,\cdot\,|_S)$
$\mathscr{E}$	strength of the electric field
$\mathcal{F}_{pq}$	integral operator corresponding to a line array of strips
$\tilde{\mathcal{F}}_{pq}$	approximation of $\mathcal{F}_{pq}$
$\mathcal{G}_{\rm free}$	free-space kernel of $\mathcal{T}$, $\mathcal{G}_{\rm free} = g_{\rm free}\mathcal{I}$
$\mathcal{G}_{\rm half}$	half-space kernel of $\mathcal{T}$
$\mathcal{G}_\Omega$	kernel of $\mathcal{T}$ for the domain Ω
$\mathscr{H}$	strength of the magnetic field
$\mathcal{I}$	identity operator
$\mathcal{I}_\mathcal{X}$	identity operator on the vector space $\mathcal{X}$
$\mathscr{J}$	current density
$\mathcal{K}_{1i,pq}, \mathcal{K}_{2,pq}$	integral operators corresponding to an array of rings ($i = 1, 2$)
$\tilde{\mathcal{K}}_{1i,pq}, \tilde{\mathcal{K}}_{2,pq}$	approximations of $\mathcal{K}_{1i,pq}, \mathcal{K}_{2,pq}$
$\mathcal{P}, \mathcal{Q}$	projections (see Subsection 2.4.1), in general $\mathcal{P} = \mathcal{W}\mathcal{W}^-$ and $\mathcal{Q} = \mathcal{V}\mathcal{V}^-$
$\mathcal{T}$	integral operator with kernel $\mathcal{G}_{\rm free}$, $\mathcal{G}_{\rm half}$, or $\mathcal{G}_\Omega$
$\mathcal{U}$	basis of eigenfunctions or eigencurrents
$\mathcal{V}, \mathcal{W}$	mappings from $\mathbb{C}^N$ to an inner-product space
$\mathcal{V}^-, \mathcal{W}^-$	mappings from an inner-product space to $\mathbb{C}^N$ corresponding to $\mathcal{V}, \mathcal{W}$ and defined by (2.111)
$\mathcal{X}, \mathcal{Y}$	1. inner-product spaces in Subsection 2.4.1

	2. domain and range of $\mathcal{Z}$ in Subsection 2.4.2
$\mathcal{X}_\mathrm{a}, \mathcal{Y}_\mathrm{a}$	domain and range of $\mathcal{Z}_\mathrm{a}$, both inner-product spaces
$\mathcal{Y}$	bi-orthogonal set of $\mathcal{U}$
$\mathcal{Z}$	impedance operator $\mathcal{Z} = (\mathcal{D}\mathcal{T}\,\cdot\,)_\mathrm{tan}$, $\mathcal{Z}\boldsymbol{J} = \boldsymbol{E}_S$
$\mathcal{Z}_\mathrm{a}$	averaged form of $\mathcal{Z}$, $\mathcal{Z}_\mathrm{a}\boldsymbol{w} = \boldsymbol{v}^\mathrm{ex}$

Greek symbols

β, β_q	ratios b/a and b_q/a_q for rings, ratios b/ℓ and b_q/ℓ_q for strips
Δ	Laplace operator
δ_{nm}	Kronecker symbol defined by $\delta_{mn} = 1$ for $m = n$ and $\delta_{mn} = 0$ for $m \neq n$
ε_0	permittivity of vacuum
ϵ	indicates the 'width' of a finite feed gap
λ	wavelength
μ_0	permeability of vacuum
ν_n, ν_{nq}	eigenvalues with indices $_n$ and $_{nq}$
$\Pi(S)$	parameter set corresponding to $\boldsymbol{x}_S$
$\Pi_\xi(S)$	defined for surfaces S for which $\Pi(S)$ can be written as $\Pi(S) = \Pi_\xi(S) \times [-\eta_1, \eta]$
ϱ	charge density
ρ	1. time-independent part of the time-harmonic charge density ϱ
	2. spherical radial coordinate
σ	conductivity
$\boldsymbol{\tau}$	tangent vector of the centerline $\boldsymbol{x}_S(\,\cdot\,, 0)$ of S, $\boldsymbol{\tau} = \boldsymbol{e}_\xi(\,\cdot\,, 0)$
$\boldsymbol{\tau}_{\partial S}$	piecewise defined tangent vector of S, if S has a piecewise and oriented boundary curve ∂S
θ, ϕ	spherical angles
$\theta_\mathrm{scan}, \phi_\mathrm{scan}$	spherical scan angles
$\theta_\mathrm{i}, \phi_\mathrm{i}$	incident angles of a plane wave
θ_1	angle that indicates the position of the main lobe of a line array
φ	angle that describes the circumference of a ring
Ψ	$\Psi = kd\cos\theta_1$
ψ, ψ_q	orientation angle of the local coordinate systems on rings
Ω	a domain in $\mathbb{R}^3$ with boundary $\partial\Omega$
Ω_v	eigenvalue of the eigenfunction v of a Sturm-Liouville problem
$\Omega_{\cos,n}$	nth eigenvalue related to a cosine eigenfunction
$\Omega_{\sin,n}$	nth eigenvalue related to a sine eigenfunction
ω	radian frequency

Supper and subscripts

*	1. complex conjugate
	2. adjoint mapping or operator
$^\vee$	$f^\vee(x) := f(-x)$
$^\perp$	orthogonal complement
^{H}	Hermitian transposed

Other symbols

$\mathbb{N}$	set of natural numbers
$\mathbb{N}^P$	set of P-tuples with components in $\mathbb{N}$ ($P = 1, 2, \ldots$)
$\mathbb{R}$	set of real numbers
$\mathbb{R}^3$	set of 3-tuples with components in $\mathbb{R}$, interpreted as vector space
$\mathbb{C}$	set of complex numbers
$\mathbb{C}^N$	set of N-tuples with components in $\mathbb{C}$
$\mathbb{C}^{M\times N}$	set of matrices of size $M \times N$
$\bullet$	scalar product on $\mathbb{R}^3$ and $\mathbb{C}^3$, also denoted as $(\,.\,\bullet\,.\,)$
$\times$	1. vector product on $\mathbb{R}^3$ and $\mathbb{C}^3$
	2. matrix size indication, e.g., $N \times N$ and $\mathbb{C}^{N\times N}$
	3. multiplication in multiple-line expressions
	4. indicator of sets such as $[a, b] \times [c, d]$
$(\,\cdot\,\circ\,\cdot\,)_N$	inner product on $\mathbb{C}^N$ with which $\mathbb{C}^N$ is an inner product space; the inner product is linear in its second argument
$(\,\cdot\,)_{\tan}$	trace operator, which restricts a vector function to the surface S and then takes the tangential component
$\vert_S$	restriction to the surface S
$.\,*\,.$	convolution
$\langle\,\cdot\,,\,\cdot\,\rangle$	inner product on a vector space, linear in its second argument, i.e., $\langle \boldsymbol{v}, \alpha\boldsymbol{w}\rangle = \alpha\langle \boldsymbol{v}, \boldsymbol{w}\rangle$ and, hence, $\langle \alpha\boldsymbol{v}, \boldsymbol{w}\rangle = \alpha^*\langle \boldsymbol{v}, \boldsymbol{w}\rangle$
$\Vert\,\cdot\,\Vert$	1. associated norm of $\langle\,\cdot\,,\,\cdot\,\rangle$
	2. norm on $\mathbb{C}^{N\times 1}$ or $\mathbb{C}^N$
$\langle\,\cdot\,,\,\cdot\,\rangle_{\mathcal{X}}$	inner product corresponding to the vector space $\mathcal{X}$
$\sqcup$	concatenation of two tuples (or row vectors) defined by (2.103)
$[\,\cdot\,]$	1. transforms a linear mapping from $\mathbb{C}^N$ to $\mathbb{C}^M$ into a matrix in $\mathbb{C}^{M\times N}$, also denoted by $[\,\cdot\,]_{M\times N}$
	2. transforms an N-tuple in $\mathbb{C}^N$ into a column vector in $\mathbb{C}^{N\times 1}$, also denoted by $[\,\cdot\,]_N$

Contents

CHAPTER 1

Introduction

On 30 April 1904, Christian Hülsmeyer patented his 'Telemobiloskop', which became the first operational radar system for detecting ships through the transmission and reception of electromagnetic waves [51, 111]. Nowadays, radar systems are widely used, for example, to control air traffic, to measure vehicle speeds, and to detect and track airplanes and ships. Thales Nederland is one of the companies that specializes in designing and producing radar systems, or more general, integrated defense systems. The company is part of the Thales group with plants in more than 30 countries. In Hengelo, the Netherlands, the focus of the design and production process is on highly advanced naval systems. Customers of Thales Nederland are marines of countries all over the world.

The principle of radar, or 'radio detection and ranging', is based on the phenomenon that metallic objects reflect electromagnetic waves. These waves are transmitted and received by the antenna of a radar system. In several systems of Thales Nederland, the antenna is a large (phased) array of single antennas. We will refer to these antennas as the (array) elements. A specific example of an antenna array of Thales Nederland is shown in Figure 1.1. The array consists of about 1000 elements, positioned on a planar antenna face of about $16\,\mathrm{m}^2$, i.e., the black surface in the figure. Figure 1.2 shows a schematic representation of one of the array elements, which are rectangular microstrip loops. The systems are designed for long-range surveillance, i.e., for detecting (metallic) objects in the range of 10 – 400 kilometers. Moreover, the systems scan in elevation by phase shifts and in azimuth by rotation. Here, azimuth is the angle related to distances around

Figure 1.1 An array of single microstrip antennas on a test tower.

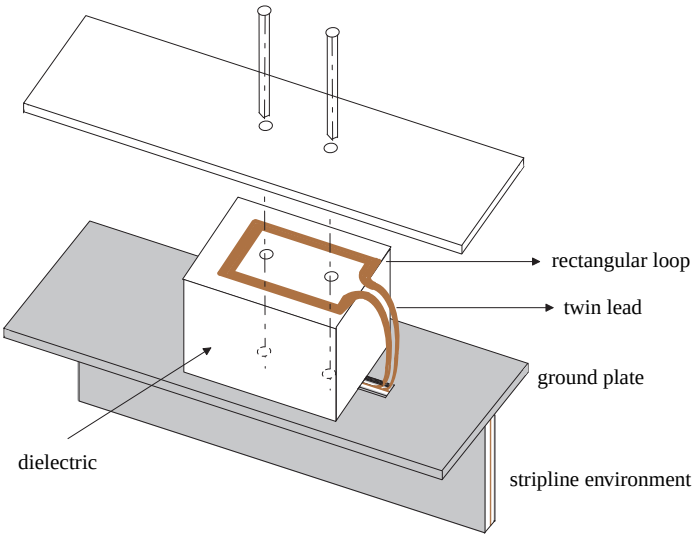

Figure 1.2 A single microstrip antenna or (array) element.

the earth's horizon, while elevation is the height above the earth's surface. As an illustration of the capability of these systems, we mention that the detection of a metallic object of the size of a tennis ball was demonstrated up to more than 50 kilometers away.

The design and development of antenna arrays is complex and costly [85, 86, 122]. To reduce design costs and design risks, and to improve the performance of the arrays, Thales Nederland uses simulations. Simulations should meet a number of criteria: they should be fast executable, they should show boundary effects and effects of mutual coupling, and they should determine the antenna performance parameters accurately. Simulations based on the generally applied infinite-array approach and simulations based on the finite-element method do not satisfy these criteria. Simulations of the first type do not describe boundary effects, while simulations of the second type are computationally too expensive. Both types of simulations do not provide direct insight into the physics relevant to the design. To overcome these disadvantages, Thales initiated a sequence of projects to develop simulation tools for arrays [7: pp. 13 – 18]. The first projects concerned mainly the modeling and analysis of a single element. The step from one element towards an array could not be taken, because simulation of a single element required too much computation time. Therefore, the focus remained on local (element) effects. In the middle of the project described in [6], we decided to shift our research towards the simulation of large (finite) antenna arrays with the focus on global (array) effects. This research resulted into a top-down approach in which we analyze an array of simple elements first. By the approach, we aimed

at finding characteristics of a single element that are essential for describing the array behavior and, therewith, for the array performance. On basis of these characteristics, we intended to develop an efficient analysis approach for finite antenna arrays with corresponding simulation tools.

In this introduction, we present an overview of our research. We describe the design process of antenna arrays in Section 1.1 and we explain our contribution to the stages in the design process. In the next section, we summarize the modeling approaches and simulation tools for antenna arrays as used by Thales Nederland. Also, recent developments in the literature are outlined to determine current needs in array modeling. Along with these needs, we describe our main objectives and modeling approach in Section 1.3. In Chapter 7, we describe the conclusions of our research in relation to these main objectives, while in Section 1.4, we describe the organization and contents of this thesis.

1.1 Design Aspects of Antenna Arrays

Each design process of an antenna, in particular an antenna array, is unique. The process is flexible, often influenced by circumstances and pragmatic decisions. For these reasons, the practice of antenna design is described in many different ways, see for example [63: p. 137]. We emphasize the main lines of the design process in the schematic representation of Figure 1.3.

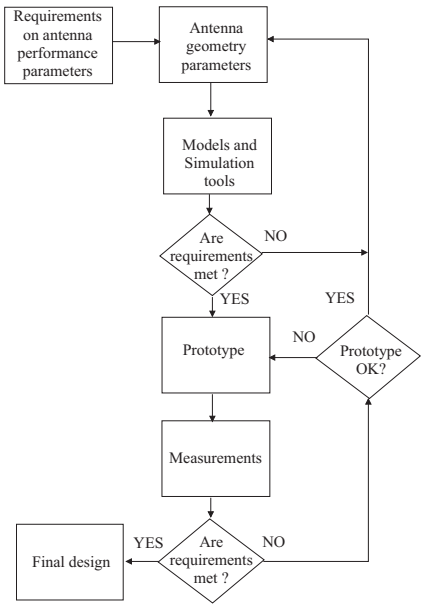

Figure 1.3 Design proces of an antenna.

Formulating the requirements on the antenna performance parameters is the start of the design process. The requirements are a quantification of the two main goals of antenna design: the input energy should be radiated in a well-defined direction and the energy loss should be minimized. We divide the performance parameters into three categories: beam parameters, mutual coupling parameters, and visibility parameters. The first category is related to the first main goal, the second category to the second goal. The last category describes the stealthiness of an entire radar system. Table 1.1 contains a selection of parameters that belong to these categories. The requirements on the parameters are specified for a certain bandwidth, or, frequency range, and for a certain scan range.

Table 1.1 Beam parameters, mutual coupling parameters, and array effects.

Beam parameters	Mutual coupling parameters	Visibility parameters
Side lobe level	(Mutual) Impedance	Radar cross section (RCS)
Beam width	Scattering parameters	
Gain	Reflection coefficients	
Polarization	Scan loss	
Axial ratio		

In close cooperation with the system engineers, the antenna engineers determine the requirements on the antenna performance parameters from the system requirements, which need to be satisfied by the entire radar system. The antenna engineers must take into account RF (Radio Frequency) performance, mechanical performance, manufacturability, development time, and costs. The next step in the design process is the selection of the antenna geometry including the selection of the antenna type. Examples of antenna types are wire antennas, reflector antennas, and antenna arrays. Within the array type, different kinds are distinguished depending on the element type, e.g., a waveguide and a microstrip patch or loop, and the array composition, e.g., uniformly spaced and sparse. The selection of the antenna type and a first estimate of suitable geometry parameters is usually done by antenna engineers with extensive experience. Subsequently, simulation tools based on array models are used to predict the array or antenna performance. As long as the requirements are not met, the selection of antenna geometry parameters is adjusted. Mostly, this process of adjusting parameters is a trial-and-error process, where the experience of the antenna designers plays an important role. Only in some cases, optimization routines are available to automate this process. In the next step of the process, a prototype is constructed and measurements are carried out. An overview of measurement techniques can be found in [55]. The outcome of the measurements determines whether the design can be finalized. In case of a negative answer, the following questions are posed.

1. Have the measurements been carried out correctly?

2. Is the prototype free of construction errors?

If the answers to both questions are positive, new antenna geometry parameters need to be chosen. To achieve this, both the accuracy of the numerical simulation and the validity of the idealizations need to be reconsidered. Moreover, if the rejection of the prototype is due to a specific performance parameter, this parameter needs to be emphasized more in the simulations. For instance, the prototype may show a high visibility, in which case the RCS performance parameter needs to be emphasized.

Having discussed the specifications of antenna design in general, we now focus on the aspects that distinguish array design from general antenna design. The main advantage of (phased)

arrays over other types of antennas is the possibility of electronic beam steering by using phase shifts between the elements [122]. Contrary to mechanical beam steering, electronic steering is accomplished without time delay due to mechanical constraints. Therefore, electronic steering in (phased) arrays facilitates multiple functions, for example, scanning, tracking, and missile guiding. On the other hand, electronic steering complicates the RF aspects of the design. The appearance of grating lobes [70: pp. 29 – 34, 81 – 86], the presence of blind scan angles [70: pp. 339 – 355], beam broadening [70: pp. 22 – 26], and a high impedance variation [53, 82] are effects that have, in general, an negative influence on the array performance.

To excite the elements of an array, a sophisticated feeding network is required. This network needs to be designed such that each element is excited with the right phase and the right amplitude, and such that the energy loss in the network is minimized. As an example, we consider the microstrip network in Figure 1.4. At each bend or junction of such a network, energy is reflected and the phase of a propagating electromagnetic wave changes. Both the amount of reflected energy and the phase change depend on the frequency. To obtain a uniform performance, reflection and phase change should be uniform over a desired frequency band. Therefore, chamfered bends [44: pp. 205 – 210 and Fig. 2.38] are often used in networks. The connections of the feeding network to the elements should have the same properties as the bends. To minimize the reflected energy, the impedances of the network connections are matched to the impedances of the elements. For this purpose, impedance transformers are used in stripline networks [44: p. 160]. A difficulty in impedance matching is that the impedance depends on the frequency and the scan angle. Moreover, the element impedance varies over the array due to the mutual coupling between the elements. Although extensive research on the relations between mutual coupling and performance parameters is described in the literature, there are no general rules. In a prototype or a final design, the mutual coupling can be measured by means of a network analyzer connected to two elements in the array, while the other elements are characteristically loaded. The scattering parameters indicate the strength of the electromagnetic coupling between the elements. Strong coupling may have a deteriorating effect on the array performance, because power radiated from one element to another flows back into the feeding network.

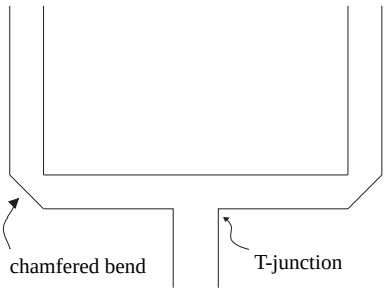

Figure 1.4 Schematic representation of a part of a microstrip network.

Our outline of array design is far from complete and shows only a limited number of difficulties that may arise. For a more extensive, recent description, we refer to [85, 86], in which array designs other than microstrip designs are considered as well. For reviews of array de-

sign in the 70s and 80s, we refer to [68, 69, 112]. Our contribution to the design process was specifically focused on the second and third stages shown in Figure 1.3, i.e., the selection of the antenna geometry parameters and the use of models and simulation tools. The modeling approach and the simulation tools we developed belong to the third stage. On basis of simulation and research results, we wanted to find characteristics that describe the (qualitative) behavior of antenna arrays. In particular, as mentioned at the beginning of this chapter, we wanted to find characteristics of a single element, which are essential for the overall array performance. In this way, we contributed to the second stage of the design process.

1.2 Simulation Tools and Analysis Approaches

We divide the analysis approaches and simulation tools which support the design process in the antenna department of Thales Nederland into two categories: an RF category and a mechanical category. The two most important simulation tools in the mechanical category are the commercial software packages Pro Engineer and ANSYS. By Pro Engineer, 3D models of mechanical designs are created. The predecessor of this package was a 2D drawing package, which has replaced the drawing tables about 20 years ago. ANSYS is used to carry out computations for the mechanical design such as computations of mechanical strength and mechanical tolerance. These computations are not only essential for a reliable mechanical design, but also for the effectiveness of a radar system as a whole. The relationship between mechanical design and radar functioning is apparent in scanning by mechanical rotation and in the stabilization of systems on ships.

The RF category is divided into two subcategories: models and tools for determining the impact of systems onto other systems, and models and tools for designing (part of) a system. In the first subcategory, analysis of electromagnetic coupling in entire systems is the main topic and simulation tools are based on asymptotic techniques [71, 87], on moment methods [76], and on combinations of mathematical and physical techniques, i.e., hybrid techniques [113]. The analysis covers the range of a single antenna up to a complete platform with more antennas, for example a ship. It is directed to topics as radar cross section, ghosts (structures on a platform which are considered as targets), blocking (visual field limited by structures on a platform), and interference. Platform analysis has become more and more important over the years, because the number of antennas on a ship increased from about 30 in the 70s to more than 100 nowadays. As an example, we mention the following interference problem in platform analysis. When a side lobe of a certain radar system on a ship is incident on an antenna array on the same ship, the limiters of the array must be capable of protecting the LNAs (Low Noise Amplifiers [37: pp. 323 – 326]).

In the second subcategory, the main aspect is the design of antennas and their feeding networks. For this purpose, Thales has available commercial software packages such as HFSS,

Momentum, and MDS, and a self-developed simulation tool called Luxaflex. Both HFSS and Luxaflex are based on the infinite-array approach, in which a periodic array is constructed from a unit cell. In HFSS, periodic boundary conditions are prescribed on the walls of the unit cell. The differential equations describing the electromagnetic field in the unit cell are solved by the finite-element method. In Luxaflex, the electromagnetic field in the unit cell is described by an integral equation with a kernel represented by a Floquet series. This equation is solved by the moment method. Both simulation tools are used for the design of arrays and frequency-selective surfaces (FSS). Like Luxaflex, Momentum is based on an integral equation formulation of the electromagnetic field; it is used for the design of several types of single antennas and network components. The software package MDS is a circuit simulator, which is used for the design of networks. Besides these packages, Thales has available several tools based on physical techniques [87], for example, techniques to predict the influence of diffraction of a (finite) ground plate on the radiation pattern of antennas. Moreover, Thales has available simulation tools for arrays of specific types of elements [35, 50, 119]; these tools are based on the infinite-array approach. Finally, for a general list of simulation tools, we refer to [23].

Most of the available (numerical) simulation tools for arrays are based on the infinite-array approach, an approach that has been extensively and successfully used for array analysis. Nevertheless, both approach and tools have several limitations.

- In the design of large arrays, often smaller 'building blocks' or subarrays are analyzed both by simulation and by measurement. *These blocks are usually too small to be analyzed by the infinite-array approach.*

- *The infinite-array approach cannot account for edge effects caused by the finiteness of the array and by the boundedness of the ground plane and dielectric layers.* With respect to the finiteness of the array, simulations and measurements show differences in side-lobe level between finite-array behavior and infinite-array simulations. When mutual coupling between the elements is strong, there can be a considerable difference between the behavior of the edge elements and their infinite-array behavior. Moreover, a significant number of elements may be affected by the edge effects. With respect to the boundedness of the ground plane, results for single elements show that the element pattern for an infinite ground plane is perturbed by the edge effects of the bounded ground plane [100]. By physical techniques such as the Uniform Theory of Diffraction (UTD), the perturbation, i.e., a ripple on the smooth pattern, is predicted.

- *Non-periodic arrays, such as sparse arrays, cannot be analyzed by the infinite-array approach. Moreover, the failure of certain elements cannot be accounted for.*

- *Differences between elements cannot be accounted for in the infinite-array approach.* For example, ideally, the elements of a planar uniform array are all positioned at the same

height above the ground plane and they are all geometrically the same. In the practice of mechanical engineering, it is very difficult to construct a flat ground plane, especially for a large array with an array face of $16\,\mathrm{m}^2$. Moreover, the elements will show slight differences in shape and height. To investigate the influence of such differences and imperfections on the array performance, a straightforward implementation of the infinite-array approach cannot be used.

A further limitation of numerical simulation tools is that they are generally not designed to provide insight into characteristics of arrays, i.e., relationships between geometry parameters and performance parameters. In practice, characteristics are determined by analyzing simulation and measurement results for various geometries. Consequently, the inventory of characteristics is fragmentary. In [8], an inventory of characteristics based on 30 articles on antenna arrays and single antennas is described. *Since characteristics serve as guidelines for the antenna designers, we preferred an analysis approach that provides direct insight into characteristics.*

To overcome the limitations, Thales initiated a sequence of projects to analyze finite antenna arrays and to develop simulation tools [3, 49, 118]. An extensive review can be found in [7: pp. 13-18]. As mentioned in the introduction of this chapter, the projects were mainly concerned with the analysis of a single element. The challenge was to find suitable functions to describe the current on the rectangular loop, as schematically depicted in Figure 1.3, while keeping the computation time short. Despite extensive research, the computation times remained too high to extend the analysis to arrays. Therefore, in the project described in [7], we started with the analysis of simpler (loop) geometries. Next, we decided to shift towards the analysis of large arrays with the focus on global (array) effects. The main motivation for this shift was to find characteristics of a single element that are essential for the array performance. Based on these characteristics, we expected to develop an efficient simulation tool. The more complex the geometry of the element, the more complicated the determination of characteristics. Because of this, we decided to consider arrays of the analyzed simple elements first. The following additional requirements for our analysis were formulated.

1. As in array design, it should be possible to use information obtained from the analysis of subarrays in the analysis of the entire array. In this respect, it is important to know which information of a subarray is essential for the description of the array behavior. Once this question is answered, the step towards a large array composed of subarrays can be made in an efficient way without the necessity of calculating again the subarray information.

2. Edge effects due to finiteness of the array should be accounted for. In our research, we did not consider edge effects caused by boundedness of the ground plane. We expect that these effects can be handled for by available techniques at Thales [13]. Effects due to the boundedness of the ground plane are discussed in Section 6.4 in relation to the analysis approach we developed in this thesis.

3. The approach should be (array) lattice independent. In other words, the approach should not be limited by specific lattices on which the building blocks or subarrays are positioned.

4. The approach should be independent of the choice of the specific elements.

Before we describe our approach, we present a list of available array-analysis approaches, especially adjustments of the infinite-array approach; we describe the benefits and limitations of these approaches. Literature on analysis of specific types of arrays, on array synthesis, and on developments in the understanding of array effects is discussed in Section 2.5 and in Chapter 6. An extensive literature list of articles on antenna arrays and related topics can be found in [8].

1. Small arrays can be analyzed by full-wave simulations of the actual array structure. To obtain higher computation speeds, iterative methods are used, such as the matrix decomposition methods described in [15, 90, 121].

2. To account for edge effects in rectangular uniform arrays, i.e., arrays with a rectangular lattice and with uniform spacing and uniform element shape, a variety of techniques is available.

   2.1 When the elements of the array are minimum scatterers with respect to impedance, admittance, or scattering parameters, results obtained by the infinite-array approach are corrected by techniques as described in [100]. Element-pattern results in this article confirm the statement of earlier work that the characteristics of only those elements in a uniform rectangular array that have at least 12 neighbors on each side are described by the infinite-array approach. Recent research [48] showed that an experimental array needs to be at least $5\lambda \times 5\lambda$, with λ the wavelength, to approximate the element characteristics of large broadband arrays. Then, the behavior of the central elements is described by the infinite array, while the behavior of the edge elements approximates the edge behavior of large arrays. For narrow-band arrays with 0.5λ spacing, the minimum size is lower than the size suggested in [100] (10×10 versus 25×25) but for wide-band arrays, it is much larger (50×50 versus 25×25).

   2.2 The infinite-array approach is adjusted by a windowing technique, which is applied both for a circuit description [52] and a field description [104, 105] of the array behavior. The basic assumption for the field description is that the current distribution on the array varies slowly from one element to another. The currents on the elements are determined in the spectral domain (with respect to position) from an electric-field integral equation, which is defined for each element separately. The kernel of this equation is a convolution of the spectral infinite-array kernel and the Fourier transform of the excitation taper, or, 'window'. The main advantage of the method is that an uncoupled system of equations needs to be solved instead of a coupled. Since

the computation of the required infinite-array data dominates the computation time of solving the uncoupled equations, the total computation time is independent of the array size.

2.3 In the casting technique in [114], the conventional set of coupled integral equations describing the array behavior is replaced by casting the corresponding moment matrix into a single integral equation for a global generating function. The kernel of the resulting equation is the product of the active admittance of the infinite array and the array factor of the uniformly excited finite array. The casting technique reduces the problem to a matrix equation which is of the same size as the equation for a single element in the windowing technique mentioned in item 2.2.

2.4 A variety of approaches takes the edge behavior into account explicitly. Based on the assumption that the edge behavior of an array is independent of the array size, the edge behavior of a large array is approximated in [77: p. 1611] by the edge behavior of a small array. More insight in edge phenomena is provided by the truncated Floquet-wave diffraction method [83, 84]. Within this method, an integral equation is solved for the fringe current, which describes the difference between the finite-array current and the associated infinite-array current. The fringe current is expanded into only a few basis functions defined on the entire array. The basis functions result from solutions of canonical problems, for example, determining (Green's) kernels for a planar semi-infinite array [16, 17, 91]. In [32, 31], the method is applied to rectangular arrays of open-ended waveguides with uniform and non-uniform amplitude excitation. Independently developed and strongly related to the truncated Floquet-wave diffraction method is the hybrid method described in [18]. The currents on the elements near the edges and corners of the array are described by separate basis functions, while the currents on the interior elements are described by a few global basis functions. In the three approaches mentioned, the number of unknowns is much lower than the number of unknowns in the element-by-element moment method. Moreover, this number is independent of the array size.

2.5 Instead of modeling a rectangular uniform array as being infinite in both length and width direction, the array is modeled as being infinite in one direction and finite in the other direction. In that case, only a single row of elements in the finite direction needs to be considered. The technique was applied to arrays of patches [77], arrays of dipoles [45, 117], and arrays of single-mode slots on an infinite ground plane [102] and on a finite-by-infinite ground plane [103]. Recently, the technique has been applied to arrays with more complex and strongly coupled elements [28, 29]. Here, the infinite and semi-infinite (half-infinite-by-infinite) array solutions are used to decompose the current on successive elements into a few standard distributions. The semi-infinite array solution is based on the moment-method solution for the

currents on a few edge elements and the assumption that the currents on the other elements equal the infinite-array solution. The decomposition of currents allows for a very fast and quite accurate approximation of the current, except near the grazing and grating-lobe scan angles.

2.6 Examples of other, mainly numerical, approaches are the combinations of the array decomposition method and the fast multipole method [56, 57], the moment method and the discrete Fourier transform method [19, 88], and the forward-backward method and the discrete Fourier transform method [22]. These hybrid approaches greatly reduce the computational effort of the element-by-element moment method.

3. To apply the approaches of item 2.2 to non-uniform arrays, the integral equation and windowing technique is reformulated in the spatial domain [106] at the cost of losing the simplicity of the spectral-domain infinite-array formulation. Solving the integral equation for the current in the space domain requires the evaluation of Sommerfeld integrals, which replaces the evaluation of Floquet series in the spectral domain. To compute these integrals rapidly, powerful numerical tools are needed.

4. To reduce the number of unknowns in the element-by-element moment method and to conserve flexibility with respect to array lattice and element shape, various techniques were developed to construct other than piecewise basis functions.

   4.1 In the expansion wave concept [33, 123], first, the currents on a single array element are determined simultaneously for its feed excitations and for waves incident on the element from different lateral directions. The reflected waves induced by these currents are determined by describing the complex amplitude by a number of basis functions. Then, the array behavior is determined from relationships between the incident and reflected expansion waves and the feed voltages. The number of unknowns equals the number of elements times the number of expansion waves determined for a single element. In [123], it is demonstrated that only 8 expansion waves are needed on a patch to reach the same accuracy as with 100 piecewise functions.

   4.2 In the synthetic basis function technique [74, 89], basis functions for array subdomains are constructed by solving on each subdomain (in isolation) an equation for the current for a number of excitations. Only a few of such functions are needed in the global array analysis. The characteristic basis function method [125] is based on the same principle and, therefore, strongly related to this technique.

5. In [36], an array mask is introduced to treat arrays of uniform elements of which the lattices are constructed from a rectangular uniform lattice by removing certain blocks of

elements. The mask describes which elements of the uniform rectangular array belong to the original array. To calculate the current, the adaptive integral method is used [12].

6. Examples of other, mainly numerical, approaches are the combination of the precorrected fast Fourier transform method and the discrete complex image method [126] and the combination of the characteristic basis function method and the finite-difference time-domain method [78]. Both approaches greatly reduce the computational effort of the element-by-element moment method and are applicable to a wider range of arrays than rectangular uniform arrays only.

Except for item 4.2, the approaches described above do not exploit the subarray idea, which is described in our additional requirement 1 above. Moreover, most of them were specifically developed for uniform arrays and, therefore, do not meet our additional requirement 3. Third, although most approaches can be applied to more types of elements, only in some cases, a general description is provided for the application to 'arbitrary-shaped' elements. According to our requirement 4, we should provide such a general description. Finally, few methods provide the direct insight into characteristics as we mentioned above. Therefore, we decided to develop an alternative analysis approach.

1.3 Main Objectives and Analysis Approach

The main objectives in the development of our analysis approach were:

I. To find characteristics of a single element that are essential for describing the array behavior.

II. To develop an efficient analysis approach for finite antenna arrays on basis of the element characteristics. The approach should provide insight into array characteristics.

III. To find characteristics that describe the behavior of arrays.

IV. Given that the infinite-array approach is most frequently used, to show in what way and to what extent our approach improves the infinite-array approach.

Within our research to reach the objectives, two phases are distinguished. The first phase was concerned with the analysis of single simple elements and the shift towards arrays of such elements. The analysis is described in Chapter 2 and Sections 3.1 – 3.3 of this thesis; results can be found in [7, 11], and in Section 2.5. The main model considerations of this phase were:

- The arrays are composed of simple elements: rectangular microstrips and ring-shaped microstrips, shortly strips and rings. Besides finding characteristics, other motivations played a role as well in the choice of (these) simple elements in the first phase.

  - To keep the computation time relatively short for large arrays.
  - Since the elements used in practice have a loop geometry, see Figure 1.2, we opted for the most simple loop geometry to be described mathematically, i.e., the ring geometry. We note that a ring is not a simple geometry from the point of view of the automatized microstrip production process due to the large number of points needed to describe a ring in a Cartesian reference frame.

- Choosing simple elements is accompanied by choosing simple excitations. Another motivation for simple excitations is that there is some doubt whether modeling the real shape of the twin lead, see Figure 1.2, makes much sense. First, the variation of the twin lead geometry from element to element will be relatively large compared to the variation of the geometry of the other antenna-element components. Second, the twin lead hardly contributes to the far-field characteristics of the array, because it hardly radiates.

- A spatial time-harmonic representation of the electromagnetic fields is employed.

- The elements are assumed so thin and well-conducting that they can be modeled as infinitely thin and perfectly conducting, see Section 2.2 for details. Then, the elements are represented by surfaces. In turn, these surfaces are assumed smooth and oriented, and their boundary curves are assumed piecewise smooth and oriented, see Section 2.3.1 for details.

- The elements are assumed so narrow, i.e., their width is much smaller than all other length scalers, that the currents on the elements may be averaged with respect to the widths, see Section 2.3 for details.

In the first phase of our research, analysis of arrays was carried out by application of the moment method to the integro-differential equations describing the currents on the arrays. Although the results were promising, computation times for arrays of simple elements were still too large to make an extension to more complex geometries possible. Moreover, characteristics of a single element could only be determined by analyzing simulation results for various geometries. Therefore, a second phase was initiated of which a first introduction is described in [10]. During the second phase, the following main features of our approach became clear:

- The behavior of arrays is reflected in their ‘eigenstates’, which we call the eigencurrents. The eigencurrents have array-independent properties. Moreover, only the ‘force’ by which the eigencurrents are excited depends on the excitation, not the eigencurrents themselves. For these reasons, the behavior of arrays can be predicted by means of their eigencurrents in an efficient way.

- As in the actual design, an array is decomposed into a hierarchy of subarrays. Then, the eigencurrents of the total array are constructed from the eigencurrents of the subsequent

subarrays. The decomposition of the array depends on the positioning of the elements and on the excitation or feeding network.

To explain the aspect of decomposition further, we consider an example. Figure 1.5 (left) shows two subarray decompositions of a uniform 4×6 array. The upper array is generated from a 1×6

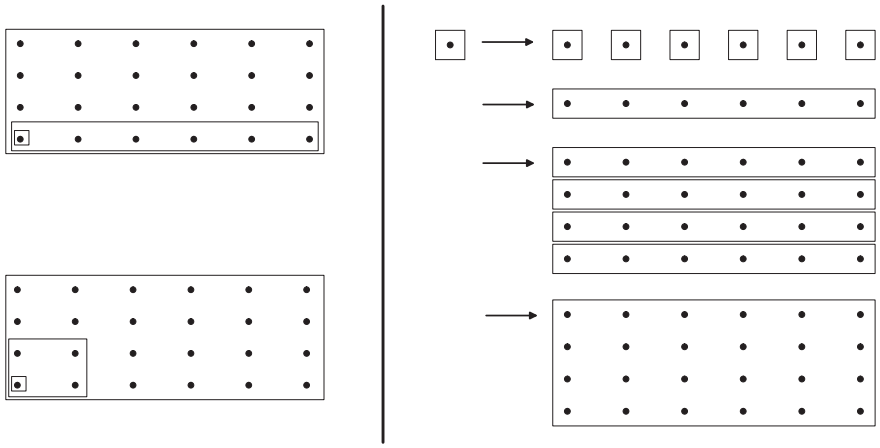

Figure 1.5 Left: Two decompositions of a rectangular 4×6 array with different (generating) subarrays. Right: Construction of a rectangular 4×6 array from subsequent (generating) subarrays.

line array, which in turn is generated from a single element. The lower array is generated from a 2×2 rectangular array, which in turn is generated from a single element. The decomposition in the upper figure is suitable if the elements of each row are excited with the same amplitude and phase, while there are amplitude and phase differences between the rows. The decomposition in the lower figure is suitable if the elements of each 2×2 block are excited with the same amplitude and phase, while there are amplitude and phase differences between the blocks.

Instead of decomposing a given array into subsequent (generating) subarrays, we can also compose an array from subsequent (generating) subarrays as illustrated in Figure 1.5 (right). The single-element subarray generates the line array and the line subarray generates the rectangular array. This composition also illustrates in what way the eigencurrents of the total array can be determined. First, the eigencurrents of a single element are determined and, next, the eigencurrents of a line array as concatenations of linear combinations of single-element eigencurrents. In other words, each eigencurrent of a line array is described as a linear combination of single-element eigencurrents. Finally, the same procedure is carried out to go from the line array to the rectangular array. Essential aspect of this approach is that, in each step, we need to take into account only those eigencurrents of the generating subarray that contribute to the mutual

coupling between the subarrays. The other eigencurrents contribute only to the local behavior of the generating subarray. This strategy saves considerable computational effort. As an example, we consider a uniform rectangular 5×30 array, which is generated from a 1×30 uniform line array. In turn, this line array is generated from a single element. In the element-by-element moment method, the current on each element is expanded into a number of expansion functions, for example, 30 piecewise functions. Then, the moment matrix describing the array behavior is a $(30 \cdot 5 \cdot 30) \times (30 \cdot 5 \cdot 30) = 4500 \times 4500$ matrix. In the proposed approach, which we call the eigencurrent approach, the eigencurrents of a single element are determined from a 30×30 matrix. Next, if only two single-element eigencurrents contribute to the mutual coupling in the line array, its (coupling) array eigencurrents are determined from a 60×60 matrix. If $N \leq 60$ eigencurrents of the line array contribute to the mutual coupling in the rectangular array, its eigencurrents are determined from a $5N \times 5N$ matrix. The matrix sizes in the eigencurrent approach are thus much smaller than the matrix size of the element-by-element moment method. Other computational advantages are discussed in the next section and in Chapters 5 and 7.

We end this section with some general remarks on the eigencurrent approach.

- The mutual coupling between the subarrays is quantified by means of a proposed measure, i.e., the spread of the eigenvalues, see Section 5.1 and Subsection 6.3.1.
- The eigencurrent approach is described in general terms in Chapter 5, but it was developed on basis of analysis of line arrays. Therefore, the examples are focussed on line arrays in particular.
- Although the examples above were uniform line arrays and rectangular arrays, the approach can be applied in principle to non-uniform arrays as well. More general, the eigencurrent approach is not lattice dependent, only subarray dependent. For a discussion, we refer to Section 5.4.
- By decomposing an excitation field of a certain array into the array eigencurrents, it can be understood which excitation fields are well-supported by that array. On a single element, the excitation field is expressed into the eigencurrents of that element. If only a few eigencurrents determine the behavior of a single element, the exact form of the excitation field is not important, but only its decomposition into these few eigencurrents. This explains once more why simple excitation fields are used.
- An overview of approaches related to the eigencurrent approach is presented in Subsection 5.1.4.

In Chapter 7, we describe the conclusions of our research and the analysis approach for finite antenna arrays that we propose. Moreover, we discuss to what extent the conclusions and the approach satisfy the main objectives in this section and the additional requirements in the previous section, see p. 8.

1.4 Organization and Contents of the Thesis

We start this thesis with the description of the classical problem of calculating the electromagnetic field induced by a current distribution in free space, see Figure 1.6. Once the model

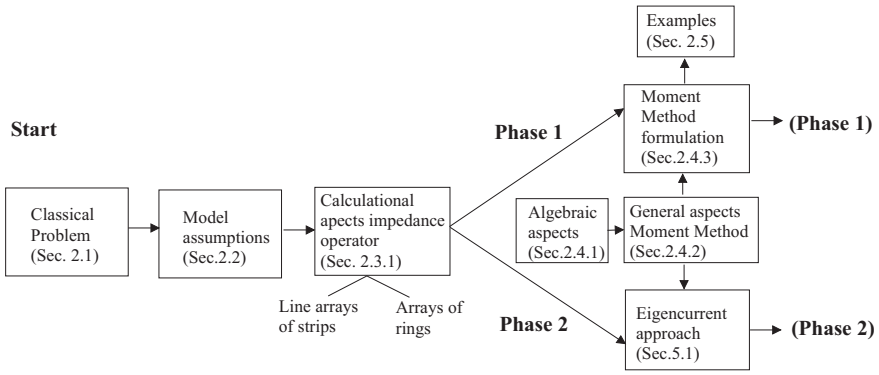

Figure 1.6 Start of the research. We note that 'Phase 1' and 'Phase 2' indicate the first and second phases of our research, while '(Phase 1)' and '(Phase 2)' indicate the connection of this scheme with the schemes in Figures 1.7 and 1.8, where the two phases are described.

assumptions for arrays of microstrips have been formulated in Section 2.2, the solution of the classical problem is used to describe the electromagnetic field induced by such an array. Basic relation is the integro-differential equation $\mathcal{Z}\boldsymbol{J} = \boldsymbol{E}_S$, also called the electric-field integral equation. It relates the current $\boldsymbol{J}$ on the conducting surface S formed by the array elements to the tangential excitation field $\boldsymbol{E}_S$ by means of the integro-differential operator $\mathcal{Z}$, which we will call the impedance operator. The tangential excitation field describes the source of the array, and is considered in detail in Chapter 4. In Section 2.3.1, an averaged form of this equation is deduced for narrow microstrips, i.e., microstrips of which the width is much smaller than the other length scales in the array and the wavelength. Next, this averaged form is elaborated for line arrays of arbitrary spaced strips with uniform geometry and to planar arrays of arbitrary positioned rings with arbitrary sizes and orientations. By dimensional analysis, terms of higher order due to the narrow-strip assumption are identified and neglected. The analysis differs from the generally applied wire analysis with reduced kernel [120: pp. 20 – 23, pp. 40 – 45] in that the scattered field is averaged instead of evaluated at the centerline, and in that the obtained integral kernels are logarithmically singular instead of continuous.

To describe the calculational aspects of both phases of our research, we introduce the required algebraic concepts as well as the moment method in Subsections 2.4.1 and 2.4.2. Next, we describe the first phase as schematically depicted in Figure 1.7. This phase starts in Subsection 2.4.3 with the general moment-method formulation for arrays. Before the aspects of this

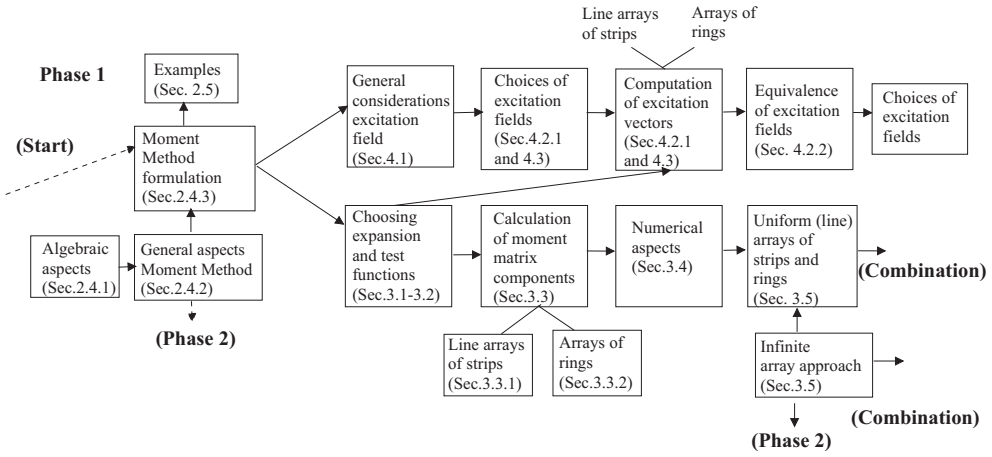

Figure 1.7 Scheme of the first research phase.

formulation are discussed in detail in Chapters 3 and 4, we present initial results for uniform and non-uniform arrays in Section 2.5. The results concern the occurrence of large current-amplitude variations in finite arrays, behavior of exponentially spaced arrays, line-array failure in rectangular arrays, and a comparison of uniform and perturbed arrays.

Choice of suitable test and expansion functions for the moment method, calculation of the moment matrix components, numerical computation of these components, and analysis of uniform (line) arrays are the aspects we discuss concerning the impedance operator in the moment-method formulation. In Sections 3.1 and 3.2, we describe the aspects of test and expansion functions commonly used in the literature from an operator-theoretical perspective. As a result of the averaging procedure in Chapter 2, the moment matrix components calculated in Section 3.3 reduce to single integrals for line arrays of strips. For line arrays of rings, they reduce to double and single integrals in case of mutual and self coupling, respectively. Two calculation procedures are explored, one in which the differential part of the averaged impedance operator is 'equally distributed' over test and expansion functions as in Green's theorem, and one in which this part is transferred to the test functions. In the second procedure, the Sturm-Liouville properties of the differential operator are exploited. In the special topic of uniform (line) arrays, the infinite-array approach is applied to approximate the current on the elements. The convergence or divergence of this approach is related to the physical phenomena of grating-lobe appearance and grazing scan. This relation extends results in the literature in that different types of line arrays are considered. Moreover, a mathematical explanation of the convergence and divergence aspects is provided based on Toeplitz properties of the impedance operator. Further investigation

of these properties and their relation to scanning are described in Chapter 5.

In Chapter 4, we discuss the tangential excitation field by which the source of arrays of strips and rings is modeled. Two types of excitation fields are considered: excitation fields related to the transmit function, also called local feeds, and excitation fields related to the receive function of the array. In particular, we investigate the consequences of expressing the tangential excitation field in terms of a finite set of expansion functions. We show that specific choices of local feeds, i.e., the delta gap, the finite feed gap, and excitation by a proximity coupled small ring, are equivalent. They generate the same current distributions up to small perturbations. Based on this result, we choose finite expansions of the delta gap as tangential excitation fields for the simulation in Chapter 6. Additionally, we discuss the equivalence of local feeds with respect to a local performance parameter, i.e., the (complex) power. Within the frame of the dimensional analysis of Chapter 2, we show that the tangential excitation field and the current may be replaced by their averaged forms in the computation of the (complex) power. Moreover, we show that the real part of the complex power equals twice the radiated power, as described in the literature. Finally, to model the receive function, we choose plane waves and we show for which plane-wave directions the averaging procedure of Chapter 2 is valid. Moreover, we show that currents induced by local feed gaps and currents induced by plane waves are approximately the same, which is explained by the reciprocity theorem.

The second phase of our research is described in Chapter 5, see Figure 1.8. In Section 5.1, the general idea of the approach suggested in this thesis, called the eigencurrent approach, is described. The eigencurrent approach consists of two main steps, called the initialization and the

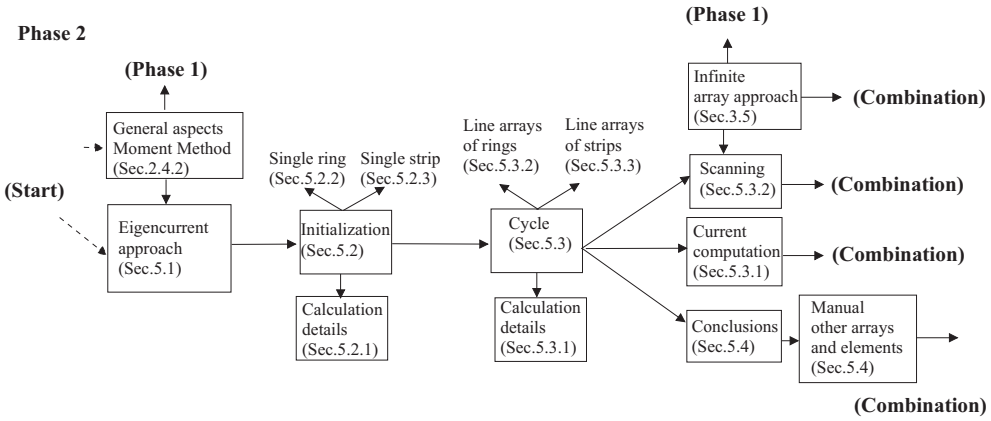

Figure 1.8 Scheme of the second research phase.

cycle. In the initialization, the eigencurrents of a single element, or more general, of the initial-

izing subarray, are determined. In the cycle, the eigencurrents of the array are determined from the eigencurrents of subsequent subarrays by an iterative process as outlined in Section 1.3. Calculational details of both steps for eigencurrents of line arrays of strips and rings are discussed in Sections 5.2 and 5.3. The excited current on line arrays of strips and rings is expressed in terms of these eigencurrents, see Section 5.3.1. In Subsection 5.3.2, we relate the eigencurrents to scanning by linear phase tapering and we compare the eigencurrent approach with the infinite-array approach. Special attention is devoted to the one-to-one correspondence between eigenvalues and scan angles and to the divergent and convergent behavior of the infinite-array solution at the grazing and grating-lobe scan angles. The main conclusions of the initialization and the cycle are summarized in Section 5.4. Moreover, we provide a manual in which the steps of the application of the eigencurrent approach to arrays of arbitrary elements are described.

The main items of both our research phases are joined in Chapter 6, see Figure 1.9. In Sec-

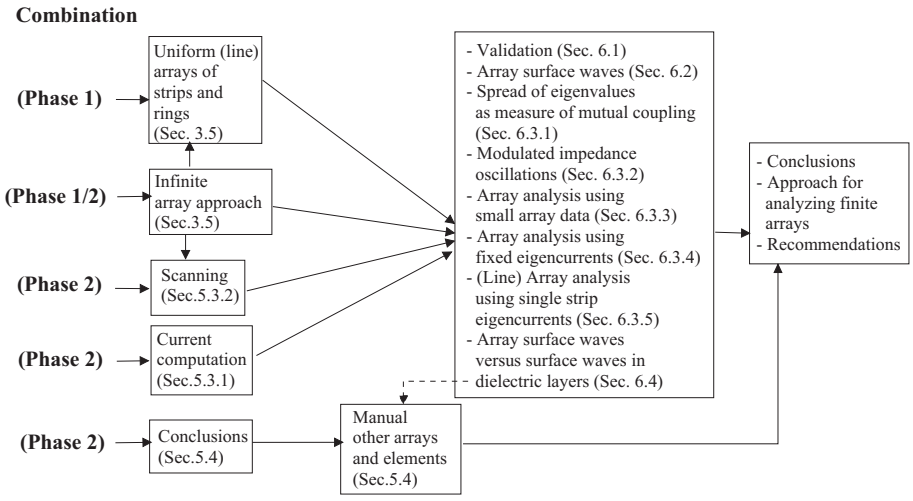

Figure 1.9 Schematic combination of the main items of both research phases.

tion 6.1, we compare results of the eigencurrent approach with results of the element-by-element moment method for various line-array sizes. Next, in Section 6.2, we show that the eigencurrent approach can predict the large variations of element-current amplitudes observed in the third example of Section 2.5. These variations, and corresponding variations of element impedances, cannot be predicted by the infinite-array approach and may decrease the performance of an array considerably. We propose an explanation, alternative to the explanation in [53, 82] based on array surface waves, for the large variations by showing that they are caused by the excitation of specific resonant eigencurrents. Moreover, we show that on basis of the behavior of the eigen-

values, resonances are predicted and suitable loads can be determined to prevent the excitation of resonant eigencurrents.

In Section 6.3, we first show that the spread of the eigenvalues is a quantitative measure for mutual coupling and, therewith, for the number of eigencurrent groups needed in the cycle of the eigencurrent approach. This investigation leads again to the identification of resonances of arrays. We show that the modulated oscillations of element impedances discussed in [30, 46] are caused by the excitation of specific resonant eigencurrents and, therewith, by the same mechanism as the variations of element impedances attributed to surface waves. Next, we show that mutual coupling between distant elements may be neglected, but that special care is needed. Except near the appearance of a grating lobe, the number of neighbors needed to describe mutual coupling is well predicted by the variation of the spread as a function of the number of elements in small arrays. Finally, we show that by fixing eigencurrents for a chosen set of geometry parameters, performance parameters for other sets of geometry parameters can be predicted in a fast and accurate way.

In Section 6.4, we show that the eigencurrent approach is capable of predicting the array behavior at the grating lobe scan angle. Moreover, we explain how this result supports our idea that the eigencurrent approach can not only handle arrays positioned in free and half space, but also arrays on dielectric layers, which may support surface waves. Finally, we present the conclusion of this chapter in Section 6.5 and we discuss to what extent the objectives of Section 1.3 were reached.

In Chapter 7, we first formulate the main conclusions of our research. Subsequently, we present the approach proposed in this thesis to analyze finite antenna arrays: the eigencurrent approach. In Section 7.3, we suggest potential modifications of this approach for a faster computation. Finally, we discuss recommendations both for array design in general and for the application of the eigencurrent approach.

Computational Details

All computations were carried out with Matlab 5.3 on a HP PC with Windows NT, an Intel Pentium 4 processor at 1.0 GHz, and 256 Mb of RAM.

CHAPTER 2

Mathematical Modeling

In this chapter, we describe the start of our research, as described by the scheme in Figure 1.6. First, the classical problem of calculating the electromagnetic field induced by a current distribution in free space is discussed. Once the model assumptions for arrays of microstrips, see for example Figure 2.1, have been formulated in Section 2.2, the solution of the classical problem is used to describe the electromagnetic field induced by such an array. The basic relation

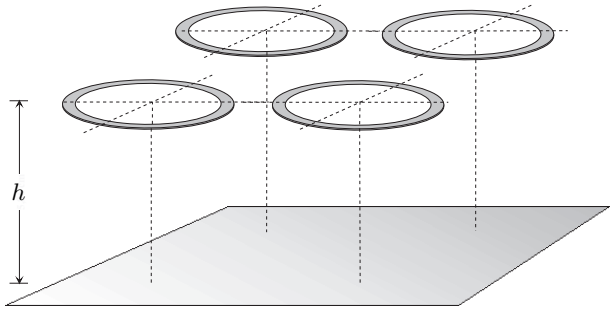

Figure 2.1 A rectangular 2×2 array of ring-shaped microstrips, shortly rings, above a ground plane.

is the integro-differential equation $\mathcal{Z}\boldsymbol{J} = \boldsymbol{E}_S$, also called the electric-field integral equation (EFIE). It relates the current $\boldsymbol{J}$ on the conducting surface S formed by the array elements to the tangential excitation field $\boldsymbol{E}_S$ by means of the integro-differential operator $\mathcal{Z}$, which we will call the impedance operator. The tangential excitation field describes the source of the array, and is considered in detail in Chapter 4. In Section 2.3.1, an averaged form of this equation is deduced for narrow microstrips, i.e., microstrips of which the width is much smaller than the other length scales in the array and the wavelength. Next, this averaged form is elaborated for line arrays of arbitrary spaced strips with uniform geometry and to planar arrays of arbitrary positioned rings

with arbitrary sizes and orientations. By dimensional analysis, terms of higher order due to the narrow-strip assumption are identified and neglected. The analysis differs from the generally applied wire analysis with reduced kernel [120: pp. 20 – 23, pp. 40 – 45] in that the scattered field is averaged instead of evaluated at the centerline, and in that the obtained integral kernels are logarithmically singular instead of continuous.

To describe the calculational aspects of both phases of our research, we introduce the required algebraic concepts as well as the moment method in Subsections 2.4.1 and 2.4.2. Next, we describe the first phase as schematically depicted in Figure 1.7. This phase starts in Subsection 2.4.3 with the general moment-method formulation for arrays. Before the aspects of this formulation are discussed in detail in Chapters 3 and 4, we present initial results for uniform and non-uniform arrays in Section 2.5. The results concern occurrence of large current-amplitude variations in finite arrays, behavior of exponentially spaced arrays, line-array failure in rectangular arrays, and comparison of uniform and perturbed arrays.

2.1 A Classical Problem

In this section, we consider the electromagnetic field in free space generated by a time-harmonic current density $\mathscr{J}$ with radian frequency ω. The field is governed by Maxwell's equations

$$\operatorname{rot} \mathscr{E} = -\frac{\partial \mathscr{B}}{\partial t}\,, \qquad \operatorname{rot} \mathscr{H} = \frac{\partial \mathscr{D}}{\partial t} + \mathscr{J}\,, \tag{2.1}$$

see [109: p. 2]. Here, $\mathscr{E}$ and $\mathscr{H}$ are the strengths of the electric and magnetic field, $\mathscr{D}$ and $\mathscr{B}$ are the densities of the electric and magnetic flux, and t is the time variable. The conservation of charge is described by the continuity equation

$$\frac{\partial \varrho}{\partial t} + \operatorname{div} \mathscr{J} = 0, \tag{2.2}$$

where ϱ is the charge density. The constitutive behavior of free space is described by

$$\mathscr{B} = \mu_0 \mathscr{H}\,, \qquad \mathscr{D} = \varepsilon_0 \mathscr{E}\,, \tag{2.3}$$

where the permittivity ε_0 and the permeability μ_0 of free space are both scalars, their values being $1/36\pi \cdot 10^{-9}\,\mathrm{A\,s/V\,m}$ and $4\pi \cdot 10^{-7}\,\mathrm{V\,s/A\,m}$. The time-harmonic behavior of the current density is modeled as

$$\mathscr{J}(\boldsymbol{x}, t) = \operatorname{Re}\left(\boldsymbol{J}(\boldsymbol{x})\, e^{j\omega t}\right) = \frac{1}{2}\left[\boldsymbol{J}(\boldsymbol{x})\, e^{j\omega t} + \boldsymbol{J}^*(\boldsymbol{x})\, e^{-j\omega t}\right], \tag{2.4}$$

where $*$ indicates the complex conjugate and the tuple $\boldsymbol{x} \in \mathbb{R}^3$ represents the position. Notice the change of notation between the vector function $\mathscr{J}$ in the space-time domain and the vector

function $\boldsymbol{J}$ in the space-frequency domain. We refer to $\boldsymbol{J}$ as the current. Incorporating the time-harmonic behavior and the constitutive behavior in Maxwell's equations and continuity equation, we arrive at

$$\operatorname{rot} \boldsymbol{E} = -j\omega\mu_0 \boldsymbol{H}\,, \qquad \operatorname{rot} \boldsymbol{H} = j\omega\varepsilon_0 \boldsymbol{E} + \boldsymbol{J}\,, \qquad j\omega\rho + \operatorname{div} \boldsymbol{J} = 0\,. \tag{2.5}$$

From (2.5), we find $\operatorname{div} \boldsymbol{H} = 0$, i.e., $\boldsymbol{H}$ is solenoidal, and $\operatorname{div} \boldsymbol{E} = \rho/\varepsilon_0$.

Next, we express $\boldsymbol{E}$ and $\boldsymbol{H}$ in the current $\boldsymbol{J}$. Since $\operatorname{div} \boldsymbol{H} = 0$ and free space is contractible, $\boldsymbol{H}$ is source free. Thus, there exists a magnetic vector potential $\boldsymbol{A}$ such that

$$\boldsymbol{H} = \operatorname{rot} \boldsymbol{A}\,. \tag{2.6}$$

Substituting (2.6) in (2.5)^1, we observe that the vector field $\boldsymbol{E} + j\omega\mu_0 \boldsymbol{A}$ is irrotational. We note that the super index ^{1} of (2.5) denotes the first equation of (2.5). Since free space is simply connected, this field is also conservative and thus there exists a scalar function ψ such that

$$\boldsymbol{E} + j\omega\mu_0 \boldsymbol{A} = -\operatorname{grad} \psi\,. \tag{2.7}$$

Substituting this expression for $\boldsymbol{E}$ in (2.5)^2, we obtain

$$\operatorname{rot}\operatorname{rot} \boldsymbol{A} = \omega^2\varepsilon_0\mu_0 \boldsymbol{A} - j\omega\varepsilon_0 \operatorname{grad} \psi + \boldsymbol{J}\,. \tag{2.8}$$

Finally, applying the vector identity $\operatorname{rot}\operatorname{rot} \boldsymbol{A} = \operatorname{grad}\operatorname{div} \boldsymbol{A} - \Delta \boldsymbol{A}$ and the Lorentz gauge $-j\omega\varepsilon_0\,\psi = \operatorname{div} \boldsymbol{A}$, we obtain the well-known Helmholtz equation for the magnetic vector potential $\boldsymbol{A}$,

$$\Delta \boldsymbol{A} + k^2 \boldsymbol{A} = -\boldsymbol{J}\,, \tag{2.9}$$

where k is the wave number defined by $k = \omega\sqrt{\varepsilon_0\mu_0}$. Moreover, by relation (2.7) and the Lorentz gauge, $\boldsymbol{E}$ is expressed in terms of $\boldsymbol{A}$:

$$\boldsymbol{E} = \mathcal{D}\boldsymbol{A}, \qquad \mathcal{D} = -jZ_0 k \left(\mathcal{I} + \frac{1}{k^2} \operatorname{grad}\operatorname{div} \right), \tag{2.10}$$

where $\mathcal{I}$ is the identity operator and $Z_0 = \sqrt{\mu_0/\varepsilon_0} = \omega\mu_0/k$ is the characteristic impedance of free space. It is well known that the solution of (2.9), supplemented by the radiation conditions at infinity, is given by

$$\boldsymbol{A} = \mathcal{T}\boldsymbol{J}, \qquad (\mathcal{T}\boldsymbol{J})(\boldsymbol{x}) = \int_{\mathbb{R}^3} \mathcal{G}_{\mathrm{free}}(\boldsymbol{x};\boldsymbol{x}')\boldsymbol{J}(\boldsymbol{x}')\,d\boldsymbol{x}', \tag{2.11}$$

where the kernel $\mathcal{G}_{\mathrm{free}}$ is defined by $\mathcal{G}_{\mathrm{free}}(\boldsymbol{x};\boldsymbol{x}') = g_{\mathrm{free}}(|\boldsymbol{x}-\boldsymbol{x}'|)\mathcal{I}$, g_{free} being a fundamental solution of the Helmholtz operator,

$$g_{\mathrm{free}}(R) = \frac{1}{4\pi}\frac{e^{-jkR}}{R}, \qquad R(\boldsymbol{x}) = |\boldsymbol{x}|\,, \tag{2.12}$$

see [80: Ch. 13, p. 1778], [124: p. 1566], and [127: pp. 496 – 497]. For a deduction of g_{free}, we refer to [127: pp. 379 – 382]. In the literature, a fundamental solution of a differential operator is often called a Green's function. However, the concepts of fundamental solution and Green's function are not the same. The universally accepted definition [66: pp. 92, 93, 105] of a fundamental solution is the definition of L. Schwartz, i.e., a fundamental solution of a differential operator $\mathcal{L}$ with respect to a point x' is defined as any distribution $f_{x'}$ that satisfies $\mathcal{L}f_{x'} = \delta_{x'}$, where $\delta_{x'}$ is the delta distribution corresponding to the point x'. For a (historical) review of the theory of distributions, we refer to [66: Ch. 6]. Green's functions were introduced by G. Green for determining the electric potential in a vacuum bounded by conductors with given potentials [66: p. 95]. A Green's function is a fundamental solution of the Laplace operator in three dimensions and satisfies (Dirichlet) boundary conditions at the boundary of a specified domain. Usually, fundamental solutions are called Green's functions when boundary conditions are imposed on these solutions, see [66: pp. 92, 93]. For a (historical) review of the development of the concepts of Green's function and fundamental solution, we refer to [66: Ch. 4]. We will refer to $\mathcal{G}_{\mathrm{free}}$ and g_{free} as the kernels of the corresponding integral operators.

2.2 Model Assumptions

We consider an array of microstrip elements and describe these elements by volumes in a space $\Omega \subset \mathbb{R}^3$ with boundary $\partial\Omega$. Let $V \subset \Omega$ be the union of these volumes. As in the classical problem, the current $\mathscr{J}$ in V induces an electromagnetic field in Ω, which is governed by Maxwell's equations. In this section, we present the assumptions for modeling such an array. We relate each model assumption to the classical problem of the previous section and show the impact of the assumption on the formulation.

1. The elements are excited by time-harmonic fields with a single frequency $f = \omega/2\pi$ only. The wavelength λ related to f is in free space given by $\lambda = c/f$, where $c = 1/\sqrt{\varepsilon_0\mu_0}$ is the speed of light. The assumption seems reasonable, if the elements are excited by a field that is approximately monochromatic. Therefore, we use only one frequency component and model the electromagnetic field as in the classical problem, see (2.4), with current $\boldsymbol{J}$. To analyze more frequency components, superposition can be applied.

2. The elements are modeled as infinitely thin, perfect conductors. In other words, V is replaced by a perfectly conducting surface S. This model assumption is supported by a dimensional analysis based on the following dimension considerations. First, the skin depth of the current is much smaller than the other characteristic length scales of the geometry and the electromagnetic field. The skin depth is defined by $\delta_{\mathrm{skin}} = \sqrt{2/\mu_0\omega\sigma}$, where σ is the conductivity of the elements. Second, the thickness of the elements is much smaller than the other characteristic length scales of the geometry and the electromagnetic

field, except for the skin-depth δ_{skin}. For example, $\delta_{\text{skin}}/2\tau \lesssim 0.05$ for copper elements with thickness $2\tau = 40$ μm excited at about 1 GHz or more. Examples of dimensional analyses can be found in [9] and [62: Ch. 7]. The analyses led to the well-known boundary conditions for infinitely thin, perfect conductors, i.e., the tangential electric field vanishes at the perfectly conducting surface and the jump of the tangential magnetic field over the surface equals the (surface) current density. These conditions are denoted as $\boldsymbol{n} \times \boldsymbol{E}|_S = \boldsymbol{0}$ and $\boldsymbol{n} \times (\boldsymbol{H}|_{S^+} - \boldsymbol{H}|_{S^-}) = \boldsymbol{J}_{\text{s}}$. Here, $\boldsymbol{J}_{\text{s}}$ is the surface current density, $S^{\pm}$ denote the sides of S, $|_S$ and $|_{S^{\pm}}$ denote the restrictions to S and $S^{\pm}$, and $\boldsymbol{n}$ is the normal on S pointing into the area at the S^+-side of S. Moreover, the vector product $\times$ of $\mathbb{R}^3$ is applied to complex vector fields.

As an example of the dimensional analyses mentioned above, we summarize the special case of a long straight thin strip, see Figure 2.2, as discussed in [9]. The strip is em-

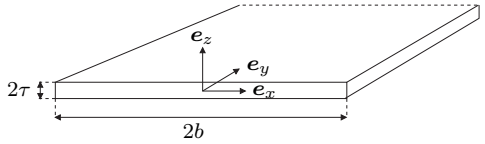

Figure 2.2 A thin strip of width $2b$ and thickness 2τ.

bedded in a dielectric medium with permittivity ε_d. First, a set of differential equations and boundary conditions for the current in the strip and the electric field in the dielectric medium are deduced from Maxwell's equations supplemented by Ohm's law for the electromagnetic field in the strip. The current is assumed to be a propagating wave in the length direction of the strip with prescribed amplitude of the total current through the cross section of the strip. Reflections at the end sections are ignored. Next, to investigate the electric field near the strip and the current inside the strip, the equations and conditions are scaled with respect to the thickness 2τ and the width $2b$ of the strip. The scaled equations incorporate the small parameter $\epsilon = \tau/b$, which is of the order 10^{-3} for the applications we consider. This parameter is responsible for boundary layers near the edges $x = \pm b$, which are ignored on basis of $\epsilon = O(10^{-3})$. Next, approximate expressions for the electromagnetic field in the dielectric medium are calculated, where radiation conditions are prescribed at infinity. In these expressions, terms of the order $\sqrt{\omega\varepsilon_d/\sigma}$ ($\lesssim 10^{-3}$), i.e., the ratio of the wavelength in the dielectric and the skin depth δ_{skin}, are neglected. The resulting electric field in the strip only exhibits a z-component and the corresponding magnetic field only exhibits an x-component. Moreover, both these fields and the surface charge density at $z = \pm b$ are completely described by the (prescribed) total amplitude of the current, the permittivity of the dielectric medium, and the permeability of vacuum.

The current in the strip only exhibits a y-component and the wave number of the current equals the wave number in the dielectric medium. The corresponding wavelength is much larger than the width of the strip, which confirms the assumption that the wave propagates in y-direction only. The current decays exponentially from the boundaries $z = \pm\tau$ with exponent $-2/\delta_{\mathrm{skin}}$. Since $\delta_{\mathrm{skin}} \lesssim 0.05$, the current is restricted to very thin layers near the boundaries. When the limit $\delta_{\mathrm{skin}} \to 0$ is taken in distributional sense, the current is restricted to the boundaries $z = \pm\tau$. In the above, the limits $\sqrt{\omega\varepsilon_d/\sigma} \to 0$ and $\delta_{\mathrm{skin}} \to 0$ were taken, which can be interpreted as $\sigma \to \infty$, i.e., the strip is a perfect conductor. Moreover, the strip can be modeled as infinitely thin, because its thickness is much smaller than all other length scales, and the current is located at the boundary. The boundary conditions for the infinitely thin, perfectly conducting strip follow from the obtained results for the electric and magnetic fields in the dielectric medium evaluated at $z = \pm\tau$. For further details, we refer to [9].

4. The spaces Ω we consider are free space and a half space bounded by a perfectly conducting plane Σ. The electromagnetic field induced by a current in free space is given by (2.10) - (2.12). For a half space, the electromagnetic field is described analogously, but with a different kernel $\mathcal{G}_{\mathrm{half}}$ defined by

$$\mathcal{G}_{\mathrm{half}}(\boldsymbol{x};\boldsymbol{x}') = \Big[g_{\mathrm{free}}\big(R(\boldsymbol{x}-\boldsymbol{x}')\big) - g_{\mathrm{free}}\big(R(\boldsymbol{x}-\mathcal{M}\boldsymbol{x}')\big)\Big]\mathcal{I}_{\mathrm{tr}} + \\ + \Big[g_{\mathrm{free}}\big(R(\boldsymbol{x}-\boldsymbol{x}')\big) + g_{\mathrm{free}}\big(R(\boldsymbol{x}-\mathcal{M}\boldsymbol{x}')\big)\Big]\mathcal{I}_{\mathrm{ax}}\,. \quad (2.13)$$

Here, $\mathcal{I}_{\mathrm{tr}}$ projects a vector on the transverse plane, i.e., the plane parallel to Σ, whereas $\mathcal{I}_{\mathrm{ax}}$ projects a vector on the axis perpendicular to the transverse plane. Moreover, $\mathcal{M}\boldsymbol{x}'$ is the mirror image of $\boldsymbol{x}'$ with respect to the plane Σ. The expression for $\mathcal{G}_{\mathrm{half}}$ can be found from (2.9) by the method of imaging and by rewriting the boundary condition $\boldsymbol{n} \times \boldsymbol{E}|_\Sigma$ to a boundary condition for $\boldsymbol{A}$, i.e., $\boldsymbol{n} \times \boldsymbol{A}|_\Sigma = \boldsymbol{0}$ and $(\partial\boldsymbol{A}/\partial n)|_\Sigma = 0$. Notice that if other spaces Ω are considered, the corresponding kernel $\mathcal{G}_\Omega$ can also be found from (2.9) together with the boundary conditions at $\partial\Omega$, but without the conditions at S. We note that the boundary conditions at $\partial\Omega$ incorporate the radiation conditions, if Ω is unbounded. If the medium in Ω is described by other constitutive equations than (2.3), they need to be accounted for in the solution for the electromagnetic field and the kernel.

The classical problem together with the assumptions suggests that the electromagnetic field generated by the current $\boldsymbol{J} := \boldsymbol{J}_{\mathrm{s}}$ is given by

$$\boldsymbol{H} = \operatorname{rot}\boldsymbol{A}\,, \quad \boldsymbol{E} = \mathcal{D}\boldsymbol{A}\,, \quad \boldsymbol{A} = \mathcal{T}\boldsymbol{J}\,, \quad (\mathcal{T}\boldsymbol{J})(\boldsymbol{x}) = \int_S \mathcal{G}_\Omega(\boldsymbol{x};\boldsymbol{x}')\boldsymbol{J}(\boldsymbol{x}')\,d\boldsymbol{x}'\,, \quad (2.14)$$

i.e., (2.6), (2.10), and (2.11) with $\mathbb{R}^3$ replaced by S. The fields $\boldsymbol{E}$ and $\boldsymbol{H}$ are the scattered electric and magnetic fields induced by the current $\boldsymbol{J}$. Since $\mathcal{G}_\Omega$ is constructed such that the

boundary conditions at $\partial\Omega$ are satisfied, only the boundary condition for $\boldsymbol{E}$ at S given in assumption 3 still needs to be applied. This condition can be written in the form $(\boldsymbol{E})_{\tan} = \mathbf{0}$. Here, $(\,\cdot\,)_{\tan}$ is a trace operator, which restricts a vector function on Ω to S and then takes the tangential component, i.e.,

$$(\boldsymbol{C})_{\tan} = \boldsymbol{C}|_S - (\boldsymbol{n} \bullet \boldsymbol{C}|_S)\,\boldsymbol{n}\,, \tag{2.15}$$

where the scalar product $(\,.\,\bullet\,.\,)$ on $\mathbb{R}^3$ is applied to complex vector fields. We note that $(\boldsymbol{C})_{\tan} = -\boldsymbol{n} \times \boldsymbol{n} \times \boldsymbol{C}|_S$. The operator $(\,\cdot\,)_{\tan}$ is only well-defined for vector fields that are continuous across S. For a discontinuous vector field, we need to distinguish between the restrictions $|_{S^+}$ and $|_{S^-}$. Using the relation between $\boldsymbol{E}$ and $\boldsymbol{J}$ given by (2.14), we obtain

$$\mathcal{Z}\boldsymbol{J} := (\mathcal{D}\mathcal{T}\boldsymbol{J})_{\tan} = \mathbf{0}\,. \tag{2.16}$$

The operator $\mathcal{Z} = (\mathcal{D}\mathcal{T}\,\cdot\,)_{\tan}$ is called the impedance operator. The electromagnetic field in Ω is now completely described by (2.14) and (2.16). However, if $\mathcal{Z}$ is injective on a suitable chosen domain for $\boldsymbol{J}$, then (2.16) yields the trivial solution $\boldsymbol{J} = \mathbf{0}$. To obtain a non-trivial solution, the right-hand side of (2.16) is replaced by a non-zero tangential vector field $\boldsymbol{E}_S$ at S, called the excitation field. Then,

$$\mathcal{Z}\boldsymbol{J} = \boldsymbol{E}_S \tag{2.17}$$

yields a unique non-trivial solution for $\boldsymbol{J}$, if $\mathcal{Z}$ is injective and $\boldsymbol{E}_S \in \mathrm{ran}(\mathcal{Z})$. Here, $\mathrm{ran}(\,\cdot\,)$ denotes the range of an operator, which depends on the domain $\mathrm{dom}(\,\cdot\,)$ of this operator. The excitation field can be interpreted as the tangential electric field at S induced by an externally applied electric field $\boldsymbol{E}^{\mathrm{ext}}$. Requiring that the total tangential electric field vanishes at S, we obtain (2.17) with $\boldsymbol{E}_S = -(\boldsymbol{E}^{\mathrm{ext}})_{\tan}$. An example of an externally applied electric field $\boldsymbol{E}^{\mathrm{ext}}$ is an incident wave, i.e., a solution $(\boldsymbol{E}^{\mathrm{ext}}, \boldsymbol{H}^{\mathrm{ext}})$ of $(2.5)^{1,2}$ with $\boldsymbol{J} = \mathbf{0}$. The total field $(\boldsymbol{E}^{\mathrm{ext}} + \boldsymbol{E}, \boldsymbol{H}^{\mathrm{ext}} + \boldsymbol{H})$ satisfies Maxwell's equations in $\Omega\backslash S$ and the boundary condition at S. Moreover, the total field satisfies the boundary conditions at $\partial\Omega$ only if $(\boldsymbol{E}^{\mathrm{ext}}, \boldsymbol{H}^{\mathrm{ext}})$ satisfies these conditions. Other examples of $\boldsymbol{E}^{\mathrm{ext}}$ are given in Chapter 4.

2.3 Calculational Aspects of the Impedance Operator

In this section, we consider the calculational aspects of the impedance operator and the related equation (2.17). First, we present a general outline of these aspects. Next, we apply the results of the outline to line arrays of rectangular microstrips, shortly strips, and to arrays of ring-shaped microstrips, shortly rings.

2.3.1 General Outline

We consider first a single microstrip element, which is modeled as a smooth oriented surface S in the space $\Omega \subset \mathbb{R}^3$. We introduce a parameter representation* $\boldsymbol{x}_S \in F(\Pi(S), \mathbb{R}^3)$ on S, where $\Pi(S)$ is the parameter set of S. Elements of $\Pi(S)$ are tuples (ξ, η). Two tangent vectors

$$\boldsymbol{e}_\xi = \frac{\partial \boldsymbol{x}_S}{\partial \xi} \Big/ \left| \frac{\partial \boldsymbol{x}_S}{\partial \xi} \right|, \quad \boldsymbol{e}_\eta = \frac{\partial \boldsymbol{x}_S}{\partial \eta} \Big/ \left| \frac{\partial \boldsymbol{x}_S}{\partial \eta} \right|, \tag{2.18}$$

correspond to the parameter representation $\boldsymbol{x}_S$, see for example Figure 2.3. They span the complex tangent plane $\text{Tang}(S, (\xi, \eta))$ at each point $\boldsymbol{x}_S(\xi, \eta)$, $(\xi, \eta) \in \Pi(S)$, of the surface S, i.e.,

$$\text{Tang}(S, (\xi, \eta)) = \{\, \alpha_\xi \boldsymbol{e}_\xi(\xi, \eta) + \alpha_\eta \boldsymbol{e}_\eta(\xi, \eta) \mid \alpha_\xi,\, \alpha_\eta \in \mathbb{C} \,\}\ . \tag{2.19}$$

Here, we extended the usual definition [27: p. 282] of tangent plane from real to complex combinations of $\boldsymbol{e}_\xi$ and $\boldsymbol{e}_\eta$, because we want to analyze the complex vector field $\boldsymbol{J}$ that is defined on S and that is tangential to S. Define the tangent bundle $\text{Tang}(S)$ of S as the union of all tangent spaces of S. Then, $\boldsymbol{J}$ and $(\mathcal{L}\boldsymbol{J})_{\tan}$ are both elements of linear spaces of functions, $F(\Pi(S), \text{Tang}(S))$. The operators $\mathcal{T}$ and $(\,\cdot\,)_{\tan}$ are linear mappings between linear spaces of functions $F(\Pi(S), \text{Tang}(S))$ and $F(\Omega, \mathbb{C}^3)$.

Another definition of tangent spaces can be found in [26: p. 63], where these spaces are introduced as function spaces. According to this definition, the tangent space of S consists of vector functions $\boldsymbol{f}$, which are defined on $\Pi(S)$ and for which $\boldsymbol{f}(\xi, \eta)$ is an element of $\text{Tang}(S, (\xi, \eta))$ in (2.19) for each $(\xi, \eta) \in \Pi(S)$. This tangent space is a subset of the function space $F(\Pi(S), \text{Tang}(S))$, because $\boldsymbol{f} \in F(\Pi(S), \text{Tang}(S))$ requires only that $\boldsymbol{f}(\xi, \eta)$ is an element of the tangent bundle $\text{Tang}(S)$ for each $(\xi, \eta) \in \Pi(S)$. We use the definition of tangent space in (2.19) and the related definition of tangent bundle.

The normal on S at $\boldsymbol{x}_S(\xi, \eta)$, say $\boldsymbol{e}_\zeta = \boldsymbol{e}_\xi \times \boldsymbol{e}_\eta$ or $\boldsymbol{e}_\zeta = -\boldsymbol{e}_\xi \times \boldsymbol{e}_\eta$, is the normal of the tangent plane at $\boldsymbol{x}_S(\xi, \eta)$. Since the surface S is oriented, there exists exactly one way in which we can obtain a smooth vector field $\boldsymbol{e}_\zeta$ choosing the direction of the normal in one point on S only. Thus, having chosen a right-handed coordinate system $\{\boldsymbol{e}_\xi(\xi_0, \eta_0), \boldsymbol{e}_\eta(\xi_0, \eta_0), \boldsymbol{e}_\zeta(\xi_0, \eta_0)\}$ for a certain tuple $(\xi_0, \eta_0) \in \Pi(S)$, we obtain the coordinate system

$$\{\boldsymbol{e}_\xi(\xi, \eta), \boldsymbol{e}_\eta(\xi, \eta), \boldsymbol{e}_\zeta(\xi, \eta)\}\,, \tag{2.20}$$

with $(\xi, \eta) \in \Pi(S)$. This system is attached to each point $\boldsymbol{x}_S(\xi, \eta)$ of S. Moreover, it is orthonormal (with respect to the Euclidean inner product on $\mathbb{R}^3$) and right-handed for all $(\xi, \eta) \in \Pi(S)$. For any vector field $\boldsymbol{C}$ in Ω, $\boldsymbol{C}|_{S^\pm}$ can be expanded into this coordinate system,

$$\boldsymbol{C}|_{S^\pm} = (\boldsymbol{e}_\xi \bullet \boldsymbol{C}|_{S^\pm})\, \boldsymbol{e}_\xi + (\boldsymbol{e}_\eta \bullet \boldsymbol{C}|_{S^\pm})\, \boldsymbol{e}_\eta + (\boldsymbol{e}_\zeta \bullet \boldsymbol{C}|_{S^\pm})\, \boldsymbol{e}_\zeta\,. \tag{2.21}$$

*By $F(A, B)$, we denote a linear space of functions, which map the elements of a set A into a set B.

Assume that the surface S has a piecewise smooth and oriented boundary curve ∂S. This curve has a piecewise defined tangent vector $\boldsymbol{\tau}_{\partial S}$, such that the orientation of ∂S induced by $\boldsymbol{\tau}_{\partial S}$ fits to the choice of the normal $\boldsymbol{e}_\zeta$ in the sense of the (right-handed) corkscrew rule related to Stokes' theorem. For every point at ∂S, there exists a piecewise vector $\boldsymbol{n}_{\partial S} \in \mathrm{Tang}(S)$ perpendicular to $\boldsymbol{\tau}_{\partial S}$ and $\boldsymbol{e}_\zeta$, i.e., $\boldsymbol{n}_{\partial S} = \boldsymbol{\tau}_{\partial S} \times \boldsymbol{e}_\zeta|_{\partial S}$. Then, $\boldsymbol{J}$ obeys the boundary condition

$$(\boldsymbol{n}_{\partial S} \bullet \boldsymbol{J}|_{\partial S}) = 0, \tag{2.22}$$

which means that the current cannot 'flow' out of S.

Using the vector prerequisites introduced above, the action of the integral operator $\mathcal{T}$ is interpreted on Ω as

$$\boldsymbol{A} = \mathcal{T}\boldsymbol{J} = \int_{\Pi(S)} \mathcal{G}\big(\,\cdot\,;\boldsymbol{x}_S(\xi',\eta')\big)\,\boldsymbol{J}(\xi',\eta')\,dS(\xi',\eta')\,, \tag{2.23}$$

where

$$dS(\xi',\eta') = S^{\mathrm{vol}}(\xi',\eta')\,d\xi' d\eta'\,, \qquad S^{\mathrm{vol}} = \left|\frac{\partial \boldsymbol{x}_S}{\partial \xi} \times \frac{\partial \boldsymbol{x}_S}{\partial \eta}\right|\,. \tag{2.24}$$

Choosing a coordinate system in Ω and expressing $\mathcal{D}$ into this system, we can calculate the scattered field $\boldsymbol{E} = \mathcal{D}\mathcal{T}\boldsymbol{J}$. For an arbitrarily chosen coordinate system, it is difficult to apply the trace operator $(\,\cdot\,)_{\tan}$ to this field, simply because the system does not 'fit' to the geometry of S. This problem can be circumvented by extending the local coordinate system in (2.20) to a global coordinate system. Then, the differential operator $\mathcal{D}$ can be expressed into this coordinate system. However, such a global extension is only possible for specific local coordinate systems, for example when $\boldsymbol{x}_S$ describes a planar, cylindrical, or spherical surface. In other cases, the local coordinate system is extended to a locally global coordinate system. This extension is based on a smooth extension $\boldsymbol{x}_S^{\mathrm{ext}}$ of the parameter representation $\boldsymbol{x}_S$ with corresponding extension $\boldsymbol{e}_\zeta^{\mathrm{ext}}$ of the field $\boldsymbol{e}_\zeta$. A locally global coordinate system can then be obtained from the mapping

$$\boldsymbol{x}(\xi,\eta,n) = \boldsymbol{x}_S^{\mathrm{ext}}(\xi,\eta) + n\boldsymbol{e}_\zeta^{\mathrm{ext}}(\xi,\eta)\,. \tag{2.25}$$

Having constructed a global or locally global coordinate system, we can calculate $\mathcal{Z}\boldsymbol{J}$ by

$$\mathcal{Z}\boldsymbol{J} = (\mathcal{D}\boldsymbol{A} - (\boldsymbol{e}_\zeta^{\mathrm{ext}} \bullet \mathcal{D}\boldsymbol{A})\boldsymbol{e}_\zeta^{\mathrm{ext}})|_S\,, \tag{2.26}$$

where $\boldsymbol{A}$ is defined as in (2.23). The differential operator in the right-hand side can be expressed into the partial derivatives with respect to ξ, η, and ζ. If this differential operator does not incorporate the normal derivative, i.e., $\partial/\partial\zeta$, we can identify an operator $\mathcal{D}_S$, which incorporates the partial derivatives with respect to ξ and η only and satisfies

$$(\mathcal{D}\,\cdot)_{\tan} = \mathcal{D}_S(\,\cdot\,|_S)\,. \tag{2.27}$$

Note that $\mathcal{D}_S$ incorporates the projection of $(\,\cdot\,)_{\tan}$ on S. A sufficient condition for the existence of $\mathcal{D}_S$ is that $A_\zeta|_S = (\mathcal{T}\boldsymbol{J})_\zeta|_S = 0$ in a neighborhood of S. In other words, $\mathcal{G}_\Omega(\,\cdot\,;\boldsymbol{x}_S(\xi',\eta'))\boldsymbol{e}$ has no normal component in this neighborhood for all $\boldsymbol{e} \in \mathrm{Tang}(S)$ and $(\xi',\eta') \in \Pi(S)$. This implies that $\mathcal{D}_S$ can be found for surfaces in free space or for surfaces parallel to the boundary of a half space, for example.

To introduce the concept of averaging a tangential vector field on S, we assume that there exists a set $\Pi_\xi(S)$ and a scalar η_1 such that $\Pi(S) = \Pi_\xi(S) \times [-\eta_1,\eta_1]$. Then, $\Pi(S)$ has a well-defined smooth centerline $\boldsymbol{x}_S(\,\cdot\,,0)$ with tangent vector $\boldsymbol{\tau} = \boldsymbol{e}_\xi(\,\cdot\,,0)$, see Figure 2.3. This

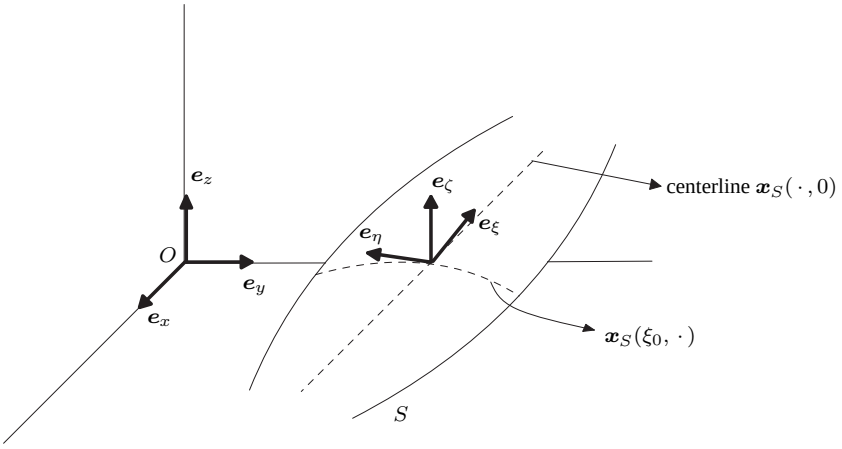

Figure 2.3 Geometry of a surface S with a centerline.

tangent vector can differ from the tangent vector $\boldsymbol{\tau}_{\partial S}$ at ∂S, see below (2.21). Let $\boldsymbol{u}$ be a tangential vector field on S and define the vector field $\mathcal{A}\boldsymbol{u}$ by

$$(\mathcal{A}\boldsymbol{u})(\xi,\eta) = u(\xi)\,\boldsymbol{\tau}(\xi), \quad (\xi,\eta) \in \Pi(S)\,, \tag{2.28}$$

where

$$u(\xi) = \left(\int_{-\eta_1}^{\eta_1} S^{\mathrm{vol}}(\xi,\eta)\,d\eta\right)^{-1} \int_{-\eta_1}^{\eta_1} u_\xi(\xi,\eta)\,S^{\mathrm{vol}}(\xi,\eta)\,d\eta\,. \tag{2.29}$$

The vector field $\mathcal{A}\boldsymbol{u}$ is uniform in η and directed along the centerline of S in each point $\boldsymbol{x}_S(\xi,\eta)$. Notice that the operator $\mathcal{A}$ satisfies the basic property of projections, i.e., $\mathcal{A}^2 = \mathcal{A}$, see also Subsection 2.4.1. The difference $\boldsymbol{u} - \mathcal{A}\boldsymbol{u}$ is given by

$$\begin{aligned}(\boldsymbol{u} - \mathcal{A}\boldsymbol{u})(\xi,\eta) = \Big[u_\xi(\xi,\eta) - u(\xi)\,\big(\boldsymbol{e}_\xi(\xi,\eta) \bullet \boldsymbol{\tau}(\xi)\big)\Big]\boldsymbol{e}_\xi(\xi,\eta) + \\ + \Big[u_\eta(\xi,\eta) - u(\xi)\,\big(\boldsymbol{e}_\eta(\xi,\eta) \bullet \boldsymbol{\tau}(\xi)\big)\Big]\boldsymbol{e}_\eta(\xi,\eta)\,.\end{aligned} \tag{2.30}$$

This difference indicates that we can replace $\boldsymbol{u}$ by $\mathcal{A}\boldsymbol{u}$ if

$$u_\xi \approx u, \qquad u_\eta/u_\xi \approx 0, \qquad (\boldsymbol{e}_\eta \bullet \boldsymbol{\tau}) \approx 0, \tag{2.31}$$

on $\Pi(S)$, where '$\approx$' needs still to be interpreted with respect to a functional metric. Such a metric depends on the antenna parameter under consideration of which examples are given in Section 1.1. The metric should relate the simulation result for a parameter to a certain reference. This reference can be a measurement result or another simulation result that is not subject to certain approximations. In Subsection 6.3.1, an example of a metric based on the L_2 norm is introduced to compare results obtained by two different approaches for the analysis of finite antenna arrays, i.e., the usual moment method and the eigencurrent approach proposed in this thesis. Moreover, it is shown that the difference between both results is also described by a measure based on the eigenvalues obtained in the eigencurrent approach. We will not go into further detail with respect to the functional metric related to (2.31). In the next sections and chapters, we only will indicate when the interpretation in terms of this functional metric is required for a certain approximation.

The first two conditions in (2.31) depend mainly on the vector field $\boldsymbol{u}$, whereas the last condition depends solely on $\boldsymbol{x}_S$ and hence on the geometry of S. If the conditions (2.31) are satisfied, we say that S is narrow with respect to the vector field $\boldsymbol{u}$. If $\boldsymbol{u}$ is replaced by $\mathcal{A}\boldsymbol{u}$, we say that $\boldsymbol{u}$ is width-averaged on S and we call $\mathcal{A}\boldsymbol{u}$ the width-average of $\boldsymbol{u}$. Integrating the width-average $\mathcal{A}\boldsymbol{u}$ over $\Pi_\xi(S)$, we obtain the average of u_ξ on S.

The surface S is generated by the set of curves K_ξ with parameter representation $\boldsymbol{x}_{K_\xi}(\eta) = \boldsymbol{x}_S(\xi,\eta)$ with $\eta \in [-\eta_1, \eta_1]$. The length of a curve K_ξ is

$$\int_{K_\xi} ds(\eta) = \int_{-\eta_1}^{\eta_1} \left| \frac{d\boldsymbol{x}_{K_\xi}}{d\eta} \right| d\eta\,. \tag{2.32}$$

If the length of all the curves K_ξ is small with respect to the wavelength, we assume that S is narrow with respect to $\boldsymbol{J}$ and, hence, that we can replace $\boldsymbol{J}$ by $\mathcal{A}\boldsymbol{J}$ in the equation for the current (2.17). Let w be the centerline component of the width-averaged current, i.e., $\mathcal{A}\boldsymbol{J} = w\,\boldsymbol{\tau}$. Replacing $\boldsymbol{J}$ in (2.17) by $\mathcal{A}\boldsymbol{J}$, we solve this equation for w instead of $\boldsymbol{J}$. The width-averaged current $\mathcal{A}\boldsymbol{J} = w\,\boldsymbol{\tau}$ satisfies the boundary condition (2.22) of $\boldsymbol{J}$ at the boundaries $\boldsymbol{x}_S(\,\cdot\,, \pm\eta_1)$ in the sense of the functional metric corresponding to (2.31). This can be shown as follows. The boundary curves $\boldsymbol{x}_S(\,\cdot\,, \pm\eta_1)$ have tangent vectors $\boldsymbol{e}_\xi(\,\cdot\,, \pm\eta_1)$. The vectors $\boldsymbol{e}_\eta(\,\cdot\,, \pm\eta_1)$ are perpendicular to these tangent vectors and are elements of $\mathrm{Tang}(S)$. Applying the boundary condition (2.22) at $\boldsymbol{x}_S(\,\cdot\,, \pm\eta_1)$ to $\mathcal{A}\boldsymbol{J}$, we obtain

$$0 = \big(\boldsymbol{e}_\eta(\xi, \pm\eta_1) \bullet (\mathcal{A}\boldsymbol{J})(\xi, \pm\eta_1)\big) = w(\xi)\,\big(\boldsymbol{e}_\eta(\xi, \pm\eta_1) \bullet \boldsymbol{\tau}(\xi)\big)\,, \tag{2.33}$$

for all $\xi \in \Pi_\xi(S)$. This shows that $\mathcal{A}\boldsymbol{J}$ satisfies the boundary condition of $\boldsymbol{J}$ at $\boldsymbol{x}_S(\,\cdot\,, \pm\eta_1)$ in the sense of the metric mentioned above.

Replacing $\boldsymbol{J}$ by $\mathcal{A}\boldsymbol{J}$ in (2.17), we average in fact the domain of the operator $\mathcal{Z}$. Averaging the range of $\mathcal{Z}$ as well, we arrive at

$$\mathcal{A}\mathcal{Z}\mathcal{A}\boldsymbol{J} = \mathcal{A}\boldsymbol{E}_S\,, \tag{2.34}$$

which raises the question whether a solution of (2.34) is an approximate solution of (2.17). By approximate we mean in the sense of the metric mentioned above. Assume that we have determined a solution of (2.34), say $\boldsymbol{J}_\mathcal{A}$. Then, $\boldsymbol{J}_\mathcal{A} \in \text{ran}(\mathcal{A})$, or $\boldsymbol{J}_\mathcal{A} = \mathcal{A}\boldsymbol{J}_\mathcal{A}$, and

$$\mathcal{Z}\boldsymbol{J}_\mathcal{A} = \boldsymbol{E}_S - (\mathcal{I}-\mathcal{A})\boldsymbol{E}_S + (\mathcal{I}-\mathcal{A})\mathcal{Z}\boldsymbol{J}_\mathcal{A}\,. \tag{2.35}$$

Hence, $\boldsymbol{J}_\mathcal{A}$ is an approximate solution of (2.17) under the condition that

$$(\mathcal{I}-\mathcal{A})\,(\mathcal{Z}\boldsymbol{J}_\mathcal{A} - \boldsymbol{E}_S) \approx \boldsymbol{0}\,. \tag{2.36}$$

In other words, $\boldsymbol{J}_\mathcal{A}$ is an approximate solution if S is narrow with respect to $\mathcal{Z}\boldsymbol{J}_\mathcal{A} - \boldsymbol{E}_S$. If S is narrow with respect to $\boldsymbol{E}_S$, so that $(\mathcal{I}-\mathcal{A})\boldsymbol{E}_S \approx \boldsymbol{0}$, the condition turns into $(\mathcal{I}-\mathcal{A})\mathcal{Z}\boldsymbol{J}_\mathcal{A} \approx \boldsymbol{0}$. This is satisfied if S is narrow with respect to $\mathcal{Z}\boldsymbol{J}_\mathcal{A}$. Finally, we notice that the solutions of (2.17) and (2.34) are approximately equal under the condition (2.36), if they are unique and depend continuously on the right-hand sides.

The domain and the range of $\mathcal{Z}$ are linear spaces of functions $F(\Pi(S), \text{Tang}(S))$. The range of $\mathcal{A}\mathcal{Z}\mathcal{A}$ is a subset of $\text{ran}(\mathcal{A})$, which consists of functions in a linear space of functions $F(\Pi(S), \text{Tang}(S))$ with centerline dependence and centerline components only. The domain can also be regarded as such a space, because $\mathcal{A}$ is applied to each function in the domain, which yields the centerline component w. Then, we can replace $\mathcal{A}\mathcal{Z}\mathcal{A}$ by the operator $\mathcal{Z}_\text{a}$, which maps the centerline component w in $\text{ran}(\mathcal{A})$ onto the corresponding centerline component v^ex in $\text{ran}(\mathcal{A}\mathcal{Z}\mathcal{A})$. We write

$$\mathcal{Z}_\text{a} w = v^\text{ex}, \tag{2.37}$$

where $v^\text{ex} = (\boldsymbol{\tau} \bullet \mathcal{A}\boldsymbol{E}_S)$ and $\mathcal{Z}_\text{a}$ is the linear operator between linear spaces $F(\Pi_\xi(S), \mathbb{C}\,)$ that corresponds to $\mathcal{A}\mathcal{Z}\mathcal{A}$.

Let us now extend the formulation to N_el microstrip elements modeled as surfaces S_q ($q = 1, \ldots, N_\text{el}$) in the space Ω. Let S be the union of these surfaces. There exists a vector function $\boldsymbol{x}_S$ on S, such that $\boldsymbol{x}_S|_{S_q}$ is the parameter representation of S_q with parameter set $\Pi(S_q)$. Moreover, there exist vector functions $\boldsymbol{e}_\xi$ and $\boldsymbol{e}_\eta$ on S, such that $\boldsymbol{e}_\xi|_{S_q}$ and $\boldsymbol{e}_\eta|_{S_q}$ belong to $F(\Pi(S_q), \text{Tang}(S_q))$ and span $\text{Tang}(S_q, (\xi,\eta))$ in every point $\boldsymbol{x}_S|_{S_q}(\xi,\eta)$. Note that $|_{S_q}$ restricts here a vector function defined on S to S_q, whereas $|_{S^\pm}$ and $|_S$ in assumption 3 of Section 2.2 restrict a vector function defined on Ω to S. We write $\boldsymbol{x}_{S_q}$ instead of $\boldsymbol{x}_S|_{S_q}$.

Let $\boldsymbol{J}$ be the current on S, $\boldsymbol{J}|_{S_q}$ being the current on S_q. The action of $\mathcal{Z}$ on $\boldsymbol{J}$ is defined by

$$(\mathcal{Z}\boldsymbol{J})|_{S_p} = \sum_{q=1}^{N_\text{el}} \big(\mathcal{Z}(\boldsymbol{J}|_{S_q})\big)\big|_{S_p}\,. \tag{2.38}$$

Here, $(\mathcal{Z}(\boldsymbol{J}|_{S_q}))|_{S_p}$ is interpreted as the tangential electric scattered field at S_p induced by the current at S_q. The action of $\mathcal{T}$ on $\boldsymbol{J}$ is defined as in (2.38) with $\mathcal{Z}$ replaced by $\mathcal{T}$, where $(\mathcal{T}\boldsymbol{J}|_{S_q})|_{S_p}$ is interpreted as the magnetic vector potential at S_p induced by the current at S_q. To arrive at (2.34), we first need to extend the coordinate systems on each S_q and, then, to identify the operators $\mathcal{D}_{S_q}$

$$(\mathcal{D}\,\cdot\,)_{\tan}|_{S_q} = \mathcal{D}_{S_q}(\,\cdot\,|_{S_q})\,, \tag{2.39}$$

as in (2.27). Analogous to the case of a single element, we assume that $\Pi(S_q) = \Pi_\xi(S_q) \times [-\eta_q, \eta_q]$. We define the average operator $\mathcal{A}$ for tangential vector fields $\boldsymbol{u}$ on S by $(\mathcal{A}\boldsymbol{u})|_{S_q} = \mathcal{A}(\boldsymbol{u}|_{S_q})$. Moreover, we call S narrow with respect to $\boldsymbol{u}$, if each S_q is narrow with respect to $\boldsymbol{u}|_{S_q}$, and we call $\mathcal{A}\boldsymbol{u}$ the width average of $\boldsymbol{u}$, if $(\mathcal{A}\boldsymbol{u})|_{S_q}$ is the width average of $\boldsymbol{u}|_{S_q}$. Then, we can replace (2.17) by (2.34), if the condition (2.36) is satisfied. Let w_q be the centerline component of $(\mathcal{A}\boldsymbol{J})|_{S_q}$ and v_q^{ex} the centerline component of $(\mathcal{A}\boldsymbol{E}_S)|_{S_q}$. If all $\Pi_\xi(S_q)$ are the same set Π_ξ, or can be scaled to such a set, then we interpret w_q and v_q^{ex} as components of vector functions $\underline{w}$ and $\underline{v}^{\mathrm{ex}}$ in linear spaces of functions $F(\Pi_\xi, \mathbb{C}^{N_{\mathrm{el}}})$. Then, analogous to (2.37), we interpret (2.34) as

$$\mathcal{Z}_{\mathrm{a}}\underline{w} = \underline{v}^{\mathrm{ex}}\,. \tag{2.40}$$

Here, we use underlined symbols for vector functions in $F(\Pi_\xi, \mathbb{C}^{N_{\mathrm{el}}})$ to distinguish them from the vector functions on S and Ω, which are typeset in boldface. Further on, we represent vector functions in $F(\Pi_\xi, \mathbb{C}^{N_{\mathrm{el}}})$ also by boldface characters, e.g., $\boldsymbol{w}$ and $\boldsymbol{v}^{\mathrm{ex}}$.

2.3.2 Line Arrays of Strips in Free Space

We consider a planar line array of parallel identical narrow strips, S_q ($q = 1, ..., N_{\mathrm{el}}$), in free space. Let 2ℓ be the length of the strips and $\boldsymbol{c}_q$ their centers, which are all positioned on the x-axis such that $c_{q,x} < c_{q+1,x}$, see Figure 2.4. The width $2b$ of the strips satisfies $\beta := b/\ell \ll 1$ and bk is of the order β. In other words, the width of the strips is of the order β with respect their lengths and with respect to the wavelength under consideration. Moreover, we assume that $b/|\boldsymbol{c}_{q+1} - \boldsymbol{c}_q|$, i.e., the ratio of the width of the strips and the distances between the strips, is of the order β. Let the parameter representation of the strip surface S_q be given by

$$\boldsymbol{x}_{S_q}(\xi, \eta) = \boldsymbol{c}_q - \eta\boldsymbol{e}_x + \xi\boldsymbol{e}_y\,, \tag{2.41}$$

where (ξ, η) is an element of the parameter set $\Pi = \Pi(S_q) = \{\,(\xi, \eta)\,|\, -\ell \le \xi \le \ell,\, -b \le \eta \le b\,\}$. Then, each parameter representation has tangent vectors $\boldsymbol{e}_\xi = \boldsymbol{e}_y$ and $\boldsymbol{e}_\eta = -\boldsymbol{e}_x$. We note that the restriction $|_{S_q}$ becomes redundant, because $\boldsymbol{e}_\xi$ and $\boldsymbol{e}_\eta$ are fixed. Since the tangent vectors correspond to a Cartesian coordinate system, the parameter representation of each strip

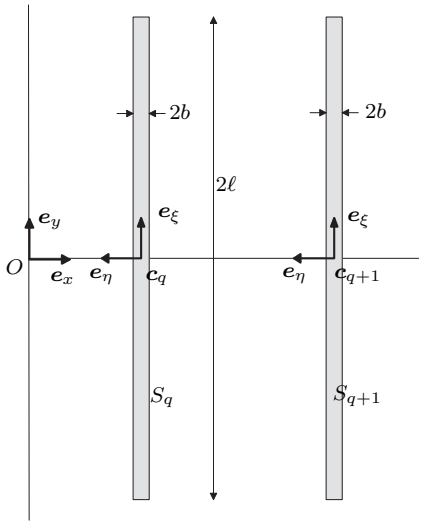

Figure 2.4 Geometry of two parallel strips.

can be extended straightforwardly to a (global) Cartesian coordinate system with $\boldsymbol{e}_\zeta = \boldsymbol{e}_z$. Moreover, since the strips are planarly positioned in free space, differential operators $\mathcal{D}_{S_q}$ as in (2.39) can be identified. From the Cartesian representation of the operator $\mathcal{D}$ defined by (2.10)[2] and the considerations above, it follows that

$$(\mathcal{Z}(\boldsymbol{J}|_{S_q}))|_{S_p} = \mathcal{D}_{S_p}\boldsymbol{A}_{pq} = -jZ_0k\left\{\left[\left(1+\frac{1}{k^2}\frac{\partial^2}{\partial\xi^2}\right)A_{pq,\xi}+\frac{1}{k^2}\frac{\partial^2}{\partial\xi\partial\eta}A_{pq,\eta}\right]\boldsymbol{e}_\xi + \right.$$
$$\left. + \left[\left(1+\frac{1}{k^2}\frac{\partial^2}{\partial\eta^2}\right)A_{pq,\eta}+\frac{1}{k^2}\frac{\partial^2}{\partial\xi\partial\eta}A_{pq,\xi}\right]\boldsymbol{e}_\eta\right\}, \quad (2.42)$$

where

$$\boldsymbol{A}_{pq} = \int_{-\ell}^{\ell}\int_{-b}^{b} g_{\mathrm{free}}\Big(R\big(\boldsymbol{x}_{S_p}(\,\cdot\,,\,\cdot\,) - \boldsymbol{x}_{S_q}(\xi',\eta')\big)\Big)\,\boldsymbol{J}|_{S_q}(\xi',\eta')\,d\eta' d\xi'. \quad (2.43)$$

The vector-valued function $\boldsymbol{A}_{pq} = (\mathcal{T}(\boldsymbol{J}|_{S_q}))|_{S_p}$ is the magnetic vector potential induced by $\boldsymbol{J}|_{S_q}$ evaluated at the surface S_p. We introduce the normalized kernel $\hat{g}_{\mathrm{free}}$ with additional normalized distance measure $\hat{R}$ and the normalized coordinates $(\hat{\xi},\hat{\eta})$ by

$$\hat{g}_{\mathrm{free}}(\hat{R}) = \frac{1}{4\pi}\frac{e^{-j\hat{R}}}{\hat{R}}, \qquad \hat{R} = kR\,, \qquad \xi = \ell\hat{\xi}, \qquad \eta = b\hat{\eta}\,, \quad (2.44)$$

where $(\xi,\eta) \in \Pi$ and $(\hat{\xi},\hat{\eta}) \in \hat{\Pi} = \{\,(\hat{\xi},\hat{\eta})\,|\,-1 \le \hat{\xi},\hat{\eta} \le l\,\}$. Notice that $g_{\rm free}(R) = k\,\hat{g}_{\rm free}(\hat{R})$. To interpret all vector functions defined on S as functions of the normalized coordinates, we need to adjust the definitions of both operators and vector functions. Interpreting $\boldsymbol{J}$ and $\mathcal{Z}\boldsymbol{J}$ as functions of the normalized coordinates, we write (2.42) as

$$(\mathcal{Z}(\boldsymbol{J}|_{S_q}))|_{S_p} = -jZ_0k^2\ell b\left\{\left[\left(1+\frac{1}{k^2\ell^2}\frac{\partial^2}{\partial\hat{\xi}^2}\right)\hat{A}_{pq,\xi}+\frac{1}{k^2\ell^2\beta}\frac{\partial^2}{\partial\hat{\xi}\partial\hat{\eta}}\,\hat{A}_{pq,\eta}\right]\boldsymbol{e}_\xi + \right.$$
$$\left. + \left[\left(1+\frac{1}{k^2\ell^2\beta^2}\frac{\partial^2}{\partial\hat{\eta}^2}\right)\hat{A}_{pq,\eta}+\frac{1}{k^2\ell^2\beta}\frac{\partial^2}{\partial\hat{\xi}\partial\hat{\eta}}\,\hat{A}_{pq,\xi}\right]\boldsymbol{e}_\eta\right\}. \quad (2.45)$$

The vector field $\hat{\boldsymbol{A}}_{pq} = \boldsymbol{A}_{pq}/\ell bk$ is given by

$$\hat{\boldsymbol{A}}_{pq} = \int_{-1}^{1}\int_{-1}^{1}\hat{g}_{\rm free}\big(\hat{R}_{pq}(\hat{\xi}-\hat{\xi}',\hat{\eta}-\hat{\eta}')\big)\,\boldsymbol{J}|_{S_q}(\hat{\xi}',\hat{\eta}')\,d\eta'd\xi'\,, \quad (2.46)$$

where

$$\hat{R}_{pq}(\hat{\xi},\hat{\eta}) = k\ell\sqrt{\hat{\xi}^2+\left(\frac{d_{pq}}{\ell}-\beta\hat{\eta}\right)^2}\;, \quad (2.47)$$

and $d_{pq} = c_{p,x} - c_{q,x}$. The relation between the normalized distance measure $\hat{R} = kR$ and the distance measure $\hat{R}_{pq}$ is

$$\hat{R}\big(\boldsymbol{x}_{S_p}(\xi,\eta) - \boldsymbol{x}_{S_q}(\xi',\eta')\big) = \hat{R}_{pq}(\hat{\xi}-\hat{\xi}',\hat{\eta}-\hat{\eta}')\,. \quad (2.48)$$

Hence, $\hat{R}_{pq}(\hat{\xi},\hat{\eta})$ is the normalized distance between an observation point $\boldsymbol{x}_{S_p}(\xi,\eta)$ on the surface S_p and the center $\boldsymbol{c}_q$ of the surface S_q, whereas $\hat{R}_{pq}(\hat{\xi}-\hat{\xi}',\hat{\eta}-\hat{\eta}')$ is the normalized distance between the former point and the source point $\boldsymbol{x}_{S_q}(\xi',\eta')$.

Given an excitation field $\boldsymbol{E}_S$, the current $\boldsymbol{J}$ can be calculated from (2.17), where $\mathcal{Z}$ is defined by (2.45) and where we interpret $\boldsymbol{E}_S$ as function of the normalized coordinates. Under the condition (2.36), Equation (2.17) can be replaced by its averaged form (2.34) and its related form (2.40). Here, we deduce an expression for the operator $\mathcal{Z}_{\rm a}$ first. Subsequently, we consider the question whether the solution of (2.34) is an approximate solution of (2.17).

Let $\boldsymbol{u}$ be a tangential vector field on S and interpret $\boldsymbol{u}$ as a function of the normalized coordinates. Then, the averaging operator $\mathcal{A}$ is defined by

$$(\mathcal{A}\boldsymbol{u})|_{S_q} = \frac{1}{2}\int_{-1}^{1} u_\xi|_{S_q}(\,\cdot\,,\hat{\eta})\,d\hat{\eta}\;\boldsymbol{e}_\xi\,, \quad (2.49)$$

which follows from the definition of $\mathcal{A}$ for functions of (ξ,η). Here, the tangent vector $\boldsymbol{\tau}$ at the centerline, given in (2.28), equals $\boldsymbol{e}_\xi$. Hence, the condition (2.31)[3] for S being narrow with

respect to $\boldsymbol{u}$ is satisfied exactly. Replacing $\boldsymbol{J}$ by $\mathcal{A}\boldsymbol{J}$ in (2.45), we obtain

$$(\mathcal{Z}\mathcal{A}(\boldsymbol{J}|_{S_q}))|_{S_p} = -jZ_0k^2\ell b\left[\left(1+\frac{1}{k^2\ell^2}\frac{\partial^2}{\partial\hat{\xi}^2}\right)\overline{\hat{A}}_{pq,\xi}\boldsymbol{e}_\xi + \frac{1}{k^2\ell^2\beta}\frac{\partial^2}{\partial\hat{\xi}\partial\hat{\eta}}\overline{\hat{A}}_{pq,\xi}\boldsymbol{e}_\eta\right], \quad (2.50)$$

where

$$\overline{\hat{A}}_{pq,\xi}(\hat{\xi},\hat{\eta}) = \int_{-1}^{1} w_q(\hat{\xi}')\, h_{pq}(\hat{\xi}-\hat{\xi}',\hat{\eta})\, d\hat{\xi}', \quad h_{pq}(\hat{\xi},\hat{\eta}) = \int_{-1}^{1} \hat{g}_{\mathrm{free}}\big(\hat{R}_{pq}(\hat{\xi},\hat{\eta}-\hat{\eta}')\big)\, d\hat{\eta}', \quad (2.51)$$

and where w_q is the centerline component of $\mathcal{A}\boldsymbol{J}$ at S_q. Note that $\overline{\hat{A}}_{pq,\eta}=0$ and that $\overline{\hat{\boldsymbol{A}}}_{pq}$ is the vector potential induced by $(\mathcal{A}\boldsymbol{J})|_{S_q}$ evaluated at S_p. Applying $\mathcal{A}$ to $\mathcal{Z}\mathcal{A}$, we obtain

$$(\mathcal{A}\mathcal{Z}\mathcal{A}(\boldsymbol{J}|_{S_q}))|_{S_p} = -\frac{1}{2}\,jZ_0k^2\ell b\int_{-1}^{1}\left(\Big(1+\frac{1}{k^2\ell^2}\frac{\partial^2}{\partial\hat{\xi}^2}\Big)\overline{\hat{A}}_{pq,\xi}\right)(\,\cdot\,,\hat{\eta})\, d\hat{\eta}\;\boldsymbol{e}_\xi\,. \quad (2.52)$$

We note that the η-component of $(\mathcal{Z}\mathcal{A}(\boldsymbol{J}|_{S_q}))|_{S_q}$ does not only vanish when we apply $\mathcal{A}$, but also when we only integrate (2.50) from -1 to 1 with respect to $\hat{\eta}$, because h_{qq} is odd in $\hat{\eta}$ and, hence, $\partial\overline{\hat{A}}_{qq,\xi}/\partial\hat{\eta}$ is odd in $\hat{\eta}$ as well. We rewrite (2.52) by interchanging the integral with respect to $\hat{\eta}'$ and the Helmholtz operator. Next, we interchange the integral with respect to $\hat{\eta}'$ and the integral with respect to $\hat{\xi}'$ in $\hat{A}_{pq,\xi}$. Moreover, we interpret the operator $\mathcal{A}\mathcal{Z}\mathcal{A}$ as $\mathcal{Z}_{\mathrm{a}}$ in (2.40) with $\boldsymbol{w}=(w_1,\ldots,w_{N_{\mathrm{el}}})\in F([-1,1],\mathbb{C}^{N_{\mathrm{el}}})$. Then,

$$(\mathcal{Z}_{\mathrm{a}}\boldsymbol{w})_p = -\frac{1}{2}\,jZ_0k^2\ell b\sum_{q=1}^{N_{\mathrm{el}}}\left(1+\frac{1}{k^2\ell^2}\frac{d^2}{d\xi^2}\right)\mathcal{F}_{pq}w_q, \quad (2.53)$$

where

$$(\mathcal{F}_{pq}w_q)(\xi) = \int_{-1}^{1} w_q(\xi')F_{pq}(\xi-\xi')\, d\xi', \;\; \xi\in[-1,1], \quad (2.54)$$

and

$$F_{pq}(\xi) = \int_{-1}^{1}\int_{-1}^{1}\hat{g}_{\mathrm{free}}\big(\hat{R}_{pq}(\xi,\eta-\eta')\big)\, d\eta' d\eta\,. \quad (2.55)$$

In these expressions, the hats on the normalized coordinates are omitted. Moreover, $\xi\in[-2,2]$ in (2.55). The function F_{pq} is called the averaged kernel. To reduce the expression for this kernel to a single integral, we introduce the following definitions. Let the inner product $\langle\,\cdot\,,\,\cdot\,\rangle_\infty$ and the convolution $.\;*\;.$ be defined by

$$\langle f,g\rangle_\infty = \int_{-\infty}^{\infty} f^*(x)\, g(x)\, dx\,, \qquad (f*g)(x) = \int_{-\infty}^{\infty} f(x')\, g(x-x')\, dx'\,, \quad (2.56)$$

for functions f and g with bounded support. We note that the superscript * denotes the complex conjugate as in (2.4). Let the characteristic function 1_χ for a set χ be defined by $1_\chi(x) = 1$ for $x \in \chi$ and $1_\chi(x) = 0$ for $x \notin \chi$. Finally, for a function g, we define the function $g^\vee$ by $g^\vee(x) = g(-x)$. Then, interpreting (2.55) as the inner product of the characteristic function $1_{[-1,1]}$ and the convolution $1_{[-1,1]} * \hat{g}_{\rm free}(\hat{R}_{pq}(\xi, \cdot))\, 1_{[-2,2]}$ and employing the identity $\langle f, g * h\rangle_\infty = \langle h^*, f^* * g^\vee\rangle_\infty$, we arrive at

$$F_{pq}(\xi) = \int_{-2}^{2} (2 - |\eta|)\, \hat{g}_{\rm free}\big(\hat{R}_{pq}(\xi,\eta)\big)\, d\eta\,, \tag{2.57}$$

where

$$\hat{g}_{\rm free}(\hat{R}_{pq}(\xi,\eta)) = \frac{1}{4\pi} \frac{\exp\left(-jk\ell\sqrt{\xi^2 + (d_{pq}/\ell - \beta\eta)^2}\right)}{k\ell\sqrt{\xi^2 + (d_{pq}/\ell - \beta\eta)^2}}\,. \tag{2.58}$$

For $p = q$, the integral in (2.57) can be rewritten as

$$F_{qq}(\xi) = \frac{1}{\pi k\ell\beta}\left[-\frac{1}{2}\log\xi^2 + \log\left(2\beta + \sqrt{4\beta^2 + \xi^2}\right)\right] + \frac{1}{2\pi j k^2\ell^2\beta^2}\Big[-\exp(-jk\ell|\xi|) + \\ + \exp\left(-jk\ell\sqrt{4\beta^2 + \xi^2}\right)\Big] + \frac{1}{\pi k\ell}\int_{\eta=0}^{2} \frac{\exp\left(-jk\ell\sqrt{\xi^2 + \beta^2\eta^2}\right) - 1}{\sqrt{\xi^2 + \beta^2\eta^2}}\, d\eta\,, \tag{2.59}$$

see Appendix A. The expressions (2.57) and (2.59) show that F_{pq} is continuous for $p \neq q$, whereas it has a logarithmic singularity for $p = q$.

The solution $\boldsymbol{w}$ of (2.40), with $\mathcal{Z}_{\rm a}$ given by (2.53), corresponds to the solution of (2.34), say $\boldsymbol{J}_{\mathcal{A}}$ with $\boldsymbol{J}_{\mathcal{A}} = \mathcal{A}\boldsymbol{J}_{\mathcal{A}}$. To answer the question whether $\boldsymbol{J}_{\mathcal{A}}$ is an approximate solution of (2.17), we need to verify the condition (2.36). By approximate we mean in the sense of the functional metric related to (2.31). However, since we have not yet specified the metric, we use here a dimensional argument to show that $\boldsymbol{J}_{\mathcal{A}}$ is an approximate solution of (2.17) in case S is narrow with respect to $\boldsymbol{E}_S$. Moreover, we show that this argument cannot be used in case S is not narrow with respect to $\boldsymbol{E}_S$. We start by considering the term $(\mathcal{Z}(\boldsymbol{J}_{\mathcal{A}}|_{S_p}))|_{S_p}$ in

$$(\mathcal{Z}\boldsymbol{J}_{\mathcal{A}})|_{S_p} = \big(\mathcal{Z}(\boldsymbol{J}_{\mathcal{A}}|_{S_p})\big)|_{S_p} + \sum_{q\neq p} \big(\mathcal{Z}(\boldsymbol{J}_{\mathcal{A}}|_{S_q})\big)\big|_{S_p}\,. \tag{2.60}$$

From the definition of $\hat{R}_{pp}$, it follows that $\partial\hat{R}_{pp}/\partial\hat{\eta}$ is of the order β^2 with respect to $\partial\hat{R}_{pp}/\partial\hat{\xi}$. Then, it follows that $\partial\hat{A}_{pp,\xi}/\partial\hat{\eta}$ is of the order β^2 with respect to $\partial\hat{A}_{pp,\xi}/\partial\hat{\xi}$. Hence, the η-component of $(\mathcal{Z}(\boldsymbol{J}_{\mathcal{A}}|_{S_p}))|_{S_p}$ is of the order β with respect to its ξ-component, see (2.50). Moreover, $\partial(\mathcal{Z}(\boldsymbol{J}_{\mathcal{A}}|_{S_p}))|_{S_p}/\partial\hat{\eta}$ is of the order β^2 with respect to $\partial(\mathcal{Z}(\boldsymbol{J}_{\mathcal{A}}|_{S_p}))|_{S_p}/\partial\hat{\xi}$. Hence, $(\mathcal{Z}(\boldsymbol{J}_{\mathcal{A}}|_{S_p}))|_{S_p}$ satisfies the conditions (2.31) for S_p being narrow with respect to

$(\mathcal{Z}(\boldsymbol{J}_{\mathcal{A}}|_{S_p}))|_{S_p}$, where '$\approx$' needs to be interpreted as equal up to terms of order β. We cannot apply the same reasoning to show that S_p is narrow with respect to $(\mathcal{Z}(\boldsymbol{J}_{\mathcal{A}}|_{S_q}))|_{S_p}$ for $q \neq p$ and thereby, that S_p is narrow with respect to $(\mathcal{Z}\boldsymbol{J}_{\mathcal{A}})|_{S_p}$ in (2.60). Since $\partial\hat{R}_{pq}/\partial\hat{\eta}$ is of the order β, and not of the order β^2, with respect to $\partial\hat{R}_{pq}/\partial\hat{\xi}$, it seems that the components of $(\mathcal{Z}(\boldsymbol{J}_{\mathcal{A}}|_{S_q}))|_{S_p}$ are of the same order. Therefore, we need another argument to show that S_p is narrow with respect to $(\mathcal{Z}(\boldsymbol{J}_{\mathcal{A}}|_{S_q}))|_{S_p}$. By the assumption $b/|d_{pq}| = O(\beta)$, it follows that $(\mathcal{Z}(\boldsymbol{J}_{\mathcal{A}}|_{S_q}))|_{S_p}$ with $q \neq p$ is of order β with respect to $(\mathcal{Z}(\boldsymbol{J}_{\mathcal{A}}|_{S_p}))|_{S_p}$. Combining this result with the result that S_p is narrow with respect to $(\mathcal{Z}(\boldsymbol{J}_{\mathcal{A}}|_{S_p}))|_{S_p}$, we find that S_p is narrow with respect to $(\mathcal{Z}\boldsymbol{J}_{\mathcal{A}})|_{S_p}$. Then, S is narrow with respect to $\mathcal{Z}\boldsymbol{J}_{\mathcal{A}}$, and hence $(\mathcal{I}-\mathcal{A})\mathcal{Z}\boldsymbol{J}_{\mathcal{A}} \approx \boldsymbol{0}$. Notice that this result is independent of $\boldsymbol{E}_S$ and that we use the property $\boldsymbol{J}_{\mathcal{A}} = \mathcal{A}\boldsymbol{J}_{\mathcal{A}}$ only. The question whether $\boldsymbol{J}_{\mathcal{A}}$ is an approximate solution of (2.17) can now be answered as follows. Since $(\mathcal{I}-\mathcal{A})\mathcal{Z}\boldsymbol{J}_{\mathcal{A}} \approx \boldsymbol{0}$, the condition (2.36) is satisfied if $(\mathcal{I}-\mathcal{A})\boldsymbol{E}_S \approx \boldsymbol{0}$, i.e., if S is narrow with respect to $\boldsymbol{E}_S$. If S is not narrow with respect to $\boldsymbol{E}_S$, this condition is in general not satisfied.

The calculation of F_{pq} from (2.57) is expensive with respect to CPU-time, because of the evaluation of the integral. To reduce computational effort, we may replace F_{pq} by an approximate kernel. As we observed above, replacing $\mathcal{Z}\boldsymbol{J} = \boldsymbol{E}_S$ by $\mathcal{A}\mathcal{Z}\mathcal{A}\boldsymbol{J} = \mathcal{A}\boldsymbol{E}_S$ means neglecting terms of order β. This suggests to approximate the kernel also by neglecting terms of order β. For $p \neq q$, we consider the kernel expression (2.57). By the assumption $b/|d_{pq}| = O(\beta)$, we obtain the asymptotic expansion

$$F_{pq}(\xi) = \frac{1}{\pi k\ell}\frac{\exp\left(-jk\ell\sqrt{\xi^2 + d_{pq}^2/\ell^2}\right)}{\sqrt{\xi^2 + d_{pq}^2/\ell^2}}\left(1 + O(\beta^2)\right), \quad p \neq q\,. \tag{2.61}$$

We note that terms of order β are annihilated by the double integration in the definition of F_{pq}. The term of order 1 in the right-hand side of (2.61) equals $4\,\hat{g}_{\mathrm{free}}(\hat{R}_{pq}(\xi,0))$.

For $p = q$, we consider the kernel expression (2.59). For $\xi = O(1)$ (as $\beta \downarrow 0$), the integral has the asymptotic expansion

$$\int_{\eta=0}^{2} \frac{\exp\left(-jk\ell\sqrt{\xi^2 + \beta^2\eta^2}\right) - 1}{\sqrt{\xi^2 + \beta^2\eta^2}}\,d\eta = \frac{2\left(\exp(-jk\ell|\xi|) - 1\right)}{|\xi|}\left(1 + O(\beta^2)\right). \tag{2.62}$$

This expansion is valid for $\xi = O(1)$. For $\xi = O(\beta)$, the term $O(\beta^2)$ is replaced by $O(\beta)$, which follows from the asymptotics of the exponential under the condition that $k\ell = O(1)$. This condition indicates that the asymptotic expansion is valid for strip lengths of the order of the wavelength and for strip lengths much smaller than the wavelength. We note that the integral in (2.62) has asymptotic expansion $-2jk\ell(1 + O(\beta))$ for $\xi = 0$, because $bk = O(\beta)$.

For the other two terms in (2.59), enclosed by $[\ldots]$, asymptotic expansions can be deduced as well. However, these expansions are not valid over the entire range of ξ. Therefore, we

choose to approximate the kernel F_{pq} by neglecting terms of order β in (2.61) and in the integral of (2.59) only. We denote the approximate kernel by $\tilde{F}_{pq}$,

$$\begin{aligned}\tilde{F}_{qq}(\xi) &= \frac{1}{\pi k\ell\beta}\left[-\frac{1}{2}\log\xi^2 + \log\left(2\beta+\sqrt{4\beta^2+\xi^2}\right)\right] + \frac{2}{\pi k\ell}\frac{\exp(-jk\ell|\xi|)-1}{|\xi|} + \\ &+ \frac{1}{2\pi jk^2\ell^2\beta^2}\left[\exp\left(-jk\ell\sqrt{4\beta^2+\xi^2}\right) - \exp(-jk\ell|\xi|)\right], \\ \tilde{F}_{pq}(\xi) &= \frac{1}{\pi k\ell}\frac{\exp\left(-jk\ell\sqrt{\xi^2+d_{pq}^2/\ell^2}\right)}{\sqrt{\xi^2+d_{pq}^2/\ell^2}}, \qquad p\neq q.\end{aligned} \tag{2.63}$$

The integral operator that results from replacing F_{pq} by $\tilde{F}_{pq}$ in (2.54) is denoted by $\tilde{\mathcal{F}}_{pq}$.

Finally, we notice that the equation $\mathcal{Z}\boldsymbol{J} = \boldsymbol{E}_S$ in (2.17) has been replaced by another operator equation in two separate steps. The first step, up to (2.59), concerns the deduction of the averaged operator $\mathcal{Z}_{\mathrm{a}}$. The second step concerns the replacement of the averaged kernel resulting from the first step by an approximate kernel.

2.3.3 Arrays of Rings in Free Space

We consider a planar array of rings, S_q ($q = 1, ..., N_{\mathrm{el}}$), in free space. Let a_q be the radii of the rings and let $\boldsymbol{c}_q$ be their centers in the xy-plane, see Figure 2.5. The widths $2b_q$ of the rings satisfy $\beta_q := b_q/a_q \ll 1$ and $b_q k = O(\beta)$ with $\beta = \max(\beta_q)$. In other words, the widths of the rings are of the order β with respect to their radii and with respect to the wavelength under consideration. Moreover, we assume that the widths of the rings are of the order β with respect to the distances between the rings, i.e., $b_q/(|\boldsymbol{c}_p - \boldsymbol{c}_q| - a_p - a_q) = O(\beta)$ for $p \neq q$.

Let the parameter representation of the ring surface S_q be given by

$$\boldsymbol{x}_{S_q}(r,\varphi) = \boldsymbol{c}_q + r\cos(\varphi+\psi_q)\boldsymbol{e}_x + r\sin(\varphi+\psi_q)\boldsymbol{e}_y\,, \tag{2.64}$$

where (r,φ) is an element of the parameter set $\Pi(S_q) = \{\,(r,\varphi)\,|\,a_q - b_q \le r \le a_q + b_q,\ -\pi < \varphi \le \pi\,\}$. Let $\boldsymbol{e}_r$ and $\boldsymbol{e}_\varphi$ be the corresponding vector fields such that $\boldsymbol{e}_r|_{S_q}$ and $\boldsymbol{e}_\varphi|_{S_q}$ are the tangent vectors of S_q. Then,

$$\begin{aligned}\boldsymbol{e}_r|_{S_q}(\varphi) &= \cos(\varphi+\psi_q)\boldsymbol{e}_x + \sin(\varphi+\psi_q)\boldsymbol{e}_y\,, \\ \boldsymbol{e}_\varphi|_{S_q}(\varphi) &= -\sin(\varphi+\psi_q)\boldsymbol{e}_x + \cos(\varphi+\psi_q)\boldsymbol{e}_y\,.\end{aligned} \tag{2.65}$$

Interpreting $\varphi \to \boldsymbol{e}_r|_{S_q}(\varphi)$ as a vector-valued function, we can describe the parameter representation (2.64) by $\boldsymbol{x}_{S_q} = \boldsymbol{c}_q + r\boldsymbol{e}_r|_{S_q}$. Since the tangent vectors correspond to cylindrical coordinate systems, the parameter representation of each ring can be extended straightforwardly

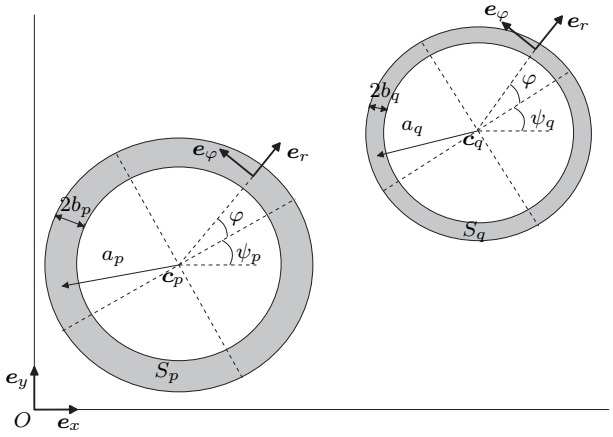

Figure 2.5 Geometry of two rings.

to a (global) cylindrical coordinate system. Moreover, since the rings are planarly positioned in free space, differential operators $\mathcal{D}_{S_q}$ as in (2.39) can be identified. From the cylindrical coordinate representation of the operator $\mathcal{D}$ defined by (2.10)[2] and the considerations above, it follows that

$$
\begin{aligned}
&(\mathcal{Z}(\boldsymbol{J}|_{S_q}))|_{S_p} = \mathcal{D}_{S_p}\boldsymbol{A}_{pq} = \\
&-jZ_0k\left\{\left[A_{pq,r} + \frac{1}{k^2}\left(\frac{\partial}{\partial r}\left(\frac{1}{r}\frac{\partial}{\partial r}\right)(rA_{pq,r}) + \frac{\partial}{\partial r}\left(\frac{1}{r}\frac{\partial}{\partial \varphi}\right)A_{pq,\varphi}\right)\right]\boldsymbol{e}_r|_{S_p} + \right. \\
&\qquad\left. + \left[A_{pq,\varphi} + \frac{1}{k^2}\left(\frac{1}{r^2}\frac{\partial^2}{\partial\varphi\partial r}(rA_{pq,r}) + \frac{1}{r^2}\frac{\partial^2}{\partial\varphi^2}A_{pq,\varphi}\right)\right]\boldsymbol{e}_\varphi|_{S_p}\right\}, \quad (2.66)
\end{aligned}
$$

where

$$
\boldsymbol{A}_{pq} = \int_{-\pi}^{\pi}\int_{a_q-b_q}^{a_q+b_q} g_{\mathrm{free}}\Big(R\big(\boldsymbol{x}_{S_p}(\,\cdot\,,\,\cdot\,) - \boldsymbol{x}_{S_q}(r',\varphi)\big)\Big)\,\boldsymbol{J}|_{S_q}(r',\varphi)\,r'\,dr'd\varphi\,. \quad (2.67)
$$

As before, $\boldsymbol{A}_{pq} = (\mathcal{T}(\boldsymbol{J}|_{S_q})|_{S_p}$ is the magnetic vector potential induced by $\boldsymbol{J}|_{S_q}$ evaluated at the surface S_p. We introduce the normalized kernel $\hat{g}_{\mathrm{free}}$ with additional normalized distance measure $\hat{R}$, see (2.44). Moreover, we introduce the normalized coordinate $\hat{r}$ by $r = a_q(1+\beta_q\hat{r})$ with $(\hat{r},\varphi) \in \hat{\Pi} = \{\,(\hat{r},\varphi)\,|\,-1 \le \hat{r} \le 1, -\pi < \varphi \le \pi\,\}$. We note that $\hat{r} = 0$ on the centerlines of the rings. To interpret all vector functions defined on S as functions of the normalized coordinates, we need to adjust the definitions of both operators and vector functions.

Interpreting $\boldsymbol{J}$ and $\mathcal{Z}\boldsymbol{J}$ as functions of the normalized coordinates, we write (2.66) as

$$(\mathcal{Z}(\boldsymbol{J}|_{S_q}))|_{S_p} = -jZ_0k^2a_qb_q\Bigg\{\Bigg[\hat{A}_{pq,r} + \frac{1}{k^2a_p^2}\Bigg(\frac{1}{\beta_p^2}\frac{\partial}{\partial\hat{r}}\left(\frac{1}{1+\beta_p\hat{r}}\frac{\partial}{\partial\hat{r}}\left((1+\beta_p\hat{r})\hat{A}_{pq,r}\right)\right) + \\ + \frac{1}{\beta_p}\frac{\partial}{\partial\hat{r}}\left(\frac{1}{1+\beta_p\hat{r}}\frac{\partial}{\partial\varphi}\right)\hat{A}_{pq,\varphi}\Bigg)\Bigg]\boldsymbol{e}_r|_{S_p} + \Bigg[\hat{A}_{pq,\varphi} + \\ + \frac{1}{k^2a_p^2(1+\beta_p\hat{r})^2}\left(\frac{1}{\beta_p}\frac{\partial^2}{\partial\varphi\partial\hat{r}}\left((1+\beta_p\hat{r})\hat{A}_{pq,r}\right) + \frac{\partial^2}{\partial\varphi^2}\hat{A}_{pq,\varphi}\right)\Bigg]\boldsymbol{e}_\varphi|_{S_p}\Bigg\}. \quad (2.68)$$

The vector field $\hat{\boldsymbol{A}}_{pq} = \boldsymbol{A}_{pq}/a_qb_qk$ is given by

$$\hat{\boldsymbol{A}}_{pq} = \int_{-\pi}^{\pi}\int_{-1}^{1}\hat{g}_{\mathrm{free}}\big(\hat{R}_{pq}(\hat{r},\hat{r}',\varphi,\varphi')\big)\,\boldsymbol{J}|_{S_q}(\hat{r}',\varphi)\,(1+\beta_p\hat{r}')\,d\hat{r}'d\varphi\,, \quad (2.69)$$

where

$$\hat{R}_{pq}(\hat{r},\hat{r}',\varphi,\varphi') = k\left|\boldsymbol{c}_p + a_p(1+\beta_p\hat{r})\,\boldsymbol{e}_r|_{S_p}(\varphi) - \boldsymbol{c}_q - a_q(1+\beta_q\hat{r}')\,\boldsymbol{e}_r|_{S_q}(\varphi')\right|. \quad (2.70)$$

Contrary to the distance measure $\hat{R}_{pq}$ of the strips in (2.46) and (2.47), the distance measure in (2.69) and (2.70) depends for $p \neq q$ on all four local coordinates of the source and observation points, $\boldsymbol{x}_{S_q}$ and $\boldsymbol{x}_{S_p}$ respectively, and for $p = q$ on r, r' and $\varphi - \varphi'$.

As in the previous subsection, we first deduce an expression for $\mathcal{Z}_{\mathrm{a}}$ and then, we construct approximations for the averaged kernels obtained in the first step. After that, we consider the question whether the solution of (2.34) is an approximate solution of (2.17). Let $\boldsymbol{u}$ be a tangential vector field on S and interpret $\boldsymbol{u}$ as a function of the normalized coordinates. Then, the averaging operator $\mathcal{A}$ is defined by

$$(\mathcal{A}\boldsymbol{u})|_{S_q} = \frac{1}{2}\int_{-1}^{1}u_\varphi|_{S_q}(\hat{r},\,\cdot\,)\,(1+\beta_q\hat{r})\,d\hat{r}\;\boldsymbol{e}_\varphi|_{S_q}\,, \quad (2.71)$$

which follows from its definition as a function (r,φ). Notice that the tangent vector $\boldsymbol{\tau}$ at the centerline, given in (2.28), equals $\boldsymbol{e}_\varphi$. Hence, the condition (2.31)^3 for S being narrow with respect to $\boldsymbol{u}$ is satisfied exactly. Replacing $\boldsymbol{J}$ by $\mathcal{A}\boldsymbol{J}$ in (2.68), we obtain for $(\mathcal{Z}\mathcal{A}(\boldsymbol{J}|_{S_q}))|_{S_p}$ the same expression as in (2.68) for $(\mathcal{Z}(\boldsymbol{J}|_{S_q}))|_{S_p}$, but with $\hat{\boldsymbol{A}}_{pq}$ replaced by $\overline{\hat{\boldsymbol{A}}}_{pq}$, i.e., $\hat{\boldsymbol{A}}_{pq}$ with $\boldsymbol{J}|_{S_q}$ replaced by $(\mathcal{A}\boldsymbol{J})|_{S_q}$. The components of $\overline{\hat{\boldsymbol{A}}}_{pq}$ are given by

$$\overline{\hat{A}}_{pq,\left\{\begin{smallmatrix}r\\ \varphi\end{smallmatrix}\right\}} = \int_{-\pi}^{\pi}h_{pq}(\hat{r},\varphi,\varphi')\,w_q(\varphi')\begin{Bmatrix}\sin(\varphi-\varphi'+\psi_p-\psi_q)\\ \cos(\varphi-\varphi'+\psi_p-\psi_q)\end{Bmatrix}d\varphi'\,, \quad (2.72)$$

$$h_{pq}(\hat{r},\varphi,\varphi') = \int_{-1}^{1}\hat{g}_{\mathrm{free}}\big(\hat{R}_{pq}(\hat{r},\hat{r}',\varphi,\varphi')\big)\,(1+\beta_q\hat{r}')\,d\hat{r}'\,, \quad (2.73)$$

where w_q is the centerline component of $\mathcal{A}\boldsymbol{J}$ at S_q. Applying $\mathcal{A}$ to $\mathcal{Z}\mathcal{A}$, we obtain

$$(\mathcal{A}\mathcal{Z}\mathcal{A}(\boldsymbol{J}|_{S_q}))|_{S_p} = -\frac{1}{2}\,jZ_0k^2a_qb_q\Bigg[\int_{-1}^{1}(1+\beta_p\hat{r})\overline{\hat{A}}_{pq,\varphi}\,d\hat{r}+$$

$$+\,\frac{1}{k^2a_p^2\beta_p}\frac{d}{d\varphi}\int_{-1}^{1}\frac{1}{1+\beta_p\hat{r}}\frac{\partial}{\partial\hat{r}}\left((1+\beta_p\hat{r})\overline{\hat{A}}_{pq,r}\right)d\hat{r}+\frac{1}{k^2a_p^2}\frac{d}{d\varphi^2}\int_{-1}^{1}\frac{\overline{\hat{A}}_{pq,\varphi}}{1+\beta_p\hat{r}}\,d\hat{r}\Bigg]\boldsymbol{e}_{\varphi}|_{S_p}\,, \tag{2.74}$$

where we interchanged integration with respect to $\hat{r}$ and differentiation with respect to φ. We rewrite the second integral by integration by parts, which yields the boundary term $\overline{\hat{A}}_{pq,r}(1,\varphi)-\overline{\hat{A}}_{pq,\varphi}(-1,\varphi)$ and an integral without derivative with respect to $\hat{r}$. After that, we rewrite the three remaining integrals in (2.74) by interchanging integrations with respect to $\hat{r}$ and φ, the latter of which is incorporated in $\overline{\hat{\boldsymbol{A}}}_{pq}$. Interpreting the operator $\mathcal{A}\mathcal{Z}\mathcal{A}$ as $\mathcal{Z}_{\mathrm{a}}$ in (2.40) with $\boldsymbol{w}=(w_1,\dots,w_{N_{\mathrm{el}}})\in F([-\pi,\pi],\mathbb{C}^{N_{\mathrm{el}}})$, we arrive at

$$(\mathcal{Z}_{\mathrm{a}}\boldsymbol{w})_p = -\frac{1}{2}\,jZ_0k^2\sum_{q=1}^{N_{\mathrm{el}}}a_qb_q\left[\mathcal{K}_{11,pq}+\frac{1}{k^2a_p^2}\left(\frac{d^2}{d\varphi^2}\mathcal{K}_{12,pq}+\frac{d}{d\varphi}\mathcal{K}_{2,pq}\right)\right]w_q\,, \tag{2.75}$$

where

$$\begin{aligned}(\mathcal{K}_{1i,pq}w_q)(\varphi) &= \int_{-\pi}^{\pi}K_{1i,pq}(\varphi,\varphi')\,\cos(\varphi-\varphi'+\psi_p-\psi_q)\,w_q(\varphi')\,d\varphi'\,,\\ (\mathcal{K}_{2,pq}w_q)(\varphi) &= \int_{-\pi}^{\pi}K_{2,pq}(\varphi,\varphi')\,\sin(\varphi-\varphi'+\psi_p-\psi_q)\,w_q(\varphi')\,d\varphi'\,.\end{aligned} \tag{2.76}$$

The kernels $K_{1i,pq}$ and $K_{2,pq}$ are defined by

$$\begin{aligned}K_{1i,pq}(\varphi,\varphi') &= \int_{-1}^{1}\int_{-1}^{1}\hat{g}_{\mathrm{free}}\big(\hat{R}_{pq}(r,r',\varphi,\varphi')\big)\,(1+\beta_pr)^{\iota(i)}(1+\beta_qr')\,dr'dr\,,\\ K_{2,pq}(\varphi,\varphi') &= \frac{1}{\beta_p}\left[h_{pq}(1,\varphi,\varphi')-h_{pq}(-1,\varphi,\varphi')\right]+K_{12,pq}(\varphi,\varphi')\,,\end{aligned} \tag{2.77}$$

where $\iota(1)=1$, $\iota(2)=-1$, and where the hat on the normalized radial coordinate is omitted.

Having deduced an expression for $\mathcal{Z}_{\mathrm{a}}$, we construct approximations for the averaged kernels $K_{1i,pq}$ and $K_{2,pq}$ in (2.77). As in the analysis of the strips, we will see that replacing $\mathcal{Z}\boldsymbol{J}=\boldsymbol{E}_S$ by $\mathcal{A}\mathcal{Z}\mathcal{A}\boldsymbol{J}=\mathcal{A}\boldsymbol{E}_S$ means neglecting terms of order β. This suggests to approximate the kernels by neglecting terms of order β as well. We consider the case $p=q$ first. The normalized distance measure $\hat{R}_{qq}$ is written as

$$\hat{R}_{qq}(r,r',\varphi)=ka_q\sqrt{\beta_q^2(r-r')^2\,+\,2\left(1+\beta_q(r+r')+\beta_q^2rr'\right)(1-\cos\varphi)}\,. \tag{2.78}$$

Here, we use that for $p = q$, all functions in (2.77) depend on $\varphi - \varphi'$ only and not on both φ and φ'. Therefore, we write $K_{1i,qq}(\varphi - \varphi')$ and $K_{2,qq}(\varphi - \varphi')$ in (2.76), and we consider all functions in (2.77) as functions of a single variable φ only. Neglecting terms of order β_q in the integrands of $K_{1i,qq}$, we arrive for both $i = 1$ and $i = 2$ at the approximate kernel

$$\breve{K}_{1,qq}(\varphi) = \int_{-1}^{1}\int_{-1}^{1} \hat{g}_{\text{free}}\big(\tilde{R}_{qq}(r-r',\varphi)\big)\, dr dr' \,, \quad \tilde{R}_{qq}(r,\varphi) = ka_q\sqrt{\beta_q^2 r^2 + 4\sin^2(\varphi/2)}\,. \tag{2.79}$$

The term $\beta_q^2 r^2$ accounts for the singular behavior of the integrand of $K_{1i,qq}$ for $(r,\varphi) = (r',\varphi')$. Therefore, this term cannot be neglected. The approximate kernel $\breve{K}_{1,qq}$ equals the averaged kernel of the strips in the following sense. Write F_{qq} in (2.57) as a function of its argument ξ and the parameters $k\ell$ and β, $F_{qq}(\xi; k\ell, \beta)$. Then, $\breve{K}_{1,qq}(\varphi) = F_{qq}(2\sin(\varphi/2); ka_q, \beta_q)$. Replacing F_{qq} by the approximate kernel $\tilde{F}_{qq}$ in (2.63), we obtain a second approximate kernel for $K_{1i,qq}$:

$$\tilde{K}_{1,qq}(\varphi) = \tilde{F}_{qq}\big(2\sin(\varphi/2); ka_q, \beta_q\big)\,. \tag{2.80}$$

To deduce an approximate kernel for $K_{2,qq}$, we consider first the difference $h_{qq}(1,\varphi) - h_{qq}(-1,\varphi)$ in (2.77)^2. By (2.73), it follows that

$$\begin{aligned} h_{qq}(1,\varphi) - h_{qq}(-1,\varphi) = \int_{-1}^{1} \Big\{ &\hat{g}_{\text{free}}\big(\hat{R}_{qq}(1,r',\varphi)\big) - \hat{g}_{\text{free}}\big(\hat{R}_{qq}(-1,-r',\varphi)\big) + \\ &+ \beta_q \Big[\hat{g}_{\text{free}}\big(\hat{R}_{qq}(1,r',\varphi)\big) + \hat{g}_{\text{free}}\big(\hat{R}_{qq}(-1,-r',\varphi)\big)\Big] r' \Big\}\, dr' \,. \end{aligned} \tag{2.81}$$

The distance measure $\hat{R}_{qq}$ is asymptotically expanded as

$$\hat{R}_{qq}(r,r',\varphi) = \tilde{R}_{qq}(r-r',\varphi)\Big(1 + \beta_q \Gamma_q(r,r',\varphi) + O(\beta_q^2)\Big), \tag{2.82}$$

where

$$\Gamma_q(r,r',\varphi) = \frac{2k^2 a_q^2 (r+r')\sin^2(\varphi/2)}{\tilde{R}_{qq}^2(r-r',\varphi)} = \frac{2(r+r')\sin^2(\varphi/2)}{\beta_q^2(r-r')^2 + 4\sin^2(\varphi/2)}\,. \tag{2.83}$$

A necessary condition for this asymptotic expansion to be valid is that $2\beta_q|\Gamma_q(r,r',\varphi)| < 1$, which is satisfied because $|\Gamma_q(r,r',\varphi)| \le |r+r'|/2 \le 1$ for $-1 \le r, r' \le 1$. Using the derived expansions

$$\hat{R}_{qq}(\pm 1, \pm r', \varphi) = \tilde{R}_{qq}(1-r',\varphi)\Big(1 \pm \beta_q \Gamma_q(1,r',\varphi) + O(\beta_q^2)\Big), \tag{2.84}$$

we deduce from (2.81)

$$h_{qq}(1,\varphi) - h_{qq}(-1,\varphi) = -\frac{\beta_q}{2\pi}\int_{-1}^{1} \frac{\exp\big(-j\tilde{R}_{qq}(1-r',\varphi)\big)}{\tilde{R}_{qq}(1-r',\varphi)} \times$$
$$\times \Big[\Gamma_q(1,r',\varphi)\Big(1+j\tilde{R}_{qq}(1-r',\varphi)+O(\beta_q)\Big) - r'\Big(1+O(\beta_q^2)\Big)\Big]\, dr' \,. \quad (2.85)$$

We return to the kernel $K_{2,qq}$ as given in (2.77)[2] and neglect terms of order β_q in the integrand of the kernel $K_{12,qq}$ and in the integrand of (2.85). Then, $K_{12,qq}$ turns into the approximate kernel (2.79)[1], which equals $F_{qq}(2\sin(\varphi/2); ka_q, \beta_q)$ as shown above. Rewriting F_{qq} as in (2.57) and replacing the integration variable in (2.85) by $\eta = 1 - r'$, we sum the two terms in $K_{2,qq}$ to obtain the approximation

$$\breve{K}_{2,qq}(\varphi) = \frac{1}{2\pi}\int_0^2 \frac{\exp(-j\tilde{R}_{qq}(\eta,\varphi))}{\tilde{R}_{qq}(\eta,\varphi)} \times$$
$$\times \left[1 - \frac{2k^2a_q^2(2-\eta)\sin^2(\varphi/2)}{\tilde{R}_{qq}^2(\eta,\varphi)}\Big(1+j\tilde{R}_{qq}(\eta,\varphi)\Big)\right] d\eta \,. \quad (2.86)$$

To reduce the computational effort of the evaluation of the kernel $K_{2,qq}$ further, we write $\breve{K}_{2,qq}(\varphi) = K(2\sin(\varphi/2); ka_q, \beta_q, 0)$, where K is defined by (A.4) in Appendix A with approximation $\tilde{K}$ given by (A.16). This approximation can be used to approximate $\breve{K}_{2,qq}$ if $ka_q = O(1)$. Then,

$$\tilde{K}_{2,qq}(\varphi) = \tilde{K}\big(2\sin(\varphi/2); ka_q, \beta_q, 0\big) \,. \quad (2.87)$$

Next, we consider the case $p \neq q$. The squared normalized distance measure $\hat{R}_{pq}^2$ can be written as

$$\hat{R}_{pq}^2(r,r',\varphi,\varphi') =$$
$$= k^2\,|\boldsymbol{d}_{pq}(\varphi,\varphi')|^2\left[1 + \frac{2b}{|\boldsymbol{d}_{pq}(\varphi,\varphi')|}\left(\frac{\boldsymbol{d}_{pq}(\varphi,\varphi')}{|\boldsymbol{d}_{pq}(\varphi,\varphi')|} \bullet \Big(\hat{b}_p r\boldsymbol{e}_r|_{S_p}(\varphi) - \hat{b}_q r'\boldsymbol{e}_r|_{S_q}(\varphi')\Big)\right) +\right.$$
$$\left. + \frac{b^2}{|\boldsymbol{d}_{pq}(\varphi,\varphi')|^2}\Big|\hat{b}_p r\boldsymbol{e}_r|_{S_p}(\varphi) - \hat{b}_q r'\boldsymbol{e}_r|_{S_q}(\varphi')\Big|^2\right], \quad (2.88)$$

where $\boldsymbol{d}_{pq} = \boldsymbol{c}_p + a_p\boldsymbol{e}_r|_{S_p} - \boldsymbol{c}_q - a_q\boldsymbol{e}_r|_{S_q}$, $b = \max(b_p, b_q)$, and $\hat{b}_i = b_i/b$. Since $|\boldsymbol{d}_{pq}(\varphi,\varphi')| \geq |\boldsymbol{c}_p - \boldsymbol{c}_q| - a_p - a_q$ and $b_q/(|\boldsymbol{c}_p - \boldsymbol{c}_q| - a_p - a_q) = O(\beta)$, the second term between the braces

is of order β and the third term is of order β^2. Neglecting terms of order β^2 in the integrands of $K_{1i,pq}$, we arrive at the approximate kernel

$$\tilde{K}_{1,pq}(\varphi,\varphi') = \frac{1}{\pi}\frac{\exp\big(-jk\,|\boldsymbol{d}_{pq}(\varphi,\varphi')|\big)}{k\,|\boldsymbol{d}_{pq}(\varphi,\varphi')|} = 4\,\hat{g}_{\rm free}(k\,|\boldsymbol{d}_{pq}(\varphi,\varphi')|)\,, \tag{2.89}$$

for both $i=1$ and $i=-1$. We note that terms of order β in the integrands of $K_{1i,pq}$ are odd in both r and r'. Hence, these terms are annihilated by the double integration in the definition of $K_{1i,pq}$.

To deduce an approximate kernel for $K_{2,pq}$, we follow the analysis for $K_{2,qq}$ above. The difference $h_{pq}(1,\varphi) - h_{pq}(-1,\varphi)$ in (2.77)^2 is given by (2.81) with $_{qq}$ replaced by $_{pq}$ and φ by φ, φ'. The distance measure $\hat{R}_{pq}$ can be asymptotically expanded as

$$\hat{R}_{pq}(r,r',\varphi,\varphi') = k\,|\boldsymbol{d}_{pq}(\varphi,\varphi')|\,\big(1+\beta\Gamma_{pq}(r,r',\varphi,\varphi')+O(\beta^2)\big)\ , \tag{2.90}$$

where

$$\Gamma_{pq}(r,r',\varphi,\varphi') = \frac{b}{\beta\,|\boldsymbol{d}_{pq}(\varphi,\varphi')|}\left(\frac{\boldsymbol{d}_{pq}(\varphi,\varphi')}{|\boldsymbol{d}_{pq}(\varphi,\varphi')|}\bullet\Big(\hat{b}_p r\boldsymbol{e}_r|_{S_p}(\varphi)-\hat{b}_q r'\boldsymbol{e}_r|_{S_q}(\varphi')\Big)\right). \tag{2.91}$$

A necessary condition for this asymptotic expansion to be valid is $\beta|\Gamma_{pq}(r,r',\varphi,\varphi')| < 1$, which is satisfied because $\Gamma_{pq}(r,r',\varphi,\varphi') = O(1)$. Using the derived expansions

$$\hat{R}_{pq}(\pm1,\pm r',\varphi,\varphi') = k\,|\boldsymbol{d}_{pq}(\varphi,\varphi')|\,\big(1\pm\beta\Gamma_{pq}(1,r',\varphi,\varphi')+O(\beta^2)\big)\,, \tag{2.92}$$

we deduce from (2.81)

$$h_{pq}(1,\varphi,\varphi') - h_{pq}(-1,\varphi,\varphi') = -\frac{\beta}{2\pi}\,\frac{\exp\big(-jk\,|\boldsymbol{d}_{pq}(\varphi,\varphi')|\big)}{k\,|\boldsymbol{d}_{pq}(\varphi,\varphi')|}\,\times$$

$$\times\int_{-1}^{1}\Big[\Gamma_{pq}(1,r',\varphi,\varphi')\Big(1+jk\,|\boldsymbol{d}_{pq}(\varphi,\varphi')|+O(\beta)\Big)-r'\big(1+O(\beta^2)\big)\Big]dr'\,. \tag{2.93}$$

We return to the expression of the kernel $K_{2,pq}$. Neglecting terms of order β in the integrand of the kernel $K_{12,pq}$, we obtain the approximate kernel $\tilde{K}_{1,pq}$ in (2.89). We neglect also terms of order β in (2.93) and calculate the integral with respect to r',

$$\int_{-1}^{1}\Big(\Gamma_{pq}(1,r',\varphi,\varphi')\big(1+jk\,|\boldsymbol{d}_{pq}(\varphi,\varphi')|\big)-r'\Big)dr' =$$

$$= \frac{2b_p\,(1+jk\,|\boldsymbol{d}_{pq}(\varphi,\varphi')|)}{\beta\,|\boldsymbol{d}_{pq}(\varphi,\varphi')|^2}\,\big(\boldsymbol{d}_{pq}(\varphi,\varphi')\bullet\boldsymbol{e}_r|_{S_p}(\varphi)\big)\,. \tag{2.94}$$

After that, we sum the two terms in $K_{2,pq}$, see $(2.77)^2$, by which we obtain an approximate kernel for $K_{2,pq}$,

$$\tilde{K}_{2,pq}(\varphi,\varphi') = \frac{1}{\pi}\,\frac{\exp\big(-jk\,|\boldsymbol{d}_{pq}(\varphi,\varphi')|\,\big)}{k\,|\boldsymbol{d}_{pq}(\varphi,\varphi')|}\Big[1-\frac{a_p k\,(1+jk\,|\boldsymbol{d}_{pq}(\varphi,\varphi')|)}{k^2|\boldsymbol{d}_{pq}(\varphi,\varphi')|^2}\,\times \\ \times\,\big(k\boldsymbol{d}_{pq}(\varphi,\varphi')\bullet\boldsymbol{e}_r|_{S_p}(\varphi)\big)\Big]. \quad (2.95)$$

From now on, we call $\tilde{K}_{1,pq}$, defined by (2.80) and (2.89), the approximate kernel of $K_{1i,pq}$ and we call $\tilde{K}_{2,pq}$, defined by (2.87) and (2.95), the approximate kernel of $K_{2,pq}$. The corresponding integral operators follow from (2.76) with $K_{1i,pq}$ and $K_{2,pq}$ replaced by $\tilde{K}_{1,pq}$ and $\tilde{K}_{2,pq}$. Denoting these operators by $\tilde{\mathcal{K}}_{1,pq}$ and $\tilde{\mathcal{K}}_{2,pq}$, we write the action of $\mathcal{Z}_{\rm a}$ in (2.75) as

$$(\mathcal{Z}_{\rm a}\boldsymbol{w})_p = -\frac{1}{2}\,jZ_0k^2\sum_{q=1}^{N_{\rm el}} a_q b_q\left[\left(1+\frac{1}{k^2a_p^2}\frac{d^{\,2}}{d\varphi^2}\right)\tilde{\mathcal{K}}_{1,pq}+\frac{1}{k^2a_p^2}\frac{d}{d\varphi}\tilde{\mathcal{K}}_{2,pq}\right]w_q\,, \quad (2.96)$$

The solution $\boldsymbol{w}$ of (2.40), with $\mathcal{Z}_{\rm a}$ given by (2.96), corresponds to the solution, say $\boldsymbol{J}_{\mathcal{A}}$, of (2.34). The question whether $\boldsymbol{J}_{\mathcal{A}}$ is an approximate solution of (2.17) cannot be answered satisfactorily. This can be explained as follows. As in the analysis of the line array of strips, we want to show that the condition (2.36) is satisfied by means of a dimensional argument. We start by considering the term $(\mathcal{Z}(\boldsymbol{J}_{\mathcal{A}}|_{S_p}))|_{S_p}$ in (2.60), which is given by (2.68) with $\boldsymbol{J}$ replaced by $\boldsymbol{J}_{\mathcal{A}}$ and $\hat{\boldsymbol{A}}_{pq}$ replaced by $\overline{\hat{\boldsymbol{A}}}_{pq}$. From the definition of $\hat{R}_{pp}$ in (2.78), it follows that $\partial\hat{R}_{pp}/\partial\hat{r}$ is of the order β with respect to $\partial\hat{R}_{pp}/\partial\varphi$. Then, it follows that $\partial(\mathcal{Z}(\boldsymbol{J}_{\mathcal{A}}|_{S_p}))|_{S_p}/\partial\hat{r}$ is of the order β with respect to $\partial(\mathcal{Z}(\boldsymbol{J}_{\mathcal{A}}|_{S_p}))|_{S_p}/\partial\varphi$, but *not* that the r-component of $(\mathcal{Z}(\boldsymbol{J}_{\mathcal{A}}|_{S_p}))|_{S_p}$ is of the order β with respect to its φ-component. Hence, the conditions $(2.31)^{1,3}$ for S_p being narrow with respect to $(\mathcal{Z}(\boldsymbol{J}_{\mathcal{A}}|_{S_p}))|_{S_p}$ are satisfied, but it is not known whether the condition $(2.31)^2$ is satisfied. Therefore, it does not follow from the above that $(\mathcal{I}-\mathcal{A})\mathcal{Z}\boldsymbol{J}_{\mathcal{A}}\approx\boldsymbol{0}$, i.e., the condition (2.36) for $\boldsymbol{J}_{\mathcal{A}}$ being an approximate solution of $\mathcal{Z}\boldsymbol{J}=\boldsymbol{E}_S$ if S is narrow with respect to $\boldsymbol{E}_S$. Hence, we cannot say whether $\boldsymbol{J}_{\mathcal{A}}$ is an approximate solution of $\mathcal{Z}\boldsymbol{J}=\boldsymbol{E}_S$.

2.3.4 Arrays in a Half Space

We consider line arrays of strips and arrays of rings in a half space bounded by a perfectly conducting plane Σ. The arrays are parallel to Σ and positioned at a height h above Σ, see Figure 2.1 for example. Let the half space Ω be given by $\Omega=\{\,\boldsymbol{x}\in\mathbb{R}^3\,|\,(\boldsymbol{x}\bullet\boldsymbol{e}_z)\geq 0\,\}$ with boundary plane Σ, i.e., the xy-plane. Then, the centers of the elements are described by $\boldsymbol{c}_q+h\boldsymbol{e}_z$, where $\boldsymbol{c}_q$ are the centers of the elements in the xy-plane as in the previous subsections. We note that for a half space, the origin of the Cartesian coordinate system is located in the plane Σ, whereas for free space, it is located in the plane of the array. To describe the current on the

elements by the operator equation $\mathcal{Z}_{\rm a}\boldsymbol{w} = \boldsymbol{v}^{\rm ex}$, we follow the analysis of the previous two subsections, where we replace the kernel $\mathcal{G}_{\rm free} = g_{\rm free}\mathcal{I}$ by the kernel $\mathcal{G}_{\rm half}$ in (2.13), see [34] for details. For a line array of strips in a half space, the result for $\mathcal{Z}_{\rm a}$ is the same as in (2.53), but with the averaged kernel F_{pq} replaced by the averaged kernel $F_{pq}^{[\rm half]}$ of a half space,

$$F_{pq}^{[\rm half]}(\xi) = F_{pq}(\xi) - F_{pq}(\sqrt{\xi^2+\gamma^2})\,. \tag{2.97}$$

Here, $\gamma = 2h/\ell$ and F_{pq} is given by (2.55) with related forms (2.57) and (2.59). Replacing F_{pq} by $\tilde{F}_{pq}$ in (2.63), we obtain an approximate kernel $\tilde{F}_{pq}^{[\rm half]}$ for the averaged kernel of a half space. Notice that in the above, we do not put a dimensional restriction on γ.

For an array of rings in a half space, the result for $\mathcal{Z}_{\rm a}$ is the same as in (2.75), but with $\hat{g}_{\rm free}(\hat{R}_{pq}(\,\cdot\,))$ replaced by

$$\hat{g}_{\rm half}(\hat{R}_{pq}(\,\cdot\,)) = \hat{g}_{\rm free}(\hat{R}_{pq}(\,\cdot\,)) - \hat{g}_{\rm free}\left(\sqrt{\hat{R}_{pq}^2(\,\cdot\,) + 4k^2h^2}\right)\,. \tag{2.98}$$

In (2.96), we have to replace the approximate kernels $\tilde{K}_{1,pq}$ and $\tilde{K}_{2,pq}$, deduced for free space, by $\tilde{K}_{1,pq}^{[\rm half]}$ and $\tilde{K}_{2,pq}^{[\rm half]}$ for a half space,

$$\begin{aligned}
&\tilde{K}_{1,qq}^{[\rm half]}(\varphi) = \tilde{F}_{qq}^{[\rm half]}(2\sin(\varphi/2); ka_q, \beta_q, \gamma_q)\,,\\
&\tilde{K}_{1,pq}^{[\rm half]}(\varphi,\varphi') = 4\,\hat{g}_{\rm free}(k\,|\boldsymbol{d}_{pq}(\varphi,\varphi')|) - 4\,\hat{g}_{\rm free}\left(k\,\sqrt{|\boldsymbol{d}_{pq}(\varphi,\varphi')|^2 + 4h^2}\right),
\end{aligned} \tag{2.99}$$

and

$$\begin{aligned}
&\tilde{K}_{2,qq}^{[\rm half]}(\varphi) = \tilde{K}(2\sin(\varphi/2); ka_q, \beta_q, 0) - \tilde{K}(2\sin(\varphi/2); ka_q, \beta_q, \gamma_q)\,,\\
&\tilde{K}_{2,pq}^{[\rm half]}(\varphi,\varphi') = \tilde{K}_{2,pq}(\varphi,\varphi', k|\boldsymbol{d}_{pq}(\varphi,\varphi')|) + \\
&\qquad\qquad - \tilde{K}_{2,pq}\left(\varphi,\varphi', k\sqrt{|\boldsymbol{d}_{pq}(\varphi,\varphi')|^2 + 4h^2}\right).
\end{aligned} \tag{2.100}$$

Here, $\gamma_q = 2h/a_q$ and $\tilde{F}_{qq}^{[\rm half]}$ is the approximate kernel of $F_{qq}^{[\rm half]}$ in (2.97), which is interpreted as a function of its argument ξ and the parameters $k\ell$, β, and γ, i.e., $F_{qq}^{[\rm half]}(\xi; k\ell, \beta, \gamma)$. Moreover, $\tilde{K}$ is defined by (A.16) and $\tilde{K}_{2,pq}$ in (2.95) is interpreted as function of φ, φ', and $k|\boldsymbol{d}_{pq}(\varphi,\varphi')|$. Notice that the second term in $\tilde{K}_{2,qq}^{[\rm half]}$ is obtained from (2.86) with $\tilde{R}_{qq}(\eta,\varphi)$ replaced by $ka_q\sqrt{\beta_q\eta^2+\xi^2+\gamma_q^2}$. The resulting function is identified as $K(2\sin(\varphi/2); ka_q, \beta_q, \gamma_q)$ defined by (A.4) and, subsequently, K is replaced by $\tilde{K}$ in (A.16).

2.4 Method of Solution

To solve the linear operator equation (2.40), i.e., $\mathcal{Z}_{\mathrm{a}}\boldsymbol{w} = \boldsymbol{v}^{\mathrm{ex}}$, we use a projection method, called the moment method. This method transforms the operator equation into a matrix equation. Many different ways of describing the method are employed in the literature, see for instance [47] and [54: pp. 329 ff.]. We describe the method by means of some algebraic concepts, which we introduce first.

2.4.1 Algebraic Concepts

Let $\mathcal{X}$ and $\mathcal{Y}$ be inner-product spaces over $\mathbb{C}$ with inner products[†] $\langle\cdot,\cdot\rangle_{\mathcal{X}}$ and $\langle\cdot,\cdot\rangle_{\mathcal{Y}}$. These spaces can be linear spaces of functions, but we do not specify $\mathcal{X}$ and $\mathcal{Y}$ further here. By $L(\mathcal{X},\mathcal{Y})$ we denote the vector space of linear mappings from $\mathcal{X}$ into $\mathcal{Y}$. If $\mathcal{X} = \mathcal{Y}$, we write $L(\mathcal{X})$. Moreover, we denote the identity mapping in $L(\mathcal{X})$ by $\mathcal{I}_{\mathcal{X}}$. Let $\mathbb{C}^N$ and $\mathbb{C}^{M\times N}$ be the vector spaces of N-tuples and $M \times N$-matrices. The nth component of $\boldsymbol{\alpha} \in \mathbb{C}^N$ is denoted as $\alpha(n)$ and the mnth component of $C \in \mathbb{C}^{M\times N}$ as $C(m,n)$. The space $\mathbb{C}^N$ is a complex inner-product space with the usual Euclidean inner product $(\,.\circ.\,)_N$, i.e.,

$$(\boldsymbol{\alpha}_1 \circ \boldsymbol{\alpha}_2)_N = \sum_{n=1}^{N} \alpha_1^*(n)\,\alpha_2(n)\,. \tag{2.101}$$

Distinguish this inner product from the scalar product $(\,.\bullet.\,)$ on $\mathbb{R}^3$. For indexing purposes, we need the spaces $\mathbb{N}^Q$, which consist of Q-tuples with components in $\mathbb{N}$. Analogously to $\mathbb{C}^N$, the qth component of $\boldsymbol{N} \in \mathbb{N}^Q$ is denoted by $N(q)$.

On the spaces $\mathbb{C}^{M\times N}$ we introduce the concept of block matrix in the usual way. Let $\boldsymbol{M} \in \mathbb{N}^P$, $\boldsymbol{N} \in \mathbb{N}^Q$, and $C_{pq} \in \mathbb{C}^{M(p)\times N(q)}$. Then, the block matrix $C \in \mathbb{C}^{|\boldsymbol{M}|\times|\boldsymbol{N}|}$ is defined by

$$C = \begin{pmatrix} C_{11} & \dots & C_{1Q} \\ \vdots & \ddots & \vdots \\ C_{P1} & \dots & C_{PQ} \end{pmatrix}, \tag{2.102}$$

where $|\boldsymbol{M}|$ and $|\boldsymbol{N}|$ denote the sums of the components of $\boldsymbol{M}$ and $\boldsymbol{N}$. On $\mathbb{C}^N$ we introduce the concept of concatenation as follows. Let $\boldsymbol{N} \in \mathbb{N}^2$ and $\boldsymbol{\alpha}_q \in \mathbb{C}^{N(q)}$ for $q = 1, 2$. Define the concatenation $\boldsymbol{\alpha}_1 \sqcup \boldsymbol{\alpha}_2$ by

$$\boldsymbol{\alpha}_1 \sqcup \boldsymbol{\alpha}_2 = (\alpha_1(1),\dots,\alpha_1(N(1)),\alpha_2(1),\dots,\alpha_2(N(2)))\,. \tag{2.103}$$

[†]We use the convention that an inner product of a complex inner product space is linear in its second argument with respect to scalar multiplication, i.e., $\langle\boldsymbol{v},\alpha\boldsymbol{w}\rangle = \alpha\langle\boldsymbol{v},\boldsymbol{w}\rangle$ and, hence, $\langle\alpha\boldsymbol{v},\boldsymbol{w}\rangle = \alpha^*\langle\boldsymbol{v},\boldsymbol{w}\rangle$. Here, * is the complex conjugate.

The generalization to $\bigsqcup_{q=1}^{Q} \boldsymbol{\alpha}_q$ is straightforward. The concepts of block matrix and concatenation are related in the following way. Let $[\,\cdot\,]_N$ be the mapping that transforms a tuple in $\mathbb{C}^N$ into a column vector in $\mathbb{C}^{N\times 1}$. Then,

$$[\boldsymbol{\alpha}_1 \sqcup \boldsymbol{\alpha}_2]_{|\boldsymbol{N}|} = \begin{pmatrix} [\boldsymbol{\alpha}_1]_{N(1)} \\ [\boldsymbol{\alpha}_2]_{N(2)} \end{pmatrix}. \tag{2.104}$$

The vector space $\mathbb{C}^{M\times N}$ can be related to the vector space $L(\mathbb{C}^N, \mathbb{C}^M)$ by the isomorphism $[\,\cdot\,]_{M\times N}$ from $L(\mathbb{C}^N, \mathbb{C}^M)$ to $\mathbb{C}^{M\times N}$,

$$[\mathcal{C}](m,n) = (\mathcal{C}\boldsymbol{e}_n)(m), \tag{2.105}$$

where $\mathcal{E}_N = \{\boldsymbol{e}_1, \ldots, \boldsymbol{e}_N\}$ is the standard basis in $\mathbb{C}^N$. Together with $[\,\cdot\,]_N$ we have the calculus

$$[\mathcal{C}\boldsymbol{\alpha}]_M = [\mathcal{C}]_{M\times N}[\boldsymbol{\alpha}]_N\,, \qquad (\boldsymbol{\zeta}\circ\mathcal{C}\boldsymbol{\alpha})_M = [\boldsymbol{\zeta}]^*_M[\mathcal{C}]_{M\times N}[\boldsymbol{\alpha}]_N\,, \tag{2.106}$$

for $\boldsymbol{\alpha} \in \mathbb{C}^N$ and $\boldsymbol{\zeta} \in \mathbb{C}^M$. The superscript $*$ indicates the adjoint, which is the Hermitian transposed for complex matrices. For $M = N$, $\mathcal{C}$ is invertible if and only if $[\mathcal{C}]_{N\times N}$ is invertible, and $[\mathcal{C}^{-1}]_{N\times N} = [\mathcal{C}]^{-1}_{N\times N}$.

We introduce the following algebraic concepts on $\mathcal{X}$ and $L(\mathcal{X},\mathcal{Y})$. Let $\{\boldsymbol{w}_1, \ldots, \boldsymbol{w}_N\}$ be a finite subset of $\mathcal{X}$. Then, the Gram matrix $G(\{\boldsymbol{w}_1, \ldots, \boldsymbol{w}_N\}) \in \mathbb{C}^{N\times N}$, shortly G, is defined by

$$G(m,n) = \langle \boldsymbol{w}_m, \boldsymbol{w}_n\rangle_{\mathcal{X}}\,. \tag{2.107}$$

The Gram matrix is invertible if and only if $\{\boldsymbol{w}_1, \ldots, \boldsymbol{w}_N\}$ is independent. Define for a subset $\mathcal{X}_1$ of $\mathcal{X}$ the orthogonal complement $\mathcal{X}_1^\perp$ by

$$\mathcal{X}_1^\perp = \{\, \boldsymbol{w} \in \mathcal{X} \,|\, \langle \boldsymbol{w}, \boldsymbol{v}\rangle_{\mathcal{X}} = 0 \;\forall\, \boldsymbol{v} \in \mathcal{X}_1 \,\}\,. \tag{2.108}$$

Then, $\mathcal{X}_1^\perp$ is a subspace of $\mathcal{X}$. Define for $\mathcal{C} \in L(\mathcal{X},\mathcal{Y})$ the adjoint mapping $\mathcal{C}^* \in L(\mathcal{Y},\mathcal{X})$ by

$$\langle \mathcal{C}^*\boldsymbol{v}, \boldsymbol{w}\rangle_{\mathcal{X}} = \langle \boldsymbol{v}, \mathcal{C}\boldsymbol{w}\rangle_{\mathcal{Y}}\,, \quad \forall\, \boldsymbol{v} \in \mathcal{Y} \quad \wedge \quad \forall\, \boldsymbol{w} \in \mathcal{X}\,. \tag{2.109}$$

Using the previous concepts on $L(\mathbb{C}^N, \mathbb{C}^M)$, $\mathcal{X}$, and $L(\mathcal{X},\mathcal{Y})$, we introduce the following concepts on $L(\mathbb{C}^N, \mathcal{X})$. Let $\mathcal{W}$ be an element of $L(\mathbb{C}^N, \mathcal{X})$ and assume that $\mathcal{W}$ is injective. Since $\mathcal{W}$ is linear, we can write the action of $\mathcal{W}$ as

$$\mathcal{W}\boldsymbol{\alpha} = \sum_{n=1}^{N} \alpha(n)\, \mathcal{W}\boldsymbol{e}_n\,, \tag{2.110}$$

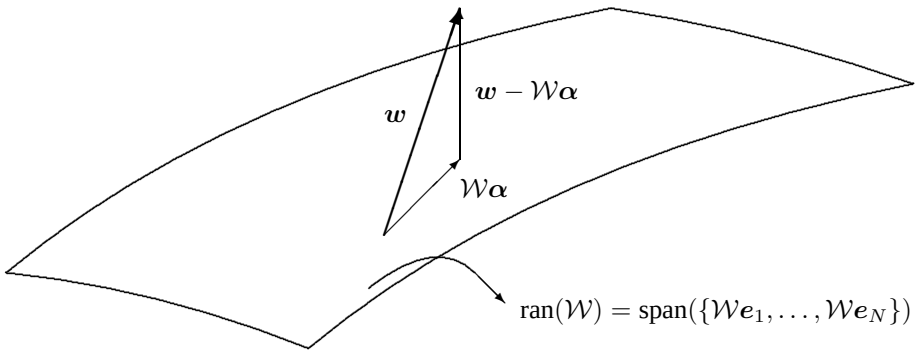

Figure 2.6 A graphical representation of $\boldsymbol{w} - \mathcal{W}\boldsymbol{\alpha}$ with respect to the linear span of the vectors $\mathcal{W}\boldsymbol{e}_n$. The linear span is graphically represented by a surface and the vectors $\mathcal{W}\boldsymbol{\alpha}$, $\boldsymbol{w} - \mathcal{W}\boldsymbol{\alpha}$, and $\boldsymbol{w}$ in $\mathcal{X}$ by arrows.

where $\boldsymbol{\alpha} \in \mathbb{C}^N$. The vectors $\mathcal{W}\boldsymbol{e}_n \in \mathcal{X}$ are the images of the unit vectors in $\mathbb{C}^N$. We observe that $\mathrm{ran}(\mathcal{W}) = \mathrm{span}(\{\mathcal{W}\boldsymbol{e}_1, \ldots, \mathcal{W}\boldsymbol{e}_N\})$, where span denotes the linear span of a set of vectors. Since $\mathcal{W}$ is injective, the set $\{\mathcal{W}\boldsymbol{e}_1, \ldots, \mathcal{W}\boldsymbol{e}_N\}$ is independent and, hence, a basis in $\mathrm{ran}(\mathcal{W})$. We refer to this basis as $\mathrm{bas}(\mathcal{W})$. Vice versa, choosing N independent vectors for $\mathrm{bas}(\mathcal{W})$ first, we can construct the corresponding injective mapping $\mathcal{W}$ from (2.110). Examples of mappings $\mathcal{W}$ are given below.

Define the mapping $\mathcal{W}^- \in L(\mathcal{X}, \mathbb{C}^N)$ by

$$\mathcal{W}^-\boldsymbol{w} = \boldsymbol{\alpha} \quad :\Leftrightarrow \quad \langle \mathcal{W}\boldsymbol{e}_n, \boldsymbol{w} - \mathcal{W}\boldsymbol{\alpha}\rangle_{\mathcal{X}} = 0 \quad \forall\, n \in \{1, \ldots, N\}\,. \tag{2.111}$$

The image $\boldsymbol{\alpha}$ is constructed such that $\boldsymbol{w} - \mathcal{W}\boldsymbol{\alpha}$ is perpendicular to the vectors $\mathcal{W}\boldsymbol{e}_n$ in the sense of the inner product on $\mathcal{X}$. Figure 2.6 shows a graphical representation. From (2.111), it follows that

$$\mathcal{W}^-\boldsymbol{w} = \boldsymbol{\alpha} \quad \Leftrightarrow \quad G(\mathrm{bas}(\mathcal{W}))\,[\boldsymbol{\alpha}]_N = [\boldsymbol{\zeta}]_N, \tag{2.112}$$

where $\boldsymbol{\zeta} \in \mathbb{C}^N$ is defined by $\zeta(n) = \langle \mathcal{W}\boldsymbol{e}_n, \boldsymbol{w}\rangle_{\mathcal{X}}$. Since G is invertible, $\mathcal{W}^-$ is well-defined, or, to every $\boldsymbol{w} \in \mathcal{X}$ corresponds exactly one image $\mathcal{W}^-\boldsymbol{w} \in \mathbb{C}^N$.

Example 1 If $\mathcal{X} = \mathbb{C}^3$ and $N = 2$, $\mathcal{W}$ maps each tuple in $\mathbb{C}^2$ onto a tuple in $\mathbb{C}^3$. If, additionally, the images of $\boldsymbol{e}_1 = (1, 0)$ and $\boldsymbol{e}_2 = (0, 1)$ in $\mathbb{C}^2$ are the unit vectors $(1, 0, 0)$ and $(0, 1, 0)$ in $\mathbb{C}^3$, $\mathcal{W}$ maps each tuple $(x, y) \in \mathbb{C}^2$ onto $(x, y, 0)$ in $\mathbb{C}^3$. Let $\mathcal{X} = \mathbb{C}^3$ be equipped with the Euclidean inner product. Then, $\mathcal{W}^-$ maps a tuple $(x, y, z) \in \mathbb{C}^3$ onto $(x, y) \in \mathbb{C}^2$. Hence, the composition $\mathcal{P} = \mathcal{W}\mathcal{W}^-$ maps a tuple $(x, y, z) \in \mathbb{C}^3$ onto $(x, y, 0) \in \mathbb{C}^3$, which shows

that $\mathcal{P}$ projects a tuple in $\mathbb{C}^3$ onto the complex xy-plane. Moreover, the mapping $\mathcal{W}^-\mathcal{W}$ maps a tuple $(x, y) \in \mathbb{C}^2$ onto $(x, y) \in \mathbb{C}^2$, which shows that $\mathcal{W}^-\mathcal{W} = \mathcal{I}_{\mathbb{C}^2}$. Below, the latter two properties are described in general.

Example 2 Let $\mathcal{X}$ be the linear space of complex valued continuous functions on $[0, 1]$ with inner product

$$\langle v, w\rangle_{\mathcal{X}} = \int_0^1 v^*(x)\, w(x)\, dx\,. \tag{2.113}$$

Let $\mathcal{W}\boldsymbol{e}_n$ be the monomials x^{n-1} for $n = 1, \ldots, N$. Then, ran$(\mathcal{W})$ is the space of polynomials with complex coefficients of degree $\leq N - 1$. Solving $\mathcal{W}\boldsymbol{\alpha} = \boldsymbol{w}$ with $\boldsymbol{w} \in \mathcal{X}$, we find the coefficients $\boldsymbol{\alpha}$ of the polynomial that fits 'best' to the function $\boldsymbol{w}$ with respect to the inner product (2.113). Here, $\alpha(n)$ is the coefficient of x^{n-1} and $\boldsymbol{\alpha} = \mathcal{W}^-\boldsymbol{w}$.

The composed operator $\mathcal{W}^-\mathcal{W}$ satisfies

$$\mathcal{W}^-\mathcal{W} = \mathcal{I}_{\mathbb{C}^N}\,. \tag{2.114}$$

The composed operator $\mathcal{P} = \mathcal{W}\mathcal{W}^-$ is the projection on ran$(\mathcal{W})$ along ran$(\mathcal{W})^\perp$. This means that:

1. every element $\boldsymbol{w} \in \mathcal{X}$ can be written uniquely as $\boldsymbol{w} = \boldsymbol{w}_1 + \boldsymbol{w}_2$ with $\boldsymbol{w}_1 \in$ ran$(\mathcal{W})$ and $\boldsymbol{w}_2 \in$ ran$(\mathcal{W})^\perp$,
2. $\mathcal{P}\boldsymbol{w} = \boldsymbol{w}$ for all $\boldsymbol{w} \in$ ran$(\mathcal{W})$,
3. $\mathcal{P}\boldsymbol{w} = \boldsymbol{0}$ for all $\boldsymbol{w} \in$ ran$(\mathcal{W})^\perp$.

Hence, ran$(\mathcal{P}) =$ ran$(\mathcal{W})$. Moreover, the projection $\mathcal{P}$ depends only on the choice of the subspace ran$(\mathcal{W})$ and on the inner product on $\mathcal{X}$. It does not on depend on the specific choices of the images $\mathcal{W}\boldsymbol{e}_n$. From (2.114), it follows that $\mathcal{P}^2 = \mathcal{P}$, which is the basic property of projections.

Both $\mathcal{W}^-$ and $\mathcal{P}$ have the property that, for $\boldsymbol{w} \in$ ran$(\mathcal{W})$, the images $\mathcal{W}^-\boldsymbol{w}$ and $\mathcal{P}\boldsymbol{w}$ do not depend on the inner product on $\mathcal{X}$. In the special case $\mathcal{X} =$ ran$(\mathcal{W})$, or, ran$(\mathcal{W})^\perp = \boldsymbol{0}$, the mapping $\mathcal{W}$ is invertible with inverse $\mathcal{W}^{-1} = \mathcal{W}^-$. Moreover, $\mathcal{P} = \mathcal{I}_{\mathcal{X}}$.

The composition of $\mathcal{W}^*$ and $\mathcal{W}$ can be related to the Gram matrix $G($bas$(\mathcal{W}))$,

$$[\mathcal{W}^*\mathcal{W}] = G(\text{bas}(\mathcal{W}))\,. \tag{2.115}$$

Since $G($bas$(\mathcal{W}))$ is invertible, $\mathcal{W}^*\mathcal{W}$ is invertible as well. Multiplying both sides of $\mathcal{I}_{\mathbb{C}^N} = (\mathcal{W}^*\mathcal{W})^{-1}(\mathcal{W}^*\mathcal{W})$ by $\mathcal{W}^-$ at the right and using that $\mathcal{W}^* = \mathcal{W}^*\mathcal{W}\mathcal{W}^-$, we obtain a relation between $\mathcal{W}^*$ and $\mathcal{W}^-$,

$$\mathcal{W}^- = (\mathcal{W}^*\mathcal{W})^{-1}\mathcal{W}^*\,. \tag{2.116}$$

As on the vector spaces $\mathbb{C}^N$, we define on the vector spaces $L(\mathbb{C}^N, \mathcal{X})$ the concept of concatenation. Let $\boldsymbol{N} \in \mathbb{N}^2$ and $\mathcal{W}_q \in L(\mathbb{C}^{N(q)}, \mathcal{X})$ for $q = 1, 2$. Define the concatenation $\mathcal{W}_1 \sqcup \mathcal{W}_2 \in L(\mathbb{C}^{|\boldsymbol{N}|}, \mathcal{X})$ by

$$(\mathcal{W}_1 \sqcup \mathcal{W}_2)(\boldsymbol{\alpha}_1 \sqcup \boldsymbol{\alpha}_2) = \mathcal{W}_1\boldsymbol{\alpha}_1 + \mathcal{W}_2\boldsymbol{\alpha}_2, \tag{2.117}$$

where $\boldsymbol{\alpha}_q \in \mathbb{C}^{N(q)}$ for $q = 1, 2$. From the definitions of the adjoint and the concatenation, it follows that $(\mathcal{W}_1 \sqcup \mathcal{W}_2)^* \boldsymbol{w} = \mathcal{W}_1^* \boldsymbol{w} \sqcup \mathcal{W}_2^* \boldsymbol{w}$. Then, using the definition of the concatenation and the concept of block matrix, we obtain from (2.112) and (2.115)

$$(\mathcal{W}_1 \sqcup \mathcal{W}_2)^- \boldsymbol{w} = \boldsymbol{\alpha}_1 \sqcup \boldsymbol{\alpha}_2 \quad \Leftrightarrow \quad \begin{pmatrix} [\mathcal{W}_1^*\mathcal{W}_1] & [\mathcal{W}_1^*\mathcal{W}_2] \\ [\mathcal{W}_2^*\mathcal{W}_1] & [\mathcal{W}_2^*\mathcal{W}_2] \end{pmatrix} \begin{pmatrix} [\boldsymbol{\alpha}_1] \\ [\boldsymbol{\alpha}_2] \end{pmatrix} = \begin{pmatrix} [\boldsymbol{\zeta}_1] \\ [\boldsymbol{\zeta}_2] \end{pmatrix}, \tag{2.118}$$

where $\boldsymbol{\zeta}_q \in \mathbb{C}^{N(q)}$ is defined by $\zeta_q(n) = \langle \mathcal{W}_q \boldsymbol{e}_n, \boldsymbol{w} \rangle_{\mathcal{X}}$. If the subspaces $\mathrm{ran}(\mathcal{W}_1)$ and $\mathrm{ran}(\mathcal{W}_2)$ of $\mathcal{X}$ are mutually orthogonal with respect to the inner product on $\mathcal{X}$, it follows that $\mathcal{W}_1^- \boldsymbol{w} = \alpha_1$ and $\mathcal{W}_2^- \boldsymbol{w} = \alpha_2$, and hence

$$(\mathcal{W}_1 \sqcup \mathcal{W}_2)^- \boldsymbol{w} = \mathcal{W}_1^- \boldsymbol{w} \sqcup \mathcal{W}_2^- \boldsymbol{w}\,. \tag{2.119}$$

The generalization to $\bigsqcup_{q=1}^{Q} \mathcal{W}_q$ is straightforward. In the following section and chapters, we omit the subscripts of the bracket operations, the inner products, and the identity mapping, if it is clear which spaces are meant.

2.4.2 Outline of the Moment Method

We consider the linear operator equation

$$\mathcal{Z}\boldsymbol{w} = \boldsymbol{v}\,, \tag{2.120}$$

where $\boldsymbol{w} \in \mathcal{X}$, $\boldsymbol{v} \in \mathcal{Y}$, $\mathcal{Z} \in L(\mathcal{X}, \mathcal{Y})$, and $\mathcal{X}$ and $\mathcal{Y}$ are inner-product spaces with inner products $\langle \cdot, \cdot \rangle_{\mathcal{X}}$ and $\langle \cdot, \cdot \rangle_{\mathcal{Y}}$. We note that, in this subsection, $\mathcal{Z}$ is not the impedance operator as defined by (2.16), but it is a certain linear mapping from $\mathcal{X}$ into $\mathcal{Y}$. To solve (2.120), we introduce first linear injective mappings $\mathcal{W} \in L(\mathbb{C}^N, \mathcal{X})$ and $\mathcal{V} \in L(\mathbb{C}^M, \mathcal{Y})$ as in the previous section. Then, we replace the operator equation by

$$\mathcal{Q}\mathcal{Z}\mathcal{P}\boldsymbol{w} = \mathcal{Q}\boldsymbol{v}\,, \tag{2.121}$$

where $\mathcal{P} = \mathcal{W}\mathcal{W}^- \in L(\mathcal{X})$ and $\mathcal{Q} = \mathcal{V}\mathcal{V}^- \in L(\mathcal{Y})$. Since $\mathcal{P}$ and $\mathcal{Q}$ are projections on the finite-dimensional subspaces $\mathrm{ran}(\mathcal{W})$ and $\mathrm{ran}(\mathcal{V})$ of $\mathcal{X}$ and $\mathcal{Y}$, respectively, the operator $\mathcal{Q}\mathcal{Z}\mathcal{P}$ is a finite-rank operator with rank M. If $M = N$, then $\mathcal{Q}\mathcal{Z}\mathcal{P}$ is invertible as element of $L(\mathrm{ran}(\mathcal{P}), \mathrm{ran}(\mathcal{Q}))$ and the solution of (2.121) is unique. The question whether the solution of

(2.121) is an approximate solution of (2.120) can be answered in a similar way as the question whether the solution $\boldsymbol{J}_{\mathcal{A}}$ of (2.34) is an approximate solution of (2.17). Assume that we have determined the solution of (2.121), say $\boldsymbol{w}_{\mathcal{P}}$. Then, $\boldsymbol{w}_{\mathcal{P}} \in \mathrm{ran}(\mathcal{P})$, or $\boldsymbol{w}_{\mathcal{P}} = \mathcal{P}\boldsymbol{w}_{\mathcal{P}}$, and

$$\mathcal{Z}\boldsymbol{w}_{\mathcal{P}} = \boldsymbol{v} - (\mathcal{I} - \mathcal{Q})\boldsymbol{v} + (\mathcal{I} - \mathcal{Q})\mathcal{Z}\boldsymbol{w}_{\mathcal{P}}\,. \tag{2.122}$$

Hence, $\boldsymbol{w}_{\mathcal{P}}$ is an approximate solution of (2.120) under the condition that

$$(\mathcal{I} - \mathcal{Q})(\mathcal{Z}\boldsymbol{w}_{\mathcal{P}} - \boldsymbol{v}) \approx \boldsymbol{0}\,. \tag{2.123}$$

Here, the approximate sign '$\approx$' needs to be interpreted in the sense of the functional metric related to (2.31). The condition (2.123) resembles the condition (2.36) for $\boldsymbol{J}_{\mathcal{A}}$ being an approximate solution of $\mathcal{Z}\boldsymbol{J} = \boldsymbol{E}_S$. The latter condition means that S is narrow with respect to $\mathcal{Z}\boldsymbol{J}_{\mathcal{A}} - \boldsymbol{E}_S$, whereas the former condition means that $\mathcal{Z}\boldsymbol{w}_{\mathcal{P}} - \boldsymbol{v}$ is approximately finite-dimensional with respect to $\mathcal{Q}$. If $(\mathcal{I} - \mathcal{Q})\boldsymbol{v} \approx \boldsymbol{0}$, the condition (2.123) turns into $(\mathcal{I} - \mathcal{Q})\mathcal{Z}\boldsymbol{w}_{\mathcal{P}} \approx \boldsymbol{0}$, i.e., $\mathcal{Z}\boldsymbol{w}_{\mathcal{P}}$ is approximately finite-dimensional with respect to $\mathcal{Q}$.

Since $\mathcal{V}$ is injective, (2.121) is equivalent to

$$\mathcal{V}^{-}\mathcal{Z}\,\mathcal{W}\,\mathcal{W}^{-}\boldsymbol{w} = \mathcal{V}^{-}\boldsymbol{v}\,, \tag{2.124}$$

This equation is transformed into a matrix equation by the bracket calculus of the previous section,

$$[\mathcal{V}^{-}\mathcal{Z}\,\mathcal{W}][\mathcal{W}^{-}\boldsymbol{w}] = [\mathcal{V}^{-}\boldsymbol{v}]\,. \tag{2.125}$$

Here, $[\mathcal{V}^{-}\mathcal{Z}\,\mathcal{W}]$ is called the moment matrix. Our definition of this matrix differs from the usual definition in the literature in the following way. According to the bracket calculus,

$$\begin{aligned} &[\mathcal{V}^{-}\mathcal{Z}\,\mathcal{W}](m,n) = (\mathcal{V}^{-}\mathcal{Z}\,\mathcal{W}\boldsymbol{e}_n)(m) = (G^{-1}[\boldsymbol{\zeta}_n])(m,1)\,,\\ &[\mathcal{V}^{-}\boldsymbol{v}](m,1) = (G^{-1}[\boldsymbol{\zeta}_0])(m,1)\,, \end{aligned} \tag{2.126}$$

where $\zeta_n(m) = \langle \mathcal{V}\boldsymbol{e}_m, \mathcal{Z}\,\mathcal{W}\boldsymbol{e}_n\rangle_{\mathcal{Y}}$, $\zeta_0(m) = \langle \mathcal{V}\boldsymbol{e}_m, \boldsymbol{v}\rangle_{\mathcal{Y}}$, and $G = G(\mathrm{bas}(\mathcal{V}))$ with respect to $\langle\cdot,\cdot\rangle_{\mathcal{Y}}$. The vectors $\mathcal{V}\boldsymbol{e}_m$ and $\mathcal{W}\boldsymbol{e}_n$ in the inner products are elements of the sets $\mathrm{bas}(\mathcal{V})$ and $\mathrm{bas}(\mathcal{W})$. If $\mathcal{X}$ and $\mathcal{Y}$ are linear spaces of functions, the elements of $\mathrm{bas}(\mathcal{V})$ are called the test functions of the moment method and the elements of $\mathrm{bas}(\mathcal{W})$ are called the expansion functions. Defining $Z(m,n) = \langle \mathcal{V}\boldsymbol{e}_m, \mathcal{Z}\,\mathcal{W}\boldsymbol{e}_n\rangle_{\mathcal{Y}}$, $V(m,1) = \langle \mathcal{V}\boldsymbol{e}_m, \boldsymbol{v}\rangle_{\mathcal{Y}}$, and $W = [\mathcal{W}^{-}\boldsymbol{w}]$, we write (2.125) as

$$G^{-1}ZW = G^{-1}V, \tag{2.127}$$

which is the usual representation of the moment-matrix equation except for multiplication by the inverse of the Gram matrix G. The usual definition of the moment matrix is Z, which is related to our definition by

$$[\mathcal{V}^{-}\mathcal{Z}\mathcal{W}] = G^{-1}Z\,. \tag{2.128}$$

Hence, our definition and the usual definition yield the same moment matrix, if the Gram matrix G is the identity matrix. If $\mathcal{Y}$ is a linear space of functions, this condition can be phrased as the test functions are orthonormal with respect to the inner product on $\mathcal{Y}$. The reason to introduce the definition (2.128) of the moment matrix besides the usual definition Z is given in Subsection 5.2.1, where we show that the definition (2.128) is essential for the eigencurrent approach in Chapter 5.

2.4.3 Application Details

We return to the operator equation $\mathcal{Z}_\mathrm{a}\boldsymbol{w} = \boldsymbol{v}^\mathrm{ex}$ in (2.40). To solve this equation by the moment method, we need:

1. to find suitable inner-product spaces $\mathcal{X}_\mathrm{a} = \mathrm{dom}(\mathcal{Z}_\mathrm{a})$ and $\mathcal{Y}_\mathrm{a} \supset \mathrm{ran}(\mathcal{Z}_\mathrm{a})$ with corresponding inner products $\langle\cdot,\cdot\rangle_{\mathcal{X}_\mathrm{a}}$ and $\langle\cdot,\cdot\rangle_{\mathcal{Y}_\mathrm{a}}$,
2. to find suitable mappings $\mathcal{W} \in L(\mathbb{C}^N, \mathcal{X}_\mathrm{a})$ and $\mathcal{V} \in L(\mathbb{C}^N, \mathcal{Y}_\mathrm{a})$ with corresponding projections $\mathcal{P} \in L(\mathcal{X}_\mathrm{a})$ and $\mathcal{Q} \in L(\mathcal{Y}_\mathrm{a})$,
3. to construct $[\mathcal{V}^- \mathcal{Z}_\mathrm{a} \mathcal{W}]$ and $[\mathcal{V}^- \boldsymbol{v}^\mathrm{ex}]$,
4. to solve (2.125).

After that, the solution of (2.121) is found as $\mathcal{W}(\mathcal{W}^-\boldsymbol{w})$, where $[\mathcal{W}^-\boldsymbol{w}]$ is the solution of (2.125). The column representation of the current $\mathcal{W}(\mathcal{W}^-\boldsymbol{w})$ on the array is $[\mathcal{W}^-\boldsymbol{w}]$. Instead of steps 3 and 4, we can also construct Z and V only and solve (2.127) to find $[\mathcal{W}^-\boldsymbol{w}]$. With respect to step 1, we notice that $\mathcal{X}_\mathrm{a}$ and $\mathcal{Y}_\mathrm{a}$ are linear spaces of functions, $F(\Pi_\xi, \mathbb{C}^{N_\mathrm{el}})$, which should be chosen in accordance with the properties of $\mathcal{Z}_\mathrm{a}$ and such that $\boldsymbol{v}^\mathrm{ex} \in \mathcal{Y}_\mathrm{a}$. In correspondence with the notation of the elements of $\mathbb{C}^N$ in Subsection 2.4.1, we denote the components of the vector functions $\boldsymbol{w} \in \mathcal{X}_\mathrm{a}$and $\boldsymbol{v} \in \mathcal{Y}_\mathrm{a}$ by $w(\,\cdot\,;q)$ and $v(\,\cdot\,;q)$ instead of w_q and v_q. Here, $q = 1, \ldots, N_\mathrm{el}$ and the dot indicates the function variable in Π_ξ. The mappings $\mathcal{W}$ and $\mathcal{V}$ in step 2 should be constructed such that they describe the dominant behavior of $\mathcal{Z}_\mathrm{a}$ in the sense of (2.123). The elements of bas$(\mathcal{W})$ and bas$(\mathcal{V})$, i.e., $\mathcal{V}\boldsymbol{e}_n$ and $\mathcal{W}\boldsymbol{e}_n$, are the expansion and test functions on the array, which are elements of linear spaces of functions $F(\Pi_\xi, \mathbb{C}^{N_\mathrm{el}})$. We construct the mappings $\mathcal{W}$ and $\mathcal{V}$ by choosing these expansion and test functions.

If the test functions are chosen the same as the expansion functions, the mappings $\mathcal{W}$ and $\mathcal{V}$ satisfy bas$(\mathcal{W})$ = bas$(\mathcal{V})$ and, hence, ran$(\mathcal{P})$ = ran$(\mathcal{Q})$. Ordering the functions in bas$(\mathcal{W})$ and bas$(\mathcal{V})$ in the same way, we obtain $\mathcal{V} = \mathcal{W}$. Strictly speaking, the mappings $\mathcal{W}^-$ and $\mathcal{V}^-$ are not equal, because they have different domains, i.e., $\mathcal{X}_\mathrm{a}$ and $\mathcal{Y}_\mathrm{a}$, and they are constructed by different inner products, i.e., $\langle\cdot,\cdot\rangle_{\mathcal{X}_\mathrm{a}}$ and $\langle\cdot,\cdot\rangle_{\mathcal{Y}_\mathrm{a}}$. The same is valid for the projections $\mathcal{P}$ and $\mathcal{Q}$. We can write $\mathcal{W}^-$ instead of $\mathcal{V}^-$ and $\mathcal{P}$ instead of $\mathcal{Q}$, if we interpret $\mathcal{W}^-$ and $\mathcal{P}$ according to the space they act on. In this way, we emphasize that the expansion and test functions are the same. In Section 3.2, we show that both for arrays of strips and for arrays of rings, there is reason to

choose the test and expansion functions the same. In that case, the finite-rank operator equation (2.121) and the moment-matrix equation (2.125) turn into

$$\mathcal{P}\mathcal{Z}_{\rm a}\mathcal{P}\boldsymbol{w} = \mathcal{P}\boldsymbol{v}^{\rm ex}\,, \qquad [\mathcal{W}^{-}\mathcal{Z}_{\rm a}\mathcal{W}][\mathcal{W}^{-}\boldsymbol{w}] = [\mathcal{W}^{-}\boldsymbol{v}^{\rm ex}]\,. \tag{2.129}$$

Here, the moment matrix $[\mathcal{W}^{-}\mathcal{Z}_{\rm a}\mathcal{W}]$ and the excitation vector $[\mathcal{W}^{-}\boldsymbol{v}^{\rm ex}]$ are given by

$$[\mathcal{W}^{-}\mathcal{Z}_{\rm a}\mathcal{W}] = G^{-1}Z, \qquad [\mathcal{W}^{-}\boldsymbol{v}^{\rm ex}] = G^{-1}V\,, \tag{2.130}$$

with $Z(m,n) = \langle \mathcal{W}\boldsymbol{e}_m, \mathcal{Z}_{\rm a}\mathcal{W}\boldsymbol{e}_n\rangle_{\mathcal{Y}_{\rm a}}$, $V(m,1) = \langle \mathcal{W}\boldsymbol{e}_m, \boldsymbol{v}^{\rm ex}\rangle_{\mathcal{Y}_{\rm a}}$, and $G = G(\mathrm{bas}(\mathcal{W}))$ with respect to the inner product on $\mathcal{Y}_{\rm a}$. We should keep in mind that $\mathcal{P}$ and $\mathcal{W}^{-}$ acting on the range of $\mathcal{Z}_{\rm a}$ are associated with the inner product on $\mathcal{Y}_{\rm a}$, while $\mathcal{P}$ and $\mathcal{W}^{-}$ acting on the domain of $\mathcal{Z}_{\rm a}$ are associated with the inner product on $\mathcal{X}_{\rm a}$. However, $\mathcal{P}$ and $\mathcal{W}^{-}$ are usually associated with the inner product on $\mathcal{Y}_{\rm a}$, because only this inner product is explicitly used in the moment method.

A common choice for the (test and) expansion functions is functions which are non-zero on a single element only. This is expressed by means of the algebraic concepts as follows. Let $\mathcal{W} = \mathcal{W}_1 \sqcup \ldots \sqcup \mathcal{W}_{N_{\rm el}}$, such that $(\mathcal{W}_q\boldsymbol{e}_n)(\,\cdot\,;q') = 0$ for all $q' \neq q$ and $n = 1,\ldots,N_{\rm exp}(q)$. In other words, the functions $\mathcal{W}_q\boldsymbol{e}_n$ are vector functions with a non-zero qth component only. The functions $(\mathcal{W}_q\boldsymbol{e}_n)(\,\cdot\,;q)$ are the (test and) expansion functions on the qth element and the vector $\boldsymbol{N}_{\rm exp}$ of length $N_{\rm el}$ represents the numbers of (test and) expansion functions on the elements. If we assume that subspaces $\mathrm{ran}(\mathcal{W}_q)$ of $\mathcal{Y}_{\rm a}$ are mutually orthogonal with respect to the inner product on $\mathcal{Y}_{\rm a}$, the mapping $\mathcal{W}$ exhibits a generalization of the property (2.119). Using this property, we rewrite the moment-matrix equation (2.129)[2] in the block form

$$\begin{pmatrix} [\mathcal{W}_1^{-}\mathcal{Z}_{\rm a}\mathcal{W}_1] & \ldots & [\mathcal{W}_1^{-}\mathcal{Z}_{\rm a}\mathcal{W}_{N_{\rm el}}] \\ \vdots & \ddots & \vdots \\ [\mathcal{W}_{N_{\rm el}}^{-}\mathcal{Z}_{\rm a}\mathcal{W}_1] & \ldots & [\mathcal{W}_{N_{\rm el}}^{-}\mathcal{Z}_{\rm a}\mathcal{W}_{N_{\rm el}}] \end{pmatrix} \begin{pmatrix} [\mathcal{W}_1^{-}\boldsymbol{w}] \\ \vdots \\ [\mathcal{W}_{N_{\rm el}}^{-}\boldsymbol{w}] \end{pmatrix} = \begin{pmatrix} [\mathcal{W}_1^{-}\boldsymbol{v}^{\rm ex}] \\ \vdots \\ [\mathcal{W}_{N_{\rm el}}^{-}\boldsymbol{v}^{\rm ex}] \end{pmatrix}. \tag{2.131}$$

In Chapters 3 and 4, we consider the four steps above to find the solution of current $\mathcal{W}(\mathcal{W}^{-}\boldsymbol{w})$, whereby we construct $\mathcal{W}$ as above, i.e., from the (test and) expansion functions defined on each element separately. In Chapter 5, we construct $\mathcal{W}$ from expansion and test functions defined on the entire array.

2.5 Examples

Before we discuss the calculational details of the moment matrix formulation, we present in this section a number of results. In [7, 11], we showed that results for the current and the electric far field of single strips and single rings agree excellently with results in the literature for wire

dipoles and wire rings [4, 20, 47, 92, 108, 118]. Therefore, we restrict ourselves to results for arrays of rings and line arrays of strips, where we compare quantitatively and qualitatively with results in the literature. All angles in the examples are spherical elevation angles, which are defined as usual within the xyz-system, see also Section 3.5, Figure 3.2. In the xz-plane and in the yz-plane, corresponding spherical azimuth angles of 0° and 90° are prescribed, respectively.

The first example is the directivity, as defined in Appendix C, of a uniform line array of 1000 strips of half a wavelength with spacing $\lambda/4$. The strips are positioned in a half space with $h = \lambda/4$. Each strip is excited by a voltage gap of 1V in its center, see Section 4.2 for details, and on each strip, one expansion function is defined, $\mathcal{W}_q \boldsymbol{e}_1 = \cos \pi\xi/2$ ($q = 1, \ldots, 1000$). Figure 2.7 (left) shows the normalized directivity in the xz-plane within one degree from broadside ($0^\circ \leq \theta \leq 0.72^\circ$). Figure 2.7 (right) shows the directivity in the same plane, but for $-90^\circ \leq \theta \leq -78^\circ$. These results agree excellently with results in [67] for the same line array but with

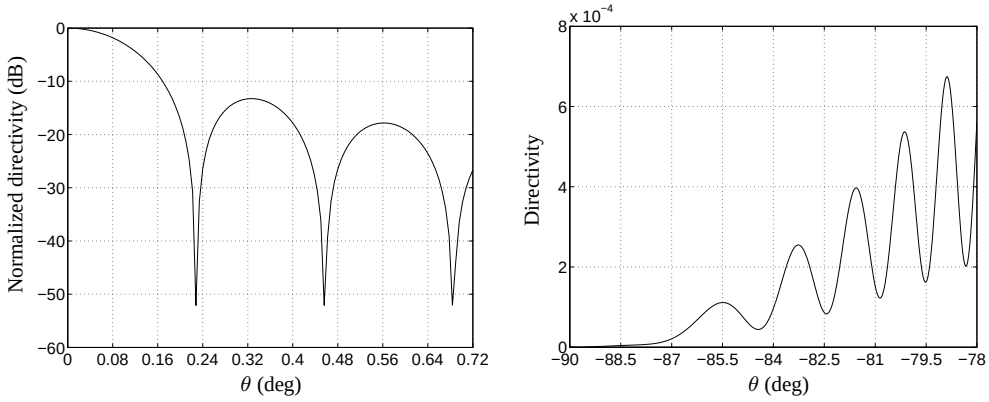

Figure 2.7 Directivity of uniform line array of 1000 strips of half a wavelength with spacing $\lambda/4$. The strips are positioned in a half space with $h = \lambda/4$ and excited by voltage gaps of 1V. Left: normalized directivity (in dB) in the xz-plane for $0^\circ \leq \theta \leq 0.72^\circ$; normalization: maximum directivity in the xz-plane. Right: directivity in the xz-plane for $-90^\circ \leq \theta \leq -78^\circ$. Parameter values: $\beta = b/\ell = 7/125$.

wires instead of strips. In the comparison, we used the rule of thumb found by Kraus [60: p. 238], which states that a thin strip of width $2b$ and a wire of cross-sectional radius $b/2$ with the same length as the strip are equivalent.

The second example is the impedance variation over a uniform line array of 201 strips of half a wavelength in free space with spacing $\lambda/2$. Each strip is excited by a voltage gap of 1V in its center and on each strip, 8 expansion functions are defined, $\mathcal{W}_q \boldsymbol{e}_n = \cos((2n-1)\pi\xi/2)$ ($n = 1, \ldots, 8$, $q = 1, \ldots, 201$). The strips are positioned on the x-axis and their indices increase in the positive direction. Figure 2.8 shows the absolute impedances of the strips as a function of

the strip index for scans at -45° and -75° in the xz-plane. For details on scanning, we refer

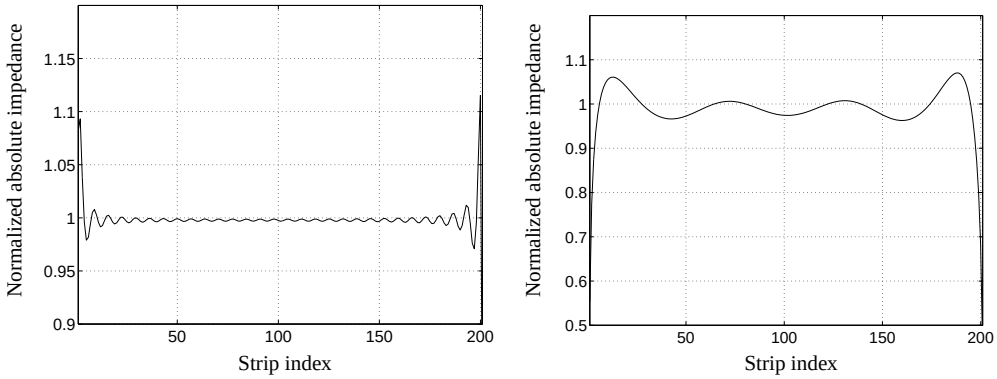

Figure 2.8 Normalized absolute strip impedances for a uniform line array of 201 strips of half a wavelength in free space with spacing $\lambda/2$. The strips are excited by voltage gaps of 1V. Left: scan at -45° in the xz-plane. Right: scan at -75° in the xz-plane. Normalization: infinite-array impedance. Parameter values: $\beta = b/\ell = 1/25$.

to Section 3.5. The impedance is normalized on the infinite-array absolute impedance, which is the same for all strips. The impedance variation shows clearly the edge effects, which cannot be described by the infinite-array approach. Up to slight amplitude differences, especially near the edges, the results agree with results in [45: Figs. 4, 6] for arrays composed of an infinite number of parallel line arrays, where each line array consists of 201 wires. The use of another array geometry explains the slight differences. As above, we applied the rule of thumb of Kraus to compare wires and strips. We note that in [45: Figs. 4, 6], the angles of scan are positive, because the corresponding azimuth angle is 180° instead of 0°.

The third example is the current-amplitude variation (in the centers of the strips) over a uniform line array of 25 strips of 15 mm long in free space with spacing 9 mm and excited at 10 GHz. In terms of the wavelength, the spacing is 0.3λ and the strip length is 0.5λ, which is about the resonant strip length. On each strip, 8 expansion functions are defined as above. The strips are either excited by voltage gaps of 1V in their centers together with a phase taper to scan at 45° in the xz-plane or by a plane wave polarized along the y-axis with incident angle -45° in the xz-plane. For details about plane waves, we refer to Section 4.3. Figure 2.9 shows that the amplitudes are very well approximated by the the amplitude obtained by the infinite-array approach except near the edges. Moreover, the amplitude variation for the plane-wave excitation is about the same as the amplitude variation for the voltage gaps. The shapes of the curves in Figure 2.9 agree very well with a result in [82: p. 3, Fig. 1.3(b)] for an array excited by a plane wave and composed of an infinite number of parallel line arrays, where each line array consists of 25 parallel wires. As above, slight quantitative differences are explained by the differences in

array geometry.

Figure 2.10 shows how the amplitude variation changes as the frequency is changed. At 8.6 GHz, the amplitude shows a much higher variation than at 9.0 GHz and 10.0 GHz. The

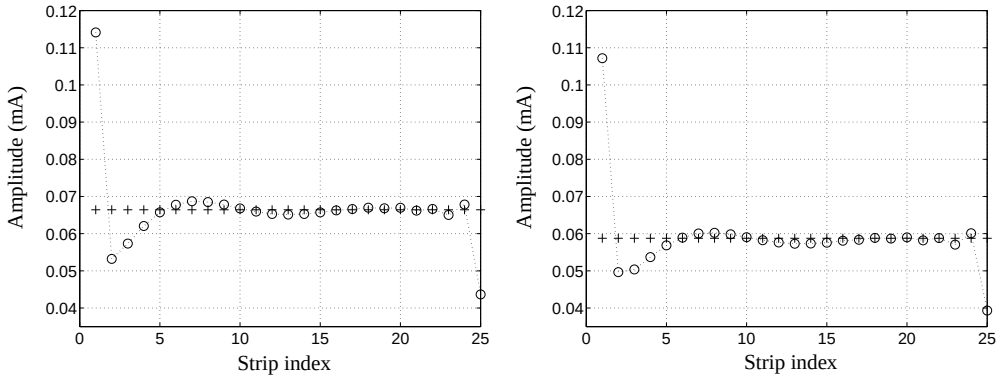

Figure 2.9 Current amplitudes (in the centers of the strips) for a uniform line array of 25 strips in free space with spacing 9 mm and excited at 10 GHz. Amplitudes computed by the element-by-element moment method ($\circ$) and by the infinite-array approach ($+$). Left: voltage gaps of 0.01V on the strips; phase taper to scan at 45° in the xz-plane. Right: plane wave excitation with incident angle -45° in the xz-plane and polarized along the y-axis with amplitude $10^{-3}\mathrm{Vm}^{-1}$. Parameter values: $2\ell = 15$ mm, $\beta = b/\ell = 3/50$.

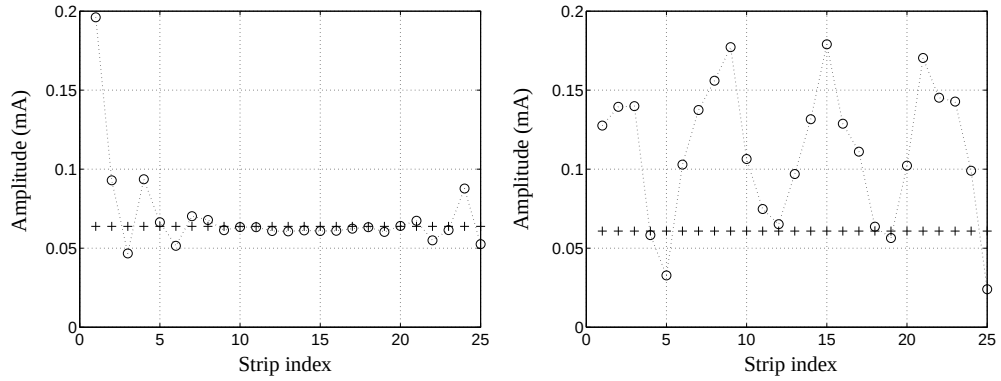

Figure 2.10 The same array as in Figure 2.9, but excited by the plane wave at 9.0 GHz (left) and 8.6 GHz (right).

frequency range in which the current shows a high variation coincides with the frequency range in which the behavior of a single strip changes from radiative to reactive. While the infinite-array current approximates the currents at 10 GHz, this approximation is highly inaccurate at

8.6 GHz, see Figure 2.10 (right). This result shows the necessity of finite-array approaches. Similar results are shown in [82: p. 3, Ch. 4], where an explanation in terms of array surface waves is proposed. In Section 6.2, we discuss the occurrence of large amplitude variations in further detail, see also the last paragraph of this section.

In the fourth example, we consider an exponentially spaced line array of 31 rings. The rings are positioned on the x-axis with $|\mathbf{c}_{q+1} - \mathbf{c}_q| = \lambda(1.12)^{q-1}/2$ ($q = 1, \ldots, 31$) and they are excited by voltage gaps of 1V positioned at $\varphi = \pi$. On each ring, 4 expansion functions are defined, $\mathcal{W}_q \boldsymbol{e}_n = \cos n\varphi$ ($n = 0, 1, 2, 3$). For the Matlab implementation described in Section 3.4 and the platform mentioned in Section 1.4, the CPU time for the construction of the moment matrix is 4 minutes and 32 seconds, while the CPU time of solving the moment-matrix equation is 1.5 seconds. As explained in [106], the advantage of exponential spacing is that a very narrow beamwidth can be obtained for much fewer elements than for a uniform spacing, given that grating lobes are unacceptable. To increase the beamwidth in uniformly spaced arrays, either the number of elements is increased or the spacing. If grating lobes are unacceptable for all scan angles, the spacing is bounded by $\lambda/2$. Hence, the number of elements needs to be increased to decrease the beamwidth, which may lead to prohibitively large numbers of elements. As

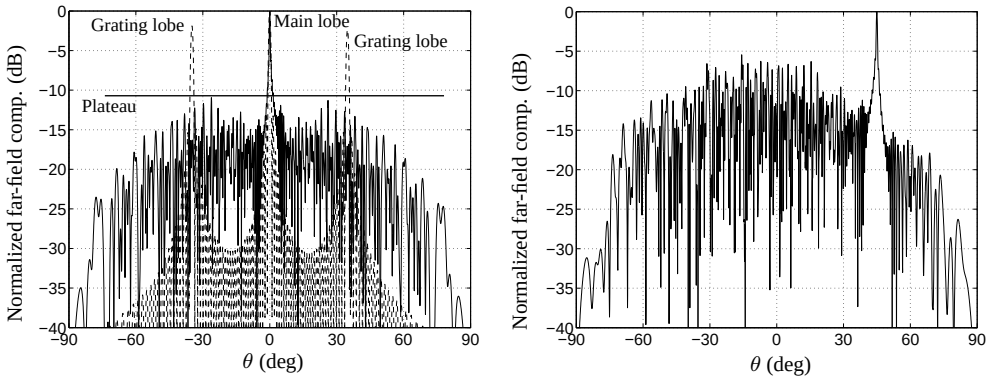

Figure 2.11 Normalized absolute ϕ-components (in dB) of the electric far fields in the xz-plane for an exponentially spaced line array with $|\mathbf{c}_{q+1} - \mathbf{c}_q| = \lambda(1.12)^{q-1}/2$ and $c_{q,y} = 0$ (solid curve), and for a uniformly spaced line array with spacing 1.75λ (dashed curve), both with 31 rings and positioned in a half space with $h = \lambda/5$. The rings are excited by voltage gaps of 1V positioned at $\varphi = \pi$. Left: for a scan at 0°. Right: for a scan at 45° (only exponential array). Normalization: maximum absolute ϕ-component for the uniform array. Parameter values: $ka = \pi/3$, $\beta = 3/100$, $\psi = 0$.

shown in Figure 2.11 (left), the beamwidth of the exponentially spaced array exhibits a grating-lobe plateau, which is higher than the side-lobe level of the uniformly spaced array, but much lower than the grating-lobe level at $\pm 34.9^\circ$. These effects are shown in [106] for a uniform

rectangular 41×41 array of rectangular patches. Figure 2.11 (right) shows a negative side effect of the exponential spacing. For a scan at 45° in the xz-plane, the side lobe level increases to -6 dB, which is in practice highly unacceptable. Finally, we note that the exponentially spaced array is much wider than the uniformly spaced array. At 10 GHz, the exponentially spaced array is 3.62 m wide, while the uniformly spaced array is only 1.58 m wide.

The fifth example concerns a uniform rectangular 20×20 array of rings with spacing $\lambda/2$ in both x and y-direction. The rings are excited by voltage gaps of 1V positioned at $\varphi = \pi$. On each ring, 3 expansion functions are defined, $\mathcal{W}_q \boldsymbol{e}_1 = 1, \mathcal{W}_q \boldsymbol{e}_2 = \cos\varphi$, and $\mathcal{W}_q \boldsymbol{e}_3 = \sin\varphi$ $(q = 1, \ldots, 400)$. For the Matlab implementation described in Section 3.4 and the platform mentioned in Section 1.4, the CPU time for the construction of the moment matrix is 3 hours and 57 minutes, while the CPU time for solving the moment-matrix equation is 5.6 seconds. Figure 2.12 shows the ϕ-component of the electric far field in the xz-plane (H-plane), both for the array in which mutual coupling is taken into account and for the array in which mutual coupling is ignored. In case mutual coupling is ignored, the maximum at 0° is about 7 dB

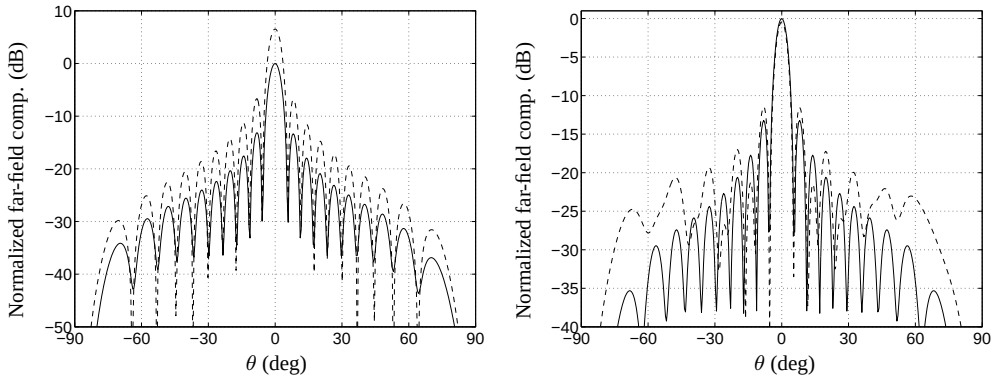

Figure 2.12 Normalized absolute ϕ-component (in dB) of the electric far field for a uniform rectangular 20×20 array of rings excited by voltage gaps of 1V positioned at $\varphi = \pi$. Left: in the xz-plane, with (solid curve) and without (dashed curve) mutual coupling. Right: in the yz-plane, with all rings excited (solid curve) and with the 9th row not excited (dashed curve). Normalization: maximum absolute ϕ-component for the array with mutual coupling. Parameter values: $ka = \pi/3$, $\beta = 3/100$, $\psi = 0$, centers: $(m\lambda/2, n\lambda/2)$ $(m, n = 0, \ldots, 19)$.

higher than in case mutual coupling is taken into account. In other words, the energy of the co-polarization is overestimated by more than a factor of 2. Since the cross-polarization, i.e., the θ-component in the xz-plane, is zero, the same is valid for the radiation intensity. These observations show that mutual coupling must be taken into account.

Figure 2.12 shows the ϕ-component of the electric far field in the yz-plane (E-plane), both for the uniformly excited array and for the array in which the 9th row is not excited. In the

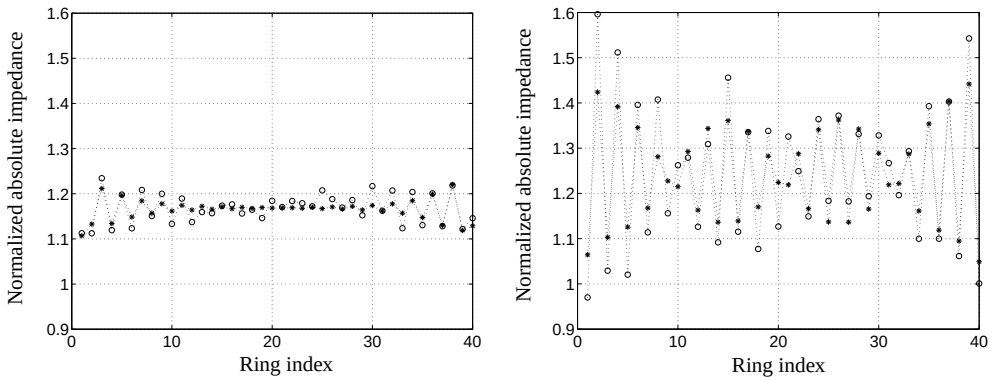

Figure 2.13 Normalized absolute ring impedances both for a uniform line array of 40 rings ($*$) of half a wavelength in free space with spacing $\lambda/2$ at $ka = \pi/3$, and for the same line array, but with a small random perturbation on the radii, widths, and centers ($\circ$). The parameter values for the random perturbation are shown in Appendix **??**. The rings are excited by voltage gaps of 1V at $\varphi = \pi$. Left: at $ka = \pi/3$. Right: the frequency is changed such that $ka = 0.943$. Normalization: for both frequencies, the absolute impedance of the single ring in the uniform line array. Parameter values: $\beta = b/a = 3/100$, $\psi = 0$, $d/a = 3$ ($d = \lambda/2$ at $ka = \pi/3$).

second case, the highest side lobes are about 1.5 dB higher and the main lobe is about 0.5 dB lower than in the first case. Moreover, other side lobes increase as well. This example shows clearly that in an array that is excited per row by means of suitable feeding networks, the failing of a row considerably decreases the array performance.

In the previous examples, we considered arrays with uniform element geometry. In practice, the element geometry and the spacing are not uniform; small differences result after the production process. To investigate the effect of such differences, the last example concerns a uniform line array of 40 rings of which the ring radii, the ring widths, and the ring centers are perturbed. The perturbations are generated randomly for a chosen tolerance of $0.5\mathrm{mm}$ for radii, widths, and center coordinates. Both line arrays are excited by voltage gaps of 1V at $\varphi = \pi$. The frequency is 1 GHz. The uniform line array exhibits a spacing of $d/a = 3$ ($d = \lambda/2$ at $ka = \pi/3$), and the ratio of half the ring width and the radius is $\beta = b/a = 3/100$. On each ring, 8 expansion functions are defined, $\mathcal{W}_q \boldsymbol{e}_n = \cos n\varphi$ ($n = 0, \ldots, 7$, $q = 1, \ldots, 40$). For the perturbed line array, also one sine function is defined to account for the asymmetry with respect to the line-array axis, $\mathcal{W} = \mathcal{W}_q^{\cos} \sqcup \mathcal{W}_q^{\sin}$ with $\mathcal{W}_q^{\cos}$ defined as $\mathcal{W}$ for the uniform line array and $\mathcal{W}_q^{\sin}$ defined by $\mathcal{W}_q^{\sin} \boldsymbol{e}_1 = \sin\varphi$. Figure 2.13 (left) shows the absolute impedances of the rings as a function of the ring indices. Both for the uniform array and for the perturbed array, the impedances vary 5% with respect to their mean value. For the unperturbed array, the absolute impedances are uniform in the middle of the array, where they equal the impedance obtained

by the infinite-array approach. At the edges, oscillations occur. For the perturbed array, the impedances are not uniform in the middle of the array, but differ at most 3.5% from their mean value. At the edges, approximately the same oscillations occur as at edges of the unperturbed array. Figure 2.13 (right) shows the impedances at $ka = 0.943$, where only k is changed by means of the frequency. The geometry parameters of the unperturbed array are not changed. The pattern of the absolute impedances of the uniform array is the same as the pattern of the perturbed array. The impedances oscillate and vary about 30% with respect to their mean value. Moreover, in both cases, the oscillations are modulated. The amplitude of the modulation is larger at the edges of the array than in the middle of the array, where the impedances vary about 10% with respect to their mean value. The differences between the impedances of the perturbed and unperturbed array are at most 5% in the middle of the array (with one exception) and run up to 15% near the edges.

The observations above indicate that the array behavior is reasonably stable for small parameter changes. The relatively large modulations reduce the performance of the array considerably. Therefore, such modulations must be avoided in the design. In this respect, we emphasize that in the example above the variations of the absolute impedances are larger for the perturbed array than for the uniform array. Hence, in practice, we may encounter larger variations of the element impedances than found by simulations of uniform arrays.

Recently, modulated oscillations of the element impedances have been found in arrays of collinear, or E-plane oriented, wires with spacing $\lambda/2$ in a half space with $h = \lambda/4$ [46]. These modulations occur at the frequency for which the elements exhibit a 'resonant broadside embedded impedance', i.e., the frequency for which the reactances of the elements are on average zero. In [46], it is mentioned that the modulations were not observed for arrays of parallel, or H-plane oriented, wires, neither for arrays in free space. In contrast, the rings in Figure 6.14 are positioned in free space and are E-plane oriented, since the voltage gaps are all positioned on the array axis. Moreover, the spacing is not equal to $\lambda/2$, but 0.464λ at $ka = 0.943$. In Chapter 6, we will explain the occurrence of modulated oscillations by showing that they are caused by the excitation of specific eigencurrents analyzed in Chapter 5. Moreover, we will show that the variations of the element impedances as shown in Figure 2.10 are explained by the same mechanism.

CHAPTER 3

The Impedance Operator

As part of the first phase of our research, see the scheme in Figure 1.7, we discuss in this chapter the impedance operator, which relates the current on the array elements to the excitation of the array. The aspects we consider are choice of suitable test and expansion functions for the moment method, calculation of the moment matrix components, numerical computation of these components, and analysis of uniform (line) arrays. In Sections 3.1 and 3.2, we describe the aspects of test and expansion functions commonly used in the literature from an operator-theoretical perspective. As a result of the averaging procedure in Chapter 2, the moment matrix components calculated in Section 3.3 reduce to single integrals for line arrays of strips. For line arrays of rings, they reduce to double and single integrals in case of mutual and self coupling, respectively. Two calculation procedures are explored, one in which the differential part of the averaged impedance operator is 'equally distributed' over test and expansion functions as in Green's theorem, and one in which this part is transferred to the test functions such that its Sturm-Liouville properties can be exploited. In the special topic of uniform (line) arrays, the infinite-array approach is applied to approximate the current on the elements. The convergence or divergence of this approach is related to the physical phenomena of grating-lobe appearance and grazing scan. This relation extends results in the literature in that different types of line arrays are considered. Moreover, a mathematical explanation of the convergence and divergence aspects is provided based on Toeplitz properties of the impedance operator. Further investigation of these properties and their relation to scanning are described in Chapter 5.

3.1 Space Characterization

We consider tangential excitation fields $\boldsymbol{E}_S$ for which $\boldsymbol{v}^{\mathrm{ex}}$ is square integrable on Π_ξ. Here, Π_ξ is the range of the parameter describing the centerline of the surface S of microstrip elements, see Subsection 2.3.1. In other words, $\boldsymbol{v}^{ex}$ belongs to the (Hilbert) space $L_2\left(\Pi_\xi, \mathbb{C}^{N_{\mathrm{el}}}\right)$ [98].

The physical interpretation of this property is that the total electric energy of the excitation field is finite. Since the current on the elements is given by $\mathcal{Z}_{\rm a}\boldsymbol{w} = \boldsymbol{v}^{ex}$, we construct $\mathcal{X}_{\rm a} = \mathrm{dom}(\mathcal{Z}_{\rm a})$ such that $\mathrm{ran}(\mathcal{Z}_{\rm a}) \subset \mathcal{Y}_{\rm a} = L_2\left(\Pi_\xi, \mathbb{C}^{N_{\rm el}}\right)$. We show that the latter can be accomplished by choosing

$$\mathcal{X}_{\rm a} = \left\{ \boldsymbol{w} \in H_{2,1}\left([-1,1], \mathbb{C}^{N_{\rm el}}\right) \,\middle|\, \boldsymbol{w}(1) = \boldsymbol{w}(-1) = \boldsymbol{0} \right\} , \tag{3.1}$$

for the strips, and

$$\mathcal{X}_{\rm a} = H_{2,1,\rm per}\left([-\pi,\pi], \mathbb{C}^{N_{\rm el}}\right) , \tag{3.2}$$

for the rings. Here, $H_{2,1}\left([-\alpha,\alpha], \mathbb{C}^N\right)$ is the subspace of $L_2\left([-\alpha,\alpha], \mathbb{C}^N\right)$ consisting of all functions with derivative in L_2, see [73: pp. 22, 50]. We omit $\mathbb{C}^N$ in this notation if $N = 1$. For $\boldsymbol{w} \in H_{2,1}\left([-\alpha,\alpha], \mathbb{C}^N\right)$, its derivative in L_2 is denoted by $\mathsf{D}\boldsymbol{w}$, i.e.,

$$\boldsymbol{w}(\xi) = \boldsymbol{w}(0) + \int_0^\xi (\mathsf{D}\boldsymbol{w})(\xi')\, d\xi' , \tag{3.3}$$

Notice the difference of notation between the differential operator $\mathcal{D}$ introduced in (2.10)[2] and the L_2-derivative D. The reason to introduce the L_2-derivative is that functions in $H_{2,1}$ are continuous, but they are not necessarily differentiable in the classical sense. With the inner product $\langle \cdot\,, \cdot \rangle_{H_{2,1}}$ defined by

$$\langle \boldsymbol{v}, \boldsymbol{w} \rangle_{H_{2,1}} = \langle \boldsymbol{v}, \boldsymbol{w} \rangle_{L_2} + \langle \mathsf{D}\boldsymbol{v}, \mathsf{D}\boldsymbol{w} \rangle_{L_2} , \quad \langle \boldsymbol{v}, \boldsymbol{w} \rangle_{L_2} = \int_{-\alpha}^{\alpha} (\boldsymbol{v}(\xi) \circ \boldsymbol{w}(\xi))\, d\xi , \tag{3.4}$$

$H_{2,1}\left([-\alpha,\alpha], \mathbb{C}^N\right)$ is a Hilbert space [58: App. A.3, p. 227], whereas with the usual L_2 inner product (3.4)[2], it is not. We note that $(\,.\,\circ\,.\,)$ is the inner product on $\mathbb{C}^N$ defined by (2.101), where we omit the subscript $_N$. Similarly, $H_{2,2}\left([-\alpha,\alpha], \mathbb{C}^N\right)$ consists of all differentiable functions on $[-\alpha,\alpha]$ for which the derivative belongs to $H_{2,1}\left([-\alpha,\alpha], \mathbb{C}^N\right)$. The spaces $H_{2,1,\rm per}\left([-\pi,\pi], \mathbb{C}^N\right)$ and $H_{2,2,\rm per}\left([-\pi,\pi], \mathbb{C}^N\right)$ consist of all functions in $H_{2,1}\left([-\pi,\pi], \mathbb{C}^N\right)$ and $H_{2,2}\left([-\pi,\pi], \mathbb{C}^N\right)$, which are periodic on the real line with period 2π. Finally, we introduce the spaces $C^\infty([-\alpha,\alpha])$ and $C^\infty([-\alpha,\alpha]^2)$, which consists of all infinitely differentiable functions on $[-\alpha,\alpha]$ and $[-\alpha,\alpha]^2 = \{\, (x,y) \,|\, x,y \in [-\alpha,\alpha] \,\}$.

Let us first consider the characterization of $\mathcal{X}_{\rm a}$ for the strips. The operators $\mathcal{F}_{pq}$ in (2.53) – (2.55) are Fredholm operators with displacement kernels F_{pq}. General theory of such operators is given in Appendix B. For $p \neq q$, the kernel F_{pq} belongs to $C^\infty([-2,2])$, and hence to $H_{2,1}([-2,2])$. For $p = q$, the kernel belongs to $L_2([-2,2])$, but not to $H_{2,1}([-2,2])$, see (2.59). Therefore, F_{qq} is decomposed into a logarithmic part, $-(\log \xi^2)/2k\ell\beta$, and a part in $H_{2,1}([-1,1])$. The kernel F_{pq} with $p \neq q$ and both parts of the kernel F_{qq} induce Fredholm operators from $L_2([-1,1])$ to $H_{2,1}([-1,1])$, see Lemmas 2 and 3 in Appendix B. Hence, for all

p, q, $\mathcal{F}_{pq} w \in H_{2,1}([-1,1])$ whenever $w \in L_2([-1,1])$. Moreover, if $w \in H_{2,1}([-1,1])$, then $\mathcal{F}_{pq} w \in H_{2,2}([-1,1])$ for $p \neq q$ and $\mathcal{F}_{qq} w \in H_{2,2}([-1,1])$ if and only if $w(1) = w(-1) = 0$, see Corollaries 1 and 2 in Appendix B. From this result and the expression for $\mathcal{Z}_\mathrm{a}$ in (2.53), we conclude that $\mathcal{Z}_\mathrm{a} \boldsymbol{w} \in L_2\left([-1,1], \mathbb{C}^{N_\mathrm{el}}\right)$ whenever $\boldsymbol{w} \in \mathcal{X}_\mathrm{a}$, where $\mathcal{X}_\mathrm{a}$ is given by (3.1). We note that the Helmholtz operator in (2.53) should be interpreted in L_2-sense, i.e., as $1+\mathsf{D}^2/k^2\ell^2$. The result $\mathcal{Z}_\mathrm{a} \boldsymbol{w} \in L_2\left([-1,1], \mathbb{C}^{N_\mathrm{el}}\right)$ is also valid when the kernels F_{pq} are replaced by the approximate kernels $\tilde{F}_{pq}$ with corresponding Fredholm operators $\tilde{\mathcal{F}}_{pq}$. The physical interpretation of the boundary conditions $\boldsymbol{w}(1) = \boldsymbol{w}(-1) = \boldsymbol{0}$ is that the current cannot 'flow' out of the strips. As shown above, these conditions are necessary to obtain $\mathrm{ran}(\mathcal{Z}_\mathrm{a}) \subset L_2\left([-1,1], \mathbb{C}^{N_\mathrm{el}}\right)$, which means that the total electric energy of the tangential scattered electric field at the strips is finite. This shows a direct link between the space characterization and the physical properties of the electromagnetic field.

For the rings, we consider only the expression (2.96) for $\mathcal{Z}_\mathrm{a}$ with the approximate kernels. Let us first consider the integral operators $\tilde{\mathcal{K}}_{1,qq}$ and $\tilde{\mathcal{K}}_{2,qq}$. These operators are Fredholm operators with displacement kernels $\tilde{K}_{1,qq}(\,\cdot\,)\cos(\,\cdot\,)$ and $\tilde{K}_{2,qq}(\,\cdot\,)\sin(\,\cdot\,)$. The kernel $\tilde{K}_{2,qq}(\,\cdot\,)\sin(\,\cdot\,)$ belongs to $H_{2,1,\mathrm{per}}([-2\pi, 2\pi])$ (period 4π), so that $\tilde{\mathcal{K}}_{2,qq} w \in H_{2,2,\mathrm{per}}([-\pi,\pi])$ whenever $w \in H_{2,1,\mathrm{per}}([-\pi,\pi])$, see Corollary 3. The kernel $\tilde{K}_{1,qq}(\,\cdot\,)\cos(\,\cdot\,)$ belongs to $L_2([-2\pi, 2\pi])$, but not to $H_{2,1,\mathrm{per}}([-2\pi, 2\pi])$. We could decompose this kernel in the same manner as F_{qq} into a part proportional to $\log\varphi^2$ and a part in $H_{2,1}([-2\pi, 2\pi])$. By doing this, we would loose the periodicity of the kernel. Therefore, we decompose the kernel into the part $-\cos\varphi \, \log\sin^2(\varphi/2) \,/\, 2k a_q \beta_q$ and a part in $H_{2,1,\mathrm{per}}([-2\pi, 2\pi])$. The first part leads to a Fredholm operator from $L_2([-\pi,\pi])$ to $H_{2,1,\mathrm{per}}([-\pi,\pi])$, see Lemma 5 in Appendix B. Moreover, if $w \in H_{2,1,\mathrm{per}}([-\pi,\pi])$, then the Fredholm operator transforms w into an element of $H_{2,2,\mathrm{per}}([-\pi,\pi])$. The second part leads to a Fredholm operator, which is treated in the same manner as $\tilde{\mathcal{K}}_{2,qq}$. Summarizing, we find that $\tilde{\mathcal{K}}_{1,qq} w, \tilde{\mathcal{K}}_{2,qq} w \in H_{2,2,\mathrm{per}}([-\pi,\pi])$ for $w \in H_{2,1,\mathrm{per}}([-\pi,\pi])$. The same result holds for $p \neq q$, because the kernels $\tilde{K}_{1,pq}$ and $\tilde{K}_{2,pq}$ belong to $C^\infty([-\pi,\pi]^2)$ and are periodic with period 2π in both their arguments. From these results and the expression of $\mathcal{Z}_\mathrm{a}$ in (2.53), we conclude that $\mathcal{Z}_\mathrm{a} \boldsymbol{w} \in L_2\left([-1,1], \mathbb{C}^{N_\mathrm{el}}\right)$ whenever $\boldsymbol{w} \in \mathrm{dom}(\mathcal{Z}_\mathrm{a})$ given by (3.2). We note that he Helmholtz operator and the single derivative in (2.96) should be interpreted in L_2-sense, i.e., as $1 + \mathsf{D}^2/k^2 a_p^2$ and $\mathsf{D}/k^2 a_p^2$.

From the above, an essential difference between the space characterizations for the strips and the rings is observed. The Fredholm operators for the rings map a function in their domain (3.2) into $H_{2,2,\mathrm{per}}([-\pi,\pi], \mathbb{C}^{N_\mathrm{el}})$, which is a subset of their domain. On the contrary, the Fredholm operators for the strips map a function in their domain (3.1) into $H_{2,2}([-1,1], \mathbb{C}^{N_\mathrm{el}})$, which is *not* a subset of their domain. This difference can be explained as follows. For the rings, the 'boundary condition' of periodicity follows from the geometry of the rings, which is satisfied by both the current and the tangential scattered field on the rings. For the strips, the boundary

condition $\boldsymbol{w}(1) = \boldsymbol{w}(-1) = \mathbf{0}$ is an impressed boundary condition on the current, which is not necessarily satisfied by the tangential scattered field.

3.2 Choosing Expansion and Test Functions

We choose the expansion and test functions as outlined in Subsection 2.4.3. Let us first consider the strips. Since the mapping $\mathcal{V}$ in the construction of the moment matrix $[\mathcal{V}^{-}\mathcal{Z}_{\mathrm{a}}\mathcal{W}]$ should be chosen in accordance with the properties of $\mathcal{Z}_{\mathrm{a}}$, the test functions $(\mathcal{V}_q \boldsymbol{e}_n)(\,\cdot\,; q)$ on the qth strip should be chosen in accordance with the properties of the operators $(1 + \mathsf{D}^2/k^2\ell^2)\mathcal{F}_{qq'}$ in (2.53) for $q' = 1, \ldots, N_{\mathrm{el}}$. In other words, these functions should be elements of the ranges of the Helmholtz operator $1 + \mathsf{D}^2/k^2\ell^2$ with domains $\mathrm{ran}(\mathcal{F}_{qq'})$. As shown in the previous section, $\mathrm{ran}(\mathcal{F}_{qq'}) \subset H_{2,2}([-1,1])$. The operator $1 + \mathsf{D}^2/k^2\ell^2$ is a Sturm-Liouville operator with the Sturm Liouville boundary conditions $w(1) = w(-1) = 0$. Examples of the application of Sturm-Liouville theory to problems of mathematical physics can be found in [101: Ch. V, Sec. 2; Ch. IX, Sec. 3] and [127: Sec. 4.3]. The operator-theoretical aspects can be found in [98]. For a direct application of these aspects to Sturm-Liouville problems, we refer to [81: pp. 361 – 369]. According to Sturm-Liouville theory, the operator $1 + \mathsf{D}^2/k^2\ell^2$ has a countable set of eigenfunctions, i.e.,

$$\cos\left(\frac{(2n-1)\pi\xi}{2}\right), \qquad \sin n\pi\xi\,, \tag{3.5}$$

with eigenvalues

$$\Omega_{\cos,n} = 1 - \frac{(2n-1)^2\pi^2}{4k^2\ell^2}\,, \qquad \Omega_{\sin,n} = 1 - \frac{n^2\pi^2}{k^2\ell^2}\,. \tag{3.6}$$

Here, $n \in \mathbb{N}$. The eigenfunctions (3.5) establish a total (or complete) orthonormal set [98: p. 67] in $L_2([-1,1])$ with respect to the L_2 inner product. Since $\mathcal{Z}_{\mathrm{a}}$ is composed of $(1+\mathsf{D}^2/k^2\ell^2)\mathcal{F}_{qq'}$, the most logical choice of the test functions $(\mathcal{W}_q \boldsymbol{e}_n)(\,\cdot\,; q)$ is (3.5).

The mapping $\mathcal{W}$ in the construction of the moment matrix $[\mathcal{V}^{-}\mathcal{Z}_{\mathrm{a}}\mathcal{W}]$ should be chosen such that the expansion functions $\mathcal{W}\boldsymbol{e}_n$ are elements of $\mathcal{X}_{\mathrm{a}}$ in (3.1). Therefore, the expansion functions $(\mathcal{W}_q \boldsymbol{e}_n)(\,\cdot\,; q)$ on the qth strip should be chosen in the set of functions $\{\, w \in H_{2,1}([-1,1]) \,|\, w(1) = w(-1) = 0 \,\}$, which is equipped with the $H_{2,1}$ inner product (3.4) as in Section 3.1. Since the linear span of the eigenfunctions (3.5) is both contained in this set and dense in this set, and since $\mathcal{F}_{qq'}$ assumes the form of a convolution integral for all values of q and q', it is reasonable to choose the expansion functions from (3.5) as well. We note that the linear span of eigenfunctions is not dense in the whole set $H_{2,1}([-1,1])$. Assuming that we can describe the domain and the range of $\mathcal{Z}_{\mathrm{a}}$ by the same *finite* subset of the countable set defined by (3.5), we choose $\mathcal{V} = \mathcal{W}$. Then, on each strip, the test and expansion functions are

the same, or, bas($\mathcal{V}$) = bas($\mathcal{W}$). As explained in Subsection 2.4.3, we can replace $\mathcal{V}^-$ by $\mathcal{W}^-$ and $\mathcal{Q}$ by $\mathcal{P}$, if we interpret $\mathcal{W}^-$ and $\mathcal{P}$ according to the space they act on. We specify the (test and) expansion functions on the array of strips by

$$\mathcal{W} = \mathcal{W}_1 \sqcup \ldots \sqcup \mathcal{W}_{N_{\mathrm{el}}}, \qquad \mathcal{W}_q = \mathcal{W}_q^{\cos} \sqcup \mathcal{W}_q^{\sin}, \tag{3.7}$$

and

$$\begin{aligned}
&(\mathcal{W}_q^{\cos}\boldsymbol{e}_n)(\xi;q) = \cos\left(\frac{(2n-1)\pi\xi}{2}\right), \qquad n = 1,2,\ldots,N_{\cos}(q)\,,\\
&(\mathcal{W}_q^{\sin}\boldsymbol{e}_n)(\xi;q) = \sin n\pi\xi, \qquad n = 1,2,\ldots,N_{\sin}(q)\,,\\
&(\mathcal{W}_q^{\cos}\boldsymbol{e}_n)(\,\cdot\,;q') = (\mathcal{W}_q^{\sin}\boldsymbol{e}_n)(\,\cdot\,;q') = 0, \qquad q' \neq q\,.
\end{aligned} \tag{3.8}$$

Here, $\boldsymbol{N}_{\exp} = \boldsymbol{N}_{\cos} + \boldsymbol{N}_{\sin}$. By (3.7) and (3.8), we specify the (test and) expansion functions as well as the order in which they appear in the moment matrix $[\mathcal{W}^-\mathcal{Z}_{\mathrm{a}}\mathcal{W}]$, see also (2.131). By decomposing each $\mathcal{W}_q$ into $\mathcal{W}_q^{\cos}$ and $\mathcal{W}_q^{\sin}$ we distinguish between 'symmetric' and 'antisymmetric' currents on the strips. We could have written the eigenfunctions as $\sin(n\pi(\xi+1)/2)$, but then, they would be alternately even and odd. The expression for $\mathcal{Z}_{\mathrm{a}}$ in (2.53) reveals that, if $\boldsymbol{v}^{\mathrm{ex}}$ is even or odd, the solution to $\mathcal{Z}_{\mathrm{a}}\boldsymbol{w} = \boldsymbol{v}^{\mathrm{ex}}$ is even or odd as well. Therefore, we choose $\boldsymbol{N}_{\sin} = \boldsymbol{0}$ if $\boldsymbol{v}^{\mathrm{ex}}$ is even and $\boldsymbol{N}_{\cos} = \boldsymbol{0}$ if $\boldsymbol{v}^{\mathrm{ex}}$ is odd. Finally, we note that the functions $\mathcal{W}_q\boldsymbol{e}_n$ are entire-domain functions with respect to the strip surface S_q, because they represent functions that are non-zero on S_q except for a subset with measure zero. The functions $\mathcal{W}_q\boldsymbol{e}_n$ are piecewise or sub-sectional functions with respect to the surface S of the complete array, because they represent functions on S that are non-zero on a single surface S_q only. If not stated otherwise, we call the functions $\mathcal{W}_q\boldsymbol{e}_n$ in (3.8) entire-domain functions.

Instead of using the entire-domain functions for the strip surfaces S_q, we can also use piecewise or sub-sectional functions. When $\mathcal{V} = \mathcal{W}$ as above, the expansion and test functions $(\mathcal{W}_q\boldsymbol{e}_n)(\,\cdot\,;q)$ on the qth strip should be elements of $H_{2,1}([-1,1])$ satisfying the Sturm-Liouville boundary conditions in order to have $\mathcal{W}\boldsymbol{e}_n \in \mathcal{X}_{\mathrm{a}}$. An obvious choice for $\mathcal{W}$ is then

$$\begin{aligned}
&\mathcal{W} = \mathcal{W}_1 \sqcup \ldots \sqcup \mathcal{W}_{N_{\mathrm{el}}},\\
&(\mathcal{W}_q\boldsymbol{e}_n)(\xi;q) = w_{\mathrm{tri}}\left(\frac{\xi-\xi_q(n)}{\Delta_{\exp}(q)}\right), \qquad w_{\mathrm{tri}}(\xi) = (1-|\xi|)\,1_{[-1,1]}(\xi)\,,\\
&(\mathcal{W}_q\boldsymbol{e}_n)(\,\cdot\,;q') = 0, \qquad q' \neq q\,,
\end{aligned} \tag{3.9}$$

where $\Delta_{\exp}(q) = 2/(N_{\exp}(q)+1)$, $\xi_q(n) = -1+n\Delta_{\exp}(q)$, and $n = 1,2,\ldots,N_{\exp}(q)$. These functions describe triangles of height 1 on a uniform grid on the interval $[-1,1]$.

For the rings, we construct only entire-domain expansion functions. The Helmholtz operators $1 + \mathsf{D}^2/k^2a_q^2$ in (2.96) are Sturm-Liouville operators with the Sturm-Liouville boundary

conditions of periodicity, i.e., $w(\pi) = w(-\pi)$ and $(\mathsf{D}w)(\pi) = (\mathsf{D}w)(-\pi)$. These operators have countable sets of eigenfunctions, i.e.,

$$\cos n\varphi, \qquad \sin n\varphi\,, \tag{3.10}$$

both with eigenvalues

$$\Omega_{q,n} = 1 - \frac{n^2}{k^2 a_q^2}\,. \tag{3.11}$$

Here, $n \in \mathbb{N} \cup \{0\}$ for the cosine functions and $n \in \mathbb{N}$ for the sine functions. According to Sturm-Liouville theory, the eigenfunctions (3.10) are orthogonal, but not normalized, with respect to the L_2 inner product and they establish a total set in $L_2([-\pi,\pi])$. Since $\mathcal{Z}_\mathrm{a}$ is composed of $(1+\mathsf{D}^2/k^2a_q^2)\tilde{\mathcal{K}}_{1,qq'}$ and $\mathsf{D}\tilde{\mathcal{K}}_{2,qq'}/k^2a_q^2$, the ranges of which are subsets of $L_2([-\pi,\pi])$ and $H_{2,1,\mathrm{per}}([-\pi,\pi])$, it is reasonable to choose the test functions $(\mathcal{V}_q\boldsymbol{e}_n)(\,\cdot\,;q)$ on the qth ring from the set defined by (3.10). The expansion functions $(\mathcal{W}_q\boldsymbol{e}_n)(\,\cdot\,;q)$ on the qth ring should be chosen in $H_{2,1,\mathrm{per}}([-\pi,\pi])$. Since the linear span of the eigenfunctions (3.10) is contained in $H_{2,1,\mathrm{per}}([-\pi,\pi])$ and dense in $H_{2,1,\mathrm{per}}([-\pi,\pi])$, and since $\tilde{\mathcal{K}}_{1,qq'}$ and $\tilde{\mathcal{K}}_{2,qq'}$ assume the form of convolution integrals for all values of q and q', it is reasonable to choose the expansion functions from (3.10) as well. Assuming that we can approximate the domain and the range of $\mathcal{Z}_\mathrm{a}$ by the same *finite* subset of the countable set defined by (3.10), we choose $\mathcal{V} = \mathcal{W}$ as in the analysis for the strips above. We specify the expansion and test functions on the array of rings by (3.7) and

$$\begin{aligned}
&(\mathcal{W}_q^{\cos}\boldsymbol{e}_n)(\xi;q) = \cos(n-1)\varphi, \qquad n = 1,2,\ldots,N_{\cos}(q)\,,\\
&(\mathcal{W}_q^{\sin}\boldsymbol{e}_n)(\xi;q) = \sin n\varphi, \qquad n = 1,2,\ldots,N_{\sin}(q)\,,\\
&(\mathcal{W}_q^{\cos}\boldsymbol{e}_n)(\,\cdot\,;q') = (\mathcal{W}_q^{\sin}\boldsymbol{e}_n)(\,\cdot\,;q') = 0, \qquad q' \neq q\,.
\end{aligned} \tag{3.12}$$

In Subsection 3.3.2, we will see that these functions are eigenfunctions of $\mathcal{Z}_\mathrm{a}$, which confirms our choice of test and expansion functions.

3.3 Calculational Aspects of the Moment-Matrix Components

The moment matrix $[\mathcal{W}^-\mathcal{Z}_\mathrm{a}\mathcal{W}]$ is composed of the blocks $[\mathcal{W}_p^-\mathcal{Z}_\mathrm{a}\mathcal{W}_q]$ with $p,q = 1,\ldots,N_\mathrm{el}$, see (2.131). From the calculus result (2.130)[1], it follows that

$$[\mathcal{W}_p^-\mathcal{Z}_\mathrm{a}\mathcal{W}_q] = G_p^{-1}Z_{pq}\,. \tag{3.13}$$

Here, $Z_{pq}(m,n) = \langle \mathcal{W}_p \boldsymbol{e}_m, \mathcal{Z}_\mathrm{a} \mathcal{W}_q \boldsymbol{e}_n \rangle_{L_2}$ ($m = 1, \ldots, N_\mathrm{exp}(p)$, $n = 1, \ldots, N_\mathrm{exp}(q)$) and $G_p = G(\mathrm{bas}(\mathcal{W}_p))$ with respect to the inner product on $\mathcal{Y}_\mathrm{a}$. Then, the Gram matrix G in (2.130) is a block-diagonal matrix with the blocks G_p on the diagonal. Moreover, the matrix Z in (2.130)[1] is a block matrix with blocks Z_{pq}. In this section, we consider the calculation of the blocks G_p and Z_{pq} for the expansion and test functions chosen in the previous section.

3.3.1 Line Arrays of Strips

For line arrays of strips, the matrices Z_{pq} are defined by $Z_{pq}(m,n) = \langle \mathcal{W}_p \boldsymbol{e}_m, \mathcal{Z}_\mathrm{a} \mathcal{W}_q \boldsymbol{e}_n \rangle_{L_2}$, where $\mathcal{Z}_\mathrm{a}$ is given by (2.53) and the L_2 inner product by (3.4)[2] with $\alpha = 1$. Since the functions $\mathcal{W}_p \boldsymbol{e}_m$ and $\mathcal{W}_q \boldsymbol{e}_n$ have for all m and n a non-zero pth and qth component only, we can interpret each Z_{pq} as a function of $(\mathcal{W}_p \boldsymbol{e}_m)(\,\cdot\,; p)$ and $(\mathcal{W}_q \boldsymbol{e}_n)(\,\cdot\,; q)$. With this interpretation, each Z_{pq} is a functional defined by

$$-\frac{2}{jZ_0 k^2 \ell b} Z_{pq}(v,w) = \int_{-1}^{1} v^*(\xi) \left(\left(1 + \frac{1}{k^2\ell^2}\mathsf{D}^2\right) \tilde{\mathcal{F}}_{pq} w \right)(\xi)\, d\xi = \\ = \langle v, (1 + \mathsf{D}^2/k^2\ell^2) \tilde{\mathcal{F}}_{pq} w \rangle_{L_2}\,, \quad (3.14)$$

for functions v and w in $H_{2,1}([-1,1])$ that vanish in 1 and -1. We write $Z_{pq}(m,n) = Z_{pq}((\mathcal{W}_p \boldsymbol{e}_m)(\,\cdot\,; p), (\mathcal{W}_q \boldsymbol{e}_n)(\,\cdot\,; q))$.

We consider two different approaches to calculate $Z_{pq}(v,w)$. In the first approach, we integrate once by parts to transfer D to the test functions and we apply Lemma 1 in Appendix B to interchange $\mathcal{F}_{pq}$ and D. Using the property of v and w that these functions vanish in 1 and -1, we obtain

$$-\frac{2}{jZ_0 k^2 \ell b} Z_{pq}(v,w) = \langle v, \tilde{\mathcal{F}}_{pq} w \rangle_{L_2} - \frac{1}{k^2\ell^2} \langle \mathsf{D}v, \tilde{\mathcal{F}}_{pq} \mathsf{D} w \rangle_{L_2}\,. \quad (3.15)$$

In the second approach, we integrate twice by parts to transfer the Helmholtz operator in (3.14) to the test functions. Using the same property of v and w as above, we obtain

$$-\frac{2}{jZ_0 k^2 \ell b} Z_{pq}(v,w) = \langle (1 + \mathsf{D}^2/k^2\ell^2) v, \tilde{\mathcal{F}}_{pq} w \rangle_{L_2} + \\ - \frac{1}{k^2\ell^2} \Big((\mathsf{D}v)(1)\, (\tilde{\mathcal{F}}_{pq} w)(1) - (\mathsf{D}v)(-1)\, (\tilde{\mathcal{F}}_{pq} w)(-1) \Big)\,. \quad (3.16)$$

In the first approach, we use only that $v, w \in H_{2,1}([-1,1])$, but in the second approach, we need also that v has a second derivative in L_2. Therefore, the first approach can be applied to both the entire-domain functions and the piecewise functions of the previous section, while the second approach can be applied to the entire-domain functions. To apply the second approach to the piecewise functions, a generalized interpretation of the second derivative is required instead of an L_2 interpretation.

We consider first the entire-domain functions defined by (3.7) and (3.8). Since these functions are orthonormal with respect to the L_2 inner product, G_p is the identity matrix and $Z_{pq} = [\mathcal{W}_p^- \mathcal{Z}_\mathrm{a} \mathcal{W}_q]$. Moreover, the matrices $[\mathcal{W}_p^- \mathcal{Z}_\mathrm{a} \mathcal{W}_q]$ are block-diagonal matrices composed of the blocks $[(\mathcal{W}_p^{\cos})^- \mathcal{Z}_\mathrm{a} \mathcal{W}_q^{\cos}]$ and $[(\mathcal{W}_p^{\sin})^- \mathcal{Z}_\mathrm{a} \mathcal{W}_q^{\sin}]$. Therefore, we need to calculate $Z_{pq}(v,w)$ only if v and w are both cosines or both sines from the set defined by (3.5). The functions of this set are the eigenfunctions of the Sturm-Liouville operator $1 + \mathsf{D}^2/k^2\ell^2$ with additional Sturm-Liouville boundary conditions. Hence, the term $(1 + \mathsf{D}^2/k^2\ell^2)v$ in (3.16) turns into $\Omega_v v$, where Ω_v is the eigenvalue of v. The form for $Z_{pq}(v,w)$ thus obtained requires the evaluation of one double integral only. This is the advantage of (3.16) over (3.15), which requires the evaluation of two double integrals. However, all L_2 inner products in (3.15) and (3.16) can be rewritten as single integrals, because the operator $\tilde{\mathcal{F}}_{pq}$ is of the convolution type. Hence, the advantage of (3.16) over (3.15) vanishes here. Since $Z_{pq}(v,w)$ is represented by two symmetric forms in (3.15), whereas it is represented by two asymmetric forms in (3.16), we decide to use (3.15) instead of (3.16). Interpreting and rewriting the inner products in (3.15) in a similar way as the kernel F_{pq} in (2.55)–(2.57), we obtain

$$-\frac{2}{jZ_0k^2\ell b}\,Z_{pq}(v,w) = \langle \tilde{F}_{pq}^*, v^* 1_{[-1,1]} * w^\vee 1_{[-1,1]} \rangle_{L_2([-2,2])} + \\ -\frac{1}{k^2\ell^2} \langle \tilde{F}_{pq}^*, (\mathsf{D}v)^*\, 1_{[-1,1]} * (\mathsf{D}w)^\vee\, 1_{[-1,1]} \rangle_{L_2([-2,2])}\,. \quad (3.17)$$

Here, the subscript $_{L_2([-2,2])}$ indicates the L_2 inner product on $[-2,2]$. Since the convolutions in the right-hand side are calculated analytically, the two inner products reduce to single integrals as mentioned above. The final result for the components of the blocks $[(\mathcal{W}_p^{\cos})^- \mathcal{Z}_\mathrm{a} \mathcal{W}_q^{\cos}]$ is

$$-\frac{1}{jZ_0k^2\ell b}\,[(\mathcal{W}_p^{\cos})^- \mathcal{Z}_\mathrm{a} \mathcal{W}_q^{\cos}](m,n) = \\ = \frac{(-1)^{m+n}}{(m+n-1)(m-n)\pi} \left\{ (2m-1)\left(1 - \frac{(2n-1)^2\pi^2}{4k^2\ell^2}\right) T_{1,pq}(2n-1) + \right. \\ \left. -\ (2n-1)\left(1 - \frac{(2m-1)^2\pi^2}{4k^2\ell^2}\right) T_{1,pq}(2m-1) \right\}, \quad (3.18)$$

for $m \neq n$, and

$$-\frac{1}{jZ_0k^2\ell b}\,[(\mathcal{W}_p^{\cos})^- \mathcal{Z}_\mathrm{a} \mathcal{W}_q^{\cos}](n,n) = 2\left(1 - \frac{(2n-1)^2\pi^2}{4k^2\ell^2}\right) T_{2,pq}(2n-1) + \\ + \frac{2}{(2n-1)\pi}\left(1 + \frac{(2n-1)^2\pi^2}{4k^2\ell^2}\right) T_{1,pq}(2n-1)\,, \quad (3.19)$$

where

$$\begin{aligned} T_{1,pq}(n) &= \int_0^1 \tilde{F}_{pq}(2\xi)\sin(n\pi\xi)\,d\xi\,, \\ T_{2,pq}(n) &= \int_0^1 (1-\xi)\tilde{F}_{pq}(2\xi)\cos(n\pi\xi)\,d\xi\,. \end{aligned} \tag{3.20}$$

The final result for the components of the blocks $[(\mathcal{W}_p^{\sin})^{-}\mathcal{Z}_{\mathrm{a}}\mathcal{W}_q^{\sin}]$ is

$$\begin{aligned} &-\frac{1}{jZ_0k^2\ell b}\,[(\mathcal{W}_p^{\sin})^{-}\mathcal{Z}_{\mathrm{a}}\mathcal{W}_q^{\sin}](m,n) = \\ &= \frac{2(-1)^{m+n}}{(m+n)(m-n)\pi}\left\{m\left(1-\frac{n^2\pi^2}{k^2\ell^2}\right)T_{1,pq}(2n) - n\left(1-\frac{m^2\pi^2}{k^2\ell^2}\right)T_{1,pq}(2m)\right\}, \end{aligned} \tag{3.21}$$

for $m \neq n$, and

$$\begin{aligned} &-\frac{1}{jZ_0k^2\ell b}\,[(\mathcal{W}_p^{\sin})^{-}\mathcal{Z}_{\mathrm{a}}\mathcal{W}_q^{\sin}](n,n) = \\ &\qquad = 2\left(1-\frac{n^2\pi^2}{k^2\ell^2}\right)T_{2,pq}(2n) + \frac{1}{n\pi}\left(1+\frac{n^2\pi^2}{k^2\ell^2}\right)T_{1,pq}(2n)\,. \end{aligned} \tag{3.22}$$

Finally, we show that (3.16) links the calculational aspects to both the space characterization and to the physical properties of the electromagnetic field. If v and w are both cosine or both sine eigenfunctions of $1+\mathsf{D}^2/k^2\ell^2$ as above, (3.16) turns into

$$-\frac{2}{jZ_0k^2\ell b}\,Z_{pq}(v,w) = \Omega_v\langle v, \tilde{\mathcal{F}}_{pq}w\rangle_{L_2} - \frac{2}{k^2\ell^2}\,(\mathsf{D}v)(1)\,(\tilde{\mathcal{F}}_{pq}w)(1)\,. \tag{3.23}$$

Physically, the second term in the right-hand side represents scattering of the electric field at the edges of the strip. Mathematically, it shows that the range of $\tilde{\mathcal{F}}_{pq}$ is not spanned by the eigenfunctions of $1+\mathsf{D}^2/k^2\ell^2$. This can be shown as follows. Since the eigenfunctions of $1+\mathsf{D}^2/k^2\ell^2$, here denoted as w_n with $n \in \mathbb{N}$, are a total orthonormal set in $L_2([-1,1])$, we may expand $\tilde{\mathcal{F}}_{pq}w$ as

$$\tilde{\mathcal{F}}_{pq}w = \sum_{n=1}^{\infty}\langle w_n, \tilde{\mathcal{F}}_{pq}w\rangle_{L_2}\,w_n\,. \tag{3.24}$$

Next, we substitute this series into the right-hand side of (3.14). If we assume that the eigenfunctions w_n span the range of $\tilde{\mathcal{F}}_{pq}$, which is a subset of $H_{2,2}([-1,1])$, we may apply $1+\mathsf{D}^2/k^2\ell^2$ termwise. Employing then the orthonormality of these eigenfunctions with respect to the L_2 inner product, we obtain the same expression for $Z_{pq}(v,w)$ as in (3.23), but without the second

term in the right-hand side. Hence, the range of $\tilde{\mathcal{F}}_{pq}$ is not spanned by the eigenfunctions w_n. This shows that the second term in the right-hand side of (3.23) is essential both from a physical and mathematical point of view. Moreover, it shows that the Fredholm operators for the strips do not map a function in their domain (3.1) into a subset of this domain, see the last paragraph of Section 3.1.

For the piecewise functions defined by (3.9), we consider the case of a single strip, i.e., $N_{\rm el} = 1$. Then, $\mathcal{W}_1 = \mathcal{W}$ and we write G and Z instead of G_1 and Z_{11}. The piecewise functions are not orthogonal with respect to the L_2 inner product and induce the tridiagonal Gram matrix G,

$$\begin{aligned} &G(m,m) = \frac{2\Delta_{\rm exp}}{3}\,, \quad G(m,m+1) = G(m+1,m) = \frac{\Delta_{\rm exp}}{6}\,, \\ &G(m,n) = 0, \quad |m-n| \geq 2\,. \end{aligned} \tag{3.25}$$

The components of Z are given by $Z(m,n) = Z(w_m, w_n)$, where Z is interpreted as in (3.14) and $w_n(\xi) = w_{\rm tri}((\xi - \xi_n)/\Delta_{\rm exp})$, see (3.9). To calculate these components, we use (3.15) to obtain

$$\begin{aligned} -\frac{2}{jZ_0k^2\ell b}\,Z(w_m,w_n) = &\int_{\xi_{m-1}}^{\xi_{m+1}} w_m(\xi) \int_{\xi_{n-1}}^{\xi_{n+1}} \tilde{F}_{11}(\xi-\xi')\,w_n(\xi')\,d\xi' d\xi + \\ &- \frac{1}{k^2\ell^2}\int_{\xi_{m-1}}^{\xi_{m+1}} (\mathsf{D}w_m)(\xi) \int_{\xi_{n-1}}^{\xi_{n+1}} \tilde{F}_{11}(\xi-\xi')\,(\mathsf{D}w_n)(\xi')\,d\xi' d\xi\,. \end{aligned} \tag{3.26}$$

Introducing the transformation of variables $y = (\xi - \xi_m)/\Delta_{\rm exp}$ and $y' = (\xi - \xi_n)/\Delta_{\rm exp}$, and using $(\mathsf{D}w_n)(\xi) = \frac{1}{\Delta_{\rm exp}}(\mathsf{D}w_{\rm tri})((\xi - \xi_m)/\Delta_{\rm exp})$, we rewrite $Z(w_m, w_n)$ as

$$\begin{aligned} -\frac{2}{jZ_0k^2\ell b}\,Z(w_m,w_n) = &\Delta_{\rm exp}^2 \int_{-1}^{1} w_{\rm tri}(y) \int_{-1}^{1} \tilde{F}_{11,m-n}(y-y')\,w_{\rm tri}(y')\,dy' dy + \\ &- \frac{1}{k^2\ell^2}\int_{-1}^{1} (\mathsf{D}w_{\rm tri})(y) \int_{-1}^{1} \tilde{F}_{11,m-n}(y-y')\,(\mathsf{D}w_{\rm tri})(y')\,dy' dy\,, \end{aligned} \tag{3.27}$$

where $\tilde{F}_{11,n}$ is defined by $\tilde{F}_{11,n}(y) = \tilde{F}_{11}(\Delta_{\rm exp} y + n)$. Interpreting and rewriting the integrals in a similar way as the kernel F_{pq} in (2.55) – (2.57), we obtain

$$\begin{aligned} -\frac{2}{jZ_0k^2\ell b}\,Z(w_m,w_n) = &\Delta_{\rm exp}^2 \langle \tilde{F}^*_{11,m-n}, w_{\rm tri} 1_{[-1,1]} * w_{\rm tri} 1_{[-1,1]} \rangle_{L_{([-2,2])}} + \\ &- \frac{1}{k^2\ell^2}\langle \tilde{F}^*_{11,m-n}, (\mathsf{D}w_{\rm tri}) 1_{[-1,1]} * (\mathcal{D}w_{\rm tri})^\vee 1_{[-1,1]} \rangle_{L_{([-2,2])}}\,. \end{aligned} \tag{3.28}$$

With (3.28), we have obtained a form for Z_{pq}, which is similar to its form (3.17) for the entire-domain functions. The convolutions are calculated analytically. The final result for the

impedance matrix Z is

$$-\frac{2}{jZ_0k^2\ell b}\,Z(m,n) = 2\left(\frac{\Delta_{\rm exp}^2}{3}-\frac{1}{k^2\ell^2}\right)T_1(m-n)+\frac{3}{k^2\ell^2}\,T_2(m-n)+$$
$$+2\left(\frac{2\Delta_{\rm exp}^2}{3}+\frac{1}{k^2\ell^2}\right)U_1(m-n)-\left(2\Delta_{\rm exp}^2+\frac{1}{k^2\ell^2}\right)U_2(m-n)+$$
$$+\Delta_{\rm exp}^2\left(-T_3(m-n)+\frac{1}{2}\,T_4(m-n)+U_3(m-n)-\frac{1}{6}\,U_4(m-n)\right)\,, \quad (3.29)$$

where

$$T_i(m)=\int_{-1}^{1}\tilde{F}_{11,m}(\xi)\,|\xi|^{i-1}d\xi, \qquad U_i(m)=\left(\int_{-2}^{-1}+\int_{1}^{2}\right)\tilde{F}_{11,m}(\xi)\,|\xi|^{i-1}d\xi\,. \quad (3.30)$$

3.3.2 Arrays of Rings

For arrays of rings, the matrices Z_{pq} are defined by $Z_{pq}(m,n)=\langle \mathcal{W}_p\boldsymbol{e}_m, \mathcal{Z}_{\rm a}\mathcal{W}_q\boldsymbol{e}_n\rangle_{L_2}$, where $\mathcal{Z}_{\rm a}$ is given by (2.96) and the L_2 inner product by (3.4)^2 with $\alpha=\pi$. In the same manner as in the previous subsection, we interpret each Z_{pq} as a functional. These functionals are defined by

$$-\frac{2}{jZ_0k^2a_qb_q}\,Z_{pq}(v,w)=\int_{-\pi}^{\pi}v^*(\xi)\left(\left(1+\frac{1}{k^2a_p^2}\,\mathsf{D}^{\,2}\right)\tilde{\mathcal{K}}_{1,pq}w+\frac{1}{k^2a_p^2}\,\mathsf{D}\tilde{\mathcal{K}}_{2,pq}w\right)(\xi)\,d\xi=$$
$$=\langle v,(1+\mathsf{D}^2/k^2a_p^2)\tilde{\mathcal{K}}_{1,pq}w\rangle_{L_2}+\frac{1}{k^2a_p^2}\langle v,\mathsf{D}\tilde{\mathcal{K}}_{2,pq}w\rangle_{L_2}\,, \quad (3.31)$$

for functions v and w in $H_{2,1,\rm per}([-\pi,\pi])$. As in the previous subsection, we write $Z_{pq}(m,n)=Z_{pq}((\mathcal{W}_p\boldsymbol{e}_m)(\,\cdot\,;p),(\mathcal{W}_q\boldsymbol{e}_n)(\,\cdot\,;q))$.

We follow only one approach to calculate $Z_{pq}(v,w)$. As in the second approach for the strips, we integrate twice by parts to transfer the differential operators to the test functions. Requiring that $v,w\in H_{2,2,\rm per}$ and that v is an eigenfunction of the Helmholtz operator $1+\mathsf{D}^2/k^2a_p^2$ with eigenvalue Ω_v, we obtain

$$-\frac{2}{jZ_0k^2a_qb_q}\,Z_{pq}(v,w)=\Omega_v\langle v,\tilde{\mathcal{K}}_{1,pq}w\rangle_{L_2}-\frac{1}{k^2a_p^2}\langle \mathsf{D}v,\tilde{\mathcal{K}}_{2,pq}w\rangle_{L_2}\,. \quad (3.32)$$

For $p=q$, the operators $\tilde{\mathcal{K}}_{1,pq}$ and $\tilde{\mathcal{K}}_{2,pq}$ with kernels $\tilde{K}_{1,qq}(\,\cdot\,)\cos(\,\cdot\,)$ and $\tilde{K}_{2,qq}(\,\cdot\,)\sin(\,\cdot\,)$ are of the convolution type. Hence, the inner products in (3.32) can be rewritten in a similar form

as in (3.17),

$$-\frac{2}{jZ_0k^2a_qb_q}\,Z_{qq}(v,w) = \Omega_v\,\langle \tilde{K}^*_{1,qq}(\,\cdot\,)\cos(\,\cdot\,), v^*1_{[-\pi,\pi]} * w^\vee 1_{[-\pi,\pi]}\rangle_{L_2([-2\pi,2\pi])} + \\ -\frac{1}{k^2a_p^2}\,\langle \tilde{K}^*_{2,qq}(\,\cdot\,)\sin(\,\cdot\,), (\mathsf{D}v)^*1_{[-\pi,\pi]} * w^\vee 1_{[-\pi,\pi]}\rangle_{L_2([-2\pi,2\pi])}\,. \quad (3.33)$$

The entire-domain functions defined by (3.7) and (3.12) are orthogonal, but not normalized with respect to the L_2 inner product. The Gram matrix G_p for these functions is a diagonal matrix of which the components are given by

$$G_p(1,1) = 2\pi\,, \qquad G_p(m,m) = \pi\,,\ m \geq 2\,, \qquad G_p(m,n) = 0\,,\ m \neq n\,. \quad (3.34)$$

The ordering of the bases $\mathrm{bas}(\mathcal{W}_p)$ and $\mathrm{bas}(\mathcal{W}_q)$ decomposes the matrix $[\mathcal{W}_p^-\mathcal{Z}_\mathrm{a}\mathcal{W}_q]$ into four blocks, $[(\mathcal{W}_p^c)^-\mathcal{Z}_\mathrm{a}\mathcal{W}_q^d]$ with $c,d = \cos,\sin$. Then, Z_{pq} is decomposed into four blocks, $Z_{pq}^{c,d}$ defined by $Z_{pq}^{c,d}(m,n) = \langle \mathcal{W}_p^c\boldsymbol{e}_m, \mathcal{Z}_\mathrm{a}\mathcal{W}_q^d\boldsymbol{e}_n\rangle_{L_2}$. These blocks can be interpreted in the sense of (3.31). Let us first consider the case $p = q$. The integral operators $\tilde{\mathcal{K}}_{1,qq}$ and $\tilde{\mathcal{K}}_{2,qq}$ are diagonal operators with respect to the eigenfunctions (3.10). This follows from the considerations with respect to the kernels $\tilde{K}_{1,qq}$ and $\tilde{K}_{2,qq}$ in Section 3.1 and from Remark 2 in Appendix B. Consequently, both blocks $Z_{qq}^{\cos,\sin}$ and $Z_{qq}^{\sin,\cos}$ are identically zero and both blocks $Z_{qq}^{\cos,\cos}$ and $Z_{qq}^{\sin,\sin}$ are diagonal matrices. The diagonal components follow from (3.33), where the convolutions are calculated analytically. The final result for the diagonal components of $Z_{qq}^{\cos,\cos}$ and $Z_{qq}^{\sin,\sin}$ is

$$-\frac{2}{jZ_0k^2a_qb_q}\,Z_{qq}^{\cos,\cos}(1,1) = 4\pi\,T_{1,q}(0), \\ -\frac{2}{jZ_0k^2a_qb_q}\,Z_{qq}^{\cos,\cos}(n,n) = 2\pi\left(\Omega_{q,n-1}T_{1,q}(n-1) + \frac{1}{k^2a_q^2}T_{2,q}(n-1)\right), \quad n \neq 1\,, \\ Z_{qq}^{\sin,\sin}(n,n) = Z_{qq}^{\cos,\cos}(n+1,n+1)\,, \quad (3.35)$$

where $\Omega_{q,n}$ is given by (3.11) and where

$$T_{1,q}(n) = \int_0^\pi \tilde{K}_{1,qq}(\varphi)\cos\varphi\cos n\varphi\,d\varphi, \qquad T_{2,q}(n) = \int_0^\pi \tilde{K}_{2,qq}(\varphi)\sin\varphi\sin n\varphi\,d\varphi\,. \quad (3.36)$$

For $p \neq q$, the components of the blocks $Z_{pq}^{c,d}$ cannot be reduced to linear combinations of single integrals by means of (3.33). Therefore, we use (3.32) to write the components as linear

combinations of double integrals. We find

$$
\begin{aligned}
-\frac{2}{jZ_0k^2a_qb_q}\,Z_{pq}^{\cos,\cos}(m,n) &= \Omega_{p,m-1}U_{1,pq}^{\cos,\cos}(m-1,n-1)+\frac{m-1}{k^2a_p^2}\,U_{2,pq}^{\sin,\cos}(m-1,n-1)\,,\\
-\frac{2}{jZ_0k^2a_qb_q}\,Z_{pq}^{\cos,\sin}(m,n) &= \Omega_{p,m-1}U_{1,pq}^{\cos,\sin}(m-1,n)+\frac{m-1}{k^2a_p^2}\,U_{2,pq}^{\sin,\sin}(m-1,n)\,,\\
-\frac{2}{jZ_0k^2a_qb_q}\,Z_{pq}^{\sin,\cos}(m,n) &= \Omega_{p,m}U_{1,pq}^{\sin,\cos}(m,n-1)-\frac{m}{k^2a_p^2}\,U_{2,pq}^{\cos,\cos}(m,n-1)\,,\\
-\frac{2}{jZ_0k^2a_qb_q}\,Z_{pq}^{\sin,\sin}(m,n) &= \Omega_{p,m}U_{1,pq}^{\sin,\sin}(m,n)-\frac{m}{k^2a_p^2}\,U_{2,pq}^{\cos,\sin}(m,n)\,,
\end{aligned}
\tag{3.37}
$$

where

$$
\begin{aligned}
U_{1,pq}^{c,d}(m,n) &= \int_{-\pi}^{\pi}\int_{-\pi}^{\pi} c(m\varphi)\,d(n\varphi')\,\cos(\varphi-\varphi'+\psi_p-\psi_q)\,\tilde{K}_{1,pq}(\varphi,\varphi')\,d\varphi' d\varphi\,,\\
U_{2,pq}^{c,d}(m,n) &= \int_{-\pi}^{\pi}\int_{-\pi}^{\pi} c(m\varphi)\,d(n\varphi')\,\sin(\varphi-\varphi'+\psi_p-\psi_q)\,\tilde{K}_{2,pq}(\varphi,\varphi')\,d\varphi' d\varphi\,.
\end{aligned}
\tag{3.38}
$$

with c and d representing the sine and cosine functions corresponding to the 'values' of the super indices ^{c,d}.

3.4 Numerical Aspects

The last step in the construction of the moment matrix concerns the numerical computation of the integrals introduced in the previous section. To determine the accuracy by which these integrals need to be computed, we consider the moment-matrix equation (2.129)^2. The solution of this equation is the projected current $\mathcal{W}(\mathcal{W}^{-}\boldsymbol{w})$. The required accuracy of this current depends on the functional metric related to (2.31). In their turn, the required accuracies of the integrals and the moment-matrix inversion depend on the required accuracy of the projected current. We consider here only the dependence of the accuracy of the integrals on the accuracy of the projected current. It goes without saying that the total CPU time of constructing the moment matrix and solving the moment-matrix equation should be minimized. We will show that the CPU time needed to construct the moment matrix dominates in general the CPU time of solving the related equation.

To determine how accurate we need to compute the integrals, we write the moment matrix $[\mathcal{W}^{-}\mathcal{Z}_{\rm a}\mathcal{W}]$ as $D+R$. Here, D consists of the diagonal blocks $[\mathcal{W}_q^{-}\mathcal{Z}_{\rm a}\mathcal{W}_q]$ of the moment matrix and R consists of the off-diagonal blocks $[\mathcal{W}_p^{-}\mathcal{Z}_{\rm a}\mathcal{W}_q]$. Then, the moment-matrix equation (2.129)^2 turns into $(I+D^{-1}R)W = D^{-1}G^{-1}V$, where I is the identity matrix and

$W = [\mathcal{W}^- \boldsymbol{w}]$. Assume that D and $G^{-1}V$ are determined exactly and that $R_{\rm cal}$ is the numerically determined off-diagonal block matrix. Let W be the exact solution of the moment-matrix equation and let $W_{\rm cal}$ be the solution replacing R by $R_{\rm cal}$,

$$(I + D^{-1}R)W = D^{-1}G^{-1}V\,, \quad (I + D^{-1}R_{\rm cal})W_{\rm cal} = D^{-1}G^{-1}V\,. \tag{3.39}$$

Write $\delta R = R_{\rm cal} - R$ and $\delta W = W_{\rm cal} - W$. Then, subtracting the equations (3.39), we obtain

$$\delta W = -(I + D^{-1}(R_{\rm cal} - \delta R))^{-1} D^{-1}\,\delta R\; W\,. \tag{3.40}$$

Of course $I + D^{-1}R_{\rm cal}$ should be invertible. Moreover, we assume that δR is so small that $\parallel (I + D^{-1}R_{\rm cal})^{-1} \parallel \parallel D^{-1}\,\delta R \parallel < 1$, which implies that $I + D^{-1}R$ is invertible, see [40: p. 59, Th. 2.3.4]. We note that $\parallel \cdot \parallel$ denotes both a norm on $\mathbb{C}^{N\times 1}$ and its sub-multiplicative associated matrix norm. Using the assumption and [40: p. 59, Lemma 2.3.3], we arrive at the estimate

$$\frac{\parallel \delta W \parallel}{\parallel W_{\rm cal} \parallel} \leq \frac{C}{1 - C\,\dfrac{\parallel D^{-1}\,\delta R \parallel}{\parallel D^{-1}R_{\rm cal} \parallel}}\;\frac{\parallel D^{-1}\,\delta R \parallel}{\parallel D^{-1}R_{\rm cal} \parallel}\;,\quad C = \parallel (I + D^{-1}R_{\rm cal})^{-1} \parallel \parallel D^{-1}R_{\rm cal} \parallel\,. \tag{3.41}$$

This means that the relative error $\parallel \delta W \parallel / \parallel W_{\rm cal} \parallel$ is determined by the relative error $\parallel D^{-1}\,\delta R \parallel / \parallel D^{-1}R_{\rm cal} \parallel$ and by the constant C. Choosing the latter error $\leq \epsilon/C(1+\epsilon)$, we obtain $\parallel \delta W \parallel / \parallel W \parallel \leq \epsilon$. If $\epsilon \ll 1$, then we may replace this choice by $\parallel D^{-1}\,\delta R \parallel / \parallel D^{-1}R_{\rm cal} \parallel \lesssim \epsilon/C$ to obtain the same, but approximate, inequality. The approximate inequality $\parallel D^{-1}\,\delta R \parallel / \parallel D^{-1}R_{\rm cal} \parallel \lesssim \epsilon/C$ is in general satisfied if each matrix component is determined with a relative error of at most ϵ provided that $C = O(1)$. Although it is expected that the norms $\parallel (I+D^{-1}R_{\rm cal})^{-1} \parallel$ and $\parallel D^{-1}R_{\rm cal} \parallel$ compensate each other, $C = O(1)$ cannot be shown satisfactorily a priori, only a posteriori. We note here only that the norm $\parallel D^{-1}R_{\rm cal} \parallel$ will in general increase as a function of the number of microstrip elements $N_{\rm el}$. A sufficient rate of convergence of the components $[\mathcal{W}_p^- \mathcal{Z}_{\rm a} \mathcal{W}_q](m,n)$ as a function of increasing $|\boldsymbol{c}_p - \boldsymbol{c}_q|$ is required to have $\parallel D^{-1}R_{\rm cal} \parallel$ bounded as $N_{\rm el} \to \infty$. This means that the mutual coupling between the microstrip elements should decrease sufficiently fast as a function of increasing distance between the elements.

The error estimate (3.41) is particularly useful for the array of rings. In this case, D is a diagonal matrix of which the diagonal components are single integrals, whereas $R_{\rm cal}$ is a dense matrix of which the off-diagonal blocks are double integrals. Hence, the construction of $R_{\rm cal}$ determines the total CPU time. Based on the error estimate, we compute first the components of D with a relative error much smaller than ϵ. Subsequently, we compute the components of $R_{\rm cal}$ with a relative error of ϵ. We choose here $\epsilon = 10^{-3}$. Let us first consider the computation of the

components of R. Since tests for the integrals (3.38) showed that the composite 2D Simpson rule requires less integration points for the same accuracy than the higher-order Newton-Coates rules, we use this rule. A Matlab implementation is given in [64: p. 191], where equal numbers of integration points for φ and φ' are chosen, i.e., $2N_{\text{int}}+1$ with N_{int} the number of subintervals on $[-\pi,\pi]$. We deduce a rule of thumb for the number of integration points required for a relative error of 10^{-3} as follows. Let $\min(N_{\text{int}})$ be the minimum N_{int} such that the relative difference between the matrix components (3.37) and certain reference values is less than 10^{-3} for all $N_{\text{int}} \geq \min(N_{\text{int}})$. These reference values are obtained by using $N_{\text{int}} = 300$ on $[-\pi,\pi]$. The minimum $\min(N_{\text{int}})$ depends on the expansion functions and the geometry parameters. For several parameter settings, we compute $\min(N_{\text{int}})$ as a function of the angular order n of the cosine and sine expansion functions $\cos n\varphi$ and $\sin n\varphi$. An example is given in Figure 3.1, where we compute $\min(N_{\text{int}})$ for $Z_{pq}^{\cos,\cos}(n,n)$ and $Z_{pq}^{\sin,\sin}(n,n)$ as a function of n for several distances between the rings. Based on these computations, we choose the number of subintervals for $Z_{pq}^{c,d}(m,n)$ as $N_{\text{int}} = 15 + 2\,\max(m,n)$ for $|\boldsymbol{c}_p - \boldsymbol{c}_q| - a_p - a_q \leq 0.5\,\lambda$ and $N_{\text{int}} = 8 + 2\,\max(m,n)$ otherwise. We tried to reduce these numbers by using different numbers of subintervals for φ and φ', but we could not find suitable rules of thumb, because the numbers of subintervals appeared to be strongly dependent on the spacing between the rings.

The integrals of the diagonal components of D are computed as follows. The integrals with respect to the logarithmically singular parts of the integrands of $(3.36)^1$ are calculated analytically with result

$$-\frac{1}{\pi k a_q \beta_q}\int_0^\pi \log(2\sin(\varphi/2))\,\cos\varphi\,\cos n\varphi\,d\varphi = \begin{cases} \dfrac{1}{2ka_q\beta_q}\dfrac{n}{n^2-1}\,, n>1\,, \\ \dfrac{1}{8ka_q\beta_q}\,, & n=1\,, \\ \dfrac{1}{2ka_q\beta_q}\,, & n=0\,. \end{cases} \tag{3.42}$$

The integrals over the $H_{2,1,\text{per}}([-\pi,\pi])$-parts and the integrals $(3.36)^2$ are computed by the 1D composite Simpson rule with $N_{\text{int}} = 100$. A description of this rule and a Matlab implementation are given in [64: p. 167].

For line arrays of strips with entire-domain expansion and test functions, the number of integration points is related to the relative error ϵ as described above for arrays of rings. Since all components of R consist of single integrals only, the CPU time for a line array of strips will be much lower than for an array of rings with the same number of elements. Therefore, we compute all integrals of R by the 1D composite Simpson rule with $N_{\text{int}} = 100$ to obtain sufficiently accurate results for the solution of the moment-matrix equation. The integrals in D are computed as follows. The integrals with respect to the logarithmically singular parts of the

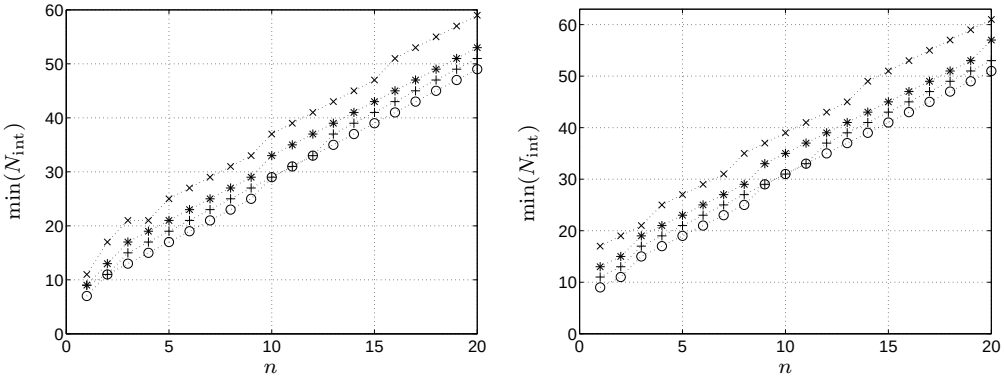

Figure 3.1 Minimum number of subintervals $\min(N_{\rm int})$ for $Z_{pq}^{\cos,\cos}(n,n)$ (left) and $Z_{pq}^{\sin,\sin}(n,n)$ (right) as a function of n for an array of rings in free space. Cross: $\boldsymbol{c}_q = (7/15\,\lambda, 0)$, asterisk: $\boldsymbol{c}_q = (8/15\,\lambda, 0)$, plus: $\boldsymbol{c}_q = (9/15\,\lambda, 0)$, circle: $\boldsymbol{c}_q = (2/3\,\lambda, 0)$. Other parameter values: $a_p = a_q = \lambda/5$, $\psi_p = \psi_q = 0$, $\boldsymbol{c}_p = \boldsymbol{0}$.

integrands of (3.20)^2 are expressed as sine integrals,

$$-\frac{1}{k\ell\beta}\int_0^1 \log(2\xi)\cos m\pi\xi\, d\xi = \frac{1}{k\ell\beta m\pi}\,\mathrm{Si}(m\pi), \qquad \mathrm{Si}(\xi) = \int_0^\xi \frac{\sin\xi'}{\xi'}\, d\xi'\,. \tag{3.43}$$

For $n \leq 20$, the sine integral is tabulated and, for higher numbers of n, it is calculated asymptotically, see [1: p. 231 – 233]. The integrals with respect to the $H_{2,1}([-1,1])$-parts and the integrals (3.36)^1 are computed by the 1D composite Simpson rule with $N_{\rm int} = 100$. Finally, the integrals for a single strip with piecewise functions are calculated similarly; the logarithmic singular parts are calculated analytically and the $H_{2,1}([-1,1])$-parts are calculated numerically with 30 integration intervals per interval of length 1.

The CPU times for the moment matrices of several line arrays of rings and strips are given in the second and third columns of Table 3.1. We have not used symmetry considerations such as the symmetry of the moment matrices of the strip arrays. Therefore, the large differences between strip and ring arrays are only due to the differences between the coupling integrals. Moreover, we observed that only for $N_{\rm el} = 50$ and $N_{\rm el} = 100$, the CPU times of the moment-matrix inversion are higher than one second, 2 seconds and 14 seconds to be precise. Here, we used the standard Matlab inversion module. For very large array sizes, the CPU time of the inversion will dominate the CPU time of the matrix construction, because the former tends as N^3, whereas the latter tends as N^2, where $N = N_{\rm el}N_{\rm exp}$ is the number of rows and columns, see [110: p. 455 – 456]. Accuracy checks for the solution of the moment-matrix equation are given in Chapter 4. For the eigenvalues of the moment matrix, such checks are given in Chapter 5.

3.5 Uniform Arrays and the Infinite-Array Approach

In the general setup, the arrays need not be uniform. Uniform arrays have uniform inter-element spacing and uniform element geometry. To compare with the infinite-array approach, we have to assume that the finite array is uniform. We consider mainly one type of uniform arrays: uniform line arrays. These arrays can be building blocks of rectangular arrays as explained in Section 1.3. Moreover, they constitute the simplest test case for a comparison between the infinite and finite-array approaches. For uniform line arrays, the expansion and test functions described by $\mathcal{W}$ can be chosen such that the moment matrices $[\mathcal{W}^- \mathcal{Z}_\mathrm{a} \mathcal{W}]$ are finite (block) Toeplitz matrices. In this section, we study the relationship between the infinite and finite-array approaches as being expressed by infinite and finite Toeplitz matrices.

A uniform line array of strips is obtained from the line array in Subsection 2.3.2 by setting the inter-element spacing $d_{q,q+1}$ in (2.47) equal to a constant d. We index the strips not from 1 to N_el as previously, but from $-N$ or $-N+1$ to N, where $N_\mathrm{el} = 2N+1$ or $N_\mathrm{el} = 2N$. Without loss of generality, we position the center of the strip with index zero in the origin, i.e., $c_{0,x} = 0$, see Figure 3.2.

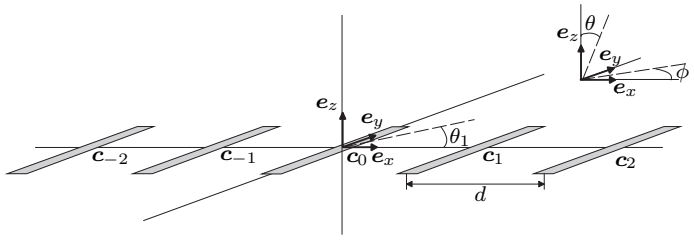

Figure 3.2 Geometry of a uniform line array of strips. The angle θ_1, i.e., the angle between the x-axis and a line through the origin at $\boldsymbol{c}_0$, indicates the position of the main lobe. The angles (θ, ϕ) are the usual spherical angles.

Uniform line arrays of rings are described in the same way as line arrays of strips. All ring geometry parameters are independent of the ring index q, i.e., $a_q = a$, $b_q = b$, and $\psi_q = \psi$, see Subsection 2.3.3. The centers $\boldsymbol{c}_q$ are positioned on the x-axis with uniform inter-element spacing d and the rings are indexed like the strips.

Let us first consider a uniform line array of strips for which the impedance operator is given by

$$(\mathcal{Z}_\mathrm{a}\boldsymbol{w})(\,\cdot\,;p) = -\frac{1}{2}\, jZ_0 k^2 \ell b \sum_{q=-N\,(+1)}^{N} \left(1 + \frac{1}{k^2\ell^2}\frac{d^2}{d\xi^2}\right) \tilde{\mathcal{F}}_{pq} w(\,\cdot\,;q)\,, \tag{3.44}$$

see (2.53), where the pth component of $\mathcal{Z}_\mathrm{a}\boldsymbol{w}$ is denoted by $(\,\cdot\,;p)$ instead of $_p$, as proposed in Section 2.4.3. The integral operators $\tilde{\mathcal{F}}_{pq}$ exhibit symmetry and translation invariance with

respect to p and q, i.e., $\tilde{\mathcal{F}}_{pq} = \tilde{\mathcal{F}}_{qp}$ and $\tilde{\mathcal{F}}_{pq} = \tilde{\mathcal{F}}_{0(q-p)}$, and hence, $\tilde{\mathcal{F}}_{pq} = \tilde{\mathcal{F}}_{0|p-q|}$. We choose the expansion and test functions as in (3.7) and (3.8). Moreover, we choose the tuples $\boldsymbol{N}_{\cos}$ and $\boldsymbol{N}_{\sin}$ uniform in their components, i.e., $N_{\cos}(q) = N_{\cos}$ and $N_{\sin}(q) = N_{\sin}$. Then, the corresponding moment matrix, given by (2.131) with adjusted numbering, is a (block) Toeplitz matrix. This means that $[\mathcal{W}_p^- \mathcal{Z}_{\rm a} \mathcal{W}_q] = [\mathcal{W}_{p+n}^- \mathcal{Z}_{\rm a} \mathcal{W}_{q+n}]$ for every admissible n. Hence, we need to calculate only the first block row and the first block column, i.e., $[\mathcal{W}_{-N}^- \mathcal{Z}_{\rm a} \mathcal{W}_q]$ and $[\mathcal{W}_q^- \mathcal{Z}_{\rm a} \mathcal{W}_{-N}]$, to construct the moment matrix. The CPU times for both the complete moment matrix and the Toeplitz blocks are given in Table 3.1 for several line arrays of strips. Unlike the results for strip arrays with $N_{\rm el} = 50, 100$ in the previous section, the CPU time of the Toeplitz blocks, which tends as $N_{\rm el}$ only, does not dominate the CPU time of the matrix inversion.

Table 3.1 CPU times for the moment-matrix construction of line arrays of $N_{\rm el}$ rings and strips in free space, obtained with the Matlab implementation of Section 3.4 and the platform mentioned in Section 1.4. Parameter values for the ring array: $a = \lambda/5$, $\beta = 1/40$, $\psi = 0$. Parameter values for the strip array: $2\ell = \lambda/2$, $\beta = 1/40$. Common parameters: $d = 3\lambda/5$, $N_{\cos} = 6$, $N_{\sin} = 0$.

	CPU time (seconds) moment matrix construction			
	Complete matrix		Toeplitz blocks	
$N_{\rm el}$	Ring array	Strip array	Ring array	Strip array
1	0.2	0.2	0.2	0.2
2	2.7	0.4	2.6	0.3
5	14.3	1.0	6.1	0.4
10	57.7	2.7	11.6	0.5
50	1450	48.6	56.9	1.9
100	4973	180	114	3.8

A general theory on Toeplitz matrices can be found in e.g. [14], while applications to arrays can be found in e.g. [110: p. 455 – 456]. The Toeplitz property holds if all elements have the same expansion functions and if a all elements have the same test functions. For the line array of strips, the moment matrix is not only Toeplitz, but also symmetric, if the expansion functions equal the test functions. Therefore, we need only to calculate the blocks $[\mathcal{W}_{-N}^- \mathcal{Z}_{\rm a} \mathcal{W}_q]$ to construct the corresponding moment matrix.

We follow the usual way to construct the moment-matrix equation for a line array of strips by the infinite-array approach. We start from the moment-matrix equation for a finite line array of strips, i.e., $[\mathcal{W}^- \mathcal{Z}_{\rm a} \mathcal{W}][\mathcal{W}^- \boldsymbol{w}] = [\mathcal{W}^- \boldsymbol{v}^{\rm ex}]$, see also Section 1.2. We write this equation in the alternative form

$$\sum_{q=-N\,(+1)}^{N} [\mathcal{W}_p^- \mathcal{Z}_{\rm a} \mathcal{W}_q][\mathcal{W}_q^- \boldsymbol{w}] = [\mathcal{W}_p^- \boldsymbol{v}^{\rm ex}]\,, \qquad p = -N\,(+1), \ldots, N-1, N\,. \quad (3.45)$$

Assuming that the excitation field $\boldsymbol{v}^{\mathrm{ex}}$ has a linear phase progression given by $v^{\mathrm{ex}}(\,\cdot\,;p) = v^{\mathrm{ex}}(\,\cdot\,;0)\,e^{-jpkd\cos\theta_1}$, we write the right-hand side of (3.45) as $[\mathcal{W}_0^-\boldsymbol{v}^{\mathrm{ex}}]\,e^{-jpkd\cos\theta_1}$. Here, the angle θ_1 indicates the scan direction of the line array, see Figure 3.2. This angle is related to the scan angle of the array, which is usually expressed in terms of spherical angles $(\theta_{\mathrm{scan}}, \phi_{\mathrm{scan}})$. In the xz-plane, the scan angle is given by $\phi_{\mathrm{scan}} = 0$ and $\theta_{\mathrm{scan}} = 90^\circ - \theta_1$. The moment-matrix equation of the infinite-array approach is obtained by letting $N \to \infty$ in (3.45). If the lowest element index is $-N$, then the limit is the principal value for arrays with odd numbers of elements. Otherwise, the limit is the principal value for arrays with even numbers of elements. We do not consider the question whether these limits are the same. The resulting equation is

$$\sum_{q=-\infty}^{\infty} [\mathcal{W}_0^-\,\mathcal{Z}_{\mathrm{a}}\mathcal{W}_{q-p}][\mathcal{W}_q^-\boldsymbol{w}] = [\mathcal{W}_0^-\boldsymbol{v}^{\mathrm{ex}}]\,e^{-jpkd\cos\theta_1}\,, \qquad p \in \mathbb{Z}\,, \tag{3.46}$$

where we used that $[\mathcal{W}_p^-\mathcal{Z}_{\mathrm{a}}\mathcal{W}_q] = [\mathcal{W}_0^-\mathcal{Z}_{\mathrm{a}}\mathcal{W}_{q-p}]$ for the infinite array. The moment matrix related to (3.46) is a (block) Laurent matrix induced by the row $(A_q)_{q=-\infty}^{\infty}$ with $A_q = [\mathcal{W}_0^-\mathcal{Z}_{\mathrm{a}}\mathcal{W}_q]$,

$$\begin{pmatrix} \ddots & \ddots & \ddots & \ddots & \ddots & \ddots \\ \dots & A_{-1} & A_0 & A_1 & \dots & \dots \\ \dots & \dots & A_{-1} & A_0 & A_1 & \dots \\ \ddots & \ddots & \ddots & \ddots & \ddots & \ddots \end{pmatrix}, \tag{3.47}$$

see [14: Ch. 1, Ch. 6]. The matrix induces an operator between two spaces consisting of sequences $\boldsymbol{\alpha} : \mathbb{Z} \to \mathbb{C}^{N_{\mathrm{exp}}}$, where $N_{\mathrm{exp}} = N_{\cos} + N_{\sin}$. If this operator is injective and the sequence induced by the right-hand side of (3.46) is an element of its range, then the solution of the infinite-array approach (3.46) is unique.

By the transformation $q' = q - p$, the parameter p in (3.46) is transferred to the second term in the left-hand side, which yields $[\mathcal{W}_{q'+p}^-\boldsymbol{w}]$. It follows that, if the blocks $[\mathcal{W}_p^-\boldsymbol{w}]$ have the same phase progression as $\boldsymbol{v}^{\mathrm{ex}}$, then (3.46) turns into

$$A(\Psi)[\mathcal{W}_0^-\boldsymbol{w}] = [\mathcal{W}_0^-\boldsymbol{v}^{\mathrm{ex}}]\,, \qquad A(\Psi) = \sum_{q=-\infty}^{\infty} A_q\,e^{-jq\Psi}, \tag{3.48}$$

where $\Psi = kd\cos\theta_1$. Hence, if the matrix-valued function $A(\Psi)$ exists and is invertible, then $\mathcal{W}^-\boldsymbol{w}$ has the same phase progression. Moreover, (3.48) yields $[\mathcal{W}_0^-\boldsymbol{w}]$, i.e., the expansion coefficients of the current on the strip with index zero. The matrix $A(\Psi)$ is called the infinite-array moment matrix. The existence and invertibility of this matrix is a basic assumption of the infinite-array approach.

In the literature, see [21, 95], the infinite-array moment matrix is often deduced from the impedance operator equation, in this case $\mathcal{Z}_{\mathrm{a}}\boldsymbol{w} = \boldsymbol{v}^{\mathrm{ex}}$. By a similar deduction as above, the

infinite-array impedance operator

$$\mathcal{Z}_{\mathrm{a}}^{\infty} = -\frac{1}{2}\, jZ_0 k^2 \ell b \sum_{q=-\infty}^{\infty} e^{-jq\Psi} \left(1 + \frac{1}{k^2\ell^2}\frac{d^2}{d\xi^2}\right) \tilde{\mathcal{F}}_{0q} \tag{3.49}$$

is obtained from (3.44) with the related operator equation $\mathcal{Z}_{\mathrm{a}}^{\infty} w(\,\cdot\,;0) = v^{\mathrm{ex}}(\,\cdot\,;0)$. This formulation is more general than (3.48) in the sense that it is valid for any choice of expansion and test functions, but the requirements for its validity are more strict. The infinite sum in (3.49) is often taken inside the integral operator, by which a new kernel is obtained, in particular, the infinite sum of the kernels $\tilde{F}_{0q}$ times the corresponding phase factors $e^{-jq\Psi}$. This formulation was reported to yield a slower numerical solution than the formulation in which the infinite sum is extracted from the moment matrix, as in (3.48), see [95: p. 604]. However, transformation of the new kernel, for example by Poisson's summation formula, may improve the rate of convergence of both formulations significantly.

We illustrate the convergence and divergence of the series describing the infinite-array moment matrix A by means of an example. Figure 3.3 (left) shows the $(1,1)$ component of A in the complex plane as a function of Ψ for prescribed parameter values. The arrow indicates the

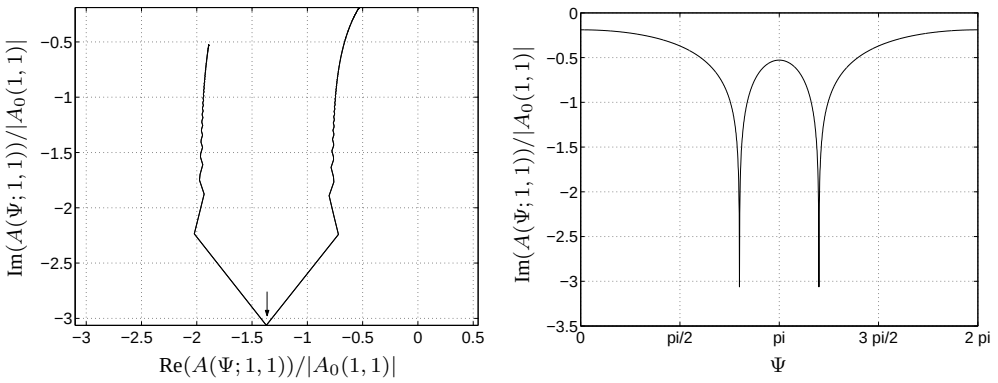

Figure 3.3 Left: normalized $A(\Psi;1,1)$ for a line array of strips in free space. Right: normalized $\mathrm{Im}(A(\Psi;1,1))$ as a function of Ψ for the same array. The function values are calculated in the points $\Psi = 2\pi i/1500$, $i = 0, 1, \ldots, 1500$, with $q = -999, \ldots, 999$ in (3.48). The arrow indicates the points $A(4\pi/5;1,1)$ and $A(6\pi/5;1,1)$. Parameter values: $2\ell = \lambda/2$, $\beta = 1/50$, $d = 3\lambda/5$, $N_{\cos} = 1$, $N_{\sin} = 0$.

points $A(4\pi/5;1,1)$ and $A(6\pi/5;1,1)$, which are the same. Near the corresponding values of Ψ, i.e., $\Psi = 4\pi/5$ and $\Psi = 6\pi/5$, the function $A(\,\cdot\,;1,1)$ varies rapidly. Together with a too low number of interpolation points, this explains the angular nature of the curve at the point indicated by the arrow. Figure 3.3 (right) suggests that the imaginary part of $A(\,\cdot\,;1,1)$ exhibits logarithmic singularities at $\Psi = 4\pi/5$ and $\Psi = 6\pi/5$. This is confirmed by Figure 3.4 (left),

which shows that the imaginary part of $A_q(1,1)\,e^{-4jq\pi/5}$ tends as $1/q$ for $q > 0$. Although shown up to $q = 50$ only, we have verified that this behavior continues up to $q = 2000$. The same behavior is observed for $\Psi = 6\pi/5$, but for $q < 0$. Hence, the series in (3.48)^2 is at most convergent in principal-value sense for $\Psi = 4\pi/5$ and $\Psi = 6\pi/5$, if it converges at all. For comparison, Figure 3.4 (right) shows the imaginary part of $A_q(1,1)$ as a function of q.

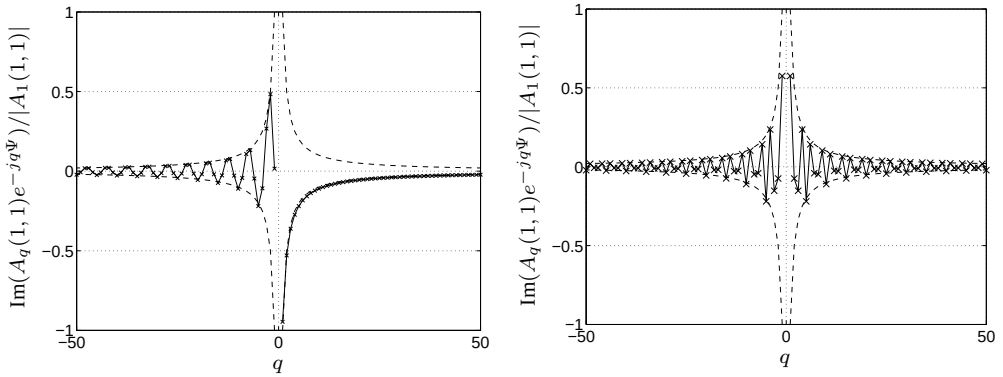

Figure 3.4 Solid curves with crosses: normalized $\mathrm{Im}(A_q(1,1)\,e^{-jq\Psi})$ as a function of q for $\Psi = 4\pi/5$ (left) and $\Psi = 0$ (right). Dashed curves: $\pm 1/|q|$. Parameter values: see Figure 3.3. Normalization: $|A_1(1,1)|$.

Numerical tests reveal that $A_q(1,1)e^{-jq\Psi}$ behaves as $1/q$ for $q = \pm|q|$ if $\Psi = \mp 2\pi d/\lambda + 2m\pi$ with $m \in \mathbb{Z}$. The angles θ_1 corresponding to these values of Ψ follow from

$$\cos\theta_1 = \mp 1 + m\lambda/d\,, \qquad 0 \le \theta_1 \le 2\pi,\ m \in \mathbb{Z}\,. \tag{3.50}$$

For $n\lambda/2 \le d < (n+1)\lambda/2$, this equation yields exactly one solution for each $m = 0, \pm 1, \ldots, \pm n$ corresponding to the sign choice of ∓ 1 in the right-hand side. For other combinations of sign choice and values of m, the equation has no real-valued solution. The solutions for $m = 0$ are the grazing angles $\theta_1 = 0^\circ$ and $\theta_1 = 180^\circ$. The solutions for $m = -1, \ldots, -n$ and $m = 1, \ldots, n$ correspond to angles θ_1 at which a grating lobe appears or disappears at 0° and 180°, respectively. Here, appearance or disappearance depends on the direction in which the interval for θ_1 is traversed. In the example of Figures 3.3 and 3.4, a grating lobe appears or disappears at 0° for $\cos\theta_1 = -2/3$, i.e., $\theta_1 = 131.8^\circ$ and $\Psi = -4\pi/5$, and at 180° for $\cos\theta_1 = 2/3$, i.e., $\theta_1 = 48.2^\circ$ and $\Psi = 4\pi/5$. This result is formulated as follows in terms of the spherical angles (θ, ϕ) and the scan angle described by the spherical angles $(\theta_{\mathrm{scan}}, \phi_{\mathrm{scan}})$. In the xz-plane, a grating lobe appears or disappears at $\theta = 90^\circ$ for the scan angle $\theta_{\mathrm{scan}} = -41.8^\circ$, and at $\theta = -90^\circ$ for the scan angle $\theta_{\mathrm{scan}} = 41.8^\circ$.

From the above, we see that the possible divergence of the series (3.48)^2 is related to the physical phenomena of grating-lobe appearance and grazing scan. Mathematically, the possible

divergence could be explained by the approximate cancelation of the phase $q\Psi$ by the phase of the kernel $\hat{g}_{\rm free}$ in the expression for $\mathcal{Z}_{\rm a}$ for large values of q, see (2.53). The mathematical implication of divergence of the series is that the Laurent matrix (3.47) induces an unbounded operator on $l_2(\mathbb{Z})$. This follows from a result in [14: pp. 3, 186], which states that the operator is bounded if and only if its related Fourier series $(3.48)^2$ generates a bounded function. This function, i.e., the infinite-array moment matrix, is called the symbol of the Laurent matrix (3.47). In Chapter 5, we show that the behavior of the spectrum of the finite-array moment matrix for $N_{\rm el} \to \infty$ is in correspondence with the possible divergence of the Fourier series by relating these eigenvalues to scan angles of the array.

The singular-like behavior of the function A appears in each of its components. Moreover, this behavior appears to be independent of the strip length and width. For spacings smaller than half a wavelength, which do not induce grating lobes, the singular behavior occurs as well, but only at grazing scan. Analogous results are obtained for line arrays of rings, where the singular behavior appears to be independent of ring circumference and width. If the rings or strips are positioned above a ground plane, the singular behavior disappears.

Divergence of the infinite-array solution is also found in [21: Sec. 6] for line arrays of collinear wires and for rectangular arrays of parallel wires, both in free space. Here, the divergence appears as a singularity in one or more expansion terms of the infinite-array integral kernel. This kernel is obtained from the exact wire kernel for the array by applying Poisson's summation formula. Condition (3.50) for divergence in free space follows also from [21: Eq. (12)] by setting $\gamma_n = 0$. As in our results, the singularities found in [21: Sec. 6] are removed when the array is positioned in a half space. Moreover, the singularities are linked to the appearance and disappearance of a grating lobe. In a general context, this link is established in [124] as well. It is shown that the resistance and reactance functions, or their derivatives, of an element in an infinite array in free space are discontinuous at the grating-lobe scan angle [124: Th. 6].

Finally, we consider briefly uniform rectangular arrays. Also for these arrays, the expansion and test functions described by $\mathcal{W}$ can be chosen such that the moment matrices $[\mathcal{W}^- \mathcal{Z}_{\rm a} \mathcal{W}]$ are block Toeplitz matrices. The interaction between the line arrays of which a rectangular array is composed is described by a block Toeplitz matrix. These blocks, which represent the self and mutual coupling of the line arrays, are block Toeplitz matrices as well. In the infinite-array approach, both the total Toeplitz matrix and its Toeplitz blocks become infinite matrices. In other words, the infinite array is represented by the Laurent matrix (3.47) of which the blocks A_q are infinite block Toeplitz matrices. If a linear phase taper is assumed in both the length and width direction of the array, the Laurent matrix is reduced to a single block as in (3.48) for line arrays.

CHAPTER 4

The Excitation Field

As part of the second phase of our research, see the scheme in Figure 1.7, we discuss in this chapter the tangential excitation field by which the source of arrays of strips and rings is modeled. Two types of excitation fields are considered: excitation fields related to the transmit function, also called local feeds, and excitation fields related to the receive function of the array. In particular, we investigate the consequences of expressing the tangential excitation field in terms of a finite set of expansion functions. We show that specific choices of local feeds, i.e., the delta gap, the finite feed gap, and excitation by a proximity coupled small ring, are equivalent. They generate the same current distributions up to small perturbations. On basis of this result, we choose finite expansions of the delta gap as tangential excitation fields for the simulations in Chapter 6. Additionally, we discuss the equivalence of local feeds with respect to a local performance parameter, i.e., the (complex) power. Within the frame of the dimensional analysis of Chapter 2, we show that the tangential excitation field and the current may be replaced by their averaged forms in the computation of the (complex) power. Moreover, we show that the real part of the complex power equals twice the radiated power, as described in the literature. Finally, to model the receive function, we choose plane waves and we show for which plane-wave directions the averaging procedure of Chapter 2 is valid. Moreover, we show that currents induced by local feed gaps and currents induced by plane waves are approximately the same, which is explained by the reciprocity theorem.

4.1 General Aspects

As mentioned in Section 2.2, the excitation field $\boldsymbol{E}_S$ can be interpreted as the tangential component of an externally applied electric field, $-(\boldsymbol{E}^{\mathrm{ext}})_{\tan}$, at the surface S of the array elements. This external field may originate from a feed including its connection to the array. The mutual coupling between the external field and the array is ignored in the model $\mathcal{Z}\boldsymbol{J} = \boldsymbol{E}_S$, or in other

words, the excitation field $\boldsymbol{E}_S$ is assumed fixed.

The solution of $\mathcal{Z}\boldsymbol{J} = \boldsymbol{E}_S$ is determined by the excitation field only, and not by the complete external field. External fields $\boldsymbol{E}^{\mathrm{ext}}$ that induce the same excitation field and, hence, induce the same solution $\boldsymbol{J}$, are called equivalent. In turn, the (numerical) solution procedure, in which $\mathcal{Z}\boldsymbol{J} = \boldsymbol{E}_S$ is replaced by the moment-matrix equation $[\mathcal{W}^- \mathcal{Z}_{\mathrm{a}} \mathcal{W}][\mathcal{W}^- \boldsymbol{w}] = [\mathcal{W}^- \boldsymbol{v}^{\mathrm{ex}}]$, gives rise to equivalent excitation fields. Fields $\boldsymbol{E}_S$ that induce the same excitation vector $[\mathcal{W}^- \boldsymbol{v}^{\mathrm{ex}}]$ and, hence, the same solution $[\mathcal{W}^- \boldsymbol{w}]$, are equivalent. Here, $\boldsymbol{v}^{\mathrm{ex}}$ represents the averaged centerline components of $\boldsymbol{E}_S$, see Subsection 2.3.1, and the excitation vector represents the expansion coefficients of $\boldsymbol{v}^{\mathrm{ex}}$ with respect to the finite basis of functions $\mathrm{bas}(\mathcal{W})$ and the inner product on $\mathcal{Y}_{\mathrm{a}}$, see Section 2.4. The finite expansion of $\boldsymbol{v}^{\mathrm{ex}}$ is square integrable, as required in the space characterization of Section 3.1, even if $\boldsymbol{v}^{\mathrm{ex}}$ itself is not square integrable. In that case, the expansion coefficients can only be calculated in generalized sense. From a practical point of view, only the expansion of $\boldsymbol{v}^{\mathrm{ex}}$ is important and not its fine structure. How accurate the expansion of $\boldsymbol{v}^{\mathrm{ex}}$ needs to be depends on the typical parameter under consideration and, hence, on the functional metric related to (2.31).

From the above, we observe that the excitation is modeled as a finite number of expansion coefficients given by the excitation vector $[\mathcal{W}^- \boldsymbol{v}^{\mathrm{ex}}]$, which can be regarded as a discretization of $\boldsymbol{E}_S$. Vice versa, the question arises whether a given excitation vector corresponds to a physically realizable excitation. The underlying assumption of each of our choices of excitation vectors is that they somehow approach a physically realizable excitation. In the next sections, we support the underlying assumptions by certain physical ideas.

4.2 Excitation Fields for Local Feeds

In this section, we first consider examples of excitation fields representing local feeds for strips and rings. Subsequently, we investigate the equivalence of these examples.

4.2.1 Examples

Feed Gaps

As a first example of a local feed, we consider the finite feed gap. The corresponding components of $\boldsymbol{v}^{\mathrm{ex}}$ are given by

$$v^{\mathrm{ex}}(\xi; q) = -\frac{V^{\mathrm{ex}}(q)}{2\epsilon\ell}\, 1_{[-\epsilon,\epsilon]}(\xi)\,, \tag{4.1}$$

for the qth strip, and by

$$v^{\mathrm{ex}}(\varphi; q) = -\frac{V^{\mathrm{ex}}(q)}{2\epsilon\pi a_q}\, 1_{[\pi(1-\epsilon)\,,\,\pi(1+\epsilon)]}(\varphi \bmod 2\pi)\,, \tag{4.2}$$

for the qth ring, see Figure 4.1. Here, $1_{[\,\cdot\,,\,\cdot\,]}$ is the characteristic function as introduced below (2.56) and mod is the modulo function. The gap width is a function of ϵ as indicated in Figure 4.1. Straightforward examples of corresponding excitation fields are $\boldsymbol{E}_S|_{S_q} = v^{\mathrm{ex}}(\,\cdot\,;q)\,\boldsymbol{e}_\xi$ and

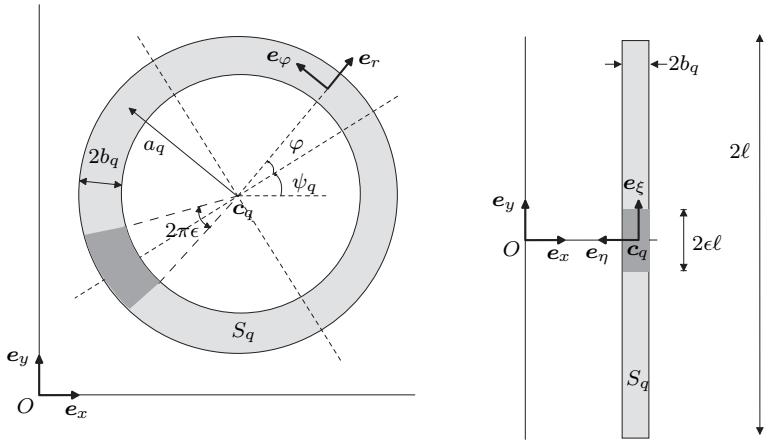

Figure 4.1 A ring and a strip with finite feed gaps.

$\boldsymbol{E}_S|_{S_q} = v^{\mathrm{ex}}(\,\cdot\,;q)\,\boldsymbol{e}_\varphi|_{S_q}$. These excitation fields are regarded as voltage jumps of magnitude $V^{\mathrm{ex}}(q)$ over a finite length on the qth strip or ring. An interpretation of such a jump is that it represents a voltage difference between the two (fictitious) terminals of a strip or a ring. For the entire-domain functions on the strips, see (3.7) and (3.8), the excitation vector corresponding to (4.1) is given by the right-hand side of (2.131), where

$$[\mathcal{W}_q^-\boldsymbol{v}^{\mathrm{ex}}] = \begin{pmatrix} [(\mathcal{W}_q^{\cos})^-\boldsymbol{v}^{\mathrm{ex}}] \\ [(\mathcal{W}_q^{\sin})^-\boldsymbol{v}^{\mathrm{ex}}] \end{pmatrix} \tag{4.3}$$

and

$$[(\mathcal{W}_q^{\cos})^-\boldsymbol{v}^{\mathrm{ex}}](n,1) = -\frac{V^{\mathrm{ex}}(q)}{\ell}\,\mathrm{sinc}\left(\frac{(2n-1)\pi\epsilon}{2}\right), \quad [(\mathcal{W}_q^{\sin})^-\boldsymbol{v}^{\mathrm{ex}}](n,1) = 0\,. \tag{4.4}$$

As in Subsection 3.3.1, we use that the entire-domain functions are orthonormal with respect to the inner product in L_2 and, hence, that the corresponding Gram matrix is the identity matrix. For the entire functions on the rings, see (3.7) and (3.12), the excitation vector is given by the right-hand side of (2.131), where

$$[\mathcal{W}_q^-\boldsymbol{v}^{\mathrm{ex}}] = G_q^{-1}\,\left[\boldsymbol{\zeta}_q^{\cos} \sqcup \boldsymbol{\zeta}_q^{\sin}\right], \tag{4.5}$$

and

$$\zeta_q^{\sin}(n) = 0\,, \qquad \zeta_q^{\cos}(n) = \frac{(-1)^n V^{\mathrm{ex}}(q)}{a_q}\,\mathrm{sinc}\big((n-1)\pi\epsilon\big)\,. \tag{4.6}$$

The Gram matrix G_q is defined by (3.34) and the concatenation $\sqcup$ by (2.103). By letting $\epsilon \to 0$ in these expressions, we obtain the non-zero components

$$[(\mathcal{W}_q^{\cos})^{-}\boldsymbol{v}^{\mathrm{ex}}](n,1) = -\frac{V^{\mathrm{ex}}(q)}{\ell}\,, \qquad \zeta_q^{\cos}(n) = (-1)^n \frac{V^{\mathrm{ex}}(q)}{a_q}\,, \tag{4.7}$$

in (4.4) and (4.6), respectively. One of the fields $\boldsymbol{v}^{\mathrm{ex}}$ corresponding to the resulting excitation vector for the strips, i.e., (4.4)[2] and (4.7)[1], is obtained as the generalized limit of (4.1). For the rings, such a field is obtained as the generalized limit of (4.2) for $\epsilon \to 0$. In both cases, the limit results in the well-known delta gap, also called voltage gap, for which $\boldsymbol{v}^{\mathrm{ex}}$ is not a square integrable function.

Excitation by Proximity Coupling

The second example of a local feed is the excitation of a ring by proximity coupling. We consider a ring with circumference of about a wavelength excited by the electromagnetic field of an electrically small ring. In turn, this small ring is excited by a delta gap. Both rings satisfy the dimension requirements of Subsection 2.3.3, but the distance between the rings is a few times the width of the large ring and, hence, not much larger than its width, i.e., $b_q/(|\boldsymbol{c}_p - \boldsymbol{c}_q| - a_p - a_q) = O(\beta)$ for $p \neq q$, see for example Figure 4.2 (left). Excitation of a ring by the external field of a proximate ring has been studied by the author in cooperation with A. Kooiker, see [59]. The objective of this study was to show equivalence between excitation by proximity coupling and excitation by finite feed gaps. The main results are presented in Subsection 4.2.2. Readers interested in the calculational details of proximity coupling find them below. The main idea is that we replace the approximate kernels as deduced in Subsection 2.3.3 by approximate kernels for electrically small spacings.

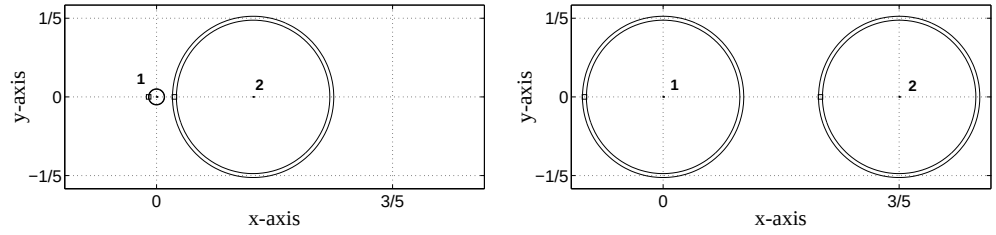

Figure 4.2 Two examples of "arrays" of two rings. The little blocks on the rings, i.e., □, indicate the position of a feed gap, if such a gap is present. Length scales are given in wavelengths.

Calculational Steps of Proximity Coupling

To study proximity coupling between two rings, we reconsider the analysis of Subsection 2.3.3. We assume that the distances between the rings are such that we may still apply the averaging operator $\mathcal{A}$, see (2.71). Depending on the distance between two rings and on their sizes, we may need other approximations for the kernels (2.77) than presented in (2.89) and (2.95) for certain values of φ and φ'. For these values, we do not approximate the distance measure $\hat{R}_{pq}$ with $p \neq q$ in (2.73) and (2.77)[1]. Hence, we need to evaluate the adjusted approximate kernels

$$\begin{aligned}
\tilde{K}_{1,pq}(\varphi,\varphi') &= \int_{-1}^{1}\int_{-1}^{1} \hat{g}_{\mathrm{free}}\big(\hat{R}_{pq}(r,r',\varphi,\varphi')\big)\,dr'dr\,,\\
\tilde{K}_{2,pq}(\varphi,\varphi') &= \frac{1}{\beta_p}\int_{-1}^{1}\Big[\hat{g}_{\mathrm{free}}\big(\hat{R}_{pq}(1,r',\varphi,\varphi')\big) - \hat{g}_{\mathrm{free}}\big(\hat{R}_{pq}(-1,r',\varphi,\varphi')\big)\Big]\,dr' + \\
&\qquad + \tilde{K}_{1,pq}(\varphi,\varphi')\,,
\end{aligned} \tag{4.8}$$

that replace the approximate kernels (2.89) and (2.95). Here, $\hat{g}_{\mathrm{free}}$ is the (normalized) kernel defined by (2.44)[1] and $\hat{R}_{pq}$ is the (normalized) distance measure defined by (2.70). In (4.8), we neglect terms of order β. We compute both integrals with the composite Simpson rule as described in Section 3.4 ($N_{\mathrm{int}} = 50$), although, for small spacings, integration intervals of equal length are not practical due to the nearly singular behavior of the integrands. To determine for which values of φ and φ' (4.8) should be used, a criterion is proposed in [59: p. 106] based on the relative difference between the distance measures $\hat{R}_{pq}(r,r',\varphi,\varphi')$ and $|\boldsymbol{d}_{pq}(\varphi,\varphi')|$, see (2.70) and (2.88). Here, we compute the kernels either completely with the approximations (4.8) or completely with the approximations (2.89) and (2.95). The coupling integrals (3.37) are computed as in Section 3.4, but with $N_{\mathrm{int}} = 50$ instead of the proposed rules of thumb.

To compare both approximations, we compute the point-wise relative differences between the corresponding results for the current for several parameter settings. The first setting concerns two rings with equal radii $a = a_1 = a_2 = \lambda/5$ and with spacing $3a$, see Figure 4.2 (right). The first ring is excited by a delta gap of $1\mathrm{V}$. Figure 4.3 (left) shows the differences for the second ring. This ring is either excited by the field of the first ring only or also by a delta gap of $1\mathrm{V}$ on itself. Figure 4.3 (right) shows the same differences, but for spacing $2a + 6b$, where $b = b_1 = b_2$ is half the width of the rings. If the second ring is not excited by a delta gap on itself, the relative differences for the larger spacing are of the same order as the maximum relative error required in Section 3.4, i.e., 0.1%. Moreover, the maximum relative difference is attained at $\varphi = -\pi$, which indicates the position on the second ring with the smallest distance to the first ring. For the smaller spacing, the relative differences are of the order of 1%. Contrary to the result for the larger spacing, the maximum relative difference is not attained at $\varphi = -\pi$, but at $\varphi = 0.95$. This value of φ indicates the position at which the current amplitude attains its minimum.

Since we neglect terms of order $\beta = b/a$ in the deduction of the kernel approximations

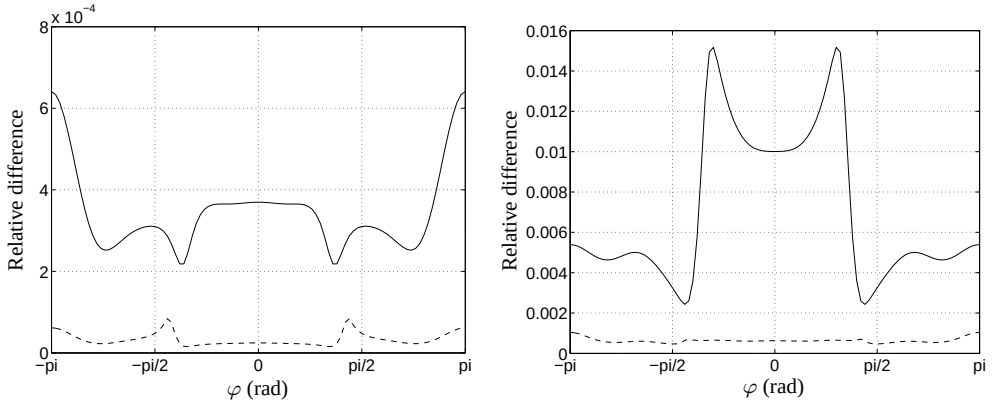

Figure 4.3 Relative differences, as a function of the angle φ, of the currents obtained by the approximations (2.89) and (2.95) and by the approximation (4.8) on the second ring of an array of two rings in free space. Left: spacing $3a$ as in Figure 4.2 (right), where $a = a_1 = a_2$. Right: spacing: $2a + 6b$, where $b = b_1 = b_2$. Dashed curve: delta gap on the second ring with $V^{\rm ex}(2) = 1\text{V}$. Solid curve: no delta gap on the second ring. Parameter values: $a = \lambda/5$, $\beta = b/a = 1/40$, $\psi_q = 0$, $V^{\rm ex}(1) = 1\text{V}$, $N_{\cos}(q) = 8$, $N_{\sin}(q) = 0$.

(2.89) and (2.95), a relative difference of order $\beta = 1/40$ is expected in the results above. Hence, for distances between the rings that are much larger than the ring widths, the accuracy of the current obtained by the kernel approximations (2.89) and (2.95) seems to be of higher order than β. Moreover, for distances of the order of the ring width of the large ring, the accuracy seems to be of the order β. In the next subsection, we use the kernel approximations (4.8) to compute the current.

The percentages above are based on the relative difference for a second ring without delta-gap excitation. If this ring is excited by a delta gap, the relative difference is much smaller, as shown in Figure 4.3. This is explained as follows. The self coupling of each ring is predominant over the mutual coupling between the rings. Hence, if a ring is excited by a local feed, its current is largely determined by the self coupling. As a result, the relative difference between the currents on the second ring in Figure 4.3 are much smaller, if this ring is excited by a delta gap.

For two closely spaced rings as in Figure 4.2 (left), we found on the second ring relative differences smaller than 1% if this ring is not excited by a delta gap, and smaller than 0.1% if this ring is excited by a delta gap of 1V. This corroborates the results above. We investigated also whether the relative differences found above are significant with respect to the numerical accuracy of the computation of (4.8) by which these differences are obtained. For $N_{\rm int} = 100$ instead of $N_{\rm int} = 50$ in this computation, we found a relative difference of 10^{-11}. Taking also

$N_{\rm int} = 100$ instead of $N_{\rm int} = 50$ in the computation of the coupling integrals (3.37), we found a relative difference of 10^{-5}. Hence, the relative differences found above are significant.

4.2.2 Equivalence

To investigate equivalence of the introduced local feeds, we consider first the coupling between a small and a large ring as shown in Figure 4.2 (left). The small ring is excited by a delta gap of 1V, whereas the second ring is not excited. Figure 4.4 shows the normalized amplitude and phase of the current on the small ring compared to the current on the same but single ring, where 'single' means without any other ring present. As expected, the current on the single ring has a small real part compared to its imaginary part, which indicates that the ring is strongly reactive. Moreover, the amplitude is almost constant. The current of the proximity coupled small ring differs pointwise only 0.1% from the current on the single ring. This difference is of the same order as the numerical accuracy required in Section 3.4 and, hence, we neglect the coupling of the large ring onto the small ring. In the moment-matrix equation $[\mathcal{W}^- \mathcal{Z}_{\rm a} \mathcal{W}][\mathcal{W}^- \boldsymbol{w}] = [\mathcal{W}^- \boldsymbol{v}^{\rm ex}]$, this can be accomplished by setting the block $[\mathcal{W}_1^- \mathcal{Z}_{\rm a} \mathcal{W}_2]$ equal to zero. Instead, we choose to construct a moment-matrix equation for the large ring only and we incorporate the excitation field induced by the small ring onto the large ring in the corresponding excitation vector. Physically speaking, we consider the current on the small ring as an impressed current and choose this current equal to the current on the small ring excited by a delta gap of 1V. The impressed current induces a fixed excitation field on the large ring. This shows a first correspondence with the feed gaps of which the excitation field is assumed to be fixed as well.

We compare the proximity coupling above with the case of a single large ring excited by a finite feed gap described by $V^{\rm ex} = 4.34 \cdot 10^{-2}$V and $\epsilon = 0.127$. The length of the feed gap is 0.16λ, while the circumference of the small ring is 0.13λ. Figure 4.5 shows that if Gibbs-like oscillations are discarded, the averaged excitation field for the feed gap is an accurate approximation of the averaged excitation field induced by proximity coupling. In this approximation, both the real parts and the imaginary parts show the same absolute difference. Figure 4.6 (left) shows that the two excitations induce currents with the same amplitudes. The difference between these excitations results in a phase difference between the corresponding currents, see Figure 4.6 (right), which is independent of the number of expansion functions. This phase difference is due to the non-zero imaginary part of the averaged excitation field of the proximity coupling as shown in Figure 4.5 (right). Without this part, the phases of the currents become identical. Moreover, their amplitudes change hardly with respect to the amplitudes in Figure 4.6 (left). Roughly speaking, the phase difference between the two currents is -0.2 rad, see Figure 4.6 (right). Hence, the two excitations can be considered equivalent up to the factor $e^{-0.2\,j}$. This factor can be interpreted as follows. The feed is not positioned on the ring, but connected to the ring by a piece of transmission line of length $0.2/k = 0.2\,\lambda/2\pi$. For more details on

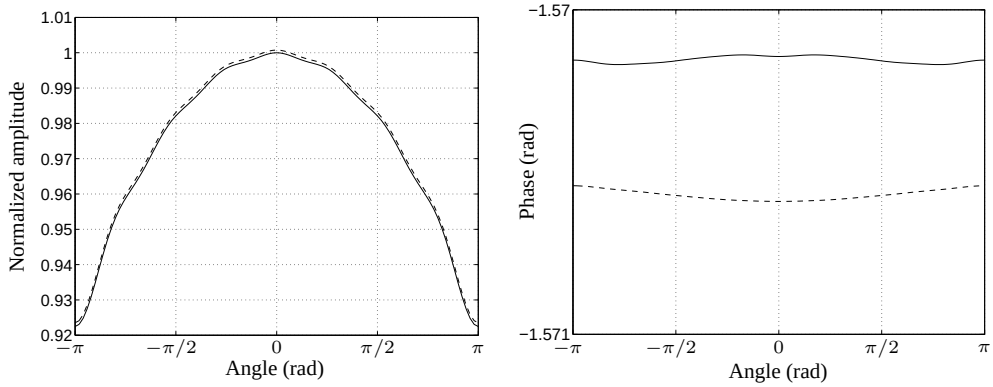

Figure 4.4 Normalized amplitude (left) and phase (right) of the current on the small ring in Figure 4.2 (left) as a function of the angle φ. Solid curve: single small ring with a delta gap of $1\mathrm{V}$. Dashed curve: no delta gap on the large ring. The rings are positioned in free space with parameter values (ring indices as in Figure 4.2): $a_2 = 10a_1 = \lambda/5$, $\beta_q = b_q/a_q = 1/40$, spacing $a_1 + b_1 + 5b_2 + a_2$, $\psi_q = 0$, $N_{\cos}(q) = 8$, $N_{\sin}(q) = 0$. Normalization: maximum current amplitude of the single ring.

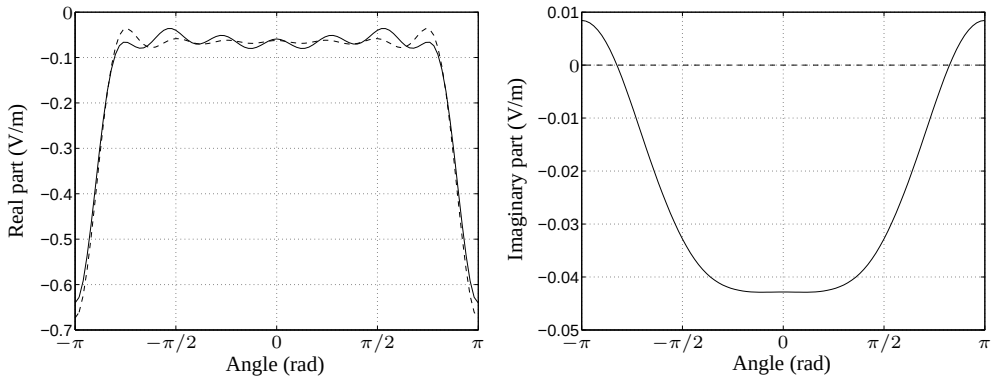

Figure 4.5 Real and imaginary part of the averaged excitation field at the large ring in Figure 4.2 (left) as a function of the angle φ. Solid curve: field induced by the small ring with a delta gap of $1\mathrm{V}$. Dashed curve: single large ring with field induced by a finite feed gap of $4.34{\cdot}10^{-2}\mathrm{V}$ with $\epsilon = 0.127$. The rings are positioned in free space with parameter values as in Figure 4.4.

transmission-line theory, we refer to [94: pp. 76 ff.].

As a second example of equivalence, we compare the finite feed gap and the delta gap for the large ring in Figure 4.2 (left). For the finite feed gap, we choose $\epsilon = 0.05$. Figure 4.7 shows that the currents induced by the finite feed gap and the delta gap have equal phase. Their amplitudes are equal up to differences of about 1% near the gaps centered at $\varphi = \pi$. Hence, the chosen excitations can be considered equivalent for the given parameter values. It goes without saying that all finite feed gaps with $0 < \epsilon < 0.05$ can be considered equivalent for the same parameter values as well.

In the two examples of equivalence above, we used $N_{\cos}(q) = 8$ entire-domain expansion functions on the rings. For $N_{\cos}(q) = 4$ and $N_{\cos} = 20$, the current amplitudes in Figure 4.6 and Figure 4.7 change only near $\varphi = \pi$, i.e., the 'position' of the local feed, and near $\varphi = 0$. This is observed by comparing the amplitudes in these figures with the amplitudes in Figure 4.8. Moreover, comparing Figure 4.6 (left) and Figure 4.8 (upper row), we observe that, regardless the number of expansion functions, the current amplitudes induced by the two local feeds of Figure 4.6 match each other, even near $\varphi = 0$, i.e., the position of the local feed. The same is valid for the current amplitudes induced by the two local feeds of Figure 4.7, but the differences near $\varphi = 0$ are larger for $N_{\cos} = 20$. The phases of the currents in Figure 4.6 and Figure 4.7 do not change. Thus, for $N_{\cos} = 4$ and $N_{\cos} = 20$, we arrive at the same conclusion, that the local feeds under consideration can be considered equivalent. Finally, in Figure 4.8 (second row, second column), the computed current amplitude of a single ring with a delta gap seems to show instabilities near $\phi = \pi$. We computed the amplitude for $N_{\cos} = 30$ and $N_{\cos} = 40$ as well, but the amplitude remained stable.

The examples above show that specific local feeds can be considered equivalent on basis of the dominant behavior of the current distributions induced by these feeds. This dominant behavior is described by a small number of entire-domain expansion functions. Because of the equivalence, we choose one local feed for the actual computation of typical parameters, namely, the delta gap described by a finite expansion. The motivation is that this specific local feed does not distinguish between the expansion functions on a single strip or ring in the sense that it 'hits' all expansion functions.

Finally, we emphasize that how accurate the expansion of $\boldsymbol{v}^{\mathrm{ex}}$ needs to be and whether certain excitations can be considered equivalent still depends on the performance parameter under consideration. As an example, we compare the complex power generated by a single ring with certain local feeds and we relate this power to the input impedance of the ring.

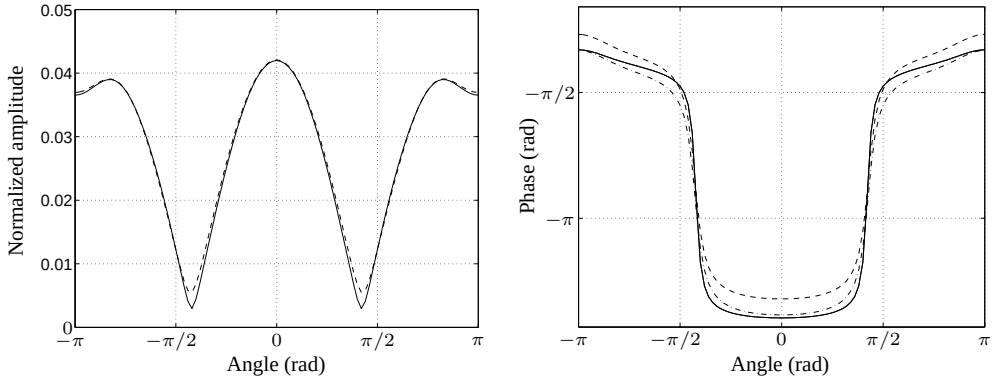

Figure 4.6 Normalized amplitude (left) and phase (right) of the current on the large ring in Figure 4.2 (left) as a function of the angle φ. Solid curve: field induced by the small ring with a delta gap of $1\mathrm{V}$. Dashed curve: single large ring with field induced by a finite feed gap of $4.34 \cdot 10^{-2}\mathrm{V}$ with $\epsilon = 0.127$. Dashed-dotted curve (right): voltage of single large ring multiplied by the phase factor $e^{-0.2\,j}$. The rings are positioned in free space with parameter values as in Figure 4.4. Normalization: maximum current amplitude of the single large ring with a delta gap of $1\mathrm{V}$.

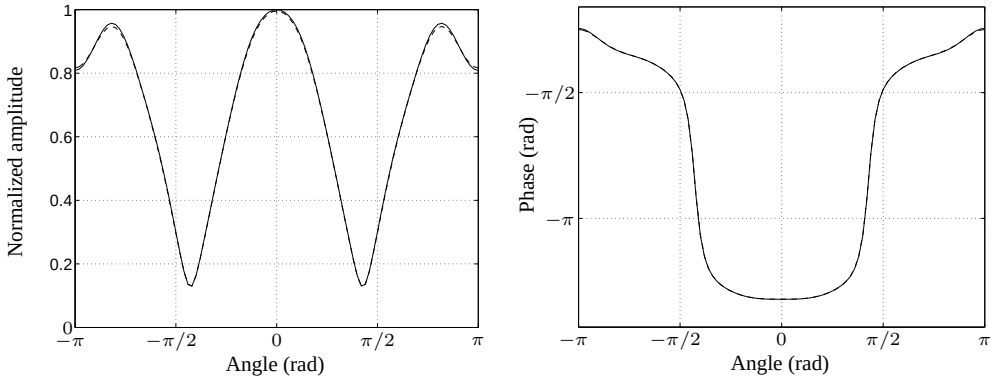

Figure 4.7 Normalized amplitude (left) and phase (right) of the current on a single ring, with the same geometry as the large ring in Figure 4.2 (left), as a function of the angle φ. Solid curve: excitation field induced by a delta gap of $1\mathrm{V}$. Dashed curve: excitation field induced by a finite feed gap of $1\mathrm{V}$ with $\epsilon = 0.05$. The rings are positioned in free space with parameter values as in Figure 4.4. Normalization: maximum current amplitude of the single large ring with a delta gap of $1\mathrm{V}$.

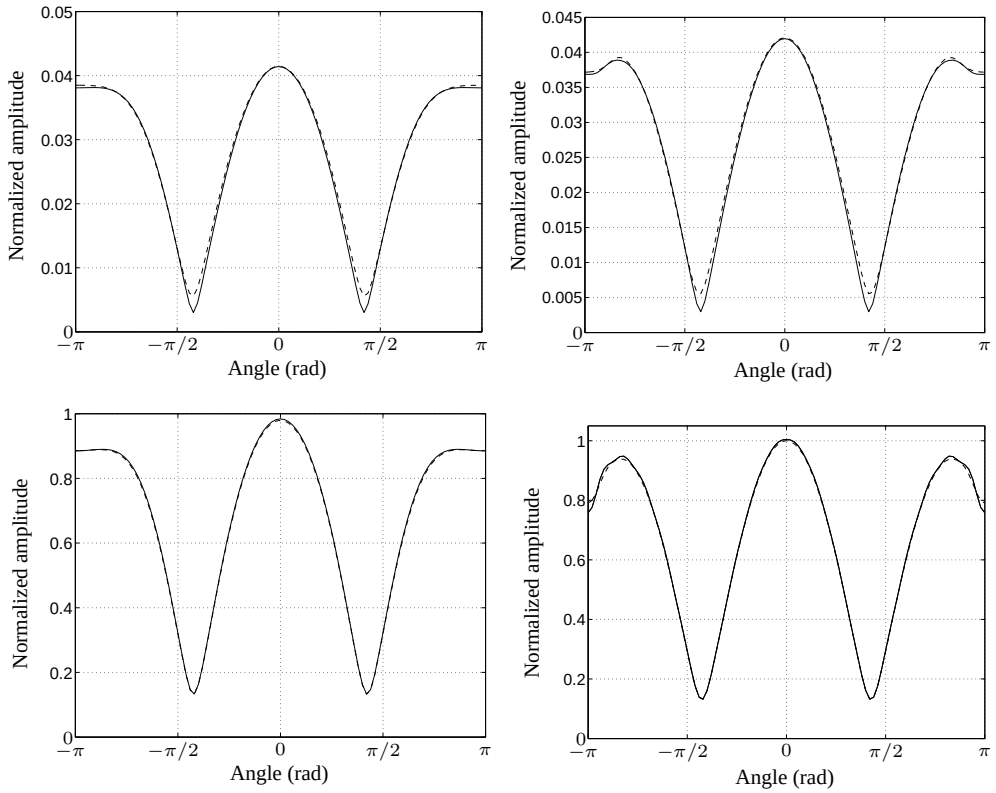

Figure 4.8 Upper row: normalized amplitudes of the currents in Figure 4.6 (left), but with $N_{\cos}(q) = 4$ (left) and $N_{\cos}(q) = 20$ (right) instead of $N_{\cos}(q) = 8$. Lower row: normalized amplitudes of the currents in Figure 4.7 (left), but with $N_{\cos}(q) = 4$ (left) and $N_{\cos}(q) = 20$ (right) instead of $N_{\cos}(q) = 8$. The rings are positioned in free space with parameter values as in the corresponding figures. Normalization: as in the corresponding figures (with $N_{\cos}(q) = 8$).

Power and Input Impedance

The complex power induced by an excitation field $\boldsymbol{E}_S$ on a surface S is defined by

$$P^{\text{ex}} = -\int_S \boldsymbol{E}_S \bullet \boldsymbol{J}^* \, dS \,. \tag{4.9}$$

For surfaces S with parameter set $\Pi(S) = \Pi_\xi(S) \times [-\eta_1, \eta_1]$, we introduced in Subsection 2.3.1 the concepts of narrow surface and width averaged vector field, see (2.28) and further. Assuming that the surface S in (4.9) is narrow with respect to $\boldsymbol{E}_S$, or, $(\mathcal{I} - \mathcal{A})\boldsymbol{E}_S \approx \boldsymbol{0}$, we may replace $\boldsymbol{E}_S$ by its width average $\mathcal{A}\boldsymbol{E}_S$. Since $\mathcal{A}\boldsymbol{E}_S$ is directed along the centerline of S, only

the centerline component of $\boldsymbol{J}$ contributes to the complex power (4.9). Moreover, since $\mathcal{A}\boldsymbol{E}_S$ is constant with respect to the width of S, the integral in (4.9) with respect to this width acts only on the product of the centerline component of $\boldsymbol{J}$ and the 'volume element' $S_{\rm vol}$ of S as defined by (2.24). Such an integral is recognized in the definition of the width average of a vector field, see (2.29). Hence, the complex power turns into

$$P^{\rm ex} = -\int_\xi (\mathcal{A}\boldsymbol{E}_S)_\xi(\xi)(\mathcal{A}\boldsymbol{J})^*_\xi(\xi)\int_{-\eta_1}^{\eta_1} S^{\rm vol}(\xi,\eta)\,d\eta\,d\xi\,, \quad \text{or,} \quad P^{\rm ex} = -\int_S \mathcal{A}\boldsymbol{E}_S \bullet \mathcal{A}\boldsymbol{J}^*\,dS\,. \tag{4.10}$$

Here, ξ is the centerline coordinate of the surface S, see Figure 2.3. The derivation of (4.10) shows that if either $\boldsymbol{E}_S$ or $\boldsymbol{J}$ in (4.9) is replaced by its width-average, the other field can be replaced by its average as well.

If S consists of $N_{\rm el}$ disjoint surfaces S_q, $\boldsymbol{v}^{\rm ex}$ and $\boldsymbol{w}$ are $N_{\rm el}$-tuples, which represent the centerline components $(\mathcal{A}\boldsymbol{E}_S)_\xi$ and $(\mathcal{A}\boldsymbol{J})_\xi$ on these elements as in (2.40). Since $\boldsymbol{v}^{\rm ex}$ and $\boldsymbol{w}$ are obtained by the moment method, they are represented by the finite expansions $\mathcal{W}\mathcal{W}^-\boldsymbol{v}^{\rm ex}$ and $\mathcal{W}\mathcal{W}^-\boldsymbol{w}$. Then, for an array of rings, the complex power is given by

$$P^{\rm ex} = -2\sum_{q=1}^{N_{\rm el}} a_q b_q \langle (\mathcal{W}\mathcal{W}^-\boldsymbol{v}^{\rm ex})(\,\cdot\,;q), (\mathcal{W}\mathcal{W}^-\boldsymbol{w})(\,\cdot\,;q)\rangle^*_{L_2}\,, \tag{4.11}$$

and for an array of strips by

$$P^{\rm ex} = -2\sum_{q=1}^{N_{\rm el}} \ell b\, \langle (\mathcal{W}\mathcal{W}^-\boldsymbol{v}^{\rm ex})(\,\cdot\,;q), (\mathcal{W}\mathcal{W}^-\boldsymbol{w})(\,\cdot\,;q)\rangle^*_{L_2} = \\ = -2\ell b\, \langle \mathcal{W}\mathcal{W}^-\boldsymbol{v}^{\rm ex}, \mathcal{W}\mathcal{W}^-\boldsymbol{w}\rangle^*_{L_2}\,. \tag{4.12}$$

Here, the L_2 inner product is defined by (3.4)^2.

Since the arrays of strips and rings are positioned in free space or in a half space, it can be shown as follows that $\mathrm{Re}(P^{\rm ex}) = 2P^{\rm rad}$, where $P^{\rm rad}$ is the total radiated power in the far field as defined by (C.18). In the complex power (4.10)^2, we replace the field $\mathcal{A}\boldsymbol{E}_S$ by $\mathcal{A}\mathcal{Z}\mathcal{A}\boldsymbol{J}$ due to the equality (2.34). Then, as shown above, we may replace $\mathcal{A}\mathcal{Z}\mathcal{A}\boldsymbol{J}$ by $\mathcal{Z}\mathcal{A}\boldsymbol{J}$. Let $\boldsymbol{E}$ and $\boldsymbol{H}$ be the electric and magnetic field induced by $\mathcal{A}\boldsymbol{J}$ according to (2.14). Then, $\mathcal{Z}\mathcal{A}\boldsymbol{J} = (\boldsymbol{E})_{\rm tan}$ and $\mathcal{A}\boldsymbol{J}$ is the jump of the tangential magnetic field over the surface S. Hence, the complex power turns into

$$P^{\rm ex} = -\int_S (\boldsymbol{E})_{\rm tan} \bullet \left(\boldsymbol{n} \times (\boldsymbol{H}|_{S^+} - \boldsymbol{H}|_{S^-})^*\right) dS\,, \tag{4.13}$$

where $\boldsymbol{n}$ is the normal on S and $S^\pm$ denote the sides of S. In this expression, we may replace $(\boldsymbol{E})_{\rm tan}$ by its restriction to S, because the jump has only a tangential component. Let $\boldsymbol{n}^\pm$ be

the normals on $S^{\pm}$ with $\boldsymbol{n}^{+} = \boldsymbol{n}$ and $\boldsymbol{n}^{-} = -\boldsymbol{n}$ as in the model assumption 2 on page 25. Applying the vector identity $\boldsymbol{A} \bullet (\boldsymbol{B} \times \boldsymbol{C}) = -\boldsymbol{B} \bullet (\boldsymbol{A} \times \boldsymbol{C})$, we rewrite (4.13) as

$$P^{\mathrm{ex}} = -\int_S \left(\boldsymbol{n}^{-} \bullet (\boldsymbol{E}|_S \times \boldsymbol{H}^*|_{S^+})\right) dS - \int_S \left(\boldsymbol{n}^{+} \bullet (\boldsymbol{E}|_S \times \boldsymbol{H}^*|_{S^-})\right) dS\,. \tag{4.14}$$

In this expression, $\boldsymbol{n}^{\pm}$ are regarded as the 'outward' normals for $\boldsymbol{H}^*|_{S^{\mp}}$. For the first integral, we interpret S as a part of a closed surface, which encloses the volume Ω^{+} at the S^{+} side of S. For the second integral, we use a similar interpretation, but with $^{+}$ replaced by $^{-}$. Both Ω^{+} and Ω^{-} do not incorporate current sources. Then, according to the complex power balance for time-harmonic fields, see [109: p. 131 – 137], the fluxes of the time-average Poynting vector $\boldsymbol{S} = \mathrm{Re}(\boldsymbol{E} \times \boldsymbol{H}^*)/2$ over $\partial\Omega^{+}$ and $\partial\Omega^{-}$ equal zero. Hence, (4.14) equals the power flux of the time-average Poynting vector over the symmetric difference of the surfaces $\partial\Omega^{+}$ and $\partial\Omega^{-}$. This symmetric difference is a surface, which encloses S. Hence, the real part of P^{ex} equals twice the flux of the Poynting vector over this surface. This statement is valid for any closed surface, which incorporates S. Choosing a sphere in free space and half a sphere together with the ground plane in a half space, we obtain $\mathrm{Re}(P^{\mathrm{ex}}) = 2\,P_{\mathrm{rad}}$, see (C.18). The derivation above is also valid for the finite expansions of $\mathcal{A}\boldsymbol{E}_S$ and $\mathcal{A}\boldsymbol{J}$. Finally, the imaginary part of P^{ex} represents the power stored in the near field of the array.

Let us consider a single ring. Then, the complex power P^{ex} in (4.11) simplifies to

$$P^{\mathrm{ex}} = -2a\,b\,\langle \mathcal{W}\mathcal{W}^{-}v^{\mathrm{ex}}, \mathcal{W}\mathcal{W}^{-}w\rangle^{*}_{L_2}\,, \tag{4.15}$$

where the subindex $_q$ is omitted. Using the definition of $\mathcal{W}$, see (2.110), we rewrite (4.11) as

$$P^{\mathrm{ex}} = -2a\,b\,[\mathcal{W}^{-}w]^{H}\,G\,[\mathcal{W}^{-}v^{\mathrm{ex}}]\,. \tag{4.16}$$

Here, $[\mathcal{W}^{-}w]$ and $[\mathcal{W}^{-}v^{\mathrm{ex}}]$ are the expansion coefficients of the averaged current w and the averaged excitation field v^{ex}, and $G = G(\mathrm{bas}(\mathcal{W}))$, i.e., the Gram matrix of the (test and) expansion functions in $\mathrm{bas}(\mathcal{W})$ with respect to the inner product on $\mathcal{Y}_{\mathrm{a}}$. As in (2.130)^2, we can write $[\mathcal{W}^{-}v^{\mathrm{ex}}] = G^{-1}V$ with $V(n,1) = \langle \mathcal{W}\boldsymbol{e}_n, v^{\mathrm{ex}}\rangle$. Then, $P^{\mathrm{ex}} = -2ab\,[\mathcal{W}^{-}w]^{H}\,V$, where the superscript ^{H} denotes the Hermitian transposed.

Table 4.1 shows the complex power P^{ex} of a ring in free space for (finite expansions of) the excitation fields of three feed gaps. Computations of the corresponding radiated powers P^{rad} showed that the relative differences between $\mathrm{Re}(P^{\mathrm{ex}})$ and $2P^{\mathrm{rad}}$ are about 0.07%. This is an important validation of the analysis for a single ring in free space. Each number of expansion (and test) functions $N_{\cos}$ in Table 4.1 yields another finite expansion of the excitation field of a feed gap. In case we fix such a finite expansion, the result for the current does not change anymore, if we increase the number of expansion (and test) functions $N_{\cos}$ in the moment method. This is due to the diagonal form of the moment matrix of a single ring with entire-domain expansion functions. Then, it is observed from Table 4.1 that the finite expansions of the delta gap

Table 4.1 The complex power $P^{\rm ex}$ $(10^{-4}{\rm W})$ for (finite expansions of) the excitation fields of three feed gaps: a delta gap of 1V and two finite feed gaps of 1V with $\epsilon = 0.05$ and $\epsilon = 0.127$. The ring is positioned in free space and its geometry is the same as the geometry of the large ring in Figure 4.2. Parameter values: $a = \lambda/5$, $\beta = b/a = 1/40$.

	Delta gap		$\epsilon = 0.05$		$\epsilon = 0.127$	
$N_{\rm cos}$	Re$(P^{\rm ex})$	Im$(P^{\rm ex})$	Re$(P^{\rm ex})$	Im$(P^{\rm ex})$	Re$(P^{\rm ex})$	Im$(P^{\rm ex})$
4	6.867	12.77	6.810	13.02	6.507	14.13
8	6.867	9.234	6.810	10.19	6.507	13.32
12	6.867	7.937	6.810	9.589	6.507	13.30
16	6.867	7.209	6.810	9.461	6.507	13.28
20	6.867	6.722	6.810	9.448	6.507	13.27

with 4, 8, 12, 16, and 20 cosine functions can be considered equivalent with respect to the total radiated power, but not with respect to the power stored in the near field of the ring. The results for the finite feed gaps with $\epsilon = 0.05$ and $\epsilon = 0.127$ show that their finite expansions for larger numbers of cosine functions can be considered equivalent with respect to the power stored in the near field. This equivalence of finite expansions is usually interpreted as convergence of the solution for the current. However, such a type of convergence may not be related to convergence in the sense of a classical norm as for example the L_2 norm. For the delta gap, we may not expect convergence of Im$(P^{\rm ex})$ for an increasing number of expansion functions, because its representation, i.e., the generalized limit of (4.2), is not square integrable and, hence, not an element of the range of $\mathcal{Z}_{\rm a}$. Finally, which finite expansion of the considered local feeds is most suitable for a certain realizable excitation is not known.

For a ring in a half space, we find similar results for the three feed gaps. Moreover, the relative difference between Re$(P^{\rm ex})$ and $2P^{\rm rad}$ is small, even for very small heights h. For $h = \lambda/100$, the difference is 0.4%, while the total radiated power is of order 10^{-3} with respect to the total radiated power in free space.

The input impedance is defined by the complex power $P^{\rm ex}$ divided by the squared absolute value of the total current through the terminals of the ring. This total current is unambiguously defined for the delta gap, with value $2b(\mathcal{W}\mathcal{W}^{-}w)(0)$, but not for the finite feed gap, because it can be defined as the average current over the gap, but also otherwise. The input impedance for the delta gap is given by

$$Z_{\rm inp} = \frac{P^{\rm ex}}{|2b(\mathcal{W}\mathcal{W}^{-}w)(0)|^2} = \frac{V^{\rm ex}}{2b(\mathcal{W}\mathcal{W}^{-}w)(0)}\,. \tag{4.17}$$

The second equality follows from (4.16) and the definition of the excitation vector $[\mathcal{W}^{-}v^{\rm ex}]$ in (4.5), (4.6)[1], and (4.7)[2]. Expression (4.17) is the network definition of the impedance, i.e., the voltage $V^{\rm ex}$ divided by the total current through the gap.

4.3 Excitation Fields for Plane Waves

A signal received by an array is usually modeled as a linear combination of plane waves. Such a wave represents an electromagnetic field in free space, propagating along a certain vector $\boldsymbol{k}^{\mathrm{i}}$ with a polarization perpendicular to $\boldsymbol{k}^{\mathrm{i}}$. Here, the upper index $^{\mathrm{i}}$ indicates that the wave is incident on the array. The field is a solution of the (time-harmonic) Maxwell's equations for free space, see (2.5) with free current equal to zero. The electric and magnetic field obey the Helmholtz equation, see (2.9) with $\boldsymbol{A}$ replaced by $\boldsymbol{E}$ or $\boldsymbol{H}$ and with zero free current. The electric field of a plane wave is given by

$$\boldsymbol{E}^{\mathrm{plane}}(\boldsymbol{x}) = \boldsymbol{E}^{\mathrm{i}} e^{j(\boldsymbol{k}^{\mathrm{i}} \bullet \boldsymbol{x})}\,, \tag{4.18}$$

where $\boldsymbol{k}^{\mathrm{i}}$ is given by

$$\frac{\boldsymbol{k}^{\mathrm{i}}}{k} = \boldsymbol{e}_\rho(\theta_{\mathrm{i}}, \phi_{\mathrm{i}}) = \sin\theta_{\mathrm{i}} \cos\phi_{\mathrm{i}}\, \boldsymbol{e}_x + \sin\theta_{\mathrm{i}} \sin\phi_{\mathrm{i}}\, \boldsymbol{e}_y + \cos\theta_{\mathrm{i}}\, \boldsymbol{e}_z\,, \tag{4.19}$$

and $\boldsymbol{E}^{\mathrm{i}}$ is a constant real vector perpendicular to $\boldsymbol{k}^{\mathrm{i}}$, or, $(\boldsymbol{e}_\rho \bullet \boldsymbol{E}^{\mathrm{i}}) = 0$. We note that $\boldsymbol{e}_\rho$ is the radial unit vector of the standard spherical coordinate system, see (C.4). The spherical angles $(\theta_{\mathrm{i}}, \phi_{\mathrm{i}})$, as shown in Figure 3.2, describe the angle of incidence of the plane wave.

As mentioned below (2.17), the excitation field $\boldsymbol{E}_S$ in the equation $\mathcal{Z}\boldsymbol{J} = \boldsymbol{E}_S$ can be described by $\boldsymbol{E}_S = -(\boldsymbol{E}^{\mathrm{ext}})_{\tan}$, where $\boldsymbol{E}^{\mathrm{ext}}$ is an externally applied field. For free space, the current induced by an incident plane wave is described by $\mathcal{Z}\boldsymbol{J} = -(\boldsymbol{E}^{\mathrm{ext}})_{\tan}$ with $\boldsymbol{E}^{\mathrm{ext}} = \boldsymbol{E}^{\mathrm{plane}}$. For a half space, the current is described analogously, but with $\boldsymbol{E}^{\mathrm{ext}}$ equal to the sum of $\boldsymbol{E}^{\mathrm{plane}}$ and the corresponding wave reflected at the boundary plane of the half space. In this way, we assure that the total field $(\boldsymbol{E}^{\mathrm{ext}} + \boldsymbol{E}, \boldsymbol{H}^{\mathrm{ext}} + \boldsymbol{H})$ satisfies Maxwell's equations and the boundary condition at the boundary plane of the half space, see below (2.17). The total field does not satisfy the radiation conditions [26: p. 113], because the plane wave does not satisfy these conditions. Only the scattered field $(\boldsymbol{E}, \boldsymbol{H})$ satisfies the radiation conditions.

We calculate the excitation vector induced by the plane wave (4.18) for arrays of strips and rings in free space. In both cases, we use entire-domain expansion functions. For arrays of strips, we find for the components of $\boldsymbol{v}^{\mathrm{ex}}$,

$$v^{\mathrm{ex}}(\xi; q) = -(\boldsymbol{e}_y \bullet \boldsymbol{E}^{\mathrm{i}})\, e^{jk(c_{q,x} \sin\theta_{\mathrm{i}} \cos\phi_{\mathrm{i}} + l\xi \sin\theta_{\mathrm{i}} \sin\phi_{\mathrm{i}})} \frac{\sin(k\ell\beta\eta \sin\theta_{\mathrm{i}} \cos\phi_{\mathrm{i}})}{k\ell\beta\eta \sin\theta_{\mathrm{i}} \cos\phi_{\mathrm{i}}}\,. \tag{4.20}$$

The corresponding excitation vector is given by the right-hand side of (2.131). Moreover, $[\mathcal{W}_q^- \boldsymbol{v}^{\mathrm{ex}}]$ is given by (4.3) and $[(\mathcal{W}_q^c)^- \boldsymbol{v}^{\mathrm{ex}}](n,1) = \langle \mathcal{W}_q^c \boldsymbol{e}_n, \boldsymbol{v}^{\mathrm{ex}} \rangle_{L_2}$ with the expansion functions $\mathcal{W}_q^c \boldsymbol{e}_n$ as defined in (3.8). As in the derivation of the approximate kernel $\tilde{F}_{qq}$ in (2.62) – (2.63), we assume that $\beta \ll 1$ and $k\ell = O(1)$ (as $\beta \downarrow 0$). Neglecting terms of order β^2, we

obtain

$$
\begin{aligned}
[(\mathcal{W}_q^{\cos})^{-}\boldsymbol{v}^{\mathrm{ex}}](n,1) &= -(\boldsymbol{e}_y \bullet \boldsymbol{E}^{\mathrm{i}})\, e^{jkc_{q,x}\sin\theta_{\mathrm{i}}\cos\phi_{\mathrm{i}}}\, \frac{(-1)^n(2n-1)\pi\cos\kappa}{\kappa^2-(2n-1)^2\pi^2/4}\,, \\
[(\mathcal{W}_q^{\sin})^{-}\boldsymbol{v}^{\mathrm{ex}}](n,1) &= -(\boldsymbol{e}_y \bullet \boldsymbol{E}^{\mathrm{i}})\, e^{jkc_{q,x}\sin\theta_{\mathrm{i}}\cos\phi_{\mathrm{i}}}\, \frac{(-1)^n 2n\pi j\sin\kappa}{\kappa^2-n^2\pi^2}\,,
\end{aligned}
\tag{4.21}
$$

where $\kappa = k\ell\sin\theta_{\mathrm{i}}\sin\phi_{\mathrm{i}}$.

For $(\boldsymbol{e}_y \bullet \boldsymbol{E}^{\mathrm{i}}) = 0$, the excitation vector in (4.21) turns to zero and, hence, the solution for the current is also zero. Moreover, for $(\boldsymbol{e}_y \bullet \boldsymbol{E}^{\mathrm{i}}) = 0$, the condition that the surface S is narrow with respect to $\boldsymbol{E}_S$, or, $(\mathcal{I}-\mathcal{A})\boldsymbol{E}_S \approx \boldsymbol{0}$, is not satisfied in general. As shown in the dimensional analysis on p. 38, this condition is necessary to replace the equation $\mathcal{Z}\boldsymbol{J} = \boldsymbol{E}_S$ by $\mathcal{A}\mathcal{Z}\mathcal{A}\boldsymbol{J} = \mathcal{A}\boldsymbol{E}_S$, or, $\mathcal{Z}_{\mathrm{a}}\boldsymbol{w} = \boldsymbol{v}^{\mathrm{ex}}$. Hence, if $E_y^{\mathrm{i}} \approx 0$, the solution of the moment-matrix equation should be handled with care.

The excitation vector for an array of rings is obtained in the same way as the excitation vector for an array of strips. Since any choice of $\boldsymbol{E}^{\mathrm{i}}$ is a linear combination of the plane waves with $\boldsymbol{E}^{\mathrm{i}} = \boldsymbol{e}_\theta(\theta_{\mathrm{i}},\phi_{\mathrm{i}})$ and $\boldsymbol{E}^{\mathrm{i}} = \boldsymbol{e}_\phi(\theta_{\mathrm{i}},\phi_{\mathrm{i}})$, we consider only these two choices. We assume $ka_q = O(1)$ (as $\beta_q \downarrow 0$) and we neglect terms of order β_q^2. Then, the excitation vector for $\boldsymbol{E}^{\mathrm{i}} = \boldsymbol{e}_\theta(\theta_{\mathrm{i}},\phi_{\mathrm{i}})$ is given by (4.5) – (4.6), where

$$
\begin{aligned}
\zeta_q^{\cos}(n) &= -\pi\cos\theta_{\mathrm{i}}\, e^{jk(\boldsymbol{e}_\rho(\theta_{\mathrm{i}},\phi_{\mathrm{i}})\bullet\boldsymbol{c}_q)}\sin((n-1)(\phi-\psi_q))\, j^{n-2}\left(J_{n-2}(\kappa_q)+J_n(\kappa_q)\right), \\
\zeta_q^{\sin}(n) &= \pi\cos\theta_{\mathrm{i}}\, e^{jk(\boldsymbol{e}_\rho(\theta_{\mathrm{i}},\phi_{\mathrm{i}})\bullet\boldsymbol{c}_q)}\cos(n(\phi-\psi_q))\, j^{n-1}\left(J_{n-1}(\kappa_q)+J_{n+1}(\kappa_q)\right),
\end{aligned}
\tag{4.22}
$$

where $\kappa_q = ka_q\sin\theta_{\mathrm{i}}$ and where J_n is the Bessel function of the first kind with index n. For $\boldsymbol{E}^{\mathrm{i}} = \boldsymbol{e}_\phi(\theta_{\mathrm{i}},\phi_{\mathrm{i}})$, the components (4.22) reduce to

$$
\begin{aligned}
\zeta_q^{\cos}(n) &= -\pi\, e^{jk(\boldsymbol{e}_\rho(\theta_{\mathrm{i}},\phi_{\mathrm{i}})\bullet\boldsymbol{c}_q)}\cos((n-1)(\phi-\psi_q))\, j^{n-2}\left(J_{n-2}(\kappa_q)-J_n(\kappa_q)\right), \\
\zeta_q^{\sin}(n) &= \pi\, e^{jk(\boldsymbol{e}_\rho(\theta_{\mathrm{i}},\phi_{\mathrm{i}})\bullet\boldsymbol{c}_q)}\sin(n(\phi-\psi_q))\, j^{n-1}\left(J_{n-1}(\kappa_q)-J_{n+1}(\kappa_q)\right).
\end{aligned}
\tag{4.23}
$$

Finally, we show that the calculated expressions for the excitation vectors above represent the electric far-field components of the corresponding arrays in the direction of $\boldsymbol{E}^{\mathrm{i}}$. Let us first consider line arrays of strips. The far field of the array is a superposition of plane waves induced by the element currents, which are described by cosines and sines. If we multiply the expressions in (4.21) by $jZ_0k\ell be^{-jk\rho}/2\pi\rho$, these expressions represent the electric far-field component in the direction of $\boldsymbol{E}^{\mathrm{i}}$, evaluated at $(\rho,\theta_{\mathrm{i}},\phi_{\mathrm{i}})$. This component is generated by the nth cosine or sine expansion function on the qth strip, which can be seen from (C.13) and (C.14) in Appendix C. In other words, the far field in the direction $(\theta_{\mathrm{i}},\phi_{\mathrm{i}})$ induced by an element current is proportional to the amplitude of this current, when the array is excited by a plane wave from the direction $(\theta_{\mathrm{i}},\phi_{\mathrm{i}})$. Moreover, the constant of proportionality is independent of the

mode and the direction. The same conclusion is valid for arrays of rings. The vector components (4.22) and (4.23) multiplied by $jZ_0ka_qb_qe^{-jk\rho}/2\pi\rho$ represent the electric far-field components evaluated at $(\rho, \theta_\mathrm{i}, \phi_\mathrm{i})$ and generated by a cosine or sine expansion function on the qth ring. Mathematically, the correspondence between the tangential electric field of an array induced by a plane wave and the far field of this array is explained from (C.9), in which the integral represents the inner product of the plane wave and the current on an element S_q. Physically, this correspondence is explained from the reciprocity theorem, which states that source and observer can be interchanged. Figure 2.9 in Section 2.5 confirms the correspondence for a line array of strips. For the dominant expansion functions, the coefficients obtained by a delta-gap excitation are approximately the same as the coefficients obtained by a plane-wave excitation.

CHAPTER 5

The Eigencurrent Approach

In this chapter, we consider the second phase of our research, see the scheme in Figure 1.8. In Section 5.1, the general idea of the approach suggested in this thesis, called the eigencurrent approach, is described. The eigencurrent approach consists of two main steps, called the initialization and the cycle. In the initialization, the eigencurrents of a single element, or more general, of the initializing subarray, are determined. In the cycle, the eigencurrents of the array are determined from the eigencurrents of subsequent subarrays by an iterative process as outlined in Section 1.3. Calculational details of both steps for eigencurrents of line arrays of strips and rings are discussed in Sections 5.2 and 5.3. The excited current on line arrays of strips and rings is expressed in terms of these eigencurrents, see Section 5.3.1. In Subsection 5.3.2, we relate the eigencurrents to scanning by linear phase tapering and we compare the eigencurrent approach with the infinite-array approach. Special attention is devoted to the one-to-one correspondence between eigenvalues and scan angles and to the divergent and convergent behavior of the infinite-array solution at the grazing and grating-lobe scan angles. The main conclusions of the initialization and the cycle are summarized in Section 5.4. Moreover, we provide a manual in which the steps of the application of the eigencurrent approach to arrays of arbitrary elements are described.

5.1 Description of the Approach

5.1.1 Idea

In the previous chapters, we described the electromagnetic behavior of an array of microstrip elements by the moment-matrix equation, or by the corresponding operator equation

$$\mathcal{P}\mathcal{Z}_{\mathrm{a}}\mathcal{P}\boldsymbol{w} = \mathcal{P}\boldsymbol{v}^{\mathrm{ex}}\,. \tag{5.1}$$

Here, $\mathcal{Z}_\mathrm{a}$ is the averaged impedance operator and $\mathcal{P}$ is the projection onto $\mathrm{ran}(\mathcal{P})$, i.e., the space spanned by the expansion functions, see Subsection 2.4.3. Equation (5.1) relates the (expanded) current on the elements to the (expanded) excitation field by means of the operator $\mathcal{P}\mathcal{Z}_\mathrm{a}\mathcal{P}$. In the previous chapters, the solution of this equation was obtained by inverting the operator $\mathcal{P}\mathcal{Z}_\mathrm{a}\mathcal{P}$. In this chapter, we describe the solution by the eigenvalues and eigenfunctions of the operator. In [115], several reasons are mentioned why eigenvalues and eigenfunctions are useful in the analysis of operators. First, since operators are diagonalized by their eigenfunctions, the solutions of various problems are obtained more rapidly. Second, the eigenvalues and eigenfunctions may provide information about the behavior of the application described by an operator. Finally, eigenvalues supplement the abstract notion of an operator by a picture in the complex plane and, therewith, they give an operator a face. Especially this last reason will become apparent from the analysis of line arrays in Subsection 5.3.2, pp. 165 ff.

Assume that the eigenfunctions $\boldsymbol{u}_n$ of the operator $\mathcal{P}\mathcal{Z}_\mathrm{a}\mathcal{P}$ span $\mathrm{ran}(\mathcal{P})$. Then, the operator is diagonalized by its eigenfunctions. If the eigenvalues are all non-zero, the solution in $\mathrm{ran}(\mathcal{P})$ of (5.1), i.e., $\boldsymbol{w}_\mathcal{P}$, is described by the eigenfunctions $\boldsymbol{u}_n$ and the eigenvalues ν_n of the operator $\mathcal{P}\mathcal{Z}_\mathrm{a}\mathcal{P}$ as

$$\boldsymbol{w}_\mathcal{P} = \sum_{n=1}^{N} \frac{1}{\nu_n} \left\langle \boldsymbol{u}_n, \mathcal{P}\boldsymbol{v}^\mathrm{ex} \right\rangle \, \boldsymbol{u}_n \,. \tag{5.2}$$

Here, N is the dimension of $\mathrm{ran}(\mathcal{P})$ and the inner product $\langle \cdot \, , \, \cdot \rangle$ on $\mathrm{ran}(\mathcal{P})$ is chosen such that the eigencurrents are orthonormal. This inner product should not be confused with the inner products $\langle \cdot, \cdot \rangle_{\mathcal{X}_\mathrm{a}}$ and $\langle \cdot, \cdot \rangle_{\mathcal{Y}_\mathrm{a}}$ defined on the spaces $\mathcal{X}_\mathrm{a} = \mathrm{dom}(\mathcal{Z}_\mathrm{a})$ and $\mathcal{Y}_\mathrm{a} \supset \mathrm{ran}(\mathcal{Z}_\mathrm{a})$, of which $\mathrm{ran}(\mathcal{P})$ is a subspace. We will see that the eigenfunctions indeed span $\mathrm{ran}(\mathcal{P})$. Moreover, the operators $\mathcal{P}\mathcal{Z}_\mathrm{a}\mathcal{P}$ that we consider will turn out almost normal with respect to the inner product on $\mathcal{Y}_\mathrm{a}$, where normal means $\mathcal{Z}\mathcal{Z}^* = \mathcal{Z}^*\mathcal{Z}$ with the adjoint $\mathcal{Z}^*$ of $\mathcal{Z}$ defined by (2.109). Hence, the eigenfunctions are almost orthogonal with respect to this inner product.

The finite expansion (5.2) provides insight into the behavior of the array. The eigenfunctions $\boldsymbol{u}_n$ of $\mathcal{P}\mathcal{Z}_\mathrm{a}\mathcal{P}$ are the eigencurrents of the array. The corresponding eigenvalues represent the characteristic impedances of these eigencurrents. Eigencurrents with larger characteristic impedances contribute less than those with smaller characteristic impedances. Moreover, if an eigenvalue is close to zero, the array shows resonant behavior. Finally, eigencurrents that match well with the (expanded) excitation field $\mathcal{P}\boldsymbol{v}^\mathrm{ex}$ contribute more than eigencurrents that do not match well. Herewith, the finite expansion gives a first insight into the relationship between the excitation field and the current.

From a calculational point of view, it is not efficient to first construct a moment matrix related to $\mathcal{P}\mathcal{Z}_\mathrm{a}\mathcal{P}$ and, subsequently, determine the eigencurrents. Therefore, we determine the finite expansion (5.2) by an alternative approach. We base this approach on the following ideas.

Let the array be composed of N_sub identical subarrays. Then, the array is described by the

position of these subarrays and the geometry of a single subarray. We say that the entire array is generated from a single subarray, which we refer to as the generating subarray. An example of such an array is discussed in Section 1.3, Figure 1.5, where a uniform rectangular 4×6 array is generated from a 1×6 line array or from a 2×2 rectangular array. Both choices of subarrays are in turn generated from a single element, which is the smallest possible generating subarray. As explained in Section 1.3, we construct the eigencurrents of an array as concatenations of linear combinations of the eigencurrents of its generating subarray. In other words, an eigencurrent of an array is described as a linear combination of subarray eigencurrents.

Assume that the generating subarray has eigencurrents $\boldsymbol{u}_n^{\mathrm{sub}}$ ($n = 1, \ldots, N_{\mathrm{eig}}^{\mathrm{sub}}$) with eigenvalues ν_n^{sub}. Let us first consider the case that all eigenvalues are different, or in other words, that the eigenvalues are non-degenerate. The case of degeneracy is considered further on. If mutual coupling between the subarrays is ignored, the eigenvalues of the complete array are the eigenvalues ν_n^{sub}, each with multiplicity N_{sub}. The eigencurrents corresponding to an eigenvalue ν_n^{sub} belong to the eigenspace spanned by N_{sub} independent currents, each of which is zero on all subarrays but one, where it equals $\boldsymbol{u}_n^{\mathrm{sub}}$. The set of these independent currents is denoted by E_n and hence, span(E_n) is the eigenspace corresponding to ν_n^{sub}. Figure 5.1 shows symbolically the currents of E_n for a line array of four subarrays. We will see that if mutual

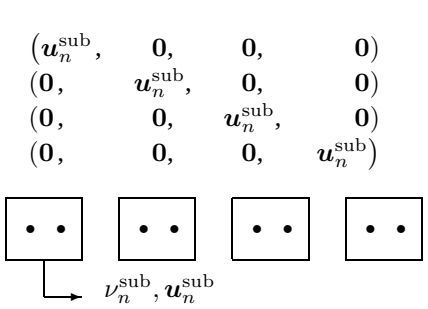

Figure 5.1 A line array of 8 elements generated from a subarray of 2 elements ($N_{\mathrm{sub}} = 4$). The elements are indicated by dots, the subarrays by blocks. The currents of E_n are symbolically denoted by 4-tuples, which indicate the currents on each of the four subarrays.

coupling is not ignored, each eigenvalue of the generating subarray yields N_{sub} eigenvalues ν_{nq} ($q = 1, \ldots, N_{\mathrm{sub}}$) of the form $\nu_{nq} = \nu_n^{\mathrm{sub}}(1 + \epsilon_{nq})$, where ϵ_{nq} are complex-valued perturbations, see for example Figure 5.2 (left). Moreover, we will see that each eigencurrent $\boldsymbol{u}_{nq}$ is a linear combination of currents of E_n, called the dominant part of the eigencurrent, plus a perturbation. The perturbation is a linear combination of the currents of the other sets $\mathsf{E}_{n'}$. The perturbations of the eigenvalues and the eigencurrents depend on the strength of the mutual coupling between the eigencurrents on the subarrays. The stronger the mutual coupling is, the larger

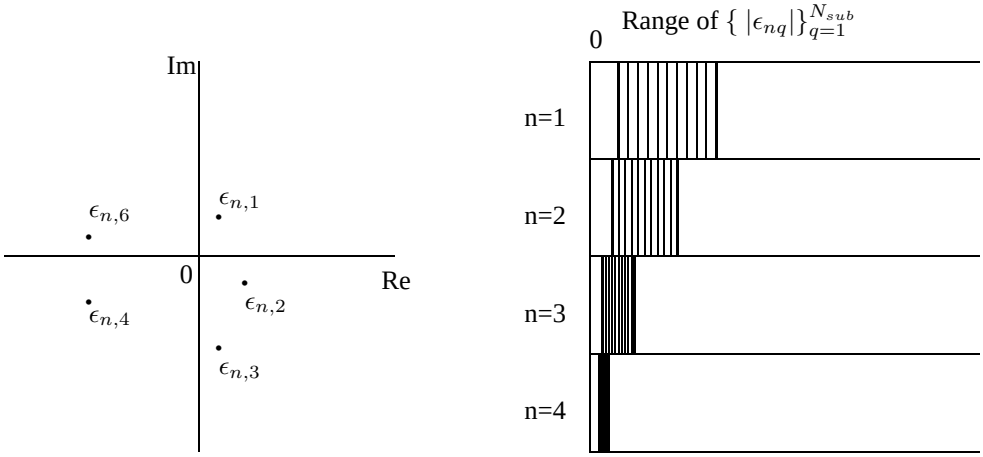

Figure 5.2 Left: Graphical representation of the (complex-valued) perturbations with index n for an array with 6 subarrays. Right: The ranges of the absolute perturbations of four groups of eigenvalues are indicated by shades areas. The thick lines indicate the maximum and minimum absolute perturbations.

the perturbations are. We emphasize that the perturbations of eigenvalues and eigencurrents do not necessarily need to be small. Nevertheless, we refer to each ϵ_{nq} as the perturbation of the eigenvalue ν_{nq} and we refer to the non-dominant part of each eigencurrent $\boldsymbol{u}_{nq}$ as its perturbation. If the perturbations are small, a perturbation technique can be applied as used in Quantum Mechanics, see item 3 in Subsection 5.1.4.

We observe that both the eigenvalues and the eigencurrents of the complete array are divided into $N_{\text{eig}}^{\text{sub}}$ groups of N_{sub} elements. For each $n \in \{1, \ldots, N_{\text{eig}}^{\text{sub}}\}$, the nth group of eigenvalues is $\{\nu_{nq}\}_{q=1}^{N_{\text{sub}}}$ and the corresponding group of eigencurrents is $\{\boldsymbol{u}_{nq}\}_{q=1}^{N_{\text{sub}}}$. The perturbations $\{\epsilon_{nq}\}_{q=1}^{N_{\text{sub}}}$ describe the spread in the complex plane of the eigenvalues of the nth group with respect to the eigenvalue ν_n^{sub}, see for example Figure 5.2 (left). This spread is a measure for both the mutual coupling among the currents of E_n and the mutual coupling between the currents of E_n and the currents of the other sets $\mathsf{E}_{n'}$. The second type of coupling does not incorporate the coupling between the currents which are non-zero on the same subarray. This coupling is the self coupling of the generating subarray, which is incorporated in the eigenvalues and eigencurrents of the subarray itself. In the literature, the self coupling is sometimes referred to as intra-mode coupling, while the other two types of coupling are referred to as inter-mode coupling. Figure 5.2 (right) shows a graphical representation of the ranges of the absolute perturbations $\{|\epsilon_{nq}|\}_{q=1}^{N_{\text{sub}}}$ for four groups of eigenvalues. These ranges are an indication of the spread of the eigenvalues.

In the ideas outlined above, the eigenvalues ν_n^{sub} and the eigencurrents $\boldsymbol{u}_n^{\text{sub}}$ belong to the

operator $\mathcal{P}_{\mathrm{sub}}\mathcal{Z}_{\mathrm{a,sub}}\mathcal{P}_{\mathrm{sub}}$ of the generating subarray. The range of the projection $\mathcal{P}_{\mathrm{sub}}$ is spanned by the eigencurrents $\boldsymbol{u}_n^{\mathrm{sub}}$. The eigenvalues ν_{nq} and the eigencurrents $\boldsymbol{u}_{nq}$ belong to the operator $\mathcal{P}\mathcal{Z}_{\mathrm{a}}\mathcal{P}$ of the array. The range of the projection $\mathcal{P}$ is spanned by the currents in the union E of the sets E_n.

The eigenvalues ν_{nq} and the eigencurrents $\boldsymbol{u}_{nq}$ can be described by a moment-matrix formulation for the operator $\mathcal{P}\mathcal{Z}_{\mathrm{a}}\mathcal{P}$ using the ideas outlined above. Assume that the eigenvalues ν_n^{sub} and the eigencurrents $\boldsymbol{u}_n^{\mathrm{sub}}$ of the generating subarray are known as well as the inner product $\langle \cdot\,, \cdot \rangle_{\mathrm{sub}}$ on $\mathrm{ran}(\mathcal{P}_{\mathrm{sub}})$ with respect to which these eigencurrents are orthonormal. By definition, the operator $\mathcal{P}_{\mathrm{sub}}\mathcal{Z}_{\mathrm{a,sub}}\mathcal{P}_{\mathrm{sub}}$ is diagonalized by its eigencurrents. If the eigencurrents are chosen as expansion functions, the moment matrix with respect to $\langle \cdot\,, \cdot \rangle_{\mathrm{sub}}$ is a diagonal matrix with the eigenvalues ν_n^{sub} on the diagonal, see for example Figure 5.3 (A). Recall that in Subsection 2.4.2, we introduced both the usual definition and our definition of the moment matrix, which are related by the Gram matrix of the test functions according to (2.128). Since the Gram matrix of the set of eigencurrents $\boldsymbol{u}_n^{\mathrm{sub}}$ with respect to $\langle \cdot\,, \cdot \rangle_{\mathrm{sub}}$ is the identity matrix, both definitions yield the same moment matrix for $\mathcal{P}_{\mathrm{sub}}\mathcal{Z}_{\mathrm{a,sub}}\mathcal{P}_{\mathrm{sub}}$.

Since the eigencurrents $\boldsymbol{u}_n^{\mathrm{sub}}$ are orthonormal with respect to $\langle \cdot\,, \cdot \rangle_{\mathrm{sub}}$, the currents of E are orthonormal with respect to the composite inner product on $\mathrm{ran}(\mathcal{P}) = \mathrm{span}(\mathsf{E})$,

$$\langle \cdot\,, \cdot \rangle_{\mathrm{comp}} = \sum_{q=1}^{N_{\mathrm{sub}}} \langle (\,\cdot\,)_q, (\,\cdot\,)_q \rangle_{\mathrm{sub}} \,. \tag{5.3}$$

Here, the dots in the inner products indicate currents on the complete array and $(\,\cdot\,)_q$ is a symbolic notation for the corresponding currents on the qth subarray. In case mutual coupling is ignored, the operator $\mathcal{P}\mathcal{Z}_{\mathrm{a}}\mathcal{P}$ is diagonalized by the currents of E. The corresponding moment matrix with respect to $\langle \cdot\,, \cdot \rangle_{\mathrm{comp}}$ is a diagonal matrix with the eigenvalues ν_n^{sub} on the diagonal, each with multiplicity N_{sub}, see for example Figure 5.3 (B). We will see that in case mutual coupling is not ignored, the operator $\mathcal{P}\mathcal{Z}_{\mathrm{a}}\mathcal{P}$ is diagonalized by the currents in the set E up to a perturbation. As above, the perturbation depends on the mutual coupling between the eigencurrents on the subarrays. The corresponding moment matrix with respect to $\langle \cdot\,, \cdot \rangle_{\mathrm{comp}}$ is a block matrix, of which the diagonal blocks equal the moment matrix of the generating subarray, while the off-diagonal blocks are dense matrices, see for example Figure 5.3 (C). The complete matrix is diagonally dominant. In Subsection 5.3.1, we will show that the eigenvalues of the moment matrix are the eigenvalues ν_{nq} of the operator $\mathcal{P}\mathcal{Z}_{\mathrm{a}}\mathcal{P}$ of the array. The eigenvectors of this matrix are the expansion coefficients of the eigencurrents $\boldsymbol{u}_{nq}$ with respect to the expansion functions in the set E, i.e., the eigencurrents of the array in which the mutual coupling between the subarrays is ignored. The composition of the moment matrix suggests the same perturbation of the eigenvalues ν_n^{sub} and the eigencurrents in E as described above. Moreover, the diagonal form of the diagonal blocks shows that the self coupling of the generating subarrays does not contribute to the spread of the groups $\{\nu_{nq}\}_{q=1}^{N_{\mathrm{sub}}}$ as observed above.

(A)

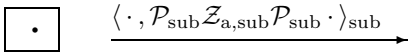

$\langle \cdot\,, \mathcal{P}_{\rm sub}\mathcal{Z}_{\rm a,sub}\mathcal{P}_{\rm sub}\,\cdot \rangle_{\rm sub}$

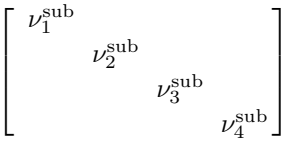

eigencurrents $\boldsymbol{u}_n^{\rm sub}$ $(n = 1, 2, 3, 4)$
as expansion functions

(B)

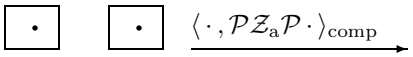

$\langle \cdot\,, \mathcal{P}\mathcal{Z}_{\rm a}\mathcal{P}\,\cdot \rangle_{\rm comp}$

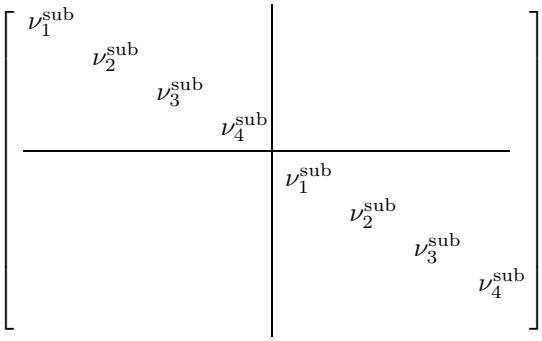

without mutual coupling;
expansion functions:
$\big(\boldsymbol{u}_n^{\rm sub}, \boldsymbol{0}\big)$ and $\big(\boldsymbol{0}, \boldsymbol{u}_n^{\rm sub}\big)$
$(n = 1, 2, 3, 4)$

(C)

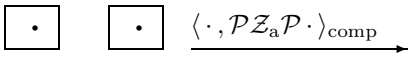

$\langle \cdot\,, \mathcal{P}\mathcal{Z}_{\rm a}\mathcal{P}\,\cdot \rangle_{\rm comp}$

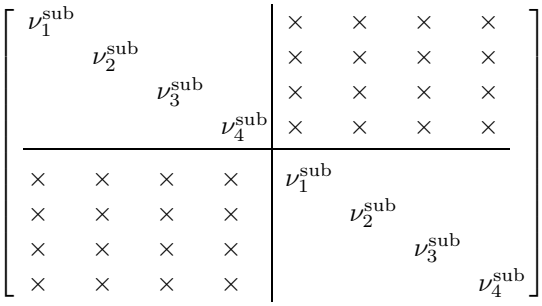

with mutual coupling

(D)

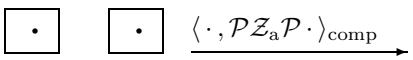

$\langle \cdot\,, \mathcal{P}\mathcal{Z}_{\rm a}\mathcal{P}\,\cdot \rangle_{\rm comp}$

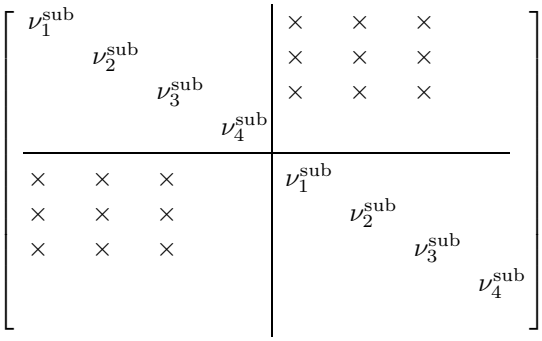

the spread of the 4th-group
of eigenvalues is negligible

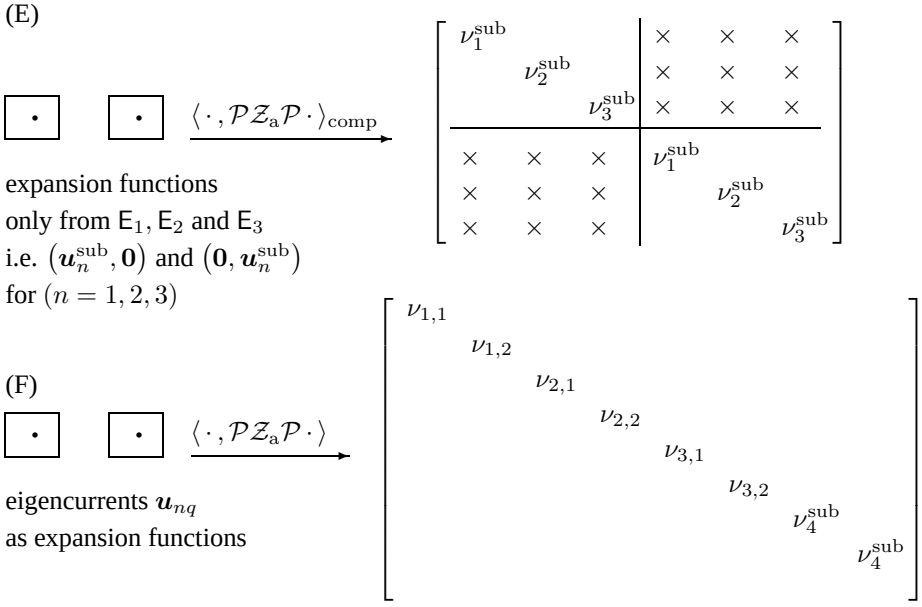

Figure 5.3 Calculation of the eigenvalues ν_{nq} and the eigencurrents $\boldsymbol{u}_{nq}$ of an array consisting of two subarrays. The generating subarray has four eigencurrents with eigenvalues ν_n^{sub}.

The eigenvalues ν_{nq} and the eigencurrents $\boldsymbol{u}_{nq}$ can be computed from the moment matrix for $\mathcal{P}\mathcal{Z}_{\mathrm{a}}\mathcal{P}$. To reduce the computational effort, we employ the ideas regarding the spread of the eigenvalues. If the spread of a group of eigenvalues, say the nth group, is negligibly small, its eigenvalues can be set equal to ν_n^{sub}. Moreover, the corresponding eigencurrents can be replaced by the currents of E_n (or, more general, by N_{sub} independent currents of span(E_n)). In that case, the currents of E_n are neither coupled with each other, nor with the currents of the other sets $\mathsf{E}_{n'}$. Hence, we can set the corresponding entries in the moment matrix equal to zero. An example is given in Figure 5.3 (D), where the spread of the fourth group of eigenvalues is negligible. The eigenvalues of the other groups can then be computed from the reduced moment matrix in Figure 5.3 (E).

The operator $\mathcal{P}\mathcal{Z}_{\mathrm{a}}\mathcal{P}$ is diagonalized by its eigencurrents $\boldsymbol{u}_{nq}$. Once these eigencurrents have been computed, an inner product $\langle \cdot, \cdot \rangle$ is constructed with respect to which they are orthonormal. The calculational details of this construction are discussed in Subsection 5.3.1. The corresponding moment matrix is a diagonal matrix with the eigenvalues ν_{nq} on the diagonal. An example is given in Figure 5.3 (F). Here, the eigenvalues ν_{4q} equal ν_4^{sub}, because the spread of the fourth group is considered negligible in Figure 5.3 (D) and Figure 5.3 (E). The array of two subarrays can be viewed as a new subarray with corresponding diagonal moment matrix. Then,

a similar procedure as above can be followed to compute the eigenvalues and eigencurrents of an array generated from this new subarray.

In general, we need to construct the moment matrix only from sets E_n that contribute to the mutual coupling between the subarrays. As in the example, these sets are not known a priori. We expect that the groups of eigenvalues corresponding to the lowest eigenvalues ν_n^{sub} have the largest spreads. In other words, we expect that the currents of the sets E_n corresponding to the lowest eigenvalues ν_n^{sub} contribute most to the mutual coupling between the subarrays. This expectation is based on the expansion (5.2), which shows that the current on the array is mainly described by the eigencurrents with the lowest eigenvalues, i.e., the eigencurrents with the lowest characteristic impedances. In the next sections, we will support the expectation by means of examples. A posteriori, it should be verified that sufficient sets E_n have been taken into account to describe mutual coupling. We will see that if the spreads of all the groups corresponding to the reduced moment matrix are significant, it may be necessary to take more sets E_n into account in this matrix. However, we also will see that it is not necessary to take more sets E_n into account, if the eigenvalues ν_n^{sub} corresponding to the groups with significant spread are much lower than the eigenvalues ν_n^{sub} corresponding to the groups with negligible spread. In Subsection 6.3.1, we introduce a definition of the spread that can handle these cases. Both the a-priori estimate of the sets E_n and the a-posteriori verification are based on arguments that are quantified by means of the eigenvalues. This explains why eigenvalues and eigencurrents are suitable for an approach to analyze arrays. Finally, we will observe that the larger eigenvalues correspond to eigencurrents that show a larger number of oscillations per wavelength. Physically, this observation is explained by the lower radiation from high-frequent currents.

Up to now, we have considered the case that the eigenvalues of the generating subarray are all non-degenerate. In case an eigenvalue is degenerate, i.e., in case an eigenvalue has multiplicity larger than one, this eigenvalue corresponds to more than one group of eigencurrents. We will consider an example of degeneracy and the corresponding consequences for the group division in Section 5.3.2, p. 163. Moreover, the consequences of degeneracy for the analysis approach outlined in the next subsection are described in the last paragraph of Subsection 6.3.5.

5.1.2 Approach

The preceding ideas to compute the eigenvalues and eigencurrents of an array from the eigenvalues and eigencurrents of its generating subarray suggest the following general approach. Assume that the eigenvalues ν_n^{sub} and the eigencurrents $\boldsymbol{u}_n^{\mathrm{sub}}$ ($n = 1, \ldots, N_{\mathrm{eig}}^{\mathrm{sub}}$) of a generating subarray are known with respect to its operator $\mathcal{P}_{\mathrm{sub}}\mathcal{Z}_{\mathrm{a,sub}}\mathcal{P}_{\mathrm{sub}}$. Here, $\mathcal{Z}_{\mathrm{a,sub}}$ is the averaged impedance operator of the generating subarray and $\mathcal{P}_{\mathrm{sub}}$ is the projection onto a finite basis of expansion functions for the subarray. Moreover, assume that the inner product $\langle \cdot, \cdot \rangle_{\mathrm{sub}}$ on $\mathrm{ran}(\mathcal{P}_{\mathrm{sub}})$ is known with respect to which the eigencurrents $\boldsymbol{u}_n^{\mathrm{sub}}$ are orthonormal. Determine

the eigencurrents of the array as follows:

I. Choose a new generating subarray of the complete array. The new subarray is considered as array generated from the original subarray with corresponding operator $\mathcal{P}_{\mathrm{sub}}\mathcal{Z}_{\mathrm{a,sub}}\mathcal{P}_{\mathrm{sub}}$. Let $\mathcal{Z}_{\mathrm{a}}$ be the averaged impedance operator of the generated array. Let N_{sub} be the number of subarrays in this array.

II. Let the sets E_n ($n = 1, \ldots, N_{\mathrm{eig}}^{\mathrm{sub}}$) and E be defined as above. In other words, each set E_n consists of N_{sub} independent currents, each of which is zero on all subarrays but one, where it equals $\boldsymbol{u}_n^{\mathrm{sub}}$. Moreover, E is the union of these sets. Then, $\mathcal{P}\mathcal{Z}_{\mathrm{a}}\mathcal{P}$ is the operator of the array, where $\mathcal{P}$ is the projection onto $\mathrm{span}(\mathsf{E})$. Next, $\mathrm{ran}(\mathcal{P}) = \mathrm{span}(\mathsf{E})$ is equipped with the composite inner product $\langle \cdot\,, \cdot \rangle_{\mathrm{comp}}$ as defined by (5.3).

III. Let $\mathsf{E}^{\mathrm{cpl}}$ be the union of the sets E_n that are expected to contribute to the mutual coupling between the subarrays. Construct the reduced moment matrix for $\mathcal{P}\mathcal{Z}_{\mathrm{a}}\mathcal{P}$ with respect to the composite inner product $\langle \cdot\,, \cdot \rangle_{\mathrm{comp}}$, where the expansion functions should be taken from the set $\mathsf{E}^{\mathrm{cpl}}$.

IV. Determine the eigenvalues ν_{nq} and the eigenvectors U_{nq} of this moment matrix. The eigenvalues are approximations of eigenvalues of the operator $\mathcal{P}\mathcal{Z}_{\mathrm{a}}\mathcal{P}$. The eigenvectors represent the expansion coefficients of the eigencurrents $\boldsymbol{u}_{nq}$ of this operator with respect to the functions in $\mathsf{E}^{\mathrm{cpl}}$. Let $\mathsf{E}^{\mathrm{eig}}$ be the set of these eigencurrents.

V. Investigate on basis of the spreads of the groups $\{\nu_{nq}\}_{q=1}^{N_{\mathrm{sub}}}$ of eigenvalues whether more sets E_n are required to describe mutual coupling. If more sets are required, return to step III.

VI. Let $\mathsf{E}^{\mathrm{unc}}$ be the union of the sets E_n that are not taken into account in the (reduced) moment matrix in step III. Then, the linear span of $\mathsf{E}^{\mathrm{eig}} \cup \mathsf{E}^{\mathrm{unc}}$ equals $\mathrm{span}(\mathsf{E}) = \mathrm{ran}(\mathcal{P})$. The operator $\mathcal{P}\mathcal{Z}_{\mathrm{a}}\mathcal{P}$ is diagonalized by the eigencurrents in $\mathsf{E}^{\mathrm{eig}} \cup \mathsf{E}^{\mathrm{unc}}$. Construct a new inner product $\langle \cdot\,, \cdot \rangle$ on $\mathrm{ran}(\mathcal{P})$ with respect to which the eigencurrents in $\mathsf{E}^{\mathrm{eig}} \cup \mathsf{E}^{\mathrm{unc}}$ are orthonormal. Then, the corresponding moment matrix is diagonal with the eigenvalues of these eigencurrents on the diagonal.

VII. Stop if the considered array equals the complete array. Otherwise return to step I, where the subarray with operator $\mathcal{P}_{\mathrm{sub}}\mathcal{Z}_{\mathrm{a,sub}}\mathcal{P}_{\mathrm{sub}}$ is the array just considered. In other words, $\mathcal{Z}_{\mathrm{a,sub}}$ is replaced by the operator $\mathcal{Z}_{\mathrm{a}}$ of the array just considered, $\mathcal{P}_{\mathrm{sub}}$ is replaced by the projection $\mathcal{P}$ in step II, and the inner product $\langle \cdot\,, \cdot \rangle_{\mathrm{sub}}$ is replaced by $\langle \cdot\,, \cdot \rangle$. Moreover, the eigencurrents $\boldsymbol{u}_n^{\mathrm{sub}}$ and the eigenvalues ν_n^{sub} are replaced by the eigencurrents in $\mathsf{E}^{\mathrm{eig}} \cup \mathsf{E}^{\mathrm{unc}}$ and their corresponding eigenvalues. Finally, $N_{\mathrm{eig}}^{\mathrm{sub}}$ is set equal to the number of eigencurrents in $\mathsf{E}^{\mathrm{eig}} \cup \mathsf{E}^{\mathrm{unc}}$.

The starting point of the eigencurrent approach sketched above is a subarray with operator $\mathcal{P}_{\mathrm{sub}}\mathcal{Z}_{\mathrm{a,sub}}\mathcal{P}_{\mathrm{sub}}$ of which the eigenvalues and eigencurrents are known. To determine the eigenvalues and eigencurrents of a first subarray, we propose the following initialization procedure:

A. Choose a subarray that generates the complete array. We consider this subarray as the initializing array. Let $\mathcal{Z}_{\mathrm{a,init}}$ be the averaged impedance operator of the initializing array and $\langle \cdot\,, \cdot \rangle_{\mathrm{init}}$ be the inner product on $\mathcal{Y}_{\mathrm{a,init}} \supset \mathrm{ran}(\mathcal{Z}_{\mathrm{a,init}})$. In Section 3.1, $\langle \cdot\,, \cdot \rangle_{\mathrm{init}}$ is the L_2 inner product.

B. Construct a finite basis of expansion functions for the initializing array with corresponding projection $\mathcal{P}_{\mathrm{init}}$. The expansion functions can be piecewise functions, for example rooftops [77: p. 1600] and Rao-Wilson-Glisson (RWG) functions [96], or entire-domain functions.

C. Construct the moment matrix for $\mathcal{Z}_{\mathrm{a,init}}$ with respect to this finite basis and the inner product $\langle \cdot\,, \cdot \rangle_{\mathrm{init}}$ on $\mathcal{Y}_{\mathrm{a,init}}$. Here, our definition of the moment matrix, as introduced in Subsection 2.4.2, must be used, see Subsection 5.2.1 for explanation.

D. Determine the eigenvalues ν_n^{init} and eigenvectors U_n^{init} of this moment matrix. The eigenvalues are also the eigenvalues of the operator $\mathcal{P}_{\mathrm{init}}\mathcal{Z}_{\mathrm{a,init}}\mathcal{P}_{\mathrm{init}}$ as we will show in Subsection 5.2.1. The eigenvectors represent the expansion coefficients of the eigencurrents $\boldsymbol{u}_n^{\mathrm{init}}$ of this operator.

E. Construct an inner product $\langle \cdot\,, \cdot \rangle_{\mathrm{sub}}$ on $\mathrm{ran}(\mathcal{P}_{\mathrm{init}})$ with respect to which these eigencurrents are orthonormal (for construction details, see Subsection 5.2.1).

F. Let $\mathcal{Z}_{\mathrm{a,sub}} = \mathcal{Z}_{\mathrm{a,init}}$, $\mathcal{P}_{\mathrm{sub}} = \mathcal{P}_{\mathrm{init}}$, $\boldsymbol{u}_n^{\mathrm{sub}} = \boldsymbol{u}_n^{\mathrm{init}}$, and $\nu_n^{\mathrm{sub}} = \nu_n^{\mathrm{init}}$. Moreover, let $N_{\mathrm{eig}}^{\mathrm{sub}}$ be the number of eigencurrents $\boldsymbol{u}_n^{\mathrm{init}}$.

5.1.3 Application Details

A successful application of the eigencurrent approach depends highly on the initialization for two reasons. First, if we make a numerical error in the initialization, this error will propagate throughout the apporach, because in each cycle, the eigenvalues of the generated array are perturbations of the eigenvalues of the generating subarray and, hence, of the initializing subarray. In the next sections, we illustrate that the loss of accuracy due to the numerical error in the initialization is of the same order as the loss of accuracy due to the numerical computation of the moment-matrix components in the usual moment method, as discussed in Section 3.4. Therefore, we do not lose accuracy with respect to the accuracy of the moment method. Second, the eigenvalues of the initializing subarray determine, to a large extent, which terms of the finite expansion (5.2) need to be taken into account. If the eigenvalues of the initializing subarray

increase rapidly as a function of their index, only a limited number of eigencurrents (one or two for a single-element subarray) will be needed to describe the electromagnetic behavior of this subarray. Moreover, in each cycle, only the eigenvalue groups corresponding to this limited number of initializing eigenvalues need to be considered, which is the second reason.

The most essential aspects of the cycle of the eigencurrent approach are, first, choosing the subsequent generating subarrays and, second, determining the eigencurrents that contribute to the mutual coupling. We explain these aspects further. By adjusting the inner product in step VI, we obtain, in step II of the next cycle, a close-to-diagonal moment matrix for the operator $\mathcal{P}\mathcal{Z}_{\mathrm{a}}\mathcal{P}$ with respect to the expansion functions in E. To what extent this moment matrix can be considered as diagonal depends on the mutual coupling between the eigencurrents on the subarrays with respect to the composite inner product $\langle \cdot\,, \cdot \rangle_{\mathrm{comp}}$ given by (5.3) and, hence, on the choice of the generating subarray. As explained in Section 1.3, the generating subarray should be chosen in correspondence with the geometry and the excitation of the generated array. The more diagonally dominant the resulting moment matrix is, the less computational effort is needed to determine the eigenvalues and eigencurrents. These observations explain the first aspect.

The second aspect is the reduction of the computational effort by reducing the size of the moment matrix in step III. This size depends quadratically on the number of subarray eigencurrents. On basis of the mutual-coupling information, which is 'grouped' by means of the eigencurrents, we only take subarray eigencurrents into account in the moment matrix of the array that contribute to the mutual coupling between the subarrays. In Section 1.3, a comparison of the matrix sizes for the eigencurrent approach and for the classical moment method is described. We note that the required number of subarray eigencurrents not only depends on the choice of the generating subarray, but also on the required accuracy for the current. This accuracy depends on the functional metric related to (2.31), see also Section 3.4.

It is not essential for the eigencurrent approach that the eigenvalues and eigencurrents of the operator $\mathcal{P}\mathcal{Z}_{\mathrm{a}}\mathcal{P}$ converge in a certain sense to the eigenvalues and eigencurrents of $\mathcal{Z}_{\mathrm{a}}$ as the dimension of $\mathrm{ran}(\mathcal{P})$ is increased. This is explained as follows. In the initialization, we choose expansion functions on the initializing subarray. In the usual moment method, we would choose the same functions, but defined on all elements of the array. Let $\mathcal{P}$ be the corresponding projection for the array. Then, by the usual moment method, we obtain a solution in the space $\mathrm{ran}(\mathcal{P})$ by solving the moment-matrix equation. In the eigencurrent approach, we determine the solution in the same space, but in the efficient way described above.

In the next sections, we discuss the calculational details of the initialization A $\rightarrow$ F and the cycle I $\rightarrow$ VII of the eigencurrent approach. Moreover, we apply the approach to uniform line arrays. In these applications, we will answer the following questions for the initialization.

- In what way can the eigenvalues ν_n^{init} and the eigencurrents $\boldsymbol{u}_n^{\mathrm{init}}$ be determined?

- How are the eigencurrents described by the set of expansion functions?
- To what extent do the eigenvalues and the eigencurrents depend on the set of expansion functions?
- How do the eigenvalues ν_n^{init}, indexed such that $|\nu_n^{\mathrm{init}}| \leq |\nu_{n+1}^{\mathrm{init}}|$, behave as function of their index?
- To what extent are the eigencurrents orthonormal with respect to $\langle \cdot, \cdot \rangle_{\mathrm{init}}$?
- To what extent do the eigencurrents and the eigenvalues depend on the geometry parameters and the frequency?

Moreover, we will answer the following questions for the cycle.

- In what way can the eigenvalues ν_{nq} and the eigencurrents $\boldsymbol{u}_{nq}$ be determined?
- Which sets E_n contribute to the mutual coupling between the subarrays?
- What can be said about the spread of the group eigenvalues as a function of the spacing between the subarrays?
- What can be said about the spread of the group eigenvalues as a function of the number of elements?
- How are the eigencurrents $\boldsymbol{u}_{nq}$ described by the eigencurrents $\boldsymbol{u}_n^{\mathrm{sub}}$?
- To what extent does this description depend on the subarray parameters and the spacing between the subarrays?
- What is the (physical) meaning of this description?

In Section 5.4, we present a summary of the answers and the obtained results. Moreover, we predict the results of the application of the eigencurrent approach to rectangular and other types of arrays.

5.1.4 Related Approaches

The eigencurrent approach is related to certain solution techniques and ideas in the literature. The correspondences and differences with these techniques and ideas are discussed.

1. The solution technique as in (5.2) is well-established if $\mathcal{Z}_{\mathrm{a}}$ is a Sturm-Liouville operator with additional Sturm-Liouville boundary conditions, see [101: Ch. V, Sec. 2; Ch. IX, Sec. 3], [127: Sec. 4.3], [81: pp. 361 – 369]. In our case, $\mathcal{Z}_{\mathrm{a}}$ is the product of an integral operator and a differential operator incorporating a Sturm-Liouville operator. We expect that $\mathcal{Z}_{\mathrm{a}}$ shows a kind of 'perturbed' Sturm-Liouville behavior.

2. For rectangular and circular waveguides, the eigenfunctions, or, eigenmodes, are known [25: Ch. 5]. These eigenfunctions are related to the Helmholtz operator. They are often used to expand the unknown electromagnetic field at waveguide discontinuities to determine this field by a mode-matching technique [25: Ch. 8].

3. The ideas concerning perturbation of eigenvalues and eigenfunctions appear in Quantum Mechanics as well. In that case, the operator $\mathcal{Z}_\mathrm{a}$ is the Hamilton operator, the eigenfunctions and eigenvalues of which are the states of a system of particles and the related energy levels, see [61: p. 591]. The eigenvalues and eigenfunctions for a perturbed system are expressed as asymptotic expansions with the unperturbed eigenvalues and eigenfunctions as the dominant terms [39: Ch. 16, Ch. 22], [43: Ch. 6]. The perturbation can for example be caused by a change of potential or by including or excluding the interaction between particles. The first case is compared to an antenna element or an array of which certain geometry parameters are perturbed. The second case is compared to the perturbation, by mutual coupling, of the eigenvalues and eigencurrents of an array in which mutual coupling is ignored. A difference with Quantum Mechanics is that the Hamilton operator is self-adjoint, while in our case $\mathcal{Z}_\mathrm{a}$ is not self-adjoint.

4. Instead of considering the eigenvalue equation $\mathcal{Z}_\mathrm{a}\boldsymbol{u}_n = \nu_n \boldsymbol{u}_n$, Harrington and Mautz [79: Ch. 3] introduced another approach for deriving eigencurrents. Applying their method in our context, the eigenvalue equation is replaced by the generalized eigenvalue equation $\mathcal{Z}_\mathrm{a}\tilde{\boldsymbol{u}}_n = \tilde{\nu}_n \mathcal{R}_\mathrm{a}\tilde{\boldsymbol{u}}_n$, where $\mathcal{R}_\mathrm{a} = (\mathcal{Z}_\mathrm{a} + \mathcal{Z}_\mathrm{a}^*)/2$. This equation is equivalent to $\mathcal{X}_\mathrm{a}\tilde{\boldsymbol{u}}_n = \lambda_n \mathcal{R}_\mathrm{a}\tilde{\boldsymbol{u}}_n$, where $\mathcal{X}_\mathrm{a} = (\mathcal{Z}_\mathrm{a} - \mathcal{Z}_\mathrm{a}^*)/2j$ and $\tilde{\nu}_n = 1 + j\lambda_n$ with λ_n real, because $\mathcal{R}_\mathrm{a}$ and $\mathcal{X}_\mathrm{a}$ are both self-adjoint. If $\mathcal{Z}_\mathrm{a}$ is normal, it follows from our eigenvalue equation together with $\mathcal{Z}_\mathrm{a}^*\boldsymbol{u}_n = \nu_n^*\boldsymbol{u}_n$ that $\mathcal{R}_\mathrm{a}\boldsymbol{u}_n = (\operatorname{Re}\nu_n)\,\boldsymbol{u}_n$ and $\mathcal{X}_\mathrm{a}\boldsymbol{u}_n = (\operatorname{Im}\nu_n)\,\boldsymbol{u}_n$. If $\operatorname{Re}\nu_n \neq 0$, then $\mathcal{X}_\mathrm{a}\boldsymbol{u}_n = (\operatorname{Im}\nu_n / \operatorname{Re}\nu_n)\,\mathcal{R}_\mathrm{a}\boldsymbol{u}_n$. In other words, the ratio $\operatorname{Im}\nu_n / \operatorname{Re}\nu_n$ and the eigenfunction $\boldsymbol{u}_n$ are a solution of the generalized eigenvalue equation of Harrington and Mautz. This result reveals a weak spot of their approach, if $\operatorname{Re}\nu_n \ll \operatorname{Im}\nu_n$. We will observe for some specific cases that if the eigenvalues of our eigenvalue equation are indexed such that $|\nu_n| \ll |\nu_{n+1}|$, their real part decreases rapidly, while their imaginary part increases rapidly. Moreover, for a single ring, $\mathcal{Z}_\mathrm{a}$ is indeed normal. Therefore, we will not use the generalized eigenvalue equation of Harrington and Mautz. Another reason is that we expect the approach to be inefficient for arrays, because the characteristic currents are determined from the moment matrix for a complete body. Constructing the characteristic currents stepwise as in our approach will affect the strongest property of the approach, namely the orthogonality of the far fields of the characteristic currents with respect to the L_2 inner product over the radiation sphere.

   Garbacz and Turpin [38] found the same characteristic currents for wires as Harrington and Mautz, but by another technique. They computed solutions of the moment-matrix

equation with minimum phase variation along the wire. In [65], the characteristic currents of Harrington and Mautz are used for pattern synthesis.

5. As stated in [115], any use of eigenvalues to derive physical predictions relies on an implicit transformation to eigenvector coordinates. For normal operators, or the almost normal operators we consider, this transformation is (almost) unitary and corresponds to a rotation or a reflection. For highly nonnormal operators, the description of the action of the operator in terms of its eigenfunctions may lead to a superposition of huge eigenfunction components that nearly cancel. To study the action of nonnormal operators, the application of the pseudo-spectrum is proposed in [75, 115]. Examples of applications where such operators are encountered are described in [75], such as the study of self-induced vibrational motion by a source of energy external to a structure and the study of parallel shear flows as a mechanism of subcritical transition to turbulence.

6. The ideas concerning the subdivision into subarrays appear in the fast multipole method as well [24, 42, 99]. The basic idea of this method is that the force exerted on a particle due to all interaction or coupling in a system of charged particles can be divided into two components. First, a force due to nearby particles that can be computed directly and, second, a force due to the distant particles approximated by their multipole expansions. The fast multipole method starts by the construction of a hierarchical spatial decomposition to divide the simulation cell into smaller subcells. Next, for all subcells, (truncated) multipole expansions are calculated. These expansions are combined in a hierarchical way to describe the behavior of larger and larger groups of particles.

5.2 Initialization

5.2.1 Calculational Details

Having chosen a subarray in step A of the initialization on p. 112, we carry out steps B and C as described in Subsection 2.4.3. For (sub)arrays of strips and rings, explicit choices of expansion functions, or mappings $\mathcal{W}$ with corresponding projections $\mathcal{P} = \mathcal{W}\mathcal{W}^{-}$, are described in Section 3.2. The calculational and computational aspects of the corresponding moment matrices are described in Sections 3.3 and 3.4. In this section, we describe steps D and E in more detail. We omit the superscripts $^{\mathrm{init}}$ and the subscripts $_{\mathrm{init}}$ in the notation.

In step D, the eigenvectors U_n ($n = 1, \ldots, N_{\mathrm{exp}}$) of the moment matrix of $\mathcal{Z}_{\mathrm{a}}$, i.e., $[\mathcal{W}^{-}\mathcal{Z}_{\mathrm{a}}\mathcal{W}]$, represent the expansion coefficients of the eigencurrents $\boldsymbol{u}_n$ in ran$(\mathcal{P})$ with respect to the expansion functions in bas$(\mathcal{W})$. Here, N_{exp} is the number of expansion functions, or, the number of elements of bas$(\mathcal{W})$. The eigenvectors and the corresponding eigenvalues ν_n are determined numerically, see the next subsections for details. Then, the eigencurrents are

described by

$$\boldsymbol{u}_n = \sum_{p=1}^{N_{\mathrm{exp}}} U_n(p,1)\, \mathcal{W}\boldsymbol{e}_p \,. \tag{5.4}$$

Here, $\{\boldsymbol{e}_1, \ldots, \boldsymbol{e}_{N_{\mathrm{exp}}}\}$ is the standard basis in $\mathbb{C}^{N_{\mathrm{exp}}}$ as in (2.110) and $\mathcal{W}\boldsymbol{e}_p$ ($p = 1, \ldots, N_{\mathrm{exp}}$) are the expansion functions in bas($\mathcal{W}$). We recall that the mapping $\mathcal{W}^-$ assigns to a function $\boldsymbol{w}$ a tuple in $\mathbb{C}^{N_{\mathrm{exp}}}$, which represents the expansion coefficients of $\boldsymbol{w}$ with respect to the expansion functions in bas($\mathcal{W}$), see (2.111). Hence, $U_n = [\mathcal{W}^-\boldsymbol{u}_n]$, where we apply the bracket calculus of Subsection 2.4.1. Since each U_n is an eigenvector of the moment matrix $[\mathcal{W}^-\mathcal{Z}_{\mathrm{a}}\mathcal{W}]$ with eigenvalue ν_n, it follows that $[\mathcal{W}^-\mathcal{Z}_{\mathrm{a}}\mathcal{W}][\mathcal{W}^-\boldsymbol{u}_n] = \nu_n[\mathcal{W}^-\boldsymbol{u}_n]$. Applying the bracket calculus to this equation, we obtain

$$\mathcal{W}^-\mathcal{Z}_{\mathrm{a}}\mathcal{W}\mathcal{W}^-\boldsymbol{u}_n = \nu_n\mathcal{W}^-\boldsymbol{u}_n \,. \tag{5.5}$$

Applying $\mathcal{W}$ to both sides of (5.5) leads to

$$\mathcal{P}\mathcal{Z}_{\mathrm{a}}\mathcal{P}\boldsymbol{u}_n = \nu_n\mathcal{P}\boldsymbol{u}_n \,. \tag{5.6}$$

Since $\mathcal{P}\boldsymbol{u}_n = \boldsymbol{u}_n$, each eigenvalue ν_n of the moment matrix is also an eigenvalue of the operator $\mathcal{P}\mathcal{Z}_{\mathrm{a}}\mathcal{P}$ with eigencurrent $\boldsymbol{u}_n$.

In the above, we used our definition of the moment matrix, i.e., $[\mathcal{W}^-\mathcal{Z}_{\mathrm{a}}\mathcal{W}]$. As explained in Subsection 2.4.2, this definition yields only the same moment matrix as the usual definition, if the Gram matrix of bas($\mathcal{W}$) with respect to the inner product in step A is the identity matrix. Hence, the eigenvalues of the moment matrix in the usual moment method are only equal to the eigenvalues of the operator $\mathcal{P}\mathcal{Z}_{\mathrm{a}}\mathcal{P}$, if the (test and) expansion functions chosen in step B are orthonormal with respect to the inner product chosen in step A. In general, these expansion functions are not orthonormal and, hence, the eigenvalues of the moment matrix defined as usual and the eigenvalues of the operator $\mathcal{P}\mathcal{Z}_{\mathrm{a}}\mathcal{P}$ are not the same. This observation reveals why our definition of the moment matrix differs from the usual definition of this matrix. For example, if all expansion functions are multiplied by a factor of 2, the eigenvalues of the moment matrix in the usual moment method are multiplied by a factor of 4. On the contrary, the eigenvalues of the moment matrix $[\mathcal{W}^-\mathcal{Z}_{\mathrm{a}}\mathcal{W}]$ remain the same due to the normalization by the Gram matrix as in (2.128).

To construct the new inner product in step E, we consider the space ran($\mathcal{P}$) = ran($\mathcal{W}$) with the initializing inner product $\langle\cdot\,,\cdot\rangle$. Since the set of eigencurrents $\{\boldsymbol{u}_1, \ldots, \boldsymbol{u}_{N_{\mathrm{exp}}}\}$ is independent in ran($\mathcal{P}$), there exists a set $\{\boldsymbol{y}_1, \ldots, \boldsymbol{y}_{N_{\mathrm{exp}}}\}$ in ran($\mathcal{P}$), such that $\langle\boldsymbol{u}_m, \boldsymbol{y}_n\rangle = \delta_{mn}$. Here, δ_{mn} is the Kronecker symbol defined by $\delta_{mn} = 1$ for $m = n$ and $\delta_{mn} = 0$ for $m \neq n$. The set $\{\boldsymbol{y}_1, \ldots, \boldsymbol{y}_{N_{\mathrm{exp}}}\}$ is called the bi-orthogonal set of $\{\boldsymbol{u}_1, \ldots, \boldsymbol{u}_{N_{\mathrm{exp}}}\}$ with respect to the initializing inner product. We calculate the elements of the bi-orthogonal set in

the next paragraph. Let the mappings $\mathcal{U}$ and $\mathcal{Y}$ be defined similarly as $\mathcal{W}$. They map tuples in $\mathbb{C}^{N_{\text{exp}}}$ onto linear expansions of functions $\mathcal{U}\boldsymbol{e}_n = \boldsymbol{u}_n$ and $\mathcal{Y}\boldsymbol{e}_n = \boldsymbol{y}_n$ as in (2.110). Then, the mapping $\mathcal{Y}\mathcal{U}^-$ maps each $\boldsymbol{u}_n$ onto $\boldsymbol{y}_n$. Hence, $\langle \boldsymbol{u}_m, \mathcal{Y}\mathcal{U}^- \boldsymbol{u}_n \rangle = \delta_{mn}$. Herewith, we have constructed an inner product on ran$(\mathcal{P})$ with respect to which the eigencurrents are orthonormal: $\langle \cdot\,, \cdot \rangle_{\text{sub}} = \langle \cdot\,, \mathcal{Y}\mathcal{U}^- \cdot \rangle$.

In the cycle of the eigencurrent approach, we will need to calculate inner products of the form $\langle \boldsymbol{u}_n, \boldsymbol{w} \rangle_{\text{sub}}$, where $\boldsymbol{w} \in \text{ran}(\mathcal{P})$. Since $\mathcal{Y}\mathcal{U}^-$ is self-adjoint with respect to the initializing inner product restricted to ran$(\mathcal{P})$, $\langle \boldsymbol{u}_n, \boldsymbol{w} \rangle_{\text{sub}}$ can be rewritten as

$$\langle \boldsymbol{u}_n, \boldsymbol{w} \rangle_{\text{sub}} = \langle \boldsymbol{u}_n, \mathcal{Y}\mathcal{U}^- \boldsymbol{w} \rangle = \langle \mathcal{Y}\mathcal{U}^- \boldsymbol{u}_n, \boldsymbol{w} \rangle = \langle \boldsymbol{y}_n, \boldsymbol{w} \rangle \,. \tag{5.7}$$

If the functions $\boldsymbol{y}_n$ are known, the inner product $\langle \boldsymbol{y}_n, \boldsymbol{w} \rangle$ can be calculated. To calculate these functions, we express each $\boldsymbol{y}_n$ into the eigencurrents $\boldsymbol{u}_n$,

$$\boldsymbol{y}_n = \sum_{p=1}^{N_{\text{exp}}} C(p,n)\, \boldsymbol{u}_p \,, \tag{5.8}$$

where the expansion coefficients $C(p,n)$ are unknown. Substituting this expression in $\langle \boldsymbol{u}_m, \boldsymbol{y}_n \rangle = \delta_{mn}$, we obtain

$$\sum_{p=1}^{N_{\text{exp}}} G_{\mathcal{U}}(m,p)\; C(p,n) = \delta_{mn} \,, \tag{5.9}$$

where $G_{\mathcal{U}} = G(\text{bas}(\mathcal{U}))$ is the Gram matrix of $\text{bas}(\mathcal{U}) = \{\boldsymbol{u}_1, \ldots, \boldsymbol{u}_{N_{\text{exp}}}\}$ with respect to the inner product $\langle \cdot\,, \cdot \rangle$. From this equation, it follows that $C = G_{\mathcal{U}}^{-1}$. Hence,

$$\boldsymbol{y}_n = \sum_{p=1}^{N_{\text{exp}}} G_{\mathcal{U}}^{-1}(p,n)\, \boldsymbol{u}_p \,. \tag{5.10}$$

The expansion coefficients of $\boldsymbol{y}_n$ with respect to the expansion functions in bas$(\mathcal{W})$ are given by

$$Y_n = [\mathcal{W}^- \boldsymbol{y}_n] = \sum_{p=1}^{N_{\text{exp}}} G_{\mathcal{U}}^{-1}(p,n)\, [\mathcal{W}^- \boldsymbol{u}_p] = \sum_{p=1}^{N_{\text{exp}}} G_{\mathcal{U}}^{-1}(p,n) U_p \,. \tag{5.11}$$

The Gram matrix $G_{\mathcal{U}}$ is obtained from the Gram matrix $G_{\mathcal{W}} = G(\text{bas}(\mathcal{W}))$ and the eigenvectors U_n. Substituting (5.4) in $G_{\mathcal{U}}(m,n) = \langle \boldsymbol{u}_m, \boldsymbol{u}_n \rangle$, we obtain

$$G_{\mathcal{U}}(m,n) = U_m^H G_{\mathcal{W}} U_n \,. \tag{5.12}$$

For the expansion functions for strips and rings as introduced in Section 3.2, the corresponding Gram matrices $G_{\mathcal{W}}$ are given in Section 3.3.

5.2.2 Single Rings

For a single ring, the eigencurrents are known. In Subsection 3.3.2, we observed that the cosine and sine expansion functions, as introduced in (3.12), diagonalize the impedance operator $\mathcal{Z}_{\mathrm{a}}$ of a single ring. Hence, the eigencurrents of a single ring are these cosine and sine functions. The eigenvalues are the diagonal components of the moment matrix $[\mathcal{W}^{-}\mathcal{Z}_{\mathrm{a}}\mathcal{W}] = G^{-1}Z$ as determined in Section 3.3, see (3.35). These components are computed as described in Section 3.4. From (3.35)^3, it follows that components corresponding to cosine and sine functions of the same angular order are equal. Hence, the constant functions establish a 1-dimensional eigenspace, while all other eigenspaces are 2-dimensional and consist of a cosine and a sine function of the same angular order. The eigenvectors of the moment matrix are the unit column vectors, each of which is zero in all entries but one, where it equals 1.

We observe that the eigencurrents depend only the angle that describes the circumference of the ring. The eigencurrents are orthogonal with respect to the L_2 inner product. To obtain an orthonormal set, we can either normalize the eigencurrents with respect to the L_2 inner product or adjust the inner product as described in the previous subsection. In the second case, the biorthogonal set $\{ y_1, \ldots, y_{N_{\mathrm{exp}}} \}$ is given by $y_n = \alpha_n u_n$, where $\alpha_n = 2\pi$ if u_n is the constant function and $\alpha_n = \pi$ otherwise. If the eigencurrents u_n are indexed in the same way as the expansion functions, then $\alpha_1 = 2\pi$ and $\alpha_n = \pi$ for $n > 1$. However, if we index the eigencurrents according to $|\nu_n| \leq |\nu_{n+1}|$, the eigencurrents will in general not be indexed in the same way as the expansion functions.

Considering the questions on pp. 113 ff., we observe that the remaining relevant questions concern the behavior of the eigenvalues as a function of their index and their dependence on the geometry parameters and the frequency. For a ring in free space, the eigenvalues depend on the dimensionless parameters ka and β, i.e., the ratio of the ring circumference and the wavelength, and the ratio of the ring width and the ring radius. Moreover, the magnitudes of the eigenvalues depend on the dimensionless parameter k^2ab, see (2.96). For a ring in a half space, the eigenvalues depend as well on the ratio h/a of the height above the ground plane and the radius.

Since the sine eigencurrents exhibit the same eigenvalues as the cosine eigencurrents with angular order larger than zero, we study here the behavior of the eigenvalues corresponding to the cosine eigencurrents. We index these eigenvalues according to $|\nu_n| \leq |\nu_{n+1}|$. Figure 5.4 shows the first 10 (normalized) absolute eigenvalues $|\nu_n|$ as a function of their index for ka between 0.75 and 1.25. Here, ka is adjusted by means of the frequency, since the ratio β remains fixed. We observe that the absolute eigenvalues increase most rapidly for $ka \approx 1$. They increase slower for $ka \approx 0.75$ and $ka \approx 1.25$. Hence, in case the ring circumference equals about a wavelength, less eigencurrents will contribute to the current on the ring than in case the ring circumference equals about 0.75λ and 1.25λ. Moreover, at $ka \approx 1$ the ring shows resonant behavior. In that case, the cosine and sine functions with angular order 1 match the ring

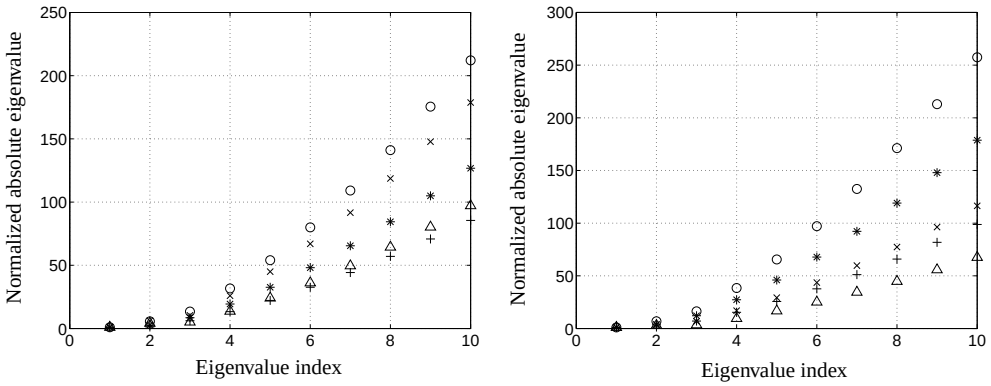

Figure 5.4 The first 10 normalized absolute eigenvalues of a single ring in both free space (left) and a half space with $h/a = 6/5$ (right). The ratios ka of ring circumferences and wavelengths are 0.75 $(+)$, 0.875 $(*)$, 1 $(\circ)$, 1.125 $(\times)$, and 1.25 $(\triangle)$. Normalization: for each value of ka, the first absolute eigenvalue. Parameter values: $\beta = b/a = 3/100$, $\psi = 0$, $N_{\cos} = 10$, $N_{\sin} = 0$.

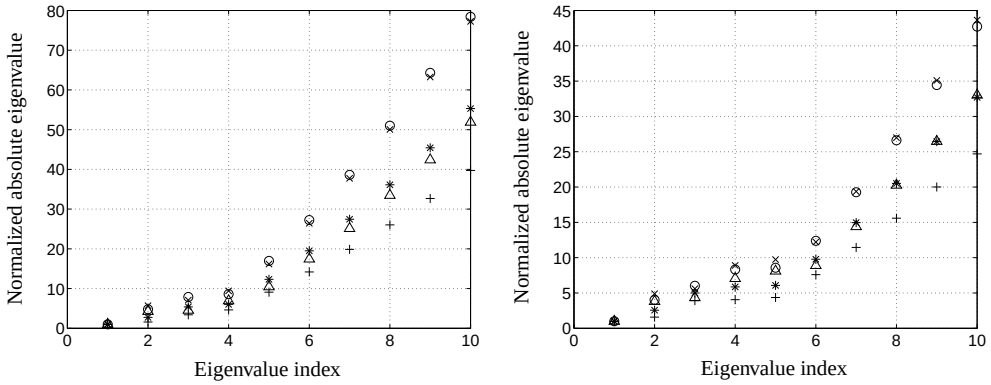

Figure 5.5 The first 10 absolute eigenvalues of a single ring in free space. The ratios ka of ring circumferences and wavelengths are $n + 0.75$ $(+)$, $n + 0.875$ $(*)$, $n + 1$ $(\circ)$, $n + 1.125$ $(\times)$, $n + 1.25$ $(\triangle)$, where $n = 1$ (left) and $n = 2$ (right). Normalization: for each value of ka, the first absolute eigenvalue. Parameter values as in Figure 5.4.

circumference. From a mathematical point of view, the resonant behavior is explained by the vanishing of the corresponding Sturm-Liouville eigenvalue as given by (3.11). Then, the first term in the right-hand side of (3.32) vanishes as well. Hence, the scattered field contributions corresponding to the cosine and sine functions with angular order 1 are entirely described by the kernel $\tilde{\mathcal{K}}_{2,pq}$, which represents the field contributions due to the curvature of the ring.

Least-square fits of the first 30 eigenvalues revealed that, in all cases, the eigenvalues tend as $n\sqrt{n}$ $(n \to \infty)$, where n is the eigenvalue index. Figure 5.5 shows similar phenomena for ka between 1.75 and 2.25, and for ka between 2.75 and 3.25. For the values of ka used in this figure, the absolute eigenvalues show the 'steepest slope' in case the circumference equals 2λ and 3λ, i.e., $ka = 2$ and $ka = 3$. As above, these circumferences correspond to resonant behavior of the ring. Further investigation revealed that both in free space and in a half space, the 'steepest slopes' are attained for values of ka between $m - 1/10$ and $m + 1/10$ $(m \in \mathbb{N})$. Moreover, the 'weakest slopes' are attained between about $m-1/2$ and $m-3/10$. For $ka \ll 1$, the slope is very steep, which indicates that only one eigencurrent, i.e., the constant function, will contribute to the current on the ring. Moreover, all eigenvalues are imaginary valued. These results are to be expected, because an electrically small ring is strongly reactive and the current along it is almost constant, see Subsection 4.2.2. Finally, for the values of ka used in Figure 5.5, the first few absolute eigenvalues do not show the $n\sqrt{n}$ behavior as in Figure 5.4 for $ka = 1$.

From the above, we observe that the number of eigencurrents needed to describe the current will increase, if the frequency is increased. This conclusion is in agreement with the remark in [79: pp. 66, 70] that only a few eigencurrents are needed to describe the current for (electrically) small and intermediate size bodies. As the results for the ring show, (electrically) larger bodies support more eigencurrents than (electrically) smaller bodies. Therefore, for larger bodies, the excitation field will have a stronger influence on the current. This is corroborated by the description (5.2) of the current. In the previous chapter, we showed that certain exterior fields induce equivalent excitation fields. This equivalence may be affected when the size of the excited body is enlarged.

The results in Figure 5.4 and Figure 5.5 suggest that the eigenvalues depend strongly on the geometry parameters and the frequency. This is corroborated by the results in Table 5.1, which shows the absolute eigenvalues and the corresponding eigencurrents of a single ring for four values of ka. As expected, the eigencurrents are distributed among the eigenvalues according

Table 5.1 The first 5 absolute eigenvalues (unit: V/A) of a single ring in free space and their corresponding eigencurrents for ka equal to 0.7, 1, 1.65, and 2. Only the cosine eigencurrents are considered. Other parameter values as in Figure 5.4.

	$ka = 0.7$		$ka = 1$		$ka = 1.65$		$ka = 2$	
n	$\lvert\nu_n\rvert$	u_n	$\lvert\nu_n\rvert$	u_n	$\lvert\nu_n\rvert$	u_n	$\lvert\nu_n\rvert$	u_n
1	11.75	1	3.078	$\cos\varphi$	12.08	$\cos 2\varphi$	4.045	$\cos 2\varphi$
2	12.33	$\cos\varphi$	17.46	1	12.74	$\cos\varphi$	19.35	$\cos\varphi$
3	68.13	$\cos 2\varphi$	41.25	$\cos 2\varphi$	29.66	1	31.91	$\cos 3\varphi$
4	146.9	$\cos 3\varphi$	97.44	$\cos 3\varphi$	47.53	$\cos 3\varphi$	34.79	1
5	244.4	$\cos 4\varphi$	166.3	$\cos 4\varphi$	90.84	$\cos 4\varphi$	68.64	$\cos 4\varphi$

to these values. For the circumferences corresponding to the resonant behavior of the ring, i.e., $ka = 1$ and $ka = 2$, the dominant eigencurrents are clearly $\cos\varphi$ and $\cos 2\varphi$. For the other two circumferences, i.e., $ka = 0.7$ and $ka = 1.65$, there are two dominant eigencurrents. Moreover, the first eigenvalues for these values of ka are larger than for $ka = 1$ and $ka = 2$. This phenomenon is explained from the need of a higher amount of energy to excite the dominant eigencurrents for the ring circumferences $0.7\,\lambda$ and $1.6\,\lambda$ than for the ring circumferences that correspond to resonant behavior. For a ring circumference close to $0.7\,\lambda$ and for a ring circumference close to $1.6\,\lambda$, the first two eigenvalues become the same. In that case, the ring exhibits a degenerate eigenvalue with an eigenspace of dimension 2 spanned by the first two eigencurrents.

The first eigenvalue depends strongly on the ratio h/a, while the other eigenvalues depend weakly on this ratio. To illustrate this dependence, Table 5.2 shows the eigenvalues and corresponding eigencurrents of a ring in free space and in a half space with $h/a = 6/5$. This

Table 5.2 The first four eigenvalues (unit: V/A) and their corresponding eigencurrents of a single ring in free space and in a half space with $h/a = 6/5$ (or, $h = \lambda/5$). Only the cosine eigencurrents are considered. Parameter values: $ka = pi/3$, $\beta = 3/100$, $\psi = 0$, $N_{\cos} = 4$, $N_{\sin} = 0$.

	Free space			Half space			
n	$\mathrm{Re}\,\nu_n$	$\mathrm{Im}\,\nu_n$	$\lvert\nu_n\rvert$	$\mathrm{Re}\,\nu_n$	$\mathrm{Im}\,\nu_n$	$\lvert\nu_n\rvert$	u_n
1	-2.68	0.49	2.72	-2.88	-1.56	3.27	$\cos\varphi$
2	-1.82	-18.27	18.36	-0.97	-18.34	18.37	1
3	-0.52	38.21	38.22	-0.33	38.30	38.30	$\cos 2\varphi$
4	-0.03	92.06	92.06	-0.01	92.12	92.12	$\cos 3\varphi$

table also shows that the real part of the eigenvalues decreases with their index n, while their imaginary part increases in absolute value. Moreover, ν_n is almost imaginary valued for $n \geq 3$. Since the eigencurrents u_n are real valued and the current on the ring is described by the finite expansion (5.2), the eigencurrents u_n with $n \geq 3$ are reactive contributions to the current.

Finally, the eigenvalues (3.11) of the Helmholtz operator differ from the eigenvalues of the ring in the sense that they are real valued, they tend as n^2, and they decrease monotonically for increasing ring circumference. Since the eigenvalues of the ring tend as $n\sqrt{n}$, the Helmholtz operator dominates the integral operator $\tilde{\mathcal{K}}_{1,pq}$, with weakly singular kernel, in (2.96).

5.2.3 Single Strips

Determining Eigenvalues and Eigencurrents

In contrast to the eigencurrents of a single ring, the eigencurrents of a single strip need to be evaluated numerically. We determine numerically the eigencurrents and the correspond-

ing eigenvalues for two different sets of expansion functions, i.e., the entire-domain functions defined by (3.7) – (3.8) and the piecewise functions defined by (3.9). For both sets, we compute the eigenvalues and eigencurrents from the moment matrix $[\mathcal{W}^- \mathcal{Z}_\mathrm{a} \mathcal{W}]$ by the Matlab function 'eig'. For the entire-domain functions, the moment matrix is a block-diagonal matrix composed of the blocks $[(\mathcal{W}^{\cos})^- \mathcal{Z}_\mathrm{a} \mathcal{W}^{\cos}]$ and $[(\mathcal{W}^{\sin})^- \mathcal{Z}_\mathrm{a} \mathcal{W}^{\sin}]$, see Subsection 3.3.1. Therefore, we can compute the eigenvalues and eigencurrents also from these blocks. Moreover, the resulting eigencurrents are either even or odd.

As mentioned in Subsection 5.1.3, numerical errors in the initialization step will propagate throughout the whole eigencurrent approach. Therefore, we investigate the numerical errors that occur in the computation of the eigenvalues and eigencurrents. These errors can be divided into two groups: errors due to the numerical approximation of the moment matrix and errors due to the numerical computation of the eigenvalues and eigenvectors of the (approximated) moment matrix. The errors of the first kind are investigated in Section 3.4. Therefore, we consider the errors of the second kind only. To investigate these errors, we computed the relative errors

$$\frac{\| \widetilde{[\mathcal{W}^- \mathcal{Z}_\mathrm{a} \mathcal{W}]} \, \tilde{U}_n - \tilde{\nu}_n \, \tilde{U}_n \|}{\| \tilde{\nu}_n \, \tilde{U}_n \|}, \qquad n = 1, \ldots, N_{\exp}\,, \tag{5.13}$$

for several strip geometries and several numbers of expansion functions. Here, $\widetilde{[\mathcal{W}^- \mathcal{Z}_\mathrm{a} \mathcal{W}]}$ is the *computed* moment matrix, and $\tilde{\nu}_n$ and $\tilde{U}_n$ are its *computed* eigenvalues and eigenvectors. Moreover, $\| \cdot \|$ is the norm on the space $\mathbb{C}^{N_{\exp} \times 1}$ of column vectors defined by $\|U\|^2 = U^H G U$, where G is the Gram matrix of $\mathrm{bas}(\mathcal{W})$ with respect to the L_2 inner product. The choice of this norm is such that $\|U\| = \|u\|_{L_2}$ for $u \in \mathrm{ran}(\mathcal{W})$ with $[\mathcal{W}^- u] = U$. Table 5.3 shows the maxima of the relative errors (5.13) for several sets of expansion functions. For each set, the maximum belongs to the smallest eigenvalue. We observe that the maximum increases with the size of the moment matrix, but even for 159 piecewise functions, the maximum is smaller than 10^{-10}. For the number of integration points as given in Section 3.4, the components of the moment matrix are computed up to relative errors of the order 10^{-3}. Hence, the numerical accuracy of the eigenvalues and eigencurrents is only determined by the approximation of the moment matrix and not by their numerical computation from this matrix. This shows that the current description by the (computed) moment matrix and the current description by the (computed) eigenvalues and eigencurrents have the same accuracy.

For the sets of expansion functions in Table 5.3, the CPU time of the matrix construction is slightly larger than the CPU time of the eigenvalue and eigenvector computation, but both CPU times are small. The maximum CPU times are 2.7 seconds and 1.2 seconds, respectively, both for 159 piecewise expansion functions.

Table 5.3 Maxima of the relative errors (5.13) for several sets of expansion functions. The mapping $\mathcal{W}$ is constructed for 5, 10, 20, 30, and 40 cosine and sine expansion functions as in (3.7) and for for 9, 19, 39, 79, and 159 piecewise expansion functions as in (3.9). Parameter values: $2\ell = \lambda/2$, $\beta = b/\ell = 1/50$.

Entire-domain exp. functions		Piecewise exp. functions	
$N_{\cos}, N_{\sin}$	max. rel. error	$N_{\exp}$	max. rel. error
5	$7.0 \cdot 10^{-14}$	9	$5.4 \cdot 10^{-14}$
10	$3.3 \cdot 10^{-13}$	19	$2.9 \cdot 10^{-13}$
20	$9.2 \cdot 10^{-13}$	39	$1.2 \cdot 10^{-12}$
30	$1.6 \cdot 10^{-12}$	79	$4.6 \cdot 10^{-12}$
40	$3.2 \cdot 10^{-12}$	159	$1.2 \cdot 10^{-11}$

Description of Eigencurrents and Dependence on Expansion Functions

In this part of Subsection 5.2.3, we will show how the eigencurrents are described by both the piecewise and the entire-domain expansion functions. Moreover, we show to what extent they depend on the set of expansion functions. Throughout this subsection, we consider a strip of half a wavelength in free space. At the end of this part, we discuss results for other strip lengths.

Let us start with the entire-domain expansion functions. Figure 5.7 shows the absolute eigenvector components for a strip of half a wavelength with 10 entire-domain expansion functions, i.e., 5 cosine and 5 sine functions, and with 20 entire-domain expansion functions, i.e., 10 cosine and 10 sine functions. The eigenvectors are indexed such that $|\nu_n| \leq |\nu_{n+1}|$. We recall that the components of each eigenvector are the expansion coefficients of an eigencurrent with respect to these functions. The first 5 and 10 coefficients, respectively, correspond to the cosine functions and the next 5 and 10 coefficients correspond to the sine functions. From the color pattern in Figure 5.7, we conclude that the eigencurrents equal the cosine and sine expansion functions up to a perturbation. For each eigencurrent, this perturbation is described by the 'neighboring' cosine or sine functions of the corresponding dominant expansion function. The perturbation is larger for eigencurrents with a dominant cosine or sine function of higher angular order. Moreover, the eigencurrents are alternately even and odd for the given strip geometry. As suggested by Figure 5.7 (left) and Figure 5.7 (right), the eigencurrents corresponding to lower eigenvalues hardly change when more expansion functions are used. This observation is corroborated by amplitude and phase plots of the eigencurrents. An example is given in Figure 5.6, which shows the first two eigencurrents for 5 and 10 cosine and sine expansion functions. The amplitude patterns show the perturbations with respect to the dominant expansion functions, while the phase patterns show that the eigencurrents have negligible imaginary parts.

For a strip of half a wavelength with piecewise expansion functions, we will show first how the eigencurrents are described by these functions. As above, the eigencurrents are indexed by

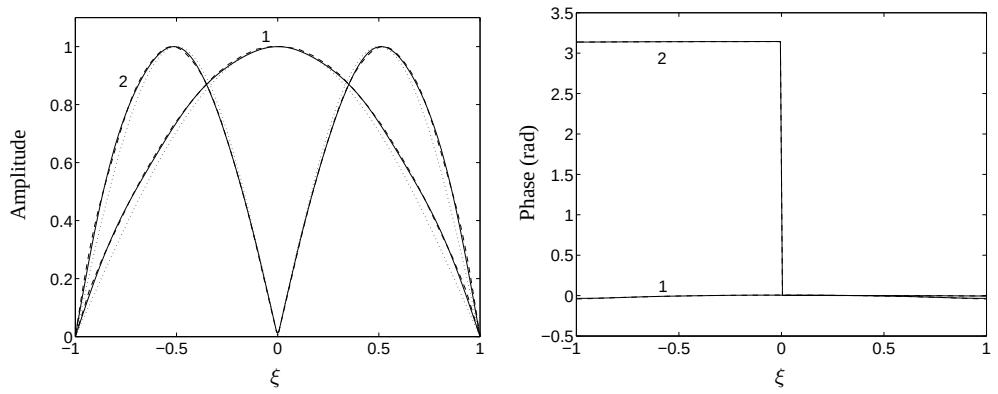

Figure 5.6 The 1st and 2nd eigencurrent for a strip of half a wavelength in free space. Solid curve: 5 cosine and 5 sine expansion functions. Dashed curve: 10 cosine and 10 sine expansion functions (indistinguishable in both figures). The dotted curves in the left figure are the functions $\cos(\pi\xi/2)$ and $\sin(\pi|\xi|/2)$. Eigencurrent normalization: absolute maximum. Parameter values as in Figure 5.7.

n such that $|\nu_n| \leq |\nu_{n+1}|$. Next, we will show that the amplitudes of the first $\lfloor N_{\text{exp}}/4 \rfloor$ eigencurrents and the phases of the first $\lfloor N_{\text{exp}}/2 \rfloor$ eigencurrents correspond to the amplitudes and phases of the first $\lfloor N_{\text{exp}}/4 \rfloor$ and $\lfloor N_{\text{exp}}/2 \rfloor$ eigencurrents obtained by the entire-domain expansion functions. This correspondence becomes less obvious for indices larger than $\lfloor N_{\text{exp}}/4 \rfloor$ and $\lfloor N_{\text{exp}}/2 \rfloor$.

Figure 5.8 (left) shows the absolute eigenvector components for 15 piecewise expansion functions. The color pattern is completely different from the patterns for the entire-domain expansion functions in Figure 5.7. It suggests that the absolute components of the nth eigenvector generate the same pattern as the absolute components of the $(16 - n)$th eigenvector. For example, the absolute components of the first and last eigenvectors generate cosine-like patterns of half a period. Moreover, the absolute components of the second eigenvector and the last but one generate absolute sine-like patterns of one period. These observations are corroborated by Figure 5.9 (left), which shows that the absolute components of the first and 15th eigenvectors are about the same as well as the absolute components of the second and 14th eigenvectors. The dotted and dashed curves between the absolute components show the patterns that these components generate; they do not have a specific meaning. Also for $n = 7$, the absolute eigenvector components of the nth and $(16 - n)$-th eigenvector exhibit the same patterns as shown in Figure 5.9 (right). Since an odd number of expansion functions is used, the 8th eigenvector does not have a corresponding eigenvector.

The color pattern in Figure 5.8 (left) shows that the absolute components of the nth eigenvector have, as a function of the component index, n local maxima if $n \leq 8$ and $16 - n$ local

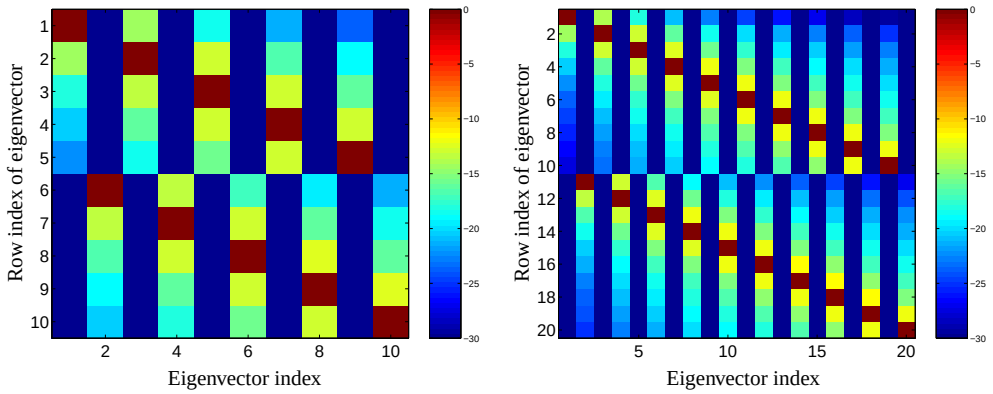

Figure 5.7 Color pattern of the absolute eigenvector components (in dB) for a strip of half a wavelength in free space. Left: 5 cosine and 5 sine expansion functions. Right: 10 cosine and 10 sine expansion functions. Eigenvector normalization: maximum component. Parameter values: $2\ell = \lambda/2$, $\beta = b/\ell = 1/50$.

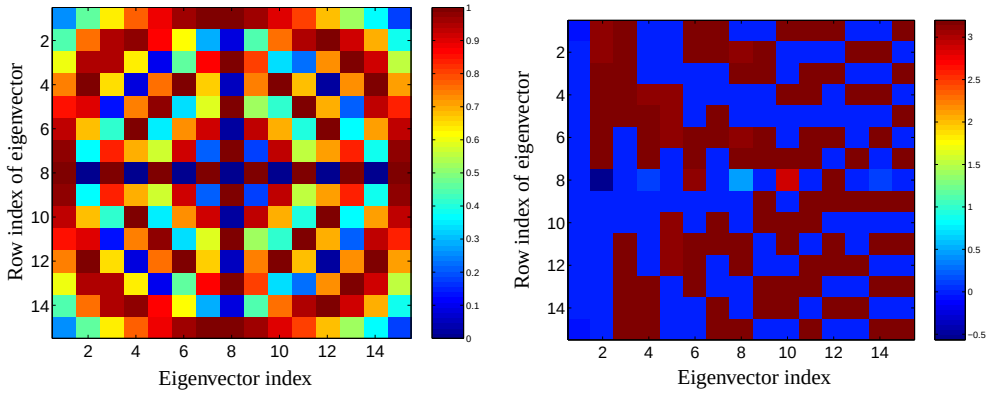

Figure 5.8 Color pattern of the absolute values (left) and the phases (right) of the eigenvector components for a strip of half a wavelength in free space with 15 piecewise expansion functions. Eigenvector normalization: maximum absolute component. Parameter values as in Figure 5.7.

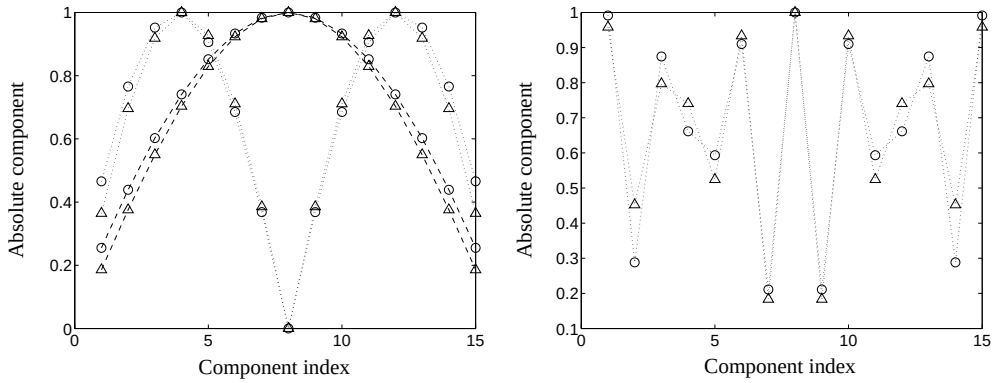

Figure 5.9 Left: absolute eigenvector components of the 1st (∘, dashed), 2nd (∘, dotted), 14th (△, dotted), and 15th (△, dashed) eigenvector for a strip of half a wavelength in free space. Right: absolute eigenvector components of the 7th (∘) and 9th (△) eigenvector for the same strip. The indices $m = 1, \ldots, 15$ of the components are transformed to the interval $[-1, 1]$ according to $m \rightarrow -1 + 2m/(N_{\text{exp}} + 1)$, where $N_{\text{exp}} = 15$. Eigenvector normalization: maximum absolute component. Parameter values as in Figure 5.7.

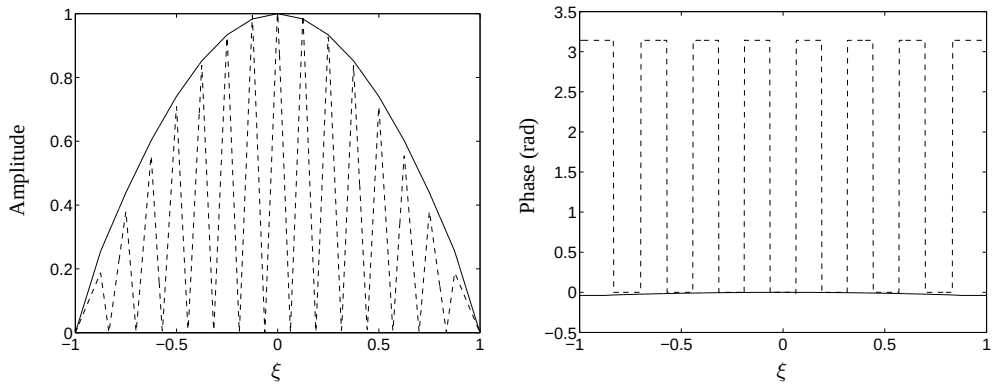

Figure 5.10 Amplitudes (left) and phases (right) of the first (solid curve) and 15th (dashed curve) eigencurrent for a strip of half a wavelength in free space with 15 piecewise expansion functions. Eigencurrent normalization: maximum amplitude. Parameter values as in Figure 5.7.

maxima if $n \geq 8$. Moreover, the components of this eigenvector have $n-1$ phase reversals (phase shifts of $180°$). Due to the increase of the number of phase reversals with the eigenvector index, the nth and $(16-n)$-th eigencurrent differ, although their absolute eigenvector components are almost equal. An example is given in Figure 5.10, which shows the amplitudes of the first and 15th eigencurrents. The amplitude of the first eigencurrent is the same as the pattern generated by the corresponding absolute eigenvector components in Figure 5.8 (left), because all eigenvector components have the same phase. The amplitude of the 15th eigencurrent is not the same as the pattern generated by the corresponding absolute eigenvector components due to a linear phase progression $m\pi$ of these components, see the color pattern of the 15th eigenvector in Figure 5.8 (right). Figure 5.10 shows that the first and the 15th eigencurrents have as many (uniformly spaced) phase reversals as the components of the first and 15th eigenvectors. Further investigation showed that for each n, the nth eigencurrent has n amplitude maxima and $n-1$ (uniformly spaced) phase reversals. Finally, Figure 5.10 (right) shows that the eigencurrents obtained by the piecewise expansion functions are real valued.

The color patterns of the absolute eigenvector components for 29 and 79 piecewise functions in Figure 5.11 show results similar to Figure 5.8. We state the following general conclusions for the eigenvectors and eigencurrents of a strip of half a wavelength with a fixed number of piecewise expansion functions N_{exp}.

1. For each $n = 1, \ldots, N_{\text{exp}}$, the absolute components of the nth and $(N_{\text{exp}}+1-n)$th eigenvector show the same patterns.

2. For each n, the components of the nth eigenvector show $\min\{n, N_{\text{exp}}+1-n\}$ absolute maxima and $n-1$ phase reversals as a function of the component index.

3. For each n, the nth eigencurrent shows n local amplitude maxima and $n-1$ (uniformly spaced) phase reversals.

Having shown the way the eigencurrents are described by the piecewise expansion functions, we compare the eigencurrents obtained by piecewise and entire-domain expansion functions. A first qualitative comparison shows that for both choices of functions, the nth eigencurrent shows n local amplitude maxima and $n-1$ (uniformly spaced) phase reversals. For a quantitative comparison, we compare four of the first 15 eigencurrents obtained by 15 and 29 piecewise functions as well as by 20 entire-domain functions, i.e., 10 cosine and 10 sine functions. From Figure 5.12, we observe that the amplitudes of the first and fourth eigencurrents obtained by 15 and 29 piecewise functions correspond to the amplitudes obtained by the entire-domain functions. For 15 piecewise functions, the amplitude of the 7th eigencurrent shows discrepancies with the amplitude obtained by the entire-domain functions. Moreover, the amplitude of the 14th eigencurrent does not correspond at all to the amplitude obtained by the entire-domain functions. For 29 piecewise functions, the amplitude discrepancies of the 7th and 14th eigencurrents are much

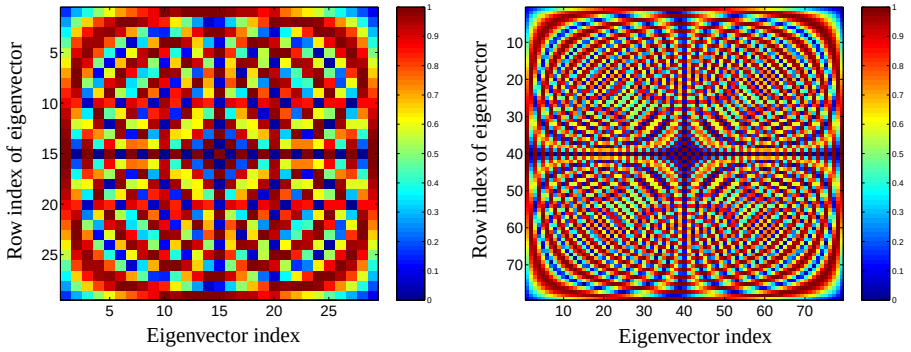

Figure 5.11 Color pattern of the absolute values of the eigenvector components for a strip in free space with 29 (left) and 79 (right) piecewise expansion functions. Eigenvector normalization: maximum component. Parameter values as in Figure 5.7.

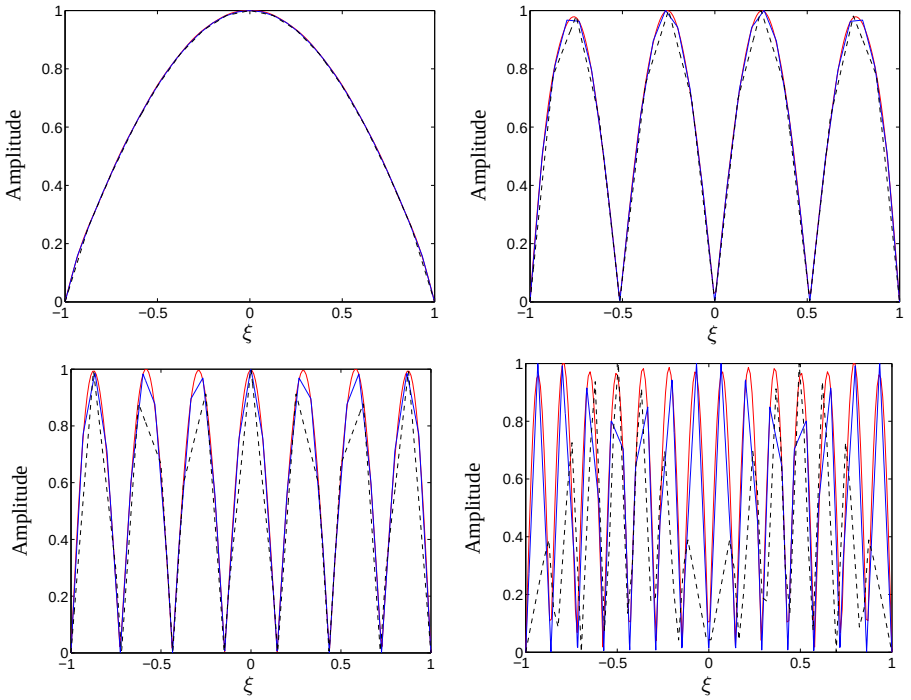

Figure 5.12 Amplitudes of the 1st, 4th, 7th, and 14th eigencurrent for a strip in free space with 15 (black dashed curve) and 29 (blue curve) piecewise expansion functions and with 10 cosine and 10 sine expansion functions (red curve). Eigencurrent normalization: maximum amplitude. Parameter values as in Figure 5.7.

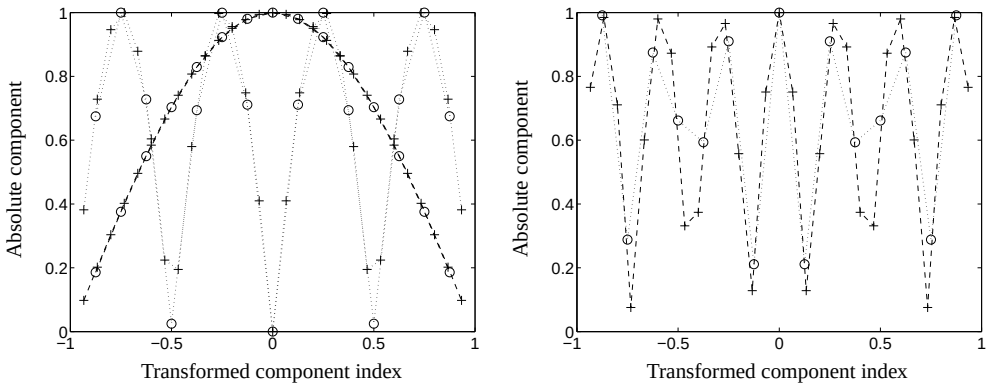

Figure 5.13 Left: absolute eigenvector components of the $N_{\rm exp}$th (dashed curve) and the $(N_{\rm exp}-3)$th (dotted curve) eigenvector for a strip of half a wavelength in free space with 15 ($\circ$) and 29 ($+$) piecewise expansion functions. Right: absolute eigenvector components of the 7th eigenvector for the same strip with 15 ($\circ$, dotted curve) and 29 ($+$, dashed curve) piecewise functions. The indices $m = 1, \ldots, 15$ of the components are transformed to the interval $[-1, 1]$ according to $m \rightarrow -1 + 2m/(N_{\rm exp}+1)$, where $N_{\rm exp} = 15, 29$. Eigenvector normalization: maximum absolute component. Parameter values as in Figure 5.7.

smaller. These results suggest that for a certain number $N_{\rm exp}$ of piecewise functions, the amplitudes of the first $\lfloor N_{\rm exp}/4 \rfloor$ eigencurrents correspond to the amplitudes of the eigencurrents obtained by the entire-domain functions. For eigencurrents with indices larger than $\lfloor N_{\rm exp}/4 \rfloor$, this correspondence deteriorates slowly as a function of the index. The deterioration starting from the index number $\lfloor N_{\rm exp}/4 \rfloor$ can be understood as follows. Since $N_{\rm exp}$ is the number of 'sampling points' and the eigencurrent with index $\lfloor N_{\rm exp}/4 \rfloor$ has $\lfloor N_{\rm exp}/4 \rfloor$ amplitude maxima, there should be at least 4 'sampling points' per amplitude maximum to obtain a good correspondence between the eigencurrents obtained by the piecewise and entire-domain functions. Investigation of the phases of the eigencurrents showed that for fixed $N_{\rm exp}$, the phases of the first $\lfloor N_{\rm exp}/2 \rfloor$ eigencurrents correspond to the phases obtained by the entire-domain functions.

Since the first $\lfloor N_{\rm exp}/4 \rfloor$ eigencurrents show convergence, the absolute components of the first $\lfloor N_{\rm exp}/4 \rfloor$ eigenvectors generate the same patterns as the first $\lfloor N'_{\rm exp}/4 \rfloor$ eigenvectors, where $N'_{\rm exp} > N_{\rm exp}$. The same is valid for the last $\lfloor N_{\rm exp}/4 \rfloor$ eigenvectors due to conclusion 1 above. This result is corroborated by Figure 5.13 (left), which shows the absolute components of the 12th and 15th eigenvectors for a strip with 15 piecewise functions and the absolute components of the 26th and 29th eigenvectors for a strip with 29 piecewise functions. The indices m of the eigenvector components are transformed to the interval $[-1, 1]$ according to $m \rightarrow -1 + 2m/(N_{\rm exp}+1)$, where the number of expansion functions $N_{\rm exp}$ equals 15 and 29. Figure 5.13 (right) shows that also for other eigenvectors similar patterns are generated. The absolute

components of the 7th eigenvector for a strip with 15 piecewise functions are all positioned on the fictitious curve generated by the absolute components of the 7th eigenvector for a strip with 29 piecewise functions.

Above, conclusions were stated for a strip of half a wavelength in free space. We verified similar results for strip lengths smaller than $11/15\,\lambda$, both in free space and in a half space. For strip lengths larger than about $11/15\,\lambda$, the order of the eigencurrents, as induced by the indexing of the eigenvalues, changes in the same way as the order for the ring, see Subsection 5.2.2. An example is given in Figure 5.15 for a strip of one wavelength with 15 piecewise expansion functions and with 10 entire-domain expansion functions, i.e., 5 cosine and 5 sine functions. Both color patterns in this figure show that the first two eigenvectors of a strip of half a wavelength are interchanged. Moreover, these patterns suggest that the eigencurrents are, up to scaling with respect to the length of the strip, the same as the eigencurrents for a strip of half a wavelength. A comparison of eigenvectors and eigencurrents for different geometry parameters is given further on. The interchange of eigencurrents affects the properties 1 - 3 described on page 128. Moreover, the first $\lfloor N_{\rm exp}/4 \rfloor$ eigencurrents obtained by $N_{\rm exp}$ piecewise functions correspond only to the eigencurrents obtained by the entire-domain functions if $N_{\rm exp}$ is sufficiently large to describe the dominant eigencurrents.

If we extrapolate the results for a strip to a more general geometry with width-averaged current, we need $4N$ piecewise expansion functions to determine the first N eigencurrents. The number N is determined by the number of eigencurrents needed to compute a certain typical parameter. Finally, the results for the piecewise and entire-domain expansion functions show that the eigencurrents depend only weakly on the set of expansion functions. Moreover, these results suggest that for each n, the eigencurrent u_n converges pointwise as the number of expansion functions increases.

Dependence of Eigenvalues on Expansion Functions

Table 5.4 shows that the computed eigenvalues ν_1 and ν_2 for a strip of half a wavelength depend only weakly on the number and the type of expansion functions. Moreover, the values seem to

Table 5.4 The first two (computed) eigenvalues (unit: V/A) for a strip of half a wavelength. The expansion functions are chosen as in Table 5.3.

$N_{\rm cos,sin}$	Re ν_1	Im ν_1	Re ν_2	Im ν_2	$N_{\rm exp}$	Re ν_1	Im ν_1	Re ν_2	Im ν_2
5	-3.005	-1.867	-0.37	38.49	9	-2.992	-1.770	-0.36	39.15
10	-3.014	-1.922	-0.37	38.33	19	-3.007	-1.878	-0.37	38.39
20	-3.018	-1.961	-0.37	38.21	39	-3.015	-1.937	-0.37	38.13
30	-3.020	-1.977	-0.37	38.16	79	-3.019	-1.976	-0.37	37.99
40	-3.021	-1.986	-0.37	38.13	159	-3.022	-2.001	-0.37	37.91

converge for $N_{\rm exp} \to \infty$. We investigated the behavior of the eigenvalues ν_1, ν_2, and ν_3 as a function of the number of expansion functions for several strip geometries. An example is given in Figure 5.14 for a strip of half a wavelength in free space. This figure shows that for

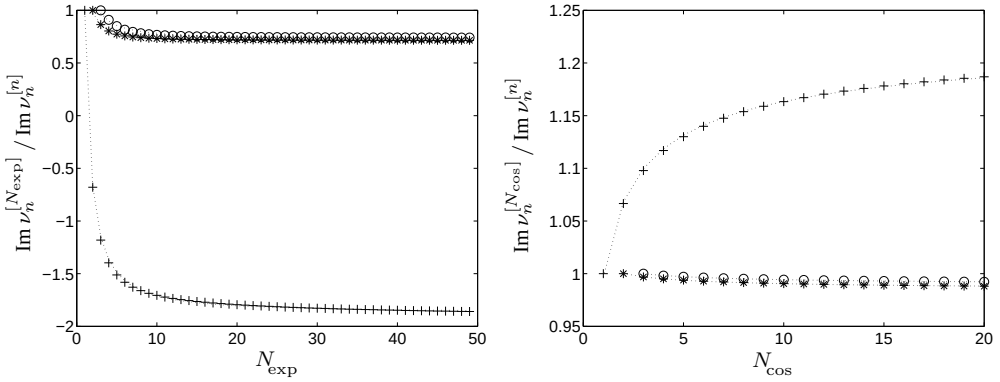

Figure 5.14 Normalized imaginary parts of the first three eigenvalues $\nu_1^{[N]}$ (+), $\nu_2^{[N]}$ (∗), and $\nu_3^{[N]}$ (∘) as a function of the number of expansion functions N for a strip of half a wavelength in free space. Each imaginary part is normalized with respect to its first estimate $\nu_n^{[n]}$. Left: piecewise functions, $N = N_{\rm exp}$. Right: cosine functions, $N = N_{\rm cos}$. Dotted curves: least-square fits (left: 1 and $1/N^{5/4}$, right: 1 and $1/\sqrt{N}$. Parameter values: $2\ell = \lambda/2$, $\beta = b/\ell = 1/50$.

the piecewise functions, the imaginary parts of the eigenvalues tend as $1/N_{\rm exp}^{5/4}$. Moreover, the relative differences between the first estimate of the imaginary part and the limiting value seem to decrease as a function of the eigenvalue index n. Tests revealed that the quality of the first estimate stabilizes as n increases.

For the entire-domain functions, we show the imaginary parts of the first three eigenvalues obtained by the cosine expansion functions, i.e., from the block $[(\mathcal{W}^{\rm cos})^- \mathcal{Z}_{\rm a} \mathcal{W}^{\rm cos}]$ of the moment matrix. As mentioned in the beginning of this subsection, the eigenvalues can be computed from the blocks $[(\mathcal{W}^{\rm cos})^- \mathcal{Z}_{\rm a} \mathcal{W}^{\rm cos}]$ and $[(\mathcal{W}^{\rm sin})^- \mathcal{Z}_{\rm a} \mathcal{W}^{\rm sin}]$ of the moment matrix. We observe that the imaginary parts tend as $1/\sqrt{N_{\rm cos}}$, where $N_{\rm cos}$ is the number of cosine expansion functions. Moreover, the relative differences between the first estimate of the imaginary part and the limiting value show the same behavior as above, i.e., they decrease as a function of the eigenvalue index n. This phenomenon is explained by the increase of the diagonal components of moment matrix for the entire-domain expansion functions, which is diagonally dominant. We observed that the imaginary parts of the first three eigenvalues obtained by the sine functions show similar properties, but they tend as $1/N^{1/4}$.

Both for the piecewise functions and for the entire-domain functions, the real parts show more rapid convergence than the imaginary parts. In contrast, the first estimates deteriorate for

larger eigenvalue indices, which is due to the decrease of the real parts of the eigenvalues with respect to the imaginary parts for larger absolute eigenvalues. Compare for example the real and imaginary parts of the first two eigenvalues in Table 5.4.

Similar results were obtained for other strip geometries in both free space and half space. In particular, the behavior of the imaginary parts of the eigenvalues as a function of the number of expansion functions is independent of the geometry parameters.

Behavior of Eigenvalues and Parameter Dependence

For a strip in free space, the eigenvalues depend on the dimensionless parameters $2\ell/\lambda$ $(= k\ell/\pi)$ and β, i.e., the ratio of the strip length and the wavelength, and the ratio of the strip width and the strip length. Moreover, the magnitudes of the eigenvalues depend on the dimensional parameter $k^2\ell b$, see (2.53). For a strip in a half space, the eigenvalues depend on the ratio h/ℓ of the height above the ground plane and the strip length as well.

The eigenvalues show a similar behavior as the eigenvalues of a ring. First, they tend as $n\sqrt{n}$, where n is the eigenvalue index. Second, the 'slope' of the absolute eigenvalues decreases non-monotonically for $2\ell/\lambda \gtrsim 0.5$, and it shows local maxima and minima for $2\ell/\lambda \approx m/2$ and $2\ell/\lambda \approx (m + 1/2)/2$ $(m \in \mathbb{N})$. Analogously to the analysis for the ring, each local maximum with index m is related to resonant behavior of the strip for which the cosine function with angular order $(2m - 1)\pi/2$ matches with the length of the strip. From a mathematical point of view, the resonant behavior is explained by the vanishing of the corresponding Sturm-Liouville eigenvalue as given by (3.6)[1]. The first term in the right-hand side of (3.16) vanishes as well. Hence, the scattered-field contribution corresponding to the cosine function with angular order $(2m - 1)\pi/2$ is entirely described by the second (boundary) term, which represents the field contributions from the edges of the strip.

For $2\ell/\lambda \ll 1$, the dependence of the slope of the absolute eigenvalues on $2\ell/\lambda$ is negligible. In other words, the ratios ν_n/ν_1 can be considered as being independent of $k\ell$. In that case, the eigenvalues are a linear function of $1/k\ell$, which can be deduced from the definition of the impedance operator for the strip as well, see (2.53). Moreover, because a small strip is strongly reactive, they are imaginary.

Orthonormality of Eigencurrents

The eigencurrents are close to an orthonormal set with respect to the natural L_2 inner product except for the first ones (4 or 6 eigencurrents). For this statement, we considered the Gram matrices of the eigencurrents for several strip geometries. These Gram matrices are computed from (5.12). An example of such a Gram matrix is given in Figure 5.16 (left) for a strip of half a wavelength in free space with 29 piecewise expansion functions. Figure 5.16 (right) shows the corresponding color pattern of the inner products between the even eigencurrents. The same

patterns are obtained for the entire-domain expansion functions. Figure 5.16 (right) shows that only two or three even eigencurrents are not orthogonal. Hence, the Gram matrix of the even eigencurrents can be approximated by the first 2×2 or 3×3 block and the remaining diagonal components. This approximation saves considerable computational time and data storage for the Gram matrix. Thus, it facilitates a faster computation of the new inner product $\langle \cdot, \cdot \rangle_{\mathrm{sub}}$. Moreover, for both the even and odd eigencurrents, the first three functions of the bi-orthogonal set $\{ y_1, \ldots, y_{N_{\mathrm{exp}}} \}$ in (5.10) equal the first three even eigencurrents up to a perturbation. The other functions y_n are proportional to u_n. The constant of proportionality equals 1, if the eigencurrents are normalized. Finally, a similar reasoning is valid for the odd eigencurrents.

Parameter Dependence of Eigenvectors and Eigencurrents

For a specified set of expansion functions, the corresponding eigenvectors and eigencurrents do not depend on the dimensionless parameters $2\ell/\lambda$ and h/a for $2\ell/\lambda \lesssim 1$ and $h/a \gtrsim 0.1$, respectively. This statement is not only valid for the 'converged' eigencurrents, but for all eigencurrents obtained by the specified set. We verified the statement for sets of 15 and 29 piecewise expansion functions and for a set of 5 cosine and 5 sine expansion functions.

The eigenvectors and eigencurrents depend weakly on the dimensionless parameter $\beta = b/\ell$ for $1/50 \leq \beta \leq 1/10$. This weak dependence is apparent from Figure 5.17, where the amplitudes of the first two eigencurrents for $\beta = 1/50$ and $\beta = 1/10$ are shown together with the amplitude of the first cosine expansion function. The results for the dimensionless parameters show that the dependence of the eigencurrents on the frequency f is negligible for $f \lesssim c/2\ell$. In that case, the strip length is smaller than or approximately equal to the wavelength. The eigencurrents depend only weakly on the length scales ℓ and b. For changes of ℓ or b for which β changes at most a factor of 2, the eigencurrents are independent of ℓ.

The independence mentioned above has computational advantages. Having calculated the eigenvalues and eigencurrents for an initial set of geometry parameters from the corresponding moment matrix, we do not need to compute the moment matrix for a new set of geometry parameters to determine the eigenvalues. Instead, we compute the Rayleigh-Ritz quotients

$$\nu_n = \frac{\langle u_n, \mathcal{Z}_{\mathrm{a}} u_n \rangle_{L_2}}{\| u_n \|_{L_2}^2} \,. \tag{5.14}$$

Since the new set of geometry parameters differs from the initial set, the impedance operator $\mathcal{Z}_{\mathrm{a}}$ in these ratios differs from the impedance operator by which the moment matrix for the initial set of expansion functions is calculated. The norms $\| u_n \|_{L_2}$ are known, since we determine the Gram matrix for the eigencurrents with respect to the L_2 inner product. The inner product $\langle u_n, \mathcal{Z}_{\mathrm{a}} u_n \rangle_{L_2}$ is calculated as described in Section 3.3.1, see (3.14) - (3.17). The eigencurrents u_n are described by expansions with respect to the prescribed expansion functions, see (5.4). It would not be efficient to substitute these expansions in $\langle u_n, \mathcal{Z}_{\mathrm{a}} u_n \rangle_{L_2}$ and to calculate all the

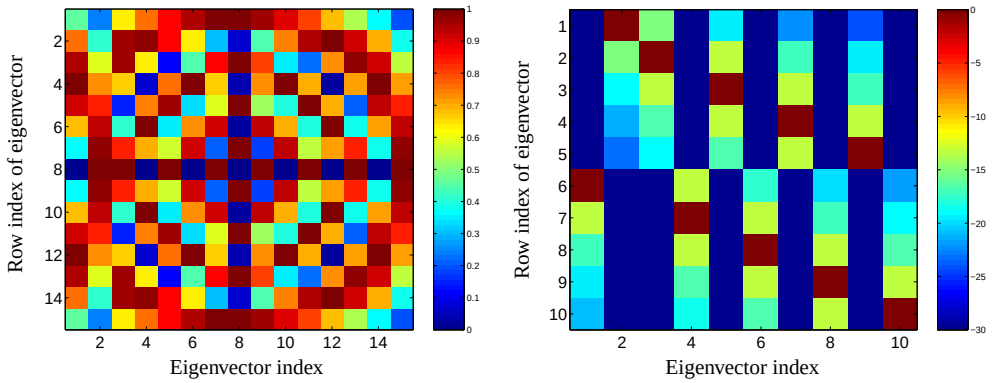

Figure 5.15 Color pattern of the absolute values of the eigenvector components for a strip of half a wavelength in free space. Left: 15 piecewise expansion functions. Right: 5 cosine and 5 sine expansion functions. Eigenvector normalization: maximum component. Parameter values: $2\ell = \lambda$, $\beta = b/\ell = 1/50$.

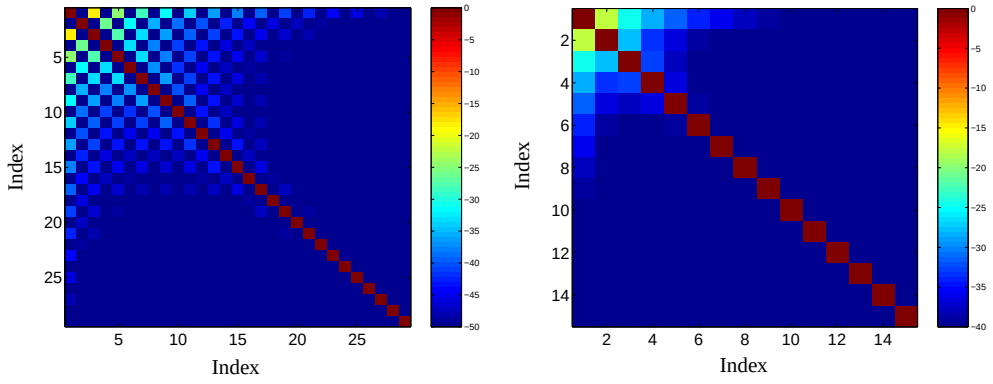

Figure 5.16 Color pattern of the absolute Gram matrix, with L_2 inner product, of the eigencurrents for a strip of half a wavelength in free space (in dB). The eigencurrents are generated with 29 piecewise expansion functions. Left: all inner products. Right: inner products between even eigencurrents. Eigencurrent normalization: L_2 norm. Parameter values: $2\ell = \lambda/2$, $\beta = b/\ell = 1/50$.

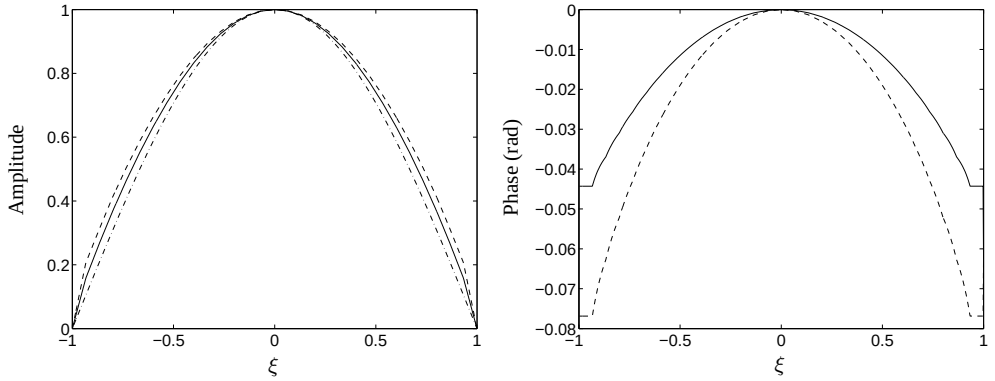

Figure 5.17 Amplitude (left) and phase (right) of the 1st eigencurrent of a strip of half a wavelength with $\beta = b/\ell = 1/50$ (solid curve) and with $\beta = 1/10$ (dashed curve). Eigencurrent normalization: maximum amplitude. Dashed-dotted curve: the function $\cos(\pi\xi/2)$.

inner products $\langle \mathcal{W}\boldsymbol{e}_s, \mathcal{Z}_\mathrm{a}\mathcal{W}\boldsymbol{e}_{s'}\rangle_{L_2}$. In that case, the computation of the eigenvalues requires as much computational effort as the computation of the moment matrix of $\mathcal{Z}_\mathrm{a}$ with respect to the expansion functions $\mathcal{W}\boldsymbol{e}_s$. Therefore, we first sample the eigencurrents and then compute the inner products $\langle u_n, \mathcal{Z}_\mathrm{a}u_n\rangle_{L_2}$. Due to the singular behavior of the kernel F of $\mathcal{Z}_\mathrm{a}$, these sampled eigencurrents may provide erroneous results for the eigenvalues. To prevent such errors, we decompose the kernel F into its logarithmically singular part and its regular part as in Section 3.1. We split $\mathcal{Z}_\mathrm{a}$ accordingly, i.e., $\mathcal{Z}_\mathrm{a} = \mathcal{Z}_{\mathrm{a,sing}} + \mathcal{Z}_{\mathrm{a,reg}}$. The singular part is, up to a factor, independent of the geometry parameters. Therefore, we can compute the inner product $\langle u_n, \mathcal{Z}_{\mathrm{a,sing}}u_n\rangle_{L_2}$ by writing u_n in terms of the expansion functions as mentioned above. The results for the inner products $\langle \mathcal{W}\boldsymbol{e}_s, \mathcal{Z}_{\mathrm{a,sing}}\mathcal{W}\boldsymbol{e}_{s'}\rangle_{L_2}$ follow from the moment matrix of $\mathcal{Z}_{\mathrm{a,sing}}$ for the initial set of geometry parameters. Moreover, we can compute $\langle u_n, \mathcal{Z}_{\mathrm{a,reg}}u_n\rangle_{L_2}$ from the sampled eigencurrents. Finally, the preceding outline to compute the eigenvalues can also be used for more complicated element structures, if the eigencurrents do not change for a certain parameter change and if the kernel is split into a singular, geometry independent, part and a regular part.

5.3 Cycle

5.3.1 Calculational Details

Having chosen a generating subarray in step I on p. 111, we describe the sets E_n in step II as follows. Let $\mathcal{W}$ be the mapping that describes the expansion functions. We construct this mapping in the same way as in Subsection 2.4.3. Let $\mathcal{W} = \mathcal{W}_1 \sqcup \ldots \sqcup \mathcal{W}_{N_\mathrm{sub}}$ and define $\mathcal{W}_q$

by $(\mathcal{W}_q \boldsymbol{e}_n)(\,\cdot\,; q) = \boldsymbol{u}_n^{\mathrm{sub}}$ and $(\mathcal{W}_q \boldsymbol{e}_n)(\,\cdot\,; q') = \mathbf{0}$ for $q \neq q'$ $(n = 1, \ldots, N_{\mathrm{eig}}^{\mathrm{sub}})$. Then, each function $\mathcal{W}_q \boldsymbol{e}_n$ is an eigencurrent of the array in which mutual coupling is ignored. Moreover, this eigencurrent is zero on all subarrays except on the qth subarray, where it equals $\boldsymbol{u}_n^{\mathrm{sub}}$. Hence, the sets E_n are defined by

$$\mathsf{E}_n = \{\, \mathcal{W}_q \boldsymbol{e}_n \,|\, q = 1, \ldots, N_{\mathrm{sub}} \,\}\,. \tag{5.15}$$

The set E is the union of these sets and $\mathcal{W}\mathcal{W}^-$ is the projection onto $\mathrm{ran}(\mathcal{P}) = \mathrm{span}(\mathsf{E})$. Let the eigenvalues ν_n^{sub} corresponding to the sets E_n be indexed such that $|\nu_n^{\mathrm{sub}}| \leq |\nu_{n+1}^{\mathrm{sub}}|$.

To describe the next steps, we assume first that all $N_{\mathrm{eig}}^{\mathrm{sub}}$ eigencurrents of the generating subarray contribute to the mutual coupling between the subarrays. This simplifies steps III and VI. Moreover, step V becomes redundant. Then, the moment matrix of $\mathcal{P}\mathcal{Z}_{\mathrm{a}}\mathcal{P}$ turns into the same form as in (2.131),

$$[\mathcal{W}^- \mathcal{P}\mathcal{Z}_{\mathrm{a}}\mathcal{P}\mathcal{W}] = \begin{pmatrix} [\mathcal{W}_1^- \mathcal{P}\mathcal{Z}_{\mathrm{a}}\mathcal{P}\mathcal{W}_1] & \ldots & [\mathcal{W}_1^- \mathcal{P}\mathcal{Z}_{\mathrm{a}}\mathcal{P}\mathcal{W}_{N_{\mathrm{sub}}}] \\ \vdots & \ddots & \vdots \\ [\mathcal{W}_{N_{\mathrm{sub}}}^- \mathcal{P}\mathcal{Z}_{\mathrm{a}}\mathcal{P}\mathcal{W}_1] & \ldots & [\mathcal{W}_{N_{\mathrm{sub}}}^- \mathcal{P}\mathcal{Z}_{\mathrm{a}}\mathcal{P}\mathcal{W}_{N_{\mathrm{sub}}}] \end{pmatrix}. \tag{5.16}$$

Each block $[\mathcal{W}_p^- \mathcal{P}\mathcal{Z}_{\mathrm{a}}\mathcal{P}\mathcal{W}_q]$ is defined by $[\mathcal{W}_p^- \mathcal{P}\mathcal{Z}_{\mathrm{a}}\mathcal{P}\mathcal{W}_q] = G_p^{-1} Z_{pq}$. Here, G_p is the Gram matrix of $\mathrm{bas}(\mathcal{W}_p)$ with respect to the composite inner product $\langle\,\cdot\,,\,\cdot\,\rangle_{\mathrm{comp}}$ given by (5.3) and

$$Z_{pq}(m,n) = \langle \mathcal{W}_p \boldsymbol{e}_m, \mathcal{P}\mathcal{Z}_{\mathrm{a}}\mathcal{P}\mathcal{W}_q \boldsymbol{e}_n \rangle_{\mathrm{comp}}\,, \tag{5.17}$$

with $m, n = 1, \ldots, N_{\mathrm{eig}}$. Since the functions in $\mathrm{bas}(\mathcal{W}_p)$ are orthonormal with respect to the inner product $\langle\,\cdot\,,\,\cdot\,\rangle_{\mathrm{comp}}$, G_p is the identity matrix for each p. Since the complete Gram matrix $G_{\mathcal{W}} = G(\mathrm{bas}(\mathcal{W}))$ is a block-diagonal matrix with the blocks G_p on the diagonal, this Gram matrix is the identity matrix as well. Hence, we do not need to calculate the Gram matrix in the cycle of the eigencurrent approach, only in the initialization. Moreover, in the cycle, the usual definition and our definition of the moment matrix yield the same result for the moment matrix of $\mathcal{P}\mathcal{Z}_{\mathrm{a}}\mathcal{P}$ with respect to the inner product $\langle\,\cdot\,,\,\cdot\,\rangle_{\mathrm{comp}}$ and the expansion functions in E.

To calculate the matrices Z_{pq}, we deduce first

$$Z_{pq}(m,n) = \langle \mathcal{W}_p \boldsymbol{e}_m, \mathcal{P}\mathcal{Z}_{\mathrm{a}}\mathcal{P}\mathcal{W}_q \boldsymbol{e}_n \rangle_{\mathrm{comp}} = \sum_{q'=1}^{N_{\mathrm{sub}}} \langle (\mathcal{W}_p \boldsymbol{e}_m)(\,\cdot\,; q'), (\mathcal{P}\mathcal{Z}_{\mathrm{a}}\mathcal{W}_q \boldsymbol{e}_n)(\,\cdot\,; q') \rangle_{\mathrm{sub}} = \\ = \langle \boldsymbol{u}_m^{\mathrm{sub}}, (\mathcal{P}\mathcal{Z}_{\mathrm{a}}\mathcal{W}_q \boldsymbol{e}_n)(\,\cdot\,; p) \rangle_{\mathrm{sub}}. \tag{5.18}$$

Next, we interpret $\mathcal{Z}_{\mathrm{a}}$ as composed of the operators $Z_{\mathrm{a},pq}$ such that the operators $\mathcal{Z}_{\mathrm{a},qq}$ describe the coupling of the generating subarray onto itself, i.e., $\mathcal{Z}_{\mathrm{a},qq} = \mathcal{Z}_{\mathrm{a,sub}}$, and the operators $\mathcal{Z}_{\mathrm{a},pq}$ $(p \neq q)$ describe the coupling between the subarrays. Then, we rewrite (5.18) as

$$Z_{pq}(m,n) = \langle \boldsymbol{u}_m^{\mathrm{sub}}, \mathcal{P}_{\mathrm{sub}} \mathcal{Z}_{\mathrm{a},pq}((\mathcal{W}_q \boldsymbol{e}_n)(\,\cdot\,; q)) \rangle_{\mathrm{sub}} = \langle \boldsymbol{u}_m^{\mathrm{sub}}, \mathcal{P}_{\mathrm{sub}} \mathcal{Z}_{\mathrm{a},pq} \boldsymbol{u}_n^{\mathrm{sub}} \rangle_{\mathrm{sub}}\,. \tag{5.19}$$

Since $\mathcal{P}_{\mathrm{sub}}\boldsymbol{u}_n^{\mathrm{sub}} = \boldsymbol{u}_n^{\mathrm{sub}}$ and $\boldsymbol{u}_n^{\mathrm{sub}}$ is an eigenfunction of $\mathcal{P}_{\mathrm{sub}}\mathcal{Z}_{\mathrm{a},qq}\mathcal{P}_{\mathrm{sub}}$ with eigenvalue ν_n^{sub}, we obtain

$$Z_{qq}(m,n) = \nu_n^{\mathrm{sub}}\delta_{mn}. \tag{5.20}$$

Hence, the blocks $Z_{qq} = [\mathcal{W}_q^-\mathcal{P}\mathcal{Z}_{\mathrm{a}}\mathcal{P}\mathcal{W}_q]$ in (5.16) are diagonal matrices with the eigenvalues of $\mathcal{Z}_{\mathrm{a,sub}}$ on the diagonal. For $p \neq q$, we need to calculate the inner products $\langle \boldsymbol{u}_m^{\mathrm{sub}}, \mathcal{P}_{\mathrm{sub}}\mathcal{Z}_{\mathrm{a},pq}\boldsymbol{u}_n^{\mathrm{sub}}\rangle_{\mathrm{sub}}$. In the first cycle after the initialization of the eigencurrent approach, this inner product can be calculated as in (5.7), where $\langle\,\cdot\,,\,\cdot\,\rangle$ is the initializing inner product.

In step IV, the eigenvectors U_m ($m = 1, \ldots, N_{\mathrm{eig}}^{\mathrm{sub}}N_{\mathrm{sub}}$) and the eigenvalues ν_m are determined numerically, see the next sections for details. We write the index $_m$ instead of the index $_{nq}$, because the group division of the eigenvalues and eigenvectors is unknown. The eigenvectors U_m represent the expansion coefficients of the eigencurrents with respect to the expansion functions in $\mathsf{E} = \mathrm{bas}(\mathcal{W})$. As explained in Section 5.1, each eigencurrent will be a linear combination of currents in a certain set E_n plus a perturbation. For each eigencurrent, this set is indicated by the index of the largest absolute component of the corresponding eigenvector, because this component will correspond to a certain current in E_n. Therefore, we determine the groups of eigenvalues and eigencurrents by grouping the eigenvectors U_m according to their largest absolute components. Having determined the groups of eigenvectors $\{U_{nq}\}_{q=1}^{N_{\mathrm{sub}}}$, we group the eigenvalues accordingly. Since we know to which set E_n each eigenvalue group $\{\nu_{nq}\}_{q=1}^{N_{\mathrm{sub}}}$ corresponds, we know also to which eigenvalue ν_n^{sub} each group corresponds. Finally, in Subsection 5.3.2, p. 163, we discuss a case in which the index of the largest absolute eigenvector component is not well-defined and we explain how this case is tackled.

The eigencurrents $\boldsymbol{u}_{nq}$ are defined as in Section 5.2.1 by $U_{nq} = [\mathcal{W}^-\boldsymbol{u}_{nq}]$ and $\boldsymbol{u}_{nq} \in \mathrm{ran}(\mathcal{P})$. Then, $\mathrm{span}(\mathsf{E}^{\mathrm{eig}}) = \mathrm{ran}(\mathcal{P})$, where $\mathsf{E}^{\mathrm{eig}}$ is the set of eigencurrents,

$$\mathsf{E}^{\mathrm{eig}} = \{\boldsymbol{u}_{nq} \,|\, n = 1, \ldots, N_{\mathrm{eig}}^{\mathrm{sub}};\ q = 1, \ldots, N_{\mathrm{sub}}\}\,. \tag{5.21}$$

Each eigencurrent $\boldsymbol{u}_{nq}$ is described by

$$\boldsymbol{u}_{nq} = \sum_{p=1}^{N_{\mathrm{eig}}^{\mathrm{sub}}N_{\mathrm{sub}}} U_{nq}(p,1)\,\mathcal{W}\boldsymbol{e}_p = \sum_{q'=1}^{N_{\mathrm{sub}}}\sum_{n'=1}^{N_{\mathrm{eig}}^{\mathrm{sub}}} [\mathcal{W}_{q'}^-\boldsymbol{u}_{nq}](n',1)\,\mathcal{W}_{q'}\boldsymbol{e}_{n'}\,, \tag{5.22}$$

where the second equality follows from $\mathcal{W}^-\boldsymbol{u}_{nq} = \mathcal{W}_1^-\boldsymbol{u}_{nq} \sqcup \ldots \sqcup \mathcal{W}_{N_{\mathrm{sub}}}^-\boldsymbol{u}_{nq}$. This description can be read in two ways. First, $\boldsymbol{u}_{nq}$ is a linear expansion of currents, or, expansion functions, in E. Second, on each subarray, the eigencurrent $\boldsymbol{u}_{nq}$ is a linear expansion of the eigencurrents $\boldsymbol{u}_{n'}^{\mathrm{sub}}$ ($n' = 1, \ldots, N_{\mathrm{eig}}^{\mathrm{sub}}$), the expansion coefficients being $[\mathcal{W}_{q'}^-\boldsymbol{u}_{nq}](n',1)$ on the q' subarray.

Analogously to the derivation corresponding to (5.5) and (5.6), it can be shown that each eigenvalue ν_{nq} of the moment matrix is an eigenvalue of the operator $\mathcal{P}\mathcal{Z}_{\mathrm{a}}\mathcal{P}$ as well. The new

inner product $\langle \cdot, \cdot \rangle$ in step VI is constructed analogously to the new inner product in step E of the initialization as described in Subsection 5.2.1. For this construction, we describe the set $\mathsf{E}^{\mathrm{eig}}$ by the mapping $\mathcal{U}$ defined by $\mathcal{U} = \mathcal{U}_1 \sqcup \ldots \sqcup \mathcal{U}_{N_{\mathrm{eig}}^{\mathrm{sub}}}$ and $\mathcal{U}_n \boldsymbol{e}_q = \boldsymbol{u}_{nq}$ $(q = 1, \ldots, N_{\mathrm{sub}})$. Then, $\mathsf{E}^{\mathrm{eig}} = \mathrm{bas}(\mathcal{U})$. From (2.115) and the definitions of the concatenation and the adjoint, it follows that the Gram matrix $G_{\mathcal{U}} = G(\mathrm{bas}(\mathcal{U}))$ is composed of the blocks $[\mathcal{U}_m^* \mathcal{U}_n]$, where $m, n = 1, \ldots, N_{\mathrm{eig}}^{\mathrm{sub}}$. The components of these blocks are given by

$$[\mathcal{U}_m^* \mathcal{U}_n](p, q) = \langle \boldsymbol{u}_{mp}, \boldsymbol{u}_{nq} \rangle_{\mathrm{comp}} = U_{mp}^H U_{nq} \,, \tag{5.23}$$

$p, q = 1, \ldots, N_{\mathrm{sub}}$, where the second equality follows from the conclusion above that the Gram matrix $G_{\mathcal{W}}$ is the identity matrix. Notice that $G_{\mathcal{U}}$ has blocks of size $N_{\mathrm{eig}}^{\mathrm{sub}} \times N_{\mathrm{eig}}^{\mathrm{sub}}$, while $G_{\mathcal{W}}$ has blocks of size $N_{\mathrm{sub}} \times N_{\mathrm{sub}}$. The functions $\boldsymbol{y}_{nq}$ in the bi-orthogonal set are described analogously to (5.10). Moreover, their expansion coefficients with respect to the set $\mathrm{bas}(\mathcal{W})$ are described analogously to (5.11),

$$Y_{nq} = [\mathcal{W}^- \boldsymbol{y}_{nq}] = \sum_{n'=1}^{N_{\mathrm{eig}}^{\mathrm{sub}}} \sum_{q'=1}^{N_{\mathrm{sub}}} G_{\mathcal{U}}^{-1}\big((n'-1)N_{\mathrm{eig}}^{\mathrm{sub}} + q', (n-1)N_{\mathrm{eig}}^{\mathrm{sub}} + q\big)\, U_{n'q'} \,. \tag{5.24}$$

Then, $\boldsymbol{y}_{nq}$ is described by (5.22) with $\boldsymbol{u}_{nq}$ and U_{nq} replaced by $\boldsymbol{y}_{nq}$ and Y_{nq}. Analogously to (5.7), the relation between the new inner product $\langle \cdot, \cdot \rangle$ and the composite inner product is given by

$$\langle \boldsymbol{u}_{nq}, \boldsymbol{w} \rangle = \langle \boldsymbol{y}_{nq}, \boldsymbol{w} \rangle_{\mathrm{comp}} \,. \tag{5.25}$$

At the beginning of this section, we assumed that all $N_{\mathrm{eig}}^{\mathrm{sub}}$ eigencurrents contribute to the mutual coupling between the subarrays. If not all eigencurrents contribute, the (reduced) moment matrix is constructed from a selection of the sets E_n. Assume that the sets $\mathsf{E}_1, \ldots, \mathsf{E}_{N_{\mathrm{cpl}}^{\mathrm{sub}}}$, with union $\mathsf{E}^{\mathrm{cpl}}$, contribute to the mutual coupling and that the contribution of the sets $\mathsf{E}_{N_{\mathrm{cpl}}^{\mathrm{sub}}+1}, \ldots, \mathsf{E}_{N_{\mathrm{eig}}^{\mathrm{sub}}}$, with union $\mathsf{E}^{\mathrm{unc}}$, to the mutual coupling is negligible. Then, we can define the corresponding mappings $\mathcal{W}^{\mathrm{cpl}}$ and $\mathcal{W}^{\mathrm{unc}}$ in the same way as we defined $\mathcal{W}$ above. These mappings satisfy $\mathcal{W} = \mathcal{W}^{\mathrm{cpl}} \sqcup \mathcal{W}^{\mathrm{unc}}$. Since the currents in $\mathsf{E}^{\mathrm{unc}}$ do not contribute to the mutual coupling, the complete moment matrix of $\mathcal{P}\mathcal{Z}_{\mathrm{a}}\mathcal{P}$ turns into the block form

$$[\mathcal{W}^- \mathcal{P}\mathcal{Z}_{\mathrm{a}}\mathcal{P}\mathcal{W}] = \begin{pmatrix} [(\mathcal{W}^{\mathrm{cpl}})^- \mathcal{P}\mathcal{Z}_{\mathrm{a}}\mathcal{P}\mathcal{W}^{\mathrm{cpl}}] & 0 \\ 0 & [(\mathcal{W}^{\mathrm{unc}})^- \mathcal{P}\mathcal{Z}_{\mathrm{a}}\mathcal{P}\mathcal{W}^{\mathrm{unc}}] \end{pmatrix} . \tag{5.26}$$

Here, $[(\mathcal{W}^{\mathrm{unc}})^- \mathcal{P}\mathcal{Z}_{\mathrm{a}}\mathcal{P}\mathcal{W}^{\mathrm{unc}}]$ is a diagonal matrix with the eigenvalues ν_n^{sub} corresponding to $\mathsf{E}^{\mathrm{unc}}$ on the diagonal. Moreover, $[(\mathcal{W}^{\mathrm{cpl}})^- \mathcal{P}\mathcal{Z}_{\mathrm{a}}\mathcal{P}\mathcal{W}^{\mathrm{cpl}}]$ is the reduced moment matrix, which is given by (5.16) with $\mathcal{W}$ replaced by $\mathcal{W}^{\mathrm{cpl}}$ and $\mathcal{W}_q$ by $\mathcal{W}_q^{\mathrm{cpl}}$. As above, but with $\mathcal{W}$ replaced by $\mathcal{W}^{\mathrm{cpl}}$, we can determine the set of eigencurrents $\mathsf{E}^{\mathrm{eig}}$ and the corresponding eigenvalues of this

matrix as well as the inner product $\langle \cdot\,, \cdot \rangle_{\rm eig}$ on $\mathrm{span}(\mathsf{E}^{\rm eig}) = \mathrm{span}(\mathsf{E}^{\rm cpl})$ with respect to which the eigencurrents are orthonormal. As in step VI, we extend the set $\mathsf{E}^{\rm eig}$ to $\mathsf{E}^{\rm eig} \cup \mathsf{E}^{\rm unc}$, the linear span of which equals $\mathrm{span}(\mathsf{E}) = \mathrm{ran}(\mathcal{P})$. Each current in this linear span can be written uniquely as a linear combination of currents $\boldsymbol{w}_1 \in \mathrm{span}(\mathsf{E}^{\rm eig})$ and $\boldsymbol{w}_2 \in \mathrm{span}(\mathsf{E}^{\rm unc})$. Then, we can define a new inner product $\langle \cdot\,, \cdot \rangle$ on $\mathrm{ran}(\mathcal{P})$ by

$$\langle \boldsymbol{v}, \boldsymbol{w} \rangle = \langle \boldsymbol{v}_1, \boldsymbol{w}_1 \rangle_{\rm eig} + \langle \boldsymbol{v}_2, \boldsymbol{w}_2 \rangle_{\rm comp}. \tag{5.27}$$

Here, $\boldsymbol{v} = \boldsymbol{v}_1 + \boldsymbol{v}_2$ and $\boldsymbol{w} = \boldsymbol{w}_1 + \boldsymbol{w}_2$, where $\boldsymbol{v}_1, \boldsymbol{w}_1 \in \mathrm{span}(\mathsf{E}^{\rm eig})$ and $\boldsymbol{v}_2, \boldsymbol{w}_2 \in \mathrm{span}(\mathsf{E}^{\rm unc})$. The eigencurrents in $\mathsf{E}^{\rm eig} \cup \mathsf{E}^{\rm unc}$ are orthonormal with respect to this new inner product. Finally, the procedure outlined above can be used as well, if another selection of sets E_n than the first $N_{\rm cpl}^{\rm sub}$ contributes to the mutual coupling between the subarrays. In that case, we re-index the eigenvalues $\nu_n^{\rm sub}$ such that $\mathsf{E}_1, \ldots, \mathsf{E}_{N_{\rm cpl}^{\rm sub}}$ are the sets that contribute to the mutual coupling and such that $\mathsf{E}_{N_{\rm cpl}^{\rm sub}+1}, \ldots, \mathsf{E}_{N_{\rm eig}^{\rm sub}}$ are the sets that do not contribute to the mutual coupling.

Calculation of the Current

Having constructed the eigencurrents of an array and the corresponding new inner product, we calculate the current by the finite expansion (5.2). Here, we explain how the current can be calculated after one cycle of the eigencurrent approach. The calculational details will be used in the next chapter to generate results for line arrays.

To calculate the current, the finite expansion (5.2) is written as

$$\boldsymbol{w}_{\mathcal{P}} = \sum_{n=1}^{N_{\rm eig}^{\rm sub}} \sum_{q=1}^{N_{\rm sub}} \frac{1}{\nu_{nq}} \langle \boldsymbol{u}_{nq}, \mathcal{P}\boldsymbol{v}^{\rm ex} \rangle \, \boldsymbol{u}_{nq}\,. \tag{5.28}$$

In this expression, ν_{nq} and $\boldsymbol{u}_{nq}$ are the eigenvalues and eigencurrents of the array and $\langle \cdot\,, \cdot \rangle$ is the inner product by which the eigencurrents are diagonalized. We consider here the line arrays of the previous sections, for which the eigenvalues ν_{nq} are perturbations of the eigenvalues $\nu_n^{\rm sub}$ of the generating element, i.e., a strip or a ring. As above, we assume that only the first $N_{\rm cpl}^{\rm sub}$ groups of eigencurrents contribute to the mutual coupling in the array. By this assumption, the eigenvalues $\nu_{nq} = \nu_n^{\rm sub}$ for $n > N_{\rm cpl}^{\rm sub}$. Moreover, the eigencurrents of the groups $\{\boldsymbol{u}_{nq}\}_{q=1}^{N_{\rm sub}}$ with index $n > N_{\rm cpl}^{\rm sub}$ are replaced by $N_{\rm sub}$ independent eigencurrents of the decoupled array, i.e., the currents in the sets E_n. As a result, $\boldsymbol{u}_{nq}$ is non-zero on the qth element only, where it equals $u_n^{\rm sub}$, i.e., the nth eigencurrent of the generating element. Then, the finite expansion (5.28) is decomposed into

$$\boldsymbol{w}_{\mathcal{P}} = \sum_{n=1}^{N_{\rm cpl}^{\rm sub}} \sum_{q=1}^{N_{\rm sub}} \frac{1}{\nu_{nq}} \langle \boldsymbol{u}_{nq}, \mathcal{P}\boldsymbol{v}^{\rm ex} \rangle \, \boldsymbol{u}_{nq} + \sum_{n=N_{\rm cpl}^{\rm sub}+1}^{N_{\rm eig}^{\rm sub}} \frac{1}{\nu_n^{\rm sub}} \sum_{q=1}^{N_{\rm sub}} \langle \boldsymbol{u}_{nq}, \mathcal{P}\boldsymbol{v}^{\rm ex} \rangle \, \boldsymbol{u}_{nq}\,. \tag{5.29}$$

Due to the decomposition, the eigencurrents $\boldsymbol{u}_{nq}$ in the first inner product are elements of span($\mathsf{E}^{\mathrm{eig}}$) and the eigencurrents $\boldsymbol{u}_{nq}$ in the second inner product are elements of span($\mathsf{E}^{\mathrm{unc}}$). To compute the inner products in the finite sums of (5.29), we need to write $\mathcal{P}\boldsymbol{v}^{\mathrm{ex}}$ as a linear combination of elements of these two linear spans. In the usual moment method, the projected excitation field $\mathcal{P}\boldsymbol{v}^{\mathrm{ex}}$ is written as

$$\mathcal{P}\boldsymbol{v}^{\mathrm{ex}} = \sum_{q'=1}^{N_{\mathrm{sub}}} \sum_{n'=1}^{N_{\mathrm{exp}}} [\mathcal{W}_{q'}^{-}\boldsymbol{v}^{\mathrm{ex}}](n',1)\, \mathcal{W}_{q'}\boldsymbol{e}_{n'}\,, \tag{5.30}$$

where the mapping $\mathcal{W}$ is defined as in Subsection 2.4.3 with $\mathcal{W}_{q'}\boldsymbol{e}_{n'}$ being the expansion functions on the array. Such an expansion function is non-zero on the q'th element only. Hence, the pth component of $\mathcal{P}\boldsymbol{v}^{\mathrm{ex}}$ is given by

$$(\mathcal{P}\boldsymbol{v}^{\mathrm{ex}})(\,\cdot\,;p) = \sum_{n'=1}^{N_{\mathrm{exp}}} [\mathcal{W}_{p}^{-}\boldsymbol{v}^{\mathrm{ex}}](n',1)\, (\mathcal{W}_{p}\boldsymbol{e}_{n'})(\,\cdot\,;p)\,. \tag{5.31}$$

The functions $(\mathcal{W}_p\boldsymbol{e}_{n'})(\,\cdot\,;p)$ are the expansion functions on the pth element, which are chosen as expansion functions in the initialization of the eigencurrent approach as well. By the relation (5.4) between these functions and the eigencurrents $\boldsymbol{u}_n^{\mathrm{sub}}$ of the generating element, we replace (5.31) by

$$(\mathcal{P}\boldsymbol{v}^{\mathrm{ex}})(\,\cdot\,;p) = \sum_{n'=1}^{N_{\mathrm{eig}}^{\mathrm{sub}}} (U^{-1}[\mathcal{W}_{p}^{-}\boldsymbol{v}^{\mathrm{ex}}])(n',1)\, u_{n'}^{\mathrm{sub}}\,, \tag{5.32}$$

where the matrix U is defined by $U(s,n) = U_n^{\mathrm{sub}}(s,1)$ with U_n^{sub} the eigenvectors corresponding to u_n^{sub}, and $N_{\mathrm{exp}} = N_{\mathrm{eig}}^{\mathrm{sub}}$. We denote the sum of the first $N_{\mathrm{cpl}}^{\mathrm{sub}}$ terms of this series by $(\mathcal{P}\boldsymbol{v}^{\mathrm{ex}})_{\mathrm{eig}}(\,\cdot\,;p)$ and the sum of the other terms by $(\mathcal{P}\boldsymbol{v}^{\mathrm{ex}})_{\mathrm{unc}}(\,\cdot\,;p)$. These sums are elements of span($\mathsf{E}^{\mathrm{eig}}$) and span($\mathsf{E}^{\mathrm{unc}}$), respectively. We substitute the decomposition of $\mathcal{P}\boldsymbol{v}^{\mathrm{ex}}$ in the inner products of (5.29). Using the definition (5.27) of the inner product $\langle\,\cdot\,,\,\cdot\,\rangle$, the relation (5.25) between this inner product and the composite inner product, and the definition (5.3) of the composite inner product, we deduce for $1 \le n \le N_{\mathrm{cpl}}^{\mathrm{sub}}$

$$\begin{aligned}\langle \boldsymbol{u}_{nq}, \mathcal{P}\boldsymbol{v}^{\mathrm{ex}}\rangle = \langle \boldsymbol{u}_{nq}, (\mathcal{P}\boldsymbol{v}^{\mathrm{ex}})_{\mathrm{eig}}\rangle_{\mathrm{eig}} = \langle \boldsymbol{y}_{nq}, (\mathcal{P}\boldsymbol{v}^{\mathrm{ex}})_{\mathrm{eig}}\rangle_{\mathrm{comp}} = \\ = \sum_{p=1}^{N_{\mathrm{sub}}} \langle y_{nq}(\,\cdot\,;p), (\mathcal{P}\boldsymbol{v}^{\mathrm{ex}})_{\mathrm{eig}}(\,\cdot\,;p)\rangle_{\mathrm{sub}}\,.\end{aligned} \tag{5.33}$$

Here, the functions $\boldsymbol{y}_{nq}$ form the bi-orthogonal set corresponding to the eigencurrents $\boldsymbol{u}_{nq}$. These functions are described by (5.22) with $\boldsymbol{u}_{nq}$ and U_{nq} replaced by $\boldsymbol{y}_{nq}$ and Y_{nq}, where Y_{nq} is computed by (5.24). Moreover, since only the first $N_{\mathrm{cpl}}^{\mathrm{sub}}$ eigencurrents of the generating

element contribute to the mutual coupling, $N_{\mathrm{eig}}^{\mathrm{sub}}$ is replaced by $N_{\mathrm{cpl}}^{\mathrm{sub}}$. The mapping $\mathcal{W}$ in (5.22) is not defined as in the excitation vector, but as in the cycle of the eigencurrent approach above. In other words, $\mathcal{W}$ describes $N_{\mathrm{eig}}^{\mathrm{sub}} N_{\mathrm{sub}}$ independent eigencurrents of the decoupled array. To distinguish this mapping from the mapping $\mathcal{W}$ above, we write $\mathcal{W}^{\mathrm{cyc}}$ instead of $\mathcal{W}$. Taking the pth component of $\boldsymbol{y}_{nq}$, we obtain

$$y_{nq}(\,\cdot\,;p) = \sum_{n'=1}^{N_{\mathrm{cpl}}^{\mathrm{sub}}} [(\mathcal{W}_p^{\mathrm{cyc}})^{-}\boldsymbol{y}_{nq}](n',1)\, u_{n'}^{\mathrm{sub}}\,. \tag{5.34}$$

The column $[(\mathcal{W}_p^{\mathrm{cyc}})^{-}\boldsymbol{y}_{nq}]$ consists of the components of Y_{nq} with indices $((p-1)N_{\mathrm{cpl}}^{\mathrm{sub}}+n',1)$, where $n'=1,\ldots,N_{\mathrm{cpl}}^{\mathrm{sub}}$. Substituting (5.34) and (5.31) in (5.33) and using the orthonormality relation $\langle u_m^{\mathrm{sub}}, u_n^{\mathrm{sub}}\rangle_{\mathrm{sub}} = \delta_{mn}$, we arrive at

$$\langle \boldsymbol{u}_{nq}, \mathcal{P}\boldsymbol{v}^{\mathrm{ex}}\rangle = \sum_{p=1}^{N_{\mathrm{sub}}} \sum_{n'=1}^{N_{\mathrm{cpl}}^{\mathrm{sub}}} [(\mathcal{W}_p^{\mathrm{cyc}})^{-}\boldsymbol{y}_{nq}]^{*}(n',1)\; (U^{-1}[\mathcal{W}_p^{-}\boldsymbol{v}^{\mathrm{ex}}])(n',1)\,. \tag{5.35}$$

The components of $[\mathcal{W}_p^{-}\boldsymbol{v}^{\mathrm{ex}}]$ are given in Chapter 4, while the components of U and $[(\mathcal{W}_p^{\mathrm{cyc}})^{-}\boldsymbol{y}_{nq}]$ are computed as in the initialization and the cycle of the eigencurrent approach in Chapter 5. For $N_{\mathrm{cpl}}^{\mathrm{sub}}+1 \le n \le N_{\mathrm{eig}}^{\mathrm{sub}}$, we deduce

$$\langle \boldsymbol{u}_{nq}, \mathcal{P}\boldsymbol{v}^{\mathrm{ex}}\rangle = \langle \boldsymbol{u}_{nq}, (\mathcal{P}\boldsymbol{v}^{\mathrm{ex}})_{\mathrm{unc}}\rangle_{\mathrm{comp}} = \sum_{p=1}^{N_{\mathrm{sub}}} \langle u_{nq}(\,\cdot\,;p), (\mathcal{P}\boldsymbol{v}^{\mathrm{ex}})_{\mathrm{unc}}(\,\cdot\,;p)\rangle_{\mathrm{sub}}\,. \tag{5.36}$$

By $u_{nq}(\,\cdot\,;p) = \delta_{pq} u_n^{\mathrm{sub}}$ for $N_{\mathrm{cpl}}^{\mathrm{sub}}+1 \le n \le N_{\mathrm{eig}}^{\mathrm{sub}}$ and $\langle u_m^{\mathrm{sub}}, u_n^{\mathrm{sub}}\rangle_{\mathrm{sub}} = \delta_{mn}$, we obtain

$$\begin{aligned}\langle \boldsymbol{u}_{nq}, \mathcal{P}\boldsymbol{v}^{\mathrm{ex}}\rangle &= \langle u_n^{\mathrm{sub}}, (\mathcal{P}\boldsymbol{v}^{\mathrm{ex}})_{\mathrm{unc}}(\,\cdot\,;p)\rangle_{\mathrm{sub}} = \\ &= \sum_{n'=N_{\mathrm{cpl}}^{\mathrm{sub}}+1}^{N_{\mathrm{eig}}^{\mathrm{sub}}} (U^{-1}[\mathcal{W}_p^{-}\boldsymbol{v}^{\mathrm{ex}}])(n',1)\, \langle u_n^{\mathrm{sub}}, u_{n'}^{\mathrm{sub}}\rangle_{\mathrm{sub}} = (U^{-1}[\mathcal{W}_p^{-}\boldsymbol{v}^{\mathrm{ex}}])(n,1)\,.\end{aligned} \tag{5.37}$$

Having computed the inner products (5.35) and (5.37) for $1 \le n \le N_{\mathrm{cpl}}^{\mathrm{sub}}$ and $N_{\mathrm{cpl}}^{\mathrm{sub}}+1 \le n \le N_{\mathrm{eig}}^{\mathrm{sub}}$, respectively, we can evaluate the series (5.29). We express the eigencurrents $\boldsymbol{u}_{nq}$ into the eigencurrents u_n^{sub} of the generating element by (5.22) and, then, we express the eigencurrents u_n^{sub} into the initializing expansion functions by (5.4). In this way, we find the expansion coefficients of the currents on the elements with respect to the initializing expansion functions.

5.3.2 Uniform Line Arrays of Rings

In this section, we consider one cycle of the eigencurrent approach for uniform line arrays of rings. These line arrays are described in Section 3.5. Choosing a single ring as the generating

subarray, we know the corresponding eigencurrents and, hence, we do not need to carry out the initialization of this approach. Since we proceed from a single ring to the entire line array, the number of subarrays N_{sub} equals the number of rings N_{el}. Moreover, since we index the eigenvalues and eigencurrents of a generating subarray such that $|\nu_n^{\mathrm{sub}}| \leq |\nu_{n+1}^{\mathrm{sub}}|$, the moment matrix of the eigencurrent approach is, up to a row and column permutation, the same as the moment matrix constructed in Subsection 3.3.2. We compute the eigenvalues and eigenvectors of this moment matrix in the same way as in the initialization for a single ring. Table 5.5 shows the maxima of the relative errors (5.13) for several line arrays of rings. For each number of

Table 5.5 Maximum relative errors (5.13) for line arrays generated from a single ring in free space. Parameter values of the generating ring: $ka = \pi/3$, $\beta = 3/100$, $\psi = 0$, $N_{\cos} = 4$, $N_{\sin} = 0$. Spacing of the line array: $d = \lambda/2$.

N_{sub}	Size moment matrix	Max. rel. error
5	20	$1.2 \cdot 10^{-14}$
10	40	$1.7 \cdot 10^{-14}$
20	80	$1.8 \cdot 10^{-14}$
40	160	$2.4 \cdot 10^{-14}$
80	320	$3.7 \cdot 10^{-14}$
160	640	$5.2 \cdot 10^{-14}$

N_{sub}, these maxima are attained for the lowest (absolute) eigenvalues. Moreover, the maxima increase more slowly with the moment matrix size than the maxima for the strip in Table 5.3. This observation is explained as follows. The moment matrix of a strip with piecewise functions is less (block-)diagonally dominant than the moment matrix of a line array of rings. Moreover, both the moment matrix of a strip with entire-domain functions and the moment matrix of a line array of rings is diagonally dominant, except for the diagonal component corresponding to the self coupling of $\cos\varphi$.

Throughout this section, we will use only two generating ring geometries, except for a part in which we investigate the dependence of the (array) eigencurrents on the generating ring eigencurrents. These geometries are the ring geometry of Table 5.5 and the same ring geometry but in a half space with $h/a = 6/5$. The corresponding eigenvalues and eigencurrents are given in Table 5.2.

Like the centers of the strips in Figure 3.2, the centers of the rings are positioned on the x-axis. In other words, the line-array axis coincides with the x-axis. Moreover, the orientation of the local coordinate systems on the rings is described by $\psi = 0$, see Figure 2.5. Then, the cosine and sine eigencurrents of the generating ring are symmetric and anti-symmetric, respectively, with respect to the line-array axis. Since a symmetric current does not couple with an anti-symmetric current, the cosine eigencurrents generate symmetric array eigencurrents with respect

to the line-array axis, while the sine eigencurrents generate anti-symmetric array eigencurrents. We will consider the anti-symmetric eigencurrents, as well as other choices of ψ, in the part about the dependence of the (array) eigencurrents only.

Spread of Eigenvalue Groups in Relation to Mutual Coupling Aspects

We determine the groups of eigenvalues $\{\nu_{nq}\}_{q=1}^{N_{\rm sub}}$ and the corresponding eigencurrents as described in Subsection 5.3.1. To determine which groups contribute to the mutual coupling in a line array, we compute for each group, with index n, the maximum and minimum of the absolute perturbations $\{|\epsilon_{nq}|\}_{q=1}^{N_{\rm sub}}$, where $\nu_{nq} = \nu_n^{\rm sub}(1+\epsilon_{nq})$, as introduced in Section 5.1, p. 106. These maxima and minima are an indication of the spread of the eigenvalues in the groups. Figure 5.18 shows that for line arrays with spacings $d = \lambda/2$ and $d = 3\lambda/5$, both in free space and in a half space, the spread of the eigenvalues decreases with the group index n. We expect that only the spreads of the first two groups are significant. This expectation is not only based on the decrease of the spread with the index n, but also on the increase of the eigenvalues $\nu_n^{\rm sub}$ of the generating ring. Due to the second property, the eigenvalues of groups with larger indices not only contribute less to the current on the line array, the spreads of these groups are also less significant than the spreads of the groups with smaller indices. Based on this expectation, we can determine the eigenvalues of the first two groups from a reduced moment matrix with only the first two eigencurrents of a single ring in free space or in a half space, see also step V of the eigencurrent approach, p. 111. The eigenvalues of the third and fourth groups can be set equal to the corresponding eigenvalues of the generating ring. This reduces the CPU time considerably, see Section 6.1 for details.

Let us consider the first two groups. Figure 5.18 (upper figures) shows that the maxima of the absolute perturbations increase with the number of elements, while the minima decrease. For all 4 line array geometries, the minima become approximately constant for $N_{\rm sub} \geq 10$, but none of the corresponding constants is zero. For the first group, these constants vary between 0.023 and 0.126 and for the second group, they vary between 0.007 and 0.026. Hence, the eigenvalues of the first and second groups differ all from the eigenvalues $\nu_n^{\rm sub}$ ($n = 1, 2$). In a half space, the maxima become constant for about $N_{\rm sub} \geq 20$. In free space, the maxima do not show this property, but for $d = 3\lambda/5$ they increase slowly. These results suggest that rings separated more than 10 or 20 times d do not show mutual coupling in the first and/or second eigencurrent(s) of the generating ring for specific line array geometries. Hence, we do not need to compute the moment-matrix components that describe the corresponding mutual coupling. We can use this observation in the eigencurrent approach as follows. The behavior of the eigenvalues of smaller line arrays, say with 10 or 20 elements, indicates for which groups the maximum and minimum of the absolute perturbations become constant as a function of the number of elements. In this way, the analysis of smaller (line) arrays provides information about the moment-matrix components to be computed for larger (line) arrays, see Subsection 6.3.3 for details.

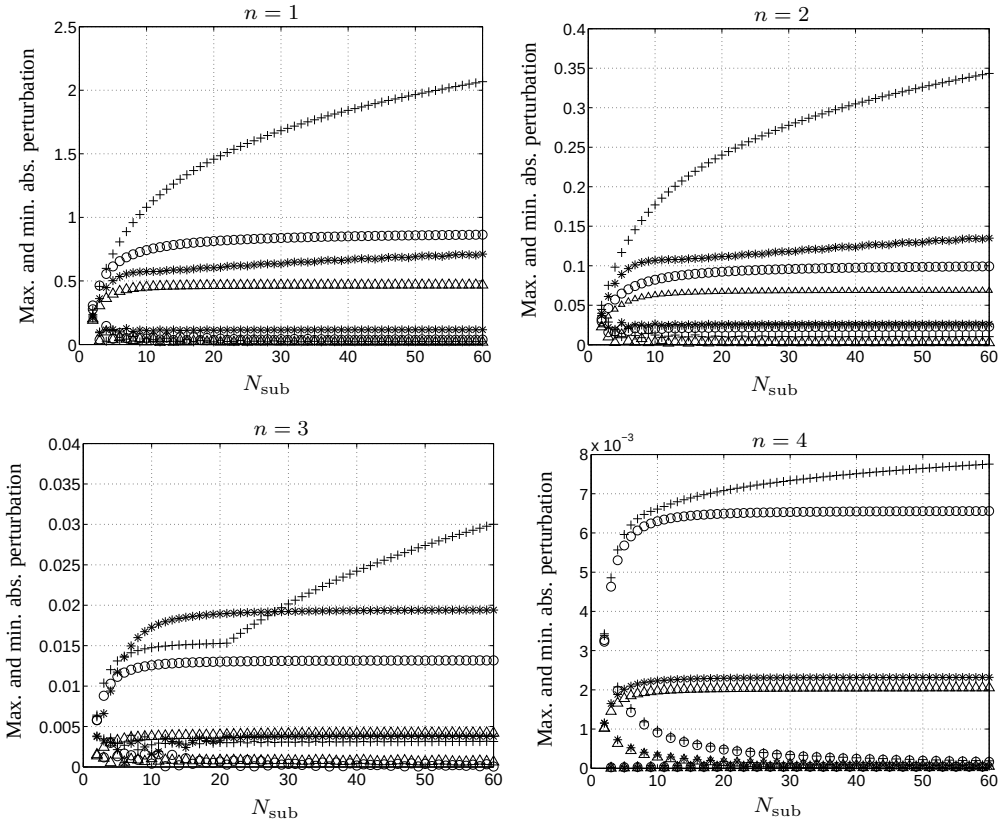

Figure 5.18 Maxima and minima of the absolute perturbations $\{|\epsilon_{nq}|\}_{q=1}^{N_{\mathrm{sub}}}$ of the first four groups of eigenvalues as a function of N_{sub}, i.e., the number of rings, for 4 different line array geometries. From upper left to lower right: group $n = 1$ to group $n = 4$. The spacing d is either $\lambda/2$ ($+$, $\circ$) or $3\lambda/5$ ($*$, $\triangle$). The generating ring is either in free space ($+$, $*$) or in a half space with $h/a = 6/5$ ($\circ$, $\triangle$). Parameter values: $N_{\mathrm{cpl}}^{\mathrm{sub}} = 4$, $ka = \pi/3$, $\beta = 3/100$, $\psi = 0$, $N_{\cos} = 4$, $N_{\sin} = 0$.

To investigate the spread of the eigenvalues as a function of the spacing, we compute the maximum and minimum of the absolute perturbations $\{|\epsilon_{nq}|\}_{q=1}^{N_{\mathrm{sub}}}$ for each group as a function of the spacing. Figure 5.19 (left) shows that for the first groups of line arrays of 5, 10, 20, and 40 rings in free space, these maxima and minima behave similarly. They decrease non-monotonically. Moreover, the maxima show local 'curve maxima' and 'curve minima' in the points $q\lambda/2$ ($q = 1, 2, 3, 4$) and $(q + 1/2)\lambda/2$ ($q = 1, 2, 3$), while for the minima, these points are interchanged. Figure 5.19 (right) shows that in a half space, the 'curve maxima' are much

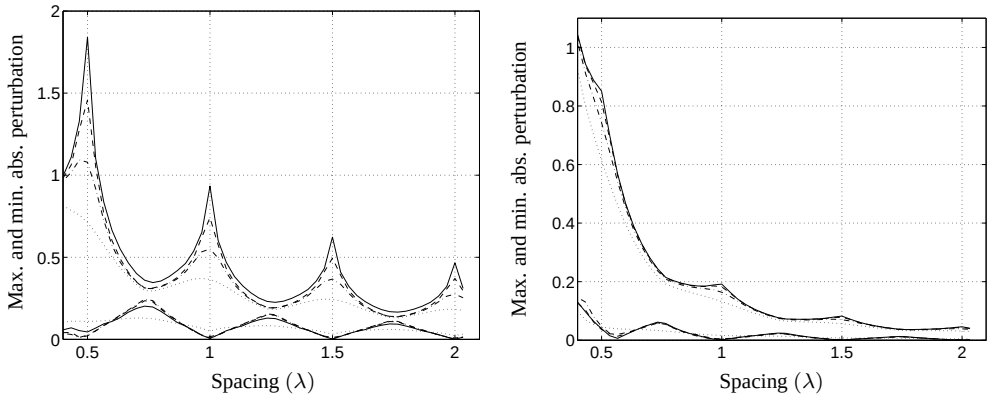

Figure 5.19 Maxima and minima of the absolute perturbations $\{|\epsilon_{1q}|\}_{q=1}^{N_{\rm sub}}$ of the 1st group of eigenvalues as a function of the spacing for line arrays of 5 (dotted curve), 10 (dashed-dotted curve), 20 (dashed curve), and 40 (solid curve) rings. Left: free space. Right: half space with $h/a = 6/5$. Parameter values: $N_{\rm cpl}^{\rm sub} = 4$, $ka = \pi/3$, $\beta = 3/100$, $\psi = 0$, $N_{\cos} = 4$, $N_{\sin} = 0$.

less pronounced and the decrease is much sharper. Both in free space and in a half space, the maxima and minima of the other three groups show similar behavior, but the magnitudes are lower. The 'curve maxima' and 'curve minima' of the maximum and minimum absolute perturbations, respectively, are related to constructive interference of the electromagnetic fields generated by the rings. In contrast, the 'curve maxima' and 'curve minima' of the minimum and maximum absolute perturbations, respectively, are related to destructive interference of the electromagnetic fields generated by the rings.

Description of Eigencurrents

To illustrate how the eigencurrents of line arrays of rings are described, we consider line arrays of 15 and 29 rings with half a wavelength spacing generated from a ring in free space. In the construction of the moment matrix, we take only the first two eigencurrents of the generating ring into account, i.e., $u_1^{\rm sub}(\varphi) = \cos\varphi$ and $u_2^{\rm sub}(\varphi) = 1$. Figure 5.20 shows the curves generated by the eigenvalues of the first and second groups in the complex plane, both for 15 and 29 rings. We conclude that each group has one curve in the complex plane, independently of the number of rings. This statement is not only valid for the first and second groups, but it is valid for each group. Near the eigenvalue ν_{n1}, the 'density' of the eigenvalues is the highest. We will discuss the behavior of the eigenvalues in detail later on. We index the eigenvalues of each group along the curve they generate in the complex plane by means of a nearest neighbor search starting at the ends indicated by the number 1. At the end of this subsection, we explain

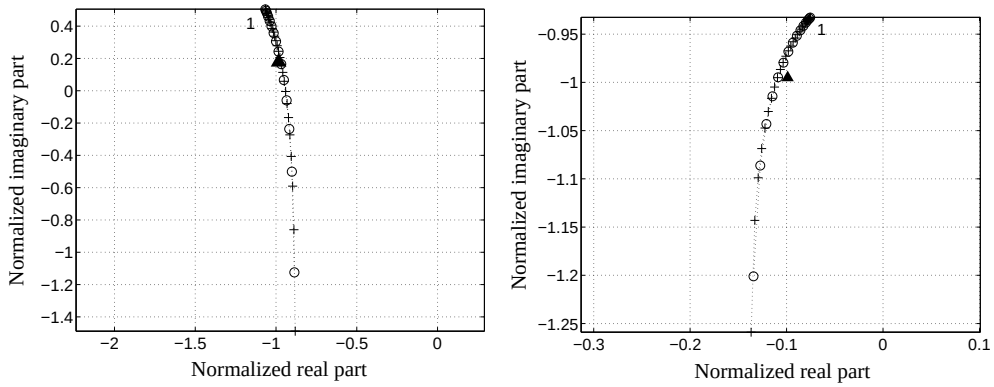

Figure 5.20 Normalized eigenvalues of the 1st (left) and 2nd group (right) of line arrays of 15 ($\circ$) and 29 ($+$) rings in free space and the corresponding normalized eigenvalues ($\blacktriangle$) of a single ring, i.e., $\nu_n^{\rm sub}$ ($n = 1, 2$). The numbers 1 indicate the first eigenvalues of the curves, i.e., ν_{n1}. Normalization: $|\nu_n^{\rm sub}|$. Parameter values: $d = \lambda/2$, $N_{\rm cpl}^{\rm sub} = 2$, $ka = \pi/3$, $\beta = 3/100$, $\psi = 0$, $N_{\cos} = 2$, $N_{\sin} = 0$.

how these ends are determined.

Figure 5.23 (left) shows the absolute values of the eigenvector components for a line array of 15 rings. The first 15 columns of the color pattern belong to the eigenvectors $\{U_{1q}\}_{q=1}^{15}$ of the first group and the last 15 columns belong to the eigenvectors $\{U_{2q}\}_{q=1}^{15}$ of the second group. The pattern confirms the conjecture in Section 5.1, p. 105, that the eigencurrents of $\{\boldsymbol{u}_{nq}\}_{q=1}^{15}$ of the nth group ($n = 1, 2$) are a linear combination of currents in E_n plus a perturbation. This is observed as follows. The eigenvector components $(2q'-1, 1)$ ($q' = 1, \ldots, 15$) are the expansion coefficients of the eigencurrents with respect to the currents in E_1, while the eigenvector components $(2q', 1)$ are the expansion coefficients of the eigencurrents with respect to the currents in E_2. The figure shows that in the first group, the eigenvector components corresponding to the currents in E_1 are much larger than the eigenvector components corresponding to the currents in E_2. The second group exhibits the same property with E_1 and E_2 interchanged. These results confirm the conjecture.

Instead of considering the eigenvectors as the expansion coefficients of the (array) currents in E_1 and E_2, we can also interpret the eigenvectors per ring. On each of the 15 rings, an eigencurrent $\boldsymbol{u}_{nq}$ is a linear combination of the eigencurrents $u_1^{\rm sub}$ and $u_2^{\rm sub}$ of a single ring. The coefficients of $u_1^{\rm sub}$ and $u_2^{\rm sub}$ on the q'-th ring are the eigenvector components $(2q'-1, 1)$ and $(2q', 1)$. Figure 5.23 (right) shows the absolute coefficient of $u_1^{\rm sub}$ on each ring for the eigencurrents $\{\boldsymbol{u}_{1q}\}_{q=1}^{15}$ of the first group. In other words, the figure shows the absolute eigenvector components $(2q'-1, 1)$ ($q' = 1, \ldots, 15$) for the first 15 eigenvectors in Figure 5.23 (left). Comparing Figure 5.23 (right) with Figure 5.8, which shows the pattern of the absolute components

of the eigenvectors of a single strip with 15 piecewise expansion functions, we come to the surprising observation that the generated patterns are almost the same. In general, we observed that the coefficients of the dominant single-ring eigencurrent in the nth group of eigencurrents, i.e., u_n^{sub}, exhibit the same patterns as the eigenvectors of a strip with piecewise expansion functions. Figure 5.21 clarifies this result in the following way. The eigenvectors of a single strip with piecewise expansion functions represent the expansion coefficients of the eigencurrents of a strip with respect to these functions. The expansion coefficients are one-to-one related to heights of the, triangular-shaped, piecewise functions. Figure 5.21 shows the pattern of these functions for the first eigencurrent of the first group. The height of each triangle corresponds to a coefficient of u_n^{sub} in the nth group of (array) eigencurrents, as indicated in the figure.

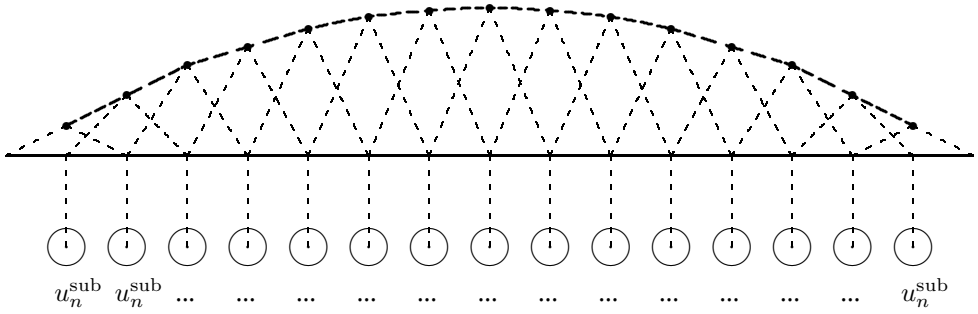

Figure 5.21 Schematic representation of the correspondence between the absolute coefficients of u_n^{sub} in the eigencurrents of the nth group of a line array of rings and the expansion coefficients of the eigencurrents of a single strip with piecewise expansion functions.

To go into more detail, Figure 5.22 (left) shows a comparison of

- the absolute coefficient of u_1^{sub} on each ring for the first and second eigencurrents of the first group,
- the absolute coefficient of u_2^{sub} on each ring for the first and second eigencurrents of the second group,
- the absolute expansion coefficients of the first and second eigencurrents of a single strip with 15 piecewise functions.

In the first two cases, the ring indices are transformed to the interval $[-1, 1]$ according to $q' \rightarrow 2q'/(N_{\mathrm{sub}} + 1)$, where N_{sub} is the number of rings. In the third case, the indices m of the expansion coefficients (or, eigenvector components) are transformed as in Figure 5.13. As in Figure 5.9, the dashed and dotted lines in Figure 5.22 are only meant for visualization

of the patterns. Figure 5.22 (right) shows a similar comparison, but the first and second eigencurrents are replaced by the 15th and 14th eigencurrents. The figures confirm that the absolute coefficients of $u_n^{\rm sub}$ in the eigencurrents of the nth group show the same behavior as the absolute expansion coefficients of the eigencurrents of a single strip with $N_{\rm sub}$ piecewise functions. Quantitatively speaking the differences are larger for eigencurrents with larger indices in a group

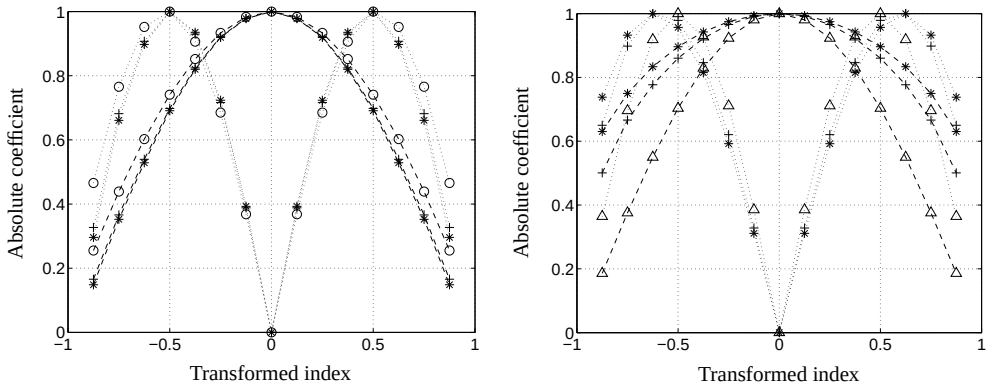

Figure 5.22 Left: for $n = 1$ (+) and $n = 2$ (∗), the absolute coefficients of $u_n^{\rm sub}$ in the 1st (dashed) and 2nd (dotted) eigencurrent of the nth group for a line array of 15 rings. Moreover, the absolute expansion coefficients of the 1st (∘, dashed) and 2nd (∘, dotted) eigencurrent of a strip with 15 piecewise expansion functions. Right: as left, but for the 15th (dashed) and the 14th (dotted) eigencurrent (symbol ∘ replaced by △). Eigencurrent normalization: maximum coefficient. Parameter values of the line array of rings as in Figure 5.20. Parameter values of the strip: $2\ell = \lambda/2$, $\beta = b/\ell = 1/50$.

than for eigencurrents with smaller indices in that group. The same results are obtained for 29 rings. The color pattern in Figure 5.24 (left) for the absolute coefficients of $u_1^{\rm sub}$ in the eigencurrents of the first group, i.e., $\{\boldsymbol{u}_{1q}\}_{q=1}^{29}$, is almost the same as the color pattern in Figure 5.11 (left), which shows the absolute expansion coefficients of the eigencurrents of a single strip with 29 piecewise expansion functions.

For a line array of 15 rings, the coefficients of $u_n^{\rm sub}$ in the eigencurrents of the nth group show also the same phase behavior as the expansion coefficients of the eigencurrents on a strip with 15 piecewise functions shown in Figure 5.8 (right). In other words, the coefficients of $u_n^{\rm sub}$ in the qth eigencurrent of the nth group, i.e., $\boldsymbol{u}_{nq}$, show $q-1$ phase reversals as a function of the ring index. As a result, each eigencurrent can be multiplied by a complex factor such that these coefficients have a negligible imaginary part. Then, the dominant part of each eigencurrent is real valued, while its complex nature is incorporated in the perturbation. An example is given at the end of this subsection.

Based on the preceding results, we state similar general conclusions as the general conclu-

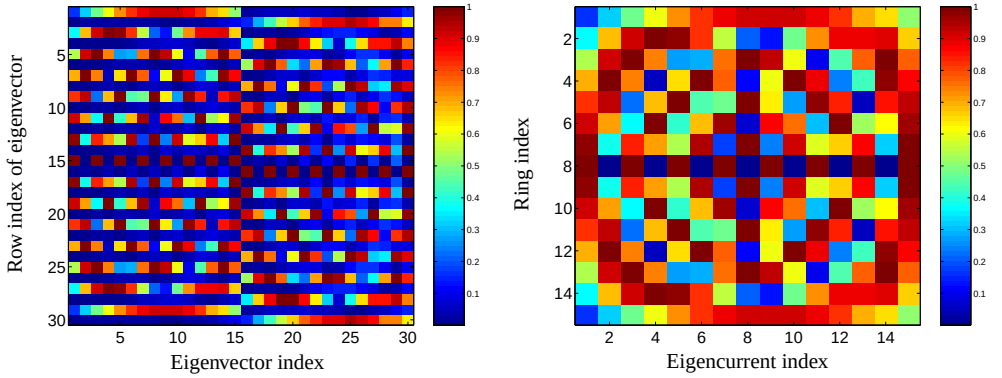

Figure 5.23 Left: color pattern of the absolute eigenvector components for a line array of 15 rings with two eigencurrents of the generating ring. Right: color pattern of the absolute coefficients of $u_1^{\rm sub}$ on the rings for the eigencurrents of the 1st group. Eigenvector normalization: maximum component. Parameter values as in Figure 5.20.

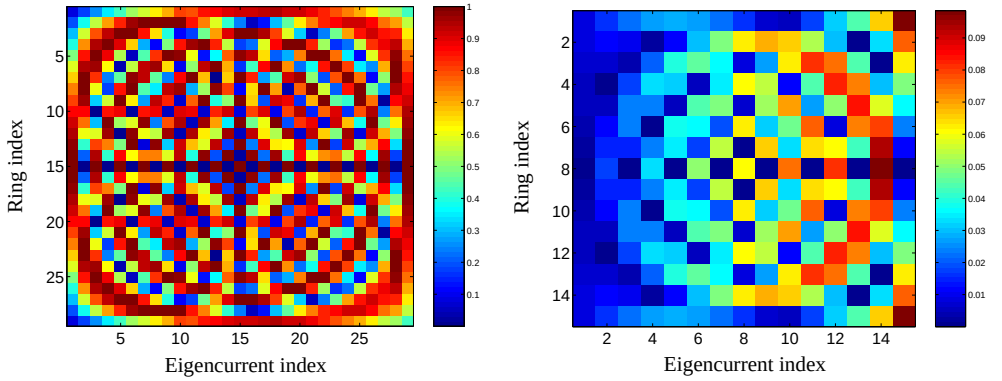

Figure 5.24 Left: color pattern of the absolute coefficients of $u_1^{\rm sub}$ in the eigencurrents of the 1st group for a line array of 29 rings. Right: color pattern of the absolute coefficients of $u_2^{\rm sub}$ in the eigencurrents of the 1st group for a line array of 15 rings. Eigencurrent normalization: maximum coefficient. Parameter values as in Figure 5.20.

sions on p. 128 for the eigenvectors of a single strip. Consider the nth group $\{\boldsymbol{u}_{nq}\}_{q=1}^{N_{\rm sub}}$ of eigencurrents, where $n = 1, \ldots, N_{\rm cpl}^{\rm sub}$.

1. For each $q = 1, \ldots, N_{\rm sub}$, the absolute coefficients of $u_n^{\rm sub}$ in the eigencurrent $\boldsymbol{u}_{nq}$ and the absolute coefficients of $u_n^{\rm sub}$ in the eigencurrent $u_{n(N_{\rm sub}+1-q)}$ show the same patterns.

2. For each q, the coefficients of $u_n^{\rm sub}$ in the eigencurrent $\boldsymbol{u}_{nq}$ show $\min\{q, N_{\rm sub} + 1 - q\}$ absolute maxima and $q - 1$ phase reversals.

Summarizing, we showed that the coefficients of the dominant single-ring eigencurrent in each group of eigencurrents of a line array of rings and the expansion coefficients of the eigencurrents of a single strip with piecewise functions generate the same patterns. There is no doubt that a strip is an entire object. Discretization of the strip by piecewise functions does not affect this statement, because in Section 5.2.3, we showed that the eigencurrents obtained by piecewise and entire functions are the same. Then, line arrays and strips generating the same patterns clearly indicate that arrays are entire objects, not collections of separate elements.

Let us return to the line array of 15 rings. Up to now, we have considered the dominant behavior of the eigencurrents in the groups. As mentioned above, the perturbations of the first group are described by the expansion coefficients of the eigencurrents with respect to the currents in E_2, while the perturbations of the second group are described by the expansion coefficients of the eigencurrents with respect to the currents in E_1. If the perturbations are interpreted per ring, the perturbations of the first group are described by the coefficients of u_2^{sub} in the eigencurrents $\{\boldsymbol{u}_{1q}\}_{q=1}^{15}$, while the perturbations of the second group are described by the coefficients of u_1^{sub} in the eigencurrents $\{\boldsymbol{u}_{2q}\}_{q=1}^{15}$. Figure 5.24 (right) shows the absolute coefficients of u_2^{sub} in the eigencurrents of the first group, or, in other words, it shows the absolute eigenvector components $(2q', 1)$ ($q' = 1, \ldots, 15$) of the first 15 eigenvectors in Figure 5.23 (left). We observe that the perturbation increases with the eigencurrent index q up to 0.1. A similar pattern is obtained for the absolute coefficients of u_1^{sub} in the eigencurrents of the second group with a maximum absolute coefficient of 0.2 instead of 0.1.

To go into more detail, Figure 5.25 shows the absolute values and the phases of the coefficients of u_1^{sub} and u_2^{sub} in the first, second, fifth, and 15th eigencurrent of the first group. For all 4 eigencurrents, we observe that not only the coefficients of the dominant single-ring eigencurrent u_1^{sub} generate patterns, but as well the coefficients of u_2^{sub}, which describe the perturbations. The absolute coefficients of u_2^{sub} have maxima and minima at rings, where the coefficients of u_1^{sub} have minima and maxima, respectively. For the first, second, and fifth eigencurrent, the phases of the coefficients of u_2^{sub} show one phase reversal more than the coefficients of u_1^{sub}, while for the 15th eigencurrent, they show one phase reversal less. Further investigation revealed that the coefficients of u_2^{sub} show q phase reversals for $q \leq 10$ and $q - 2$ phase reversals for $11 \leq q \leq 15$. More general, the coefficients of u_2^{sub} in the eigencurrent $\boldsymbol{u}_{1q}$ show q phase reversals for $q \approx \lfloor 2N_{\mathrm{sub}}/3 \rfloor$ and $q - 2$ phase reversals for larger values of q. In the second group, we observe the same behavior as above for the coefficients that describe the perturbations in this group, i.e., the coefficients of u_1^{sub}.

Figure 5.26 describes a situation in which more single-ring eigencurrents are taken into account, $N_{\mathrm{cpl}}^{\mathrm{sub}} = 6$ to be precise. In this case, the figure shows that the absolute coefficients of all non-dominant single-ring eigencurrents in the first eigencurrent of the first and second groups generate either the same pattern as the dominant single-ring eigencurrent or the same pattern as the coefficients of u_2^{sub} in the preceding results. Further investigation revealed that the

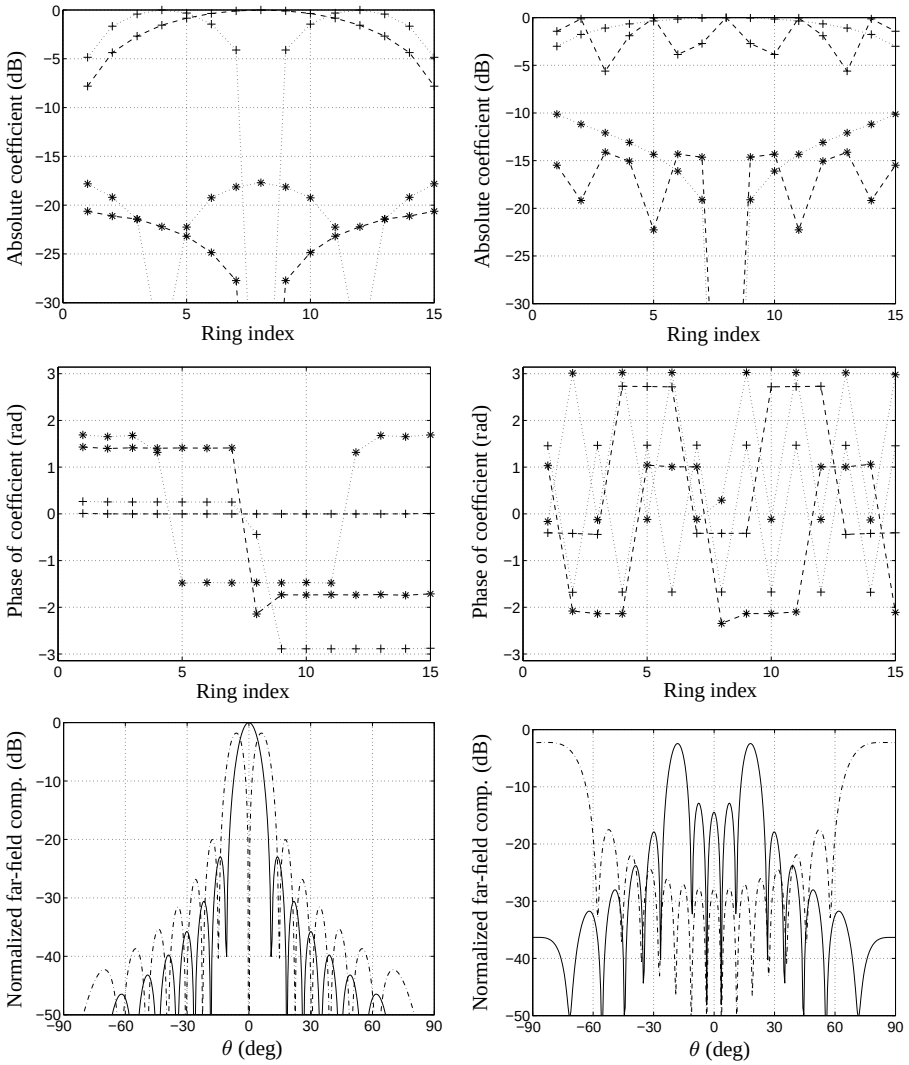

Figure 5.25 Left: absolute values (in dB) and phases of the coefficients of u_1^{sub} $(+)$ and u_2^{sub} $(*)$ in the 1st (dashed curves) and 2nd eigencurrent (dotted curves) of the 1st group for a line array of 15 rings, and the corresponding normalized absolute ϕ-components (in dB) of the electric far field in the plane $\phi = 0$ (dashed $\rightarrow$ solid and dotted $\rightarrow$ dashed-dotted). Right: as left, but for the 5th and 15th eigencurrents. Eigencurrent normalization: maximum coefficient. Far-field normalization: maximum absolute ϕ-component of the 1st eigencurrent. Parameter values as in Figure 5.20.

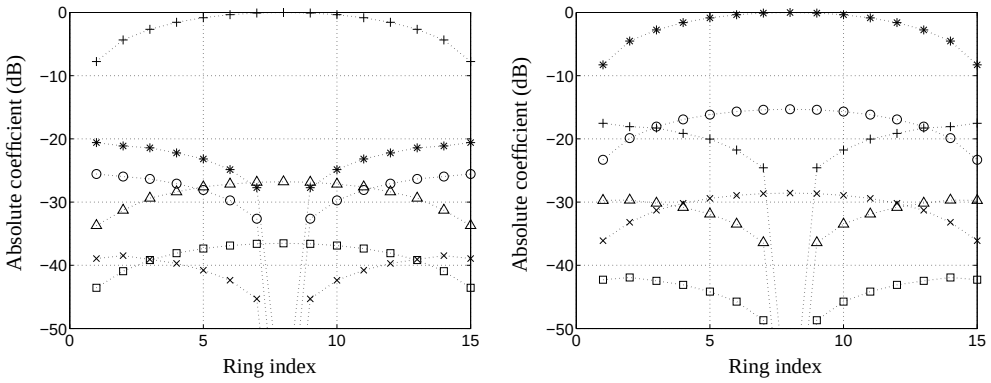

Figure 5.26 Absolute coefficients (in dB) of the single-ring eigencurrents $u_1^{\rm sub}$ (+), $u_2^{\rm sub}$ (∗), $u_3^{\rm sub}$ (○), $u_4^{\rm sub}$ (△), $u_5^{\rm sub}$ (×), and $u_6^{\rm sub}$ (□) in the 1st eigencurrent of the 1st group ($\boldsymbol{u}_{11}$, left) and in the 1st eigencurrent of the 2nd group ($\boldsymbol{u}_{21}$, right). Eigencurrent normalization: maximum coefficient. Parameter values as in Figure 5.20, but with $N_{\cos} = 6$.

absolute coefficients of $u_m^{\rm sub}$ and $u_{m'}^{\rm sub}$ in a certain eigencurrent $\boldsymbol{u}_{nq}$ generate the same pattern, if the eigencurrents $u_m^{\rm sub}$ and $u_{m'}^{\rm sub}$ have the same even or odd symmetry with respect to the line parallel to the y-axis through the center of the ring. We note that the rings are all positioned on the x-axis.

The two figures in the last row of Figure 5.25 show the electric far fields in the xz-plane in Figure 3.2, i.e., the plane $\phi = 0$, for the first, second, fifth, and 15th eigencurrent of the first group. These far fields are determined by the far-field expressions for arrays of rings in Appendix C. The spherical angles (θ, ϕ) are defined by (C.4), where θ is the angle with respect to the z-axis. The first eigencurrent induces a broadside beam with a maximum side-lobe level of about -23 dB. This low sidelobe level is due to the cosine-like pattern of the corresponding absolute coefficients of the dominant single-ring eigencurrent $u_1^{\rm sub}$, see Figure 5.25 (first row, first column, dashed curve). The pattern can be interpreted as an amplitude taper on the line array. The corresponding uniform phase distribution can be interpreted as a phase taper on the line array. The second eigencurrent induces two main lobes, which are symmetrically positioned around 0°. In contrast to the first eigencurrent, the corresponding phase distribution of the dominant single-ring eigencurrent exhibits one phase reversal half way the line array, see Figure 5.25 (second row, first column, dashed curve). The last 7 elements exhibit an opposite phase with respect to the first 7 elements and no current is induced on the center ring. In the literature, the electric far field of the first eigencurrent is referred to as the sum pattern of the array, while the electric far field of the second eigencurrent is referred to as the difference pattern or monopulse of the array. Both phase distributions are used in practice. The sum pattern is used to detect objects, while the difference pattern is used to track objects [85]. Both patterns are eigenstates

of the array, which explains why the techniques of broadside scan and monopulse work so well.

The electric far fields of the fifth and 15th eigencurrent in Figure 5.25 (third row, second column) each show two main lobes, which are positioned at $\theta = \pm 18^\circ$ and $\theta = \pm 90^\circ$, respectively. Moreover, these far fields have 3 and 13 side lobes between their main lobes. This observation suggests how the far fields of the eigencurrents evolve. For $q > 1$, the qth eigencurrent has 2 main lobes with $q - 2$ side lobes in between. This statement is not only true in this particular case, but it is true in general for the group with dominant single-ring eigencurrent $\cos\varphi$. Although the coefficients of the dominant single-ring eigencurrents of the other groups are about the same as the coefficients of $\cos\varphi$ in this group, the far fields of the other groups may differ. These differences are explained by the differences between the element patterns, or electric far fields, of the single-ring eigencurrents. For example, Figure 5.27 (left) shows that the electric far field of the first eigencurrent of the second group is not a broadside beam as in the first group, but a monopulse beam. Moreover, the electric far field of the 15th eigencurrent

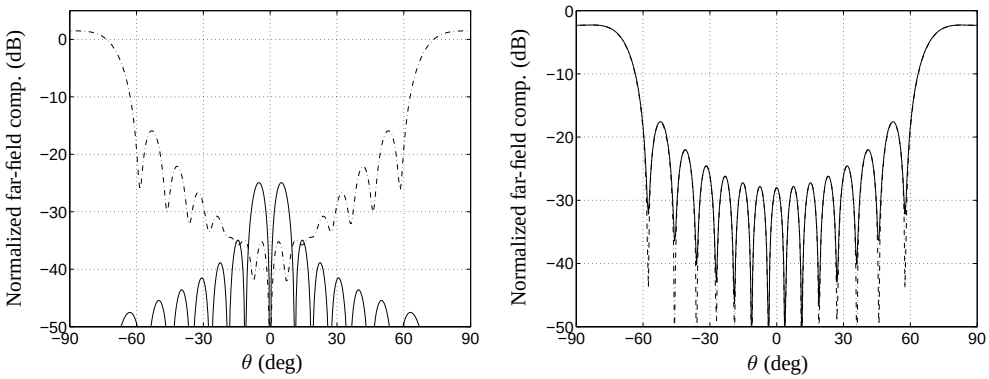

Figure 5.27 Left: normalized absolute ϕ-component (in dB) of the electric far field in the plane $\phi = 0$ for the 1st (solid curve) and 15th (dashed-dotted curve) eigencurrent of the 2nd group of a line array of 15 rings. Right: the same component, but for the 'exact' (solid curve) and 'approximated' (dashed-dotted curve) 15th eigencurrent of the 1st group. Eigencurrent normalization: maximum coefficient. Normalization each far field: maximum absolute ϕ-component of the 1st eigencurrent in the 1st group. Parameter values as in Figure 5.20.

of the second group has 14 instead of 13 side lobes between its two main lobes. In general, for $q \geq 1$, the qth eigencurrent of the second group has $q - 1$ side lobes between its two main lobes. The differences between the first group and the second group are due to the differences between the radiation intensities induced by $u_1^{\mathrm{sub}} = \cos\varphi$ and $u_2^{\mathrm{sub}} = 1$. The radiation intensity of the constant eigencurrent has a null at $\theta = 0^\circ$, while the radiation intensity of the cosine eigencurrent has a maximum at $\theta = 0^\circ$, see [7: Fig. 2.27] and [60: pp. 163 ff.]. The maxima of the element pattern of the constant eigencurrent at endfire, i.e., $\theta = \pm 90^\circ$, explain the large

intensity differences between the main lobes of the first and 15th eigencurrents in Figure 5.27 (left).

These observations show that each eigencurrent and, therewith, each eigenvalue, is related to certain main lobes in the far field. The corresponding positions, or angles, of these main lobes seem to correspond to scan angles of the line array. Moreover, the main lobes of the far field of the 15th eigencurrent seem to be the scan lobe at $\theta = \pm 90^\circ$ together with the corresponding grating lobe at $\theta = \mp 90^\circ$. We will discuss these observations in detail in a separate part about scanning and the infinite-array approach on pp. 165 ff.

To investigate the contribution of the perturbations of the eigencurrents to their far fields, Figure 5.27 (right) shows the far fields of both the 'exact' 15th eigencurrent and the 'approximated' 15th eigencurrent of the first group. Here, 'exact' means that the contributions of both single-ring eigencurrents, i.e., u_1^{sub} and u_2^{sub}, are taken into account. 'Approximated' means that only the contribution of the dominant single-ring eigencurrent of the first group, i.e., u_1^{sub}, is taken into account. The figure shows that the contribution of the perturbations is negligibly small up to about -32 dB with respect to the magnitudes of the main lobes. Since the perturbations increase with the index q of the eigencurrents $\boldsymbol{u}_{nq}$, the match between 'exact' and 'approximated' is even better for the other eigencurrents in the first group. As observed above, the perturbations in the second group are slightly larger than in the first group. On the other hand, the eigencurrents in the second group correspond to a larger single-ring eigenvalue and, hence, their far fields will contribute less to the total far field of the line array. Thus, we conclude that the contribution of the perturbations of the eigencurrents to their far fields is negligible. In Chapter 6, we investigate whether the perturbation is negligible for mutual-coupling performance parameters as well.

As in the initialization of the strip, we investigate the level of orthogonality of the eigencurrents. Figure 5.30 shows the Gram matrices of the eigencurrents of line arrays of 15 and 29 rings with respect to the composite inner product. The blocks of these matrices are computed by (5.23), i.e., the Euclidean inner products of the eigenvectors. The matrices consist of 4 blocks with sizes 15×15 and 29×29, respectively, which represent the self and mutual coupling of the 2 groups. Both kinds of coupling are described by band matrices. The self coupling of the first group is described by the diagonal and the two second co-diagonals, while the self coupling of the second group is somewhat more pronounced and described by the second, fourth, and 6th co-diagonal. Moreover, the odd-indexed co-diagonals are negligibly small. Hence, the coupling between eigencurrents with even and odd numbers of phase reversals in their coefficients of the dominant single-ring eigencurrent is negligibly small. In Figure 5.22, we visualized the behavior of the coefficients of the dominant single-ring eigencurrent in the first and second groups of eigencurrents versus the behavior of the expansion coefficients of a single strip with piecewise functions. Here, we compare the self-coupling blocks for a line array with 29 rings in Figure 5.30 (right) with the Gram matrix for a strip with 29 piecewise functions in Figure 5.16 (left).

We observe that the self-coupling blocks for the line array are less diagonally dominant than the Gram matrix for the strip. Moreover, for the strip, the coupling is restricted to the first few eigencurrents.

Contrary to the self-coupling blocks, the mutual-coupling blocks have negligibly small even-indexed co-diagonals, while the odd-indexed co-diagonals vary from 0.001 to 0.2. Hence, the coupling between eigencurrents with both an even or odd number of phase reversals in their coefficients of the dominant single-ring eigencurrent is negligibly small. In contrast, the coupling between eigencurrents with even and odd numbers of phase reversals in these coefficients are not negligible. This difference with the self-coupling blocks is explained as follows. In the inner products of the mutual-coupling blocks, the coefficients of the dominant single-ring eigencurrent in an eigencurrent of the first group are multiplied by the coefficients of the perturbation in an eigencurrent of the second group and vice versa. In each eigencurrent, the coefficients of the perturbations exhibit either one phase reversal more or one phase reversal less than the coefficients of the dominant single-ring eigencurrent. These observations explain the difference between the self and mutual-coupling blocks, because the eigencurrents of different groups show mutual coupling if their coefficients of corresponding single-ring eigencurrents have either both an even or both an odd number of phase reversals. As illustrated by the color pattern in Figure 5.30, the mutual coupling becomes stronger for eigencurrents with more phase reversals in the coefficients of their dominant single-ring eigencurrent. This is explained by the increase of the perturbation with the index q of the eigencurrents $\boldsymbol{u}_{nq}$.

To complete this section, we explain first how the starting points of the eigenvalue curves are determined. Next, we consider the conjecture on p. 149 that each eigencurrent can be multiplied by a complex factor such that the coefficients of its dominant single-ring eigencurrent have negligible imaginary parts. We recall that the coefficients of the dominant single-ring eigencurrent of the qth eigencurrent in each group have $q-1$ phase reversals. Since the eigenvalues of each group are indexed along the curve they generate in the complex plane, see Figure 5.20, the number of phase reversals increases along this curve. Hence, the starting point of each eigenvalue curve is the eigenvalue corresponding to the eigencurrent without phase variance in the coefficients of the dominant single-ring eigencurrent. In Figure 5.25, we multiplied each computed eigencurrent by $e^{-j\alpha}$, where α is the mean phase of the coefficients of its dominant single-ring eigencurrent. Instead of this value of α, we may also choose another value. For example, Figure 5.25 (first row, first column) shows that the coefficients of u_1^{sub} in the first eigencurrent of the first group exhibit a maximum at the 8th ring. We multiplied the complete eigencurrent by $e^{-j\alpha}$ with α being the phase of the coefficient of u_1^{sub} at the 8th ring. The resulting real and imaginary parts of the coefficients of u_1^{sub} and u_2^{sub} are shown in Figure 5.28 (left). The figure shows that the imaginary parts of the coefficients of u_1^{sub} are small ($< 10^{-2}$) with respect their real parts. Moreover, the real parts of the coefficients of u_2^{sub} are small with respect to their imaginary parts. Hence, in this case, the dominant part of each eigencurrent is real, while its

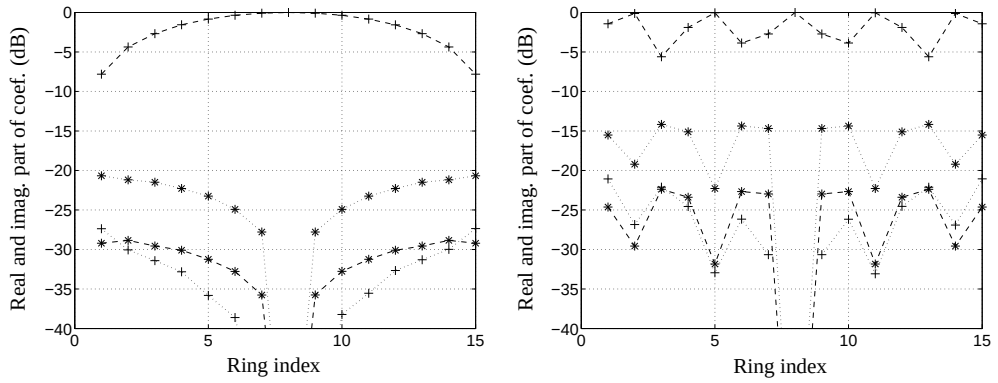

Figure 5.28 Real (dashed curves) and imaginary (dotted curves) coefficients (in dB) of the single-ring eigencurrents $u_1^{\rm sub}$ ($+$) and $u_2^{\rm sub}$ ($*$) in the 1st (left) and 5th (right) eigencurrent of the 1st group. Eigencurrent normalization: maximum coefficient. Parameter values as in Figure 5.20.

perturbation is imaginary. The same observations are valid for the real and imaginary parts of the coefficients of $u_1^{\rm sub}$ and $u_2^{\rm sub}$ in the fifth eigencurrent, see Figure 5.28 (right), where we multiplied this eigencurrent by $e^{-j\alpha}$ with α being the phase of the coefficient of $u_1^{\rm sub}$ at the 8th ring. These two examples confirm the conjecture on p. 149.

Parameter Dependence of Eigencurrents

Having described the array eigencurrents, we investigate their dependence on the geometry parameters and the frequency. In Subsection 5.2.3, we carried out such an investigation for the eigencurrents of a single strip. We showed that the dependence of the single-strip eigencurrents on the geometry parameters and the frequency is negligible. Since the eigencurrents of a single strip with piecewise functions correspond to the array eigencurrents in the way explained above, we may expect that the dependence of the dominant coefficients of the array eigencurrents on the geometry parameters and the frequency is negligible as well. Since we considered only a single strip geometry to show the correspondence, we consider first the comparison between the single-strip eigencurrents and the array eigencurrents in more detail.

With respect to this comparison we have two comments. First, it is not clear which choices of strip parameters fit best to certain choices of array parameters. Second, the comparison of the results for 15 and 29 rings in Figure 5.23 (right) and Figure 5.24 (left), and the results for 15 and 29 piecewise functions in Figure 5.8 (left) and Figure 5.11 (left) is not completely justified. This second comment is explained as follows. The parameters of line arrays of rings and the parameters of strips can be related as in Table 5.6. The array size is defined such that the ratio array size versus spacing equals the ratio striplength versus interval length if $N_{\rm exp} = N_{\rm sub}$.

Table 5.6 Parameters of a line array of rings related to parameters of a strip with piecewise functions. Both kind of parameters are normalized with respect to the wavelength.

Number of rings	N_{sub}	N_{exp}	Number of piecewise functions
Array size	$(N_{\mathrm{sub}}+1)\,d/\lambda$	$2\,\ell/\lambda$	Strip length
Spacing	d/λ	$2\,\ell/(N_{\mathrm{exp}}+1)\lambda$	Distance between two triangle center points
Ring circumference	$ka(=2\pi a/\lambda)$	$2\,\ell/(N_{\mathrm{exp}}+1)\lambda$	Half the triangle base

The ring radius and half the triangle base are separated from the other parameters, because these two parameters describe the geometry of a single microstrip element, while the other parameters describe the geometry of the entire array or strip. Here, we imagine the piecewise functions as currents on overlapping microstrips. For the strips, N_{exp} is varied and 2ℓ ($\lambda/2$) is constant, while for the line arrays, N_{sub} is varied and d ($\lambda/2$) is constant. In Subsection 5.2.3, we showed that the eigenvectors of a strip do not depend on the strip length. This observation justifies the comparison mentioned above only if the eigencurrents are independent of (half) the triangle base, because both the distance between two triangle center points and (half) the triangle base vary (linearly) with the strip length. Due to the formulation for a single strip with piecewise functions, we cannot vary the length without varying both the distance between two triangle maxima and (half) the triangle base. The base of every triangle overlaps half the base of each of its neighbors. For a one-to-one comparison of strips and line arrays of rings, we would need to introduce an independent parameter Δ_{width}, which describes half the normalized triangle base as $\ell\Delta_{\mathrm{width}}/\lambda$. Then, the normalized distance between two triangle center points is $2\ell(1-\Delta_{\mathrm{width}})/(N_{\mathrm{exp}}-1)\lambda$. Moreover, the normalized strip length needs to be replaced by $2\ell(1-\Delta_{\mathrm{width}})/\lambda$.

The observations above show that a one-to-one comparison between the eigencurrents of single strips with piecewise functions and the eigencurrents of line arrays of rings is not possible due to our formulation for the strip. In the remainder of this section, we investigate the dependence of the eigencurrent coefficients of line arrays on the number of rings, the spacing, and the generating-ring parameters. We compare the results for line arrays of rings with the results for strips according to Table 5.6.

Number of Rings

Increasing of the number of rings extends each group by eigencurrents with more rapidly varying absolute coefficients, see Figure 5.23 (right) and Figure 5.24 (left). An example of an eigencurrent with rapidly varying absolute coefficients is given in Figure 5.29 for a line array of 60 rings.

Both the absolute coefficients of u_1^{sub} and the coefficients of u_2^{sub} show modulated oscillations as a function of the ring index. Moreover, the absolute coefficients of u_1^{sub} show the same behavior as the absolute expansion coefficients of the 21st eigencurrent of a strip with 60 piecewise functions, which confirms the correspondence between line arrays and strips.

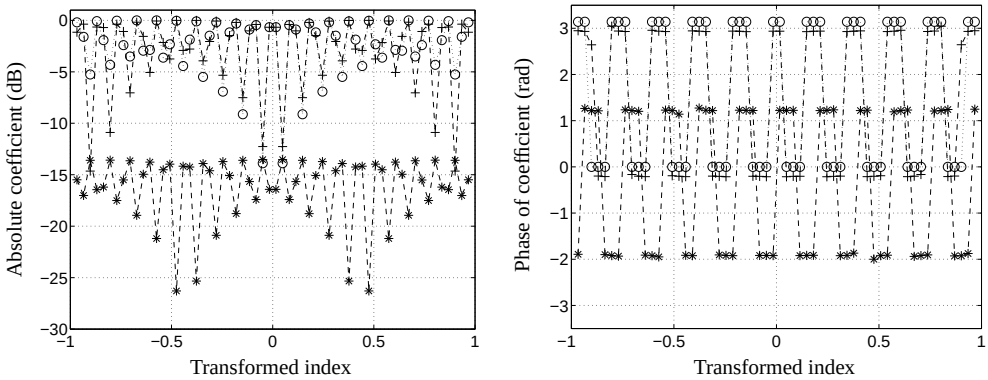

Figure 5.29 Absolute values (in dB) and phases of the coefficients of u_1^{sub} $(+)$ and u_2^{sub} $(*)$ in the 21st eigencurrent of the 1st group for a line array of 60 rings. Absolute values and phases of the expansion coefficients of the 21st eigencurrent of a strip with 60 piecewise functions $(\circ)$. Indices are transformed as in Figure 5.22. Eigencurrent normalization: maximum coefficient. Parameter values as in Figure 5.20.

The absolute coefficients of the dominant single-ring eigencurrent u_n^{sub} of the nth group show the same patterns for different numbers of rings as illustrated by Figure 5.31. Moreover, for a given array geometry, the absolute coefficients are positioned on a fictitious curve, independently of the number of rings. The same phenomenon has been observed for a strip with piecewise functions, see Figure 5.13. Figure 5.31 shows that this phenomenon occurs also for the coefficients of u_2^{sub}, which describe the perturbation of the second last eigencurrent. The coefficients of u_2^{sub}, which describe the perturbation of the third eigencurrent, show the same patterns, but the fictitious curves do not coincide. Instead, the coefficients decrease with the number of rings and, consequently, the perturbation decreases.

Finally, the pattern of the Gram matrix does not change in case the number of rings is increased, which is observed by comparing Figure 5.30 (left) and 5.30 (right).

Spacing

The absolute coefficients of the dominant single-ring eigencurrent u_n^{sub} in the eigencurrents of the nth group show the same global behavior for different spacings as illustrated by Figure 5.32. For eigencurrents $\boldsymbol{u}_{nq}$ with lower index q, these coefficients are totally independent of

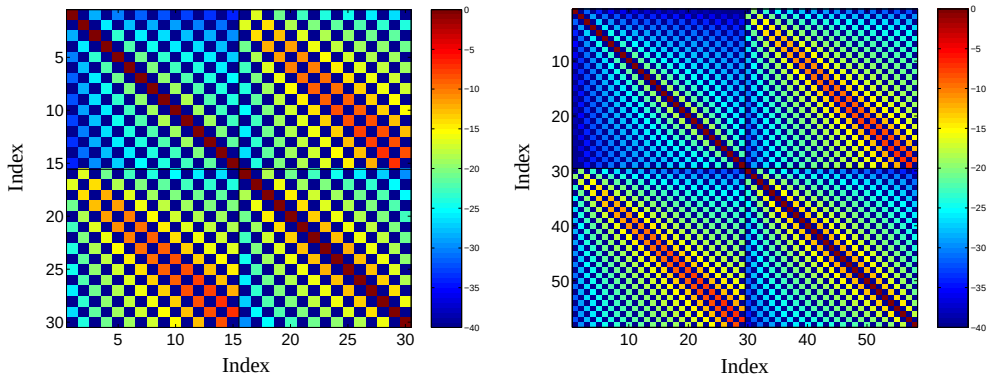

Figure 5.30 Color pattern of the absolute Gram matrix, with inner product $\langle \cdot\,, \cdot \rangle_{\mathrm{comp}}$, of the eigencurrents for line arrays with 15 and 29 rings in free space (in dB). Eigencurrent normalization: associated norm of $\langle \cdot\,, \cdot \rangle_{\mathrm{comp}}$. Parameter values as in Figure 5.20.

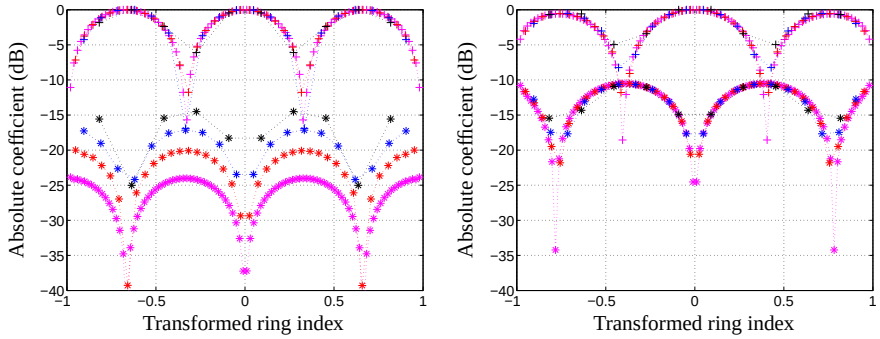

Figure 5.31 Absolute coefficients (in dB) of u_1^{sub} $(+)$ and u_2^{sub} $(*)$ in the 3rd (left) and $(N_{\mathrm{sub}}-2)$th eigencurrent of the 1st group for line arrays of $N_{\mathrm{sub}} = 10$ (black), 20 (blue), 40 (red), and 100 (purple) rings. Eigencurrent normalization: maximum coefficient. Parameter values as in Figure 5.20.

the spacing, while for eigencurrents with higher index, their actual values depend weakly on the spacing. In particular, Figure 5.32 (lower right) shows that for $d = \lambda/2$, the coefficients of the dominant single-ring eigencurrent u_1^{sub} in the last eigencurrent of the first group are larger at the boundaries of the line array than for the other spacings. Similar differences were observed in the comparison between a strip of half a wavelength with 15 piecewise expansion functions and a line array of 15 rings with $d = \lambda/2$, see Figure 5.22 (dashed curves). This suggests that a better comparison between line arrays of rings and strips with piecewise functions is obtained for other cases than the spacing of $\lambda/2$, which was considered in Figure 5.22.

Figure 5.32 confirms that for $d = \lambda/2$, the perturbation of the eigencurrents, described by

the coefficients of u_2^{sub}, increases with the index q of the eigencurrents $\boldsymbol{u}_{nq}$. For the other spacings, the perturbation increases for lower values of q and decreases for higher values of q. Further investigation revealed that the perturbation increases up to about $q = 32$ for $d = 2\lambda/5$ and $d = 3\lambda/5$, and up to about $q = 24$ for $d = 7\lambda/10$. For $d = 3\lambda/5$, the value $q = 32$ is clearly observed from Figure 5.33 (left), which shows the color pattern of the absolute coefficients of u_2^{sub} in the eigencurrents of the first group. For $d = 2\lambda/5$, a similar pattern is obtained. Comparing Figure 5.33 (left) with Figure 5.24 (right), we clearly observe the differences between the perturbations for $d = 3\lambda/5$ and for $d = \lambda/2$. Moreover, comparing Figure 5.33 (right) and Figure 5.30, we observe that for $d = 3\lambda/5$, the self coupling of the eigencurrent groups with respect to the inner product $\langle \cdot\,, \cdot \rangle_{\mathrm{comp}}$ is higher than for $d = \lambda/2$.

Figure 5.34 shows that the phases corresponding to the absolute coefficients of u_1^{sub} in the 9th and 40th eigencurrents shown in Figure 5.32 are the same. This illustrates that the phases of the dominant single-ring eigencurrent u_n^{sub} in the eigencurrents of the nth group are the same for different spacings. Phase differences occur only for relatively small absolute coefficients.

Because of the weak dependence of the eigencurrents on the spacing, we can choose a certain spacing and compute the eigencurrents. Then, for other spacings, the eigenvalues are approximated by the Rayleigh Ritz quotient,

$$\nu_{nq} = \frac{\langle \boldsymbol{u}_{nq}, \mathcal{Z}_{\mathrm{a}} \boldsymbol{u}_{nq} \rangle_{\mathrm{comp}}}{\| \boldsymbol{u}_{nq} \|_{\mathrm{comp}}^2} \,. \tag{5.38}$$

Here, $\boldsymbol{u}_{nq}$ is an eigencurrent of the chosen spacing, $\mathcal{Z}_{\mathrm{a}}$ is the impedance operator for the new spacing, and $\| \cdot \|_{\mathrm{comp}}$ is the associated norm of the composite inner product.

Generating-Ring Parameters

As observed in Subsection 5.2.2, the eigencurrents of a single ring are a function of the angle that describes the circumference; their dependence on the ratios $\beta = b/a$ and h/a is negligible. Moreover, in free space, the eigenvalues depend strongly on ka $(2\pi a/\lambda)$ and weakly on β; in a half space, they also depend strongly on h/a. Since the off-diagonal blocks of the moment matrix of a line array of rings are independent of β and the diagonal blocks are diagonal matrices with the single-ring eigenvalues on the diagonal, the eigenvectors of a line array of rings depend weakly on β. Hence, the same is valid for the coefficients of the single-ring eigencurrents in the array eigencurrents. Numerically, we found that the dependence of the coefficients of the dominant single-ring eigencurrent on ka and h/a is negligible. Moreover, the coefficients describing the perturbation depend weakly on these parameters with differences of the order of 1 dB at -10 dB or less. Fixing the coefficients of the array eigencurrents as obtained for certain generating-ring eigencurrents, we can compute the eigenvalues for other generating-ring eigencurrents by (5.38).

For a single ring, the choice of the orientation angle ψ is arbitrary. For a line array, this

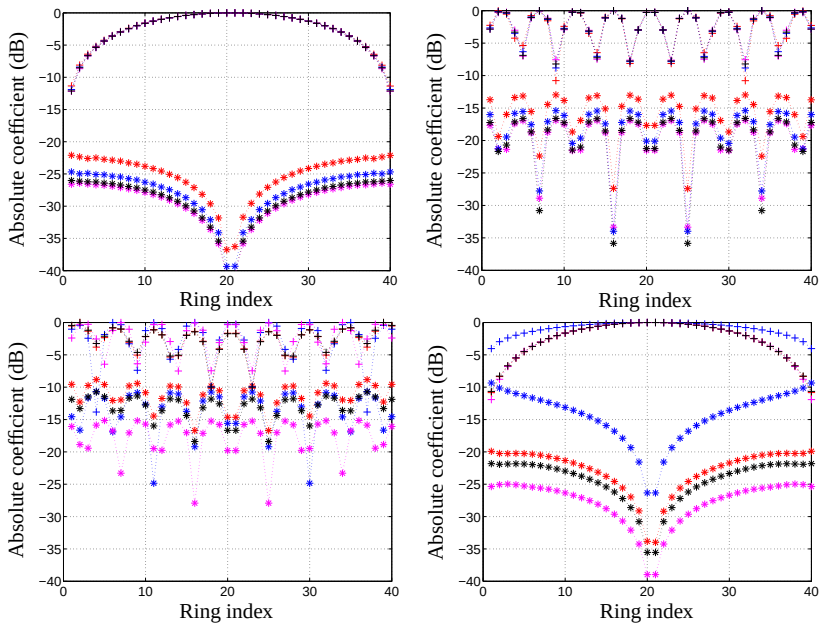

Figure 5.32 Absolute coefficients (in dB) of u_1^{sub} $(+)$ and u_2^{sub} $(*)$ in the 1st (upper left), 9th (upper right), 32nd (lower left), and 40th (lower right) eigencurrent of the 1st group for line arrays of 40 rings with spacings $2\lambda/5$ (red), $\lambda/2$ (blue), $3\lambda/5$ (black), $7\lambda/10$ (purple). Eigencurrent normalization: maximum coefficient. Parameter values of the generating ring as in Figure 5.20.

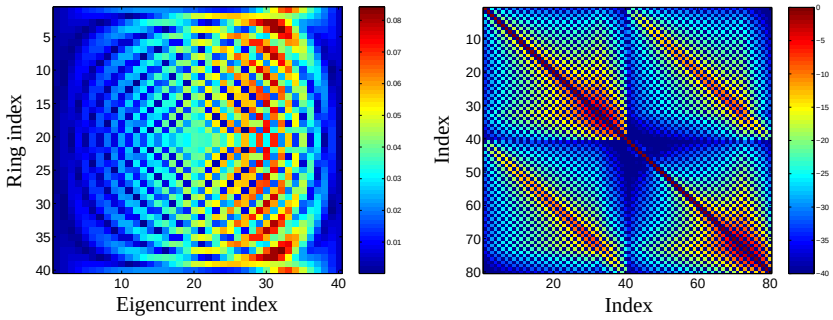

Figure 5.33 Left: color pattern of the absolute coefficients of u_2^{sub} in the eigencurrents of the 1st group for a line array of 40 rings in free space (in dB). Right: color pattern of the absolute Gram matrix, with inner product $\langle \cdot\,, \cdot \rangle_{\mathrm{comp}}$, of the eigencurrents of the same line array (in dB). Eigencurrent normalization: maximum coefficient (left) and associated norm of $\langle \cdot\,, \cdot \rangle_{\mathrm{comp}}$ (right). Parameter values of the generating ring as in Figure 5.20, but with $d = 3\lambda/5$ instead of $d = \lambda/2$.

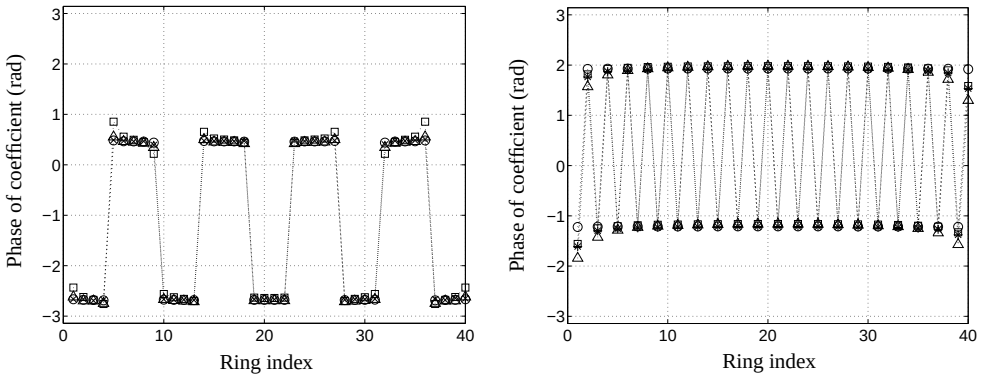

Figure 5.34 The phases corresponding to the absolute coefficients of u_1^{sub} in the 9th and 40th eigencurrents as shown in Figure 5.32 (upper right and lower right) for the spacings $2\lambda/5$ ($\times$), $\lambda/2$ ($\circ$), $3\lambda/5$ ($\triangle$), $7\lambda/10$ ($\square$).

angle describes the position of the local feeds, as introduced in Section 4.2, with respect to the line-array axis. Therefore, ψ is a line-array parameter, although it is prescribed for a single ring. The choice of ψ determines which cosine and sine single-ring eigencurrents are symmetric and anti-symmetric with respect to the line-array axis. Up to now, we have considered the symmetric single-ring eigencurrents, which are described by the cosines for $\psi = 0$ and which generate symmetric array eigencurrents (with respect to the line-array axis). As mentioned in the introduction of this section, the anti-symmetric array eigencurrents are described by the sines. These eigencurrents do not couple with the symmetric eigencurrents and can therefore be calculated independently. The coefficients describing the anti-symmetric array eigencurrents show the same patterns and have the same properties as the symmetric array eigencurrents. An example is given in Figure 5.35 (left), which shows the absolute coefficients of the 18th eigencurrent both for the first group of the symmetric array eigencurrents and for the first group of the anti-symmetric array eigencurrents. Here, $u_1^{\mathrm{sub}}(\varphi) = \cos\varphi$ and $u_2^{\mathrm{sub}}(\varphi) = 1$ for the symmetric eigencurrents and $u_1^{\mathrm{sub}}(\varphi) = \sin\varphi$ and $u_2^{\mathrm{sub}}(\varphi) = \sin 2\varphi$ for the anti-symmetric eigencurrents. Figure 5.35 (right) shows the spread of the first group of eigenvalues for the anti-symmetric eigencurrents of the 4 different line array geometries considered in Figure 5.18. This spread is of the same order as the spread of the first group of eigenvalues for the symmetric eigencurrents as shown in Figure 5.18 (upper left). We observed that the spread of the second group of eigenvalues for the anti-symmetric eigencurrents is of the same order as the spread of the third group of eigenvalues for the symmetric eigencurrents. Since this third group is not taken into account to describe the mutual coupling in line arrays of rings, only one group of anti-symmetric eigencurrents needs to be taken into account to describe the mutual coupling.

We also investigated the case $\psi = \pi/4$ for which the single-ring eigencurrents $\cos\varphi$ and $\sin\varphi$ are neither symmetric nor anti-symmetric with respect to the line-array axis. As mentioned

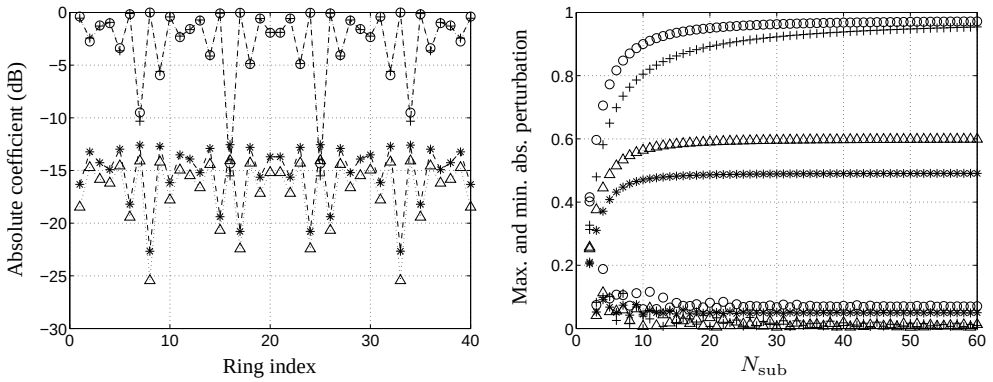

Figure 5.35 Left: absolute coefficients of u_1^{sub} and u_2^{sub} in the 18th eigencurrent of the 1st group for a line array of 40 rings ($d = \lambda/2$) in free space generated from single rings with $N_{\cos} = 2$ and $N_{\sin} = 0$ (u_1^{sub}: $+$, u_2^{sub}: $*$) and with $N_{\cos} = 0$ and $N_{\sin} = 2$ (u_1^{sub}: $\circ$, u_2^{sub}: $\triangle$). Right: maximum and minimum of the absolute perturbations of 1st group of eigenvalues as a function of N_{sub} for the 4 different line array geometries specified in Figure 5.18. Parameter values of the generating ring: $ka = \pi/3$, $\beta = 3/100$, $\psi = 0$.

in Section 5.2.2, these eigencurrents span a 2-dimensional eigenspace, because they have the same eigenvalues. In the line-array analysis, the dominant single-ring eigencurrents of the first and second groups appear to be $\cos\varphi \pm \sin\varphi = \cos(\varphi \pm \pi/4)$ instead of $\cos\varphi$ and $\sin\varphi$, which are prescribed. These eigencurrents are symmetric and anti-symmetric with respect to the line-array axis. Hence, despite the prescription of non-symmetric single-ring eigencurrents, the array eigencurrents are symmetric and anti-symmetric with respect to the line array axis, i.e., the symmetry line of the array. This observation is in correspondence with physical views, because the symmetry of a single ring is determined by its excitation, while a line array of rings is symmetric with respect to the line-array axis. Hence, the observation is a validation of the eigencurrent approach. The consequence of prescribing the cosine and sine functions instead of $\cos(\varphi \pm \pi/4)$ is that the two corresponding groups will not be identified correctly, because the coefficients of $\cos\phi$ and $\sin\phi$ in the array eigencurrents are on each ring of equal magnitude. Therefore, these groups are joined together at the cost of computational efficiency. In general, groups corresponding to a degenerate single-element eigenvalue are joined together, if no a priori information is available about the excitation field. Otherwise, such information should be used to choose the single-element eigencurrents corresponding to a degenerate eigenvalue.

Finally, by varying the frequency, we vary both the single-ring parameters and the spacing. Therefore, the array eigencurrents will show both types of behavior described above. In Section 6.2, we will show an example in which the dominant eigencurrent behavior at the frequency for which the elements of an array exhibit a 'resonant broadside embedded impedance' is the same

as the dominant eigencurrent behavior at frequencies 15% and 19% below this frequency. We recall that the elements exhibit a 'resonant broadside embedded impedance', if their reactances are on average zero.

Scanning

Supported by Figure 5.25, we stated that each eigencurrent and, consequently, each eigenvalue, is related to certain main lobes in the far field. In this subsection, we will show in detail how the main lobes correspond to specific scan angles of the line array. Figures 5.36 – 5.38 show results for line arrays of 40 rings with spacings $3\lambda/5$ and $2\lambda/5$. The single-ring parameters are chosen as in the description of the eigencurrents above. We first discuss the results for the spacing $3\lambda/5$. The eigenvalue curve of the first group is shown in Figure 5.36 (left), where the first, 32nd, 36th, 39th, and 40th eigenvalue are indicated by their index. Figure 5.37 (left) shows

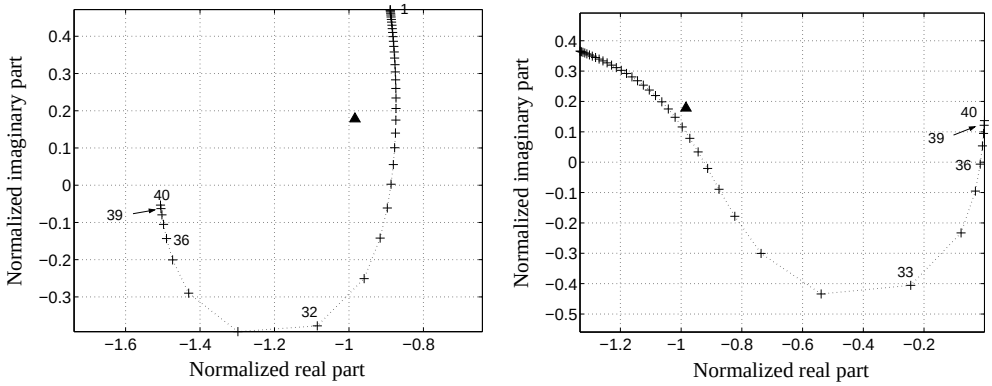

Figure 5.36 Normalized eigenvalues of the 1st group for two line arrays of 40 rings in free space and the corresponding normalized eigenvalues (▲) of a single ring, i.e., ν_1^{sub}. Normalization: $|\nu_1^{\mathrm{sub}}|$. Left: $d = 3\lambda/5$. Right: $d = 2\lambda/5$. Parameter values: $N_{\mathrm{cpl}}^{\mathrm{sub}} = 2$, $ka = \pi/3$, $\beta = 3/100$, $\psi = 0$, $N_{\cos} = 2$, $N_{\sin} = 0$.

that the electric far field of the 32nd eigencurrent exhibits 4 main lobes in the xz-plane, to be precise, main lobes at $\theta = \pm 41.8°$ and $\theta = \pm 90.0°$. As described in Section 3.5, for the spacing $3\lambda/5$, the angles $\pm 41.8°$ are scan angles for which a grating lobe appears at $\mp 90.0°$. Hence, the main lobes in Figure 5.37 (left) represent the scan lobes at $\pm 41.8°$ and the corresponding grating lobes at $\mp 90°$. Similar phenomena are observed for the 36th and 39th eigencurrents. In the far field of the 36th eigencurrent shown in Figure 5.37 (left, dashed curve), the two main lobes at $\pm 68.9°$ are the grating lobes for the scan angles $\mp 47.3°$, which are exactly the positions of the other two main lobes in the pattern. In the far field of the 39th eigencurrent shown in Figure 5.37 (right, dashed curve), the angles corresponding to the grating lobes and the scan directions

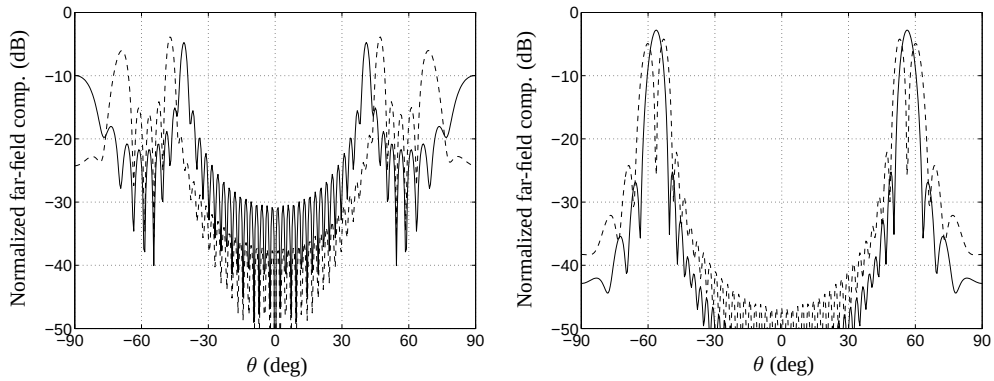

Figure 5.37 Normalized absolute ϕ-components (in dB) of the electric far fields in the xz-plane for the 32nd (solid curve, left), 36th (dashed curve, left), 39th (dashed curve, right), and 40th (solid curve, right) eigencurrent of a line array of 40 rings in free space. Normalization: maximum absolute ϕ-component of the 1st eigencurrent. Parameter values as in Figure 5.36.

are $\pm 60.1^\circ$ and $\mp 53.1^\circ$, respectively. The far field of the 40th eigencurrent shows only two main lobes positioned at $\pm 56.2^\circ$, because scanning at these angles results into grating lobes at $\mp 56.2^\circ$. For scanning at angles larger than 56.2°, the grating lobes in the electric far fields of the eigencurrents 32 – 40 become the scan lobes and vice versa.

For the line array considered in Figure 5.37, the main lobes at $\pm 90^\circ$ appear in the 32nd eigencurrent. For the spacings $7\lambda/10$ and $4\lambda/5$, instead of $3\lambda/5$, we found these main lobes in the 24th and 16th eigencurrents, respectively. These observations raise the question whether there is a relation between the spacing and the index of the eigencurrent that induces main lobes at $\pm 90^\circ$. Numerically, we found for $d \geq \lambda/2$ that the eigencurrent with index

$$\text{index} = \left\lceil \left(1 - \frac{d \bmod (\lambda/2)}{\lambda/2} \right) N_{\text{sub}} \right\rceil \tag{5.39}$$

induces these main lobes lobes. As in the example of Figure 5.37, the main lobes of the far-field patterns with index larger or equal to (5.39) represent both main lobes and grating lobes. For a line array with 15 rings and spacing $\lambda/2$, as in Figure 5.25, the grating lobes appear in the 15th eigencurrent, which is in correspondence with (5.39).

To show how the far fields of the eigencurrents evolve for indices just below (5.39), we consider the far fields of the 30th and 31st eigencurrents of the line array of 40 rings with spacing $3\lambda/5$. Figure 5.38 (left) shows that these far fields have side lobes at $\pm 90^\circ$, which are 17.5 dB and 12.2 dB lower than the corresponding main lobes. The lobes $\pm 90^\circ$ of the far field of the 32nd eigencurrent are only 5.2 dB lower than the lobes at 41.8°.

For a line array of 40 rings with spacing $2\lambda/5$, Figure 5.36 (right) shows the eigenvalue

curve. Since the spacing in the array is smaller than half the wavelength, we do not expect grating lobes. Numerically we verified that the first 32 eigencurrents have only two main lobes in their far fields, with the exception of the first eigencurrent, which has one main lobe. The far field of the 33rd eigencurrent in Figure 5.38 (right) shows 2 main lobes at $\pm 90^\circ$, which are the grazing scan angles of the array. Although the spacing is smaller than $\lambda/2$, we observe that

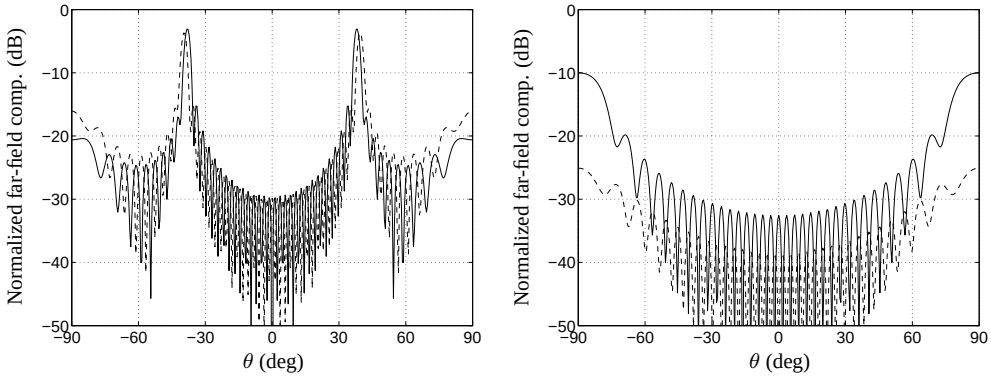

Figure 5.38 Normalized absolute ϕ-components of the electric far fields in the xz-plane for the 30th (solid curve) and 31st (dashed curve) eigencurrent of the line array in Figure 5.36 (left). Right: idem, but for the 32nd and 36th eigencurrent of the line array in Figure 5.36 (right).

the index 33 follows from (5.39) with a difference of only 1. Further investigation showed that for spacings smaller than half a wavelength, (5.39) indicates the eigencurrent, which generates the grazing scan angles. Since we observed that main lobes are both scan lobes and grating lobes for indices larger than or equal to (5.39), we do not expect grating lobes for indices larger than 33 in the line array of Figure 5.38 (right). This is confirmed by the numerical results. The figure shows that the 36th eigencurrent does not have a clear main lobe. Moreover, the radiation intensity is 20 dB lower than the main lobe of the first eigencurrent.

The results discussed above confirm that each eigencurrent corresponds to a scan angle. If a grating lobe is present at such a scan angle, the electric far field of the corresponding eigencurrent shows both the scan lobe and the grating lobe. Given a scan angle, there exist an eigencurrent such that the difference between the angle of one of its main-lobes and the scan angle is minimal. We expect that if the array is scanned at this scan angle, the resulting scan lobe is composed of that main lobe and main lobes of one or two neighboring eigencurrents. This expectation is based on the following reasoning.

Ideally, if the selected scan lobe corresponds to the eigencurrents $\boldsymbol{u}_{1,q_1}, \ldots, \boldsymbol{u}_{1,q_k}$ ($1 \leq q_1, \ldots, q_k \leq N_{\mathrm{sub}}$) of the first group, the excitation should be chosen as a linear combination of these eigencurrents. In practice, an array is scanned at a certain scan angle by means of a linear phase taper. To link the eigencurrent approach to practice, we search a relationship

between choices of linear phase tapers and choices of excited eigencurrents. As observed in the description of the eigencurrents, the coefficients of $\boldsymbol{u}_1^{\mathrm{sub}}$ in an eigencurrent $\boldsymbol{u}_{1q}$ show $q-1$ phase reversals as a function of the ring index. The total phase difference equals $(q-1)\pi$. Therefore, if the total phase difference of the linear phase taper equals $(q-1)\pi$, the eigencurrent $\boldsymbol{u}_{1q}$ is excited. To show the validity of this statement, we consider a line array of 15 rings in free space with spacing $\lambda/2$. Table 5.7 shows the main lobe positions of the eigencurrents of the first group. Corresponding electric far fields are depicted in Figure 5.25 for the of the first, second, fifth, and 15th eigencurrent. Also, the table shows the scan angles obtained by the linear phase tapers with

Table 5.7 Main lobe positions of the eigencurrents of the first group of a line array of 15 rings in free space. The scan angles of the same line arrays for prescribed phase progressions $kd\sin\theta_{\mathrm{scan}}$. Parameter values as in Figure 5.36.

Index	1	2	3	4	5	6	7
Main lobe eigenc.	$0°$	$\pm 6.3°$	$\pm 10.3°$	$\pm 14.0°$	$\pm 18.0°$	$\pm 22.1°$	$\pm 26.1°$
Phase progression	0	$\pm\pi/14$	$\pm 2\pi/14$	$\pm 3\pi/14$	$\pm 4\pi/14$	$\pm 5\pi/14$	$\pm 6\pi/14$
Scan angle	$0°$	$\pm 4.1°$	$\pm 8.2°$	$\pm 12.4°$	$\pm 16.6°$	$\pm 20.9°$	$\pm 25.4°$

8	9	10	11	12	13	14	15
$\pm 30.1°$	$\pm 34.7°$	$\pm 39.5°$	$\pm 44.5°$	$\pm 49.8°$	$\pm 56.1°$	$\pm 63.9°$	$\pm 90°$
$\pm 7\pi/14$	$\pm 8\pi/14$	$\pm 9\pi/14$	$\pm 10\pi/14$	$\pm 11\pi/14$	$\pm 12\pi/14$	$\pm 13\pi/14$	$\pm\pi$
$\pm 30.0°$	$\pm 34.8°$	$\pm 40.0°$	$\pm 45.6°$	$\pm 51.8°$	$\pm 59.0°$	$\pm 68.2°$	$\pm 90°$

total phase differences $(q-1)\pi$ and $-(q-1)\pi$. The corresponding scan angles are defined by $(q-1)\pi/14 = kd\sin\theta_{\mathrm{scan}}$. For the first 12 eigencurrents, the differences between the scan angles and the main lobe positions are smaller than $2.2°$. For the 13th and 14th eigencurrents, the differences are $2.9°$ and $4.3°$. The beam width of the main lobe of the 15th eigencurrent is large and, hence, the scan angle is not well determined. Considering the differences between the linear phase tapers and the eigencurrents, we conclude that the total phase difference of a phase taper that 'fits to' the qth eigencurrent is not exactly $\pm(q-1)\pi$. This phenomenon is explained by the averaging effect of the linear phase progression on the eigencurrents, as illustrated by Figure 5.39 for the phase distribution of the coeffients of u_1^{sub} in the third eigencurrent. A single eigencurrent cannot be excited by a linear phase progression.

Except for the first eigencurrent, the electric far field of each eigencurrent has two main lobes if there are no grating lobes. A linear phase taper induces only one main lobe. For example, the third eigencurrent of a line array of 15 rings in free space with $d = \lambda/2$ has two main lobes at $\pm 10.3°$, see Figure 5.7. If a linear phase taper with $\theta_{\mathrm{scan}} = 10.3°$ is applied, only the corresponding main lobe is excited. In Section 6.2, we illustrate this by an example.

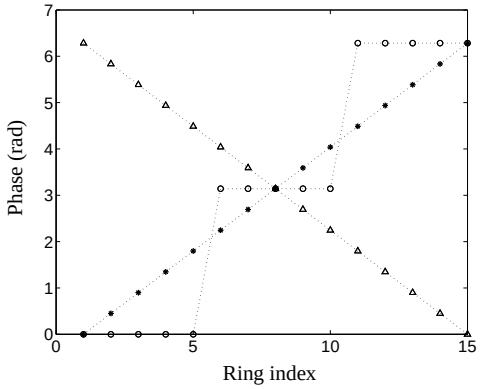

Figure 5.39 Phase distribution ($\circ$) of the coefficients of u_1^{sub} in the 3rd eigencurrent of the 1st group for a line array of 15 rings and the phase distribution on the array for the linear phase progressions with $\theta_{\mathrm{scan}} = 8.2^\circ$ ($\triangle$) and $\theta_{\mathrm{scan}} = -8.2^\circ$ ($*$).

Comparison with the Infinite-Array Approach

In the infinite-array approach, a fixed linear phase taper on the array is assumed, see (3.46). The eigencurrents of the array exhibit the same phase distribution as the phase taper. In contrast, the eigencurrents of the finite array have a block-like phase distribution as in Figure 5.39. This is a first indication that a finite array will never show the same behavior as the infinite array, no matter the size of the finite array.

For the infinite-array approach, the eigencurrents are determined from the infinite-array moment matrix $A(\theta_{\mathrm{scan}})$, see (3.48) with $\Psi = kd\sin\theta_{\mathrm{scan}}$. Since the matrix depends on the scan angle, the eigenvalues and eigencurrents depend in general on the scan angle as well. Each eigenvalue of the single ring corresponds to an eigenvalue $\nu_n(\theta_{\mathrm{scan}})$ of the matrix $A(\theta_{\mathrm{scan}})$. For the finite-array approach, each ring eigenvalue ν_n corresponds to a finite and discrete group of eigenvalues $\{\nu_{nq}\}_{q=1}^{N_{\mathrm{sub}}}$. Analogously, for the infinite-array approach, each eigenvalue ν_n corresponds to a continuum group of eigenvalues parameterized by θ_{scan}. In both approaches, each eigenvalue in a group is related to one scan angle. Of course, the question arises whether in the limit for a finite array the discrete groups tend to the continuum groups of the corresponding infinite array. To investigate this, we consider two examples.

First, we consider two line arrays of 15 and 40 rings with spacing $\lambda/2$. Figure 5.40 (left) shows that the eigenvalues of the first group of the finite-array moment matrices all coincide with certain eigenvalues of the first group of the infinite-array moment matrix. To compute the spectrum of the infinite-array moment matrix, we have to truncate the Fourier series $(3.48)^2$ that describes $A(\theta_{\mathrm{scan}})$. Therefore, the curve for the infinite-array spectrum is suggestive. For larger truncation numbers than in Figure 5.40, we observed that the curve is stretched down-

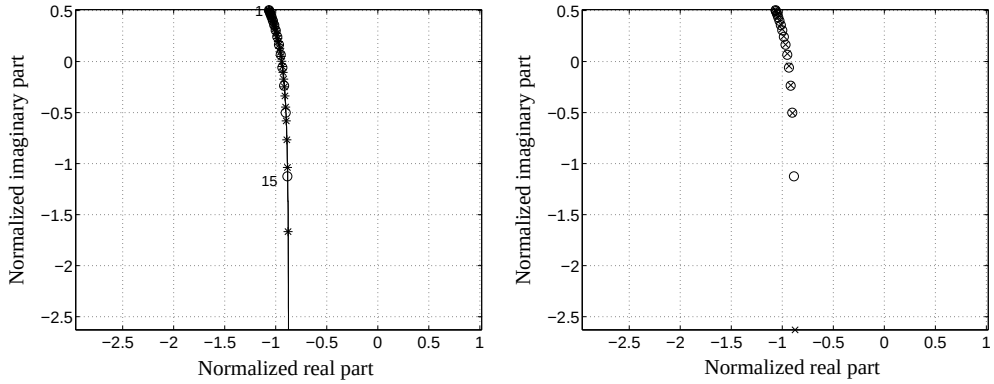

Figure 5.40 Left: normalized eigenvalues of the 1st group for line arrays of 15 ($\circ$) and 40 ($*$) rings in free space, and the normalized eigenvalues of the 1st group for the same line array, but computed by the infinite-array approach (solid curve: $q = -100, \ldots, 100$ in the series (3.48)^2). Right: as left, but only the eigenvalues for 15 rings and the eigenvalues obtained by the infinite-array approach for the positive-valued main-lobe positions in Table 5.7 (2nd row) are shown ($\times$). Normalization: $|\nu_1^{\rm sub}|$. Parameter values as in Figure 5.36, but with $d = \lambda/2$.

wards. Figure 5.40 (right) shows that the eigenvalues $\{\nu_{1q}\}_{q=1}^{15}$ of the line array of 15 rings are very well approximated by the infinite-array eigenvalues $\{\nu_1(\theta_q)\}_{q=1}^{15}$ obtained for the scan angles $\{\theta_q\}_{q=1}^{15}$ that correspond to the positive-valued main-lobe positions of the finite-array eigencurrents in Table 5.7, except for the last eigenvalue. The same is valid for the negative valued main-lobe positions. This observation indicates once more that there is a one-to-one correspondence between the finite-array eigenvalues and a discrete set of scan angles.

Second, we consider line arrays of 40, 100, 200, and 400 rings in free space with spacing $3\lambda/5$. The geometry parameters are the same as in Figure 5.36 (left). Figure 5.41 (left) shows that the curve of the infinite-array eigenvalues is stretched downward if more terms in the Fourier series describing $A(\theta_{\rm scan})$ are taken into account. As a result, not all eigenvalues of the finite arrays coincide with infinite-array eigenvalues. Moreover, if an eigenvalue of a finite array differs from the infinite-array eigenvalues, it differs from the eigenvalues of the other finite arrays as well. For example, for the line array of 40 rings, the 32nd and 33rd eigenvalue differ significantly from both the infinite-array eigenvalues and the eigenvalues of the other arrays. Figure 5.41 (right) shows that at the 26th eigenvalue, the eigenvalues $\{\nu_{1q}\}_{q=1}^{40}$ of the finite-array moment matrix start to deviate from the eigenvalues $\{\nu_1(\theta_q)\}_{q=1}^{40}$ of the infinite-array moment matrix obtained for the positive-valued main-lobe positions $\{\theta_q\}_{q=1}^{40}$ of the finite-array eigencurrents. We note that $\theta_{26} = 32.4^\circ$, $\theta_{28} = 35.1^\circ$, $\theta_{30} = 38.1^\circ$, and $\theta_{32} = 41.8^\circ$. The observed differences are explained as follows. In Section 3.5, we found that the infinite-array moment matrix for line arrays in free space is possibly divergent at the grazing scan angles

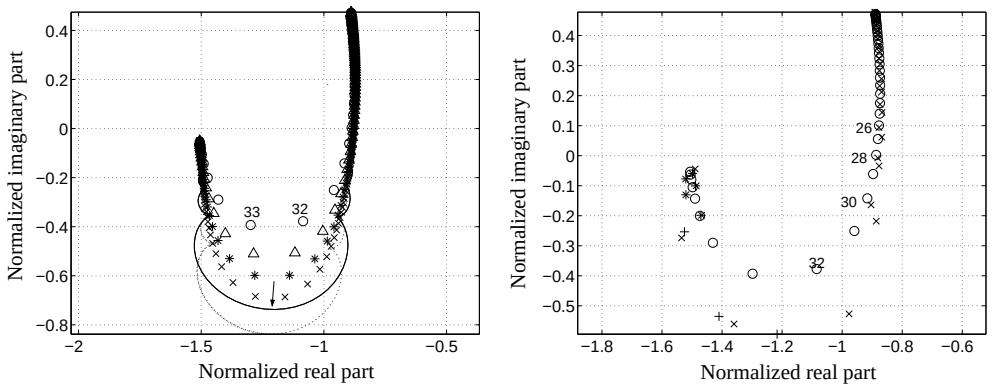

Figure 5.41 Left: normalized eigenvalues of the 1st group for line arrays of 40 (○), 100 (△), 200 (∗), and 400 (×) rings in free space and the corresponding infinite-array eigenvalues (solid curve: $q = -100, \ldots, 100$ in the series (3.48)^2; dotted curve: $q = -200, \ldots, 200$). Right: as left, but only the eigenvalues for the finite array of 40 rings and the eigenvalues obtained by the infinite-array approach for the main-lobe positions of the finite-array eigencurrents (× for scan angles $\leq 56.2^\circ$ and + otherwise). Normalization: $|\nu_1^{\mathrm{sub}}|$. Parameter values as in Figure 5.36 with $d = 3\lambda/5$.

$\pm 90^\circ$ and at the grating-lobe scan angles, i.e., the scan angles for which a grating lobe appears or disappears at $\pm 90^\circ$. In other words, the Fourier series (3.48)^2 describing this matrix does not converge. The differences occur, because the 32nd eigenvalue corresponds to the grazing and grating-lobe scan angles. A similar phenomenon is observed in Figure 5.40 of the previous example, where the 15th eigenvalue corresponds to the grazing (and grating-lobe) scan angles.

The two examples suggest that, for an increasing number of rings, the sequence of eigenvalues corresponding to the grazing and grating-lobe scan angles tends to infinity. Mathematically, this observation could be explained as follows. As mentioned in Section 3.5, the infinite-array moment matrix is called the symbol of the Laurent matrix (3.47). Both the Laurent matrix and any related finite-array moment matrix are generated by the symbol $A(\theta_{\mathrm{scan}})$ expanded into a Fourier series as in (3.48)^2. The finite-array moment matrix is a truncated Laurent matrix. Then, according to the extension of [14: Th. 4.13] stated on [14: p. 197], the largest singular value of the finite-array moment matrix tends to infinity as the number of rings tends to infinity, if the symbol is unbounded. In Section 3.5, numerical results for the range of the symbol, supported by analytical explanations, suggest that the symbol is indeed unbounded. At the grazing and grating-lobe scan angles, the symbol seems to exhibit logarithmic singularities. Since the finite-array moment matrix is almost normal, the absolute eigenvalues approximate the singular values. The largest eigenvalue of the finite-array moment matrix corresponds to the index given by (5.39) and, herewith, to the grazing and grating-lobe scan angles. Hence, the sequence of

eigenvalues corresponding to the grazing and grating-lobe scan angles tends to infinity. The observation explains why the spreads of the first groups of eigenvalues in Figure 5.19 increase with the number of rings.

Numerical results showed that the curve of the infinite-array eigenvalues in Figure 5.41 (left) equals the range of the symbol for any choice of the truncation number. In [14: Th. 1.2], such a result is generally given for bounded symbols. According to Theorem 5.5 in [116], the singular values of the finite-array moment matrix follow the absolute range of the symbol, if the symbol is a square integrable function and if only one expansion function per element is used. We observed numerically that all eigenvalues of the finite-array moment matrix follow the range, except the eigenvalues with indices equal or close to (5.39), i.e., those corresponding to the grazing and grating-lobe scan angles.

We recall two statements of Section 3.5 in the context of this section. First, for spacings smaller than half a wavelength, the divergence of the Fourier series describing the infinite-array moment matrix appears only at grazing scan. For the line array in Figure 5.36 (right) with spacing $2\lambda/5$, the grazing scan is described by the 33rd eigencurrent, which is shown in the figure. The eigenvalue curve suggests the same divergent behavior of the eigenvalues as the behavior for the spacing $3\lambda/5$ in Figures 5.36 (left) and 5.41. Second, in a half space, the Fourier series describing the infinite-array moment matrix converges at the grazing and grating-lobe scan angles. This is confirmed by Figure 5.42 (left), which shows the normalized eigenvalues for the line arrays of 40 and 100 rings with $d = 3\lambda/5$ and the corresponding infinite-array eigenvalues. The eigenvalue curves are totally different from the eigenvalue curves for free space as shown in Figure 5.41. In free space, the largest eigenvalue of the first group corresponds to the grazing and grating lobe scan angles. In a half space, the largest eigenvalue is the first eigenvalue, which is fixed for increasing numbers of elements and which corresponds to the broadside scan angle. In contrast to free space, the eigenvalues of finite arrays in a half space coincide all with infinite-array eigenvalues. Moreover, the curve describing the infinite-array eigenvalues converges with the truncation number of the corresponding Fourier series. As a result, the eigenvalues for larger numbers of rings can be estimated from the distribution of eigenvalues on this curve for lower numbers of rings.

Figure 5.42 (right) shows that the eigenvalues $\{\nu_{1q}\}_{q=1}^{40}$ of the line array of 40 rings are the same as the eigenvalues $\{\nu_1(\theta_q)\}_{q=1}^{40}$ of the infinite-array moment matrix obtained for the positive-valued main-lobe positions $\{\theta_q\}_{q=1}^{40}$ of the finite-array eigencurrents. At the 32nd eigenvalue, the eigenvalue curve shows a bend, which is also present in the eigenvalue curve of the infinite-array moment matrix. In free space, this eigenvalue corresponds to the grazing and grating-lobe scan angles and its index is described by the general relation (5.39). In a half space, the 32nd eigencurrent does not generate main lobes at $\pm 90^\circ$ as observed from Figure 5.43 (left). The 33rd eigencurrent generates two main lobes at $\pm 42.3^\circ$ and two main lobes of low intensity at $\pm 79.4^\circ$. The positions of the second two main lobes differ 4.3° from the

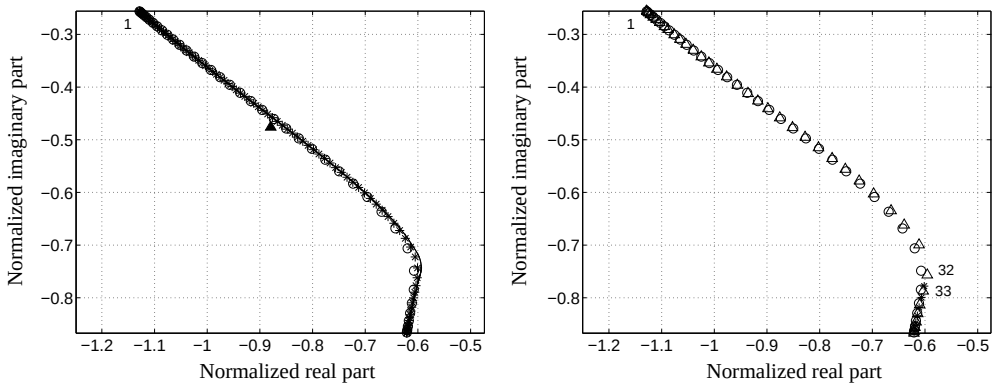

Figure 5.42 Left: normalized eigenvalues of the 1st group for line arrays of 40 ($\circ$) and 100 ($*$) rings in a half space with $h = 6/5$, the corresponding normalized eigenvalue ν_1^{sub} ($\blacktriangle$) of a single ring, and the corresponding infinite-array eigenvalues (solid curve: both $q = -100, \ldots, 100$ and $q = -400, \ldots, 400$ in the series (3.48)^2). Right: as left, but only the eigenvalues for the array of 40 rings and the eigenvalues obtained by the infinite-array approach for the positive-valued main-lobe positions of the finite-array eigencurrents ($\triangle$ for scan angles $\leq 56.2^\circ$ and $*$ otherwise). Normalization: $|\nu_1^{\mathrm{sub}}|$. Parameter values as in Figure 5.36 with $d = 3\lambda/5$.

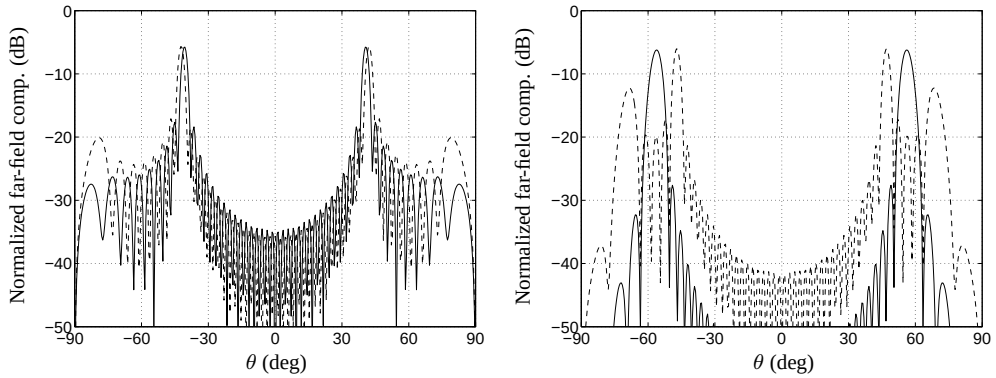

Figure 5.43 Normalized absolute ϕ-components (in dB) of the electric far fields in the xz-plane for the 32nd (solid curve, left), 33rd (dashed curve, left), 36th (dashed curve, right), and 40th (solid curve, right) eigencurrent of a line array of 40 rings in a half space space with $h/a = 6/5$. Normalization: maximum absolute ϕ-component of the 1st eigencurrent. Parameter values as in Figure 5.42.

grating-lobe positions for the scan angles $\pm 42.3^\circ$, i.e., $\mp 83.7^\circ$. For the 36th eigencurrent in Figure 5.43 (right), the main-lobe positions correspond to the main-lobe positions obtained for free space and, hence, the main lobes represent scan lobes and their corresponding grating lobes. The same behavior is observed for the 40th eigencurrent, which generates only two main lobes as the 40th eigencurrent in free space.

The absence of main lobes at $\pm 90^\circ$ in the far field of the 32nd eigencurrent and the low intensity of two main lobes of the 33rd eigencurrent are explained by the behavior of the element patterns, or electric far fields, of the single-ring eigencurrents in a half space. These patterns exhibit zeros at $\pm 90^\circ$ and, hence, the far field of the array must exhibit zeros at $\pm 90^\circ$ as well.

5.3.3 Uniform Line Arrays of Strips

In this subsection, we compare the behavior of the eigenvalues of line arrays of strips with the behavior of the eigenvalues of line arrays of rings. Line arrays of strips are described in Section 3.5. The approach to calculate the eigenvalues is the same as the approach for line arrays of rings. Thus, we choose a single strip as the generating subarray and we compute the eigenvalues and eigencurrents of this strip as in Subsection 5.2.3. Next, we proceed from a single strip to a whole line array such that the number of subarrays N_{sub} equals the number of elements N_{el}. The centers of the strips are positioned on the x-axis as shown in Figure 3.2. The eigencurrents of a single strip composed of cosine expansion functions are symmetric with respect to the line-array axis, while the eigencurrents composed of sine expansion functions are anti-symmetric. Since a symmetric current does not couple with an anti-symmetric current, the cosine expansion functions generate symmetric array eigencurrents, while the sine expansion functions generate anti-symmetric array eigencurrents. These two types of array eigencurrents can be determined independently.

Calculation of the Moment Matrix

The moment matrix for a (uniform) line array of strips generated from a single strip is a block matrix, the diagonal blocks being diagonal matrices with the eigenvalues of a single strip on the diagonal. The off-diagonal blocks are dense matrices described by (5.19), where u_n^{sub} ($n = 1, \ldots, N_{\mathrm{cpl}}^{\mathrm{sub}}$) are the eigencurrents of a single strip that contribute significantly to the mutual coupling in the line array. To rewrite (5.19), we use the relationship (5.7) between the subarray inner product and the initializing L_2 inner product on the interval $[-1, 1]$. Then, we obtain

$$Z_{pq}(m,n) = \langle y_m^{\mathrm{sub}}, \mathcal{Z}_{\mathrm{a},pq} u_n^{\mathrm{sub}} \rangle_{L_2} \,, \tag{5.40}$$

where the functions y_n^{sub} form the bi-orthogonal set corresponding to the eigencurrents of a single strip. The functions y_n are calculated from (5.10) and their expansion coefficients with respect to the expansion functions on a single strip by (5.11). The projection $\mathcal{P}_{\mathrm{sub}}$ is omitted

in the inner product (5.40), because the functions y_n^{sub} are elements of ran$(\mathcal{P}_{\mathrm{sub}})$ and $\mathcal{P}_{\mathrm{sub}}$ is constructed by the L_2 inner product.

Like the components of the usual moment matrix in Subsection 3.3.1, Z_{pq} can be interpreted as a function of y_m^{sub} and u_n^{sub}. With this interpretation, Z_{pq} is a functional, which is calculated as in (3.15) with v replaced by y_m^{sub} and w replaced by u_n^{sub}. The remaining inner products incorporate the integral operator $\tilde{\mathcal{F}}_{pq}$ with kernel $\tilde{F}_{pq}$, which is singular for $p = q$ and regular for $p \neq q$. To calculate these inner products, we can substitute in (3.15) the expansions of y_m^{sub} and u_n^{sub} with respect to the expansion functions on a single strip. However, this way of computing the moment matrix is in general not efficient, because we may need to compute as many inner products as in the usual moment method. Therefore, we sample the functions y_n^{sub}, u_n^{sub}, and their derivatives first and, then, we compute the inner products by a 2D composite Simpson rule. To reduce the computational effort, we sample the kernel $\tilde{F}_{pq}$ before calculating the block matrix Z_{pq}. If this kernel is singular, the sampled eigencurrents might provide erroneous results for the moment-matrix components. However, since $p \neq q$ in (5.40), all integrands are regular. As mentioned above, the components of the block matrices Z_{qq}, which exhibit the singular behavior of the kernel $\tilde{F}_{qq}$, are diagonal matrices with the eigenvalues of a single strip on the diagonal. In more general terms, the singular behavior of the kernel plays a role in the initialization only. In the cycle, this behavior is incorporated in the eigenvalues of a single strip.

Comparison with Uniform Line Arrays of Rings

In general, the behavior of the eigenvalues and eigencurrents of line arrays of strips is the same as described in Subsection 5.3.2 for line arrays of rings. Moreover, relations between scanning, eigenvalues and eigencurrents, and the infinite-array approach are analogously described. Therefore, for line arrays of strips, we will specifically focus on the correspondences and differences with line arrays of rings.

As in Subsection 5.3.2, we first consider the spreads of the eigenvalues. Figure 5.44 (left) shows the maxima and minima of the absolute perturbations of the second group of eigenvalues for line arrays of half-wavelength strips with two different spacings, both in free space and in a half space with $h/\ell = 4/5$. Comparing the order of magnitude of the spread, i.e., 10^{-2}, with the orders of magnitude obtained for line arrays of rings, see Figure 5.18, we observe that this spread has the same order of magnitude as the spread of the third group of the line arrays of rings. Since we do not need to take into account this third group, we need not take into account the second group of line arrays of strips either.

Figure 5.44 (right) shows the maxima and minima of the absolute perturbations of the first group of eigenvalues as a function of the spacing for line arrays of 5, 10, 20, and 40 strips in a half space with $h/\ell = 4/5$. Since the strips can be positioned closer to each other than the rings, the maxima and minima are depicted for smaller spacings than 0.4λ for the line arrays of rings in Figure 5.19. The spread for line arrays of strips shows the same behavior as the spread for the

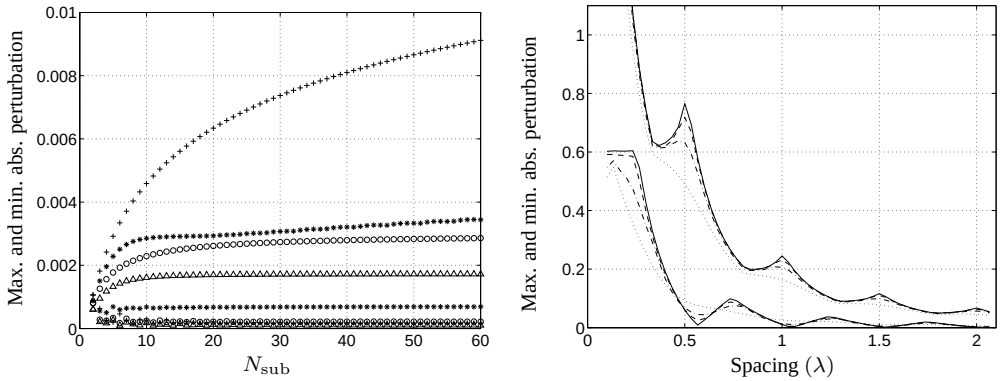

Figure 5.44 Left: the maximum and minimum absolute perturbation of the eigenvalues of the 2nd group for line arrays of strips as a function of the number of elements N_{sub}; the strip geometries corresponding to the different symbols are the same as specified in Figure 5.18. Right: the maximum and minimum absolute perturbation of the eigenvalues of the 1st group for line arrays of strips in a half space with $h/\ell = 4/5$; the numbers of elements corresponding to the different curve styles is the same as specified in Figure 5.19. Parameter values: $N_{\mathrm{cpl}}^{\mathrm{sub}} = 4$, $2\ell = \lambda/2$, $\beta = 1/50$, $N_{\cos} = 15$, $N_{\sin} = 0$.

line arrays of rings, but the local maxima are more pronounced, especially at half a wavelength.

We consider two different line array settings to compare the coefficient distributions of the eigencurrents of line arrays of rings and strips. First, we consider line arrays of rings and strips in free space with 10 elements and spacing $\lambda/2$. In both line arrays, we use the first two (symmetric) single-element eigencurrents to describe the mutual coupling. For a ring with a circumference of about a wavelength ($ka = \pi/3$), the eigencurrents are $u_1^{\mathrm{sub}}(\varphi) = \cos\varphi$ and $u_2^{\mathrm{sub}}(\varphi) = 1$. For a strip of half a wavelength, Figure 5.6 shows the eigencurrents. Figure 5.45 shows the absolute coefficients of u_1^{sub} and u_2^{sub} in the first and last eigencurrents of the first group and the corresponding phases of the coefficients of u_1^{sub}. Both the absolute values and the phases of the coefficients of u_1^{sub}, which describe the dominant behavior of the eigencurrents for the two line arrays, agree very well. The coefficients of u_2^{sub}, which describe the perturbation, do not match. The perturbations are larger for the line array of rings than for the line array of strips, because the mutual coupling between the single-element eigencurrents u_2^{sub} for the rings is stronger than the mutual coupling for the strips. Moreover, the behavior of the perturbations differs, which is explained by the same reasoning as described in relation to Figure 5.26. The absolute coefficients of u_m^{sub} and $u_{m'}^{\mathrm{sub}}$ in a certain eigencurrent $\boldsymbol{u}_{nq}$ generate the same patterns, if the eigencurrents u_m^{sub} and $u_{m'}^{\mathrm{sub}}$ have the same even or odd symmetry with respect to the line parallel to the y-axis through the center of the element. For the line array of strips, u_1^{sub} and u_2^{sub} have the same symmetry, but for the line array of rings, they do not have the same symmetry.

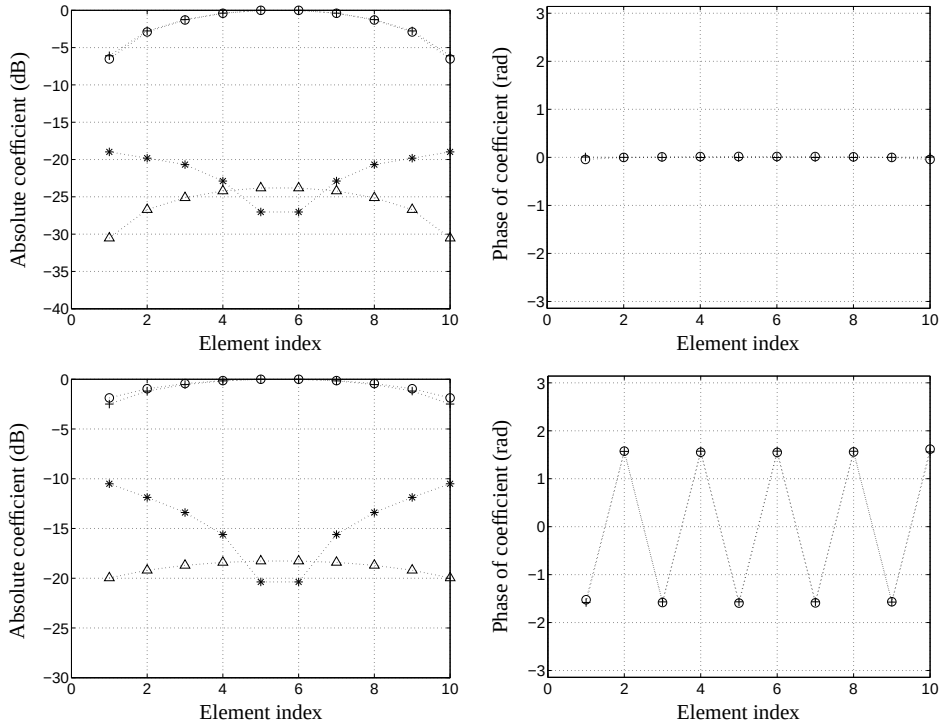

Figure 5.45 Left column: Absolute coefficients (in dB) of u_1^{sub} (rings: $+$, strips: $\circ$) and u_2^{sub} (rings: $*$, strips: $\triangle$) in the 1st (upper left) and 10th (lower left) eigencurrent of the 1st group for a line array of 10 rings and a line array of 10 strips in free space. Right column: phases corresponding to the coefficients of u_1^{sub}. Eigencurrent normalization: maximum coefficient. Parameter values of the line array of rings: $N_{\mathrm{cpl}}^{\mathrm{sub}} = 2$, $d = \lambda/2$, $ka = \pi/3$, $\beta = 3/100$, $\psi = 0$, $N_{\cos} = 2$, $N_{\sin} = 0$. Parameter values of the line array of strips: $N_{\mathrm{cpl}}^{\mathrm{sub}} = 2$, $d = \lambda/2$, $2\ell = \lambda/2$, $\beta = b/\ell = 1/50$, $N_{\cos} = 15$, $N_{\sin} = 0$.

Therefore, the behavior of the perturbations differs.

Finally, we consider line arrays of rings and strips in a half space ($h = \lambda/5$) with 40 elements and spacing $3\lambda/5$. As in the first example, we use the first two (symmetric) single-element eigencurrents to describe the mutual coupling. Figure 5.46 shows the absolute coefficients of u_1^{sub} and u_2^{sub} in the 13th, 19th, and 35th eigencurrents of the first group and the corresponding phases of the coefficients of u_1^{sub}. As in Figure 5.45, the coefficients of u_1^{sub} match very well, while the coefficients of u_2^{sub} differ. *Thus, we conclude that the eigencurrents of line arrays of rings and strips have the same dominant coefficient distribution. Based on this conclusion, we expect that the coefficient distribution of the eigencurrents of (line) arrays is independent of the element shape.*

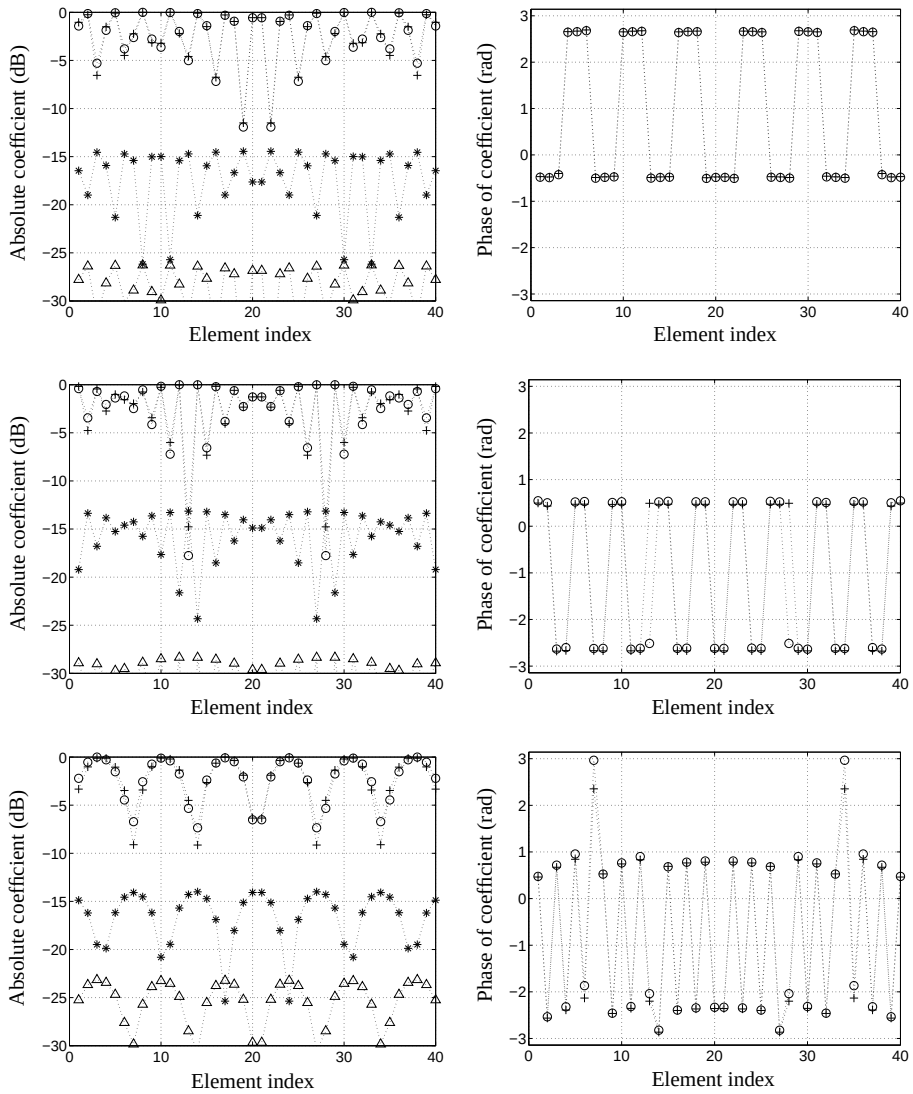

Figure 5.46 Left column: absolute coefficients (in dB) of u_1^{sub} (rings: $+$, strips: $\circ$), and u_2^{sub} (rings: $*$, strips: $\triangle$) in the 13th (1st row), 19th (2nd row), and 35th (3rd row) eigencurrents of the 1st group for a line array of 40 rings and a line array of 40 strips in a half space with $h = \lambda/5$. Right column: phases corresponding to the coefficients of u_1^{sub}. Eigencurrent normalization: maximum coefficient. Parameter values as in Figure 5.45, but with $d = 3\lambda/5$.

5.4 Summary of the Conclusions and Discussion

In this section, we summarize point-by-point the main conclusions obtained for a single ring/strip, and for line arrays of rings/strips. Moreover, based on these conclusions, we arrive at recommendations for the application of the proposed eigencurrent approach to arrays of arbitrary elements. We describe first the results for a single ring/strip.

1. *For ring circumferences and strip lengths up to a few times the wavelength, a low number ($\lesssim 10$) of eigencurrents is sufficient to describe the current accurately. The exact number depends on the excitation.*

   The eigenvalues ν_n of rings and strips tend as $n\sqrt{n}$. The slope of the eigenvalue curve decreases non-monotonically with the ratio of wavelength and ring circumference or strip length.

2. *For a strip, the approximation of the first eigencurrents is independent of the chosen expansion functions. The eigencurrents of a ring are known in closed form, i.e., cosine and sine functions, which depend only on the angle that describes the circumference.*

   The eigencurrents of a strip are evaluated numerically both for entire-domain and piecewise expansion functions. The entire-domain expansion functions show that the eigencurrents are cosine and sines plus a perturbation. The first $\lfloor N_{\mathrm{exp}}/4 \rfloor$ eigencurrents obtained by N_{exp} piecewise expansion functions equal the first $\lfloor N_{\mathrm{exp}}/4 \rfloor$ eigencurrents obtained by the entire-domain expansion functions.

3. *The eigencurrents for a single element depend only weakly on the geometry parameters, if they depend at all. As a result, if the eigencurrents for one setting of geometry parameters are computed, the eigenvalues for other settings can be calculated from the Rayleigh-Ritz quotient (5.14).*

   The eigencurrents of a ring do not depend on the geometry parameters. The eigencurrents of a strip do not depend on the ratio of length and wavelength and the ratio of height above the ground plane and wavelength. They depend only weakly on the ratio of width and length.

4. *The eigencurrent corresponding to the smallest eigenvalue (in absolute sense) contributes most to the radiated energy, if this eigencurrent matches well the excitation field.*

   The current is expanded into the set of (approximated) eigencurrents. In the resulting series, each eigencurrent is multiplied by its corresponding inverted eigenvalue.

5. *The inner product with respect to which the eigencurrents are orthogonal can be evaluated efficiently. This saves computational effort in the cycle of the eigencurrent approach.*

The eigencurrents of a ring are orthogonal with respect to the L_2 inner product. Only the first few eigencurrents of a strip are non-orthogonal.

Next, we describe the results for line arrays of rings/strips.

6. *For line arrays of rings, only the first two or three single-ring eigencurrents contribute to the mutual coupling. For line arrays of strips, only the first one or two single-strip eigencurrents contribute to the mutual coupling. The other single-element eigencurrents only influence the local behavior of the elements.*

   For line arrays of strips/rings with symmetric eigencurrents only, the spreads of the second and third groups, respectively, is of the order 10^{-2}. For line arrays of rings with anti-symmetric eigencurrents only, the spread of the second group is of the order 10^{-2}. The physical explanation of these observations is that the electromagnetic fields induced by the eigencurrents with larger eigenvalues are much more reactive than the electromagnetic fields induced by eigencurrents with lower eigenvalues.

7. *The eigencurrents of an array are described as concatenations of linear combinations of the single-element eigencurrents. In this description, the coefficients of the dominant single-element eigencurrent depend negligibly on the element shape.*

   Line arrays of strips and line arrays of rings generate the same coefficients for the dominant single-element eigencurrent in each group of array eigencurrents. Moreover, for line arrays of rings, these coefficients depend negligibly on the ring geometry parameters.

8. *Arrays are entire objects rather than collections of separate elements.*

   The coefficients of the dominant single-element eigencurrent in each group of eigencurrents of a line array of rings or strips and the expansion coefficients of the eigencurrents of a single strip with piecewise functions generate the same patterns. Since a strip is an entire object, line arrays are entire objects as well.

9. *The broadside scan, the monopulse, and the grating lobe are reflected in specific eigencurrents of the array.*

   We note first that the eigenvalues of each group are indexed according to the (oriented) curve they generate in the complex plane. The coefficient distributions of the array eigencurrents of line arrays of rings and strips are amplitude and phase tapers on the elements. The electric far field of the first eigencurrent of the first group is an amplitude-tapered broadside scan beam with side lobes of about -24 dB. The electric far field of the second eigencurrent is an amplitude-tapered monopulse. The eigencurrent with index given by (5.39) represents the $\pm 90^\circ$ scan for spacings smaller than half a wavelength. For larger spacings, this eigencurrent generates main lobes at the grating-lobe scan angle with corresponding grating lobes at $\pm 90^\circ$.

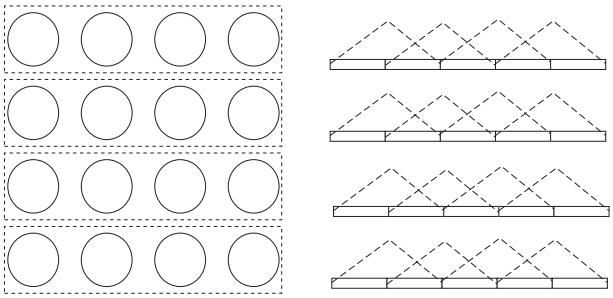

Figure 5.47 Schematic comparison two arrays. Left: a rectangular array of rings with a line array as generating subarray. Right: a line array of strips with piecewise functions defined on the strips.

10. *All array eigenvalues are related to specific scan angles of the array. These scan angles are the positions of the main lobes in the far fields of the corresponding eigencurrents.*

    The linear phase taper corresponding to a specific scan angle averages the block-like phase distribution (with phase shifts of $180°$) of the eigencurrents of line arrays. The eigencurrent with closest total phase shift will be stronger excited than the other eigencurrents. Since each eigencurrent generates an electric far field with certain main lobes, one of the main lobes of the excited eigencurrent will be the main lobe of the array.

11. *Finite arrays with and without ground plane show the same eigencurrent behavior. The difference is in the eigenvalues of the moment matrix. The eigenvalue range is bounded for a half space and tends to become unbounded for free space.*

    The eigenvalues of a finite array can be grouped, where each group corresponds to an eigenvalue of a single element. For an infinite array, the same statement is valid. For a half space, the finite-array groups converge to the infinite-array groups as the number of elements tends to infinity. Our conjecture is that this is not true for free space.

12. *The impedance operator of line arrays of rings and strips is almost normal and, hence, the corresponding eigencurrents are almost orthogonal.*

    This statement is confirmed numerically by analyzing Gram matrices of eigencurrent sets of line arrays of rings and strips.

We end this section with recommendations how the proposed eigencurrent approach should be applied in the determination of eigencurrents of arrays of arbitrary elements. Let us first consider rectangular arrays of rings and strips. Figure 5.47 (left) shows a rectangular array of elements, in this case rings, with a line array as generating subarray. The array eigencurrents are then described as concatenations of linear combinations of the subarray eigencurrents. Based on the

following observations, we expect that the coefficients of the subarray eigencurrents generate the same patterns as line arrays of rings and strips. Line arrays of rings and a strip with piecewise functions generate the same coefficient patterns. Moreover, line arrays of strips generate the same coefficient patterns as line arrays of rings. Interpreting line arrays of strips as rectangular arrays of overlapping microstrip pieces, we come to the given expectance for rectangular arrays.

If the element is not a ring or a strip, but a more complex element such as the one used by Thales shown in Figure 1.2, the analysis is analogous to the one for line arrays of strips/rings. First, the eigencurrents of a single element are determined by choosing certain expansion functions, for example piecewise functions such as rooftops [77: p. 600] and Rao-Wilson-Glisson (RWG) functions [96]. Next, only a few eigencurrents are used in the array analysis. As in the analysis of line arrays of strips/rings, the level of mutual coupling is described by the spread of the eigenvalues. For elements of which the current cannot be averaged, the behavior of the single-element eigenvalues will be more complicated. For example, for a patch, the eigenvalues are of the form of the eigenvalues of a rectangular membrane. Since the eigenvalues of a rectangular membrane are $\pi(m^2/a^2+n^2/b^2)$, where a and b are the length and width, the eigenvalues of a patch will exhibit such a form as well.

For other array compositions, the analysis is analogous to the analysis for line arrays of strips and rings as well. Each subarray decomposition depends on the spacing and the excitation as explained in Section 1.3. If the space surrounding the elements is changed, for example by inserting a dielectric layer, the integral kernel is changed as well, but the eigencurrent analysis will remain the same. Stronger mutual coupling, for example due to surface waves in the dielectric, may increase the number of single-element eigencurrents that contribute to the mutual coupling in an array. Although not confirmed by our research, we believe that the number of coupling single-element eigencurrents will not increase in this case. Our reasons are, first, that the single-element eigencurrents incorporate the main effect of the dielectric layer. Second, the number of coupling groups is not only dependent on the spread, but also on the behavior of the single-element eigenvalues. Finally, the stronger mutual coupling due to, for example, surface waves may increase the spread in the eigenvalue groups. This effect can be handled by the eigencurrent approach, because the perturbation of the eigenvalues does not necessarily need to be small, as mentioned in Section 5.

CHAPTER 6

Test Cases for the Eigencurrent Approach

In this chapter, the main items of both our research phases, i.e., the phase concerning the element-by-element moment method and the phase concerning the eigencurrent approach, are joined, see the scheme in Figure 1.9. In Section 6.1, we compare results of the eigencurrent approach with results of the element-by-element moment method for various line-array sizes. Next, in Section 6.2, we show that the eigencurrent approach can predict the large variations of element-current amplitudes observed in the third example of Section 2.5. These variations, and corresponding variations of element impedances, cannot be predicted by the infinite-array approach and may decrease the performance of an array considerably. We propose an explanation, alternative to the explanation in [53, 82] based on array surface waves, for the large variations by showing that they are caused by the excitation of specific resonant eigencurrents. Moreover, we show that on basis of the behavior of the eigenvalues, resonances are predicted and suitable loads can be determined to prevent the excitation of resonant eigencurrents.

In Section 6.3, we first show that the spread of the eigenvalues is a quantitative measure for mutual coupling and, therewith, for the number of eigencurrent groups needed in the cycle of the eigencurrent approach. This investigation leads again to the identification of resonances of arrays. We show that the modulated oscillations of element impedances discussed in [30, 46] are caused by the excitation of specific resonant eigencurrents and, therewith, by the same mechanism as the variations of element impedances attributed to surface waves. Next, we show that mutual coupling between distant elements may be neglected, but that special care is needed. Except near the appearance of a grating lobe, the number of neighbors needed to describe mutual coupling is well predicted by the variation of the spread as a function of the number of elements in small arrays. Finally, we show that by fixing eigencurrents for a chosen set of geometry parameters, performance parameters for other sets of geometry parameters can be predicted in a fast and accurate way.

In Section 6.4, we show that the eigencurrent approach is capable of predicting the array behavior at the grating lobe scan angle. Moreover, we explain how this result supports our idea

that the eigencurrent approach can not only handle arrays positioned in free and half space, but also arrays on dielectric layers, which may support surface waves. Finally, we present the conclusions of this chapter in Section 6.5.

6.1 Validation

To validate the eigencurrent approach and its implementation, we consider three test cases of line arrays of strips and rings, for which the element geometry and the spacing are chosen as in many practical applications. The ring circumference is about wavelength and both the strip length and the spacing are half a wavelength. Other array geometries are considered extensively in the next sections. The following three test cases are considered.

- A line array of 40 rings in free space with spacing $\lambda/2$. Each ring is excited by a voltage gap of 1V. Figure 6.1 shows the normalized ϕ-component of the electric field for a scan at 0° and a scan at 45° in the xz-plane and the corresponding (normalized) ring impedances. For details on scanning, see below. The definition of impedance is given in Section 4.2.2 and the electric far field is described in Appendix C.

- A line array of 10 strips of half a wavelength in a half space with $h/\ell = 4/5$ and with spacing $\lambda/2$. Each strip is excited by a voltage gap of 1V. Figure 6.2 shows the normalized ϕ-component of the electric far field for a scan at 55° in the xz-plane and the corresponding normalized absolute strip impedances.

- Line arrays of 100 rings and 100 strips with spacing $\lambda/2$ in free space and in a half space with $h/\ell = 4/5$, respectively. Each element is excited by a voltage gap of 1V. Figure 6.3 shows the normalized absolute element impedances for scans at 70° in the xz-plane.

In this chapter, all line arrays are positioned in the xy-plane with centers on the x-axis and their indices increase in the positive x-direction. The scan angles and the incident angles of plane waves are spherical elevation angles in the xz-plane, where a corresponding spherical azimuth angle of 0° is prescribed, see Section 3.5 for details on scanning and Section 4.3 for details on plane waves. The voltage gaps of the strips are positioned at their centers. If not mentioned otherwise, the voltage gaps of the rings are positioned on the x-axis, to be precise, at $\varphi = \pi$, where $\psi = 0$, see Section 4.2.

In all three test cases, we choose 8 cosine expansion functions on each ring or strip. In the element-by-element moment method, we construct the moment matrix with these functions. In the eigencurrent approach, we compute the eigencurrents of a single element prescribing these functions. Next, we calculate the eigencurrents of the line arrays with only one or two single-element eigencurrents per element, or, with only one or two groups of coupling eigencurrents.

The electric far-field components, obtained by the eigencurrent approach with one group of coupling eigencurrents, match the results of the moment method perfectly for the broadside scan of the line array of 40 rings and for the 55° scan of the line array of 10 strips. Only close to endfire slight differences occur. For the 45° scan of the line array of 40 rings, the main and side lobes obtained by the eigencurrent approach are about 0.6 dB lower than the main and side lobes obtained by the moment method. For two coupling eigencurrents, we found a perfect match.

Both for one and two groups of coupling eigencurrents, the curves describing the impedance variation obtained by the eigencurrent approach show the same shape as the curve obtained by the (element-by-element) moment method. For the line arrays of 10 and 100 strips, the differences between the absolute impedances obtained by the moment method and by the eigencurrent approach are less than 1.2% and 0.3% for one and two groups of coupling eigencurrents. For the line array of 100 rings, these differences are 5.9% and 1.9%. The percentages confirm the statement of the previous chapter that two groups of coupling eigencurrents are needed for line arrays of rings and only one group of coupling eigencurrents is needed for line arrays of strips. For the line array of 40 rings, the differences between the absolute impedances obtained by the moment method and by the eigencurrent approach for both one and two groups of coupling eigencurrents are smaller than 1%. The differences for only one group are somewhat smaller than the differences for two groups. However, especially for 45°, the results for two groups are more accurate than the results for one group, because the phase differences between the impedances obtained by the moment method and by the eigencurrent approach run up to 0.1 rad for one group, while they are smaller than 0.01 rad for two groups. For one group, the phase differences are approximately uniform over the array.

Table 6.1 shows the computation times for line arrays of rings in free space, both for the moment method and for the eigencurrent approach with one and two groups of coupling eigencurrents. The computations are carried out with a Matlab implementation on the platform men-

Table 6.1 CPU times (seconds) for the current on line arrays of 10, 40, 100, 200, and 400 rings in free space with spacing $\lambda/2$ for a Matlab implementation on the platform mentioned in Section 1.4. Parameter values: $ka = \pi/3$, $\beta = 3/100$, $\psi = 0$, $N_{\cos} = 8$, $N_{\sin} = 0$.

Number of rings	Moment Method	Eigencurrent approach 1 group	Eigencurrent approach 2 groups
10	35	$\langle$ 1	$\langle$ 1
40	118	2	3
100	303	4	15
200	730	19	90
400	–	106	1035

tioned in Section 1.4. For only one group of coupling eigencurrents, the computation times for the eigencurrent approach are at least 40 times smaller than the computation times for the element-by-element moment method. For two groups of coupling eigencurrents, the computation time for the eigencurrent approach is for 10 rings about 70 times lower than the computation time for the moment method, while for 200 rings, this factor reduces to 7. The reduction is mainly due to the increase of the time needed to determine the eigencurrents, which is, for a given matrix size, larger than the matrix inversion time. The problem of efficiency reduction of the approach can be avoided in two ways. First, since the dominant behavior of the eigencurrents depends negligibly on the geometry parameters, see Section 5.4, we need to compute the eigencurrents only once, while we need to carry out a matrix inversion for each new set of geometry parameters. The computational reduction obtained in the eigencurrent approach by fixing the eigencurrents is discussed in Section 6.3 in further detail. Second, instead of the standard Matlab function 'eig', which is based on the QR decomposition, other methods and corresponding implementations can be used to compute the eigenvalues and eigencurrents. In [2: Sec. 2.6, Ch. 7], several methods are described for computing the eigenvalues and eigenvectors of non-hermitian matrices.

An important advantage of the eigencurrent approach over the usual moment method is that the eigencurrent approach keeps the moment-matrix size relatively small. This advantage is apparent from Table 6.1. The standard Matlab function 'eig' calculates the eigencurrents of a line array of 400 rings both for one and two groups of coupling eigencurrents. Once these eigencurrents have been computed, the computation of the currents takes only 31 seconds and 64 seconds, respectively. In contrast, the standard Matlab matrix inversion in the moment method implementation runs out of memory for the same line array of 400 rings with 8 expansion functions per ring. The construction of the moment matrix takes 1482 seconds in this case, which is more than the total computation time of the implementation of the eigencurrent approach with two groups of coupling eigencurrents.

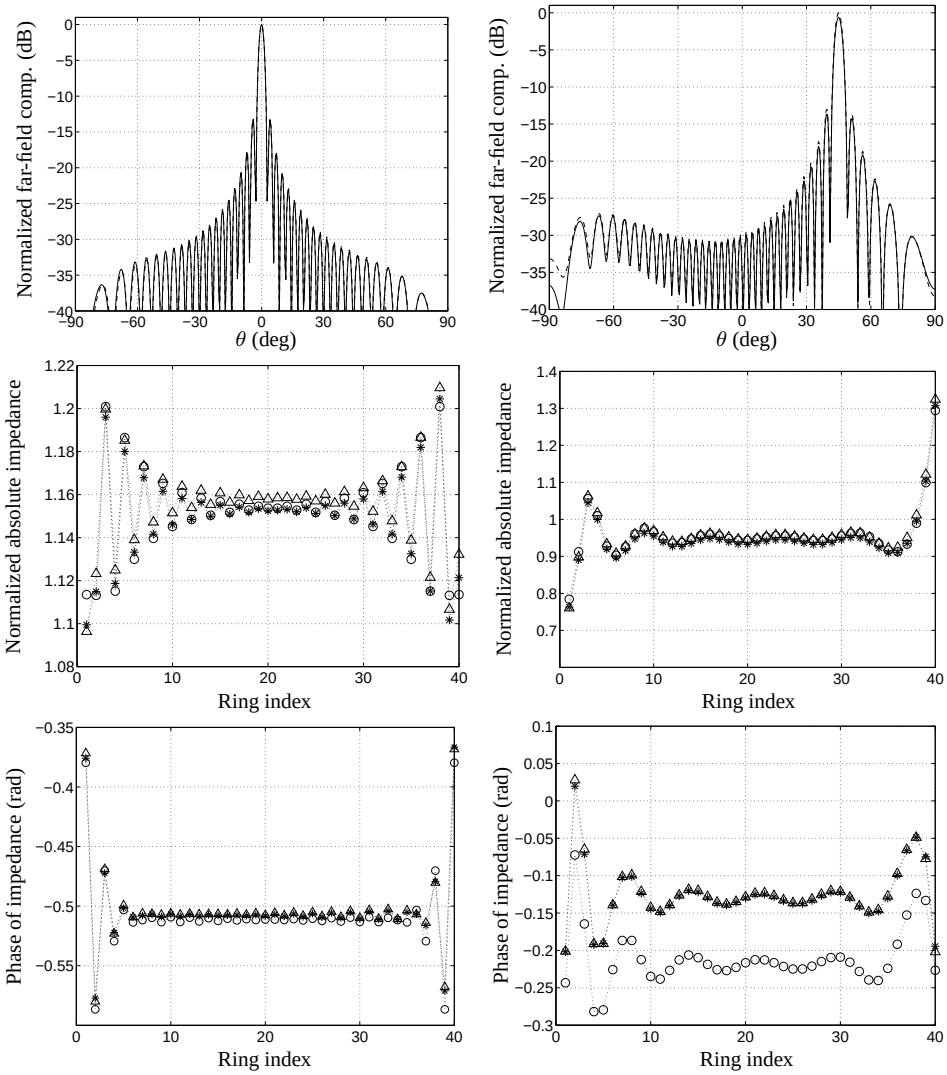

Figure 6.1 First row: the normalized absolute ϕ-components (in dB) of the electric far field in the xz-plane for a line array of 40 rings in free space for a scan at 0° (left) and for a scan at 45° (right), computed by the moment method (solid curve) and by the eigencurrent approach with one group of coupling eigencurrents (dashed curve). Second and third rows: the corresponding normalized absolute values and phases of the ring impedances ($*$: moment method, $\circ$: one group, $\triangle$: two groups). Excitation: voltage gaps of 1V on the rings. Normalization far field: maximum absolute component in the xz-plane. Normalization impedance: single-ring impedance. Parameter values: $d = \lambda/2$, $ka = \pi/3$, $\beta = 3/100$, $\psi = 0$, $N_{\cos} = 8$, $N_{\sin} = 0$.

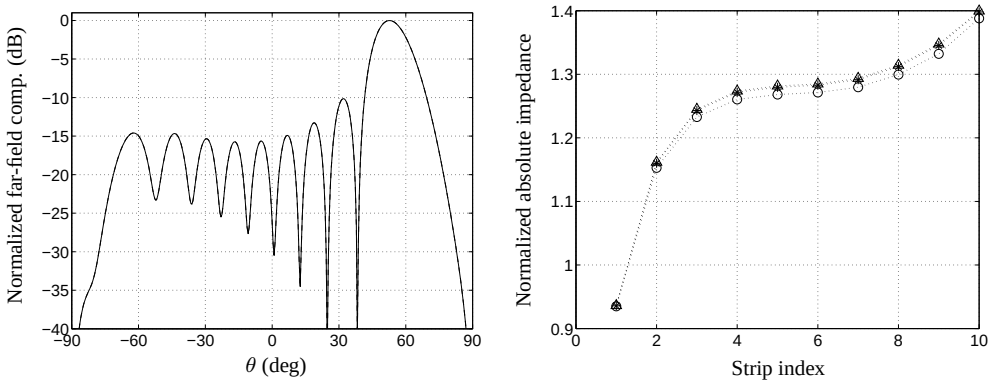

Figure 6.2 Left: normalized absolute ϕ-components (in dB) of the electric far field in the xz-plane for a line array of 10 strips in a half space with $h/l = 4/5$ for a scan at $55°$, computed by the moment method (solid curve) and by the eigencurrent approach with one group of coupling eigencurrents (dashed curve (indistinguishable)). Right: the corresponding normalized absolute impedances computed by the moment method ($*$) and by the eigencurrent approach with one ($\circ$) and two ($\triangle$) groups of coupling eigencurrents. Normalization and excitation as in Figures 6.1. Parameter values: $d = \lambda/2$, $2\ell = \lambda/2$, $\beta = b/\ell = 1/50$, $N_{\cos} = 8$, $N_{\sin} = 0$.

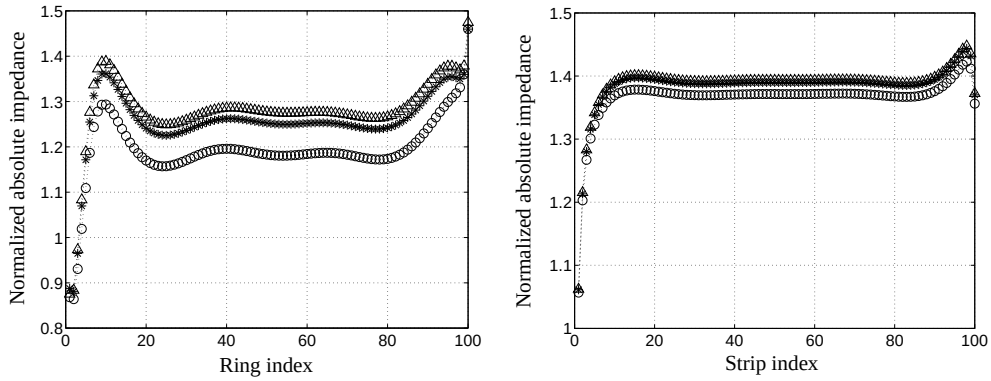

Figure 6.3 Normalized absolute element impedances for line arrays of 100 rings (left) and 100 strips (right) in free space and in a half space with $h/\ell = 4/5$, respectively, computed by the moment method ($*$) and by the eigencurrent approach with one ($\circ$) and two ($\triangle$) groups of coupling eigencurrents. Scan angle: $70°$. Normalization, excitation, and parameter values as in Figures 6.1 and 6.2.

6.2 Impedance Variation, Array Surface Waves, and Design

Strong variation of the current amplitudes over an array and, consequently, strong variation of element impedances, may decrease the performance of the array considerably. To explain this, we first mention that, in various types of arrays, certain groups of elements are all matched with the same impedance to the feeding network of the array. An example is the rectangular array of rings as discussed in the fifth example of Section 2.5, see Figure 2.12 (right), which is excited per row by means of suitable feeding networks. The elements of each row are matched with the same impedance to the feeding network of the row. Next, we consider the third example of Section 2.5 (Figures 2.9 and 2.10), which concerns a line array of 25 strips. In this example, the current amplitudes at 10 GHz are almost uniform, while they show a strong variation at 8.6 GHz. If all strips are matched with the same impedance to a feeding network, the energy reflection of the strips is almost uniform at 10 GHz. For the same matching, huge differences in energy reflection occur at 8.6 GHz. Consequently, the total radiated power decreases and the far field is distorted.

Recently, the occurrence of (array) surface waves carried by the elements of (finite) arrays has been studied in detail in [53, 82] to explain the change from a low variation of element-current amplitudes into a high variation. These waves have a main component that propagates along the plane of the array. In this section, we show that the high variation of element-current amplitudes and element impedances is caused by the excitation of specific resonant eigencurrents. Moreover, we show that the eigencurrent approach is capable of predicting the change. To this end, we show first that the positions of the main lobes in the far fields of the eigencurrents of an array are indeed specific scan angles of this array, as stated in Section 5.4.

Let us consider the example of Section 5.3.2 of a line array of 15 rings in free space with spacing $\lambda/2$. We recall that the eigencurrents and eigenvalues of an array can be divided into groups, where each group corresponds to a single-element eigenvalue. In the example, the eigencurrents of the first group, which corresponds to the lowest single-ring eigenvalue, generate far fields with main-lobe positions shown in Table 5.7. The main lobes of the first and 7th eigencurrents are positioned at 0° and $\pm 26.1^\circ$, respectively. As discussed in Subsection 5.3.2, we expect that for scans at 0° and 26.1°, these eigencurrents are excited especially. This is confirmed by Figure 6.4, which shows, for scans at 0° and 26.1°, the normalized absolute coefficients in the finite expansion (5.28) of the current in terms of the eigencurrents. The (expansion) coefficients are $\langle \boldsymbol{u}_{nq}, \mathcal{P}\boldsymbol{v}^{\mathrm{ex}} \rangle / \nu_{nq}$, i.e., the product of the inverted eigenvalues and the inner products of the eigencurrents and the excitation field. Only the coefficients of the first group are shown, i.e., $n = 1$. For the scan at 0°, the coefficient of the first eigencurrent is at least three times larger than the coefficients of the other eigencurrents. For the scan at 26.1°, the coefficient of the 7th eigencurrent is at least four times larger than the coefficients of the other eigencurrents, except for its neighbors. Hence, the scan lobe at 26.1° is composed of the far fields of the 6th, 7th,

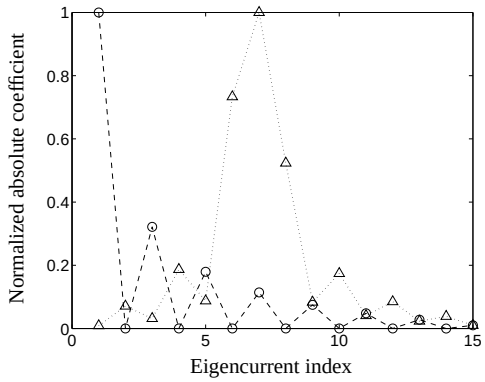

Figure 6.4 Normalized absolute coefficients in the finite expansion (5.28) of the current for a uniform line array of 15 rings in free space with spacing $\lambda/2$ for a scan at 0° ($\circ$) and a scan at 26.1° ($\triangle$). Only the coefficients of the first group of eigencurrents are shown. Excitation: voltage gaps of 1V on the rings. Normalization: maximum coefficient for each scan angle. Parameter values: two groups of coupling eigencurrents, $ka = \pi/3$, $\beta = b/a = 3/100$, $\psi = 0$, $N_{\cos} = 8$, $N_{\sin} = 0$.

and 8th eigencurrent. The composition is shown in Figure 6.5 (left) for the ϕ-component of the electric far field in the xz-plane. Figure 6.5 (right) shows the total ϕ-component in this plane. These results confirm the statement of Section 5.4 that the positions of the main lobes in the far

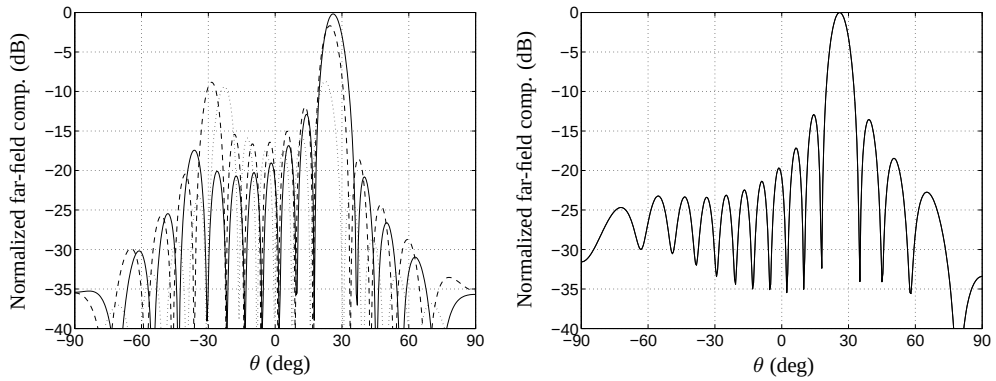

Figure 6.5 Normalized absolute ϕ-component (in dB) of the electric far field in the xz-plane for the line array of Figure 6.4. Left: only the first 6 (dotted curve), 7 (dashed curve), and 8 (solid curve) eigencurrents of the first group are taken into account in the finite expansion (5.28) of the current. Right: all terms are taken into account. Normalization: maximum absolute component in the xz-plane for all terms.

fields of the eigencurrents of an array are specific scan angles of this array. Finally, the series coefficients of the second group show about the same behavior as the series coefficients of the first group, because the coefficients of the dominant single ring eigencurrents in the first and second groups exhibit the same behavior as observed in Subsection 5.3.2. The magnitude of the series coefficients of the second group is about 10 times lower than the magnitude of the series coefficients of the first group. This is partly explained by the difference of about a factor of 5 between the eigenvalues of the first and second groups.

Next, we consider the third example of Section 2.5, i.e., a line array of 25 strips in free space with spacing 9 mm. The array is excited by a plane wave with incident angle -45° and polarized along the y-axis. As mentioned at the beginning of this section, at 10 GHz, the current amplitude in the centers of the strips is almost uniform as a function of the strip index. In contrast, large variations of element-current amplitudes occur at 8.6 GHz. Figure 6.6 shows the normalized absolute coefficients in the finite expansion (5.28) of the current for three frequencies. Only the coefficients of the first group are shown. At 9 GHz and 10 GHz, the largest coefficients

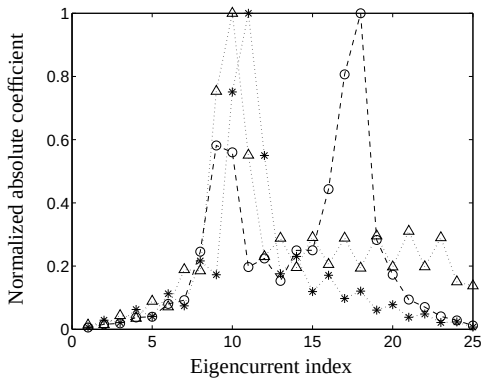

Figure 6.6 Normalized absolute coefficients in the finite expansion (5.28) of the current for a line array of 25 strips in free space with spacing 9 mm and excited at 8.6 GHz ($\circ$), 9 GHz ($\triangle$), and 10 GHz ($*$) by a plane wave with incident (elevation) angle -45° and polarized along the y-axis with amplitude $10^{-3}\mathrm{Vm}^{-1}$ Coefficients computed by the eigencurrent approach with two groups of coupling eigencurrents; only the coefficients of the first group are shown. Normalization: maximum coefficient for each frequency. Parameter values: one group of coupling eigencurrents, $2\ell = 15$ mm, $\beta = b/\ell = 3/50$, $N_{\cos} = 8$, $N_{\sin} = 0$.

correspond to the 9th and 10th eigencurrents and to the 10th and 11th eigencurrents, respectively. These eigencurrents induce main lobes at $\pm 42.4^\circ$, $\pm 47.5^\circ$, and $\pm 55.6^\circ$. At 8.6 GHz, the 9th and 10th eigencurrents exhibit large coefficients as well, but the coefficients corresponding to the 17th and 18th eigencurrents are larger. Hence, the 17th and 18th eigencurrents dominate the behavior of the current. Figure 6.7 shows that the current-amplitude variation observed

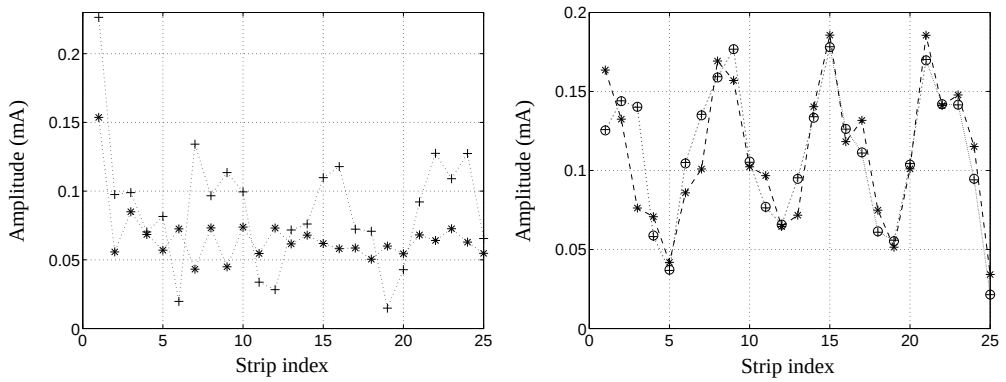

Figure 6.7 Current amplitudes (in the centers of the strips) for the line array of Figure 6.6 excited at 8.6 GHz. Left: only the first 14 ($*$) and the first 17 ($+$) eigencurrents of the first group are taken into account in the finite expansion (5.28). Right: the first 18 eigencurrents of the first group ($*$), all 25 eigencurrents of the first group ($+$), and all eigencurrents ($\circ$) are taken into account.

in the third example of Section 2.5, see Figure 2.10, is to a large extent determined by these eigencurrents. If only the first 14 eigencurrents are taken into account in the finite expansion of the current, the large variation is absent, see Figure 6.7 (left). For 18 eigencurrents, the current-amplitude variation is globally the same as the variation for all 25 eigencurrents of the first group as well as the variation for all eigencurrents, see Figure 6.7 (right). Further investigation revealed that the current-amplitude variation is globally described by the 8th – 18th eigencurrent of the first group. The result for all 25 eigencurrents of the first group and the result for all eigencurrents match almost perfectly. Differences are less than 1%, which is explained by the large differences (a factor of 30 or more) between the single-strip eigencurrent corresponding to the first group and the single-strip eigencurrents corresponding to the other groups. Moreover, both results differ at most 3% from the moment-method result in Figure 2.10 (right), which is explained by the use of only one group of coupling eigencurrents in the eigencurrent approach. These two observations illustrate why the single-mode approximation frequently applied in the literature is a good approximation for strips.

One could think that the excitation of the 17th and 18th eigencurrents is due to differences between the eigencurrents at 8.6 GHz and the eigencurrents at 10 GHz. However, in Section 5.4, we concluded that the eigencurrents of an array are described as concatenations of linear combinations of single-element eigencurrents, where the coefficients of the dominant single-element eigencurrents depend negligibly on the element shape and the frequency. This conclusion is based on numerical results for various geometries. Figure 6.8 shows that the statement is valid for large variations of frequency as well. Both absolute values and phases of the coefficients

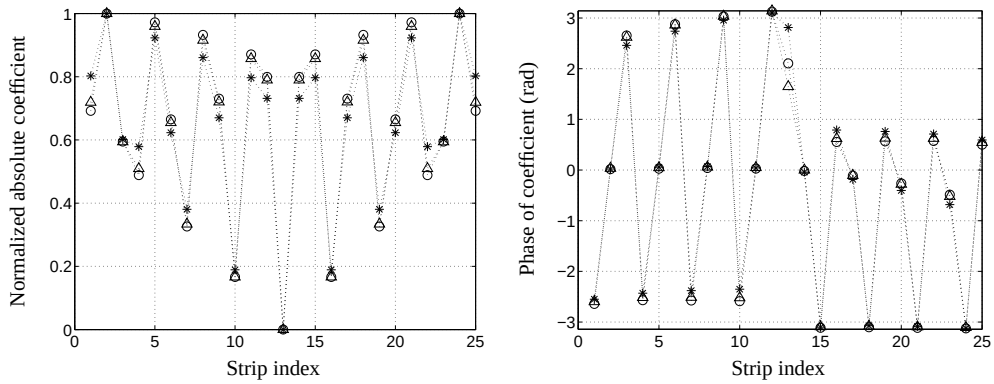

Figure 6.8 Absolute values (left) and phases (right) of the coefficients of the dominant single-strip eigencurrents in the 18th (array) eigencurrent of the first group for the array in Figure 6.6 with plane-wave excitation at 8.6 GHz (○), 9 GHz (△), and 10 GHz (∗). Normalization: maximum coefficient.

of the dominant single-strip eigencurrents in the 18th (array) eigencurrent are at 8.6 GHz the same as they are at 9 GHz and 10 GHz. Since single-element eigencurrents change negligibly except for scaling with the size of the element, also the eigencurrents themselves are the same at 8.6 GHz as at 9 GHz and 10 GHz. Hence, the excitation of the 17th and 18th eigencurrents at 8.6 GHz is not due to changes of the eigencurrents. Moreover, when in Figure 6.6 the inner products $\langle \boldsymbol{u}_{nq}, \mathcal{P}\boldsymbol{v}^{\mathrm{ex}} \rangle$ are plotted instead of the coefficients $\langle \boldsymbol{u}_{nq}, \mathcal{P}\boldsymbol{v}^{\mathrm{ex}} \rangle / \nu_{nq}$, the peak at the 17th and 18th eigencurrents disappears completely and the curve at 8.6 GHz becomes about the same as the one at 10 GHz. Hence, the peak is caused by a change of the eigenvalues.

Figure 6.9 (left) shows the eigenvalues in the complex plane for different frequencies, or, values of ka. Surprisingly, the eigenvalues of the first group are mainly shifted by the change of frequency, where the 25th eigenvalue of the curve remains on the imaginary axis (see p. 156 for details on the indexation of the eigenvalues). This suggests that the eigenvalues for different frequencies can be estimated, if the shift as a function of the frequency is somehow described. We leave the investigation of such an approximation as a topic of further research. Figure 6.9 (right) shows that at 10 GHz, the absolute eigenvalues are all of order 1, if they are normalized on the single-strip eigenvalue. In contrast, at 8.6 GHz, the eigenvalue of the 18th eigencurrent becomes very small, where the normalization is the same as at 10 GHz. Moreover, the neighboring eigenvalues are small as well. Consequently, the inverted eigenvalues become large and, hence, the corresponding series coefficients become large if the excitation field $\mathcal{P}\boldsymbol{v}^{\mathrm{ex}}$ matches sufficiently well with the eigencurrents. We have to write here 'sufficiently well' for the following reason. The difference between the series coefficients of the 9th and 18th eigencurrents is only a factor of 1.7, but the difference between the corresponding absolute eigenvalues is about a factor of

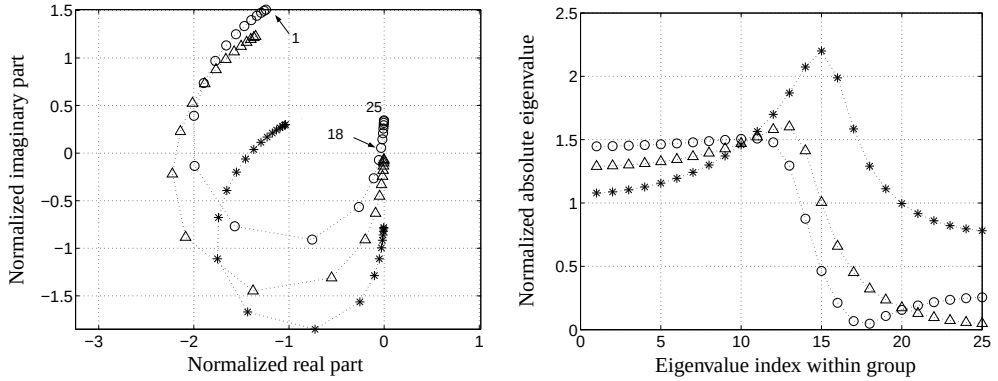

Figure 6.9 Normalized eigenvalues of the first group (left) and their absolute values (right) for the line array of strips in Figure 6.6 with plane-wave excitation at 8.6 GHz (○), 9 GHz (△), and 10 GHz (∗). Normalization: absolute value of the first single-strip eigenvalue at 10 GHz.

30. Hence, the 18th eigencurrent does not match that well to the excitation field; its excitation is mainly due to the decrease of its eigenvalue. Physically, this decrease can be interpreted as an increase of the energy level of the 18th eigencurrent. The same interpretation is found in the Quantum Mechanical description of particle behavior as discussed in Subsection 5.1.4. Finally, the increase of the series coefficients 15 – 25 at 9 GHz with respect to their values at 10 GHz is explained analogously.

Do there exist combinations of geometry parameters and frequencies in our model for which an eigenvalue becomes identically zero? This question is interesting from a mathematical point of view. In practice, the combination of geometry parameters and frequency will never be exactly the same as the combination for which an eigenvalue becomes zero. Moreover, in that case, the corresponding eigencurrent exhibits an infinitely high energy level. Finally, numerically, we will not find the exact combinations, if they exist, due to numerical approximation. From a practical point of view, it is more interesting to investigate the array behavior near the 'resonances'. The observations above show that large variations of element-current amplitudes and element impedances occur if one or more eigenvalues are relatively close to zero. Here, we must write 'relatively', because only the ratios of the eigenvalue related to the scan angle and all other (array) eigenvalues are of importance. In particular, we want to know in which frequency range(s) the large variations of element-current amplitudes occur. Moreover, we want to know to what extent these variations depend on the frequency. In this respect, it is important to realize that the behavior of both eigencurrents and eigenvalues observed above is 'stable'. The eigencurrents do not change with the geometry parameters and the frequency, while the eigenvalues are mainly shifted. Considering the eigenvalue curve in Figure 6.9 (left), we conclude that the large variations of current-amplitude occur below 9 GHz, at 8.94 GHz to be precise. Then, the normalized

last eigenvalue is much closer to the origin than the 9th and 10th eigenvalues that correspond to the scan angle. The variation of element-current amplitudes at 8.94 GHz exhibits an alternating phase with phase shifts of about $180°$, which corresponds specifically to the last eigencurrent. The number of maxima of the absolute current amplitude equals 8, which is close to the number of maxima of the 9th and 10th eigencurrents that induce the scan lobe at $45°$. If the frequency decreases, the 24th – 18th eigenvalue pass the origin. Hence, the large variations will occur at least over the range 8.6 GHz – 9 GHz. Globally the same variations of element impedances as at 8.6 GHz are obtained on the range 8.56 GHz – 8.61 GHz, where the impedance shows 4 peaks as in Figure 6.7 at about the same positions, see Figure 6.10. Considering Figure 6.10 in detail, we observe that the absolute impedances change for frequency changes of 20 MHz, but their global behavior remains the same. The same is valid for the corresponding phases.

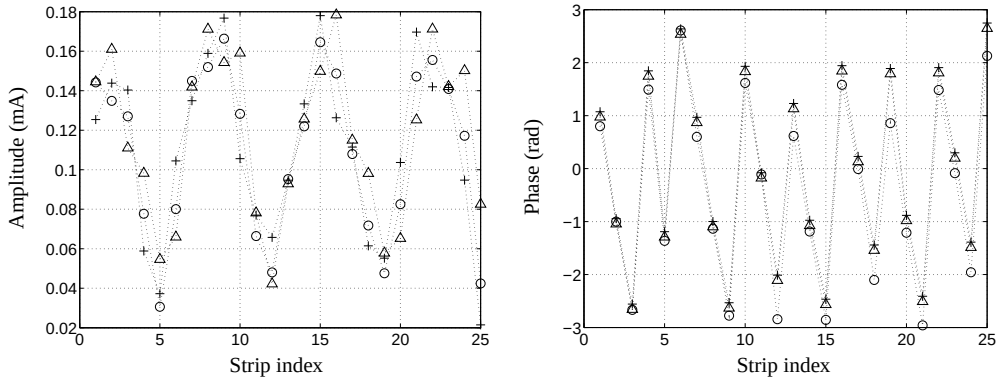

Figure 6.10 Current amplitudes (in the centers of the strips) and corresponding phases for the line array of Figure 6.6 excited at 8.6 GHz (+), 8.58 GHz (○), and 8.56 GHz (△). The amplitudes were obtained by the moment method; for the eigencurrent approach, the same amplitudes were obtained as in Figure 6.6.

Since the change of current-amplitude variation is caused by the excitation of specific eigencurrents, the question arises in what way they are related to the array surface waves studied in [53, 82]. The following relations are mentioned.

- In [82: p. 132], it is stated that array surface waves exist only on finite arrays, not on infinite arrays. In Subsection 5.3.2, we observed that the eigencurrents of a finite array are not the same as the eigencurrents of an infinite array, no matter the size of the finite array. The eigencurrents of the finite array have a block-like phase distribution, while the eigencurrents of the infinite array have a linear phase distribution. Moreover, the spectrum of finite array is discrete, while the spectrum of the infinite array is continuous, see Section 5.3.2, pp. 169 ff. For a given linear phase taper, only one eigencurrent is excited on the

infinite array, which corresponds to the direction of scan. In contrast, on the finite array, all eigencurrents are excited. Since the eigencurrents that cause the change of impedance variation are not related to the direction of scan, such eigencurrents are not excited on the infinite array for a given linear phase taper. This confirms the statement in [82: p. 132].

- In [82: p. 133], it is stated that array surface waves (on a finite array) radiate. This is confirmed by a result in [82: p. 96], which shows that the maximum lobe level of the far fields induced by the surface-wave currents is about 20 dB lower than the main lobe of the total far field. A similar result is found for the eigencurrents that cause the change of impedance variation. In the example above, the 17th and 18th eigencurrents do not induce main lobes. The ϕ-components of their far fields attain maxima at $\pm 90^\circ$ in the xz-plane, which at 8.6 GHz are 19 dB lower than the maximum of the first eigencurrent. At 10 GHz, the shape of the pattern is the same as the one at 8.6 GHz, but the maxima at $\pm 90^\circ$ are only 9 dB lower than the maximum of the first eigencurrent.

- In [82: p. 5], it is stated that array surface waves exist only for spacings smaller than half a wavelength. Similarly, only for spacings smaller than half a wavelength, eigencurrents without main lobes exist. In the example above, the spacing is 0.3λ for 10 GHz and 0.26λ for 8.6 GHz. Moreover, in the example of Figure 5.38 (right), where the 33rd – 40th eigencurrent do not show main lobes, the spacing is 0.4λ. For spacings larger than half a wavelength, all eigencurrents show main lobes and possibly also grating lobes, see Subsection 5.3.2.

- In [82: p. 88], a criterion is given for the occurrence of surface waves. This criterion must predict the resonant behavior studied above as well. Further research needs to be carried out on the criterion in relation to the resonant behavior.

- In [82: p. 5], the current is decomposed into Floquet currents, surface-wave currents, and end currents. The Floquet currents are currents with equal amplitudes on the array and a phase matching that of an incident plane wave, or in other words, currents that occur on an infinite array. The end currents are the total currents minus the Floquet and surface-wave currents. This decomposition depends strongly on the geometry parameters and the frequency. In contrast, the coefficients of the dominant single-element eigencurrents in the (array) eigencurrents depend negligibly on the geometry parameters and the frequency, as observed in Subsection 5.3.2. The global behavior of these coefficients remains the same, even when the frequency is 19% below the frequency for which the elements exhibit a 'resonant broadside embedded impedance', i.e., the reactances of the elements are on average zero. Only the eigenvalues change. Our decomposition is more physical than a decomposition into Floquet currents and other types of currents, because, on finite arrays, eigencurrents exist in contrast to Floquet currents.

On basis of the observations in this section, we conclude that eigencurrents describe array surface wave phenomena and related variations of element-current amplitudes and element impedances. More specifically, surface wave phenomena and the related variations are described by a limited number of coupling eigencurrents only. The example above illustrates that these eigencurrents are the eigencurrents of the first group. In this example, the 8th – 11th eigencurrent of the first group describe the scan behavior of the array, while the 16 – 18th eigencurrent describe the surface wave behavior.

We mentioned that the occurrence of a strong impedance variation decreases the performance of an array considerably. Therefore, it must be avoided in the design. In the example above, the impedance variation occurs about 19% below the frequency for which the array exhibits a 'resonant broadside embedded impedance'. Hence, the variations shown here are in general not present in a narrow-band design. For designs with a wider frequency band, the variations must be taken care of. In [82: Sec. 1.4], the application of loads on the elements is proposed to reduce the variations. As an example of loading, we consider here uniform surface loading. Contrary to the second model assumption in Section 2.2, the elements of an array are in practice never perfectly conducting. This non-perfectness may prevent resonances from occurrence. Moreover, if resonances occur, they can be prevented by the application of materials that exhibit a lower conductivity for example. To explain this from the point of view of our model, we consider the relation $\mathcal{Z}\boldsymbol{J} = \boldsymbol{E}_S$ between the current $\boldsymbol{J}$ and the (tangential) excitation field $\boldsymbol{E}_S$. Often, uniform surface loads are modeled by adding an extra term $\alpha\mathcal{I}$ to this relation: $(\mathcal{Z} + \alpha\mathcal{I})\boldsymbol{J} = \boldsymbol{E}_S$. Here, the scalar α indicates the surface load and $\mathcal{I}$ is the identity operator. Then, the eigenvalues ν_{nq} obtained by the eigencurrent approach are shifted in the complex plane and become $\nu_{nq} + \alpha$. Considering the representation in the complex plane of the eigenvalues in Figure 6.9 (left) for example, we observe that a suitable choice of α will move the eigenvalues such that no eigenvalue is relatively close to zero according to our definition. Then, due to the relationship between the eigenvalues and specific scan angles of the array, we know that for all scan angles, the resonant behavior is reduced or even annihilated. Finally, we leave the further investigation of the reduction of resonant behavior by means of surface loading, including the investigation of the relation between material properties and the scalar α, as a topic of research.

6.3 Parametric Study

6.3.1 Spread of eigenvalues as Measure of Mutual Coupling

In Chapter 5, we showed that the eigenvalues of an array can be divided into groups $\{\nu_{nq}\}_{q=1}^{N_{\rm sub}}$, where each group corresponds to a single element eigenvalue $\nu_n^{\rm sub}$. Here, $N_{\rm sub}$ is the number of elements and n is the group index. In this subsection, we investigate whether the spread of the eigenvalue groups is a qualitative measure for mutual coupling and, therewith, for the number of groups of coupling eigencurrents needed in the cycle of the eigencurrent approach. To this end, we need to define the spread of the eigenvalue groups first. In Chapter 5, we considered the spread as the maximum and minimum of the absolute perturbations $\{|\epsilon_{nq}|\}_{q=1}^{N_{\rm sub}}$ of the group eigenvalues with respect to the corresponding single-element eigenvalue, i.e., $\nu_{nq} = \nu_n^{\rm sub}(1+\epsilon_{nq})$, see Section 5.1, p. 106. To describe the approximation error of the current due to neglecting the mutual coupling of a group of eigencurrents, or, due to taking $\epsilon_{nq} = 0$ for a certain value of n, we need to consider the maximum absolute perturbation of the group eigenvalues relative to the first absolute single-element eigenvalue. In other words, we need to define the spread as

$$MRP_n^{[N_{\rm sub}]} = \max\{|\epsilon_{nq}|\}_{q=1}^{N_{\rm sub}} \cdot |\nu_1^{\rm sub}|/|\nu_n^{\rm sub}|\,, \tag{6.1}$$

which we call the maximum relative perturbation of the nth group. This definition is explained by the approximation error of the current being of the order $MRP_n^{[N_{\rm sub}]}$. To compare the currents obtained by the eigencurrent approach, which describe a part of the mutual coupling, and the currents obtained by the moment method, which describe all mutual coupling (within the set of expansion functions), we introduce the maximum relative L_2 difference

$$MRD_{L_2} = \max_{q=1,\ldots,N_{sub}} \frac{\|w_{\rm eig}(\,\cdot\,;q) - w_{\rm mom}(\,\cdot\,;q)\|_{L_2}}{\|w_{\rm mom}(\,\cdot\,;q)\|_{L_2}}\,. \tag{6.2}$$

Here, $w_{\rm eig}(\,\cdot\,;q)$ and $w_{\rm mom}(\,\cdot\,;q)$ are the currents on the qth element obtained by the eigencurrent approach and the moment method, respectively. For our investigation, we consider two examples.

The first example concerns a line array of 40 strips of half a wavelength in a half space with $h/\ell = 4/5$. The strips are excited by voltage gaps of 1V. The spacing is varied from 0.1λ to 0.6λ. Figure 6.11 (left) shows that $MRP_n^{[40]}$ of the first three groups of eigenvalues all show the same behavior as a function of the spacing. The maximum relative perturbations decrease monotonically up to about 0.4λ and have local maxima at 0.5λ. The perturbations of the second and third groups are 25 dB – 40 dB and 35 dB – 50 dB lower than the perturbations of the first group. Figure 6.11 (right) shows that MRD_{L_2} exhibits about the same behavior as the maximum absolute perturbations. For a scan at 0°, MRD_{L_2} decreases monotonically both for one and two groups of coupling eigencurrents, while for a scan at 60°, MRD_{L_2} decreases

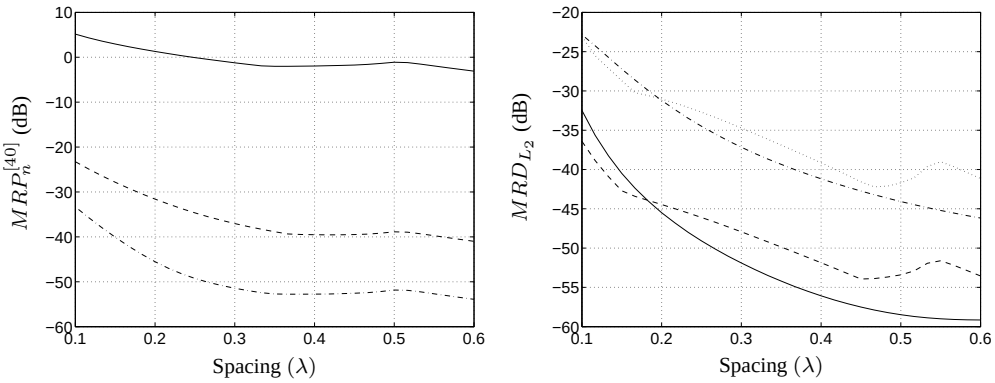

Figure 6.11 Left: $MRP_n^{[40]}$ (in dB) of the 1st (solid curve), 2nd (dashed curve), and 3rd (dashed-dotted curve) group of eigenvalues as a function of the spacing in a uniform line array of 40 strips of half a wavelength in a half space with $h/\ell = 4/5$. Excitation: voltage gaps of 1V. Right: MRD_{L_2} for scans in the xz-plane; solid curve: 2 groups of coupling eigencurrents, 0° scan; dashed curve: 2 groups, 60° scan; dashed-dotted curve: 1 group, 0° scan; dotted curve: 1 group, 60° scan. Parameter values: $\beta = b/\ell = 1/50$, $N_{\cos} = 8$, $N_{\sin} = 0$.

monotonically up to about 0.45λ with local maxima at about 0.55λ. For two groups of coupling eigencurrents, MRD_{L_2} is 10 dB – 12 dB lower than for one group of coupling eigencurrents both at 0° and at 60°. Why the curves for 60° exhibit local maxima and the curves for 0° do not exhibit such maxima, is explained after the second example. In case the striplength is changed from $\lambda/2$ to $3\lambda/5$, the absolute perturbations and MRD_{L_2} show the same behavior as well, as illustrated by Figure 6.12. The results above show that the spread of the eigenvalue groups is

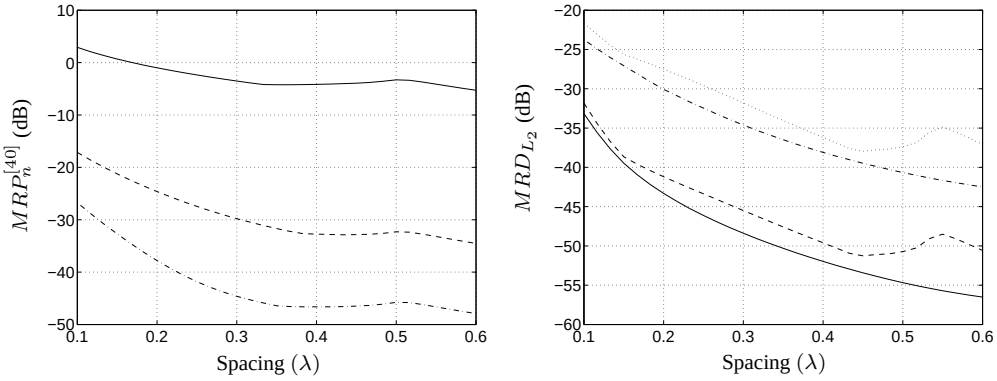

Figure 6.12 As Figure 6.11, but the strip length is $3\lambda/5$ instead of $\lambda/2$.

a good qualitative measure for the number of groups of coupling eigencurrents needed in the cycle of the eigencurrent approach.

The second example is a line array of 40 rings in free space with a spacing equal to three times the ring radius. The rings are excited by voltage gaps of 1V. The frequency is varied such that ka varies from 0.75 to 1.4. Figure 6.13 (left) shows that the maximum relative perturbation of the first group increases up to $ka \approx 1.04$ and then decreases. This value of ka corresponds to the frequency for which the array exhibits a 'resonant broadside embedded impedance', or, for which the reactances of the rings are on average zero. The perturbation of the second group

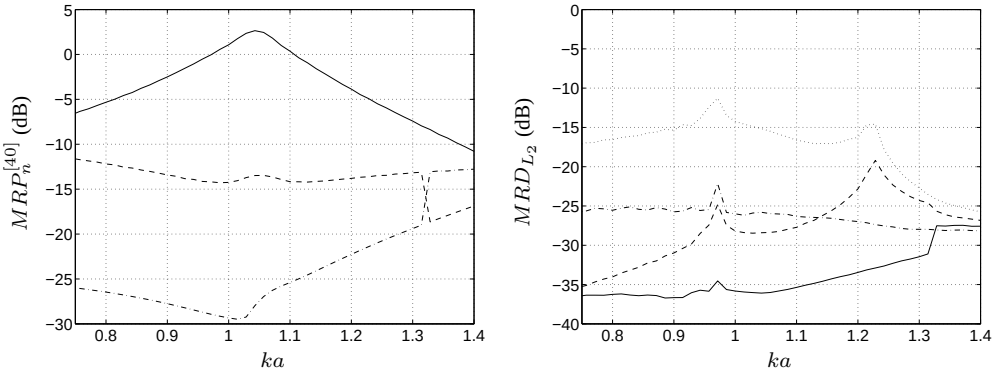

Figure 6.13 Left: $MRP_n^{[40]}$ (in dB) of the 1st (solid curve), 2nd (dashed curve), and 3rd (dashed-dotted curve) group of eigenvalues as a function of the frequency (ka with a fixed) in a uniform line array of 40 rings in free space excited by voltage gaps of 1V. Right: MRD_{L_2} for scans in the xz-plane; solid curve: 2 groups of coupling eigencurrents, 0° scan; dashed curve: 2 groups, 45° scan; dashed-dotted curve: 1 group, 0° scan; dotted curve: 1 group, 45° scan. Parameter values: $d/a = 3$ ($d = \lambda/2$ at $ka = \pi/3$), $\beta = b/a = 3/100$, $\psi = 0$, $N_{\cos} = 8$, $N_{\sin} = 0$.

decreases monotonically up to $ka \approx 1$. At $ka \approx 1.06$, the perturbation exhibits a local maximum. For larger values of $ka \gtrsim 1.1$, the perturbation increases up to $ka \approx 1.32$, where it suddenly decreases. At the same value of ka, the perturbation of the third group increases suddenly. The sudden changes are explained by the interchange of the single-ring eigencurrents that correspond to these groups. For $ka \lesssim 1.32$, the constant single-ring eigencurrent corresponds to the second group, while the eigencurrent $\cos 2\varphi$ corresponds to the third group. For $ka \gtrsim 1.3$, the eigencurrents are interchanged. Figure 6.13 (right) shows MRD_{L_2} as a function of ka for four parameter settings. Both for a scan at 0° and for a scan at 45°, MRD_{L_2} is about 10 dB smaller for two groups of coupling eigencurrents than for one group of coupling eigencurrents, except for $ka \gtrsim 1.3$, which is explained by the interchange of eigencurrents as observed above. For $ka \gtrsim 1.3$, the maximum relative perturbation of the third group is of the same order of

magnitude as the perturbation of the first group and much larger than the perturbation of the second group. This indicates that the third group should be taken into account to describe the coupling and it explains why taking two groups of coupling eigencurrents instead of one does not improve the solution for the current. These results confirm that the spread of the eigenvalue groups is an appropriate qualitative measure for the number of groups of coupling eigencurrents needed in the cycle of the eigencurrent approach.

We recall that we still need to explain the local maxima of MRD_{L_2} in Figure 6.11 as well as the local maxima of MRD_{L_2} in the other two figures. Partly, these maxima are related to grating-lobe behavior. For the scan at 60° in Figures 6.11 (right) and 6.12 (right), the maxima occur at the spacing for which a grating lobe appears or disappears at -90°. For the scan at 45° in Figure 6.13 (right), the maxima at $ka \approx 1.23$ occur at the frequency for which a grating lobe appears or disappears at -90°. The maxima at $ka \approx 0.97$ are not related to grating-lobe behavior, but to resonant behavior, specifically at 0° of scan, which is explained in detail in the next subsection.

The slight increase of MRD_{L_2} near the frequency for which a grating lobe appears or disappears at -90° is more pronounced in free space than in a half space, because in contrast to free space, the grating lobe is canceled in a half space. Only a large side lobe near the plane of the array is present. Consequently, no power is transported along the array plane, while in free space the radiation intensity in the array plane is of the same order as in the scan direction. Both in free space and in a half space, the power radiated along or nearly along the array plane excites slightly some higher order eigencurrents, which explains the increase of MRD_{L_2}.

6.3.2 Modulated Oscillations of Impedance Described by Eigencurrents

As mentioned in Section 6.2, large variations of element impedances across an array reduce its performance considerably. Recently, modulated oscillations of the element impedances have been found [46], that occur at the frequency for which the elements exhibit a 'resonant broadside embedded impedance'. If the amplitudes of the modulated oscillations are large, they reduce the performance of an array as well. In [30], the modulations are explained by the phase velocity of the waves diffracted by the edges of the array being slightly larger than the free space velocity of light. In this subsection, we show that the occurrence of modulated oscillations is caused by the excitation of specific eigencurrents and, hence, by the same mechanism as the variations of element impedances studied in Section 6.2. Moreover, we show that the eigencurrent approach approximates the modulated oscillations very well. To this end, we start by showing that the maxima of MRD_{L_2} at $ka \simeq 0.97$ for the line array of 40 rings in Figure 6.13 are related to resonant behavior.

In Figure 6.14, we depict the normalized absolute impedances of the rings for the frequencies with $ka = 0.94$ and $ka = 0.971$ for scans at 0°. The value $ka = 0.971$ corresponds with the

position of the local maxima in Figure 6.13; the value $ka = 0.943$ was chosen arbitrarily. The figures show modulated oscillations of the impedance. For $ka = 0.971$, these modulations exhibit a shorter period than for $ka = 0.943$. The absolute impedances vary in both cases about 50% with respect to their mean value. For $ka = 0.971$, these large variations extend over the entire array. In contrast, for $ka = 0.943$, they are concentrated at the edges of the array. In the middle of the array the absolute impedances vary about 10% with respect to their mean values. We emphasize that the eigencurrent approach with two groups of coupling eigencurrents

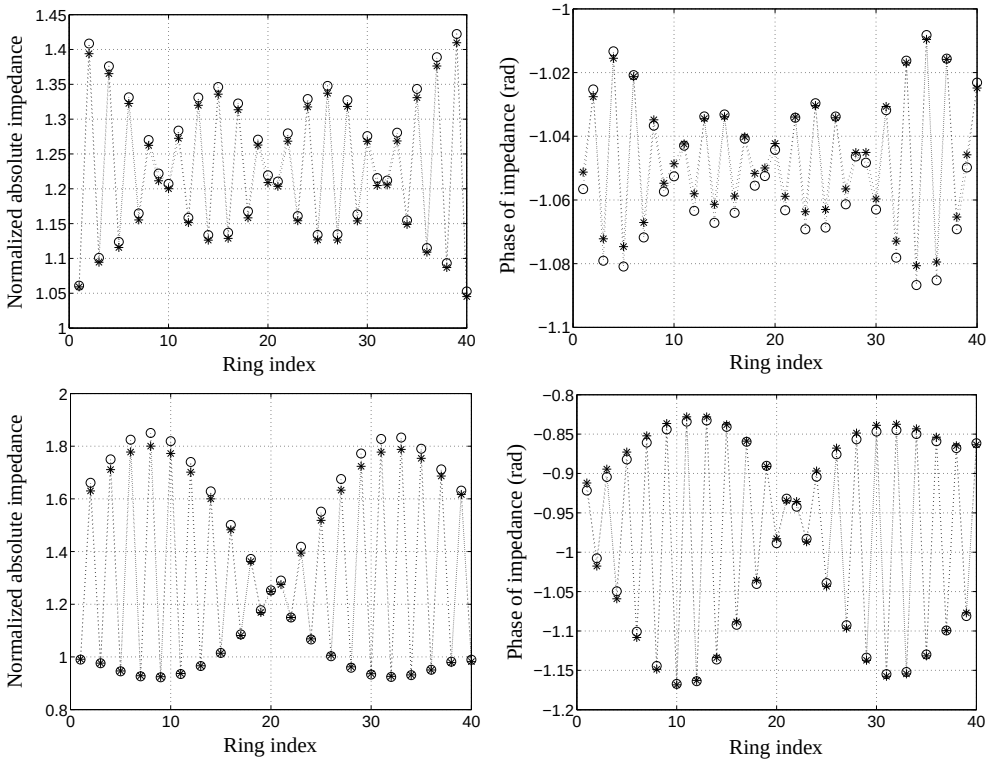

Figure 6.14 Normalized absolute ring impedances (left) and corresponding phases (right) for a line array of 40 rings in free space excited by voltage gaps of 1V for a scan at 0°. Upper figures: frequency with $ka = 0.943$. Lower figures: frequency with $ka = 0.971$. Impedances computed by both the moment method ($*$) and by the eigencurrent approach with two groups of coupling eigencurrents ($\circ$). Figure 6.13 shows the related spreads of eigenvalue groups. Normalization: for each frequency, the corresponding impedance of a single ring. Parameter values: $d/a = 3$ ($d = \lambda/2$ at $ka = \pi/3$), $\beta = b/a = 3/100$, $\psi = 0$, $N_{\cos} = 8$, $N_{\sin} = 0$.

is capable of approximating accurately the modulated oscillations of absolute impedances and corresponding phases.

The same kind of modulated oscillations are discussed in [46] for arrays of collinear, or E-plane oriented, wires with spacing $\lambda/2$ in a half space with $h = \lambda/4$. The modulated oscillations are not observed for arrays of parallel, or H-plane oriented, wires, neither for arrays in free space. In contrast, the rings in Figure 6.14 are positioned in free space and are H-plane oriented, since the voltage gaps are all positioned on the array axis. Moreover, the spacing is not equal to $\lambda/2$. As indicated in Figure 6.13, the spacing is $\lambda/2$ for the frequency with $ka = \pi/3$. For $ka = 0.971$ and $ka = 0.943$, the spacing is 0.464λ and 0.450λ, respectively.

To explain the cause of the modulation, Figure 6.15 shows the normalized absolute expansion coefficients in the finite expansion (5.28) of the current for three values of ka. Only the coefficients of the eigencurrents of the first group are shown. For $ka = 1$, the coefficients of

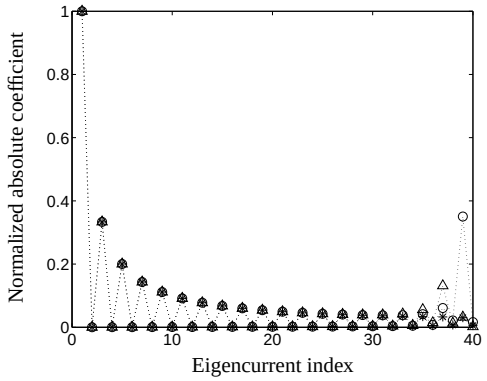

Figure 6.15 Normalized absolute coefficients in the finite expansion (5.28) of the current on the line array of 40 rings in Figure 6.14 for the frequencies with $ka = 0.971$ ($\circ$), $ka = 0.943$ ($\triangle$), and $ka = 1$ ($*$). Only the coefficients of the eigencurrents of the first group are shown. Normalization: maximum coefficient.

odd eigencurrents, i.e., the coefficients with even indices, are zero, while the coefficients of odd eigencurrents form a monotonically decreasing sequence. The corresponding ring impedances behave as the ring impedances in Figure 6.1 for $ka = \pi/3$. For $ka = 0.971$ and $ka = 0.943$, the coefficients show the same behavior as the coefficients for $ka = 1$, but the 39th and 37th (array) eigencurrents, respectively, have a much higher coefficient. The coefficients of the dominant single-ring eigencurrents in the 39th and 37th (array) eigencurrents show an alternating pattern modulated by a sine of one and two periods, respectively. Since these eigencurrents are especially excited, the impedances in Figure 6.14 show such a pattern as well.

As described in Section 6.2, large variations and modulations of element impedances occur, if one or more eigenvalues are relatively close to the origin. The behavior of the eigenvalues in

the complex plane for varying frequency and the corresponding behavior of their absolute values is illustrated in Figure 6.16. The minimum absolute eigenvalues for $ka = 0.943$ and $ka = 0.971$ are the 37th and 39th eigenvalues, which correspond to the eigencurrents in Figure 6.15 with the small peaks at the 37th and 39th eigencurrents, respectively. For $ka = 0.943$, the 37th eigenvalue is only 6 times lower than the first eigenvalue, which corresponds to the 0° scan angle. Hence, although the 37th eigenvalue at $ka = 0.943$ is not relatively close to zero according to

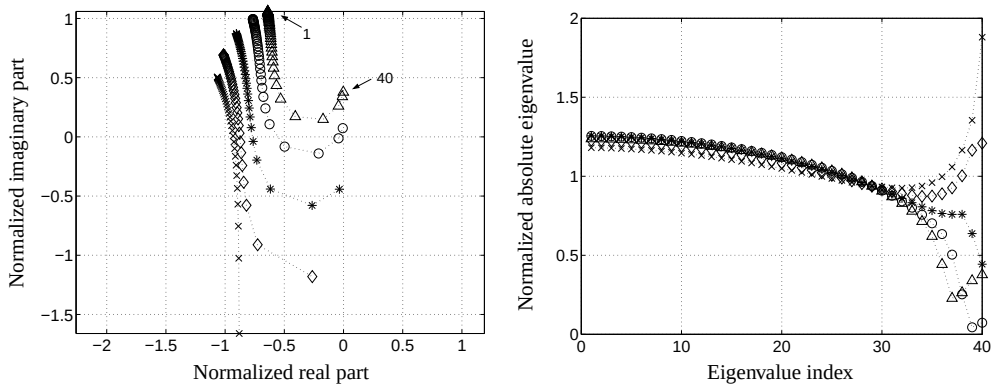

Figure 6.16 Normalized eigenvalues of the first group (left) and their absolute values (right) for the line array of 40 rings in Figure 6.14 for the frequencies with $ka = 0.943$ ($\triangle$), $ka = 0.971$ ($\circ$), $ka = 1$ ($*$), $ka = 1.027$ ($\diamond$), and $ka = \pi/3$. Normalization: for each frequency, the corresponding absolute single-ring eigenvalue.

our definition, its corresponding eigencurrent generates the modulations in Figure 6.14 (upper figures). This indicates that there exist large variations and modulations for a wide frequency range around the 'resonant' frequency. Further investigation revealed that the modulations occur approximately in the range $0.93 \lesssim ka \lesssim 0.99$, where the absolute impedances vary from 10% to more than 100% with respect to their mean value. For a design with $ka = 1.047$ ($\approx \pi/3$) and $d = \lambda/2$ at 1 GHz, the modulated oscillations occur for $0.89\,\mathrm{GHz} \lesssim f \lesssim 0.94\,\mathrm{GHz}$. The frequency for which the elements exhibit a 'resonant broadside embedded impedance' is in this in this case 1.061 GHz. Hence, the modulated impedance oscillations occur between 11% and 16% below this frequency. For frequencies with ka outside the range given, the impedance shows a behavior as in Figure 6.1 for $ka = \pi/3 \approx 1.047$, where the absolute impedances vary only 5%.

The modulations appear also in a half space, where they depend on the height above the ground plane. Figure 6.17 shows the modulated oscillations of the absolute impedances for the same line array of 40 rings as above, but in a half space with $h/a = 3/2$ and in a half space with $h/a = 6/5$. The array is excited with the frequency for which $ka = 0.991$ as in Figure 6.14 (upper figures). The relatively large difference between the two used values of h/a indicates that

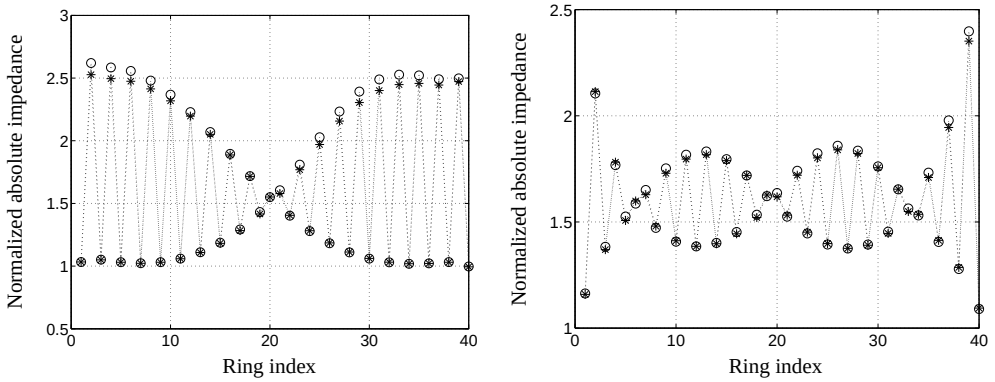

Figure 6.17 Normalized absolute ring impedances for a line array of 40 rings in a half space with $h/a = 3/2$ (left) and in a half space with $h/a = 6/5$ (right) ($h = \lambda/4$ for $ka = \pi/3$), excited by voltage gaps of 1V for a scan at 0°. The frequency is such that $ka = 0.991$. The impedances are computed by the moment method ($*$) and by the eigencurrent approach with two groups of coupling eigencurrents ($\circ$). Normalization: for each frequency, the corresponding impedance of a single ring. Parameter values: $d/a = 3$ ($d = \lambda/2$ at $ka = \pi/3$), $\beta = b/a = 3/100$, $\psi = 0$, $N_{\cos} = 8$, $N_{\sin} = 0$.

we may expect moderate to large variations and modulations over a wide range of h/a. Figure 6.18 shows that the modulations at $h/a = 3/2$ fade out for a frequency shift of -0.5%, while the modulations at $h/a = 6/5$ do not fade out. For $h/a = 3/2$ with the frequency shift of -0.5%, the same pattern of the impedance is obtained as the pattern for $h/a = 6/5$. Hence, for $h/a = 3/2$ with frequency $0.995 f_0$ and for $h/a = 6/5$ with frequency f_0, the same eigencurrent is excited especially. The coefficients of the dominant single-ring eigencurrents in this (array) eigencurrent form an alternating pattern modulated by a sine of two periods. For a design with $ka = 1.047$, $d = 3a = \lambda/2$, and $h = 3a/2 = \lambda/4$ or $h = 6a/5 = \lambda/5$ at 10 GHz, the modulations occur at $f_0 = 9.46$ GHz. The frequency shifts of 0.25% are in that case 24 MHz.

To study the occurrence of (modulated) oscillations of the impedance as a function of the scan angle, we consider the behavior of the eigenvalues in Figure 6.16 for a line array of 40 rings in free space. In Section 5.3.2, we showed that all eigenvalues are related to specific scan angles of the array. For $ka = 0.943$, the first eigenvalue in Figure 6.16 (right) corresponds to 0°, while the 30th and 37th eigenvalues correspond to 55° and 90°, respectively. The last three eigenvalues correspond to eigencurrents that induce far fields with maxima at $\pm 90^\circ$ in the xz-plane, which are much lower than the maxima of the far fields of the other eigencurrents. Since the first 30 eigenvalues are about a factor of 6 larger than the 37th eigenvalue, that causes the (modulated) oscillations of the impedance at 0°, the oscillations occur over a wide range of scan angles. Whether the oscillations are modulated depends on the the interaction between

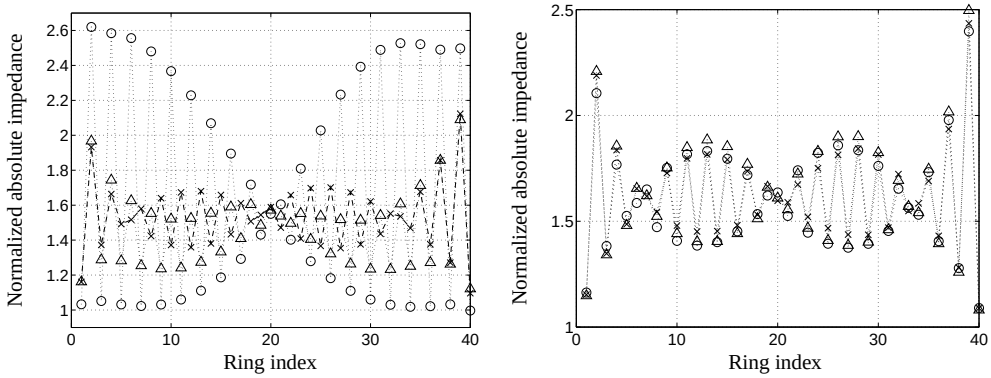

Figure 6.18 Normalized absolute ring impedances for the line array in Figure 6.17 with $h/a = 3/2$ (left) and $h/a = 6/5$ (right) for the frequencies f_0 ($\circ$), $0.9975 f_0$ ($\triangle$), and $0.995 f_0$ ($\times$), where f_0 corresponds to $ka = 0.991$. Other geometry parameters as in Figure 6.17. The impedances are computed by the eigencurrent approach with two groups of coupling eigencurrents and match the impedances obtained by the moment method. Normalization: for each frequency, the corresponding impedance of a single ring.

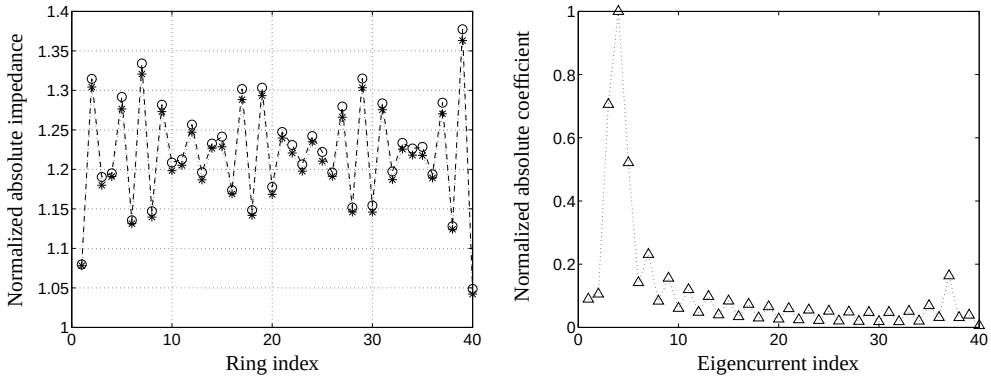

Figure 6.19 Left: normalized absolute ring impedances for the line array of 40 rings in Figure 6.14 (upper figures) with scan angle $5.85°$; impedances computed by the eigencurrent approach with two groups of coupling eigencurrents ($\circ$) and by the moment method ($*$). Right: corresponding normalized absolute coefficients of the eigencurrents of the first group in the finite expansion (5.28) of the current. Normalization impedances: corresponding impedance of a single ring. Normalization coefficients: maximum coefficient.

especially the 37th eigencurrent and the eigencurrents that induce the scan lobe. As an example, Figure 6.19 (left) shows that the oscillations of the normalized absolute impedances of the same line array as in Figure 6.14 (upper figures) for a scan at $5.85°$ are modulated. Figure 6.19 (right) shows that, for this scan angle, the scan lobe is composed of the main lobes of the third, fourth, and fifth eigencurrents. Beside the even (array) eigencurrents, also a number of odd (array) eigencurrents are excited, because the excitation of the array is not symmetric. If the scan angle of the array equals one of the scan angles corresponding to the 37th eigenvalue, i.e., $\pm 90°$, the scan lobe of the array is one of the two main lobes of the far field of the 37th eigencurrent. Since these main lobes have a large beamwidth, we excite the 37th eigencurrent at lower scan angles as well. For example, Figure 6.20 (left) shows the normalized absolute impedances for the same line array as above, but with scan angle $80°$. The absolute impedances of the elements are in

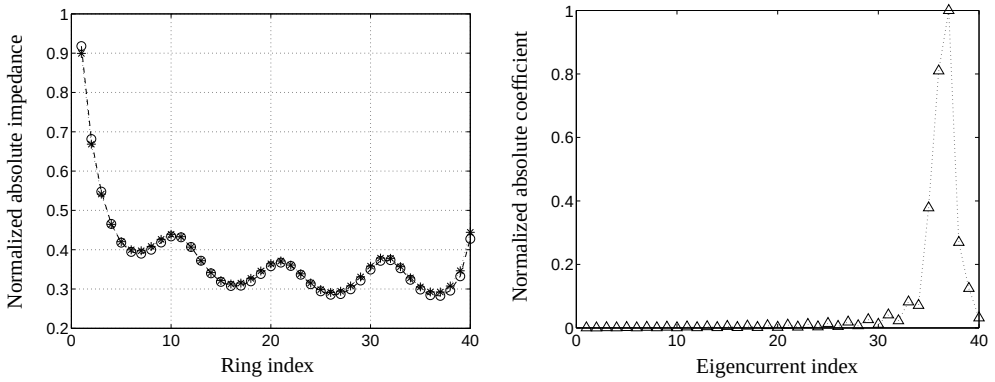

Figure 6.20 As Figure 6.19, but with scan angle $80°$.

this case much lower than the corresponding absolute impedance of a single ring. Figure 6.20 (right) shows that especially the 36th and 37th eigencurrents are excited. The eigencurrents 1 – 30 are hardly excited. Finally, the excitation of the 37th eigencurrent generates a large amount of energy, which can be disastrous for the array due to heating of the array structure.

In [46, 30], it is shown that the period of the modulations in uniform arrays of wires changes in case the wire radius is changed. In arrays of rings and arrays of strips, the same effects occur. Moreover, the number of modulations is in correspondence with the eigencurrents that are excited. For example, Figure 6.21 shows the normalized absolute coefficients in the finite expansion of the current for two different ring widths; the ring radius is constant. Only the coefficients of the eigencurrents of the first group are shown. For $\beta = 3/100$, the 95th eigencurrent is especially excited, while for $\beta = 1/100$, both the 95th and the 93rd eigencurrent are excited. The coefficients of the dominant single-ring eigencurrents in the 95th and 93rd eigencurrents exhibit alternating patterns modulated by a sine with 3 and 4 periods, respectively. The patterns of these eigencurrents are reflected in the modulated impedance oscillations of the array. Fig-

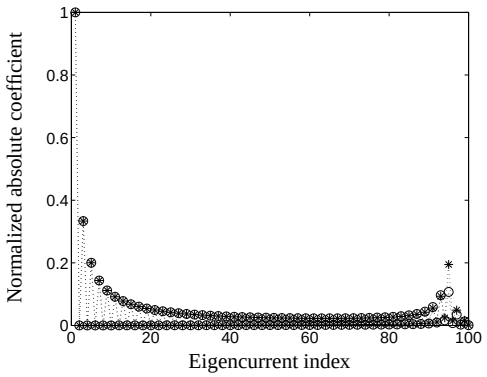

Figure 6.21 Normalized absolute coefficients in the finite expansion (5.28) of the current for a line array of 100 rings in a half space with $h/a = 1.270$ excited by voltage gaps of 1V at the frequency with $ka = 0.990$ and with scan angle 0°. The ring widths are chosen such that $\beta = 3/100$ ($*$) and $\beta = 1/100$ ($\circ$). Coefficients computed by the eigencurrent approach with two groups of coupling eigencurrents; only the coefficients of the first group are shown. Normalization: maximum absolute coefficient. Parameter values: $d/a = 3$ ($d = \lambda/2$ at $ka = \pi/3$), $\psi = 0$, $N_{\cos} = 8$, $N_{\sin} = 0$.

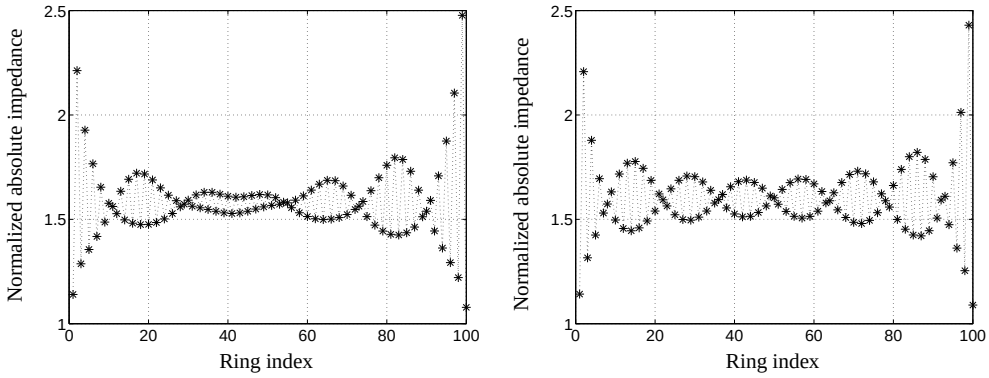

Figure 6.22 The normalized absolute ring impedances for the line arrays in Figure 6.21 computed by the eigencurrent approach with. Left: $\beta = 3/100$. Right: $\beta = 1/100$.

ure 6.22 shows that for $\beta = 3/100$, the impedance oscillations are modulated by a sine with 2.5 periods, while for $\beta = 1/100$, the impedance oscillations are modulated by a sine of 3.5 periods. Simulations showed that the dependence of the modulation on the width does not occur for all geometry settings. If we increase the height of the array above the ground plane to $h/a = 1.59 \approx \lambda/4$ in the array of Figure 6.21, we do not observe dependence on the width. In that case the oscillations raise to the height of the edge oscillations in Figure 6.22, because the

95th eigencurrent becomes resonant. The oscillations are then clearly modulated by a sine with 3 periods.

The modulations are observed in line arrays of parallel, or H-plane oriented, strips as well. Figure 6.23 (left) shows the normalized absolute ring impedances for a line array of 40 strips in a half space with $h/\ell = 1.027$, excited by voltage gaps of 1V at the frequency for which $2\ell/\lambda = 0.429$. The spacing equals $d = 2.053\ell$. The oscillations of the impedance are modulated

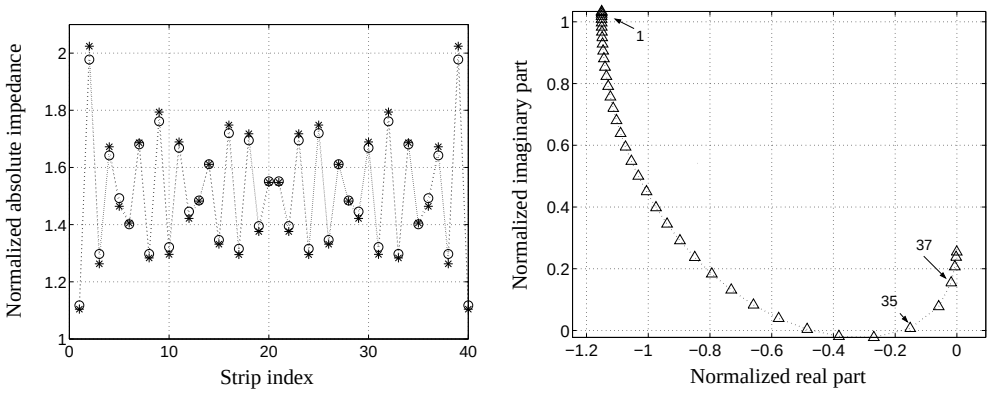

Figure 6.23 Left: normalized absolute ring impedances for a line array of 40 strips in a half space with $h/\ell = 1.027$ and with spacing $d = 2.053\ell$, excited by voltage gaps of 1V at the frequency for which $2\ell = 0.429\lambda$ with scan angle 0°; impedances computed by the eigencurrent approach with two groups of coupling eigencurrents ($\circ$) and by the moment method ($*$). Note that $h = \lambda/4$ and $d = \lambda/2$ for $2\ell = \lambda/2$. Right: corresponding normalized eigenvalues of the first group. Normalization impedances: corresponding impedance of a single strip. Normalization eigenvalues: single-strip eigenvalue corresponding to the first group. Parameter values: $\beta = b/\ell = 0.0205$, $N_{\cos} = 8$, $N_{\sin} = 0$.

by sines with 2 and 3 periods. These sines correspond to the 37th and 35th eigencurrents of which the eigenvalues are relatively close to zero as shown by Figure 6.23 (right). Also the eigenvalue of the 36th eigencurrent is relatively close to zero, but this eigencurrent is odd and, therefore, not excited for a scan at 0°.

Up to now, we have only considered H-plane oriented elements, i.e., rings with voltage gaps on the line array axis and parallel strips with voltage gaps in their centers. To consider E-plane oriented elements, we position the voltage gaps of a line array of 40 rings on lines perpendicular to the line array axis. In other words, we take $\psi = \pi/2$ instead of $\psi = 0$. As observed in [46, 30], for E-plane oriented elements, modulated oscillations of the element impedances occur at a frequency that is much closer to the frequency for which the array exhibits a 'resonant broadside embedded impedance' than the frequency at which these oscillations occur for the H-plane oriented elements considered above. Figure 6.24 (left) shows modulated oscillations of the

element impedances for a line array of 40 rings excited by voltage gaps of 1V at the frequency for which $ka = 1.038$. The line array exhibits a 'resonant broadside embedded impedance' for the frequency with $ka = 1.011$. Hence, the modulated oscillations shown in Figure 6.24 (left) occur only 2.7% above this frequency. Figure 6.24 (right) shows the corresponding behavior of the eigenvalues. As in Figure 6.14, the 37th eigencurrent becomes resonant.

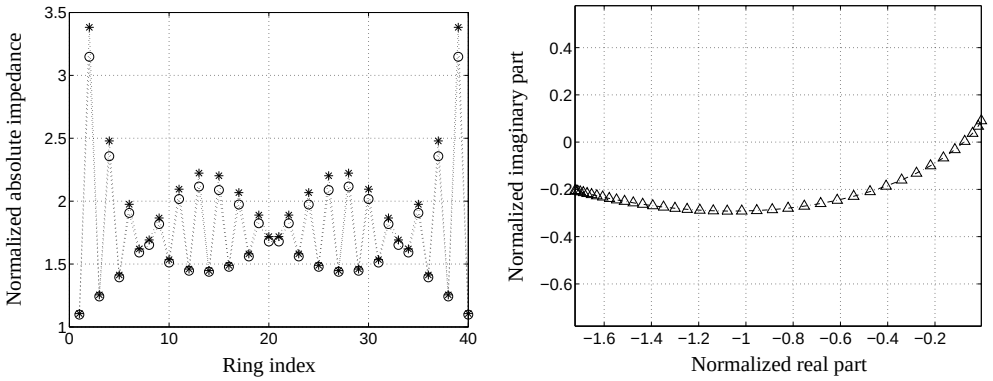

Figure 6.24 Left: normalized absolute ring impedances for a line array of 40 rings in a half space with $h/a = 3/2$ and with spacing $d = 3a = 0.495\lambda$, excited by voltage gaps of 1V at the frequency for which $ka = 1.038$ with scan angle 0°; impedances computed by the eigencurrent approach with two groups of coupling eigencurrents ($\circ$) and by the moment method ($*$). Note that $h = \lambda/4$ and $d = \lambda/2$ for $2\ell = \lambda/2$. Right: corresponding normalized eigenvalues of the first group. Normalization impedances: corresponding impedance of a single strip. Normalization eigenvalues: single-strip eigenvalue corresponding to the first group. Parameter values: $\beta = b/\ell = 0.0205$, $N_{\cos} = 8$, $N_{\sin} = 0$.

Based on the observations above, we conclude that eigencurrents describe modulated oscillations of the element impedances. Specifically, modulated oscillations of the element impedances are described by a limited number of coupling eigencurrents only. The examples above reveal that these eigencurrents are the eigencurrents of the first group. The scan behavior of the array is described by two or three eigencurrents, while the modulated oscillations are due to the excitation of one or two higher-order eigencurrents.

This conclusion and the conclusion of Section 6.2 shows that *modulated oscillations of element impedances and variations of element impedances attributed to surface waves are caused by the excitation of specific eigencurrents and, therewith, by the same mechanism. Both these array effects are due to resonant behavior.* There are certain frequency ranges in which the effects occur. In the examples above of modulated oscillations in uniform line arrays of H-plane oriented rings, the frequency ranges from 11% to 16% and from 14% to 20%, respectively, below the frequency for which the array exhibits a 'resonant broadside embedded impedance'. For

E-plane oriented rings, the modulated oscillations occur 2.7% above this frequency.

In the practice of mechanical engineering, it is very difficult to construct a flat ground plate or (approximately) uniform element geometries, see also item 4 on p. 7. In Section 2.5, we showed an example of a randomly perturbed uniform line array that is excited at a frequency for which resonant behavior occurs, see Figure 2.13. Although the modulated oscillations, the general pattern remains unchanged and the modulations are present. This shows that large variations and modulated oscillations of element impedances are not merely an artefact of uniform line arrays. Our idea is that the spectra and the eigencurrents will show a 'stable' behavior with respect to small geometry perturbations, but that the array performance may change considerably as observed in this section. Moreover, (small) differences in element geometry and height above the groundplane can be dealt with by the proposed eigencurrent approach by allowing for differences between the single-element eigencurrents in which the array eigencurrents are decomposed. For arrays of rings, such an extension is straightforward, because the single-ring eigencurrents are invariant with respect to the ring geometry and depend only on the angle that describes the circumference. Moreover, an impedance operator that allows for differences between ring radii and ring widths, and a corresponding moment matrix was deduced in Chapter 2 and 3. We mention that whether the resonances studied in this section occur in practice, depends on the actual design, in particular the conductivity of the microstrip material used. If they occur, loading can prevent the large modulated oscillations. As in Section 6.2, the eigenvalues predict the required uniform surface loads.

6.3.3 Line Array Analysis Using Small Array Information

In Section 5.3.2, we suggested to use information about the spread of the eigenvalues obtained for relatively small arrays in the analysis of large(r) arrays as follows. First, we analyze the spread of each group of eigenvalues for some relatively small arrays, say with 4, 8, and 12 elements. We expect that if the spread of a group of eigenvalues tends to become constant as the number of elements increases, for the corresponding single-element eigencurrent we need only the coupling between each element and, e.g., its first 3 or 7 neighbors on both of its sides. Next, in the eigencurrent approach, we construct the moment matrices of larger arrays by calculating only the relevant coupling between eigencurrents. If for each group of coupling eigencurrents only the coupling between each element and its first M neighbors on both sides, i.e., $2M$ neighbors in total, need to be taken into account, the number of Toeplitz blocks in the moment matrix of the eigencurrent approach reduces from $2N_{\mathrm{sub}} - 1$ to $2M + 1$, where N_{sub} is the number of elements.

We define the spread of a group of eigenvalues as in Section 6.3.3, namely as the maximum absolute perturbation. In that section, we wanted to know whether the eigenvalues of a group are approximately the same as the corresponding single-element eigenvalue. In this section, we

want to investigate to what extent the spread of the eigenvalues is a measure for the number M. Therefore, we are also interested in the finer structure of the spread. Despite this, we think that it is not necessary to consider, for example, the minimum absolute perturbations of the groups as well, because in Section 5.3.2, we showed that the minimum tends to become constant more rapidly than the maximum.

The maximum absolute perturbations of the first and second groups of eigenvalues as a function of the number of elements in two different line arrays shown in Figure 6.25 are discussed in detail in Subsection 5.3.2, see Figure 5.18. For the line array in free space, the maximum ab-

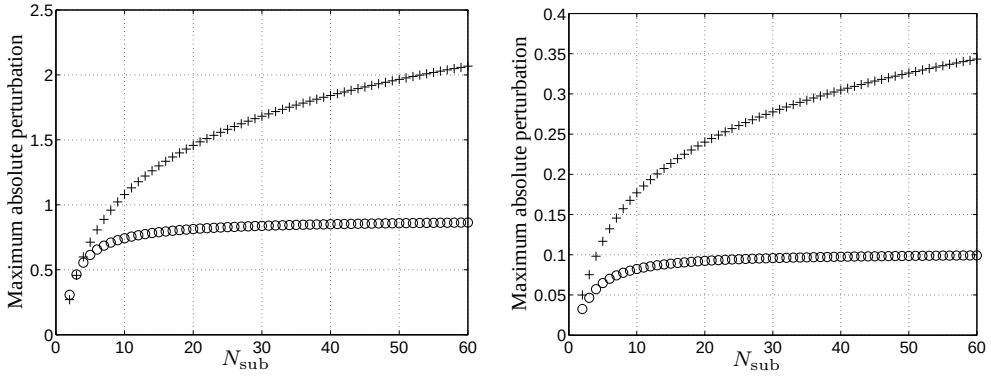

Figure 6.25 Maxima and minima of the absolute perturbations $\{|\epsilon_{nq}|\}_{q=1}^{N_{\mathrm{sub}}}$ of the first (left) and the second (right) group of eigenvalues as a function of N_{sub}, i.e., the number of rings, for a line array of 40 rings, with spacing $\lambda/2$, in free space ($+$) and in a half space with $h/a = 6/5$ ($\circ$). Parameter values: four groups of coupling eigencurrents, $ka = \pi/3$, $\beta = 3/100$, $\psi = 0$, $N_{\cos} = 4$, $N_{\sin} = 0$.

solute perturbations increase monotonically, which is discussed on pp. 169 ff. in relation to the divergence of the infinite-array solution at the grating-lobe scan angle. In contrast, the maxima for the line array in half space with $h/a = 6/5$ ($h = \lambda/5$) become constant for line arrays of 20 elements or more. Based on these observations and our theory on the number of neighbors needed, we would say that for the line array in half space, we need the first 20 neighbors to describe mutual coupling, while for the line array in free space we cannot neglect any mutual coupling between the single-element eigencurrents of the first and the second group. That this estimation is too pessimistic is shown by Figures 6.26 and 6.27. For the line array in half space, $M = 5$ is sufficient to obtain an accurate impedance approximation for a scan at $45°$. A rough approximation is obtained with $M = 1$. For the line array in free space, $M = 5$ provides an accurate approximation of the absolute impedances, but not of their phases. The approximation of the phases is much more accurate for $M = 10$, but the approximation of the absolute values deteriorates slightly. Further investigation revealed that a perfect match is obtained with

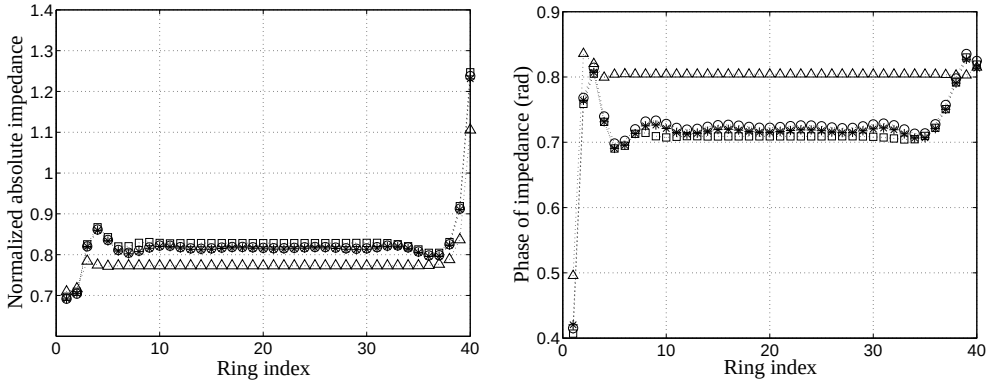

Figure 6.26 Normalized absolute values (left) and phases (right) of the ring impedances for a line array of 40 rings in a half space space with $h/a = 6/5$ and with spacing $\lambda/2$ ($d = 3a$). The rings are excited by voltage gaps of 1V for a scan at 45°. The impedances are computed by the moment method ($*$), by the eigencurrent approach ($\circ$), and by the eigencurrent approach with $M = 1$ ($\triangle$) and $M = 5$ ($\square$). Normalization: Absolute impedance of a single ring. Parameter values: two groups of coupling eigencurrents, $ka = \pi/3$, $\beta = 3/100$, $\psi = 0$, $N_{\cos} = 8$, $N_{\sin} = 0$.

$M = 20$. Finally, we found similar results for 0°.

The pessimistic estimate of the number of neighbors for the line array in free space is explained as follows. In that case, the maximum absolute perturbation of a group belongs to the eigenvalue corresponding to the grating lobe scan angle. On pp. 169 ff., we showed that this eigenvalue tends to become infinite as the number of elements increases. Therefore, the maximum absolute perturbation will not become constant. For line arrays in a half space, we illustrated that the eigenvalues of each group are bounded, which explains why the estimate of the number of neighbors provides accurate results.

To obtain a better estimate for M, we first define the quantity

$$\Delta_n^{[N_{\rm sub}]} = \frac{|MRP_n^{[N_{\rm sub}+1]} - MRP_n^{[N_{\rm sub}-1]}|\,|\nu_n^{\rm sub}|^2}{2\,|\nu_1^{\rm sub}|^2}\,, \tag{6.3}$$

where $MRP_n^{[N_{\rm sub}]}$ is the spread of the nth eigenvalue group as defined in Section 6.3.1. This quantity is a measure for the slopes of the curves described by the spreads of the groups as a function of the number of elements $N_{\rm sub}$. Examples of such curves are shown in Figure 6.25. The factor $|\nu_n^{\rm sub}|^2/|\nu_1^{\rm sub}|^2$ is meant to account for the differences in the absolute perturbations of different groups. We call (6.3) the relative variation of the spread. For the line array in free space, the relative variation of the spread of the first and second groups for 20 elements are $\Delta_1^{[21]} = 0.028$ and $\Delta_2^{[21]} = 0.031$, while for the line array in half space, the relative variations

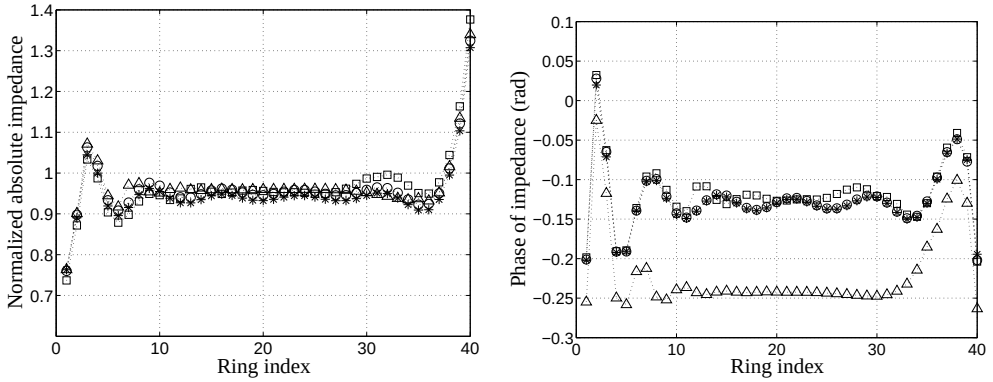

Figure 6.27 As Figure 6.26, but the line array is in free space. Moreover, the values of M are $M = 5$ ($\triangle$) and $M = 10$ ($\square$). Only the impedances for a scan at 45° are shown.

are $\Delta_1^{[6]} = 0.035$ and $\Delta_2^{[6]} = 0.027$. The differences are due to the rapid changes of the relative variation near $N_{\rm sub} = 6$, by which the values for the line array in half space vary strongly, if $N_{\rm sub}$ is varied. These results indicate that a fixed tolerance may exist for the groups. The relative variation of the spread $\Delta_n^{[N_{\rm sub}]}$ should be smaller than about 0.03 to take $M = N_{\rm sub} - 1$.

To investigate whether the relative variation is indeed a good measure for M, we consider the same line arrays as above, but with spacing $3\lambda/5$. The maximum and minimum absolute perturbations as a function of the number of rings are shown in Figure 5.18. For the line array in free space, the relative variations of the first and second groups are $\Delta_1^{[6]} = 0.026$ and $\Delta_2^{[6]} = 0.041$ and for the line array in half space, they are $\Delta_1^{[5]} = 0.028$ and $\Delta_2^{[5]} = 0.028$. These values of the relative variations are approximately the same as above for the spacing $\lambda/2$. Therefore, we expect that the approximations of the impedances have the same accuracy as above. For the line array in half space, we obtained a good match between the solution obtained by the eigencurrent approach with $M = 4$ and the solution obtained by the moment method, even near the grating-lobe scan angle 41.8°. For the line array in free space, we obtained a good match for $M = 5$ between both solutions for scans up to 10°. For larger scan angles, the approximation with $M = 5$ slowly deteriorates. At 20°, the impedance variation is approximated accurately with $M = 10$, while Figure 6.28 shows that the impedance variation at 30° is approximated accurately with $M = 20$ instead of $M = 5$.

The increase of M in free space for scan angles larger than 10° can be explained as follows. First, in Subsection 6.3.1, we observed that the appearance of a grating lobe increases the maximum relative difference in L_2 sense between the element currents obtained by the moment method solution and by the eigencurrent approach. This effect, which influences the approximation of the impedance, is more pronounced for arrays in free space than for arrays in half space. Second, $MRP_1^{[N_{\rm sub}]}$ and $MRP_2^{[N_{\rm sub}]}$ increase slowly but monotonically with $N_{\rm sub}$ for the line

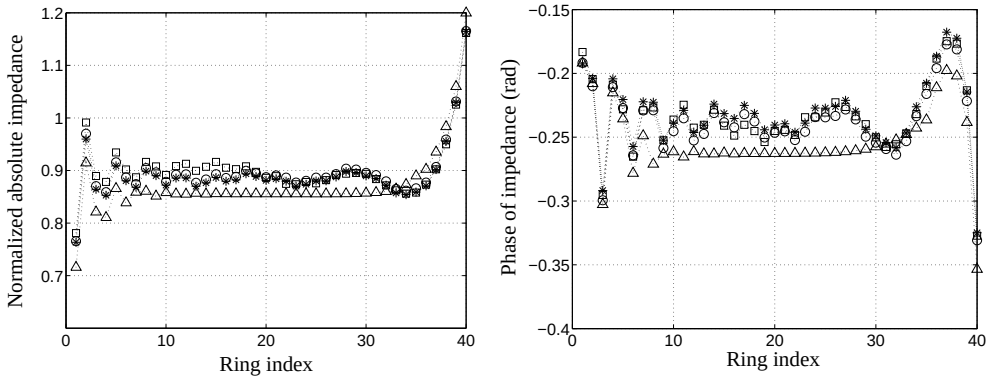

Figure 6.28 As Figure 6.26, but the line array is in free space with spacing $3\lambda/5$ and the scan angle is 30°. Moreover, $M = 5$ ($\triangle$) and $M = 20$ ($\square$).

array in free space, while they become constant for the line array in half space, see Figure 5.18. These observations indicate that we need to be careful with neglecting mutual coupling between elements near the appearance of a grating lobe in free space. The examples show that for scan angles within 25° from grating-lobe appearance, about 5 – 10 more neighbors should be taken into account than predicted by $\Delta_n^{[N_{\rm sub}]} \lesssim 0.03$.

Near resonant behavior, the estimate of M by means of the relative variation of the spread provides reasonably accurate results, but smaller values of M do in general not show the modulation observed in the previous subsection. For example, Figure 6.29 shows that if we take $M = 6$ at $ka = 0.943$, we obtain a totally incorrect impedance pattern. Instead of being modulated, it resembles a common broadside impedance pattern as shown in Figure 6.1. Hence, the modulation is the result of mutual coupling between elements that are relatively far away from each other. The relative variation with tolerance 0.03 as above provides the estimate $M = 8$, because $\Delta_1^{[8]} = 0.032$ and $\Delta_1^{[9]} = 0.023$. This value of M is too low. Figure 6.29 (right) shows that for $M = 10$, the modulation is predicted, but the amplitude is too small. For $M = 20$, the amplitude of the modulation obtained by the eigencurrent approach is about the same as the amplitude obtained by the moment method.

The difference between the predicted value $M = 8$ and the required value $M = 20$ is not due to the resonant behavior. As observed above, $MRP_1^{[N_{\rm sub}]}$ increases slowly but monotonically in free space and, therefore, the relative variation does not give a correct indication of M for the tolerance 0.03. For line arrays in half space with resonant behavior, the number M is much better estimated by the relative variation. For example, by analyzing impedance patterns, we found that the resonant behavior of the line array of 40 rings shown in Figure 6.17 is well-described by the choice $M = 7$ for both $ka = 0.972$ and $ka = 0.943$. In both cases, $\Delta_1^{[8]} \approx 0.023$ and $\Delta_2^{[8]} \approx 0.014$. These values are smaller than the fixed tolerance 0.03 chosen above and, hence,

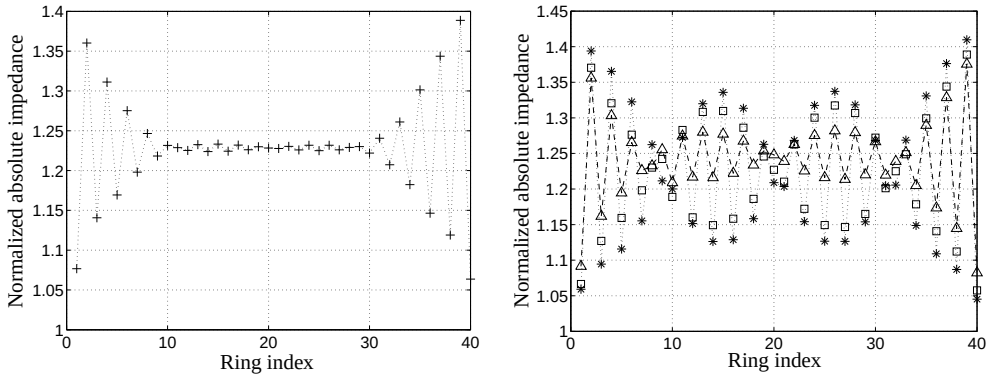

Figure 6.29 Normalized absolute impedances of the line array of Figure 6.26, but the line array is positioned in free space and excited at the frequency with $ka = 0.943$; scan angle is 0°. Left: the impedances are computed by the eigencurrent approach with $M = 6$. Right: the impedances are computed by the moment method ($*$) and by the eigencurrent approach with $M = 10$ ($\triangle$) and $M = 20$ ($\square$). Normalization: absolute impedance of a single ring.

the relative variation provides the correct estimate of M.

Incorrect impedance patterns for small M, both for resonant behavior and non-resonant behavior, are due to incorrect eigenvalues and eigencurrents. In the example of resonant behavior, the eigenvalues for $M = 6$ and $M = 10$ are perturbed with respect to the eigenvalues for the case in which all coupling in the first two groups is taken into account, i.e., $M = 39$, as shown in Figure 6.30. In Subsection 6.3.2, we observed that the modulations at $ka = 0.943$ in this example are caused by the excitation of the 37th eigencurrent. For $M = 39$ and $M = 10$, the 37th eigenvalue is about 1.7 and 1.1 times smaller than the 40th eigenvalue, respectively. In contrast, for $M = 6$, the 37th eigenvalue is about 1.7 times larger than the 40th eigenvalue. Therefore, the 37th eigencurrent is not excited if $M = 6$ is used, while it is excited if $M = 10$ or $M = 39$ is used. The differences between the eigenvalues for different values of M are accompanied by differences in eigencurrents. For smaller values of M, the dominant behavior of the eigencurrents is too much perturbed. In other words, the coefficients of the dominant single-element eigencurrents in the array eigencurrents of a group are too much perturbed. Since these coefficients depend negligibly on the geometry parameters and the frequency, negative side effects of choosing a small value of M can be prevented by computing the eigencurrents first for a frequency, or more general, for a parameter setting, for which no resonant behavior occurs. Subsequently, the eigenvalues are computed by means of the Rayleigh-Ritz quotient as will be explained in the next subsection.

The results above show that we may neglect mutual coupling, but that we need to be care-

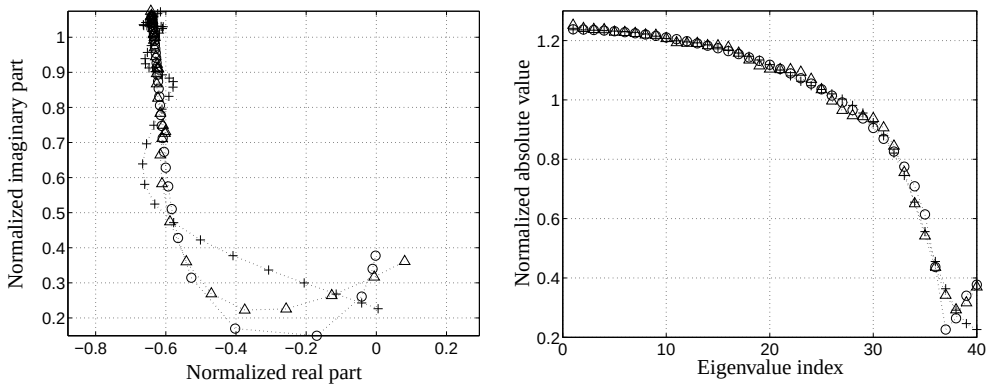

Figure 6.30 The eigenvalues of the first group corresponding to the cases $M = 6$ ($\triangle$) and $M = 10$ ($\square$) in Figure 6.29 together with the eigenvalues for the case in which all elements couple ($M = 39$, $\circ$). Normalization: absolute single-ring eigenvalue.

ful. Except near the appearance of a grating lobe, the number of neighbors needed to describe mutual coupling is well predicted by the variation of the spread as a function of the number of elements in small arrays. Empirically we deduced that if $\Delta_n^{[N_{\rm sub}]}\, \nu_1^{\rm sub}/\nu_n^{\rm sub}$ is smaller than 0.03, only the coupling of each element with its first $N_{\rm sub} - 1$ neighbors needs to be considered for the single-element eigencurrent corresponding to the nth group of eigencurrents. In half space, the estimate of the number of neighbors provides accurate results. In free space, the estimate may be a few elements too small due to the monotonic, but possibly slow increase of the spread. To relate the tolerance on the relative variation to a certain maximum error of the impedance, further investigation is needed. In this respect, we should keep in mind that by evaluating the impedance of the elements, we point-evaluate the currents. The results of these point evaluations are sensitive to parameter variations. Therefore, we recommend relating the tolerance to the maximum relative L_2 difference MRD_{L_2} introduced in Subsection 6.3 instead of to the impedance.

Regarding the computation times in Table 6.1, we note that the computation times for 100, 200, and 400 rings reduce about 20% if $M = 10$. This reduction is not so large, because for increasing numbers of elements, the computation time of the eigencurrents and eigenvalues dominates the computation time of the (reduced) moment matrix from which the eigencurrents and eigenvalues are determined. Moreover, the CPU time of moment matrices for uniform line arrays tends as $N_{\rm sub}$ in contrast to the CPU time for non-uniform arrays, which tends as $N_{\rm sub}^2$. To avoid eigenvalue computation from (reduced) moment matrices, we discuss in the next section the computation of eigenvalues and performance parameters by choosing a fixed set of eigencurrents for various parameter settings.

6.3.4 Line Array Analysis Using a Fixed Set of Eigencurrents

In Subsection 5.3.2, we proposed to approximate the (coupling) array eigencurrents for a certain parameter setting as follows: their expansion coefficients with respect to the single-element eigencurrents are approximated by the expansion coefficients obtained for another parameter setting. This approximation is based on the weak dependence of the coefficients on the geometry parameters and the frequency as demonstrated in Subsection 5.3.2. In this subsection, we show some examples of this approximation.

The first example concerns a line array of 40 rings in free space with spacing $\lambda/2$. The rings are excited by voltage gaps of 1V. Only one group of coupling eigencurrents is used. The expansion coefficients of these eigencurrents are approximated by the expansion coefficients obtained for the spacing $3\lambda/5$. Next, the eigenvalues are approximated by the Rayleigh-Ritz quotient (5.38). Figure 6.31 shows the absolute values and the phases of the ring impedances for a scan at 45°. Both absolute values and phases show the same curve shapes as the absolute values and phases obtained by the eigencurrent approach and the moment method. For the

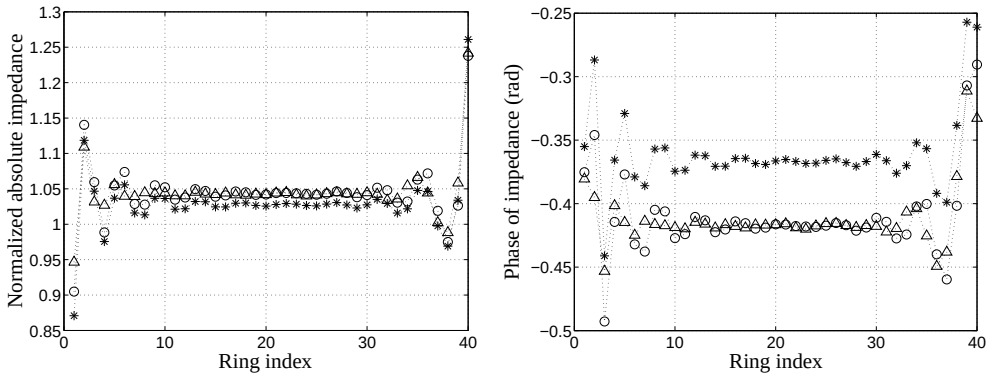

Figure 6.31 Normalized absolute values (left) and phases (right) of the ring impedances for a line array of 40 rings in free space with spacing $\lambda/2$. The rings are excited with voltage gaps of 1V for a scan at 30°. The impedances are computed by the moment method ($*$), by the eigencurrent approach with one group of coupling eigencurrents ($\circ$), and by the eigencurrent approach with eigencurrents obtained for the spacing $3\lambda/5$ ($\triangle$). Normalization: single-ring impedance. Parameter values: $ka = \pi/3$, $\beta = 3/100$, $\psi = 0$, $N_{\cos} = 8$, $N_{\sin} = 0$.

middle 20 rings, absolute values and phases match perfectly the absolute values and phases obtained by the eigencurrent approach. Near the edges, the differences in absolute value and phase run up to 3% and 0.05 rad, respectively. As observed in Section 6.1, the phase difference between the impedances obtained by the moment method and by the eigencurrent approach with only one group of coupling eigencurrents is almost uniform with value 0.05 rad. If two groups

are taken into account, this difference almost vanishes.

The second example concerns the same line array. We denote the frequency at which the array is excited by f_0 and the corresponding wavelength by λ_0. The spacing is $\lambda_0/2$. The expansion coefficients of the eigencurrents are approximated by the expansion coefficients obtained for the frequency $1.1f_0$. For a scan at $45°$, Figure 6.32 shows that the normalized absolute impedances thus obtained match very well the normalized absolute impedances obtained by the eigencurrent approach (without the described eigencurrent approximation) and the moment method, if one group of coupling eigencurrents is used. The phases of the impedances

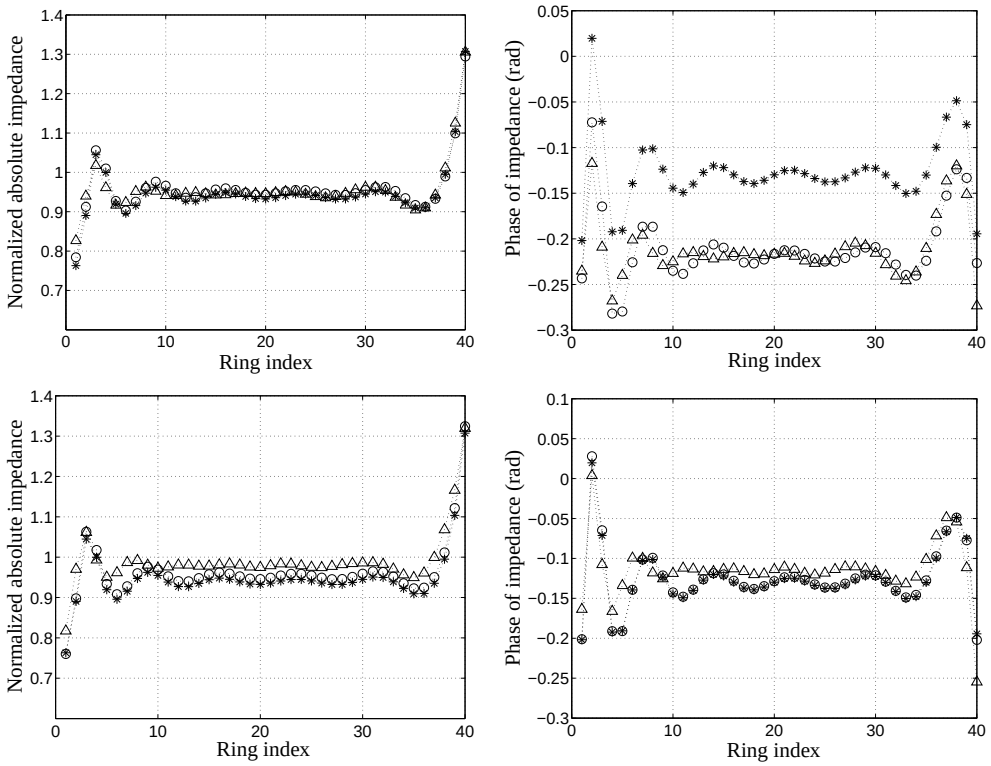

Figure 6.32 Normalized absolute values (left) and phases (right) of the ring impedances for a line array of 40 rings in free space with spacing $\lambda_0/2$. The rings are excited with voltage gaps of 1V at the frequency f_0 for a scan at $45°$. The impedances are computed by the moment method ($*$), by the eigencurrent approach ($\circ$), and by the eigencurrent approach with eigencurrents computed at the frequency $1.1f_0$ ($\triangle$). Upper figures: one group of coupling eigencurrents. Lower figures: two groups of coupling eigencurrents. Normalization: single-ring impedance (at f_0). Parameter values: $k_0a = \pi/3$, $\beta = 3/100$, $\psi = 0$, $N_{\cos} = 8$, $N_{\sin} = 0$.

match very well the phases obtained by the eigencurrent approach. The phase difference with the impedances obtained by the moment method is about 0.1 rad. For two groups of coupling eigencurrents, the phase approximation improves considerably and mimics the phases obtained by the eigencurrent approach and the moment method quite well. The approximation of the absolute impedance is slightly worse than for one group of coupling eigencurrents. We note that for two groups of coupling eigencurrents, the phases obtained by the eigencurrent approach (without the described eigencurrent approximation) match the phases obtained by the moment method perfectly.

One could think that the differences between the impedances obtained by the eigencurrent approaches with and without approximated eigencurrents are not only small because of the weak dependence of the eigencurrents on the geometry parameters and the frequency, but also, because of small differences between the impedances at the frequencies f_0 and $1.1f_0$. However, at $1.1f_0$, the impedances differ considerably from the the impedances at f_0. This follows from a comparison of Figure 6.32 with Figure 6.33, which shows the impedances of the same array as in Figure 6.32, but excited at $1.1f_0$ instead of f_0. The eigencurrents are determined at f_0 instead of $1.1f_0$. Contrary to Figure 6.32, the phases obtained by the approximation match the phases obtained by the eigencurrent approach and the moment method reasonably well for one group of coupling eigencurrents. The absolute values differ about 8% from the absolute values obtained by the moment method, while they match the absolute values obtained by the eigencurrent approach approximately. For two groups of coupling eigencurrents, the absolute impedances and the corresponding phases obtained by the approximation match the absolute values and phases obtained by the moment method, except near the left edge of the array.

Up to now, we have not applied the matrix-reduction suggested in the previous subsection. We consider the last example of the previous subsection, i.e., a line array of 40 rings in free space excited at the frequency with $ka = 0.943$. At this frequency, the line array exhibits resonant behavior. First, we compute the eigencurrents for the same line array, but excited at the frequency with $ka = 1.026$. Next, we apply the Rayleigh-Ritz quotient to the computed eigencurrents to approximate the eigenvalues at $ka = 0.943$. Both in the eigencurrent approach and in the Rayleigh-Ritz quotient, we neglect mutual coupling by taking $M = 6$ and $M = 20$, where M is number of neighbors that couple with an element. As observed in the previous subsection, for $M = 6$, we obtain an impedance pattern without modulation. The eigenvalues of the first group are incorrect and the impedance pattern does not show the modulations, see Figure 6.34. For $M = 20$, the modulations are well predicted. This number of M corresponds with the estimate for M found in the previous subsection, see Figure 6.29. We conclude that even at the resonant frequency, we may neglect mutual coupling between elements according to the rule of thumb proposed in the previous subsection.

Regarding the quantitative differences observed in the results of this subsection, we should keep in mind that differences between impedances obtained by the moment method and the

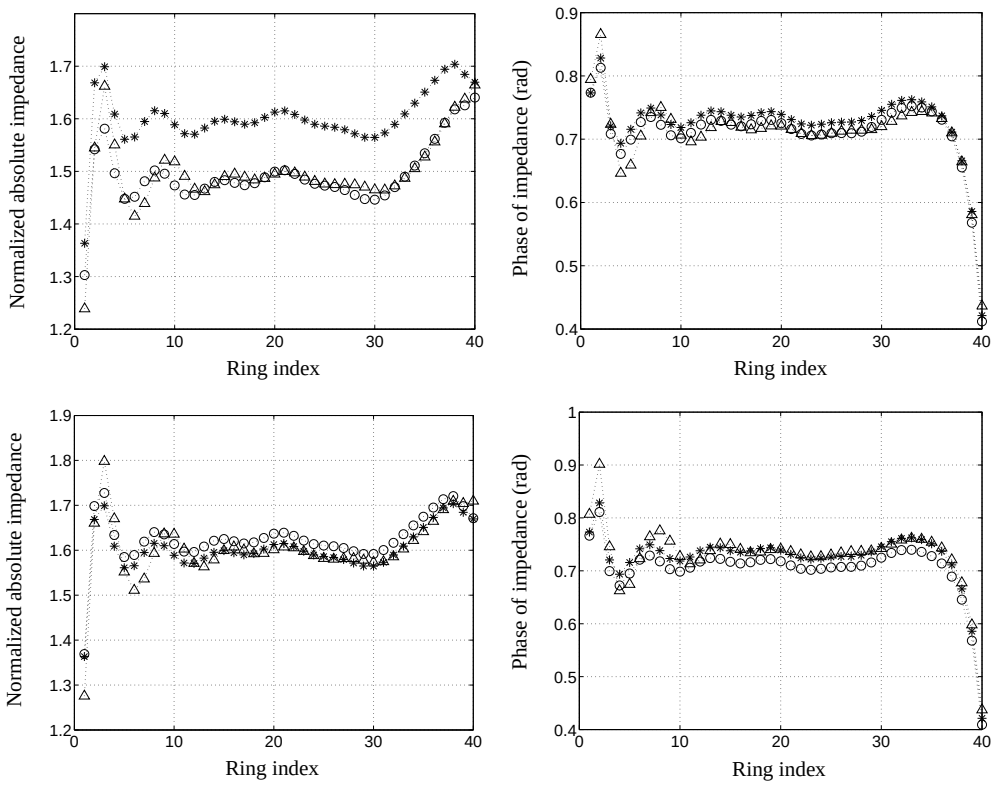

Figure 6.33 As Figure 6.32, but the array is excited at the frequency $1.1 f_0$, while the eigencurrents to obtain the third curve ($\triangle$) are computed at the frequency f_0. The normalization is the single-ring impedance at $1.0 f_0$ as in Figure 6.32.

eigencurrent approach may be larger than the differences obtained for the maximum relative L_2 difference introduced in Subsection 6.3.1, see also Section 6.3.3. Moreover, differences between impedance results do not necessarily mean that other performance parameters show large differences as well. For the electric far fields of the scans at 30° and 45°, perfect matches were obtained except near the grazing angles $\pm 90^\circ$. Thus, we conclude that, for large parameter variations, both the element impedances and the far-field performance parameters are approximated accurately for a fixed set of eigencurrent coefficients.

This conclusion can be used in computations of the array perfomance parameters for a given excitation as follows. First, for a given parameter setting, we compute the eigenvalues and eigencurrents. Next, we fix the computed eigencurrents. For a new parameter setting, we approximate the eigenvalues by the Rayleigh-Ritz quotient applied to the fixed eigencurrents. Both in the computation of the eigencurrents in the first step and in the computation of the eigenvalues

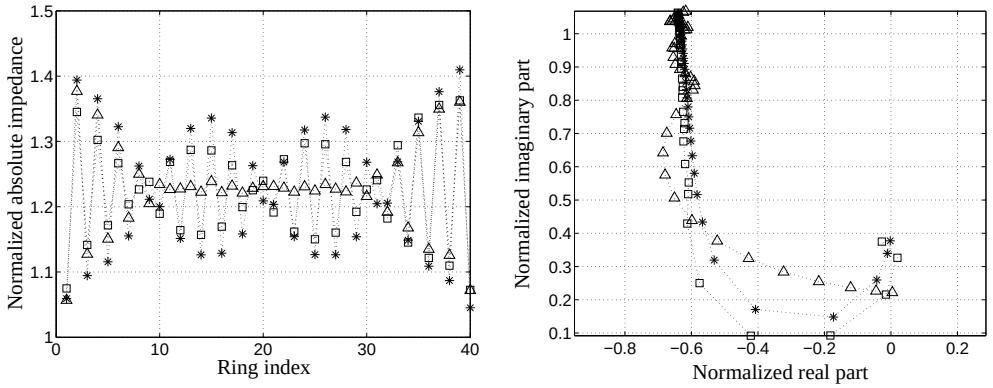

Figure 6.34 Left: normalized absolute ring impedances for a line array of 40 rings in free space excited at the frequency with $ka = 0.943$ by voltage gaps of 1V for a scan at 0°. Impedances computed by the eigencurrent approach with two groups of coupling eigencurrents ($*$) and by the eigencurrent approach with eigencurrents computed at the frequency with $ka = 1.206$, both for $M = 6$ ($\triangle$) and $M = 20$ ($\square$). Normalization: corresponding impedance of a single ring. Right: eigenvalues of the first group for $M = 6$ ($\triangle$), $M = 20$ ($\square$), and $M = 39$ ($*$). Normalization: absolute single-ring eigenvalue. Parameter values: $d/a = 3$ ($d = \lambda/2$ at $ka = \pi/3$), $\beta = b/a = 3/100$, $\psi = 0$, $N_{\cos} = 8$, $N_{\sin} = 0$.

in the second step, we restrict mutual coupling on basis of calculations of the relative variation $\Delta_n^{[N_{\text{sub}}]}$ for small arrays as explained in the previous subsection.

6.3.5 Line Array Analysis Using Single Strip Eigencurrents

In addition to the approximation of (coupling) array eigencurrents as discussed in the previous subsection, we proposed in Subsection 5.3.2 to approximate the array eigencurrents and eigenvalues as follows. First, compute the expansion coefficients of the eigencurrents of a single strip obtained by piecewise linear expansion functions. Next, consider these expansion coefficients as the coefficients of the dominant single-element eigencurrents in the array eigencurrents. In this way, approximated array eigencurrents are obtained. Finally, compute the eigenvalues of the line array by applying the Rayleigh Ritz quotient to the approximated (array) eigencurrents. The approximation is based on the correspondence between the coefficient distributions of the eigencurrents of a single strip and the coefficient distributions of line arrays of strips and rings, as discussed in Subsection 5.3.2.

For a line array of 40 rings excited by voltage gaps of 1V to scan at 45°, Figure 6.35 shows a comparison of the moment method, the eigencurrent approach with one group of coupling eigencurrents, and the eigencurrent approach with approximated eigencurrents. The eigencur-

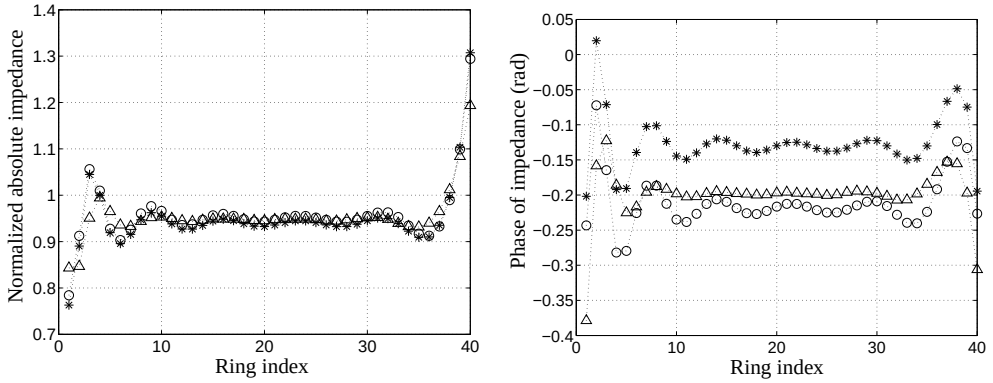

Figure 6.35 Normalized absolute values (left) and phases (right) of the ring impedances for a line array of 40 rings in free space with spacing $\lambda/2$. The rings are excited with voltage gaps of 1V for a scan at 45°. The impedances are computed by the moment method ($*$), by the eigencurrent approach ($\circ$), and by the eigencurrent approach with eigencurrents obtained from the eigencurrents of a single strip in free space with 40 piecewise expansion functions ($\triangle$). One group of coupling eigencurrents is used. Parameter values of the rings: $ka = \pi/3$, $\beta = 3/100$, $\psi = 0$, $N_{\cos} = 8$, $N_{\sin} = 0$. Parameter values of the single strip: $2\ell = \lambda/2$, $\beta = 1/50$, $N_{\cos} = 8$, $N_{\sin} = 0$.

rent coefficients of the approximation are obtained form a strip of half a wavelength with 40 piecewise functions. The absolute impedances obtained by the approximation match the absolute impedances obtained by the eigencurrent approach (without the described eigencurrent approximation) and the moment method reasonably well. The phase difference with the phases obtained by the moment method is about 0.1 rad, which is about the same as the difference between the phases obtained by the eigencurrent approach and the moment method. Contrary to the eigencurrent approach, the phases of the approximation mimic the pattern of the phases obtained by the moment method less well.

Taking two groups of coupling eigencurrents instead of one, we do not obtain a much better result for the phases obtained by the approximation as in the previous subsection. This is explained as follows. Only the dominant behavior of the eigencurrents of the first and second groups of eigencurrents can be described by the eigencurrent coefficients of the strip, not their perturbations. These perturbations are discussed in Subsection 5.3.2, see for example Figure 5.25 and the related paragraphs. They are described by the coefficients of the non-dominant single-element eigencurrents in each group. Since the magnitudes of the perturbations are between -10 dB and -20 dB with respect to the dominant behavior of the eigencurrents, the perturbations contribute to the local performance parameters of the elements. Especially the perturbations in the first and second groups that are of the order -10 dB may contribute more to

these parameters than the dominant part of eigencurrents in the third or fourth group, because the groups with higher index correspond to higher single-element eigenvalues.

The eigencurrent approach itself can handle large perturbations or perturbations that vary with the parameter setting, because it computes the eigenvalues and eigencurrents for each setting separately. The approximations of Subsections 6.3.4 and 6.3.5 are applicable if either the perturbations depend negligibly on the geometry parameters and the frequency, or if the perturbations are of second order with respect to the dominant behavior of the eigencurrents. The eigencurrents of the arrays we considered exhibit the second property. The perturbations of eigencurrents may become large if there is a degenerate eigenvalue. In that case, there is an eigenspace of more than one independent single-element eigencurrent. We encountered such a case in Subsection 5.3.2, p. 163, for a line array of rings with both cosine and sine eigencurrents prescribed on the elements. These eigencurrents exhibit the same eigenvalue and span together an eigenspace. Moreover, they are orthogonal with respect to the initializing L_2 inner product. In the general case, it is not essential that the eigencurrents obtained from the moment matrix of a single element are orthogonal with respect to the initializing inner product. It is only essential that they are independent. In this respect, it is important to note that independency does not depend on the inner product. Having computed the eigencurrents of a single element, we construct the new inner product in step E of the initialization of the eigencurrent approach, see Subsection 5.1.2. The eigencurrents corresponding to a degenerate eigenvalue are orthonormal by the definition of this inner product.

6.4 Array Surface Waves versus Surface Waves in Dielectric Layers

Up to now, we have considered arrays in free and half space. In practice, the elements are positioned on a dielectric layer on the ground plane. Such a layer can carry surface waves. If such a wave occurs, most of the power is carried along the array surface instead of radiated into space. Consequently, the array becomes 'blind'. In the literature, blindness is considered by many authors, see for example [107, 95, 93]. In this section, from an eigencurrent point of view, we discuss the correspondences between array surface waves and surface waves in dielectric layers. Moreover, we discuss whether the eigencurrent approach with only a limited number of groups of coupling eigencurrents can treat arrays positioned on grounded dielectric layers. To this end, we consider first the application of the infinite-array approach to arrays in free space.

To compute the currents on the elements of an array by the infinite-array approach, the 'infinite-array series' is truncated. We showed that the infinite-array approach does not provide a convergent solution at the grating-lobe scan angle, see Section 3.5. Hence, if the current at this scan angle is evaluated by the infinite-array approach with a truncated series, the result depends

on the truncation number. To evaluate the current accurately, the finite array must be considered.

In the practice of the moment, the array is not scanned up to the grating-lobe scan angle. Therefore, evaluation of the impedance at this angle is hardly considered. However, for us, it is important for the following reason. If a grating lobe appears in the plane of the array, a large amount of energy is radiated along the surface of the array. The same phenomenon occurs if the elements are positioned on a dielectric layer, which carries a surface wave. We show that the eigencurrent approach with only three groups of coupling eigencurrents computes the currents on the elements and related performance parameters sufficiently accurate at the grating-lobe scan angle. Thus, we are strengthened in our idea expressed in Section 5.4 that the eigencurrent approach can treat not only arrays in free and half space, but also arrays positioned on a grounded dielectric layer.

Figure 6.36 (upper figures) shows the impedances for a line array of 40 rings in free space excited by voltage gaps of 1V at the frequency for which $ka = 1.23$ to scan at $45.3°$. Since the spacing is $d = 3a = 0.587\lambda$, a grating lobe occurs at $-90°$ for this scan angle. Both for one and two groups of coupling eigencurrents, the absolute impedances obtained by the eigencurrent approach differ at most 2.5% from the absolute impedances obtained by the moment method. The phase differences are approximately uniform over the array, being 0.07 rad and 0.05 rad for one and two groups of coupling eigencurrents. Figure 6.36 (lower figures) shows that phase differences are slightly larger if the number of elements is increased to 201. Finally, the behavior of the absolute impedances and the corresponding phases at the grating-lobe scan angle for a line array of 201 H-plane oriented rings is in general the same as the behavior of arrays composed of an infinite number of parallel line arrays, where each line array consists of 201 parallel wires of about half a wavelength, see [46: Figs. 6, 7].

The phase differences observed above are not specifically due to the appearance of a grating lobe. Figure 6.37 shows that if the frequency is changed such that $ka = 1.047$, the phases obtained by the eigencurrent approach with two groups of coupling eigencurrents differ less than 0.02 rad from the phases obtained by the moment method. Why this phase difference is much smaller than the phase difference at $ka = 1.23$ is explained as follows. In Section 6.3.1, we investigated for the line array of 40 rings the spreads of the eigenvalue groups as a function of the frequency and we related the behavior of the spreads to the maximum relative L_2 difference between the solutions obtained by the moment method and the eigencurrent approach. At $ka = 1.23$, the L_2 difference becomes indeed larger due to the appearance of the grating lobe, but it is still below 2%. More important is the conclusion in Section 6.3.1 that on basis of the behavior of the spreads of the eigenvalue groups, the third group is needed to describe mutual coupling for ka near 1.3. At this value of ka, the single-ring eigenvalues corresponding to the second and third groups become approximately the same. Consequently, the second and third single-ring eigencurrents become equally important in the description of the current on a single ring. A test revealed that if the third group of eigencurrents is taken into account,

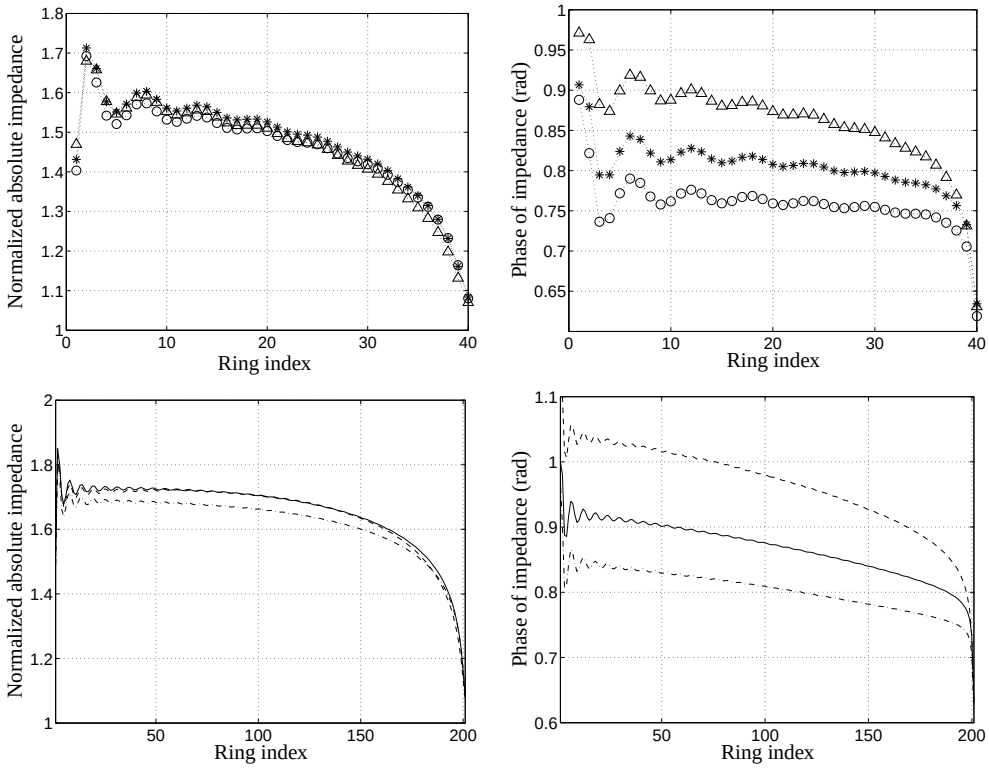

Figure 6.36 Normalized absolute values (left) and phases (right) of the ring impedances for line arrays of 40 and 201 rings in free space. The rings are excited with voltage gaps of 1V at the frequency with $ka = 1.23$ for a scan at 45.3°. The impedances are computed by the moment method ($*$) and by the eigencurrent approach ($\circ$). Parameter values: one group of coupling eigencurrents, $d = 3a$ ($d = \lambda/2$ at $ka = \pi/3$), $\beta = b/a = 3/100$, $\psi = 0$, $N_{\cos} = 8$, $N_{\sin} = 0$.

the phase difference of the impedances in Figure 6.36 reduce to 0.02 rad. For $ka \approx 1$, the single-ring eigenvalue of the third group is much larger than the single-ring eigenvalue of the second group. Therefore, only two groups of groups of coupling eigencurrents are needed to describe mutual coupling. These results show that grating lobe behavior is described by only two or three groups of coupling eigencurrents for ring circumferences of less than 1.5 times the wavelength. Moreover, the results confirm that the element shape determines which single-element eigencurrents can be excited; whether they are excited is determined by the excitation field of the array. Only single-element eigencurrents with small eigenvalues are excited and, hence, only these eigencurrents need to be taken into account as coupling eigencurrents in the

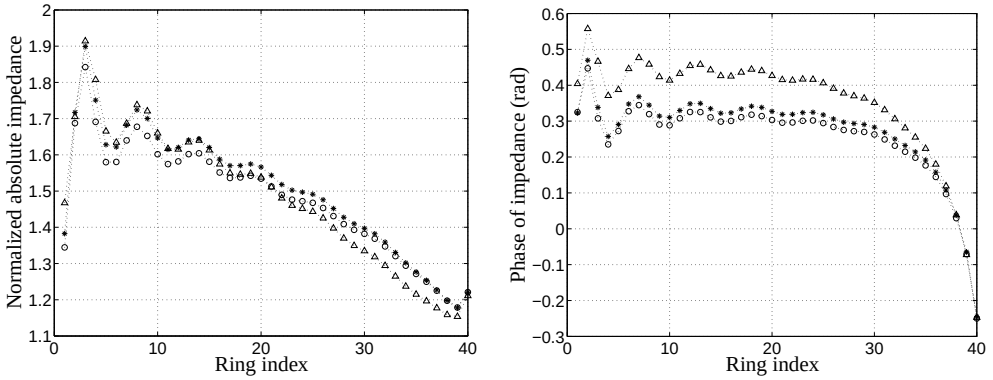

Figure 6.37 As Figure 6.36, but the frequency is changed such that $ka = 1.047$. Only the impedances of the line array of 40 rings are shown.

cycle of the eigencurrent approach.

Taking three instead of two groups of coupling eigencurrents into account increases the computation time of the eigencurrent approach. This can be prevented as follows. Since the coefficients of the dominant single-element eigencurrent in the array eigencurrents of each group are the same, see Subsection 5.3.2 and conclusion 7 in Section 5.4, we can approximate the eigencurrents of the third group by the dominant behavior of the eigencurrents of the first group. Then, we compute the eigenvalues of the third group by the Rayleigh-Ritz quotient. As discussed in relation to the single-strip eigencurrents in Subsection 6.3.5, by this approximation, we ignore the perturbation of the eigencurrents of the third group. This perturbation is of less importance than the perturbation of the first group, because the single-element eigenvalue corresponding to the third group is higher than the one corresponding to the first group. Therefore, the approximation will not affect the result for the currents on the elements and the related performance parameters.

Finally, we discuss the correspondences and differences between array surface waves, surface waves in dielectric layers, and grating-lobe appearance. The effect of surface waves in dielectric layers resembles the effect of grating-lobe appearance in the sense that a large amount of power is transported along the surface of the array. Since a grating lobe is represented by a specific eigencurrent, we think that a surface wave in a dielectric layer is represented by a specific eigencurrent as well. In contrast to the far field of the eigencurrent related to the grating lobe, the far field of the eigencurrent related to a surface wave will have main lobes at $\pm 90^\circ$ only. The eigenvalue corresponding to this eigencurrent will correspond to the blind scan angle in the same way as the eigenvalue of the 'grating-lobe' eigencurrent corresponds to the grating-lobe scan angle. As shown in Section 6.2, the occurrence of array surface waves corresponds to resonant behavior of the array. According to our definition, grating-lobe appearance is only

resonant behavior of the array, if the eigenvalue corresponding to the grating-lobe scan angle is relatively close to zero. In other words, if the eigencurrent corresponding to the grating-lobe scan angle exhibits a relatively small eigenvalue, i.e., a relatively low characteristic impedance. We think that a surface wave in a dielectric layer is only resonant behavior of the array, if the corresponding eigenvalue is relatively close to zero according to our definition. Resonant behavior due to a surface wave can occur both in a dielectric layer of finite extent and in a dielectric layer of infinite extent. In a dielectric layer of infinite extent, a propagating surface wave becomes a standing wave for certain sizes of the array, which is positioned in/on the dielectric layer. In a dielectric layer of finite extent, a propagating surface wave becomes a standing wave both for certain sizes of the array and for certain sizes of the dielectric layer.

6.5 Summary of the Conclusions

In this section, we first summarize point-by-point the main conclusions of this chapter. Next, we discuss to what extent our analysis as described in Chapters 5 and 6 meets the four requirements formulated in Chapter 1, p. 1.2, and to what extent our analysis provides insight into characteristics of arrays.

1. *Eigencurrents describe array surface wave phenomena and related variations of element-current amplitudes and element impedances.*

   Specifically, surface wave phenomena and the related variations are described by only a limited number of coupling eigencurrents. The examples of this chapter reveal that these eigencurrents are the eigencurrents of the first group. Four eigencurrents describe the scan behavior of the array, while three eigencurrents describe the surface-wave behavior. [Section 6.2]

2. *Eigencurrents describe modulated oscillations of the element impedances.*

   Specifically, modulated oscillations of the element impedances are described by a limited number of coupling eigencurrents only. Again, the examples of this chapter reveal that these eigencurrents are the eigencurrents of the first group. The scan behavior of the array is described by two or three eigencurrents, while the modulated oscillations are due to the excitation of one or two higher-order eigencurrents. [Subsection 6.3.2]

3. *Variations of element impedances attributed to surface waves and modulated oscillations of element impedances are caused by the excitation of specific eigencurrents and, therewith, by the same mechanism. Both these array effects are due to resonant behavior.*

   There are certain frequency ranges in which the effects occur. In the examples in this chapter of modulated oscillations in line arrays of H-plane oriented rings, the frequency

ranges from 11% to 16% and from 14% to 20%, respectively, below the frequency for which the array exhibits a 'resonant broadside embedded impedance'. In the examples of variations of element impedances in line arrays of H-plane oriented strips, the frequency ranges from 14% to 20% below this frequency. Finally, for line arrays of E-plane oriented rings, the modulated oscillations occur about 2.7% above this frequency. In contrast to the large variations of element impedances in item 1, the modulated oscillations do not occur over their entire frequency range. [Section 6.2 and Subsection 6.3.2]

4. *On basis of the eigenvalue distribution of the first group of (array) eigenvalues, (uniform) element surface loads required to reduce resonant behavior can be determined.* [Section 6.2]

5. *The spread of the eigenvalue groups is an appropriate qualitative measure to determine the number of groups of coupling eigencurrents needed to describe mutual coupling.*

   Here, the spread of an eigenvalue group is defined as the product of the maximum absolute eigenvalue perturbation, i.e., $\max\{|\epsilon_{nq}|\}_{q=1}^{N_{\rm sub}}$, and the ratio of the first absolute single-element eigenvalue, $|\nu_1^{\rm sub}|$, and the absolute single-element eigenvalue corresponding to this group, $|\nu_n^{\rm sub}|$. In formula, $\max\{|\epsilon_{nq}|\}_{q=1}^{N_{\rm sub}} \cdot |\nu_1^{\rm sub}|/|\nu_n^{\rm sub}|$. The single-element eigenvalues are indexed according to increasing absolute value. [Subsection 6.3.2]

6. *In the cycle of the eigencurrent approach for uniform line arrays generated from a single element, mutual coupling between distant elements may be neglected, but special care is needed. Except near the appearance of a grating lobe, the number of neighbors needed to describe mutual coupling is well predicted by the relative variation of the spreads for small arrays. Here, the relative variation of the spreads are defined as in Subsection 6.3.3.*

   Empirically, we deduced that if the relative variation of the spread $\Delta_n^{[M+1]}$ is smaller than 0.03, in line arrays of more than $M+1$ elements, only the coupling of each element with its first M neighbors needs to be considered for the single-element eigencurrent corresponding to the nth group of eigencurrents. Here, the relative variation is defined as in Subsection 6.3.3. In half space, the estimate of the number of neighbors provides accurate results, even for resonant behavior. In free space, the estimate may be a few elements too small due to the monotonic, but possibly slow increase of the spread. [Subsection 6.3.3]

7. *For large parameter variations, both the element impedances and the far-field performance parameters are approximated accurately for a fixed set of expansion coefficients of the array eigencurrents with respect to the single-element eigencurrents.*

   This conclusion can be used in computations of the array perfomance parameters for a given excitation as follows. First, for a given parameter setting, we compute the eigenvalues and eigencurrents. Next, we fix the computed eigencurrents. For a new parameter

setting, we approximate the eigenvalues by the Rayleigh-Ritz quotient applied to the fixed eigencurrents. Both in the computation of the eigencurrents in the first step and in the computation of the eigenvalues in the second step, we restrict mutual coupling on basis of calculations of the relative variation of the spreads for small arrays as explained in the previous conclusion. [Subsection 6.3.4]

8. *A first-order approximation of the performance parameters of uniform line arrays is obtained as follows. First, compute the expansion coefficients of the eigencurrents of a single strip obtained by piecewise linear expansion functions. Next, consider these expansion coefficients as the coefficients of the dominant single-element eigencurrents in the array eigencurrents. In this way, approximated array eigencurrents are obtained. Finally, compute the eigenvalues of the line array by applying the Rayleigh Ritz quotient to the approximated (array) eigencurrents.*

   In case only one group of coupling (array) eigencurrents needs to be considered, this approximation is in general more accurate than in case more groups of coupling eigencurrents need to be considered. [Subsection 6.3.5]

9. *In the eigencurrent approach, grating-lobe behavior is described by at most three groups of coupling eigencurrents.*

   For arrays of rings with circumference close to 1.5 times the wavelength, three groups of coupling eigencurrents are needed, while for rings with circumference close to or less than the wavelength, only two groups of coupling eigencurrents are needed. This observation confirms that the element shape determines, which single-element eigencurrents can be excited; whether they are excited is determined by the excitation field of the array. Only single-element eigencurrents with small eigenvalues are excited and, hence, only these eigenvalues need to be taken into account as coupling eigencurrents in the cycle of the eigencurrent approach. [Section 6.4]

10. *In contrast to array surface waves, grating-lobe appearance is non-resonant behavior of the array, if the eigenvalue corresponding to the grating-lobe scan angle is not relatively close to zero according to our definition.*

    The effect of surface waves in dielectric layers resembles the effect of grating-lobe appearance in the sense that a large amount of power is transported along the surface of the array. Since a grating lobe is represented by a specific eigencurrent, we think that a surface wave in a dielectric layer is represented by a specific eigencurrent as well. In contrast to the far field of the eigencurrent related to the grating lobe, the far field of the eigencurrent related to a surface wave will have main lobes at $\pm 90^\circ$ only. The eigenvalue corresponding to this eigencurrent will correspond to the blind scan angle in the same way as the eigenvalue of the 'grating-lobe' eigencurrent corresponds to the grating-lobe scan angle. As shown in

Section 6.2, the occurrence of array surface waves corresponds to resonant behavior of the array. According to our definition, grating-lobe appearance is only resonant behavior of the array, if the eigenvalue corresponding to the grating-lobe scan angle is relatively close to zero. In other words, if the eigencurrent corresponding to the grating-lobe scan angle exhibits a relatively small eigenvalue, i.e., a relatively low characteristic impedance. We think that a surface wave in a dielectric layer is only resonant behavior of the array, if the corresponding eigenvalue is relatively close to zero according to our definition. Resonant behavior due to a surface wave can occur both in a dielectric layer of finite extent and in a dielectric layer of infinite extent. In a dielectric layer of infinite extent, a propagating surface wave becomes a standing wave for certain sizes of the array, which is positioned in/on the dielectric layer. In a dielectric layer of finite extent, a propagating surface wave becomes a standing wave both for certain sizes of the array and for certain sizes of the dielectric layer. [Section 6.4]

11. *The eigencurrent approach proposed in this thesis describes resonant behavior of finite arrays accurately. In contrast, resonant behavior cannot be tackled by the infinite-array approach, no matter the size of the finite array.* [Section 6.2 and Subsection 6.3.2]

CHAPTER 7

Conclusions and Recommendations

The research on analysis and design of antenna arrays discussed in this thesis was assigned by and carried out at Thales Nederland in Hengelo, the Netherlands, in the period August 2000 to August 2004. The first part of the research, from August 2000 to April 2001 was carried out as final project of the postgraduate program Mathematics for Industry at the Technische Universiteit Eindhoven. In this chapter, we first summarize the conclusions of the research. Second, we outline the new approach proposed in this thesis to analyze antenna arrays, called the eigencurrent approach. Both for the conclusions and for the approach, we discuss to what extent they satisfy the main objectives I – IV in Section 1.3 and the requirements 1 – 4 in Section 1.2, p. 8. Third, we suggest potential modifications of the approach for a faster computation. Finally, we present recommendations for the future analysis and design of antenna arrays.

7.1 Conclusions

In this section, we discuss first the conclusions of this thesis. Next, we discuss to what extent they satisfy the objectives and requirements mentioned above.

1. The most important aspect of antenna-array analysis is determining the eigencurrents of a single element (or a subarray). For single rings and for single strips, we observed that the eigencurrents depend negligibly on the geomertry parameters.

2. The array eigencurrents are described as concatenations of linear combinations of the single-element eigencurrents. In this description, the coefficients of the dominant single-element eigencurrent depend negligibly on the element shape, as observed for line arrays of rings and line arrays of strips. Moreover, these coefficients depend negligibly on the spacing in line arrays.

3. The eigencurrents and eigenvalues of an array with uniform element geometry can be divided into groups; each group corresponds to an eigencurrent of the single element, i.e., the dominant single-element eigencurrent of the group. The coefficients of the dominant single-element eigencurrents are in each group the same. The eigenvalues are perturbations, not necessarily small, of the corresponding single-element eigenvalue. If mutual coupling is neglected, these perturbations are zero.

4. The spread of a group of eigenvalues, as defined by (6.1), is a quantitative measure for the mutual coupling both among the eigencurrents of that group and between the eigencurrents of that group and the eigencurrents of other groups. In an implementation of an analysis approach based on eigencurrents, an upper bound can be specified for the spread in order to neglect mutual coupling automatically.

5. The mutual coupling behavior of arrays consisting of elements that are typically designed to excite only one eigencurrent, or one main mode, can be described by a limited number of groups, typically one or two, of coupling eigencurrents.

6. Arrays are entire objects rather than collections of separate elements. For, the coefficients of the dominant single-element eigencurrent in each group of eigencurrents of a line array of rings or strips and the expansion coefficients of the eigencurrents of a single strip with piecewise functions generate the same patterns. Since a strip is an entire object, line arrays are entire objects as well.

7. All array eigenvalues are related to specific scan angles of the array. These scan angles are the positions of the main lobes in the far fields of the corresponding eigencurrents. The broadside scan, the monopulse, and the grating lobe are represented by specific eigencurrents of the array.

8. The eigencurrents of a finite array describe its characteristic behavior completely. The corresponding eigenvalues represent their characteristic impedance. The lower the impedance of an eigencurrent, the less excitation energy is required.

9. As a tool to calculate the array eigencurrents, the eigencurrent approach proposed in this thesis describes the characteristic behavior of finite antenna arrays accurately. In contrast, the infinite-array approach cannot describe the characteristic behavior of finite antenna arrays completely, no matter the size of the finite array.

10. The eigencurrents of finite arrays are standing waves. In contrast, eigencurrents related to the infinite-array approach are propagating waves. A finite line array can be regarded as a finite microstrip, or in mechanical terms, a finite string. Applying the infinite-array approach to finite arrays can be compared to replacing a finite microstrip, or a finite string, by an infinite one.

11. Characteristic behavior of finite arrays is due to resonance, and resonance is due to the excitation of specific, resonant, eigencurrents. The eigenvalues, or impedances, of these resonant eigencurrents are relatively close to zero compared to the eigenvalues of the non-resonant eigencurrents according to our definition in Section 6.2 and Subsection 6.3.2.

12. Variations of element-current amplitudes and element impedances attributed to array surface waves [82], and modulations of element impedances [46, 30] can explained from the excitation of specific eigencurrents of the array and, therewith, by the same mechanism.

13. On basis of the eigenvalue distribution of the first group of (array) eigenvalues, uniform surface loads required to reduce resonant behavior can be straightforwardly determined for the elements of an array. Uniform loading is equivalent to shifting the eigenvalues.

14. Grating-lobe appearance is resonant behavior of the array, if the eigenvalue corresponding to the grating-lobe scan angle is relatively close to zero in comparison with the other eigenvalues.

15. The difference between arrays in free space and arrays in half space is reflected in the far fields of the eigencurrents. In free space, there is a single eigencurrent that excites the grating lobe in the plane of the array. In half space, the same eigencurrent exists, but does not excite the grating lobe.

On basis of these conclusions, we come to the following **final conclusion** of this thesis:

The design characteristics of antenna arrays are one-to-one related to the excitation of specific eigencurrents of the array. The eigencurents are one-to-one related to scan lobes, grating lobes, monopulse lobes, impedance variations, modulated impedance oscillations, et cetera.

By this final conclusion, Objective III in Section 1.3 is satisfied. The eigencurrents are the characteristics that describe the behavior of arrays. Moreover, these characteristics are up to certain extent independent of the array geometry, see Conclusions 2, 3 and 6. With respect to Objective I, the characteristics of a single element that are essential for describing the array behavior are the single-element eigencurrents that contribute to the mutual coupling, see Conclusion 5 and the strongly related conclusions 1 and 4. Objective II is considered in the next section. Finally, the question in Objective IV about how and to what extent our approach improves the infinite-array approach is answered by the Conclusions 9 and 10.

Next, we consider the requirements 1 – 4 in Section 1.2, p. 8. Requirement 1 is satisfied, because once the eigencurrents of a single element or a single subarray are determined, these eigencurrents can be used for all arrays composed of the same elements, see Conclusion 2 and 3. The edge effects mentioned in Requirement 2 are described by the eigencurrents for

finite arrays. Moreover, the eigencurrents describe the resonant behavior of finite arrays. Therewith, requirement 2 is satisfied. Since the expansion coefficients of the dominant single-element eigencurrents in the array eigencurrents depend negligibly on the element shape and the spacing, coefficient distributions of eigencurrents can be used to analyze different array geometries using the same distributions. Therefore, an analysis approach based on eigencurrents will not be array-lattice and element-shape dependent, by which Requirements 3 and 4 will be satisfied. More details with respect to the requirements are discussed in the next section.

7.2 Approach for Analysis of Finite Antenna Arrays

We propose to analyze finite antenna arrays with the eigencurrent approach as described in this thesis. This proposal is supported by the conclusion of the previous section and, more specifically, the conclusions in Sections 5.4 and 6.5. We applied the eigencurrent approach successfully to line arrays of strips and rings, and we discussed the application of the eigencurrent approach to other types of elements and array geometries in Section 5.4 and Section 6.4. The eigencurrent approach is suitable for analyzing finite antenna arrays in an efficient way, keeping track of the characteristic behavior of arrays. It has two main steps, i.e., initialization and cycle. In this section, we outline the eigencurrent approach for arrays of uniform element geometry.

Initialization:

1. Choose suitable expansion functions for the single element. If the element has no specific shape, the choices of rooftop functions and Rao-Wilson-Glisson functions are suggested.

2. Construct the moment matrix for the single element, such that the matrix exhibits the same eigenvalues as the projected impedance operator. In contrast to the moment matrix defined as usual, the moment matrix defined as in Section 2.4.2 exhibits this property for all choices of expansion functions.

3. Compute the eigencurrents and eigenvalues from the moment matrix.

4. Construct the inner product with respect to which the eigencurrents are orthonormal.

Cycle:

1. Estimate how many single-element eigencurrents are needed to describe mutual coupling in the array from the behavior of their eigenvalues. Only single-element eigencurrents with eigenvalues that are small with respect to the other eigenvalues need to be taken into account.

2. Construct the moment matrix of the array for these single-element eigencurrents with respect to the inner product composed of the new single-element inner products.

3. Compute the eigencurrents and eigenvalues of the array from this moment matrix.

4. Group the (array) eigencurrents according to their corresponding single-element eigencurrent and single-element eigenvalue. Index the groups according to increasing single-element eigenvalues.

5. Verify that the spread of the eigenvalues of higher-order groups is small. If not, repeat steps 2 and 3 of the cycle with more single-element eigencurrents. Here, the spread of a group is defined as in Subsection 6.3.1.

6. Construct the inner product with respect to which both the coupling (array) eigencurrents and the non-coupling (array) eigencurrents are orthonormal.

Once the eigencurrents of the array have been computed, the current induced by a given excitation is computed by the (finite) expansion of the current with respect to the (array) eigencurrents.

The eigencurrent approach satisfies Objective II in Section 1.3 in the sense that it is efficient, see Section 6.1, and in the sense that it describes the characteristic behavior of arrays accurately, see Conclusions 9 and 10 of the previous section. Therewith, all objectives and requirements are satisfied, except that the application of the eigencurrent approach to other array geometries than line arrays is required to verify Requirements 3 and 4 more thoroughly. In this respect, we note that, above, only one cycle of the eigencurrent approach is described. An extension to more cycles is described in Chapter 5.

7.3 Modifications for Faster Computation

The eigencurrent approach as outlined in the previous section can be adjusted in several ways for a faster computation of the current. We mention the following four adjustments, which are investigated in this thesis.

- In the cycle of the eigencurrent approach, we may neglect mutual coupling between distant elements, but special care is needed. Except near the appearance of a grating lobe, the number of neighbors required to describe mutual coupling is well predicted by the relative variation of the spread for small arrays. Here, the relative variation of the spread is defined as in Subsection 6.3.3. For a given tolerance on the relative variation, such as the one deduced in Subsection 6.3.3, the number of neighbors required can be estimated automatically. [Conclusion 6, Section 6.5]

- Fix the eigencurrents computed for a certain parameter setting. Approximate the eigenvalues for a new parameter setting by the Rayleigh-Ritz quotient applied to these eigencurrents. In this way, the computation of the eigenvalues and eigencurrents from the moment matrix for each parameter setting is avoided, which saves considerable computation time. [Conclusion 7, Section 6.5]

- If groups of higher index, say 3 or 4, are needed in the eigencurrent approach, the computation time of the eigencurrents from the moment matrix in step 3 of the cycle may become large. To avoid this, compute first the eigencurrents for the groups of lower index, say 1 or 2, from the moment matrix in step III. Next, approximate the coefficients of the dominant single-element eigencurrents of the groups of higher index by the the coefficients of the dominant single-element eigencurrents of the first group. In this way, only the self coupling of the groups of higher index is considered, not the coupling between the groups of higher index and those of lower index. Approximate the eigenvalues for a given parameter setting for the array by applying the Rayleigh-Ritz quotient to the thus obtained eigencurrents of the groups of higher index.

- A first-order approximation of the performance parameters of uniform line arrays is obtained as follows. First, compute the expansion coefficients of the eigencurrents of a single strip obtained by piecewise linear expansion functions. Next, consider these expansion coefficients as the coefficients of the dominant single-element eigencurrents in the array eigencurrents. In this way, approximated array eigencurrents are obtained. Finally, compute the eigenvalues of the line array by applying the Rayleigh Ritz quotient to the approximated (array) eigencurrents. In this way, the dcomputation of the eigenvalues and eigencurrents from the moment matrix is not needed at all. [Conclusion 8, Section 6.5]

7.4 Recommendations

On basis of our research on antenna arrays, we come to the following recommendations in the fields of array design (1), application and validation of the eigencurrent approach (2 – 5), and implementation (6). The second and third recommendations are especially meant to verify Requirements 3 and 4 of Section 1.2, p. 8. The fourth recommendation is a general validation of the eigencurrent approach with experiments.

- Separate element design and array design. This recommendation is supported by the conclusions of the eigencurrent approach, in particular that the eigencurrents show this separated behavior.

- Apply the eigencurrent approach to other array geometries, in particular, to rectangular arrays. We suggest to use the multi-cycle approach as suggested in Chapter 5. General ideas for the application of the eigencurrent approach to other array geometries are described in Section 5.4.

- Apply the eigencurrent approach to arrays positioned on grounded dielectric layers. In that case, the kernel of the impedance operator needs to be changed. Kernels for grounded dielectric layers can be found in the literature, e.g., [5] and [72]. Finally, general ideas for the application of the eigencurrent approach to arrays positioned on grounded dielectric layers are described in Sections 5.4 and 6.4.

- Validate the proposed method by an experiments. We suggest the following. First, measure performance parameters of a uniform line array of existing elements. Next, compute the eigencurrents of this element by the initialization of the eigencurrent approach. Third, approximate the coefficients of the single-element eigencurrents in the array eigencurrents by the coefficients obtained for line arrays of strips or rings. Fourth, compute the eigenvalues of the array by applying the Rayleigh-Ritz quotient to the array eigencurrents thus obtained. Here, the first modification proposed in the previous section can be applied. Next, compute the current and the array performance parameters for some excitation fields. Finally, compare measurement results with simulation results.

- Apply eigencurrents for pattern synthesis, or in other words, apply eigencurrents to construct the specified far field of an antenna array. This recommendation is based on the conclusion that eigencurrents describe the characteristic behavior of arrays, in particular, the far field.

- Implement the eigencurrent approach in a programming language more suitable for commercial applications, such as the C programming language and the Fortran programming language.

APPENDIX A

Calculation of the Averaged Kernels

A.1 The Averaged Kernel F_{qq}

For $p = q$, the kernel F_{pq} in (2.57) is split into

$$F_{qq} = F_1 + F_2 + F_3, \tag{A.1}$$

where the functions F_1, F_2, and F_3 are defined by

$$F_1(\xi) = \frac{1}{\pi k\ell} \int_0^2 \frac{1}{\sqrt{\xi^2 + \beta^2\eta^2}}\, d\eta, \quad F_2(\xi) = \frac{1}{\pi k\ell} \int_0^2 \frac{\exp(-jk\ell\sqrt{\xi^2 + \beta^2\eta^2}) - 1}{\sqrt{\xi^2 + \beta^2\eta^2}}\, d\eta,$$

$$F_3(\xi) = -\frac{1}{2\pi k\ell} \int_0^2 \frac{\eta \exp(-jk\ell\sqrt{\xi^2 + \beta^2\eta^2})}{\sqrt{\xi^2 + \beta^2\eta^2}}\, d\eta. \tag{A.2}$$

The functions F_2 and F_3 are continuous. The integrand of F_1 is continuous as function of ξ except in the point 0, where it exhibits a linear singularity. Therefore, F_1 is logarithmic singular in 0, as can also be seen from

$$F_1(\xi) = \frac{1}{\pi k\ell\beta} \left[-\frac{1}{2} \log \xi^2 + \log \left(2\beta + \sqrt{4\beta^2 + \xi^2} \right) \right] . \tag{A.3}$$

This is the term $[\ldots]/\pi k\ell\beta$ in (2.59). The function F_3 equals the term $[\ldots]/2\pi j k^2\ell^2\beta^2$ in (2.59).

A.2 The Approximate Kernel $\breve{K}_{2,qq}$

The approximate kernel in (2.86) can be written as $\breve{K}_{2,qq}(\varphi) = K(2\sin(\varphi/2); ka_q, \beta_q, 0)$, where K is defined by

$$K(\xi;\alpha,\beta,\gamma) = \frac{1}{2\pi\alpha}\int_0^2 \frac{\exp\left(-j\alpha\sqrt{\beta^2\eta^2+\xi^2+\gamma^2}\right)}{\sqrt{\beta^2\eta^2+\xi^2+\gamma^2}}\left\{1+ \right. \\ \left. -\frac{(1-\eta/2)\xi^2}{\beta^2\eta^2+\xi^2+\gamma^2}\left(1+j\alpha\sqrt{\beta^2\eta^2+\xi^2+\gamma^2}\right)\right\} d\eta\,. \quad \text{(A.4)}$$

In this appendix, we deduce an approximation for K. We consider K as function of ξ with parameters $\alpha, \beta > 0$, and $\gamma \geq 0$, which are independent of ξ. We assume that $\beta \ll 1$ and approximate K as follows. First, we decompose K into two parts,

$$K(\xi;\alpha,\beta,\gamma) = K_1(\xi;\alpha,\beta,\gamma) + K_2(\xi;\alpha,\beta,\gamma), \quad \text{(A.5)}$$

where

$$K_2(\xi;\alpha,\beta,\gamma) = \frac{\xi^2}{4\pi\alpha}K_{21}\left(\sqrt{\xi^2+\gamma^2}\,;\alpha,\beta\right) - \frac{j\xi^2}{4\pi}K_{22}\left(\sqrt{\xi^2+\gamma^2}\,;\alpha,\beta\right), \quad \text{(A.6)}$$

and

$$K_1(\xi;\alpha,\beta,\gamma) = \frac{1}{2\pi\alpha}\int_0^2 \frac{\exp\left(-j\alpha\sqrt{\beta^2\eta^2+\xi^2+\gamma^2}\right)}{\sqrt{\beta^2\eta^2+\xi^2+\gamma^2}}\left(1-\frac{\xi^2}{\beta^2\eta^2+\xi^2+\gamma^2}\right)d\eta\,,$$

$$K_{21}(y;\alpha,\beta) = \int_0^2 \frac{\exp\left(-j\alpha\sqrt{\beta^2\eta^2+y^2}\right)}{\sqrt{\beta^2\eta^2+y^2}}\frac{\eta}{\beta^2\eta^2+y^2}\,d\eta\,, \quad \text{(A.7)}$$

$$K_{22}(y;\alpha,\beta) = \int_0^2 \exp\left(-j\alpha\sqrt{\beta^2\eta^2+y^2}\right)\frac{2-\eta}{\beta^2\eta^2+y^2}\,d\eta\,.$$

The functions K_2 and K_3 are both continuous as functions of y. The function K_1 is continuous as function of ξ except for $\gamma = 0$, where it exhibits a logarithmic singularity in $\xi = 0$. Under the condition that $\alpha = O(1)$ (as $\beta \downarrow 0$), we deduce

$$K_1(\xi;\alpha,\beta,\gamma) \approx \frac{1}{2\pi\alpha}\exp\left(-j\alpha\sqrt{\xi^2+\gamma^2}\right)\int_0^2 \frac{\beta^2\eta^2+\gamma^2}{(\beta^2\eta^2+\xi^2+\gamma^2)\sqrt{\beta^2\eta^2+\xi^2+\gamma^2}}\,d\eta = \\ = \frac{1}{2\pi\alpha}\exp\left(-j\alpha\sqrt{\xi^2+\gamma^2}\right)\left\{\frac{1}{\beta}\left(\log\left(2\beta+\sqrt{4\beta^2+\xi^2+\gamma^2}\right)-\log\left(\sqrt{\xi^2+\gamma^2}\right)\right)+ \right. \\ \left. -\frac{2\xi^2}{(\xi^2+\gamma^2)\sqrt{4\beta^2+\xi^2+\gamma^2}}\right\} =: \tilde{K}_1(\xi;\alpha,\beta,\gamma)\,. \quad \text{(A.8)}$$

This approximation is not appropriate for the imaginary part of K_1 if $\gamma = 0$. It is observed that the imaginary part of the approximation with $\gamma = 0$ tends to zero as $\xi \to 0$, whereas

$$\mathrm{Im}(K_1(0;\alpha,\beta,0)) = -\frac{1}{2\pi\alpha}\int_0^2 \frac{\sin(\alpha\beta\eta)}{\beta\eta}\,d\eta\,, \tag{A.9}$$

which is in general not zero. Therefore, the imaginary part of K_1 is approximated by

$$\begin{aligned}\mathrm{Im}(K_1(\xi;\alpha,\beta,\gamma)) &\approx -\frac{1}{2\pi\alpha}\frac{\sin(\alpha\sqrt{\xi^2+\gamma^2})}{\sqrt{\xi^2+\gamma^2}}\int_0^2 \frac{\beta^2\eta^2+\gamma^2}{\beta^2\eta^2+\xi^2+\gamma^2}\,d\eta = \\ &= -\frac{1}{2\pi\alpha}\frac{\sin(\alpha\sqrt{\xi^2+\gamma^2})}{\sqrt{\xi^2+\gamma^2}}\left(2-\frac{\xi^2}{\beta\sqrt{\xi^2+\gamma^2}}\arctan\left(\frac{2\beta}{\sqrt{\xi^2+\gamma^2}}\right)\right) = \\ &=: \mathrm{Im}(\tilde{K}_1(\xi;\alpha,\beta,\gamma))\,. \end{aligned} \tag{A.10}$$

This approximation is not only appropriate for the case $\gamma = 0$ and $\xi \to 0$, but also otherwise, provided that $\alpha = O(1)$ as above.

We rewrite the integral K_{21} by transforming the integration variable into $t = \eta^2$ first. Then, integrating by parts, we obtain

$$\begin{aligned}K_{21}(y;\alpha,\beta) &= \frac{1}{2}\int_0^4 \frac{\exp\left(-j\alpha\sqrt{\beta^2 t+y^2}\right)}{(\beta^2 t+y^2)^{\frac{3}{2}}}\,dt = \\ &= -\frac{1}{\beta^2}\left\{\frac{\exp\left(-j\alpha\sqrt{4\beta^2+y^2}\right)}{\sqrt{4\beta^2+y^2}} - \frac{\exp\left(-j\alpha|y|\right)}{|y|}\right\}+ \\ &\qquad - \frac{j\alpha}{2}\int_0^4 \frac{\exp\left(-j\alpha\sqrt{\beta^2 t+y^2}\right)}{\beta^2 t+y^2}\,dt\,. \end{aligned} \tag{A.11}$$

The integral K_{22} is decomposed into two parts and the integration variable of one of these parts is transformed into $t = \eta^2$,

$$K_{22}(y;\alpha,\beta) = 2\int_0^2 \frac{\exp\left(-j\alpha\sqrt{\beta^2\eta^2+y^2}\right)}{\beta^2\eta^2+y^2}\,d\eta - \frac{1}{2}\int_0^4 \frac{\exp\left(-j\alpha\sqrt{\beta^2 t+y^2}\right)}{\beta^2 t+y^2}\,dt\,. \tag{A.12}$$

We approximate the integral with respect to η in K_{22} in the same way as the integral K_1. In

other words, the real part is approximated by

$$\int_0^2 \frac{\cos\left(\alpha\sqrt{\beta^2\eta^2+y^2}\right)}{\beta^2\eta^2+y^2}\,d\eta \approx \cos(\alpha|y|)\int_0^2 \frac{1}{\beta^2\eta^2+y^2}\,d\eta = \\ = \frac{\cos(\alpha|y|)}{\beta|y|}\arctan\left(\frac{2\beta}{|y|}\right), \quad \text{(A.13)}$$

and the imaginary part by

$$\int_0^2 \frac{\sin\left(\alpha\sqrt{\beta^2\eta^2+y^2}\right)}{\beta^2\eta^2+y^2}\,d\eta \approx \frac{\sin(\alpha|y|)}{|y|}\int_0^2 \frac{1}{\sqrt{\beta^2\eta^2+y^2}}\,d\eta = \\ \frac{\sin(\alpha|y|)}{\beta|y|}\left[-\log|y| + \log\left(2\beta+\sqrt{4\beta^2+y^2}\right)\right]. \quad \text{(A.14)}$$

Summing K_{21} and K_{22} as in (A.6) to obtain K_2, we observe that the integrals with respect to t in K_{21} and K_{22} vanish. Hence, the approximation for K_2 is given by

$$\tilde{K}_2(\xi;\alpha,\beta,\gamma) = -\frac{\xi^2}{4\pi\alpha\beta^2}\left\{\frac{\exp\left(-j\alpha\sqrt{4\beta^2+\xi^2+\gamma^2}\right)}{\sqrt{4\beta^2+\xi^2+\gamma^2}} - \frac{\exp\left(-j\alpha\sqrt{\xi^2+\gamma^2}\right)}{\sqrt{\xi^2+\gamma^2}}\right\}+ \\ -\frac{j\xi^2}{2\pi\beta\sqrt{\xi^2+\gamma^2}}\cos\left(\alpha\sqrt{\xi^2+\gamma^2}\right)\arctan\left(\frac{2\beta}{\sqrt{\xi^2+\gamma^2}}\right)+ \\ -\frac{\xi^2}{2\pi\beta\sqrt{\xi^2+\gamma^2}}\sin\left(\alpha\sqrt{\xi^2+\gamma^2}\right)\left[-\log\sqrt{\xi^2+\gamma^2}+\right. \\ \left.+\log\left(2\beta+\sqrt{4\beta^2+\xi^2+\gamma^2}\right)\right]. \quad \text{(A.15)}$$

Finally, the integral K is approximated by

$$\tilde{K} = \tilde{K}_1 + \tilde{K}_2\,, \quad \text{(A.16)}$$

where the real and imaginary part of $\tilde{K}_1$ are given by (A.8) and (A.10), respectively, and $\tilde{K}_2$ is given by (A.15).

APPENDIX B

Fredholm Operators with Weakly Singular Displacement Kernels

In this appendix, we study Fredholm operators with weakly singular displacement kernels. For $k \in L_2([-2\alpha, 2\alpha])$, $\alpha > 0$, we introduce the Fredholm operator $\mathcal{K}$ by

$$(\mathcal{K}\phi)(x) = \int_{-\alpha}^{\alpha} k(x-y)\phi(y)\,dy, \qquad x \in [-\alpha, \alpha]\,. \tag{B.1}$$

The Cauchy-Schwarz inequality reveals that $\mathcal{K}\phi \in L_2([-\alpha, \alpha])$ for $\phi \in L_2([-\alpha, \alpha])$. Starting from this result, we formulate several statements below, which we use in the characterization of the domain and the range of the operator $\mathcal{Z}_{\rm a}$ in Chapter 3. With the notation of Section 3.1, we introduce the Lebesgue spaces $L_2([-\alpha, \alpha])$ and $H_{2,m}([-\alpha, \alpha])$ and the L_2-derivative D. In most of the statements, we take $\alpha = 1$, but these statements are valid for any $\alpha > 0$.

Lemma 1 Let $k \in L_2([-2, 2])$ and $\phi \in H_{2,1}([-1, 1])$. Then, $\mathcal{K}\phi \in H_{2,1}([-1, 1])$ with L_2-derivative

$$\mathsf{D}(\mathcal{K}\phi) = \mathcal{K}(\mathsf{D}\phi) + \phi(-1)k(x+1) - \phi(1)k(x-1)\,. \tag{B.2}$$

▲ For $x \in [-1, 1]$,

$$\begin{aligned}(\mathcal{K}\phi)(x) &= \int_{-1}^{1} \mathsf{D}_y \left\{ -\int_0^{x-y} k(\xi)\,d\xi \right\} \phi(y)\,dy = \\ &= \phi(-1)\int_0^{x+1} k(\xi)\,d\xi - \phi(1)\int_0^{x-1} k(\xi)\,d\xi + \int_{-1}^{1} \left\{ \int_0^{x-y} k(\xi)\,d\xi \right\} (\mathsf{D}\phi)(y)\,dy\,,\end{aligned} \tag{B.3}$$

where D_y indicates the L_2-derivative with respect to y. Differentiating both sides with respect to x yields (B.2). Moreover, $\mathsf{D}\mathcal{K}\phi \in L_2([-1,1])$, because the terms in the right-hand side of (B.2) are all elements of $L_2([-1,1])$. ■

Lemma 2 Let $k \in H_{2,1}[-2,2]$ and $\phi \in L_2([-1,1])$. Then, $\mathcal{K}\phi \in H_{2,1}([-1,1])$ and

$$(\mathsf{D}\mathcal{K}\phi)(x) = \int_{-1}^{1} (\mathsf{D}k)(x-y)\phi(y)\,dy\,. \tag{B.4}$$

▲ By the definition of the L_2-derivative k we obtain from (B.1)

$$\begin{aligned}(\mathcal{K}\phi)(x) &= c\int_{-1}^{1}\phi(y)\,dy + \int_{-1}^{1}\left\{\int_{0}^{x-y}(\mathsf{D}k)(\xi)\,d\xi\right\}\phi(y)\,dy = \\ &= c\int_{-1}^{1}\phi(y)\,dy - \int_{-1}^{1}\int_{0}^{y}(\mathsf{D}k)(\xi-y)\,d\xi\,\phi(y)\,dy + \int_{0}^{x}\int_{-1}^{1}(\mathsf{D}k)(\xi-y)\phi(y)\,dy d\xi\,,\end{aligned} \tag{B.5}$$

where $c = k(0)$. The first two terms in the right-hand side are constant. Differentiating both sides with respect to x, we obtain (B.4). Since $\mathsf{D}k \in L_2[-2,2]$ and $\phi \in L_2([-1,1])$, it follows that $\mathsf{D}\mathcal{K}\phi \in L_2([-1,1])$. ■

Corollary 1 Let $k \in H_{2,1}[-2,2]$ and $\phi \in H_{2,1}([-1,1])$. Then, $\mathcal{K}\phi \in H_{2,2}([-1,1])$.

▲ From Lemma 2, it follows that $\mathcal{K}\mathsf{D}\phi \in H_{2,1}([-1,1])$, and hence $\mathsf{D}\mathcal{K}\phi \in H_{2,1}([-1,1])$ by Lemma 1. ■

Lemma 3 Let k be the function $k(\xi) = \frac{1}{2}\log\xi^2$ and $\phi \in L_2([-1,1])$. Then, $\mathcal{K}\phi \in H_{2,1}([-1,1])$.

▲ See [97: p. 37] ■

Corollary 2 Let $\phi \in H_{2,1}([-1,1])$ in the previous lemma. Then, $\mathcal{K}\phi \in H_{2,2}([-1,1])$ if and only if $\phi(1) = \phi(-1) = 0$. Under this condition, $\mathsf{D}\mathcal{K}\phi = \mathcal{K}\mathsf{D}\phi$.

▲ It follows from Lemma 1 and Lemma 3 that $\mathcal{K}\phi \in H_{2,2}([-1,1])$ if and only if $\phi(-1)\log(1+x) - \phi(1)\log(1-x) \in H_{2,1}([-1,1])$. The latter is equivalent to $\phi(-1) = \phi(1) = 0$, which implies $\mathsf{D}\mathcal{K}\phi = \mathcal{K}\mathsf{D}\phi$ by lemma 1. ■

Remark 1 The previous lemmas and corollaries are valid for all $\alpha > 0$.

Lemma 4 Let the functions N_0, $N_{\cos,n}$, and $N_{\sin,n}$ $(n = 1, 2, ...)$ be defined by

$$N_0 = \frac{1}{\sqrt{2\pi}}\,, \qquad N_{\cos,n}(x) = \frac{1}{\sqrt{\pi}}\cos nx\,, \qquad N_{\sin,n}(x) = \frac{1}{\sqrt{\pi}}\sin nx\,. \tag{B.6}$$

Then, $f \in H_{2,m,per}[-\pi,\pi]$ if an only if there exist a_0, a_n, b_n $(n = 1, 2, ...)$, such that

$$f = a_0 N_0 + \sum_{n=1}^{\infty} \left(a_n N_{\cos,n} + b_n N_{\sin,n}\right)\,, \qquad \sum_{n=1}^{\infty}(1+n^2)^m(a_n^2+b_n^2) < \infty\,. \tag{B.7}$$

Lemma 5 Let k be defined by $k(\xi) = -\frac{1}{2}\cos\xi\,\log\sin^2(\xi/2)$. Let $\phi \in L_2[-\pi,\pi]$. Then, $\mathcal{K}\phi \in H_{2,1,per}[-\pi,\pi]$. If $\phi \in H_{2,1,per}([-\pi,\pi])$, then $\mathcal{K}\phi \in H_{2,2,per}([-\pi,\pi])$ and $\mathsf{D}\mathcal{K}\phi = \mathcal{K}\mathsf{D}\phi$.

▲ From the expansion of $\log(2\cos(\xi/2))$, $-\pi < \xi < \pi$, see [41: p. 38, Eq. 1.441.4], it follows that

$$-\frac{1}{2}\log\sin^2\left(\frac{\xi}{2}\right) = \log 2 + \sum_{n=1}^{\infty}\frac{\cos n\xi}{n}, \qquad -2\pi < \xi < 2\pi, \xi \neq 0\,. \tag{B.8}$$

Then,

$$-\cos\xi\;\log\sin^2\left(\frac{\xi}{2}\right) = 1 + 2\left(\log 2 + \frac{1}{4}\right)\cos\xi + \sum_{n=2}^{\infty}\frac{2n}{n^2-1}\cos n\xi\,. \tag{B.9}$$

By this expression, we write the kernel $k(x-y)$ as

$$\begin{aligned} k(x-y) = \pi N_0^2 + \pi\left(\log 2 + \frac{1}{4}\right)\left(N_{\cos,1}(x)N_{\cos,1}(y) + N_{\sin,1}(x)N_{\sin,1}(y)\right) + \\ + \pi\sum_{n=2}^{\infty}\frac{n}{n^2-1}\left(N_{\cos,n}(x)N_{\cos,n}(y) + N_{\sin,n}(x)N_{\sin,n}(y)\right)\,, \end{aligned} \tag{B.10}$$

where the functions N_0, $N_{\cos,n}$, and $N_{\sin,n}$ $(n = 1, 2, ...)$ are defined as in Lemma 4. These functions form a total orthonormal set in $L_2([-\pi,\pi])$. Then, we may expand $\phi \in L_2([-\pi,\pi])$ into the functions of this set,

$$\phi = a_0 N_0 + \sum_{n=1}^{\infty}\left(a_n N_{\cos,n} + b_n N_{\sin,n}\right)\,, \qquad \sum_{n=1}^{\infty}\left(a_n^2+b_n^2\right) < \infty\,. \tag{B.11}$$

The latter implies the convergence of the series expansion for ϕ on basis of Banach's criterion. Using (B.10) and (B.11), we obtain for $\mathcal{K}_\pi\phi$

$$(\mathcal{K}\phi)(x) = \pi a_0 N_0(x) + \pi\left(\log 2 + \frac{1}{4}\right)(a_1 N_{\cos,1}(x) + b_1 N_{\sin,1}(x)) + \\ + \pi\sum_{n=2}^{\infty}\frac{n}{n^2-1}\left(a_n N_{\cos,n}(x) + b_n N_{\sin,n}(x)\right), \quad \text{(B.12)}$$

Then, according to Lemma 4, $\mathcal{K}\phi \in H_{2,1,per}([-\pi,\pi])$ for $\phi \in L_2([-\pi,\pi])$. Moreover, if $\phi \in H_{2,1,per}([-\pi,\pi])$, then $\mathcal{K}\phi \in H_{2,2,per}([-\pi,\pi])$ and $\mathsf{D}\mathcal{K}\phi = \mathcal{K}\mathsf{D}\phi$, the latter of which follows from straightforward calculation. ■

Corollary 3 Replace the function k in the previous lemma by a function $k \in H_{2,1,per}([-\pi,\pi])$. Then, the same conclusions hold as in this lemma.

Remark 2 From (B.12), it follows that the Fredholm operator $\mathcal{K}$ induced by the kernel k in Lemma 5 is a diagonal operator with respect to the total orthonormal set defined by (B.6) in $L_2([-\pi,\pi])$. The same yields for the kernels k in Corollary 3.

APPENDIX C

Far-Field Approximations

In this appendix, we deduce expressions for the electric field far away from an array of strips or rings. By far away, we mean that the distance to a fixed point on the array is much larger than both the characteristic length L of the array and the wavelength λ.

Let us consider an array in free space described by a surface S as in Subsection 2.3.1. The electric field generated by the averaged current $\mathcal{A}\boldsymbol{J}$ on the surface S in free space is given by

$$\boldsymbol{E} = \sum_{q=1}^{N_{\mathrm{el}}} \boldsymbol{E}_q\,, \qquad \boldsymbol{E}_q = \mathcal{D}\boldsymbol{A}_q = \mathcal{D}\mathcal{T}(\mathcal{A}\boldsymbol{J})|_{S_q}\,, \tag{C.1}$$

where

$$\boldsymbol{A}_q(\boldsymbol{x}) = \mathcal{T}(\mathcal{A}\boldsymbol{J})|_{S_q}(\boldsymbol{x}) = \int_{\Pi(S_q)} g_{\mathrm{free}}\Big(R\big(\boldsymbol{x}-\boldsymbol{x}_{S_q}(\xi,\eta)\big)\Big)\,(\mathcal{A}\boldsymbol{J})|_{S_q}(\xi,\eta)\,dS_q(\xi,\eta)\,, \tag{C.2}$$

and

$$(\mathcal{A}\boldsymbol{J})|_{S_q}(\xi,\eta) = w_q(\xi)\,\boldsymbol{e}_\xi(\xi,0), \qquad dS_q(\xi,\eta) = S_q^{\mathrm{vol}}(\xi,\eta)\,d\eta\,d\xi\,. \tag{C.3}$$

We note that g_{free} is defined by (2.12), S_q^{vol} by (2.24)^2, and $\mathcal{D}$ by (2.10). We express the tuple $\boldsymbol{x} \in \mathbb{R}^3$ into the standard spherical coordinate system given by

$$\begin{aligned}
\boldsymbol{e}_\rho(\theta,\phi) &= \sin\theta\cos\phi\,\boldsymbol{e}_x + \sin\theta\sin\phi\,\boldsymbol{e}_y + \cos\theta\,\boldsymbol{e}_z,\\
\boldsymbol{e}_\theta(\theta,\phi) &= \cos\theta\cos\phi\,\boldsymbol{e}_x + \cos\theta\sin\phi\,\boldsymbol{e}_y - \sin\theta\,\boldsymbol{e}_z,\\
\boldsymbol{e}_\phi(\theta,\phi) &= -\sin\phi\,\boldsymbol{e}_x + \cos\phi\,\boldsymbol{e}_y.
\end{aligned} \tag{C.4}$$

Then, $\boldsymbol{x}(\rho,\theta,\phi) = \rho\boldsymbol{e}_\rho(\theta,\phi)$ and

$$R\big(\boldsymbol{x}(\rho,\theta,\phi) - \boldsymbol{x}_{S_q}(\xi,\eta)\big) = \sqrt{\rho^2 - 2\rho\,(\boldsymbol{e}_\rho(\theta,\phi)\bullet\boldsymbol{x}_{S_q}(\xi,\eta)) + |\boldsymbol{x}_{S_q}(\xi,\eta)|^2}\,. \tag{C.5}$$

Moreover, in spherical coordinates, the action of $\mathcal{D}$ on $\boldsymbol{A}_q$ is given by

$$\mathcal{D}\boldsymbol{A}_q = -jZ_0k\left[\boldsymbol{A}_q + \frac{1}{k^2}\left(\boldsymbol{e}_\rho\frac{\partial}{\partial\rho} + \boldsymbol{e}_\phi\frac{1}{\rho\sin\theta}\frac{\partial}{\partial\phi} + \boldsymbol{e}_\theta\frac{1}{\rho}\frac{\partial}{\partial\theta}\right)\right.$$
$$\left.\left(\frac{1}{\rho^2}\frac{\partial}{\partial\rho}(\rho^2 A_{q,\rho}) + \frac{1}{\rho\sin\theta}\frac{\partial}{\partial\theta}(A_{q,\theta}\sin\theta) + \frac{1}{\rho\sin\theta}\frac{\partial A_{q,\phi}}{\partial\phi}\right)\right]. \quad \text{(C.6)}$$

The components $A_{q,\rho}$, $A_{q,\theta}$, and $A_{q,\phi}$ are obtained by expressing $\boldsymbol{e}_\xi(\xi,0)$ into the Cartesian coordinate system and then by expressing the vectors of this system into the spherical coordinate system. For ρ so large that the sphere with radius ρ contains S, we may reverse the integrals in these components and the partial derivatives in (C.6). Then, the partial derivatives act on the kernel $g_{\rm free}(R(\boldsymbol{x}(\rho,\theta,\phi) - \boldsymbol{x}_{S_q}(\xi,\eta)))$ in (C.2). For the ρ-derivatives of this kernel, we obtain

$$\frac{\partial^n g_{\rm free}\Big(R\big(\boldsymbol{x}(\rho,\theta,\phi) - \boldsymbol{x}_{S_q}(\xi,\eta)\big)\Big)}{\partial\rho^n} = \frac{(-jk)^n}{\rho}\times$$
$$\times\ \exp\left(-jk\sqrt{\rho^2 - 2\rho\,(\boldsymbol{e}_\rho(\theta,\phi)\bullet\boldsymbol{x}_{S_q}(\xi,\eta)) + |\boldsymbol{x}_{S_q}(\xi,\eta)|^2}\right)\left(1 + O\Big(\frac{L+1/k}{\rho}\Big)\right), \quad \text{(C.7)}$$

where L is the characteristic length scale of the surface S and $n = 0, 1, 2$. As mentioned above, we assume that $L/\rho \ll 1$ and $1/k\rho \ll 1$. Moreover, the parameter descriptions $\boldsymbol{x}_{S_q}$ are chosen such that $|\boldsymbol{x}_{S_q}(\xi,\eta)|/\rho \ll 1$. It follows from (C.6) and (C.7) that the dominant terms of $(\mathcal{D}\boldsymbol{A}_q)_\rho$ are $A_{q,\rho}$ and $\partial^2 A_{q,\rho}/\partial^2\rho^2$. The other terms in $(\mathcal{D}\boldsymbol{A}_q)_\rho$ are of $O((L+1/k)/\rho)$ with respect to these terms. Hence, it seems that the dominant term of $(\mathcal{D}\boldsymbol{A}_q)_\rho$ is $A_{q,\rho} + \partial^2 A_{q,\rho}\,/\,k^2\,\partial^2\rho^2$. However, it follows from (C.7) that this term vanishes up to terms of $O((L+1/k)/\rho)$. This implies that $(\mathcal{D}\boldsymbol{A}_q)_\rho$ is of $O((L+1/k)/\rho)$ with respect to $(\mathcal{D}\boldsymbol{A}_q)_\theta$ and $(\mathcal{D}\boldsymbol{A}_q)_\phi$. From (C.6) and (C.7), it follows also that $A_{q,\theta}$ and $A_{q,\phi}$ are the dominant terms of $(\mathcal{D}\boldsymbol{A}_q)_\theta$ and $(\mathcal{D}\boldsymbol{A}_q)_\phi$. The other terms are of $O((L+1/k)/\rho)$. Then, neglecting terms of $O(L^2/\rho^2)$ in the phase term of (C.7) with $n = 0$, and neglecting terms of $O((L+1/k)/\rho)$ in the other terms of the electric field $\boldsymbol{E}_q$, we find that

$$\boldsymbol{E}_q = -jZ_0k\,(A_{q,\theta}\boldsymbol{e}_\theta + A_{q,\phi}\boldsymbol{e}_\phi)\ , \quad \text{(C.8)}$$

where the components $A_{q,\theta}$ and $A_{q,\phi}$ follow from

$$\boldsymbol{A}_q(\rho,\theta,\phi) = \frac{e^{-jk\rho}}{4\pi\rho}\int_{\Pi(S_q)} e^{jk\left(\boldsymbol{e}_\rho(\theta,\phi)\bullet\boldsymbol{x}_{S_q}(\xi,\eta)\right)}\,w_q(\xi)\,\boldsymbol{e}_\xi|_{S_q}(\xi,0)\,S_q^{\rm vol}(\xi,\eta)\,d\eta\,d\xi\,. \quad \text{(C.9)}$$

The magnetic field $\boldsymbol{H}_q$ corresponding to $\boldsymbol{E}_q$ follows from (2.14)[1], i.e., $\boldsymbol{H}_q = \mathrm{rot}\,\boldsymbol{A}_q$. By a similar dimensional analysis as above, it is shown that the ρ-component of this field vanishes

and that the θ and ϕ-components are given by $H_{q,\theta} = -\partial A_{q,\phi}/\partial\rho$ and $H_{q,\phi} = \partial A_{q,\theta}/\partial\rho$. From (C.7) we obtain two equivalent expressions for $\boldsymbol{H}_q$,

$$\boldsymbol{H}_q = jk\,(A_{q,\phi}\boldsymbol{e}_\theta + A_{q,\theta}\boldsymbol{e}_\phi)\,, \qquad \boldsymbol{H}_q = \boldsymbol{e}_\rho \times \boldsymbol{E}_q \,/\, Z_0\,, \tag{C.10}$$

where $\boldsymbol{E}_q$ is given by (C.8). The expressions (C.8) and (C.10)[2] are the well-known far-field expressions, see for example [110: pp. 31 – 32].

Let us now consider an array of strips in free space as described in Subsection 2.3.2. For the parameter description $\boldsymbol{x}_{S_q}$ given by (2.41), the origin of the spherical coordinate system is located in the plane of the array. The vector $\boldsymbol{e}_\xi|_{S_q}$ in (C.2) equals $\boldsymbol{e}_y$ and $S_q^{\mathrm{vol}} = 1$. Using $\boldsymbol{e}_y = \sin\theta\sin\phi\,\boldsymbol{e}_\rho + \cos\theta\sin\phi\,\boldsymbol{e}_\theta + \cos\phi\,\boldsymbol{e}_\phi$, we obtain from (C.9)

$$A_{q,\left\{\begin{smallmatrix}\theta\\ \phi\end{smallmatrix}\right\}}(\rho,\theta,\phi) = \begin{Bmatrix}\cos\theta\sin\phi\\ \cos\phi\end{Bmatrix} A_q(\rho,\theta,\phi)\,, \tag{C.11}$$

where A_q is given by

$$A_q(\rho,\theta,\phi) = \frac{\ell b}{4\pi}\,\frac{e^{-jk\rho}}{\rho}\,e^{jkc_{q,x}\sin\theta\cos\phi}\int_{-1}^{1} e^{jk\ell\xi\sin\theta\sin\phi} w_q(\xi)\,d\xi \int_{-1}^{1} e^{-jk\ell\beta\eta\sin\theta\cos\phi}\,d\eta\,. \tag{C.12}$$

In these expressions, we normalized the integration variables with respect to ℓ and b, and that we interpreted w_q as a function of the normalized coordinate ξ. As in the deduction of the approximate kernel $\tilde{F}_{qq}$ in (2.62), we assume that $\beta \ll 1$ and $k\ell = O(1)$ (as $\beta \downarrow 0$). Neglecting terms of order β^2, we approximate the integral with respect to η by 2. To calculate the integral with respect to ξ, we need to specify w_q. For the entire-domain expansion functions (3.8), w_q is a linear combination of the expansion functions $(\mathcal{W}_q^{\cos}\boldsymbol{e}_n)(\,\cdot\,;q)$, $n = 1, 2, \ldots, N_{\cos}(q)$, and $(\mathcal{W}_q^{\sin}\boldsymbol{e}_n)(\,\cdot\,;q)$, $n = 1, 2, \ldots, N_{\sin}(q)$. The expansion coefficients corresponding to these functions are $[(\mathcal{W}_q^{\cos})^{-}\boldsymbol{w}](n,1)$ and $[(\mathcal{W}_q^{\sin})^{-}\boldsymbol{w}](n,1)$, which follow from the solution of the moment-matrix equation $[\mathcal{W}^{-}\mathcal{Z}_{\mathrm{a}}\mathcal{W}][\mathcal{W}^{-}\boldsymbol{w}] = [\mathcal{W}^{-}\boldsymbol{v}^{ex}]$. Having calculated the integral with respect to ξ for each expansion function in (3.8), we construct the electric field from (C.1)[1], (C.8), (C.11), and (C.12). We obtain

$$\boldsymbol{E}(\rho,\theta,\phi) = -jZ_0k\,(\cos\theta\sin\phi\,\boldsymbol{e}_\theta + \cos\phi\,\boldsymbol{e}_\phi)\sum_{q=1}^{N_{\mathrm{el}}} A_q(\rho,\theta,\phi)\,, \tag{C.13}$$

where

$$A_q(\rho,\theta,\phi) = \frac{\ell b}{2\pi}\frac{e^{-jk\rho}}{\rho}\, e^{jkc_{q,x}\sin\theta\cos\phi}\left(\sum_{n=1}^{N_{\cos}(q)}[(\mathcal{W}_q^{\cos})^{-}\boldsymbol{w}](n,1)\,\frac{(-1)^n(2n-1)\pi\cos\kappa}{\kappa^2-(2n-1)^2\pi^2/4}+\right.$$
$$\left.+\sum_{n=1}^{N_{\sin}(q)}[(\mathcal{W}_q^{\sin})^{-}\boldsymbol{w}](n,1)\,\frac{(-1)^n 2n\pi j\sin\kappa}{\kappa^2-n^2\pi^2}\right), \quad \text{(C.14)}$$

and $\kappa = k\ell\sin\theta\sin\phi$.

Let us consider an array of rings as described in Subsection 2.3.3. As above, the origin of the spherical coordinate system is located in the plane of the array for the parameter description $\boldsymbol{x}_{S_q}$ given by (2.64). The vector $\boldsymbol{e}_\xi|_{S_q}$ in (C.2) is given by $\boldsymbol{e}_\theta|_{S_q}$ in (2.65)[2] and S_q^{vol} is given by $S_q^{\mathrm{vol}}(r,\varphi) = r$. Using $\boldsymbol{e}_x = \sin\theta\cos\phi\,\boldsymbol{e}_\rho + \cos\theta\cos\phi\,\boldsymbol{e}_\theta - \sin\phi\,\boldsymbol{e}_\phi$, and $\boldsymbol{e}_y = \sin\theta\sin\phi\,\boldsymbol{e}_\rho + \cos\theta\sin\phi\,\boldsymbol{e}_\theta + \cos\phi\,\boldsymbol{e}_\phi$, we obtain from (C.9)

$$A_{\left\{\begin{smallmatrix}\theta\\ \phi\end{smallmatrix}\right\}}(\rho,\theta,\phi) = \begin{Bmatrix}\cos\theta\\ 1\end{Bmatrix}\frac{a_q b_q}{4\pi}\frac{e^{-jk\rho}}{\rho}\, e^{jk(c_{q,x}\sin\theta\cos\phi + c_{q,y}\sin\theta\sin\phi)}\times$$
$$\times\int_{-\pi}^{\pi}\exp\big(jka_q\sin\theta\cos(\phi-\varphi-\psi_q)\big)\,w_q(\varphi)\begin{Bmatrix}\sin(\phi-\varphi-\psi_q)\\ \cos(\phi-\varphi-\psi_q)\end{Bmatrix}\times$$
$$\times\int_{-1}^{1}\exp\big(jka_q\beta_q r\sin\theta\cos(\phi-\varphi-\psi_q)\big)\,(1+\beta_q r)\,dr\,d\varphi. \quad \text{(C.15)}$$

As the integral with respect to η above, we approximate the integral with respect to r by 2, where we assume that $\beta_q \ll 1$ and $ka_q = O(1)$ (as $\beta \downarrow 0$). To calculate the integral with respect to φ, we specify w_q as above for the strips, where the entire-domain expansion functions are given by (3.12). Then, we obtain

$$E_{\left\{\begin{smallmatrix}\theta\\ \phi\end{smallmatrix}\right\}}(\rho,\theta,\phi) = -jZ_0k\begin{Bmatrix}\cos\theta\\ 1\end{Bmatrix}\frac{e^{-jk\rho}}{2\rho}\sum_{q=1}^{N_{\mathrm{el}}}a_q b_q e^{jk(c_{q,x}\sin\theta\cos\phi + c_{q,y}\sin\theta\sin\phi)}\times$$
$$\times\left(\sum_{n=1}^{N_{\cos}(q)}[(\mathcal{W}_q^{\cos})^{-}\boldsymbol{w}](n,1)\begin{Bmatrix}\sin(n-1)(\phi-\psi_q)\\ \cos(n-1)(\phi-\psi_q)\end{Bmatrix}j^{n-2}\big(J_{n-2}(\kappa_q)\pm J_n(\kappa_q)\big)+\right.$$
$$\left.+\sum_{n=1}^{N_{\sin}(q)}[(\mathcal{W}_q^{\sin})^{-}\boldsymbol{w}](n,1)\begin{Bmatrix}-\cos n(\phi-\psi_q)\\ \sin n(\phi-\psi_q)\end{Bmatrix}j^{n-1}\big(J_{n-1}(\kappa_q)\pm J_{n+1}(\kappa_q)\big)\right), \quad \text{(C.16)}$$

where $\kappa_q = ka_q\sin\theta$.

For arrays of strips or rings in a half space, the deduction of the electromagnetic far fields runs analogously. Due to the description of the centers of the elements in Subsection 2.3.4, the origin of the spherical coordinate system is not in the plane of the array as above, but in the boundary plane of the half space. The components of the corresponding electric far fields are given by (C.13) and (C.16), both multiplied $2j\sin(hk\cos\theta)$, see [34] for details. Here, h is the height above the ground plane and the spherical coordinates correspond to the new origin. The factor $2j\sin(hk\cos\theta)$ is the same as the factor for an infinitesimal dipole in a half space, see [4: Eq. (4-116)].

We compare the far field (C.16) of the rings with results for a single wire ring as described in the literature. For $N_{\mathrm{el}} = 1$, $N_{\sin}(1) = 0$, $c_{1,x} = c_{1,y} = 0$, and $\psi_1 = 0$, we can rewrite (C.16) as

$$E_{\left\{\begin{smallmatrix}\theta\\ \phi\end{smallmatrix}\right\}}(\rho,\theta,\phi) = \frac{\omega\mu_0 a_1 e^{-jk\rho}}{4j\rho} \begin{Bmatrix} -\cos\theta \\ j \end{Bmatrix} \times \\ \times \sum_{n=-N_{\cos}(1)+1}^{N_{\cos}(1)-1} \alpha_n j^n e^{jn\phi}\big(J_{n+1}(\kappa_1) \pm J_{n-1}(\kappa_1)\big), \quad \text{(C.17)}$$

where $\alpha_0 = 2b_1\,[(\mathcal{W}_1^{\cos})^{-}\boldsymbol{w}](1,1)$ and $\alpha_n = \alpha_{-n} = b_1\,[(\mathcal{W}_1^{\cos})^{-}\boldsymbol{w}](n+1,1)$ for $n > 0$. These expressions for the electric far-field components are the same as the expressions (5-49) and (5-50) in [47: p. 92] for a wire ring, if we identify α_n and V_s/Z_{nn} in [47: p. 92]. Moreover, putting also $N_{\cos}(1) = 1$ in (C.16), we find the same far-field components as in [4: p. 219] for a wire ring with constant current. Here, we identify the total current $2b_1\,[(\mathcal{W}_q^{\cos})^{-}\boldsymbol{w}](1,1)$ through the strip and the total current I_0 through the wire in [4: p. 219].

For the strips, it can be shown that the far-field expression (C.13) yields the same result as in [4: p. 162], but then we need to align the z-axis along the strip. This is accomplished by the permutation $(x,y,z) \to (z,x,y)$ in (C.4).

Finally, we calculate the total radiated power in the far field. The time-average Poynting vector $\boldsymbol{S}$ defined by $\boldsymbol{S} = \mathrm{Re}(\boldsymbol{E}\times\boldsymbol{H}^*)/2$ represents the radiation power density averaged with respect to time, see [109: p. 137]. By (C.10)^2, the Poynting vector in the far field can be written as $\boldsymbol{S} = (\boldsymbol{E}\bullet\boldsymbol{E}^*)\boldsymbol{e}_\rho/2Z_0$. The total radiated power of an array in free space is the total flux of $\boldsymbol{S}$ over a sphere with radius ρ,

$$P^{\mathrm{rad}} = \int_0^{2\pi}\int_0^{\pi} (\boldsymbol{S}\bullet\boldsymbol{n})\,\rho^2\sin\theta\,d\theta\,d\phi = \int_0^{2\pi}\int_0^{\pi} U(\theta,\phi)\,\sin\theta\,d\theta\,d\phi\,. \quad \text{(C.18)}$$

where $U(\theta,\phi) = (\boldsymbol{E}\bullet\boldsymbol{E}^*)\rho^2/2Z_0$ is the radiation intensity. For a half space, the range of θ reduces to the interval $[0,\pi/2]$. The integrand in (C.18) is independent of ρ as can be seen from the far-field expressions in this appendix. The quantity $4\pi U(\theta,\phi)/P^{\mathrm{rad}}$ is the directivity of the array.

Bibliography

[1] M. Abramowitz and I. A. Stegun. *Handbook of Mathematical Functions with Formulas, Graphs, and Mathematical Tables*. Applied Mathematics Series 55. National Bureau of Standards, Oxford, 7th edition, 1968.

[2] Z. Bai, J. Demmel, J. Dongarra, A. Ruhe, and H. van der Vorst. *Templates for the solution of Algebraic Eigenvalue Problems: A Practical Guide*. SIAM, Philadelphia, 2000.

[3] O. C. Balan. *Antenna Design*. Final Report of the Postgraduate Program Mathematics for Industry. Eindhoven University of Technology, Eindhoven, 2000. ISBN 90-444-0009-6.

[4] C. A. Balanis. *Antenna Theory: Analysis and Design*. Wiley, New York, reprinted (1997) edition, 1982.

[5] S. Barkeshli, P. H. Pathak, and M. Marin. An asymptotic closed-form microstrip surface green's function for the efficient moment method analysis of mutual coupling in microstrip antennas. *IEEE Transactions on Microwave Theory and Techniques*, 38(9):1374–1383, September 1990.

[6] D. J. Bekers. *Finitely Large Phased Arrays of Microstrip Antennas – Analysis and Design*. Final Report of the Postgraduate Program Mathematics for Industry. Technische Universiteit Eindhoven, Eindhoven, 2001. ISBN 90-444-0147-5.

[7] D. J. Bekers. *Finitely Large Phased Arrays of Microstrip Antennas*. Engineering and Analysis Report of Thales Nederland, Hengelo, the Netherlands, 2002. Document Subject: EAR 9501 027 223.

[8] D. J. Bekers. *Phased Arrays and Single Antennas - Inventory of Literature and Characteristics*. To be published as EAR. Thales Nederland, Hengelo, 2004.

[9] D. J. Bekers, S. J. L. van Eijdnhoven, and A. A. F. van de Ven. Modeling and analysis of a long thin conducting stripline. *Journal of Engineering Mathematics*, 49(4):373–390, 2004.

[10] D. J. Bekers, S. J. L. van Eijndhoven, A. A. F. van de Ven, P-P. Borsboom, and A. G. Tijhuis. Modeling and analysis of finite phased arrays of microstrip antennas – an eigenvector approach. In *Proceedings of the International conference on Electromagnetism in Advanced Applications*, pages 561–564, Torino, September 2003. ISBN 88-8202-008-8.

[11] D. J. Bekers, S. J. L. van Eijndhoven, A. A. F. van de Ven, P-P. Borsboom, and E. W. Kolk. Finitely large phased arrays of microstrip antennas – analysis and design. In *Scientific Computing in Electrical Engineering*, volume 4 of *Mathematics in Industry*, pages 120 – 127. Springer, Berlin, 2004. ISBN 3-540-21372-4.

[12] E. Bleszynski, M. Bleszynski, and T. Jaroszewicz. Aim: Adaptive integral method for solving large scale electromagnetic scattering and radiation problems. *Radio Science*, 31:1225–1251, 1996.

[13] P.-P. Borsboom. Personal communication, 2001.

[14] A. Böttcher and B. Silbermann. *Introduction to Large Truncated Toeplitz Matrices*. Springer, New York, 1999.

[15] Y. Brand, A. K. Skrivervik, and J. R. Mosig. An interative scheme solution for the analysis of printed arrays. *Microwave and Optical Technology Letters*, 16(2):106–115, October 1997.

[16] F. Capolino, M. Albani, S. Maci, and L. B. Felsen. Frequency-domain green's function for a planar periodic semi-infinite phased array - part i: Truncated floquet wave formulation. *IEEE Transactions on Antennas and Propagation*, 48(1):67–74, January 2000.

[17] F. Capolino, M. Albani, S. Maci, and L. B. Felsen. Frequency-domain green's function for a planar periodic semi-infinite phased array - part ii: Diffracted wave phenomenology. *IEEE Transactions on Antennas and Propagation*, 48(1):75–85, January 2000.

[18] O. A. Çivi, P. H. Pathak, H-T. Chou, and P. Nepa. A hybrid uniform geometrical theory of diffraction - moment method for efficient analysis of electromagnetic radiation/scattering from large finite planar arrays. *Radio Science*, 35(2):607–620, March-April 2000.

[19] O. A. Çivi, V. B. Ertürk, and H-T. Chou. Efficient analysis of large finite arrays via mom formulation with dft based acceleration algorithms. In *Proceedings of the International conference on Electromagnetism in Advanced Applications*, pages 337–340, Torino, September 2003. ISBN 88-8202-008-8.

[20] N. J. Champagne, J. T. Williams, and D. R. Wilton. The use of curved segments for numerically modeling thin wire antennas and scatterers. *IEEE Transactions on Antennas and Propagation*, 40(6):682–688, June 1992.

[21] V. W. H. Chang. Infinite phased dipole array. *IEEE Transactions on Antennas and Propagation*, 56(11):1892–1900, November 1968.

[22] H.-T. Chou and H.-K. Ho. Implementation of a forward-backward procedure for the fast analysis of electromagnetic radiation/scattering from two-dimensionl large phased arrays. *IEEE Transactions on Antennas and Propagation*, 52(2):388–396, February 2004.

[23] Circuitsage. http://www.circuitsage.com .

[24] R. Coifman, V. Rokhlin, and S. Wandzura. The fast multipole method for the wave equation: A pedestrian prescription. *IEEE Antennas and Propagation Magazine*, 35(3):7–12, June 1993.

[25] R. E. Collin. *Field Theory of Guided Waves*. IEEE Press, New York, 1991.

[26] D. Colton and R. Kress. *Integral Equation Methods in Scattering Theory*. Wiley, New York, 1983.

[27] R. Courant and F. John. *Introduction to Calculus and Analysis*, volume 2. Wiley, New York, 1974.

[28] C. Craeye, A. B. Smolders, D. H. Schaubert, and A. G. Tijhuis. An efficient computation scheme for the free space green's function of a two-dimensional semiinfinite phased array. *IEEE Transactions on Antennas and Propagation*, 51(4):766–771, April 2003.

[29] C. Craeye, A. G. Tijhuis, and D. H. Schaubert. An efficient mom formulation for finite-by-infinite arrays of two-dimensional antennas arranged in a three-dimensional structure. *IEEE Transactions on Antennas and Propagation*, 52(1):271–281, January 2004.

[30] C. Craeye and M. Arts. Modulated oscillations appearing in the scan impedance of a finite phased array. *IEEE Transactions on Antennas and Propagation*, 51(9):2054–2056, September 2003.

[31] A. Cucini, M. Albani, and S. Maci. Truncated floquet wave full-wave analysis of large phased arrays of open-ended waveguides with a nonuniform amplitude excitation. *IEEE Transactions on Antennas and Propagation*, 51(6):1386–1394, June 2003.

[32] A. Cucini, M. Albani, and S. Maci. Truncated floquet wave full-wave (t(fw)^2) analysis of large periodic arrays of rectangular waveguides. *IEEE Transactions on Antennas and Propagation*, 51(6):1373–1385, June 2003.

[33] F. J. Demuynck, G. A. E. Vandenbosch, and A. R. Van de Capelle. The expansion wave concept - part i: Efficient calculation of spatial green's functions in a stratified dielectric medium. *IEEE Transactions on Antennas and Propagation*, 46(3):397–406, March 1998.

[34] W. Dijkstra. *A Planar Array of Narrow Ring-shaped Microstrips in a Half Space*. Document Subject: 9501 027 224, Type: EAR. Thales Nederland, Hengelo, 2002.

[35] B. Dunnebier. *Large Microstrip Phased Array Antennas, Analysis and Numerical Implementation*. Final Report for the Postgraduate Program Information and Communication Technology. Eindhoven University of Technology, Eindhoven, 1999. ISBN 90-5282-987-X.

[36] B. Fasenfest, F. Capolino, D. R. Wilton, D. R. Jackson, and N. Champagne. General mom solutions for large arrays. In *Proceedings of the International conference on Electromagnetism in Advanced Applications*, pages 609–612, Torino, September 2003. ISBN 88-8202-008-8.

[37] N. Fourikis. *Phased Array-Based Systems and Applications*. Wiley, New York, 1997.

[38] R. J. Garbacz and R. H. Turpin. A generalized expansion for radiated and scattered fields. *IEEE Transactions on Antennas and Propagation*, AP-19(3):348–358, May 1971.

[39] S. Gasiorowicz. *Quantum Physics*. Wiley, New York, 1974.

[40] G. H. Golub and C. F. Van Loan. *Matrix Computations*. Hopkins University Press, Baltimore, 2nd edition edition, 1989.

[41] I. Gradshteyn and I.M. Ryzhik. *Table of Integrals, Series and Products*. Academic Press, New York, 1965.

[42] L. Greengard and V. Rokhlin. A fast algoririthm for particle solutions. *Journal of Computational Physics*, 73:325–348, 1987.

[43] D. J. Griffiths. *Introduction to Quantum Mechanics*. Prentice Hall, Upper Saddle River, 1995.

[44] K. C. Gupta, Ramesh Garg, Inder Bahl, and Prakash Bartia. *Microstrip Lines and Slotlines*. Artech House, Boston, 1996.

[45] R. C. Hansen. A gibbsian model for finite scanned arrays. *IEEE Transactions on Antennas and Propagation*, 44(2):243–248, February 1996.

[46] R. C. Hansen. Anomalous edge effects in finite arrays. *IEEE Transactions on Antennas and Propagation*, 47(3):549–554, March 1999.

[47] R. F. Harrington. *Field Computation by Moment Methods*. Macmillan, New York, 1968.

[48] H. Holter and H. Steyskal. On the size requirement for finite phased-array models. *IEEE Transactions on Antennas and Propagation*, 50(6):836–840, June 2002.

[49] M. Horstman. *The Design of Phased Array Antennas*. Final Report of the Postgraduate Program Mathematics for Industry. Eindhoven University of Technology, Eindhoven, 2000.

[50] S. Hulshof. *Analysis of Infinite Arrays of Vivaldi-like Antennas*. M.Sc. Thesis, EM-4-97, Department of Electrical Engineering. Eindhoven University of Technology, Eindhoven, 1997.

[51] C. Hülsmeyer. Verfahren, um entfernte metallische gegenstände mittels elektrischer wellen einem beobachter zu melden. Eurpean Patent Office, Patentschrift DE165546, 30 April 1904.

[52] A. Ishimaru, R. J. Coe, G. E. Miller, and W. P. Geren. Finite periodic structure approach to large scanning array problems. *IEEE Transactions on Antennas and Propagation*, AP-33(11):1213–1220, November 1985.

[53] D. S. Janning and B. A. Munk. Effects of surface waves on the currents of truncated periodic arrays. *IEEE Transactions on Antennas and Propagation*, 50(9):1254–1265, September 2002.

[54] D. S. Jones. *Methods in Electromagnetic Wave Propagation*. Clarendon Press, Oxford, 1979.

[55] W. P. M. N. Keizer. An overview of test techniques for characterizing active phased array antennas. In *Proceedings of the Conference Perspectives on Radio Astronomy - Technologies for Large Antenna Arrays*, pages 191–200, Dwingeloo, the Netherlands, April 1999. ISBN 90-805434-2-X, http://www.astron.nl/documents/conf/ .

[56] R. W. Kindt and J. L. Volakis. Finite array analysis using a multi-dimensional, multi-cell hybrid array decomposition fast multipole method. In *Proceedings of the International conference on Electromagnetism in Advanced Applications*, pages 317–320, Torino, September 2003. ISBN 88-8202-008-8.

[57] R. W. Kindt, K. Sertel, E. Topsakal, and J. L. Volakis. Array decompostion method for the accurate analysis of finite arrays. *IEEE Transactions on Antennas and Propagation*, 51(6):1364–1372, June 2003.

[58] A. Kirsch. *An Introduction to the Mathematical Theory of Inverse Problems*. Springer, Berlin, 1996.

[59] H. A. Kooiker. *Excitation Models for Finitely Large Phased Arrays of Microstrip Antennas*. Document Subject: 9501 027 994XX, Type: EAR. Thales Nederland, Hengelo, 2003.

[60] J. Kraus. *Antennas*. McGraw-Hill, New York, 1950.

[61] E. Kreyszig. *Introductory Functional Analysis with Applications*. Wiley, New York, 1978.

[62] L. D. Landau and E. M. Lifshitz. *Electrodynamics of Continuous Media*. Pergamon Press, Oxford, 1960.

[63] H. F. Lee and W. Chen. *Advances in Microstrip and Printed Antennas*. Wiley, New York, 1997.

[64] G. Lindfield and J. Penny. *Numerical Methods Using Matlab*. Prentice Hall, Upper Saddle River, New Yersey, 2nd (2000) edition, 1995.

[65] D. Liu, R. J. Garbacz, and D. M. Pozar. Antenna synthesis and optimization using generalized characteristic modes. *IEEE Transactions on Antennas and Propagation*, 38(6):862–868, June 1990.

[66] J. Lützen. *The Prehistory of the Theory of Distributions*. Springer, New York, 1982.

[67] J. L. Luzwick, E. C. Ngai, and A. T. Adams. Analysis of a large linear antenna array of uniformly spaced thin-wire dipoles parallel to a perfectly conducting plane. *IEEE Transactions on Antennas and Propagation*, 70(3):246–291, March 1982.

[68] R. J. Mailloux. Phased array theory and technology. *Proceedings of the IEEE*, 70(3):246–291, March 1982.

[69] R. J. Mailloux. Antenna array architecture. *Proceedings of the IEEE*, 80(1):163–172, January 1992.

[70] R. J. Mailloux. *Phased Array Antenna Handbook*. Artech House, Boston, 1994.

[71] R. J. Marhefka and W. D. Burnside. Antennas on complex platforms. *Proceedings of the IEEE*, 80(1):204–207, January 1992.

[72] M. A. Marin and P. H. Pathak. An asymptotic closed-form representation for the grounded double-layer surface green's function. *IEEE Transactions on Antennas and Propagation*, 40(11):1357–1366, November 1992.

[73] J. T. Marti. *Introduction to Sobolev Spaces and Finite Element Solution of Elliptic Boundary Value Problems*. Academic Press, London, 1986.

[74] L. Matekovits, G. Vecchi, G. L. Dassano, and M. Orefice. Synthetic function analysis of large printed structures. *Digest of 2001 IEEE Antennas and Propagation Society International Symposium*, pages 568–571, 2001. 8 - 13 July 2001, Boston, Massachusetts.

[75] R. V. N. Melnik. Topological analysis of eigenvalues in engineering computations. *Engineering Computations*, 17(4):386 – 416, 2000.

[76] E. K. Miller and G. J. Burke. Low-frequency computational electromagnetics for antenna analysis. *Proceedings of the IEEE*, 80(1):24–42, January 1992.

[77] R. Mittra, C. H. Chan, and T. Cwik. Techniques for analyzing frequency selective surfaces – a review. *IEEE Proceedings*, 76:1593–1614, December 1988.

[78] R. Mittra and N.-T. Huang. Numerically efficient analysis of large array and fss radome composites with dissimilar periodicities. In *Proceedings of the International conference on Electromagnetism in Advanced Applications*, pages 313–316, Torino, September 2003. ISBN 88-8202-008-8.

[79] R. Mittra(ed.). *Topics in Applied Physics: Numerical and Asymptotic Techniques in Electromagnetics*, volume 3. Springer, Berlin, 1975.

[80] P. M. Morse and H. Feshbach. *Methods of Theoretical Physics*, volume II. McGraw-Hill, New York, 1953.

[81] A. Mukherjea and K. Pothoven. *Real and Functional Analysis*. Plenum Press, New York, 1978.

[82] B. A. Munk. *Finite Antenna Arrays and FSS*. Wiley, New York, 2003.

[83] A. Neto, S. Maci, G. Vecchi, and M. Sabbadini. A truncated floquet wave diffraction method for the full wave analysis of large phased arrays - part i: Basic principles and 2-d cases. *IEEE Transactions on Antennas and Propagation*, 48(3):594–600, March 2000.

[84] A. Neto, S. Maci, G. Vecchi, and M. Sabbadini. A truncated floquet wave diffraction method for the full wave analysis of large phased arrays - part ii: Generalization to 3-d cases. *IEEE Transactions on Antennas and Propagation*, 48(3):601–611, March 2000.

[85] D. Parker and D. C. Zimmermann. Phased arrays - part i: Theory and architectures. *IEEE Transactions on Microwave Theory and Techniques*, 50(3):678–687, March 2002.

[86] D. Parker and D. C. Zimmermann. Phased arrays - part ii: Implementations, applications, and future trends. *IEEE Transactions on Microwave Theory and Techniques*, 50(3):688–697, March 2002.

[87] P. H. Pathak. High-frequency techniques for antenna analysis. *Proceedings of the IEEE*, 80(1):44–65, January 1992.

[88] P. H. Pathak, P. Janpugdee, P. Mahachoklertwattana, and P. Nepa. A fast analysis of the radiation and scattering from a large microstrip antenna array. In *Proceedings of the International conference on Electromagnetism in Advanced Applications*, pages 329–332, Torino, September 2003. ISBN 88-8202-008-8.

[89] P. Pirinoli, F. Vipiana, L. Matekovits, and G. Vecchi. Multliscale analysis of large complex arrays. pages 605–608, September 2003. ISBN 88-8202-008-8.

[90] J.-R. Poirier, P. Borderies, R. Mittra, and V. Varadarajan. Numerically efficient solution of dense linear system of equations arising in a class of electromagnetic scattering problems. *IEEE Transactions on Antennas and Propagation*, 46(8):1169–1175, August 1998.

[91] A. Polemi, A. Toccafondi, and S. Maci. High-frequency green's function for a semi-infinite array of electric dipoles on a grounded slab - part i: Formulation. *IEEE Transactions on Antennas and Propagation*, 49(12):1667–1677, December 2001.

[92] D. Poljak. Finite element integral equation modelling of a thin wire loop antenna. *Communications in Numerical Methods in Engineering*, 14(4):347–354, 1998.

[93] D. M. Pozar. Analysis of finite phased arrays of printed dipoles. *IEEE Transactions on Antennas and Propagation*, AP-33(10):1045–1053, October 1985.

[94] D. M. Pozar. *Microwave Engineering*. Addison-Wesley, Reading, Massachusetts, reprinted (1993) edition, 1990.

[95] D. M. Pozar and D. H. Schaubert. Scan blindness in infinite phased arrays of printed dipoles. *IEEE Transactions on Antennas and Propagation*, AP-32(6):602–610, June 1984.

[96] S. M. Rao, D. R. Wilton, and A. W. Glisson. Electromagnetic scattering by surfaces of arbitrary shape. *IEEE Transactions on Antennas and Propagation*, AP-30(2):409–418, May 1982.

[97] G. R. Richter. On weakly singular fredholm integral equations with displacement kernels. *Journal of Mahemarical Analysis and Applications*, 55:32–42, October 1976.

[98] F. Riesz and B. Sz.-Nagy. *Functional Analysis*. Frederick Ungar Publishing, New York, 4th edition edition, 1965.

[99] V. Rokhlin. Rapid solution of integral equations of classical potential theory. *Journal of Computational Physics*, 60:187–207, 1983.

[100] A. J. Roscoe and R. A. Perrott. Large finite array analysis using infinite array data. *IEEE Transactions on Antennas and Propagation*, 42(7):983–992, July 1994.

[101] H. Sagan. *Boundary and Eigenvalue Problems in Mathematical Physics*. Wiley, New York, 1961.

[102] R. W. Scharstein. Mutual coupling in a slotted phased array, infinite in e-plane and finite in h-plane. *IEEE Transactions on Antennas and Propagation*, 38(8):1186–1191, August 1990.

[103] J. P. Skinner, C. C. Whaley, and T. K. Chattoraj. Scattering from finite-by-infinite arrays of slots in a thin conducting wedge. *IEEE Transactions on Antennas and Propagation*, 43(4):369–375, April 1995.

[104] A. K. Skrivervik and J. R. Mosig. Finite phased array of microstrip patch antennas: The infinite array approach. *IEEE Transactions on Antennas and Propagation*, 40(5):579–582, May 1992.

[105] A. K. Skrivervik and J. R. Mosig. Analysis of finite phase arrays of microstrip patches. *IEEE Transactions on Antennas and Propagation*, 41(8):1105–1114, August 1993.

[106] A. K. Skrivervik and J. R. Mosig. Analysis of printed array antennas. *IEEE Transactions on Antennas and Propagation*, 45(9):1411–1418, September 1997.

[107] L. Stark. Microwave theory of phased-array antennas - a review. *IEEE Transactions on Antennas and Propagation*, 62(12):1661–1701, December 1974.

[108] J. E. Storer. Impedance of thin-wire loop antennas. *AIEE Transactions (Part I. Communication and Electronics)*, 75:606–619, November 1956.

[109] J. A. Stratton. *Electromagnetic Theory*. McGraw-Hill, New York, 1941.

[110] W. L. Stutzman and G. A. Thiele. *Antenna Theory and Design*. Wiley, New York, 1998.

[111] S. S. Swords. *Technical History of the Beginnings of Radar*. Peregrinus, London, 1986.

[112] R. Tang and R. W. Burns. Array technology. *Proceedings of the IEEE*, 80(1):173–182, January 1992.

[113] G. A. Thiele. Overview of selected hybrid methods in radiating system analysis. *Proceedings of the IEEE*, 80(1):66–78, January 1992.

[114] B. Tomasic and A. Hessel. Analysis of finite arrays - a new approach. *IEEE Transactions on Antennas and Propagation*, 47(3):555–564, March 1999.

[115] L. N. Trefethen. Pseudospectra of linear operators. *Siam Review*, 39(3):383–406, September 1997.

[116] E. E. Tyrtyshnikov. A unifying approach to some old and new theorems on distribution and clustering. *Linear Algebra and its Applications*, 232:1–43, 1996.

[117] J. M. Usoff and B. A. Munk. Edge effects of truncated periodic surfaces of thin wire elements. *IEEE Transactions on Antennas and Propagation*, 42(7):946–953, July 1994.

[118] K. Valkering. *Developing a Design Tool for Finite Array Antennas*. Final Report of the Postgraduate Program Mathematics for Industry. Eindhoven University of Technlogy, Eindhoven, 1998. ISBN 90 5282 912 8.

[119] M. C. van Beurden. *Analysis of Infinite Phased Arrays of Printed Antennas*. M.Sc. Thesis, EM-4-97, Department of Electrical Engineering. Eindhoven University of Technology, Eindhoven, 1997.

[120] M. C. van Beurden. *Integro-differential Equations for Electromagnetic Scattering - Analysis and Computation for Objects with Electric Contrast*. Phd. Thesis. Eindhoven University of Technology, Eindhoven, 2003.

[121] H. van der Vorst. *Iterative Krylov Methods for Large Linear Systems*. Cambridge University Press, Cambridge, 2003.

[122] P. van Genderen. State of the art trends in phased array radar. In *Proceedings of the Conference Perspectives on Radio Astronomy - Technologies for Large Antenna Arrays*, pages 1–10, Dwingeloo, the Netherlands, April 1999. ISBN 90-805434-2-X, http://www.astron.nl/documents/conf/ .

[123] G. A. E. Vandenbosch and F. J. Demuynck. The expansion wave concept - part ii: A new way to model mutual coupling in microstrip arrays. *IEEE Transactions on Antennas and Propagation*, 46(3):407–413, March 1998.

[124] D. Varon and G. I. Zysman. Some properties and limitations of electronically steerable phased array antennas. *The Bell System Technical Journal*, pages 1561–1586, September 1967.

[125] J. Yeo, V. V. S. Prakash, and R. Mittra. Efficient analysis of a class of microstrip antennas using the characteristic basis function method. *Microwave and Optical Technology Letters*, 39(6):456–464, December 2003.

[126] N. Yuan, X.-C. Nie, and L. W. Li. A fast analysis of scattering and radiation of large microstrip antenna arrays. *IEEE Transactions on Antennas and Propagation*, 51(9):2218–2226, September 2003.

[127] E. Zauderer. *Partial Differential Equations of Applied Mathematics*. Wiley, New York, 2nd edition edition, 1989.

Samenvatting

Radar, voluit ‘radio detection and ranging’, wordt gebruikt voor velerlei doeleinden, zoals het regelen van luchtverkeer, het doen van snelheidsmetingen in het verkeer, en het lokaliseren en volgen van schepen en vliegtuigen. Het principe van radar is gebaseerd op het fenomeen dat metalen objecten radiogolven reflecteren. De radiogolven worden uitgezonden en ontvangen door de antenne van een radarsysteem. Het ontwerp van een dergelijke antenne kent twee hoofddoelen: de energie die in de antenne in de vorm van electromagnetische straling opgewekt wordt, moet in een specifieke richting worden uitgestraald en de energie-overdracht van bron naar elektromagnetische straling moet optimaal zijn. Voorbeelden van antenne types zijn draadantennes, paraboolantennes, en antenne-arrays.

Antenne-arrays bestaan uit separate antennes, die elementen worden genoemd. Het aantal elementen varieert van een tiental tot vele honderden. In veel gevallen hebben de elementen dezelfde vorm en zijn geordend in een regelmatige geometrie. Antenne-arrays hebben als groot voordeel boven andere antenne-types dat zij de gebruiker de mogelijkheid bieden de bundel van elektromagnetische straling te besturen door middel van faseverschillen tussen de elementen. Deze bundel is vergelijkbaar met een lichtbundel bij toneelvoorstellingen, maar is onzichtbaar voor het menselijk oog. De elektronische besturing kan vrijwel instantaan worden bewerkstelligd, dit in tegenstelling tot mechanische besturing van de bundel. Aan elektronische besturing danken antenne-arrays hun multifunctionaliteit die onder meer bestaat uit scannen van het luchtruim, volgen van doelen, en leiden van raketten naar een doel.

Het ontwerp en de ontwikkeling van radarsystemen is complex en kostbaar. Om de kosten en risico’s bij het ontwerp te verkleinen, en om de prestatie van systemen te verbeteren, gebruikt men simulaties. Simulaties moeten voldoen aan een aantal criteria: ze moeten snel uitvoerbaar zijn, ze moeten randeffecten tonen alsmede effecten van mutuele elektromagnetische koppeling tussen de elementen, en ze moeten in grote nauwkeurigheid de prestatieparameters bepalen. Simulaties gebaseerd op de oneindige array aanpak en simulaties gebaseerd op de eindige elementen methode voldoen niet aan deze criteria. Eerstgenoemde beschrijven geen randeffecten en laatstgenoemde leiden tot trage berekeningen. Geen van deze simulaties geeft direct inzicht in de fysica die relevant is voor het ontwerp. In dit proefontwerp stellen we een aanpak voor die

voldoet aan bovengenoemde criteria en bovendien inzicht verschaft in de fysica. Deze aanpak kan de nadelige en desastreuze invloed van staande golven op de prestatie van eindige arrays voorspellen en geeft aan hoe dit gedrag kan worden voorkomen voor het hele scanbereik van het array. De aanpak van dit proefontwerp is getest op lijnarrays met regelmatige geometrie, waarbij de elementen rechthoekige microstrips of ringvormige microstrips zijn. In beide gevallen zijn de arrays gepositioneerd in de vrije ruimte of boven een geleidend oppervlak. In tegenstelling tot de lengte en omtrek van de microstrips is hun breedte klein ten opzichte van de golflengte. Richtlijnen voor het toepassen van de aanpak op andere array-geometrieën met andere element-geometrieën en op arrays waarbij kleine verschillen tussen de elementen bestaan, worden uitvoerig beschreven.

In de voorgestelde aanpak wordt het gedrag van een eindig array beschreven door zijn eigentrillingen of eigenstromen. Deze eigenstromen zijn de eigenfuncties van de impedantie-operator die de stromen op de elementen relateert aan hun excitatievelden, afkomstig van bijvoorbeeld een invallende golf of van lokale bronnen. Uit fysisch oogpunt zijn de eigenstromen staande golven van het array. De bijbehorende eigenwaarden representeren de karakteristieke impedanties van de eigenstromen. Hoe groter de karakteristieke impedantie van een eigenstroom, des te minder zal deze eigenstroom bijdragen aan de stroom op de elementen bij een gegeven excitatieveld. Het concept eigenstroom blijkt uitermate geschikt voor het ontwerpen van arrays, omdat de ontwerp-karakteristieken waarnaar men ontwerpt één-op-één gerelateerd zijn aan de excitatie van specifieke eigenstromen. Uit dit proefontwerp blijkt dat eigenstromen en hun bijbehordende eigenwaarden één-op-één gerelateerd zijn aan scanbundels, aan monopulsbundels, aan gratingbundels, aan gemoduleerde impedantie-oscillaties, aan impedantievariaties toegeschreven aan oppervlaktegolven van de arraystructuur, en aan veel andere eigenschappen van het array. Behoudens een fysische interpretatie blijkt de aanpak met eigenstromen te leiden tot snel uit te voeren simulaties; immers, hoewel de prestatieparameters van een array veranderen als functie van de geometrieparameters en de frequentie, veranderen de eigenstromen nauwelijks. In feite veranderen alleen de eigenwaarden, zij het regelmatig, als functie van geometrieparameters en de frequentie. Derhalve kunnen de eigenstromen verkregen voor een zekere keuze van parameters vastgelegd worden om ze vervolgens te gebruiken voor simulaties bij andere parameterwaarden. De bijbehorende eigenwaarden worden benaderd middels het Rayleigh-Ritz quotient.

Uitgangspunt van de voorgestelde aanpak is het bepalen van de eigenstromen van een element en de bijbehorende eigenwaarden. De eigenstromen en eigenwaarden worden berekend uit een ‘genormaliseerde’ momentenmatrix gerelateerd aan gekozen ontwikkelfuncties voor de stroom op het element. Vervolgens wordt een inproduct bepaald ten opzichte waarvan deze element-eigenstromen orthonormaal zijn. De bijbehorende momenten matrix in termen van deze eigenstromen is een diagonaal matrix ten opzichte van het nieuwe inproduct. In de tweede stap wordt een gereduceerde momenten matrix berekend ten opzichte van de samenstelling van

de nieuwe element-inproducten, waarbij de ontwikkelfuncties de eigenstromen per element zijn. Alleen eigenstromen die bijdragen aan de mutuele koppeling in het array worden in rekening gebracht. Omdat deze eigenstromen a priori niet bekend zijn, wordt eerst het aantal koppelende element-eigenstromen geschat aan de hand van het gedrag van de element-eigenwaarden. Element-eigenstromen met grote eigenwaarden, zullen niet of nauwelijks bijdragen aan de mutuele koppeling. Het resultaat van de tweede stap zijn de array-eigenstromen die beschreven zijn als concatenaties van lineaire combinaties van koppelende element-eigenstromen. De array-eigenstromen en hun bijbehorende eigenwaarden zijn verdeeld in groepen, waarbij elke groep correspondeert met één element-eigenstroom, de zogenoemde dominante element-eigenstroom van de groep. De eigenwaarden in een groep zijn perturbaties van de eigenwaarde van de dominante element-eigenstroom. Deze perturbaties zijn niet noodzakelijk klein. Hun spreiding blijkt een kwantitatieve maat te zijn voor de mutuele koppeling in het array. Als de spreiding van een groep klein is, hoeft de koppeling van deze groep met zichzelf en met andere groepen niet in rekening te worden gebracht. A posteriori kan dus aan de hand van de spreidingen bepaald worden of voldoende element-eigenstromen in rekening zijn gebracht voor het beschrijven van mutuele koppeling. Numerieke simulaties laten zien dat met één of twee groepen van koppelende eigenstromen de mutuele koppeling in arrays, opgebouwd uit elementen die typisch ontworpen zijn voor de excitatie van één specifieke eigenstroom, beschreven kan worden. Door het verwaarlozen van mutuele koppeling worden tijdwinsten van een factor 10 tot een factor 50 geboekt ten opzichte van de conventionele momenten methode. De spreiding is tevens een kwantitatieve maat om het aantal buren van een element te bepalen dat moet worden meegenomen om mutuele koppeling te beschrijven. Het verwaarlozen van koppeling tussen buren leidt tot een verdere reductie van de rekentijd.

Nadere bestudering van de eigenstromen van lijnarrays bestaande uit ringen en strips heeft tot een tweetal belangrijke observaties geleid. Ten eerste hangen de coëfficiënten van de dominante element-eigenstroom in elke groep niet of nauwelijks af van de elementvorm. Op grond van deze observatie blijkt dat een eerste orde schatting van het gedrag van lijnarrays met complexe elementen wordt beschreven door de coëfficiëntverdelingen van de eigenstromen van lijnarrays met eenvoudiger elementen. Ten tweede vertonen de coëfficiënten van de dominante element-eigenstroom dezelfde patronen als de coëfficiënten van de eigenstromen van één strip verkregen met stuksgewijs lineaire functies. Op grond van deze observatie blijkt een eerste orde schatting van het gedrag van lijnarrays met complexe elementen te worden beschreven door de coëfficiëntverdelingen van de eigenstromen van één strip met stuksgewijze functies. Verwacht wordt dat de coëfficiëntverdelingen van de eigenstromen van een rechthoekige patch kunnen worden gebruikt voor een eerste orde schatting van het gedrag van een rechthoekig array. Uit de tweede observatie leiden we af dat een array één geheel is en niet een verzameling van losse elementen.

Het mag beslist niet onvermeld blijven dat het karakteristieke gedrag van arrays wordt

veroorzaakt door resonant gedrag en dat resonant gedrag wordt veroorzaakt door de excitatie van specifieke eigenstromen. De eigenwaarden, of karakteristieke impedanties, van deze eigenstromen zijn klein in vergelijking met de eigenwaarde die hoort bij de scanbundel. Zowel gemoduleerde impedantie-oscillaties als variaties van elementimpedanties toegeschreven aan oppervlaktegolven van de arraystructuur worden veroorzaakt door de excitatie van eigenstromen met relatief kleine eigenwaarden. De verdeling in de groep met de laagste eigenwaarden voorspelt welke belasting van het systeem nodig is om resonant gedrag te vermijden. Tot besluit vermelden we dat de relevantie van het concept eigenstroom in dit proefontwerp aangetoond wordt aan de hand van een aantal specifieke fysische effecten die in de praktijk van het antenneontwerp zijn waargenomen.

About the Author

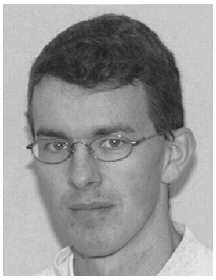

Dave Johannes Bekers was born on August 19, 1974 in Breda, the Netherlands. In June 1993, he finished secondary school at the OLV Lyceum in Breda. From September 1993 until February 1999, he studied Mathematics at the Technische Universiteit Eindhoven. He completed his studies by a final project of ten months at Axxicon Moulds in Eindhoven. For his master's thesis 'Microscopic Flow Behaviour in the Injection Moulding of Compact Discs' he received the Mignot Prize of the Technische Universiteit Eindhoven in June 2000. From April 1999 until April 2001, he followed the postgraduate program Mathematics for Industry at the Stan Ackermans Instituut of the Technische Universiteit Eindhoven. Within the frame of this program, he carried out several projects for companies such as Fontijne Holland and Philips. To prepare for the final project of this program, he joined the Laboratoire d'Electromagnétisme et d'Acoustique (LEMA) of the Ecole Polytechnique Fédérale de Lausanne in Switzerland for a project of three months from April 2000 until June 2000. From August 2000 until April 2001, he carried out the final project at the company Thales Nederland in Hengelo, the Netherlands. With the financial support of Thales Nederland and the Stan Ackermans Institute, this project was continued as a Ph.D. on design. From May 2001 until till June 2004, Dave was a Ph.D. student in the Applied Analysis group of the Department of Mathematics and Computing Science at the Technische Universiteit Eindhoven; his research in the field of antenna arrays was carried out at Thales Nederland in the group JRS-TU Antenna. From the first of November 2004 Dave will join the Fysisch en Electrotechnisch Laboratorium of TNO in The Hague, the Netherlands.